ISSW 2023

19th International
Ship Stability Workshop
İstanbul, Turkey, 11-13 September

Proceedings of the 19th

International
Ship Stability Workshop

11-13 September 2023, İstanbul, Turkey

Editors
Ismail H. Helvacioglu & Metin Taylan

ISSW 2023

19th International
Ship Stability Workshop
İstanbul, Turkey, 11-13 September

Proceedings of the 19th

International
Ship Stability Workshop

11-13 September 2023, İstanbul, Turkey

Arranged and hosted by Piri Reis University and Istanbul Technical University

Main sponsors:

Silver sponsor:

Skipsteknisk

Proceedings of the 19th International Ship Stability Workshop (ISSW 2023)

Istanbul, Turkey, 11-13 September, 2023
Editors: Ismail H. Helvacioglu & Metin Taylan

ABOUT INTERNATIONAL SHIP STABILITY WORKSHOP

International Ship Stability Workshop (ISSW) is a part of a longstanding series of international technical meetings in the field of ship stability, dynamics and safety, consisting of the STAB conferences, which are held every third year, and the ISSW workshops, which are held in the years between the conferences. These conferences and workshops are initiated and supervised by an International Standing Committee (ISC) and arranged and hosted by a Local Organizing Committee, each time in different corners of the world. General information about ISSW, STAB, ISC, SRDC (Stability Research and Development Committee), proceedings from past events, and other information concerning ship stability, dynamics and safety, can be found at www.shipstab.org.

PREVIOUS INTERNATIONAL SHIP STABILITY WORKSHOPS

1995, Glasgow, UK
1996, Osaka, Japan
1997, Hersonissos, Crete, Greece
1998, St. John's, Newfoundland, Canada
2001, Trieste, Italy
2002, New York, USA
2004, Shanghai, China
2005, Istanbul, Turkey
2007, Hamburg, Germany
2008, Daejeon, Korea
2010, Wageningen, the Netherlands
2011, Washington, USA
2013, Brest, Brittany, France
2014, Kuala Lumpur, Malaysia
2016, Stockholm, Sweden
2017, Belgrade, Serbia
2019, Helsinki, Finland
2022, Gdansk, Poland

ACKNOWLEDGEMENTS

We would like to thank our sponsors, the Turkish Chamber of Shipping (IMEAK-DTO), the Turkish Shipbuilders Association (GISBIR), Skipsteknisk Engineering A.Ş. for their financial support. All the web related work has been carried out by Dr. Gabriele Bulian. So, we thank him for his patience and efforts. The assistance from Earthlight Travel Services is also gratefully acknowledged.

DISCLAIMER

The opinions expressed in the papers are those of the authors and not necessarily those of any organization with which the authors have been associated.

CONTENTS

Session 1: Viscous effect on ship stability

Session 2: Damage stability

Session 3: Operational aspects of intact stability

Session 4: Stochastic approach to intact stability assessment

Session 9: Locally organized session

Towards the uncertainty quantification of a roll damping model

Shawn Aram, David Taylor Model Basin (NSWCCD), shawn.aram.civ@us.navy.mil
Kenneth M. Weems, David Taylor Model Basin (NSWCCD), kenneth.m.weems2.civ@us.navy.mil
Vadim Belenky, David Taylor Model Basin (NSWCCD), vadim.belenky.civ@us.navy.mil

ABSTRACT

Predictions of ship motions with seakeeping simulation tools typically rely on roll damping models in order to account for viscous effects that are not included in their potential flow solution of hydrodynamic forces. Various models have been developed to represent the roll damping of surface ships, ranging from generic models developed from systematic experimental studies to ship-specific models fitted to data from roll decay model tests or high-fidelity computational fluid dynamic (CFD) simulations. The accuracy of these models can greatly influence the predicted ship response, especially near the resonance conditions. It is therefore highly desirable to quantify the uncertainty associated with the adopted reduced order models and identify contributors to the modelling uncertainty. The present study seeks to develop a roll damping model for the LAMP (Large Amplitude Motions Program) and SimpleCode seakeeping codes through a series of CFD simulations with forced and free roll motions, quantify the uncertainty of the resulting roll damping model, and then evaluate the influence of this uncertainty on the predicted responses. The coefficients of the rolldamping model are obtained through an optimization procedure to minimize the difference between the hydrodynamic forces calculated by CFD and LAMP or SimpleCode under forced roll motions.

Keywords: *Roll Damping Model, Uncertainty Quantification, Computational Fluid Dynamics.*

1. INTRODUCTION

Since full viscous flow solvers are still too expensive for the practical evaluation of ship responses over a range of irregular wave conditions, such analyses typically rely on hybrid seakeeping simulation tools incorporating roll damping models in order to account for viscous effects that are not included in their potential flow solution of hydrodynamic forces (Reed and Beck, 2016). Various models have been developed to represent the roll damping of surface ships. These range from generic models developed from systematic experimental studies to ship-specific models fitted to data from roll decay model tests or high-fidelity computational fluid dynamics (CFD) simulations. The accuracy of these models can greatly influence the predicted ship roll response, especially near resonant conditions. It is therefore highly desirable to quantify the uncertainty associated with the adopted reduced order models and identify contributors to the modelling uncertainty.

The present study seeks to develop roll damping models for the LAMP (Large Amplitude Motions Program, Shin et al., 2003) seakeeping code or SimpleCode reduced order seakeeping simulation (Weems, et al., 2023) through a series of CFD simulations with forced and free roll motions, quantify the uncertainty of the resulting roll damping model, and then evaluate the influence of this uncertainty on the predicted responses. A polynomial damping model is used with coefficients obtained through an optimization procedure to minimize the difference between the hydrodynamic forces calculated by CFD and LAMP or SimpleCode under prescribed roll motions.

2. CFD ANALYSIS OF ROLL MOTION

CFD simulations of free and forced roll motions are performed for DTMB (David Taylor Model Basin) Model 5613-1, which is the Tumblehome configuration of the ONR (Office of Naval Research) Topsides Series, commonly referred to as ONRTH (Bishop et al., 2005). The CFD

configuration (Figure 1) includes bilge keels, rudders, shafts and struts, but not propellers.

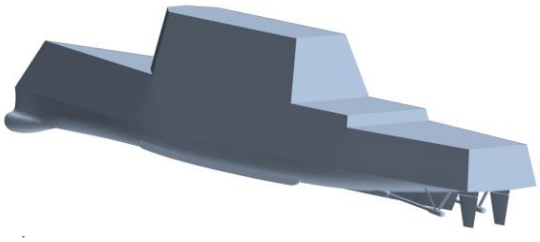

Figure 1: Perspective view of ONRTH model 5613-1.

The period of the forced roll motions is set to the natural roll period obtained from a six-degrees-of-freedom (6-DOF) CFD simulations of free roll motion (roll decay). The forced roll motion in this study is 1-DOF motion that allows roll to follow a prescribed sinusoidal path with an amplitude ranging from 3° to 12°. The roll moment generated by hull, bilge keels and rudders are calculated in the CFD simulations and utilized for developing a roll damping model in LAMP. CFD simulation of a 1-DOF (free to roll) free roll motion is also performed.

Numerical methodology

Simcenter™ STAR-CCM+ software, a commercial CFD simulation tool that is part of the Siemens Xcelerator portfolio, is employed in this study to model the free and forced roll motions of the ONRTH hull. The software for marine hydrodynamics applications has been utilized and validated the predictions against model tests (Aram and Wundrow, 2022; Aram and Park, 2022, Aram and Mucha, 2023). The finite volume (FV) method is adopted to solve the Navier-Stokes equations:

$$\frac{\partial}{\partial t}\int_V \rho \, \mathrm{d}V + \int_S \rho \boldsymbol{v} \, \mathrm{d}S = 0 \tag{1}$$

$$\frac{\partial}{\partial t}\int_V \rho \boldsymbol{v} \, \mathrm{d}V + \int_S \rho(\boldsymbol{v}\boldsymbol{v}) \cdot \boldsymbol{n} \, \mathrm{d}S = \int_S \boldsymbol{T} \cdot \boldsymbol{n} \, \mathrm{d}S + \int_V \rho \boldsymbol{b} \, \mathrm{d}V \tag{2}$$

where $\boldsymbol{v}$ is the fluid velocity vector, ρ is the fluid density, $\boldsymbol{n}$ is the normal vector of S (area of the surface of control volume V), $\boldsymbol{T}$ is the stress tensor and $\boldsymbol{b}$ is a vector representing a force per unit mass. The surface and volume integrals of convective and diffusive fluxes in these equations are approximated with the mid-point rule. Semi-Implicit Method for Pressure Linked Equations (SIMPLE) algorithm provides a segregated solution to the velocity-pressure coupling problem. Time-accurate discretization of the equations is achieved by adopting an implicit second-order three-level scheme. Volume of Fluid (VOF) method with a High-Resolution Interface Capturing (HRIC) scheme in the software offers a sharp representation of free surface. Overset grid method, which allows for multiple grids within one computational background domain to overlap arbitrarily, models the ship motions. The *k-ω* Shear Stress Transport (SST) (Menter, 1994), a two-equation turbulence model widely applied in the ship hydrodynamic community under the Reynolds Averaged Navier-Stokes (RANS) simulation approach, is employed in this study.

Computational setup

A perspective view of the ONRTH model 5613-1 geometry investigated in this study is in Figure 1. The model is equipped with a skeg, bilge keels, twin rudders, shafts and struts. Both the full scale and model scale ship with the scaling factor of 49 are examined in this study. Table 1 summarizes the configuration particulars given in the SIMMAN2020 website (https://simman2020.kr/), a workshop on the verification and validation of ship maneuvering simulation methods.

Table 1: Particulars for ONRTH model 5613-1.

Main Particulars	Model Scale	Full Scale
Displacement, Δ (kg)	72.6	6.77e6
Waterline Length, *L* (m)	3.147	154
Waterline Beam, *B* (m)	0.384	18.8
Draft, *T* (m)	0.112	5.5
Wetted Surface Area, *S* (m^2)	1.5	3602
LCB (m aft of FP)	1.625	79.6
VCG (m from keel)	0.156	7.65
Roll Radius of Gyration, k_{xx}/B	0.344	0.344
Pitch Radius of Gyration, k_{yy}/L	0.246	0.246
Yaw Radius of Gyration, k_{zz}/L	0.246	0.246
Propeller Diameter, D_p (m)	0.1066	5.25
Propeller Shaft Angle (deg)	5	5

The grid resolution adopted in the study is based on coarse grid applied to the same ship in the previous study by Aram and Park (2022). A limited grid sensitivity analysis was performed, where the size of cells for the fine grid in all three principal directions was half of the coarse grid (1/8 in cell volume), and reported an independence of computed

roll motion to the grid spacing under a 6-DOF free roll decay test. The top and stern views are in Figure 2 of the computational grid with hexahedral-dominant unstructured-grid topology and prism layers for a boundary layer that forms on the solid surface. Instead of resolving the boundary layer region and as a practical approach to surface ship hydrodynamic analysis, the first cell height on the model surface is chosen to achieve the required range suitable for activating the wall functions. Local volume refinements are applied to generate required grid resolutions in the large gradient regions. The resulting number of volume cells are 8.8×10^6 and 27.7×10^6 for the model and full-scale ship, respectively. Except for the outlet, which is set to the zero-gradient boundary condition for velocity, a Dirichlet condition with zero value for velocity is applied to all computational boundaries of the rectangular domain.

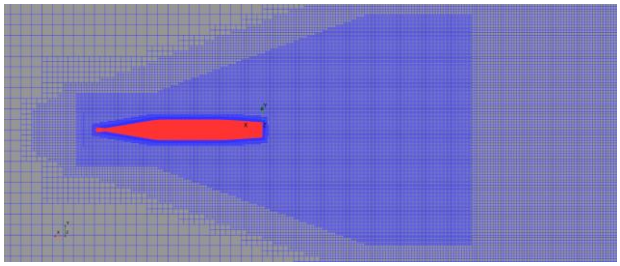

(a) Top view

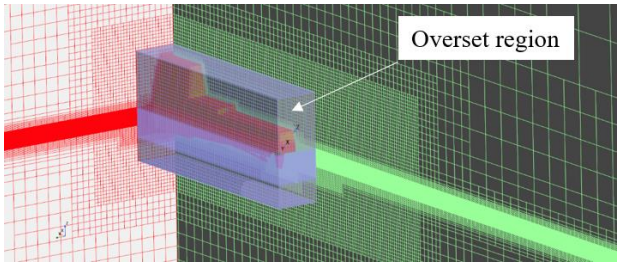

(b) Stern view

Figure 2: (a) Top and (b) stern views of computational grid.

Results and discussion

Forced roll motions with roll amplitudes a = 3°, 6°, 9° and 12° are modeled at a constant period and the Froude number (Fr) of 0.0 and 0.2. The period of the roll motions is equal to the natural period of the model obtained from the roll decay CFD simulations described in Aram and Park (2022). Figure 3 has the roll decay period from a curve fit of an exponential cosine function on the CFD motion for the initial roll amplitudes of 6°, 9.3° and 12°. The period varies (linearly) with the initial roll amplitude, which may be related to the geometric nonlinearity. The average of the natural period between 5° and 15° initial roll amplitude (1.57 s) is for the forced roll motions in this study.

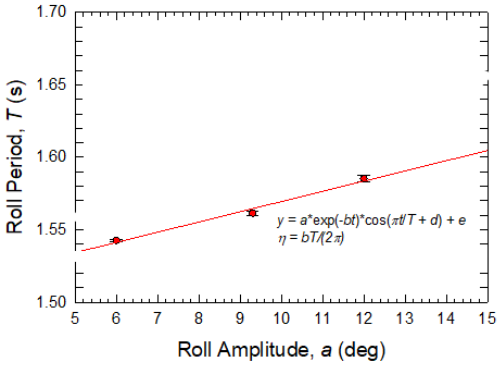

Figure 3: ONRTH roll period from exponential cosine function (Aram and Park, 2022).

Figure 4 depicts the contours of streamwise vorticity on multiple planes along the ship length for the 12° amplitude forced roll motion at Fr = 0.0 during the first half a cycle. The ship is in an upright position at the start of the cycle. The evolution of the vorticity with negative value formed in the previous cycle at the tip of bilge keel and rudder is observed. The vorticity goes through stretch, growth, and detachment from these appendages along with weakening and disappearance. The formation and growth of the vorticity with an opposite sign (positive in these snapshots) is also observed. The subtle presence of a weak positive vorticity wrapping around the negative tip vorticity formed in the previous cycle is also noticeable in these snapshots. The vorticity varies along the bilge keel length with cores that are stronger and larger than those generated by the rudder.

Figure 5 compares the streamwise vorticities between various roll motion amplitudes at $t = T/8$ of the cycle and Fr = 0.0. The size and extent of the core vortices generated by the bilge keel and rudder grow with the roll amplitude. The strength and extent of the bilge keel vortices are greater than rudder vortices.

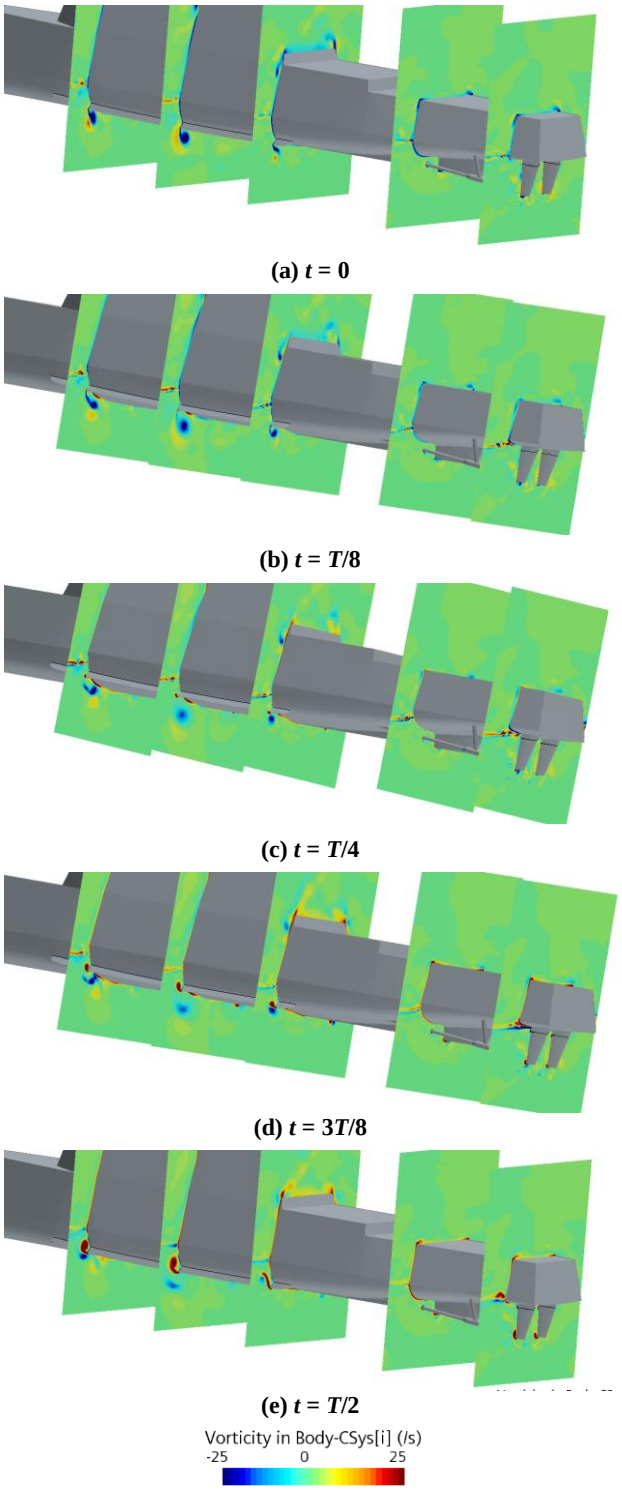

Figure 4: Contours of streamwise vorticity on multiple planes along length of model scale ONRTH under 12º amplitude forced roll motion at *Fr* = 0.0.

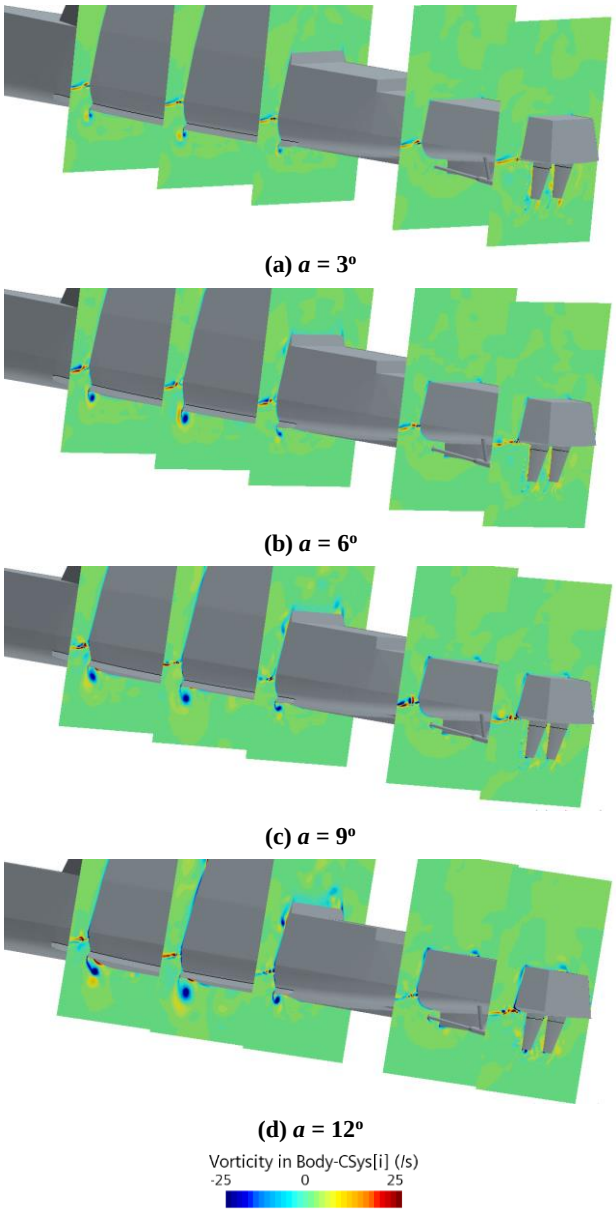

Figure 5: Contours of streamwise vorticity on multiple planes along length of model scale ONRTH at t = *T*/8 under forced roll motion at *Fr* = 0.0.

Figure 6 plots the time histories of the roll moments on the hull (bare hull, shafts, struts), port bilge keel (index "P" is for port throughout this paper), and port rudder of the model scale ONRTH under forced roll motion at *Fr* = 0.0. The moments on the starboard bilge keel and rudder have a 180º phase shift with an opposite sign compared to the moment on the port side. The peak moment is greatest on the hull, while the rudder moment is negligible. The amplitude of the roll moment increases with the roll amplitude, and the peak roll of the hull occurs near the maximum roll acceleration with slight dependence to the roll amplitude. However, the peak roll moment

generated by the bilge keel and rudder occurs at a different time partly due to the formation and evolution of vortices at the tip of these appendages, which influence the pressure distribution on their surfaces, as depicted in Figure 4 and 5.

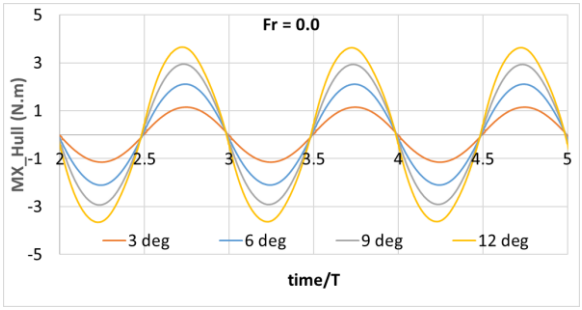

(a) Hull roll moment

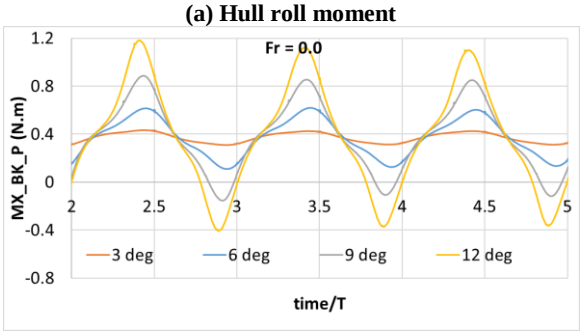

(b) Port bilge keel roll moment

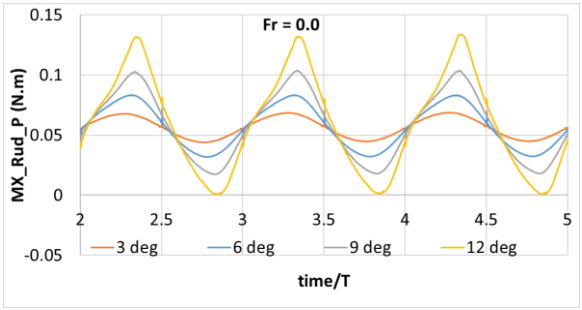

(c) Port rudder roll moment

Figure 6: Roll moment on (a) hull, (b) port bilge keel, (c) port rudder of model scale ONRTH under forced roll motions at *Fr* = 0.0.

The pressure and frictional contributions to the hull roll moment for the model scale ship at *Fr* = 0.0 are in Figure 7. The amplitudes of the pressure moments are significantly greater than the frictional moment for all roll amplitudes, in which the frictional moment can be neglected. Both moment components increase with the roll amplitude.

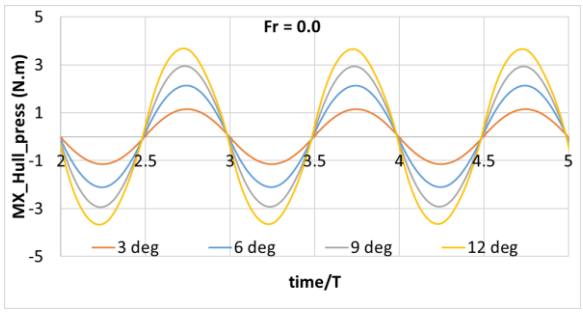

(a) Pressure

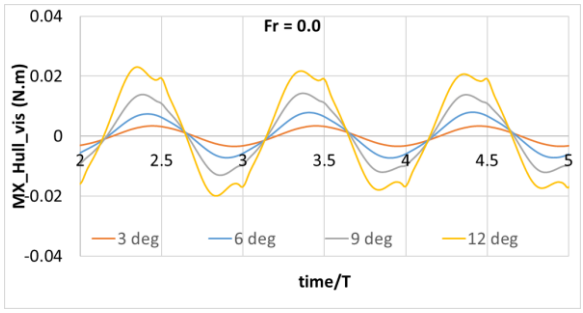

(b) Friction

Figure 7: (a) Pressure and (b) frictional contribution to hull roll moment of model scale ONRTH under forced roll motions at *Fr* = 0.0.

Figure 8 compares the streamwise vorticity contours for *Fr* = 0.0 and 0.2 with 12° roll for the model scale ship at *T*/8. The core vortices are further from the bilge keel and slightly larger for *Fr* = 0.0. The vorticity grows and extends as traveling along the bilge keel at *Fr* = 0.2, partly due to the growth of boundary layer on this appendage.

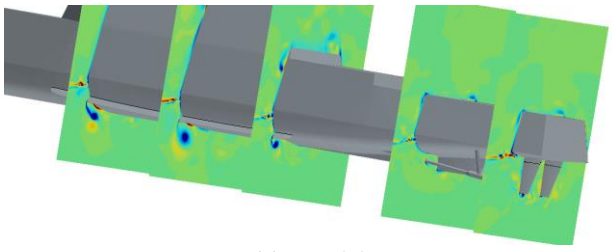

(a) *Fr* = 0.0

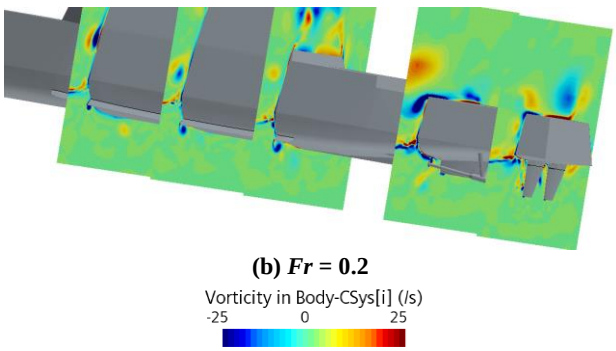

(b) *Fr* = 0.2

Figure 8: Contours of streamwise vorticity on multiple planes along length of model scale ONRTH at t = *T*/8 under 12° forced roll motion at *Fr* = 0.0 and 0.2.

The total roll moment is compared in Figure 9, as well as contributions from hull, port bilge keel and rudder between Fr = 0.0 and 0.2 for forced roll motion of model scale ship with 12° roll amplitude. Fr indicates slight influence on the amplitude and phase of the hull roll moment. However, the amplitude of bilge moment is reduced for ship with forward speed, which is consistent with the differences in the vortices in Figure 8. Significant differences in the rudder moment observed between the two speeds are mainly due to the hull wave effects on the rudders for the ship at surge speed condition. Despite the differences in the moment generated by these appendages, the total roll moment between two ship speeds is comparable, since the hull is the dominant contributor to the total moment for both speeds.

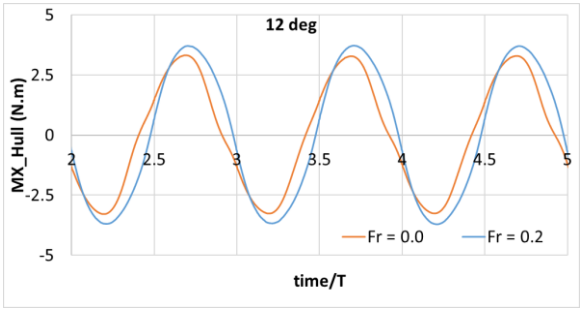

(a) Hull roll moment

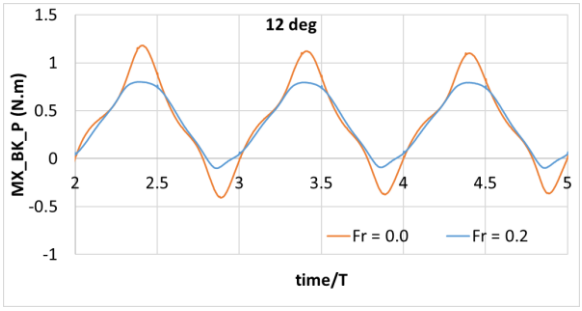

(c) Port bilge keel roll moment

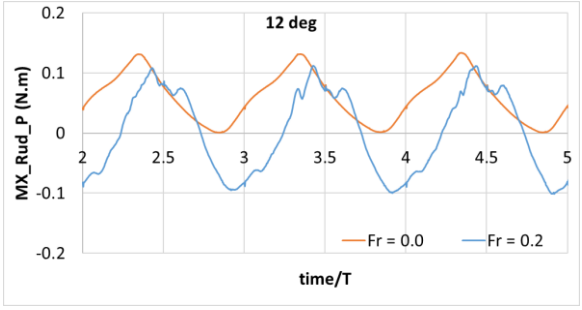

(c) Port rudder roll moment

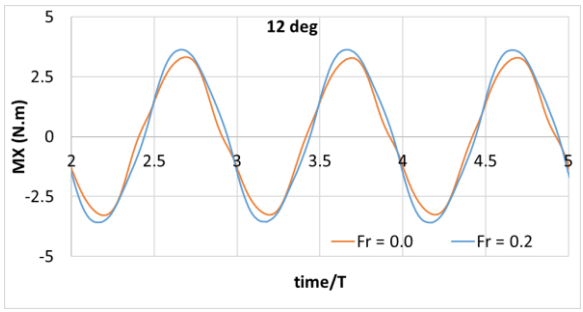

(d) Ship roll moment

Figure 9: (a) Hull roll moment, (b) port bilge keel roll moment, (c) port rudder roll moment, and (d) ship roll moment on model scale ONRTH under 12° amplitude forced roll motion for *Fr* = 0.0 and *Fr* = 0.2.

Figure 10 presents the scale effects on the roll moment at Fr = 0.0 and 0.2 under forced roll motion with 12° amplitude. The moment in this figure is scaled by $1/2\rho V_c^2 L^3$, where $V_c = L/T$. The scale effects are marginal for both Froude numbers. The only noticeable difference is found in the frictional component of the hull moment (not shown here). However, due to the small magnitude of this component compared to the total moment, the effect is negligible.

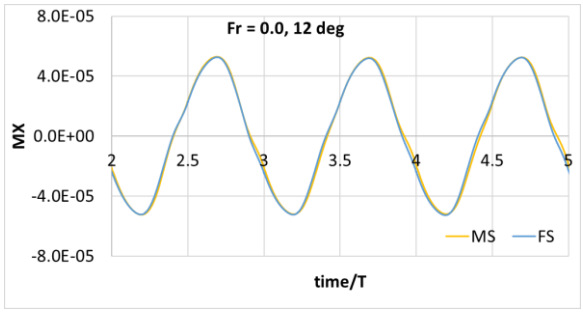

(a) *Fr* = 0.0

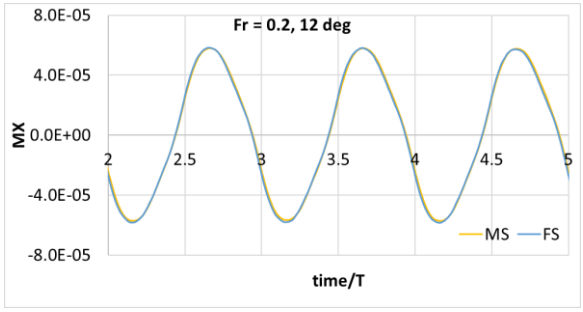

(b) *Fr* = 0.2

Figure 10: Effect of scaling on total roll moment for (a) *Fr* = 0.0 and (b) *Fr* = 0.2.

In addition to the forced motion cases, a 1-DoF free rolling simulation was run at Fr = 0.0 with an initial roll angle of 12°. This simulation has previously been validated against model test performed at the Iowa Institute of Hydraulic Research (Aram and Park, 2022). In the present roll

damping study, this case can be used for either fitting the roll damping coefficients or evaluating the responses of the seakeeping codes with computed coefficients. Figure 11 compares the roll motion response between model and full-scale simulations. Similar to the forced motion, the scale effect is negligible.

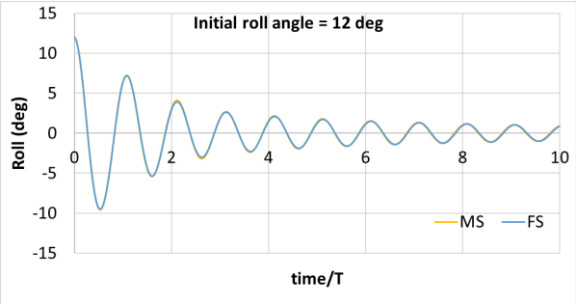

Figure 11: Free roll response from 12° (roll decay) *Fr* = 0.0.

3. ROLL DAMPING MODEL

The general form of the roll moment model, that will be fitted to the CFD data, has the following form:

$$Mx(t) = -a_{44}\ddot{\phi}(t) - b_{44}^{1}\dot{\phi}(t) - b_{44}^{2}\dot{\phi}(t)\left|\dot{\phi}(t)\right| - b_{44}^{3}\dot{\phi}(t)^{3} \quad (3)$$

where $\dot{\phi}(t)$ and $\ddot{\phi}(t)$ are the roll rate and roll acceleration, respectively. Since this model includes an acceleration term, it is not strictly a roll damping model but would perhaps be better described as a roll radiation force model. In classical seakeeping theory, radiation forces are the hydrodynamic forces associated with the ship's motion. In this context, a_{44} can be referred to as an added mass coefficient. As the model in Equation (3) may well be used with a hybrid code involving potential flow forces and appendage models, it may be better to call this a "supplemental moment model" or even a "moment correction." However, it will be called a damping model in the present discussion.

In a traditional seakeeping analysis, these coefficients would typically be estimated through roll decay matching. The peaks of an experimental or CFD roll decay time history would be extracted, and used to compute the roll period and roll decrement for each pair of successive peaks. The analysis would be repeated for a numerical simulation of the same roll decay test and the results plotted over the experimental/CFD values. The added mass coefficient a_{44} could then be adjusted to match the roll period, while the damping coefficients would be adjusted to match the roll decrements. When plotted on a logarithmic scale, the linear damping term b_{44}^{1} controls the height of the decrement curve, the quadratic term b_{44}^{2}controls the slope of the decrement curve and the cubic term b_{44}^{3} (when used) controls the curvature of the decrement curve.

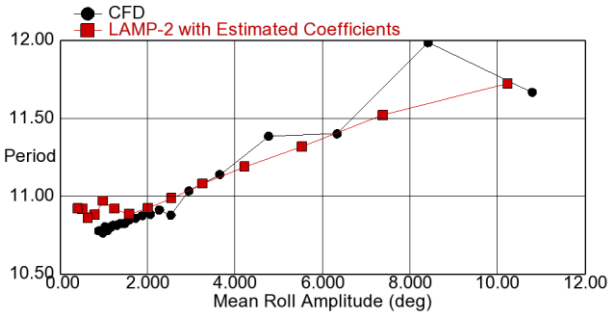

Figure 12: Roll period plot for ONRTH free roll decay run at *Fr* = 0.0.

Roll period and decrement plots are in Figure 12 and 13, respectively, for the ONRTH at 0 knots with traditionally fitted linear and quadratic damping. A significant decrease occurs in the roll period as the roll amplitude decreases. This somewhat unusual result is a product of the "tumblehome" nature of the hull form (Figure 1).

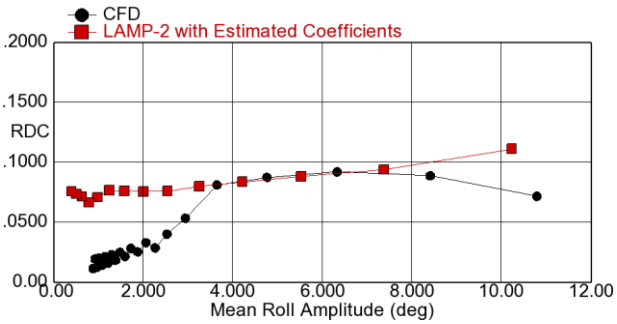

Figure 13: Log roll decrement plot for ONRTH free roll decay run at *Fr* = 0.0.

In the present approach, regression will fit the coefficients to the moments from the forced roll CFD simulations. The exact roll moment that will be fitted will depend on the intended use of the roll moment model.

Modeling All Hydrodynamic Moments

With a simplified ordinary differential equation (ODE) ship motion model or a simplified numerical code such SimpleCode or LAMP-0 ("hydrostatics-only") option in LAMP, this model may be applied for all of the roll forces except for the hydrostatic,

incident wave (Froude-Krylov) and diffraction (if modeled) forces. For such cases, the roll moment that will be fitted will be the total moment from the calm water CFD simulations subtracted by an estimate of the nonlinear hydrostatic restoring forces.

$$Mx^{fit}(t) = Mx_{Tot}^{CFD}(t) - Mx_{HS}(t) \qquad (4)$$

In the present application, the restoring moment $Mx_{HS}(t)$ is computed with the body-nonlinear hydrostatic and Froude-Krylov moment from a LAMP simulation by the same forced roll motion as the CFD run. For these calm water cases, this will be the hydrostatic restoring moment.

Figure 14 illustrates the calculation of the hydrodynamic roll moment to be fitted for the *Fr* = 0.2 run (15 knots) with 12° forced roll. The red curve is the total roll moment from the CFD calculation, scaled to full scale (kN·m). The green curve is the body-nonlinear hydrostatic moment computed by LAMP. The blue curve is the difference between these two and is the moment that will be fitted in order to compute coefficients for use with SimpleCode, LAMP-0, etc.

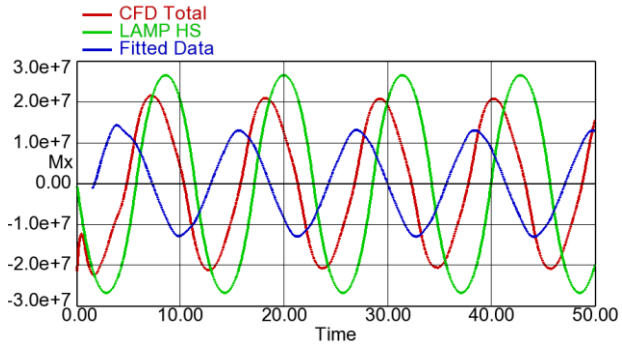

Figure 14: Fitted roll moment *Fr* = 0.2 (15 knots), 12° roll – fitting all hydrodynamic forces.

In this type of force fitting, the calculation of the subtracted restoring moment $Mx_{HS}(t)$ does not necessarily have to match the simulation code for the damping model. For example, the hydrostatic moments could be computed with LAMP even when the roll damping model was to be employed with a linear set of ODEs. However, the forces should provide an accurate estimate of the non-linear restoring. If they do not, the coefficients may be attempting to fit a part of the nonlinear restoring, which can be both large and non-linear, especially for a hull like ONRTH.

Modeling Damping and Correction Moments

If the roll damping model is in a typical hybrid seakeeping code that incorporates potential flow wave-body hydrodynamics, appendage models, etc., the fitting procedure and roll velocity and acceleration data will be the same but the moment that is to be fitted will be different. In this case, the fitted moment will be the total from the CFD simulation subtracted by the total of the hybrid seakeeping code *except* for the tunable damping terms.

$$Mx^{fit}(t) = Mx_{Tot}^{CFD}(t) - (Mx_{Tot}(t) - Mx_{Damp}(t)) \qquad (5)$$

In this situation, other elements of the hybrid seakeeping code compute parts of the hydrodynamic roll moment, such as potential-flow radiation forces, while the model in Equation (3) computes additional forces due to viscosity, appendage lift, etc. If the hybrid code includes models for appendages, the damping model can provide a correction or adjustment to those models. In any event, the total moments that need to be modeled by Equation (3) would be expected to be smaller than in the "all hydrodynamic force" fit. For this case, imperatively, the subtracted forces are computed with the same hybrid seakeeping code and options that will be used with the computed coefficients.

For the present applications, the damping model is to be set for calculations made with the LAMP's standard potential-flow hydrodynamics option LAMP-2. The LAMP-2 simulation will incorporate a body-nonlinear calculation of the hydrostatic restoring forces, a body-linear solution of the wave-body hydrodynamic interaction problem, and semi-empirical models for the forces on the bilge keels and rudders. The wave-body hydrodynamics solution is computed by a 3-D panel method with Rankine singularities distributed over the mean wetted hull surface and a local portion of the mean free surface. The pressure forces from the potential-flow solution provide the added mass and damping associated with the ship-generated wave field.

In order to get the $(Mx_{Tot}(t) - Mx_{Damp}(t))$ moments that will need to be subtracted for the data fit, a series for forced motion simulations are set up with all of the options and models (including appendages) *except* that the supplemental damping and added mass terms are turned off. The total roll

moments from these LAMP simulations will be subtracted from the CFD moments to get the roll moments used in the coefficient fit.

This data setup is illustrated by Figure 15, which has the CFD moment, the subtracted LAMP-2 moment and the resulting "supplemental" moment that will need to be fitted. Comparing this result to Figure 14, the fitted moment in this case is considerably smaller than for the "all hydrodynamic forces" fit.

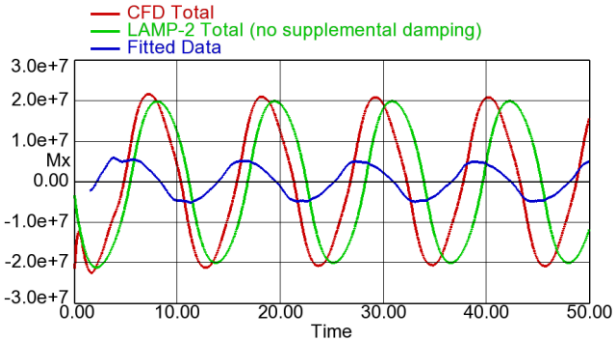

Figure 15: Fitted roll moment 15 knots, 12° roll – fitting viscous/correction moments.

However, not all seakeeping codes have a supplemental added mass term or a cubic damping term. In fact, most traditional roll damping tuning only considered the linear and quadratic damping terms (at best). The present approach will work without these terms, but if the prediction has a significant difference the added mass term, perhaps due to a neglect of the appendage added masses, the error in the fitting of the moment coefficients may be large.

Additionally, the fit approach described here is not restricted to sinusoidal forced motion. As long the appropriate $Mx_{HS}(t)$ or $(Mx_{Tot}(t) - Mx_{Damp}(t))$ forces can be computed for the motions from the CFD cases, the fit can be done for any free or forced motion case. If a hybrid code computes the $Mx_{HS}(t)$ or $(Mx_{Tot}(t) - Mx_{Damp}(t))$ forces, it will be necessary to be able to prescribe the motion time histories in the corresponding hybrid code runs.

Regression Fit

The coefficients are computed through a straightforward regression approach (*e.g.* Faraway, 2005) in which an over-determined system of linear equations are set up as follows:

$$\boldsymbol{X}\vec{c} = \vec{Y} \tag{6}$$

where $\vec{c}$ is the vector of 4 added mass and damping coefficients, $\vec{Y}$ is a vector of fitted moment values at Nt times (response vector), and $\boldsymbol{X}$ is $4 \times Nt$ matrix of velocity and acceleration terms at those times (matrix of predictors). $\vec{c}$, $\vec{Y}$, and $\boldsymbol{X}$ are described in Equations (7) through (9).

$$\vec{c} = \begin{pmatrix} -a_{44} \\ -b_{44}^{1} \\ -b_{44}^{2} \\ -b_{44}^{3} \end{pmatrix} \tag{7}$$

$$\vec{Y} = \begin{pmatrix} Mx^{fit}(t_1) \\ Mx^{fit}(t_2) \\ \vdots \\ Mx^{fit}(t_{Nt}) \end{pmatrix} \tag{8}$$

$$\boldsymbol{X} = \begin{pmatrix} \ddot{\phi}(t_1) & \dot{\phi}(t_1) & \dot{\phi}(t_1)|\dot{\phi}(t_1)| & \dot{\phi}(t_1)^3 \\ \ddot{\phi}(t_2) & \dot{\phi}(t_2) & \dot{\phi}(t_2)|\dot{\phi}(t_2)| & \dot{\phi}(t_2)^3 \\ \vdots & \vdots & \vdots & \vdots \\ \ddot{\phi}(t_{Nt}) & \dot{\phi}(t_{Nt}) & \dot{\phi}(t_{Nt})|\dot{\phi}(t_{Nt})| & \dot{\phi}(t_{Nt})^3 \end{pmatrix} \tag{9}$$

This system can be solved with a least squares approach:

$$\boldsymbol{X}^T\boldsymbol{X}\vec{c} = \boldsymbol{X}^T\vec{Y} \tag{10}$$

Solving this system computes a set of coefficients which minimizes the error $\|B - Ax\|_2^2$, where $\|\cdot\|_2$ denotes the Euclidean norm.

Fit to the CFD Forced Motion Data

The CFD forced motion data were computed for 2 speeds (Fr = 0.0 and 0.2, which correspond to 0 and 15 knots full scale) and 4 roll amplitudes (3°, 6°, 9° and 12°). In addition, a 0 knot free roll decay case is available. The amount of data needed for the coefficient fit depends on the intended use of damping model. To maximize the relevance of the model, the fitted data should cover the range of conditions expected in the simulations. To maximize the accuracy (i.e. minimize the fit error) of the model, the range might want to be restricted.

As the CFD data indicate a significant difference in the moment values for the different speeds (Figure 9) and the damping model (Equation 3) does not implicitly include speed dependence, to do separate fits for the two speed might be best and use speed dependent coefficients in the hybrid code simulations. If speed dependent coefficients are not supported in the simulation code or are impractical in the analysis, data for all speeds should be fitted

simultaneously, which may be more likely to produce a larger error in certain conditions.

As an irregular sea analysis will cover a range of roll angles in each simulation and the model includes amplitude dependence through the non-linear terms, the data from the different roll angle should be combined in a single fit for each speed or all speeds combined.

Table 2 lists the coefficients for several fits to the "All Hydrodynamic Moments" data, with rows for the separate and combined speed fits.

Table 2: Damping model coefficients fitted to all hydrodynamic moments.

A44	B44_1	B44_2	B44_3	Case(s) Fitted
2.91E+6	238265	370483	-35044	0 knots; all forced roll
2.44E+6	988012	71676	-2941	15 knots; all forced roll
2.68E+6	613139	221080	-18992	all forced roll
2.67E+6	537761	244372	-20991	all cases

The last line in Table 2 lists a fit, which includes the 0-knot free decay CFD data as well as the forced decay data. In this case, the extra data do not make much difference, but free roll data should be employed with care, as it is likely to include very little data at larger roll velocities and accelerations and much data at lower values. The nonlinearity in the roll moment data will tend to be under emphasized.

The values in Table 2 suggest that the damping at 15 knots appears to be dominated by the linear term while the nonlinear terms are relatively more important in the 0-knot data. This may be due to the effect of the shedding of the vorticity from the bilge keels, which stays around the ship in the 0-speed problem but is left behind in the forward speed problem.

Visually, these fits can be checked by plotting the fitted moment data versus the moments calculated with the computed coefficients. Figure 16 has the fit check for the four 15-knot forced roll cases with coefficients fitted to all of the 15-knot CFD cases. The fit matches the phasing and magnitude of the data well with a discrepancy evident only at the largest peaks.

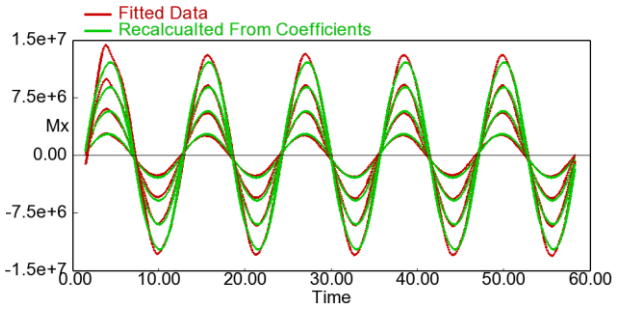

Figure 16: Roll moment fit Check, 15 knots – fitting all hydrodynamic forces from 15-knot forced roll data.

The fit check for the 9° forced forces cases with coefficients computed from CFD data at both speeds is plotted in Figure 17. Since the damping model does not implicitly include speed dependent terms and the same coefficients are used for both speeds, the moments from the coefficients are the same for both speeds, so a single curve "Coefficient Fit" is included for those results. The fitted data are not the same for the two speeds, but the difference is not large. This type of plot can provide a visual check on the effectiveness of speed-dependent vs. speed-independent coefficients.

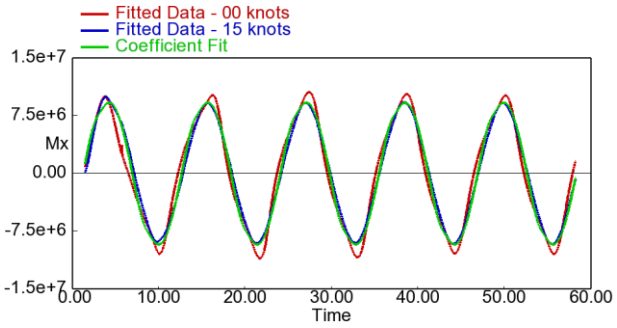

Figure 17: Roll moment fit check, 9° – fitting all hydrodynamic forces from all forced roll data.

4. UNCERTAINTY QUANTIFICATION OF ROLL DAMPING MODEL

In the plots above, the fit of the coefficient-based force model will not be perfect, which will lead to some uncertainty in the damping force model. It would be highly beneficial to be able to quantify this uncertainty, both as way to assess the accuracy of the data fit and to provide a mechanism by which the uncertainty in the model can be propagated though the lower fidelity predictions in a multi-fidelity analysis.

Confidence Interval of the Coefficients

The residuals of the fit are the difference between the original data values and the values

predicted with the computed coefficients. A vector of the residuals at each time step can be readily computed as:

$$\vec{\varepsilon} = \vec{Y} - \boldsymbol{X}\vec{c} \tag{11}$$

These residuals provide a measure of the error of the coefficient fit and can compute a confidence interval for each coefficients as:

$$c_i^{low} = c_i - QT\ \sigma \sqrt{\boldsymbol{XTXI}_{i,i}} \tag{12}$$

$$c_i^{high} = c_i + QT\ \sigma \sqrt{\boldsymbol{XTXI}_{i,i}} \tag{13}$$

where σ is the residual standard error that can be computed as:

$$\sigma = \sqrt{(\vec{\varepsilon} \cdot \vec{\varepsilon})/(Nt - p)} \tag{14}$$

where p is the number of predictors (4 in this case), QT is the quantile of the Student-t distribution corresponding to the desired probably level, such as 0.95, and $\boldsymbol{XTXI}$ is the unscaled covariance matrix:

$$\boldsymbol{XTXI} = (\boldsymbol{X}^T\boldsymbol{X})^{-1} \tag{15}$$

These formulae can compute the uncertainty of the coefficients as part of the regression fit. Table 3 lists the confidence intervals for the four coefficients computed for the "all hydrodynamic moments" problem with data from the 15-knot roll CFD simulations in Figure 16. The probability level of the confidence interval is 0.95. In this example, the confidence interval is quite small, which coincides with the close fit in the visual check.

Table 3: Confidence intervals for damping model coefficients fitted to 15-knot forced roll CFD data – all hydrodynamic moments.

Prob=0.95	A44	B44_1	B44_2	B44_3
Low end of CI	2.441E+6	963078	59412	-4347
Estimate	2.447E+6	988012	71676	-2941
High end of CI	2.453E+6	1012946	83940	-1535

Prediction Interval for a Single Point Prediction

The confidence intervals of the individual coefficients could readily be propagated through the seakeeping simulations by repeating the simulations with different combinations of the high and low-end values. However, this approach has some drawbacks. To know beforehand, which combination of high and low values may lead to the largest uncertainty, may be difficult. More importantly, the dependency of the terms is not considered.

A more effective approach would be to implement a prediction interval for each evaluation of the damping model. Such a prediction interval can be evaluated as (e.g. Faraway, 2005):

$$Mx^{low}(t) = \vec{c} \cdot \vec{x}(t) - QT\ \sigma \sqrt{1 + \vec{x}(t) \cdot (\boldsymbol{XTXI} \cdot\ \vec{x}(t))} \tag{16}$$

$$Mx^{high}(t) = \vec{c} \cdot \vec{x}(t) + QT\ \sigma \sqrt{1 + \vec{x}(t) \cdot (\boldsymbol{XTXI} \cdot\ \vec{x}(t))} \tag{17}$$

where $\vec{x}(t)$ is a vector of roll acceleration and velocity terms:

$$\vec{x}(t) = \begin{pmatrix} \ddot{\phi}(t) \\ \dot{\phi}(t) \\ \dot{\phi}(t)|\dot{\phi}(t)| \\ \dot{\phi}(t)^3 \end{pmatrix} \tag{18}$$

This expression could be implemented in a simulation code to allow a case to be run with "high" or "low" damping.

A disadvantage of the prediction interval approach is that it has to be implemented within the simulation code, while an approach based on the confidence intervals of the individual coefficients can be used by simply modifying the code input.

Irregular Sea Roll Response with Uncertainty

In order to demonstrate the propagation of the uncertainty of the roll damping model in the seakeeping simulations, irregular sea simulations are set up with damping model coefficients spanning their confidence interval. The first example is a LAMP-2 run for the ONRTH at 15 knots in a quartering Sea State 6 ($H^{1/3}$ = 5.0m, T_0 = 12.3s). As this is a 3-DOF (heave-roll-pitch) LAMP-2 run including potential-flow hydrodynamics and appendage models, the damping model coefficients have been fitted to the damping and correction moments as described in Equation (5). Table 4 lists the computed coefficients with confidence intervals for a probability of 0.95. These coefficients were computed from the four 15-knot CFD forced motion simulations.

Table 4: Confidence intervals for damping model coefficients fitted to 15-knot forced roll CFD data – damping and correction moments.

Prob = 0.95	A44	B44_1	B44_2	B44_3
Low end of CI	426697	378966	89079	-1913
Estimate	420590	354107	76851	-3315

High end of CI	414482	329247	64624	-4717

LAMP responses were predicted with the estimated coefficient values and the values at the low and high end of the confidence interval. The roll response for ONRTH at 15 knots in quartering Sea State 6 is in Figure 18. For this case, the effect of the coefficient uncertainty is small, only ~ 0.1° at the peak values. This is reasonable as the error in the coefficient fit was not large and the roll motion for this case, while not small, is not driven by resonance. The principal encounter period here is about 15 seconds while the roll natural period is 10-11 seconds in Figure 12.

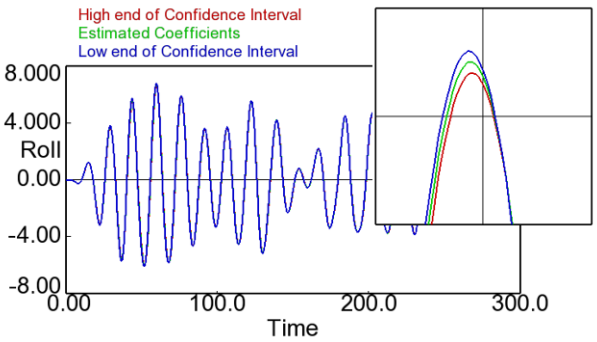

Figure 18: LAMP-2 roll response for ONRTH at 15 knots in quartering Sea State 6 – effect of uncertainty in the damping model coefficients.

This set of calculations is now repeated for the same seaway but at 0 knots. At this speed, the encounter period will be closer to the ship's roll natural period, so the roll response is expected to be both larger and more sensitive to damping. Damping model coefficients were computed from the four 0-knot CFD forced motion simulations, and are with confidence interval (probability of 0.95) in Table 5. As the model fit for the 0-knot coefficients was not a close as the 15-knot coefficients, the confidence intervals are wider than the 15-knot results in Table 5.

Table 5: Confidence Intervals for Damping Model Coefficients Fitted to 0-knot Forced Roll CFD Data – Damping and Correction Moments

Prob = 0.95	A44	B44_1	B44_2	B44_3
Low end of CI	5.88E+06	9.99E+08	4.64E+07	-7.17E+09
Estimate	9.33E+06	1.10E+09	4.72E+07	-6.53E+09
High end of CI	1.28E+07	1.20E+09	4.81E+07	-5.89E+09

A portion of the roll response for these LAMP simulations is in Figure 19. The roll response is larger than for the 15-knot case, and the effect of the uncertainty in the damping model coefficients is more significant.

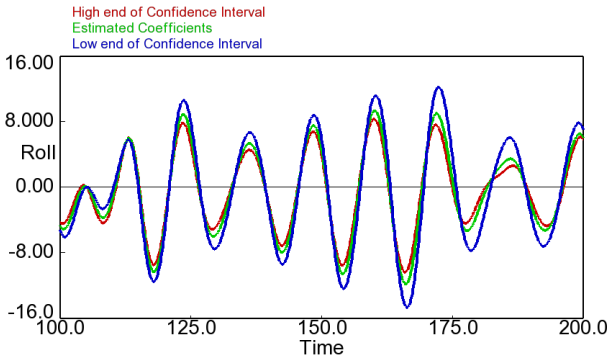

Figure 19: LAMP-2 roll response for ONRTH at 0 knots in quartering Sea State 6 – effect of uncertainty in the damping model coefficients.

The peak roll response with coefficients at the high end of the confidence interval is 6 % lower than with the estimated coefficients themselves, while the peak roll response for coefficients from the low end of the confidence interval is 25 % higher than with the estimated coefficients.

As described above, a better way to include the damping uncertainty in the seakeeping simulation would be to implement the prediction interval from Equations (16) and (17) for each damping moment evaluation. This approach is preferable because it accounts for the dependency between the terms of the damping model but has the drawback that the evaluation needs to be implemented in the seakeeping code, rather than simply being a modification of the code input.

5. COMPONENTS OF ROLL DAMPING

A significant advantage of the present set of CFD roll motion simulations is that they include separate values for the forces and moments due to hull pressure, hull shear force, bilge keels, etc. This decomposition of the forces and moments provides insight into the contributions to the ship roll moments and can build or refine force models for hybrid seakeeping codes such as LAMP.

In the present study, this has led to a refinement of the added mass term in LAMP's bilge keel model, and further work in this area is anticipated. However, this work is outside of the scope of the present paper.

SUMMARY AND FUTURE WORK

A series of 1-DOF free and forced roll motion CFD runs were performed for the ONRTH hull for the purpose of developing roll damping models for seakeeping predictions made with hybrid codes such as LAMP and SimpleCode. The force motion CFD simulations included two speeds (Fr = 0.0 and 0.2) and 4 roll amplitudes (3°, 6°, 9° and 12°). The output of the CFD simulations include forces and moments due to hull pressure, hull shear force, bilge keels and rudders.

The moments from these simulations computed hull and speed specific coefficients for a roll damping model including terms for linear added mass and linear, quadratic and cubic damping. The coefficients were computed by a least-squares regression of the fitted roll moment vs. the instantaneous roll rate and acceleration. For the use of the damping model with a potential-flow based seakeeping code like LAMP, the fitted roll moment is the difference between the CFD moments and the LAMP roll moments for the same motion history. In this usage, the damping model is a supplemental or correction model, which accounts for viscous forces not included in the potential flow model as well as deficiencies or approximations in the code's appendage force models.

For use with a reduced order seakeeping tool such as SimpleCode, the fitted roll moment is the total CFD moment minus a body-nonlinear hydrostatic restoring moment. In this usage, the damping model accounts for all of the hydrodynamic forces due to ship roll motion.

With either usage, the residual of the regression procedure, which is the difference between the fitted moment and the moment predicted by the computed coefficients, evaluates an uncertainty in the roll damping model. This uncertainty is a "modeling uncertainty" which quantifies the error in the damping forces due to the simplifications in the form of the damping model versus the complexity of the actual flow. A confidence interval is computed from the residual error for each coefficient in the damping model, which can be propagated through production level seakeeping simulations in order to evaluate the effect of the uncertainty on the ship roll response.

The residual has also been utilized to compute a prediction interval that can quantify the uncertainty in each evaluation of the damping moment. While more challenging to implement, this approach provides a more robust evaluation of the uncertainty as it includes the dependency between the terms in the damping model. The prediction interval approach is currently being implemented in LAMP and SimpleCode.

Several advantages exist in using forced roll motion rather than free roll motion (roll decay) in the CFD simulations to set up the roll damping models. It simplifies the CFD simulations by eliminating the need for a full dynamic solver. More importantly, it allows a more balanced fit to large and small amplitude roll motion. Roll decay runs typically have very few large amplitude cycles and these may be significantly affected by transient behavior in the CFD simulation. Tuning of roll damping to free roll data must take care not to over-emphasize the damping at low velocities, which may have little importance to large amplitude roll responses.

The decomposition of the moments in the present CFD simulations also provides insight into the contributions for the roll damping forces and are well suited toward refining the appendage force models in codes like LAMP. These results have already refined the added mass term in LAMP's bilge keel force model and will continue to evaluate and refine the appendage force models, especially at zero speed.

ACKNOWLEDGEMENTS

The work presented in this paper has been funded by the Office of Naval Research (ONR) under Dr. Woei-Min Lin.

REFERENCES

Aram, S. and P. Mucha, 2023, "Computational Fluid Dynamics Analysis of Different Propeller Models for a Ship Maneuvering in Calm Water," *Ocean Eng.* Vol. 276, pp. 1-18.

Aram, S. and J. Park, 2022, "On the Uncertainty Quantification of Roll Decay Test," *Proc. 18th Intl. Ship Stability Workshop*, Gdansk, Poland, pp. 21-32.

Aram, S. and D. Wundrow, 2022, "Application of Blended-Method and CFD to Ship Maneuvering Prediction," 34th Symposium on Naval Hydrodynamics, Washington, DC, USA.

Bishop, R. C., W. Belknap, C. Turner, B. Simon, and J. H. Kim,

2005, "Parametric Investigation on the Influence of GM, Roll damping, and Above-Water Form on the Roll Response of Model 5613," Hydromechanics Department, Naval Surface Warfare Center Carderock Division, West Bethesda, Maryland, USA, Report NSWCCD-50-TR-2005/027.

Faraway, J., 2005, Linear Models with R, CRC Press, Boca Raton, ISBN 0-203-50727-4.

Menter, F. R., 1994, "Two-Equation Eddy-Viscosity Turbulence Models for Engineering Applications," *AIAA Journal*, Vol. 32, pp. 1598-1605.

Reed, A. M and Beck, R. F., 2016, "Advances in the Predictive Capability for Ship Dynamics in Extreme Waves," *SNAME Transactions*, Vol. 124, pp. 2-39.

Shin, Y. S, Belenky, V. L., Lin, W.-M., Weems, K. M., and A. H. Engle, 2003, "Nonlinear Time Domain Simulation Technology for Seakeeping and Wave-Load Analysis for Modern Ship Design," *SNAME Transactions*, Vol. 111, pp. 557-578.

Weems, K.M., Pipiras, V. and Belenky, V., 2023, "Multifidelity Fast Code for Direct Stability Assessment," *Proc. 19th Intl. Ship Stability Workshop*, Istanbul, Turkey.

Effects of height of roll axis on pressure distribution on hull caused by bilge-keels

Toru Katayama, *Osaka Metropolitan University,* katayama.marine@omu.ac.jp
Naofumi Yoshida, *Osaka Metropolitan University,* sa22743t@st.omu.ac.jp

ABSTRACT

Recently, Ikeda's method for roll damping is used for wide-breadth and shallow-draught vessels with low KG. However, the estimated results may be overestimate, because the estimated bilge-keel roll damping by Ikeda's method does not sufficiently include the effects of shallow-draught and low KG. To improve Ikeda's method, Katayama et al. (2019, 2021, 2022) have investigated their effects on normal force component of bilge-keel roll damping with and without free surface and proposes some modifications. However, it is indicated that the estimated results by the Ikeda's method including the modifications is not always enough by comparing to the measured results, because the effects on hull pressure component of bilge-keel roll damping is not taken account. In this study, the effects on hull pressure component of roll damping are investigated numerically to improve Ikeda's method. As the results, it is found that the larger $B/2d$ at KG/d=1.0 (or OG=0.0) makes larger difference of pressure distributions on hull surfaces around two bilge-keels, and it is also cleared that the negative pressure coefficients C_P^- are affected by $B/2d$ and becomes smaller than the results of Ikeda' method.

Keywords: *Roll damping, Ikeda's method, Bilge-keel component.*

1. INTRODUCTION

The characteristics of roll motion are one of important factors for ship safety. However, it is difficult to estimate roll motion accurately by only potential theory because of significant viscous effects on roll damping.

As one of estimation methods of the viscous effects on roll damping, Ikeda's method (Ikeda et al., 1978a, b) is well-known. However, it is pointed out by Tanaka et al. (1981) that the method may overestimate roll damping for vessels with shallow-draught and low KG.

To improve Ikeda's method, Katayama et al. (2019, 2020) investigate the effects of H_0 (=$B/2d$: half breadth to draught ratio) and KG/d on the coefficient f which is a correction factor to take account of the increment flow velocity at bilge on hull and propose two new coefficients $g(H_0)$ and h(KG/d). Moreover, Katayama et al. (2022) investigate the effects of free surface on drag coefficient of bilge-keel C_D and propose new coefficient i(KG/d, H_0). However, the estimated results by Ikeda's method including the modifications have not always enough accuracy and especially for low KG even if draught is not shallow. One of reasons is supposed that the effects of H_0 and KG/d on hull pressure component of bilge-keel roll damping is not considered yet.

In this study, the effects of H_0 at KG/d=1.0 (or OG=0) on hull pressure component of bilge-keel roll damping are investigated numerically to improve Ikeda's method.

2. BILEGE-KEEL ROLL DAMPING COMPINENT OF IKEDA'S METHOD

2. 1 Original method

In Ikeda's method, bilge-keel component B_{BK} of roll damping coefficient is composed of two components

$$B_{BK} = B_N + B_S \,, \tag{1}$$

where B_N is normal force component due to normal force acting on bilge-keels and B_S is hull pressure

component due to pressure on hull surface created by bilge-keels.

Equivalent linear sectional normal force component B'_N is

$$B'_N = \frac{8}{3\pi}\rho\, r^2 \omega\, \phi_a\, b_{BK}\, f^2 C_D\, l_1, \qquad (2)$$

where ρ [kg/m^3] is density of fluid, r [m] is the distance from roll axis G to hull surface attached on bilge-keel, ω [rad/s] is roll angular frequency and ϕ_a [rad] is roll amplitude, b_{BK} [m] is breath of bilge-keel and l_1 [m] is the distance from roll axis G to the normal vector to bilge-keel which through the point where is on hull attached bilge-keel. C_D is drag coefficient and f is the correction factor to take account of increment of flow velocity caused by hull form at the point on hull surface where bilge-keel is attached, and they are determined by measured data as follows

$$C_D = \frac{22.5}{K_C \cdot f} + 2.4 \quad (4 < K_C < 20) \qquad (3)$$

$$f = 1 + 0.3e^{\{-160(1-\sigma)\}}, \qquad (4)$$

where σ is area coefficient of cross-section and K_C is Keulegan-Carpenter number as follows

$$K_C = \frac{U_{\max} T}{D} = \frac{\pi r \phi_a}{b_{BK}}, \qquad (5)$$

where T [s] is period of the oscillation, $U_{\max}$ [m/s] is amplitude of characteristic velocity and D [m] is characteristic length. In the case of this study, T is roll period, $U_{\max}$ is the velocity caused by rolling at the point on hull surface where bilge-keel is attached and D is twice of breadth of bilge-keel.

Equivalent linear sectional hull pressure component B'_S is

$$B'_S = \frac{4}{3\pi}\rho\, r^2 \omega\, \phi_a\, f^2 \int_G C_P \cdot l\, dG, \qquad (6)$$

where G [m] is girth length along hull, l [m] is moment lever, C_P is hull pressure coefficient and its values for front and back face of bilge-keels are

$$C_P = \begin{cases} 1.2 & (\text{for } C_P^+) \\ 1.2 - C_D & (\text{for } C_P^-) \end{cases}. \qquad (7)$$

Fig.1 shows two pressure distributions on hull measured by Ikeda et al. (1978b). To simplify the distribution as shown in Fig. 2, positive pressure coefficient C_P^+ is empirically taken as 1.2 at front of bilge-keels and 0 at water surface and keel. And negative pressure coefficient C_P^- is 1.2 - C_D from the relation of $C_D = C_P^+ + C_P^-$. Length of the negative-pressure S_0 [m] is obtained as

$$\frac{S_0}{b_{BK}} = 0.3\left(\frac{\pi f r \phi_a}{b_{BK}}\right) + 1.95. \qquad (8)$$

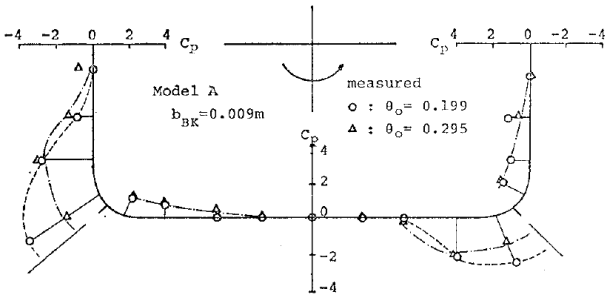

Fig. 1 : Pressure distributions on hull measured by Ikeda et al. (1978b).

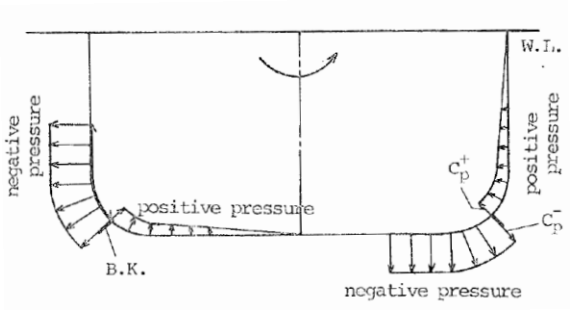

Fig. 2 : Assumed pressure distribution on hull created by bilge-keels by Ikeda et al. (1978b).

2. 2 Effects of H_0 and KG/*d on f*

Tanaka et al. (1981) point out that Ikeda's method overestimates the roll damping when the method is applied to a ship with shallow-draught, and the tendency is more significant as KG of the ship is lower. Moreover, it is explained that the reasons of the overestimation are that the interactions of waves made by hull and bilge-keels decrease wave making roll damping component and the free surface effects decrease the size of shedded

vortexes by bilge-keels and their roll damping component.

Katayama et al. (2019, 2020) focus on the correction factor f and investigate the effects of H_0 and KG/d on f by using CFD. And new coefficients g and h to include the effects of H_0 and KG/d at small roll amplitude are proposed as

$$g = \frac{0.35}{H_0} + 0.75 \quad (\text{for } 1.0 \le H_0 \le 4.5), \qquad (9)$$

$$h = 0.44 \tanh\left(0.80 \frac{\mathrm{KG}}{d}\right) + 0.70 \quad (\text{for } 1.0 \le H_0 \le 4.5 \text{ and } 0.5 \le \frac{\mathrm{KG}}{d} \le 4.5), \qquad (10)$$

where KG is the height of roll axis from keel line.

2. 3 Effects of free surface on C_D

Katayama et al. (2022) propose the coefficient i to include the free surface effects on drag coefficient of bilge-keel C_D.

$$i = a \cdot \left(\frac{KG}{d}\right) + b \quad (\text{for } 0.6 \le \frac{KG}{d} \le 2.7) \qquad (11)$$

$$\begin{cases} a(H_0) = 0.1366 H_0^2 - 0.9164 H_0 + 1.557 \\ b(H_0) = -0.1391 H_0^2 + 0.7497 H_0 - 0.2877 \end{cases} \quad (\text{for } 1.0 \le H_0 \le 4.2) \qquad (12)$$

2. 4 Effectiveness of modifications

Fig. 3 shows the comparisons among the estimated bilge-keel roll damping coefficients by the original Ikeda's method, the modified method and the measurement by Katayama et al. (2019). In this figure, the modified method including the coefficients g, h and i is better than the original method. Fig. 4 shows the ratio of the bilge-keel roll damping coefficients estimated by the modified method to the measured results. From this figure, the modified method overestimates B_{BK} at H_0 < 3.0. The reasons for this overestimation are supposed that the modified method has not included enough the effects of H_0 and KG/d on hull pressure component of bilge-keel roll damping yet.

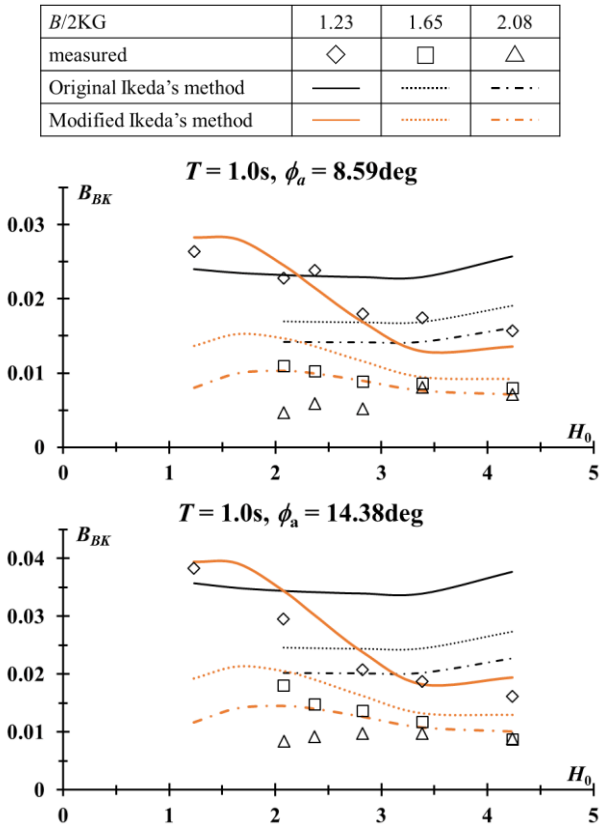

Fig. 3 : Comparisons among estimated bilge-keel components by the original Ikeda's method, the modified methods and measured results.

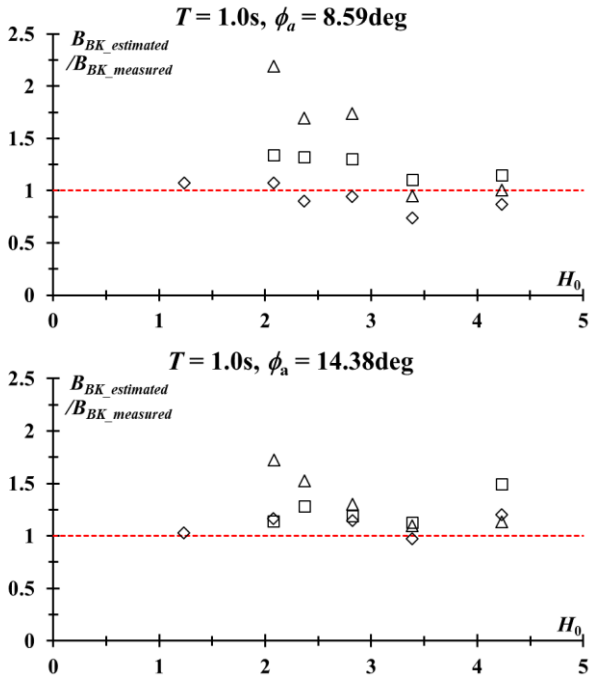

Fig. 4 : Ratio of bilge-keel components estimated by the modified Ikeda's method to the measured results. Marks in this figure is the same as shown in Fig. 3.

3. EFFECTS OF HALF BREADTH TO DRAUGHT RATIO

3. 1 Subject model and set up of CFD

Table 1 shows the principle particulars of the subject model. The model is similar to one of the used models when Ikeda's original method was developed (Ikeda et al., 1978a, b).

Fig. 5 shows the relations of KG/d and H_0 between the 2D-models and existing vessels in recent years. Two dotted lines shows H_0 =B/2d=1.23 and KG/d = 1.0 and the values relates to Ikeda's subject ships when Ikeda's method was developed. In this study, to investigate the effects of H_0 on the hull pressure component indicated in the subsection 2.4, H_0 is determined at KG/d = 1.0 (and OG=0.0).

Fig 6 is the calculation domains for 2D-model without free surface. The boundary condition on the hull surface is non-slip and that on the semicircle dummy superstructure is free-slip.

Table 2 shows computational conditions of CFD and Table 3 shows calculation conditions of forced roll test in CFD. In the forced roll test, to remove the Kc effects on vortex shedding from bilge-keels, Kc is constant but roll amplitude is not constant.

Table 1 : Principle particulars of 2D-model.

breadth: B [m]	0.237
KG [m]	0.1185, 0.096, 0.072, 0.057, 0.042
KG/d (or OG)	1.0 (0.0)
H_0 (=B/2d)	1.00, 1.23, 1.65, 2.08, 2.82
sectional area coefficient σ	0.981, 0.977, 0.969, 0.961, 0.947
bilge radius [m]	0.035
b_{BK}×t_{BK} [m×m]	0.01×0.001

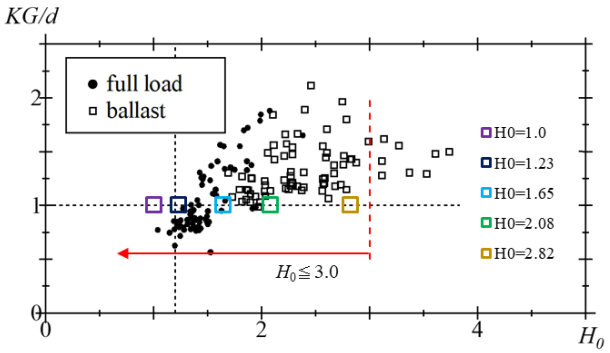

Fig. 5 : Relations of KG/d and H_0 between the 2D-models and existing vessels in recent years.

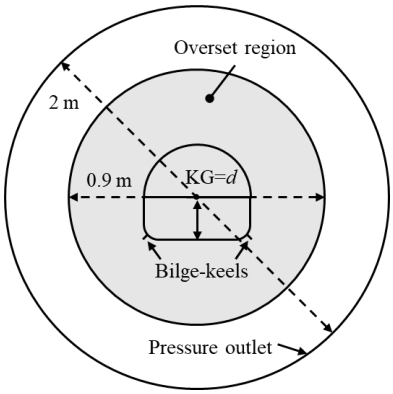

Fig. 6 : Schematic view of calculation model without free surface.

Table 2 : Computational conditions of CFD.

turbulent model	SST k-ω
time discretization	second-order accuracy
minimum mesh size [m]	0.00125
minimum time step [s]	0.0002

Table 3 : Calculation conditions of forced roll test in CFD.

roll period [s]	1.0
K_C in Eq. (5)	6.283
total calculation cycles	8

3. 2 Hull pressure coefficient and measurement points of pressure on hull

Pressure on hull surface P^* is obtained as average value at four different moments when roll angular velocity is maximum to remove numerical noise. Measuring points of P^* on hull for different H_0 at OG=0 are shown in Fig. 7.

Hull pressure coefficient C_P is obtained as following

$$C_P = \frac{2P^*}{\rho(r\phi_a\omega)^2}. \qquad (13)$$

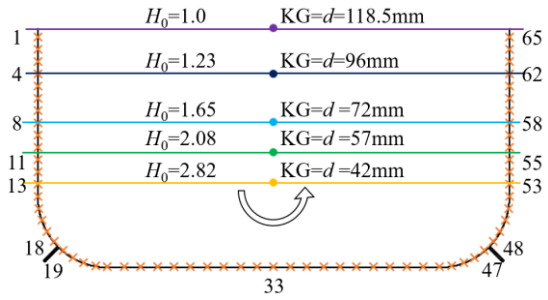

Fig. 7: Measuring points of hull pressure and their number for different H_0.

3. 3 Calculated pressure distribution and velocity

In Fig. 8, the distributions of C_P for H_0= 1.23, 2.08 and 2.82 at OG=0 are shown. The horizontal axis indicates the point number. At H_0=1.23 which is the standard condition of Ikeda's method, C_P^+ of the fore and the aft bilge-keels are almost same, and C_P^- of the fore and the aft bilge-keels are also almost same. However, according to increase in H_0, the difference of C_P^+ and C_P^- of the fore and the aft bilge-keels are larger.

Fig. 9 shows the pressure coefficients C_P^+ and C_P^- on the measuring point number 18, 19, 47 and 48 where are at the root of bilge-keels for different H_0. In this figure, at No. 18 and 19 (the root of the aft bilge-keel), according to increase in H_0, C_P^+ increases and C_P^- decreases. On the other hand, at No. 48 and 49 (the root of the fore bilge-keel), both C_P^+ and C_P^- decrease, according to increase in H_0.

Fig. 10 shows pressure and velocity around bilge-keels for H_0=1.23, 2.08 and 2.82 at the moment when roll angular velocity is maximum. At the aft bilge-keel, according to increase in H_0, the size of vortex shedded by bilge-keel becomes smaller. At the fore bilge-keel, accoding to increase in H_0, the vortex shedded by bilge-keel go farther from hull.

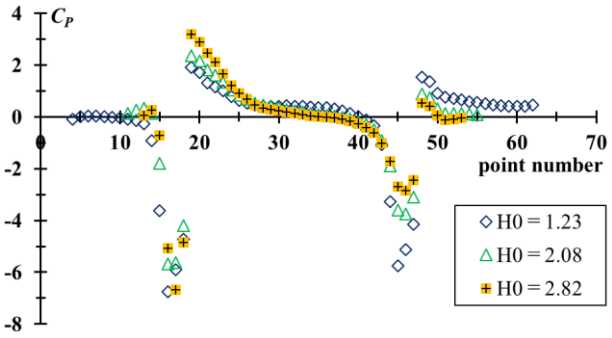

Fig. 8 : Distributions of hull pressure coefficient C_P for H_0=1.23, 2.08 and 2.82.

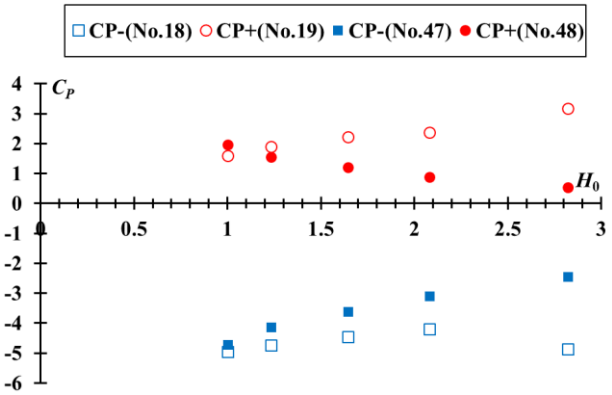

Fig. 9 : C_P^+ and C_P^- at the points where is the root of front and back of bilge-keels for different H_0.

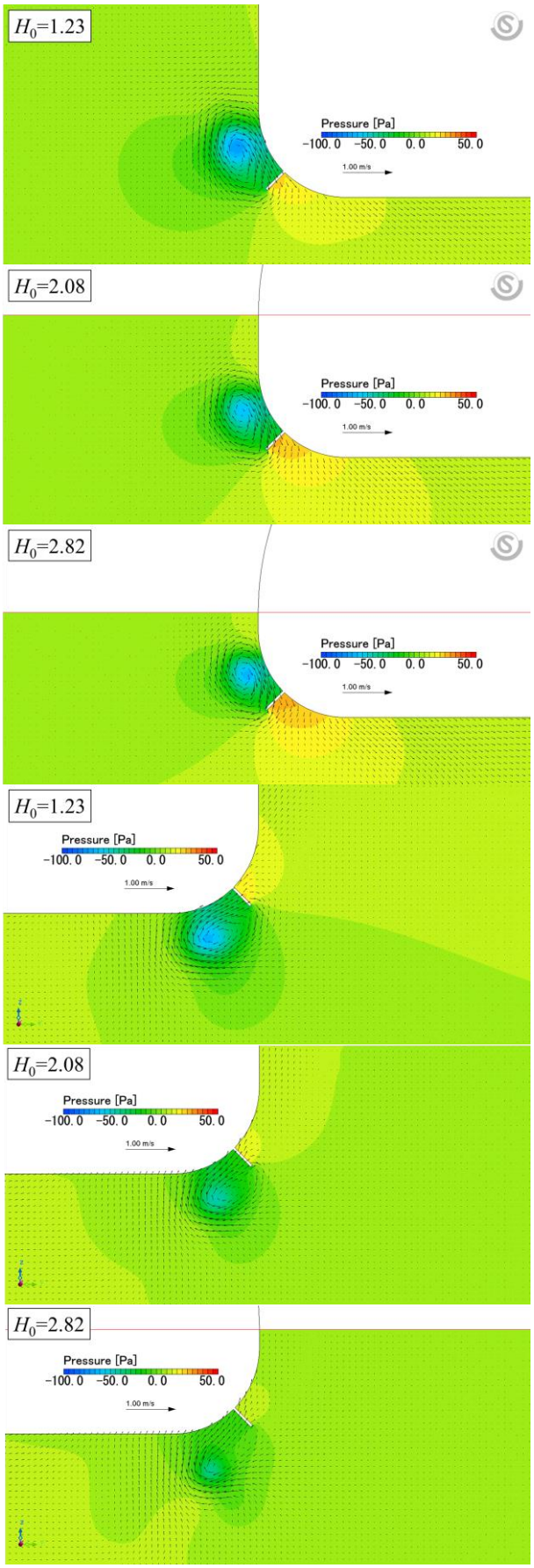

Fig. 10 : Pressure and velocity around bilge-keels for H_0 =1.23, 2.08 and 2.82 (upper: aft bilge-keel, lower: fore bilge-keel). Red line shows the draught line.

3.4 Effects of H_0 on C_P^+ and C_P^-

Fig. 11 shows the ratios of four C_P at the root of bilge-keels for different H_0 to the C_P for H_0=1.23. In this figure, according to increase in H_0, the ratio of C_P^+ for the aft bilge-keel increases, the ratio of C_P^+ for the fore bilge-keel decreases and the ratio of C_P^- for the aft and the fore bilge-keels decrease.

Fig. 12 shows the ratio of the average C_P^+ and C_P^- of for the aft and the fore bilge-keels for different H_0 to those for H_0=1.23. For example, the average C_P^+ means the average value of C_P^+ of the fore bilge-keel and C_P^+ of the aft bilge-keel. In this figure, the ratio of the average C_P^+ is almost constant regardless of H_0, on the other hand, the ratio of the average C_P^- decreases.

From the results, C_P^+ and C_P^- are affected by H_0. To improve the Ikeda's method, it is requierd to consider the effects of H_0 on the four C_P or the two average C_P.

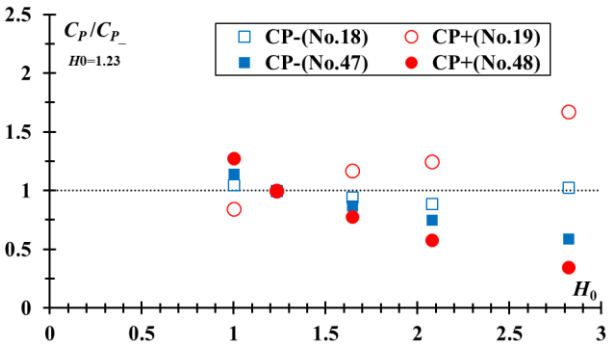

Fig. 11 : Ratio of C_P at the root of bilge-keels to C_P for H_0=1.23.

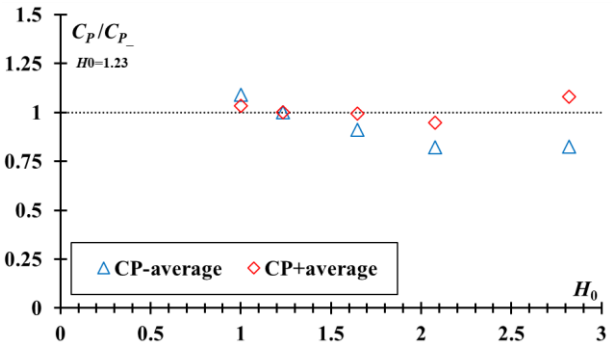

Fig. 12 : Ratio of average C_P of both sides for each H_0 to C_P for H_0=1.23.

4. CONCLUSIONS

In this study, the effects of half breadth to draght ratio H_0 on the pressure distribution on hull caused by bilge-keels are investigated by using CFD to improve Ikeda's method. The following conclusions are obtained.

1) Accoding to increase in H_0, the difference of C_P^+ and C_P^- of the fore and the aft bilge-keels are larger. The C_P^+ at the root of the fore bilge-keel decreases and that at the root of the aft bilge-keel increases. On the other hand, the C_P^- at the root of both bilge-keels decrease.
2) When H_0 changes, The angle of flude inflow to bilge-keel is changed and it affects magnitude of the shedded vortexes by bilge-keels and their directions.
3) The ratio of C_P at the root of bilge-keels for different H_0 to the C_P for H_0 =1.23 which is associated with the target ships which are used when Ikeda's method was developed are obtained. Accoding to increase in H_0, the ratio of C_P^+ for the aft bilge-keel increases and that for the fore bilge-keel decreases. The ratio of C_P^- for the aft and the fore bilge-keels decrease.
4) The ratio of the average C_P^+ is almost constant regardless of H_0, on the other hand, the ratio of average C_P^- decreases.
5) To improve Ikeda's method, it is required to consider the effects of H_0 on the four C_P or the two average C_P.

ACKNOWLEDGEMENT

Part of this research was supported by ClassNK and JSPS KAKENHI Grant Number 21K04502.

REFERENCES

Ikeda, Y., Himeno, Y., Tanaka, N., 1978a, "On roll damping force of ship -effects of friction of hull and normal force of bilge keels", Report of Department of Naval Architecture, University of Osaka Prefecture, No.00401.

Ikeda, Y., Himeno, Y., Tanaka, N., 1978b, "A Prediction method for Ship Roll Damping, Report of Department of Naval Architecture", University of Osaka Prefecture, No.00405.

Katayama, T., Matsuoka, M., Adachi, T., Ikushima, K., 2019, "Effects of half breath to draught ratio of hull under water surface on bilge-keel roll damping component", Ocean Engineering, Vol. 188.

Katayama, T., Adachi, T., Sugimoto, K., Fukumoto, Y., 2020,

"Estimation Method of Bilge-keel Roll Damping Component Applicable for Wide-breadth and Shallow-draught Ship-Effects of Draught, Height of Roll Center and Free Surface on Normal Force on Bilge-keel -", Conference Proceedings of the Japan Society of Naval Architects and Ocean Engineers, Vol. 30, pp. 417-423. (in Japanese)

Katayama, T., Yoshida, N., Yamamoto, Y., 2022, "Effects of Free Surface on Normal Force Component of Bilge-keel Roll Damping and Improvement of Ikeda's method", Proceedings of the 18th International Ship Stability Workshop.

Stability in Waves Committee, 2011, ITTC Recommended Procedure Numerical Estimation Method of Roll Damping, International Towing Tank Conference, 26th ITTC, Report 7.5-02-07-04.5.

Tanaka, N., Himeno, Y., Ikeda, Y., Isomura, K., 1981, "Experimental study on bilge-keel effect for shallow-draft ship", J. Kansai Soc. Nav. Archit. Japan. 180, pp.69–75. (in Japanese)

Experimental investigation of wave excitation roll moment in irregular beam waves

Toru Katayama, *Osaka Metropolitan University,* katayama.marine@omu.ac.jp
Yusuke Yamamoto, *Osaka Metropolitan University,* yamamoto.marine@omu.ac.jp
Atsuo Maki, *Osaka University,* maki@naoe.eng.osaka-u.ac.jp
Kei Sugimoto, *Class NK,* sugimoto@classnk.or.jp

ABSTRACT

In the previous study on short-term prediction of roll in beam sea, the results solved one-degree of non-linear roll motion equation with MSC (Monte Carlo Simulation) are different from the measured results. The primary difference of the results is that the simulated average roll period is shorter than the measured one. In the simulation, the power spectrum of roll excitation moment in irregular waves for fully captive hull is used. Therefore, it is supposed that the peak frequency of power spectrum is affected by sway significantly. The wave excitation roll moment for partly captured hull are measured, and it is confirmed that the measured power spectrum at high frequency range is smaller than one for fully captive hull.

Keywords: *Short-term Prediction, Roll, Wave Excitation Moment, Non-Gaussian Distribution.*

1. INRODUCTION

The current formula to determine the roll angle for structural strength assessment in Class NK's Technical Rule and Guidance gives a value based upon maximum roll amplitude at probability Q=10^{-8} on long term prediction of roll amplitude. The probability Q is defined as the number of encounter waves, which is roughly corresponding to 25years of designed life of a ship divided by 10s of average encounter wave period. The long-term prediction is obtained from combining short-term prediction of roll amplitude and a probability of occurrence of short-term irregular sea in long term. And the short-term prediction is the energy spectrum method based on the principle of linear superposition, which uses roll response function at small wave height and wave spectrum of short-term irregular waves. Additionally, non-linearity of roll is included as some correction coefficients obtained from model experiments and empirical knowledge at the time of development. However, the type of vessels has increased after the time of developed the coefficients, and the coefficients are not always suitable for the newest vessels.

Therefore, the fundamental revision is required, which is not only revision of correction coefficients to apply the present formula to all type vessels in recent years, but also proposal of rational new method to be able to apply to the vessel which will be further diversified in the future.

In our research group, short-term prediction of roll in beam sea has been studying using the non-linear roll motion equation. In the previous study, it is found that the results by Monte Carlo simulation (MCS) method for the non-linear equation differ from the measured results. Its primary difference is that the mean roll period obtained by MCS is different form the measured one. One of reasons is supposed that the power spectrum of excitation roll moment used in MCS is different from one for roll motion measurement, because the power spectrum is measured by fully captive model test.

Then, in this study, the wave excitation roll moment with the partly captured model whose sway (and drift) is free is carried out and the results are compared with the results by the fully captive model test.

2. SUBJECT SHIP

Subject ship is typical large PCC in recent years. Fig.1 shows the body plan of the model, and Table 1 shows its principal particulars. Height of the center of gravity KG and natural roll period T_n are obtained

from an inclining test and a free roll decay test, respectively.

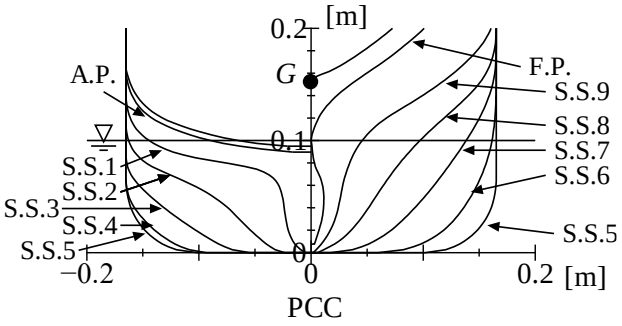

Fig. 1: Body plan of PCC model.

Table 1: Principal particulars of the model PCC.

scale	1/97.5
overall length: L_{OA} [m]	2.054
breadth: B [m]	0.330
depth: D [m]	0.351
draught: d [m]	0.100
ship weight: W [N]	359.46
height of the center of gravity: KG [m]	0.152
metacentric height GM [m]	0.0126
natural roll period: T_n [s]	1.96
position of bilge keels	s.s.3.4 - s.s.5.6.
initial trim [m]: $d_a - d_f$	0
LCG [m] from midship (+ aft)	0.0615

3. WAVE EXCITATION ROLL MOMENT

Wave excitation roll moment acting on the model in irregular beam waves are measured at the towing tank of Osaka Metropolitan University. Fig.2 shows the fully captive model test that the model is mounted under a 3-component load cell. Fig.3 shows the partly captured model test. The load cell mounted on model is attached to the drifting carriage through the device whose heave is free to avoid large heave load.

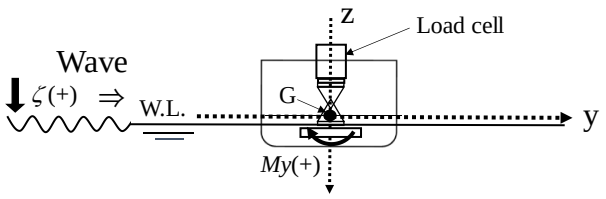

Fig. 2: Schematic view of the wave excitation roll moment measurement with fully captive model.

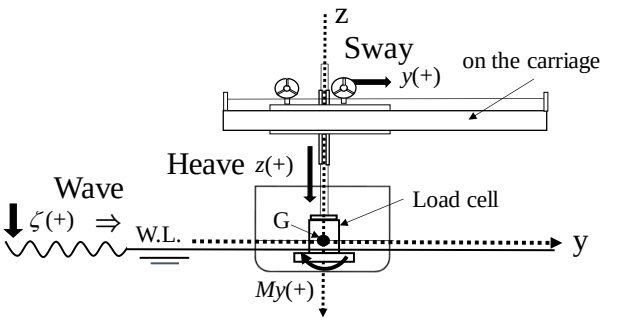

Fig. 3: Schematic view of the wave excitation roll moment measurement with partly captured model whose sway (and drift) and heave are free.

Table 2 shows the condition of measurements. The conditions are same as one for roll measurement in previous study (Katayama et al, 2023). Here, two significant wave heights which do not cause water on deck in model tests are set. Irregular wave spectrum is ISSC spectrum, sampling frequency of measurement is 100 Hz. The number of encounter waves is at least 200 waves each case. To avoid the effects of reflected wave by the end of towing tank, the time of one measurement is about 40 s and the measurement for one wave spectrum is repeated 7 times at the spectrum with different phase differences. The measured wave power spectrums are shown in Fig.4.

Table 2: Wave condition in the tests.

Wave spectrum	ISSC spectrum
Significant wave height: $H_{1/3}$ [m]	0.03, 0.06
Average wave period: T [s]	1.392

Figs.5, 6 show the power spectrum of wave excitation roll moment by the fully captive model test and the partly captured model test. The results by the fully captive model test are the almost same as the results in previous study (Katayama et al, 2023). However, the results by the partly captured model test show higher peak than that by the fully captive model test and its peak frequency is near the peak frequency of the incident wave spectrum shown in Fig.4.

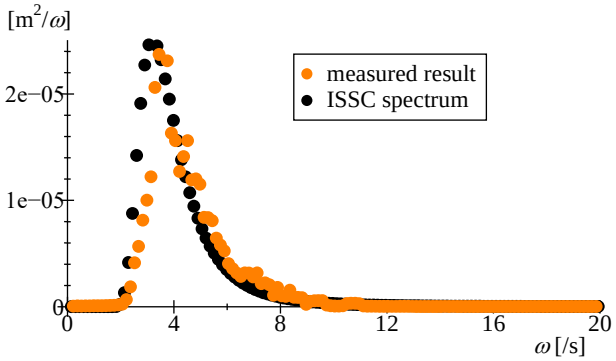

$H_{1/3}$=0.03 m

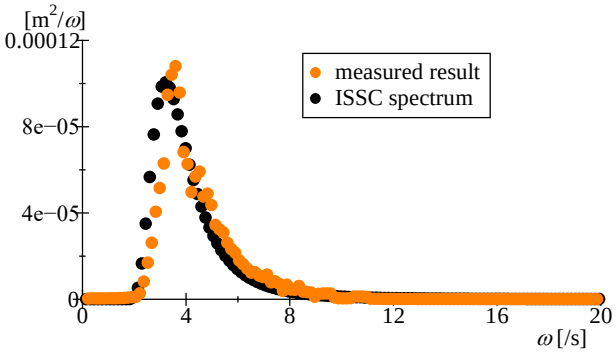

$H_{1/3}$=0.06 m

Fig. 4: Power spectrums of measured and set incident waves.

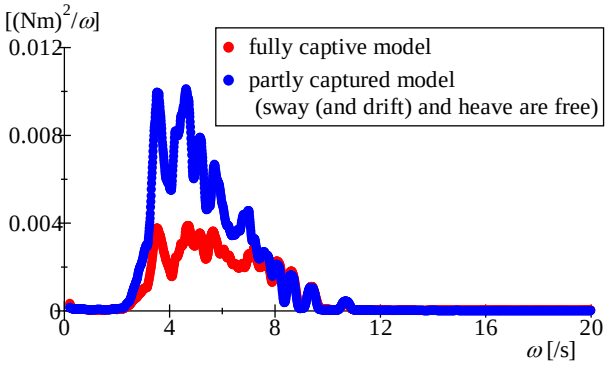

Fig. 5: Power spectrums of measured wave excitation roll moment at $H_{1/3}$= 0.03 m.

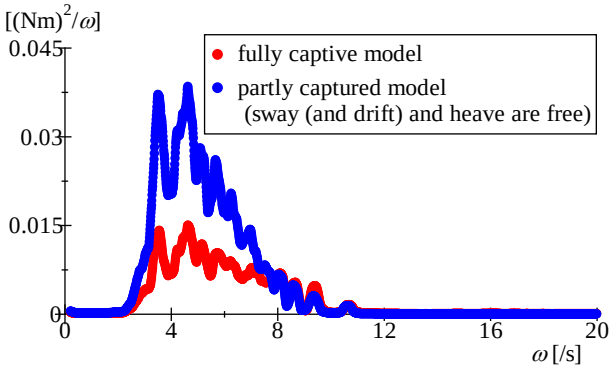

Fig. 6: Power spectrums of measured wave excitation roll moment at $H_{1/3}$= 0.06 m.

4. PROBABILITY DENSITY OF ROLL MOTION

Roll Motion equation

If roll motion can be expressed by a one degree of freedom motion equation, a non-linear roll equation can be given as (Maki, 2017, Maki et al, 2018)

$$\ddot{\phi} + \alpha\dot{\phi} + \beta\dot{\phi}\left|\dot{\phi}\right| + \frac{W}{I_{xx}}\mathrm{GZ}(\phi) = M_{wave}(t)$$
$$\mathrm{GZ}(\phi) = \mathrm{GM}\phi + \mathrm{GZ}_2\phi^2 + \mathrm{GZ}_3\phi^3 + \mathrm{GZ}_4\phi^4 + \mathrm{GZ}_5\phi^5 \quad (1)$$

where t is time, α is liner damping coefficient, β is quadratic damping coefficient, W is ship weight. GZ(ϕ) is lever of roll restoring moment and is indicated as a polynomial expression. $M_{wave}(t)$ is wave excitation moment in irregular waves shown as

$$M_{wave}(t) = \frac{W \cdot \mathrm{GM}}{I_{xx}} \sum_{i=1}^{8000} \gamma_i \ \Theta_i \sin(\omega_i t - \varepsilon_i), \quad (2)$$

where I_{xx} is moment of inertia, γ is effective wave slope and Θ is the maximum wave slope for each wave frequency component. In the calculation, the frequency of the wave spectrum is divided into 8000 components by the same frequency. In this study, γ and Θ are obtained from the measurements of wave excitation roll moment. The maximum wave slopes for frequency components is obtained from the power spectrum of incident waves, and γ that becomes the wave excitation roll moment is obtained using Eq.(2) from the power spectrum of the wave excitation roll moment.

Results of MSC

Figs.7, 8 show probability density of roll motion obtained by MCSs which use the wave excitation roll moments obtained from the fully captive model test and the partly captured model test, respectively. In these figures, the measured roll motion in irregular beam waves are also shown. The results of MCS using the moment by the fully captive model is almost same as the results in previous study (Katayama et al, 2023). On the other hand, the results of MSC using the moment by the partly

captured model test agrees with the measured roll motion.

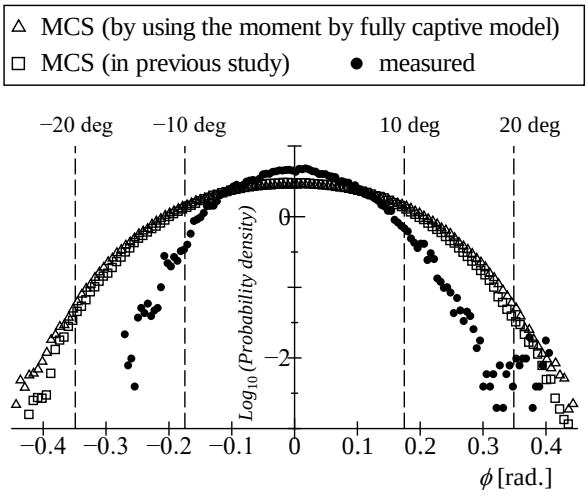

Fig. 7: Probability density of roll angle obtained by MCS using the wave excitation roll moment with the fully captive model.

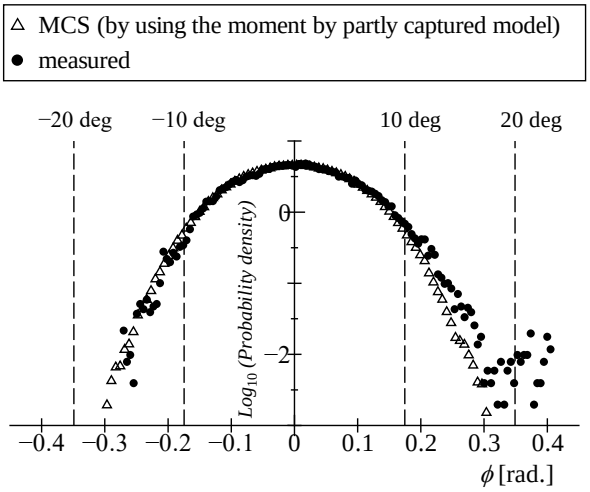

Fig. 8: Probability density of roll angle obtained by MCS using the wave excitation roll moment with the partly captured model whose sway, drift and heave are free.

5. CONCLUTIONS

In this study, it is assumed that the reason of the difference between the results by MCS of the non-linear equation and the measured results of roll motion in previous study is wave excitation moment, and the wave excitation roll moments are measured by two different tests which are the fully captive model test and the partly captured model test (sway, drift and heave free), and the following conclusions are obtained.

1. The power spectrum of the wave excitation roll moment by the partly captured model test has higher peak than that by the partly captured model test and its peak frequency is near the peak frequency of the incident wave spectrum.

2. The MCS using the wave excitation roll moment obtained by the partly captured model test is agreed with the measured results of roll motion.

ACKNOWLEDGEMENT

Part of this research was supported by ClassNK.

REFERENCES

Katayama, T., Kankaku, M., Maki, A., Sugimoto, K., Fukumoto, Y., 2023, “Study on Short-term Prediction of Roll in Beam Sea.”, Contemporary Ideas on Ship Stability: From Dynamics to Criteria edited by Kostas J. Spyrou, Vadim L. Belenky, Toru Katayama, Igor Backalov, Alberto Francescutto, pp. 143-156.

Maki, A., 2017, “Estimation method of the capsizing probability in irregular beam seas using non-Gaussian probability density function”. Journal of Marine Science and Technology, Vol. 22, No. 2, pp.351–360.

Maki, A., Sakai, M. and Umeda, N., 2018, “Estimating a non-Gaussian probability density of the rolling motion in irregular beam seas”, Journal of Marine Science and Technology, doi.org/10.1007/s00773-018-0606-7 (First Online).

Experimental and numerical investigation of viscous effects on parametric roll motion

Hasan Islam Copuroglu, *Karadeniz Technical University - Turkey,* hasancopuroglu@ktu.edu.tr
Emre Pesman, *Karadeniz Technical University - Turkey,* pesman@ktu.edu.tr
Hiroki Morata, *Osaka Metropolitan University - Japan,*
Naofumi Yoshida, *Osaka Metropolitan University - Japan,* sa22743t@st.omu.ac.jp
Yusuke Yamamoto, *Osaka Metropolitan University - Japan,*
Toru Katayama, *Osaka Metropolitan University - Japan,* katayama.marine@omu.ac.jp

ABSTRACT

The chaotic behavior of parametric roll motion is widely known. Briefly, disregarding viscous effects may have an impact on roll amplitudes, particularly around the velocities where bifurcation takes place. In the presented study, experimental, numerical, and analytical analyses are used to examine how the behavior of the ship is altered when viscous effects in parametric roll motion are neglected. In order to compare it with the approximate analytical solution of the 1 DOF nonlinear equation of parametric roll motion, 6 DOF experiments are conducted with constant velocities. While there are viscous effects in the experiments, viscous effects are neglected in the analytical solution since the GZ curves used in the analytical solution are obtained by hydrostatic methods and does not contain viscous effects. Then, various CFD analyses are carried out to determine updated GZ curves, which include viscous effects. So, the updated GZ curves that are obtained from CFD analyses are adapted to the analytical solution, and the results are compared with over the viscous effects.

Keywords: *parametric roll, computational fluid dynamics, viscous effect.*

1. INTRODUCTION

The fact that ships are capsized by parametric resonance in head or following waves has made this previously known physical phenomenon an important issue, especially due to the increase in accidents related to this phenomenon in recent years. Today, this physical phenomenon, which researchers, classification societies and rule-making institutions focus on, has been modeled in different ways and has been a popular subject whose problems are still being tried to be solved. Despite meeting the IMO rules and current IS code established based on static or semi-static stability in calm water, ships can still overturn. In order to develop and renew the existing stability rules, taking into account the nature of the sea and the dynamic responses of the ship, the movement of the ship between the waves must be modeled accurately.

In the 1930s and 1940s, Watanabe (1934) and Kempf (1938) published the first works on parametrically excited roll motion. Numerous scholars have investigated the roll motion of ships in longitudinal waves, including Graff, Heckscher (1941), Kerwin (1955), Paulling, and Rosenberg (1959). Paulling et al. (1972) conducted the first experimental observation of parametric roll in San Francisco Bay. Despite being theoretically possible for a very long time, parametric roll has recently received a lot of attention because of incidents that have caused damage (France et. al., 2003; BSU, 2009). Studies on the Post-Panamax C11 class containership, which suffered significant loss and damage to deck-stowed containers in October 1998, revealed that these ships frequently exhibit parametric roll motion in severe weather (France et. al., 2003). These fatalities prompted further research and investigations from designers, researchers, and regulatory authorities. Researchers Neves and Rodrigues (2006) and Spyrou (2000) as well as Bulian et al. (2004) concentrated on nonlinear features and impacts of modifying tuning variables on parametric roll motion. Additionally, some researchers (Shin et. al., 2004; ABS, 2008; Belenky, 2004; Hashimoto et. al., 2006; Bulian et. al., 2006; Francescutto, 2007) focused on the probabilistic characteristics of parametric roll.

Both numerical and analytical methods have been used in the literature to examine the parametric roll resonance phenomenon. Depending on the application, each approach to a solution has its own benefits. For the solution of coupled motions in the time domain, numerical methods are appropriate. A set of equations for coupled heave, pitch, and roll motion with second- and third-order nonlinearities characterizing the restoring action are analyzed in two dimensions by Neves and Rodriguez (2005). Coupled nonlinear equations of motion in the time domain with 3 and 5 degrees of freedom (DOF) are employed by Levadou and Van't Veer (2006). Analytical techniques, on the other hand, have certain useful advantages, such as the capacity to identify roll amplitudes and bifurcations over the stability threshold. With the quasi-static Froude-Krylov assumption, it is possible to reduce the number of DOF from 3 to 1 using an alternate simplified technique (Bulian, 2004; 2006).

The parametric rolling behavior of ship models in test tanks is successfully reported by Bulian (2008) and Hashimoto (2011).

Numerous research has been conducted recently on the parametric roll phenomena prediction, assessing the possible risk to ships. In a hybrid method developed by Zhou et al. (2015) and according to Zhou (2019), the three-dimensional (3D) CFD methodology is used to determine the roll damping while the potential theory method is used to forecast the parametric roll characteristics. A series of scaled model experiments are carried out by Schumacher et al. (2016) to examine the occurrence of parametric roll for a containership under various wave conditions. A nonlinear time domain model's output is contrasted with the results of an experiment. The relationship between the parametric roll and additional resistance is researched by Lu et al. in 2016. The findings demonstrated that the additional resistance rises with the parametric roll's amplitude. To study the parametric roll of a containership, Liu and Papanikolaou (2016) used a 3D nonlinear time-domain technique based on the impulse response function. Ma et al. (2018) used model testing and numerical predictions to investigate the parametric roll of a containership in regular waves. It is found that the numerical outcomes offer accurate predictions for the parametric roll. A 3D mixed-source coupled three-degree-of-freedom (3DOF) model was used by Bu et al. (2019) to study the parametric roll. The outcomes demonstrated a nonlinear relationship between heeling angles and wave amplitudes. A method to evaluate the susceptibility of a ship's parametric roll in a genuine random seaway is described by Somayajula et al. (2019). An accurate estimate of ship stability is provided using the stochastic averaging technique. Yu et al. (2019) used a 5DOF nonlinear time-domain model to provide parametric roll prediction for a containership. The outcomes shown that the roll damping has an impact on the amplitudes of parametric roll. Acanfora et al. (2020) applied a 6DOF blended nonlinear model to generate the roll motions from irregular waves in the time domain. The findings demonstrated that, similarly to a regular wave, the roll amplitude controls the resonance time in an irregular wave.

In the presented study it is aimed to show viscous effect on parametric roll motion by using different GZ surface approaches. Generally, GZ surfaces related with position of wave crest and heel angle are calculated simply with neglecting viscous effects. GZ values can simply calculated with software based on hydrostatic calculations. However, ships in waves cannot be thought of as static. Ships have motions due to waves and fluid around them. And there is also ship velocity which changes the results.

2. EXPERIMENTAL AND COMPUTATIONAL METHOD

Sample Ship Model and Environmental Conditions

The sample ship used throughout the analysis is of a ro-ro form and its experimental tests are carried out at the towing tank of Osaka Metropolitan University-Japan. The experiments are carried out for 6 DOF. The sample ship has no bilge keels and appendages. The main characteristics of the sample ship, named Model 35, are given in Figure 1 and Table 1, respectively.

Table 1: Main characteristics of the sample ship model

Name	Type	LBP	B	T	KG
Model 35	Ro-Ro	1.12 m	0.24 m	0.059 m	0.107m

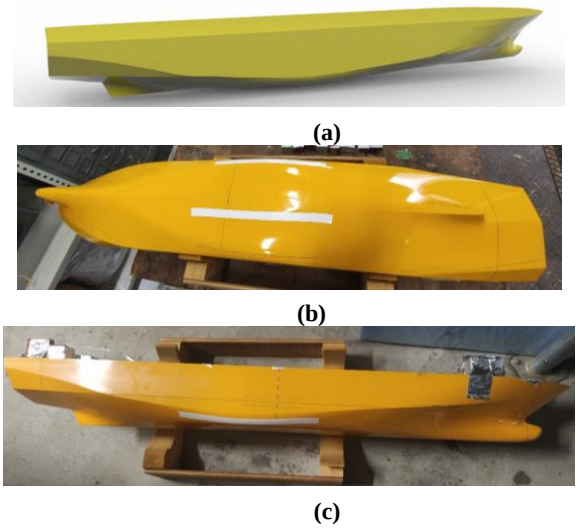

Figure 1: Model 35 (a) solid cad geometry (b) view from the bottom (c) profil view

Experimental Setup

Experiments are carried out in Osaka Metropolitan University, Katayama Laboratory. Model 35 is towed with the capability of 6 Degrees of Freedom (DOF) motions. The model is joined to towing car with ropes. The joint point of the model is on the longitudinal direction line of the gravity center. The model can make roll motion by the capability of joint point hinge on model as shown in Figure 2.

The ship model is pulled with towing car at various constant velocities from 0.3 to 0.55 m/s.The head wave that is used for experiments has $\lambda_W/L_S=1$ and $H_W/\lambda_W=0.38$ values.

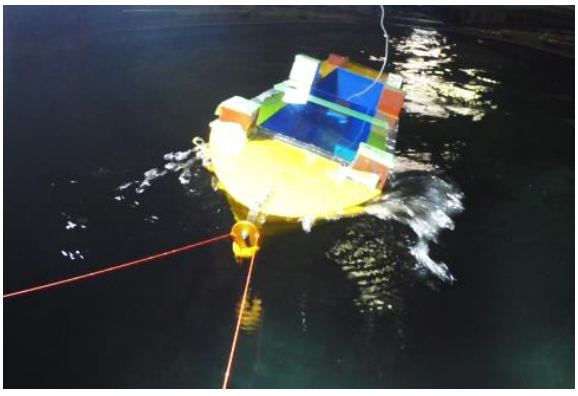

Figure 2: Ropes and joint point of the Model 35 (Model velocity is 0.4 m/s, roll angle is 20º)

The data of ship motions were measured by an accelerometer sensor for 0.01 seconds time steps as shown in Figure 3. Accelerometer was located at gravity center of the model.

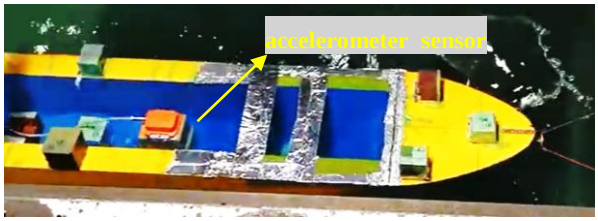

Figure 3: Accelerometer location on ship model

Mathematical Model Set Up

In the presented study simplified version of one degree of freedom (1DOF) nonlinear parametric roll motion equation is utilized (Shin et. al., 2004). The equations that are used for analytical solutions can be seen below.

$$\ddot{\phi} + 2\mu\dot{\phi} + \beta\dot{\phi}|\dot{\phi}| + \delta\dot{\phi}^3 + \frac{{\omega_0}^2}{GM_0} f(\phi, x) = 0 \qquad (1)$$

$$f(\phi, x) = sign(\phi) GZ(|\phi|, x) \qquad (2)$$

$$x = Vt - Lfloor\left(\frac{Vt}{\lambda}\right) \qquad (3)$$

CFD Simulation Setup

In numerical analysis, the same scale (1/50) model is used. GZ surfaces are calculated for different heeling angles The dimensions of the solution volume are taken as the same as the dimensions of the towing tank in which the experiments are carried out. In order to prevent wave reflections, the transverse walls of the model are taken as symmetry. The distances between the model and the wall have been chosen according to the ratio recommended by ITTC (2014b), which will not disturb the flow.

The particle density structure for 0º heeling angle case is represented as adaptive, the particle densities can be seen from different views in the figures below.

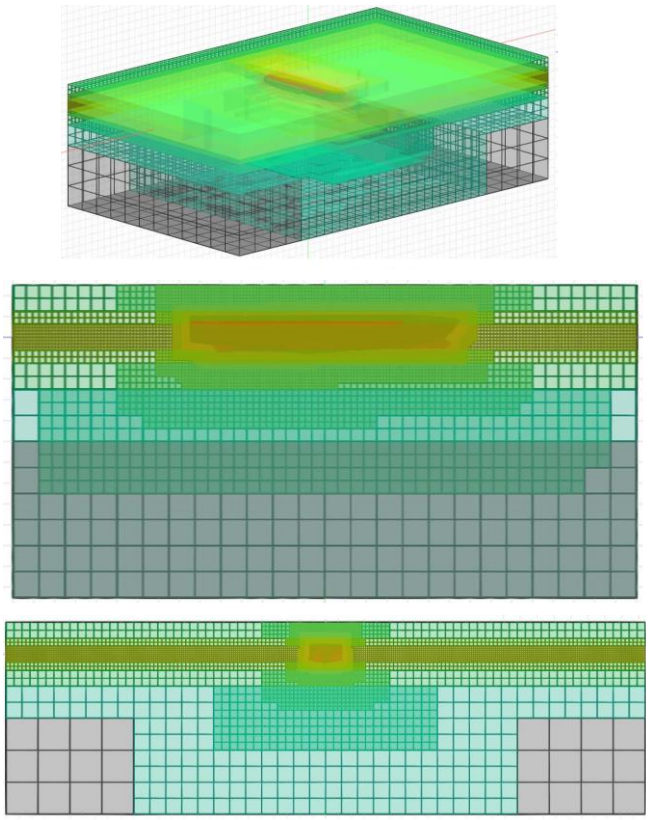

Figure 4: The particle density structure

As can be seen, the particle density increases as getting closer to the ship model. In the relevant simulation model, the minimum particle density (distance between particles) is 0.003 m and the maximum particle density is 0.3 m.

There are initial parameters that need to be addressed for the solution to be carried out correctly. These parameters are summarized in the table below.

Table 2: Parameters used in simulations.

Parameter	Value
Flow Dimension	3D
Turbulance Model	WALE
Cx, Cw	0,5
Gravitational acceleration	9,81 m⁄s^2
Water height (From Base)	1,8 m
Water temperature	288,15 K
Water density	998,3 kg⁄m^3
Wall model	Enhanced Wall-Function
Wall roughness	0 m
Time Step	Fixed Automatic
Courant Number	1

3. RESULTS

The GZ surfaces are found by hydrostatic calculations, poly-cos (polynomial-cosines function) approximation and CFD method. The comparison of the GZ surfaces is given in Figure 4,5 and 6 respectively.

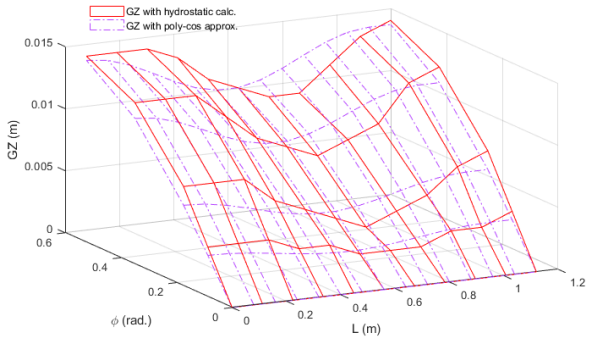

Figure 4: GZ surface comparison of hydrostatic calculations and poly-cos approximation methods

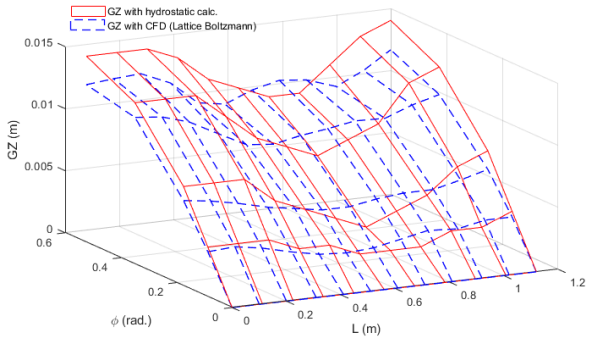

Figure 5: GZ surface comparison of hydrostatic calculations and CFD methods

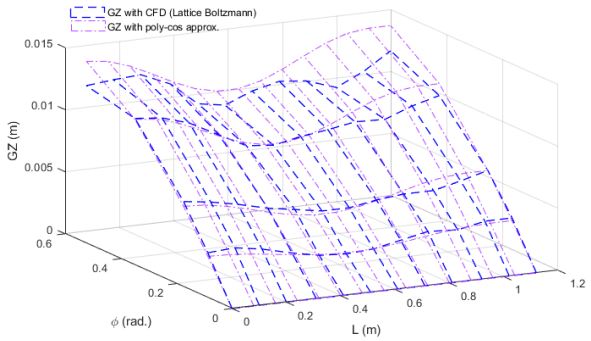

Figure 6: GZ surface comparison of poly-cos approximation and CFD methods

In the figures above, all GZ calculations are shown in comparison with each other. It can be seen

that there is a very significant difference between the results of hydrostatic calculations in which viscous effects are neglected and the GZ surface obtained by using CFD. It is seen that the GZ surface created with the poly-cos functions is in good agreement with the GZ surface obtained with the CFD specific to this study. However, it should be noted that this is an exception.

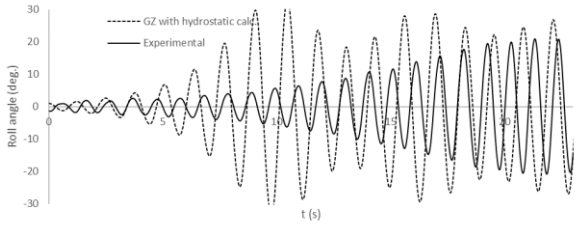

Figure 7: The comparison of roll angle respect to time for GZ that is calculated by hydrostatic calculations and experiments.

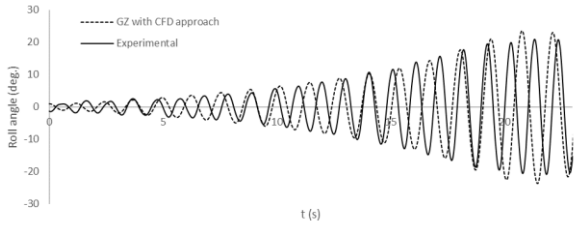

Figure 8: The comparison of roll angle respect to time for GZ that is calculated by CFD method and experiments.

In Figure 7 above, the time dependent roll angle values obtained and the hydrostatic calculation are compared with the experimental results and it can be seen that the results are far from being in agreement. In Figure 8, it is seen that the results of the roll angle obtained using the GZ surface calculated from CFD and the results obtained from the experiment are in good agreement.

Comparisons of roll amplitudes for different GZ approaches are given below.

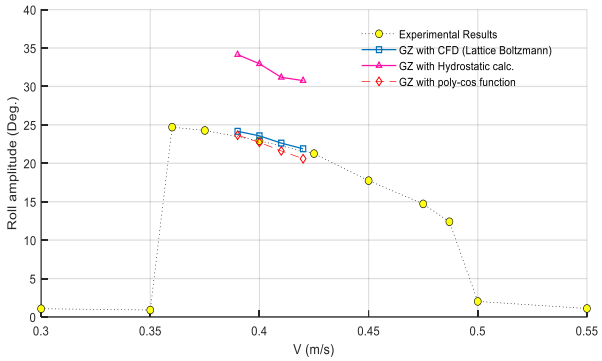

Figure 9: Comparison of roll amplitudes for different GZ approaches

In Figure 9, roll amplitudes around 0.4 m/s are given in comparison with the experimental results depending on the ship speed. As can be seen, the results obtained by the hydrostatic calculation, since the viscous effects are neglected, show that the maximum roll amplitudes are above 30 degrees and are quite different from the data obtained from the experiments. In addition, since the GZ surfaces obtained from CFD and ploy-cos are close to each other, the results are calculated in accordance with the experimental results.

4. CONCLUSIONS

In this study, the difference between the results obtained by including the dynamic and viscous effects depending on the ship speed and the results obtained by using the hydrostatic GZ is examined.

As can be seen from the results, the results obtained for the case where the viscous effects are not neglected are quite close to the experimental results. Since there is no static situation, viscous effects are physically present in natural situations. Due to the effect of viscous effects on energy conservation, results in which the viscous effect is neglected show high roll amplitudes. However, viscous effects reduce the roll amplitudes due to the energy spent.

Not neglecting the viscous effects in the parametric roll analyses will provide a better representation of the real physical problems.

5. ACKNOWLEDGEMENTS

The experimental study in this paper is carried out at Osaka Metropolitan University, Katayama Laboratory.

The authors sincerely thank the above organization and individuals.

REFERENCES

ABS, 2004, "Guide for the assessment of parametric roll resonance in the design of container carriers," American Bureau of Shipping, Houston.

Acanfora, M., Balsamo, F., Lauria, D., & Rizzuto, E. 2020, "A new identification method for non-linear roll resonance in irregular waves," *Ocean Engineering*, 197, 106809.

Belenky, V.L., 2004, "On risk evaluation at extreme seas," In Proceedings of the 7th International Stability Workshop, Shanghai, China, 188-202.

Bulian, G., Francescutto, A., & Lugni, C., 2004, "On the nonlinear modeling of parametric rolling in regular and irregular waves," *International Shipbuilding Progress*, 51, 205-220.

Bulian, G., Francescutto, A., Umeda, N., & Hashimoto, H., 2008, "Qualitative and quantitative characteristics of parametric ship rolling in random waves in the light of physical model experiments," *Ocean Engineering*, 35(17-18), 1661-1675.

Bulian, G., 2004, "Approximate analytical response curve for a parametrically excited highly nonlinear 1-DOF system with an application to ship roll motion prediction," *Nonlinear Analysis: Real World Applications*, 5(4), 725-748.

Bu, S., Gu, M., Lu, J., & Abdel-Maksoud, M., 2019, "Effects of radiation and diffraction forces on the prediction of parametric roll," *Ocean Engineering*, 175, 262-272.

France, W.N., Levaduo, M., Treakle, T.W., Paulling, J.R., Michel, R.K., & Moore, C., 2003, "An investigation of head-sea parametric rolling and its influence on container lashing systems," *Marine Technology*, 40(1), 1-19.

Francescutto, A., 2007, "Intact stability of ships - recent developments and trends," In Proceedings of the 10th International Symposium on Practical Design of Ships and Other Floating Structures (PRADS'07), Vol. 1, Houston, 487-496.

Graff, W., & Heckscher, E., 1941, "Widerstand und Stabilität Versuche mit Drei Fischdampfer Modellen," *Werft Reederei Hafen*, 22, 115-120.

Hashimoto, H., Umeda, N., & Matsuda, A., 2006, "Experimental and numerical study on parametric roll of a Post-Panamax container ship in irregular waves," In Proceedings of STAB'06 9th International Conference on Stability of Ships and Ocean Vehicles, Rio de Janeiro, Brazil, 181-190.

Hashimoto, H., Umeda, N., & Matsuda, A., 2011, "Experimental Study on Parametric Roll of a Post-panamax Containership in Short-Crested Irregular Waves," Springer, Netherlands.

Kempf, G., 1938, "Die Stabilität Beanspruchung der Schiffe Durch Wellen und Schwingungen," *Werft Reederei Hafen*, 19, 200-202.

Kerwin, J.E., 1955, "Note on rolling in longitudinal waves," *International Shipbuilding Progress*, 2(16), 597-614.

Levadou, M., & Van't Veer, R., 2006, "Parametric roll and ship design," In Proceedings of the Ninth International Conference on Stability of Ships and Ocean Vehicles (STAB'06), Vol. 1, 191-206.

Liu, S., & Papanikolaou, A., 2016, "Prediction of parametric rolling of ships in single frequency regular and triple frequency group waves," *Ocean Engineering*, 120, 274-280.

Ma, S., Ge, W., Ertekin, R.C., He, Q., & Duan, W., 2018, "Experimental and numerical investigations of ship parametric rolling in regular head waves," *China Ocean Engineering*, 32(4), 431-442.

Neves, M.A.S., & Rodriguez, C.A., 2005, "A coupled third-order model of roll parametric resonance," In Proceedings of the Maritime Transportation and Exploitation of Ocean and Coastal Resources, London, 243-253.

Neves, M.A.S., & Rodriguez, C.A., 2006, "Influence of non-linearities on the limits of stability of ships rolling in head seas," *Ocean Engineering*, 34, 1618-1630.

Paulling, J.R., & Rosenberg, R.M., 1959, "On unstable ship motions resulting from nonlinear coupling," *Journal of Ship Research*, 3, 36-46.

Paulling, J.R., Kastner, S., & Schaffran, S., 1972, "Experimental Studies of capsizing of intact ships in heavy seas," U.S. Coast Guard Technical Report (also IMO Doc. STAB/7, 1973).

Sakai, M., Umeda, N., & Maki, A., 2019, "Encounter frequency effect on the simplified design criteria against parametric roll," *Ocean Engineering*, 182, 21-2

Schumacher, A., Ribeiro E Silva, S., & Guedes Soares, C., 2016, "Experimental and numerical study of a containership under parametric rolling conditions in waves," *Ocean Engineering*, 124, 385-403.

Somayajula, A., Falzarano, J., & Lutes, L., 2019, "An efficient assessment of vulnerability of a ship to parametric roll in irregular seas using first passage statistics," *Probabilistic Engineering Mechanics*, 58, 102998.

Spyrou, K.J., 2000, "Designing against parametric instability in following seas," *Ocean Engineering*, 27, 625-653.

Yu, L., Ma, N., & Wang, S., 2019, "Parametric roll prediction of the KCS containership in head waves with emphasis on the roll damping and nonlinear restoring moment," *Ocean Engineering*, 188, 106298.

Zhou, Y., 2019, "Further validation study of hybrid prediction method of parametric roll," *Ocean Engineering*, 186,

106103.

Zhou, Y., Ma, N., Lu, J., & Gu, X., 2015, "A study on applicability of CFD approach for predicting ship parametric rolling," In Proceedings of the 12th International Conference on the Stability of Ships and Ocean Vehicles, Glasgow, UK.

Flooding Risk Assessment of Motor Bancas Operating in the Philippines

Dracos Vassalos, *Sharjah Maritime Academy, 180018, Khorfakkan, Sharjah, UAE,* dvassalos@sma.ac.ae
Donald Paterson, *Sharjah Maritime Academy, 180018, Khorfakkan, Sharjah, UAE,* dpaterson@sma.ac.ae
Francesco Mauro, *Sharjah Maritime Academy, 180018, Khorfakkan, Sharjah, UAE,* Francesco.Mauro@sma.ac.ae
Hongseok Bae, *Sharjah Maritime Academy, 180018, Khorfakkan, Sharjah, UAE,* hbae@sma.ac.ae

ABSTRACT

This paper focuses on describing the process of assessing the flooding risk, as well as identifying and implementing cost-effective solutions, for designing new or for retrofitting existing motor bancas, representative of some 10,000 of these boats, serving most of the domestic trade in the Philippines. To this end, the selected design has been subjected to a systematic process of damage stability and flooding risk analysis in order to identify design vulnerabilities, leading to risk estimation in the form of PLL. A number of risk control options have then been identified, enabling a thorough risk assessment and identification of cost-effective RCOs, as well as impact assessment, using IMO risk acceptance criteria as the basis and the metric of Potential Loss of Life, facilitating estimation. The process of risk analysis and risk assessment is then detailed, the latter providing a cost-benefit assessment to aid decision-making in the RCOs selection, practical implementation, and impact.

Keywords: *Motor bancas, Philippines, Damage stability, Time to capsize, Flooding Risk Assessment, RCOs, Recommendations*

1. INTRODUCTION

One way of ensuring that action is taken before a disaster occurred is to use a process known as a formal safety assessment (FSA, MSC-MEPC.2/Circ.12/Rev.2.). This has been described as "a rational and systematic process for assessing the risks associated with shipping activity and for evaluating the costs and benefits of IMO's options for reducing these risks.". Such options have invariably been extended to other stakeholders (Flags, Administrations, Class, Shipyards and Ship operators), aiming at identifying cost-effective solutions to improve the safety standards of existing ships and new buildings. As the nature of this undertaking is highly technical, it is vitally important that the proposed solutions in the form of recommendations are properly communicated to ensure that all stakeholders gain sufficient information at a level that is readily understood to support effective decision-making (Vassalos et al., 2022a). One way to achieve this is by comparing proposed changes with existing standards, targeting life-cycle implications (design, operation, emergencies) to enable a balance to be drawn between technical and operational issues, including the human element as well as between safety (Delta Risk) and cost (Delta cost) in the implementation of the proposed recommendations (Goerlandt, F. & Montewka, J., 2015, Puisa et al., 2021).

This paper focuses on describing the process of assessing the risk (Aven, 2012, 2022), as well as identifying and implementing cost-effective solutions for the design of new ships or for retrofitting existing ships (Vassalos et al., 2021,2022b) to achieve higher safety standards with a focus on the highest risk contributor, as previously identified, namely inadequate damage stability and the ensuing risk to human life (Vassalos et al., 2019).

To this end, following a ship selection process of representative ships from the whole fleet currently engaged in domestic voyages in the Philippines, three ships have been selected, namely (a) a small motor banca; (b) a medium-sized modern RoPax and (c) a large older design RoPax. In this paper, only the first category is being addressed. The process of risk analysis and risk assessment is detailed, the latter

providing a cost-benefit assessment to aid decision-making in the Risk Control Options (RCOs) selection, practical implementation, and impact.

2. ADOPTED METHODOLOGY FOR FLOODING RISK ESTIMATION

2.1 Survivability Assessment

The methodology adopted in the FSA Philippines project, has been tailored to cater for flooding risk estimation (using different risk metrics), pertinent to static assessment and statutory requirements, leading to risk-informed performance in relevant conditions and environments. This, in turn, facilitates the design and implementation of pertinent RCOs to prevent, mitigate and control flooding risk in domestic passenger ships and is comprised of eight distinct phases, as elaborated in the following and shown in Figure 1. The process begins by addressing damage stability assessment based upon conventional hydrostatic techniques (Bulian et al., 2016, Ruponen et al., 2018, Mauro & Vassalos, 2022). Such assessment is conducted in accordance with applicable IMO statutory instruments, which vary depending on vessel age, type, and size. When assessing new build vessels engaged in international voyage, this relates to the requirements of either SOLAS 2009 (IMO, 2009) or SOLAS 2020 (IMO, 2020), as applicable. This form of assessment enables a quantifiable baseline risk level to be established from which the impact of RCOs can then be measured and compared (Vassalos et al., 2022b). Unfortunately, a great deal of existing ships and domestic vessels are regulated based on older prescriptive regimes, with an implicit but not explicitly quantifiable safety level. This is by using the Index of Subdivision (A-Index) as the risk metric to facilitate comparisons in the attained "risk" level and for evaluation of various design options to enhance ship damage stability. This means that the choice of risk control options is somewhat shaped by the elements of assumption, generalisation and simplification that are commonplace within technical standards.

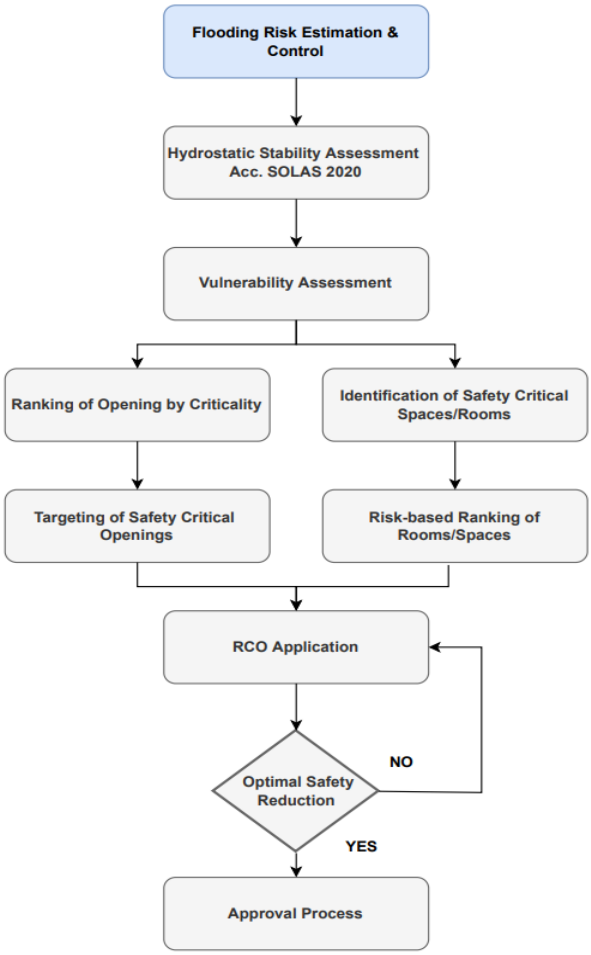

Figure 1: Methodology Adopted

3. RISK ASSESSMENT

3.1 General Considerations

Building upon the developments in risk models over the past 30 years, a generic risk quantification process and modelling is presented in this section, geared towards domestic passenger ships operating in the Philippines. In this respect, a generalised way of considering flooding risk in the form of PLL_A (Attained Potential Loss of Life) is given in equations (1) (Vassalos et al. 2023) with a detailed description in Figure 2.

$$PLL = Probability \times Consequences \quad (1)$$

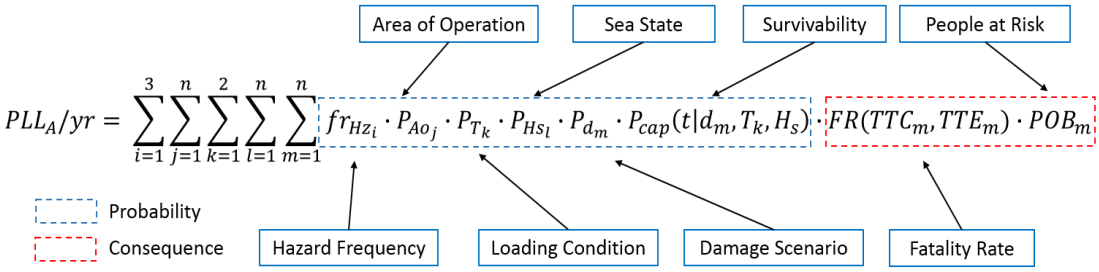

Figure 2: Description of Risk Estimation (PLL) Components

3.2 Flooding Risk Quantification – Input Data and Parameters

3.2.1 Sample ships – Initial ship data and preliminary analysis

The first item considered in analysing domestic passenger fleet data pertaining to the Philippines, has been to observe the fleet demographics in terms of ship type and age, as shown in Figure 3.

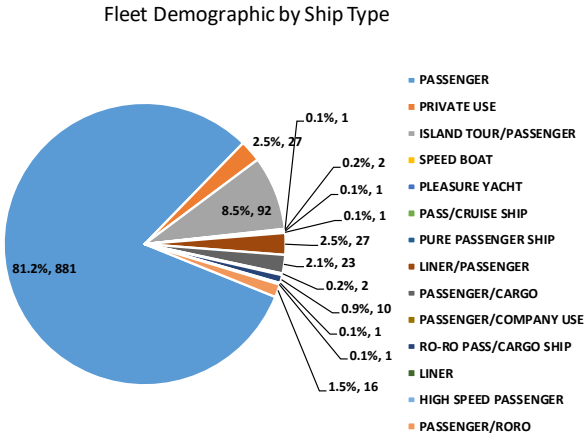

Figure 3: Ship Demographics by Ship Type and Ship Age

Here, the following key observations can be made:

- 93% of the fleet is less than 100 GT;
- 98% of the fleet is less than 1,000 GT;
- 37% of the fleet is less than 10 m length;
- 83% of the fleet is less than 20 m length.

In addition, the domestic passenger vessel fleet has also been analysed in terms of PAX capacity, Gross Tonnage and Length, as shown in Figure 4, Figure 5 and Figure 6.

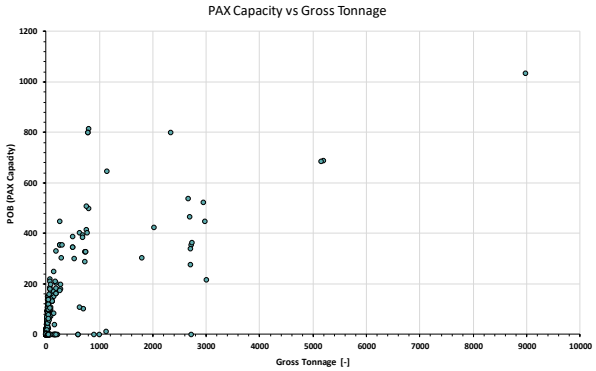

Figure 4: Fleet at Risk – PAX capacity Vs Gross Tonnage

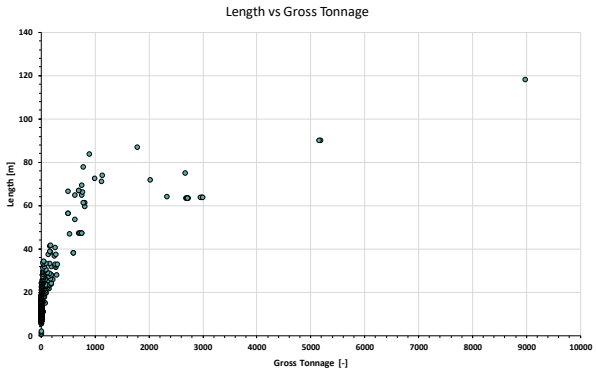

Figure 5: Fleet at Risk – Length Vs Gross Tonnage

3.2.2 Sample ships selection

Figure 6 (Pax Capacity Vs Length) outlines the vessels selected for the FSA study, representing the full size-range, on the basis of which quantitative risk assessment has been undertaken, in particular damage stability calculations and risk analysis in the FSA study. The red markers in the figure are the ships selected in order to provide a representative picture of the whole range of vessels comprising the fleet at risk. This, in turn, supports the argument that a weighted (based on the number of ships in each of the four selected bands) risk evaluation will suitably represent the whole fleet at risk.

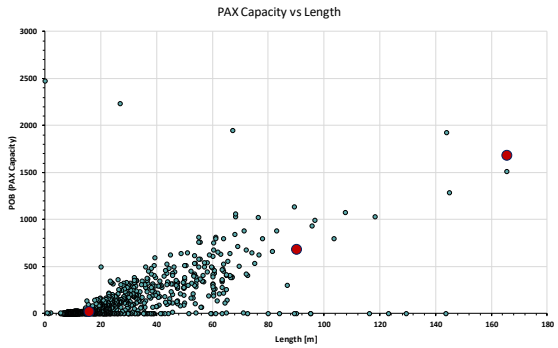

Figure 6: Vessel selection for the FSA study

Table 1: Representative ships and associated characteristics selected for the FSA study.

Name	Service	Homeport	Registry	Build Yr.	Rig	Hull	Length	Breadth	GRT	
Kate Alleson	Passenger	Surigao City	Surigao City	2019	MBCA	WOOD	15.75	1.24	3.86	2
Starlite Venus	Passenger	Batangas	Batangas	2020	MV	STEEL	90.11	16.3	1616	6
ST. POPE JOHN PAUL II	PASSENGER/CARGO	MANILA	CEBU	1984	MV	STEEL	165.31	26.8	19317	1

3.3 Frequency estimation of a loss scenario

1. Hazard frequency: This needs to be ship and area specific as well as hazard specific. In the absence of all the requisite information, we take frequencies from the database pertaining to each hazard in question (collision, bottom grounding, side grounding).

Table 2: Hazard frequencies for the domestic ferries in the Philippines

Hazard type	Domestic Ferries in the Philippines	
	Frequency 1/ship year	
	Motor Banca	RoPax
Collision	**4.55E-04**	**1.68E-03**

2. Scenario frequency: This is the frequency of a given scenario occurring, conditional on the hazard being addressed, as defined by the p-factor. The product of 1 and 2 gives the frequency of the loss scenario being considered.
3. PLL calculation: Ship level PLL can be calculated by substituting scenario specific 1-s values, with the compliment of the Attained Index as an estimation of capsize probability.

3.4 PLL_A Quantification

3.4.1 Consequence estimation of a loss scenario

As the expected number of fatalities depends on the time to capsize and static analysis does not account for time, some approximation is called for to estimate the fatality rate. This is conditional on fast or slow capsize and assumptions relating to the percentage of passengers lost. To simplify the methodology and to account for the dependencies between survivability and fatality rate, the following simplifying assumptions are made (based on work performed in Project FLARE), Eq. (3) and Eq. (4):

If 0 < s-factor <1 → Fatality rate = 5% (3)

If s-factor = 0 → Fatality rate= 80% (4)

This simple and conservative approach is in line with the method used in the EMSA III Project and for the development of SOLAS2020. Moreover, research in Project FLARE (Cardinale, 2022) indicated that collated information from time-domain simulations on cruise and RoPax vessels that the majority of damage scenarios in a survivability assessment are transient capsize cases, in which case no time for evacuation is available (on average 5 minutes for RoPax). In the absence of other evidence, it is assumed that for domestic ferries this value also applies (potentially even less time will be available).

3.4.2 Main assumptions and considerations

Drawing from Eq. (1), the following main assumptions are made for risk estimation:

i	Only collision is considered (1=collision)
j	Area of operation is considered with Hs=4 m, as per SOLAS
k	Three loading conditions are accounted for
$FR(s)$	Fatality Rate as a function of s-factor according to eq. (4) and eq. (5)
POB	Persons on board (people at risk) according for the operational profile of each selected vessel
$PLL_{A/yr}$	Attained Potential Loss of Life per year of exposure.

On the basis of the above, Eq. (1), with all the variables set to unit values, i.e., PLL for collision, per loading condition and scenario, becomes:

$$\frac{PLL_A}{yr} = hazard fequency \; x \; scenario \; frequency \; x \; capzize \; probability \; x \; fatality \; rate \; x \; PoB \quad (2)$$

Where,

- Hazard frequency for domestic ferries in the Philippines (Table 2).

- Scenario frequency is the p-factor corresponding to the breach being examined (damage scenario)
- Capsize probability is the complement of the scenario s-factor, i.e., (1-s)
- SOLAS breach distribution for collision
- Calculations by software NAPA rel.2020.2

4. CASE STUDY NO.2 – SMALL MOTOR BANCA VESSEL

4.1 Vessel Principal Particulars

The vessel principal particulars are outlined in Table 3. Here, it can be observed that the vessel is a small traditional Motor Banca, with a length of approximately 16 m and a capacity of 24 persons.

Table 3: Vessel Particulars

Property	Value
Length O.A. [m]	15.75
Length B.P. [m]	15.75
Breadth Mld. [m]	1.94
Depth Mld. [m]	1.8
GT [-]	15.89
NT [-]	6.89
Pax Capacity	24

4.2 Coordinate System

A right-handed coordinate system has been used in defining the vessel stability model. The origin is located at frame #0, and locations in the ship are designated in accordance with a Cartesian coordinate system, where the axes are placed as follows:

- X-axis: longitudinal coordinate, positive in the direction of the bow, zero at frame #0,
- Y-axis: transverse coordinate, positive direction to port side, zero at the centre line,
- Z-axis: vertical coordinate, positive upwards, zero at the baseline.

In addition, trim is positive to stern and negative to bow. The heeling angle is positive when the vessel heels to the port side.

4.3 Stability Model

The ship model used in the damage stability calculations has been defined from the baseline to the upper extremity of the primary hull. The resultant calculation sections of the model are shown in Figure 7 below, with the profile and body plan illustrated in Figure 8, and the General Arrangement plan in Figure 9.

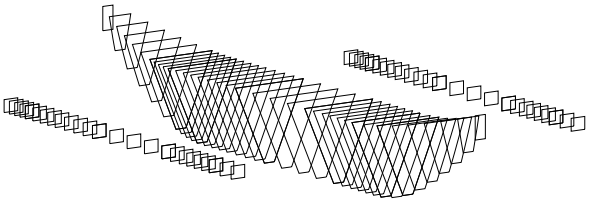

Figure 7: Vessel Calculation Sections

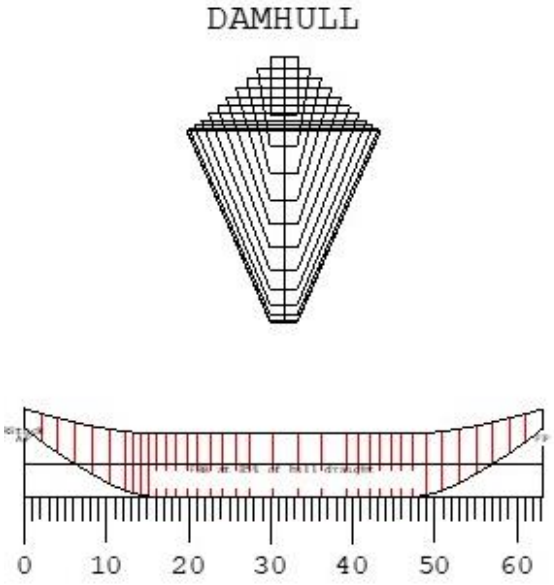

Figure 8: Vessel Body Plan & Profile

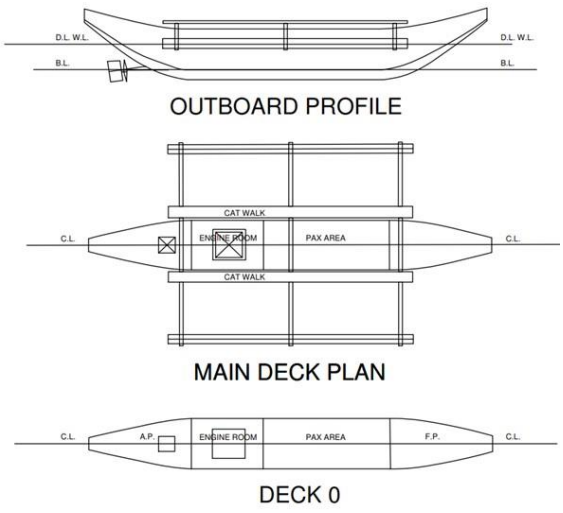

Figure 9: Vessel General Arrangement Plan

4.4 Relevant Openings

A list of all relevant openings considered within the damage stability calculations is presented in Table 4, indicating:

- **ID**: identification code used within NAPA model,
- **Description**: outline of opening purpose,
- **Type**: opening watertight rating,
- **Frame**: opening location relative to frame scale,
- **X**: x-coordinate of opening from frame zero (m),
- **Y**: y-coordinate of opening from vessel centreline (m),
- **Z**: z-coordinate of opening from vessel baseline (m),
- **Connection**: spaces linked by respective openings.

Table 4: Relevant Openings

ID	Type [-]	FR + Dist.	X [m]	Y [m]	Z [m]	Connected Rooms
OPE1	Hatch	#11-0.010	2.74	0.31	2.05	R001 SEA
OPE2	Hatch	#11-0.040	2.71	-0.31	2.05	R001 SEA
OPE3	Hatch	#20-0.120	4.88	0.6	1.94	R002 SEA
OPE4	Hatch	#20-0.120	4.88	-0.6	1.94	R002 SEA
OPE5	Unprotected Opening	#27+0.100	6.85	0.37	1.94	R003 SEA
OPE6	Unprotected Opening	#47+0.050	11.8	0.37	1.94	R003 SEA
OPE7	Unprotected Opening	#27+0.100	6.85	-0.37	1.94	R003 SEA
OPE8	Unprotected Opening	#47+0.050	11.8	-0.37	1.94	R003 SEA

4.5 Subdivision Arrangement

In the calculation of the Attained Subdivision Index, the vessel subdivision has been discretised into 6 zones as illustrated in Figure 10.

Note: Though not apparent within the diagram, the vessel outriggers have been considered within the zonal discretisation.

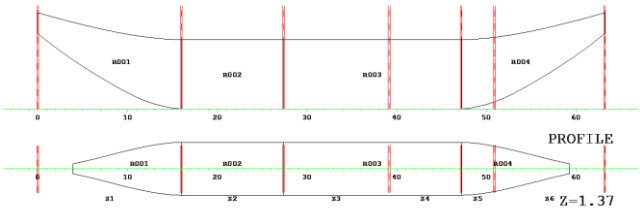

Figure10: Subdivision Arrangement Plan

4.6 Permeabilities

The permeabilities used in the damage stability calculations are summarised in the tables below, in accordance with the SOLAS 2020 prescribed values:

Table 5: Category-specific Compartment Permeabilities

Space Category	Permeability
Appropriated to stores	0.60
Occupied by accommodation	0.95
Occupied by machinery	0.85
Intended for liquids	0.95
Void spaces	0.95

4.7 Compartment and Tank Volumes

The following table outlines the vessel compartment/tank volumes, permeabilities, and centres of gravity, in accordance with space category.

Table 6: Compartment and Tank Properties

Purpose	Description	Volume	Perm	CGX	CGY	CGZ
		m3	[-]	m	m	m
VOID	Void Sp.	22.6	0.95	8.58	0	1.342
MMA	Machinery Sp.	6.2	0.8	5.425	0	1.21
TOTAL		28.7	[-]	7.901	0	1.313
Name	**Description**	**Volume**	**Perm**	**CGX**	**CGY**	**CGZ**
		m3	[-]	m	m	m
		Void Space				
R001	Aft Peak	4.8	0.35	2.616	0	1.484
R003	Pax Space	10.7	0.95	9.325	0	1.21
R004	Fore Peak	4.8	0.35	13.184	0	1.484
ORS2	Void	0.3	0.95	5.425	-5	1.36
ORS3	Void	0.3	0.95	8.32	-5	1.36
ORS4	Void	0.2	0.95	10.795	-5	1.36
ORS5	Void	0.1	0.95	12.265	-5	1.36
ORP1	Void	0.1	0.95	3.55	5	1.36
ORP2	Void	0.3	0.95	5.425	5	1.36
ORP3	Void	0.3	0.95	8.32	5	1.36
ORP4	Void	0.2	0.95	10.795	5	1.36
ORP5	Void	0.1	0.95	12.265	5	1.36
ORS1	Void	0.1	0.95	3.55	-5	1.36
		Machinery Sp.				
R002	Engine Space	6.2	0.85	5.425	0	1.21

4.8 Moments Due to Wind and Passenger Crowding

4.8.1 Wind Induced Moment

The projected windage area of the vessel and corresponding moment lever are shown in Figure 10. The wind induced heeling moment regarded in the damage stability calculations is calculated with the following formula:

$$\boldsymbol{M_{wind} = (P \cdot A \cdot Z)/9.806\ (tm)}$$

Where,

P = 120 (N/m^2)

A = Windage area (m^2), measured in accordance with the projected lateral area relating to each calculation draft.

Z = Distance from T/2 to the centroid of windage area (m)

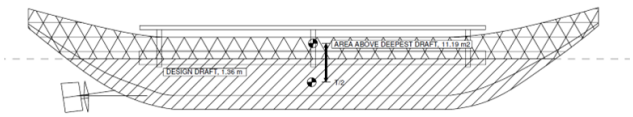

Figure 11: Wind Profile

4.8.2 Moment Resulting from Passenger Crowding

The moment resulting from passenger crowding has been calculated in accordance with the maximum passenger capacity of the vessel (24 persons). A conservative transverse lever of B/2 (0.97 m) from the centreline has been assumed and the weight attributed to each passenger is 75 Kg.

Moment by crowding of passengers = 1.746 tm

4.9 Required Subdivision Index R

The vessel's Required Subdivision Index has been calculated as 0.722.

4.10 Attained Subdivision Index Calculation under Operational GM Conditions

An initial damage stability assessment has been conducted on the vessel in the as-built condition. The results of this analysis are presented in the tables below, indicating an Attained Index of 0.6741, or in other terms, a survival probability of 67.41%. Based on current SOLAS standards, the vessel fails to comply by some margin, demonstrating a less than 1-compartment damage standard. Clearly some measures need to be taken if such vessels were to be operated safely.

Table 6: Attained Subdivision Index Calculation – As-Built Operational GM Conditions

Initial Condition	T [m]	TR [m]	GM [m]	A/R	COEF	A*COEF
DL	1.345	-0.100	12.242	0.997	0.200	0.144
DP	1.354	0.000	12.024	0.944	0.400	0.273
DS	1.360	0.000	11.857	0.892	0.400	0.257
Attained Subdivision Index A						0.6741
Required Subdivision Index R						0.722

Following this, the Risk Profile has been calculated with the aim to identify areas of heightened vulnerability within the vessel, as shown in Figure12. Here it can be observed that there is a concentration of vulnerable areas towards amidships, where larger compartment volumes are present. Furthermore, the predominant risk can be seen as resulting predominantly from 2-compartment damage scenarios.

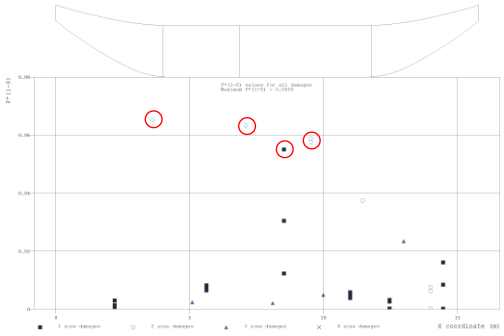

Figure 12: Vessel Risk Profile Under Operational GM Conditions (High risk shown in red)

4.11 RCO 1 – Increased Outrigger Volume

4.11.1 Description of RCO

The first RCO considered, has been to examine the potential benefit of increasing the volume of the vessel outriggers. The impetus behind exploring this RCO has been to provide the vessel with both a larger GM (intact and damaged), whilst at the same time offering additional reserve buoyancy in the damaged condition. In order to ascertain the optimal configuration, a form of sensitivity analysis has been undertaken, in which varying degrees of increased outrigger volume have been assessed. When scaling the outriggers, a ratio of 1:2 in beam to height has been adhered to and the lower extremity of the outrigger has been fixed, i.e., the draft of the outrigger has been kept constant. In relation to the former, a greater degree of vertical scaling has been favoured in order to provide reserve buoyancy, that will come into effect when the vessel is inclined. Furthermore, having vertically distributed reserve buoyancy will work to prevent the vessel from being too stiff, and thus uncomfortable to passengers. However, some degree of transverse scaling has also been considered as this increases the waterplane inertia and thus GM. The lower extremity of the outriggers has been kept constant again as a means of enhancing reserve buoyancy, with the majority of the added volume lying above the waterline. This also reduces the degree to which the resistance properties of the vessel will be impacted, as the immersed hull form is only marginally affected. Figure 13 below, provides an illustration of the scaling process that has been employed.

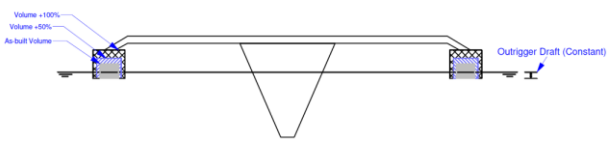

Figure 13: Outrigger volumetric increase diagram

4.11.2 RCO Impact on Intact GM & Attained Subdivision Index

The impact of RCO 1 has first been measured in terms of increased initial GM. The results of this analysis are presented in Figure 14, where a linear relationship between increased initial GM and outrigger volume can be observed. The reason for this primarily comes as a result of increased volume within the outriggers, which increases waterplane area inertia and also results in a greater transverse shift in the centre of buoyancy outwards (increased metacentric radius), both of which act to increase GM.

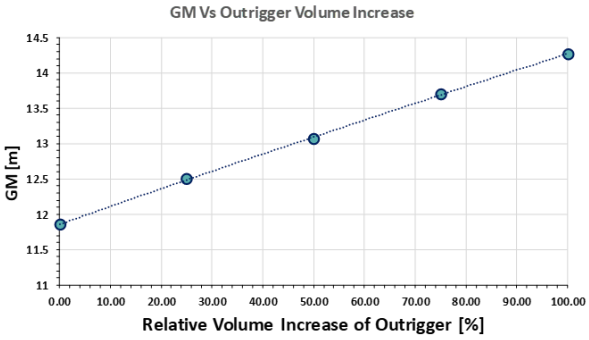

Figure 14: Impact of Outrigger Volume Increase on Vessel Intact GM

In addition to alterations in GM, and perhaps more importantly, variations in the vessel Attained Subdivision Index have also been evaluated. The aim here has been to identify the optimal increase in volume relative to enhanced survivability. This is identified as the point of diminishing returns in the relationship between the Attained Subdivision Index and outrigger volume, as shown in Figure 15. Here, an optimum volume increase of approximately 75% can be identified, leading to an Attained Index of 0.7988, which is SOLAS 2020 compliant.

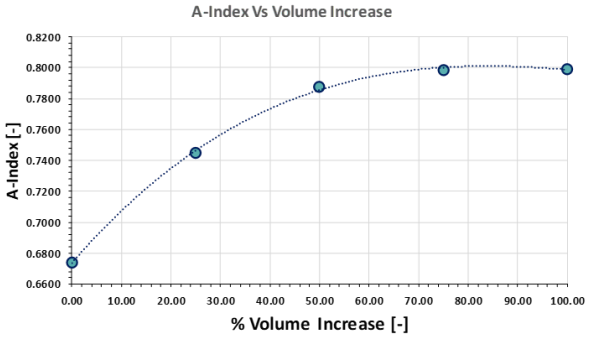

Figure 15: Impact of Outrigger Volume on Attained Subdivision Index

Table 7: Optimum Outrigger Volume

Outrigger Volume Increase (%)	A
0.00	0.6741
25.00	0.7450
50.00	0.7876
75.00	0.7988
100.00	0.7990

4.12 RCO 2 – Reduction in Outrigger Beam

4.12.1 Description of RCO

A further assessment has been conducted examining the potential to reduce the outrigger beam offset. The motivation behind such an assessment relates to reducing vessel susceptibility to damage, whilst also improving the operability of the vessel in relation to its size. To this end, a further sensitivity analysis has been conducted in which varying degrees of outrigger offset have been explored and the impact on Attained Index measured. The results of this process are presented in Figure 16 and Table 7, where an outrigger beam reduction of at least 0.75m is achievable, without significantly impacting the Attained Index.

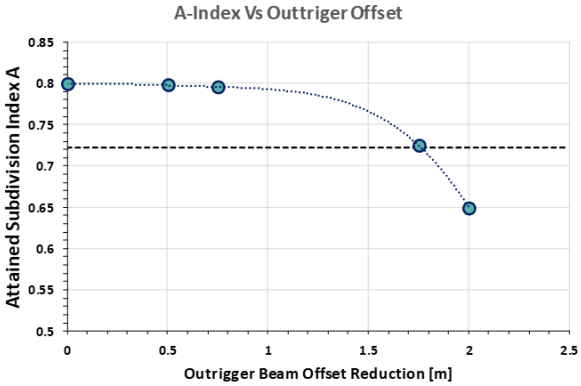

Figure 16: Attained Subdivision Index Sensitivity to Outrigger Beam Offset

Table 7: Impact of Outrigger Offset on Attained Subdivision Index

Outrigger Beam Offset Reduction [m]	A-Index
0.00	0.79909
0.50	0.79749
0.75	0.79564
1.75	0.72499
2.00	0.64937

4.13 RCO 3 – Passive foam installations

4.13.1 Description of RCO

Passive foam installation has been identified as the most efficient and cost-effective RCO during the EC-funded project FLARE and has again been

considered in this instance. Unfortunately, the highest risk areas within the vessel are the passenger seating area and engine room, where it would not be possible to install foam. However, both the fore and aft peak voids and the outriggers have been targeted, as shown in Figure 16. This protects all the most exposed areas of the vessel, and although the high-risk spaces could not be targeted for foam application directly, the fore and aft peak voids, in addition to the outriggers, will now be able to provide additional buoyancy in cases where multiple compartments are breached.

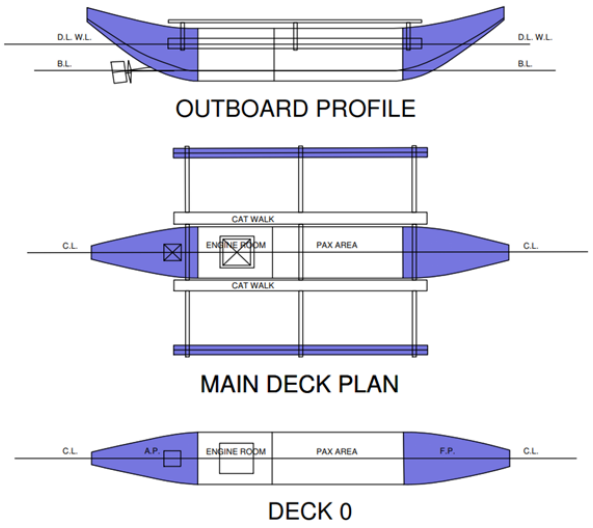

Figure 16: Foam Installation Locations (10m^3 foam volume)

4.13.2 Re-evaluation of Attained Subdivision Index

Having implemented the foam solution in addition to the proposed outrigger modifications, the vessel Attained Index has once again been calculated. The results of this process are provided within Table 8, where it can be observed that an Attained Index value of 0.874 has been achieved, which greatly surpasses the SOLAS 2020 requirement of 0.722.

Table 8: Updated Attained Index Calculation - Passive Foam & Outrigger Modifications

Initial Condition	T [m]	TR [m]	GM [m]	A/R	COEF	A*COEF
DL	1.345	-0.1	14.741	1.258	0.2	0.182
DP	1.354	0	14.473	1.99	0.4	0.346
DS	1.36	0	14.273	1.99	0.4	0.346
Attained Subdivision Index A						0.874
Required Subdivision Index R						0.722

4.13.3 Re-evaluation of the Risk Profile

The updated risk profile of the vessel has been produced following the RCO implementation and is provided within Figure 17. Here, it is evident that the RCOs have worked to eradicate the majority of the flooding risk within the vessel design, with only a single damage scenario presenting significant risk when the two midships compartments are breached.

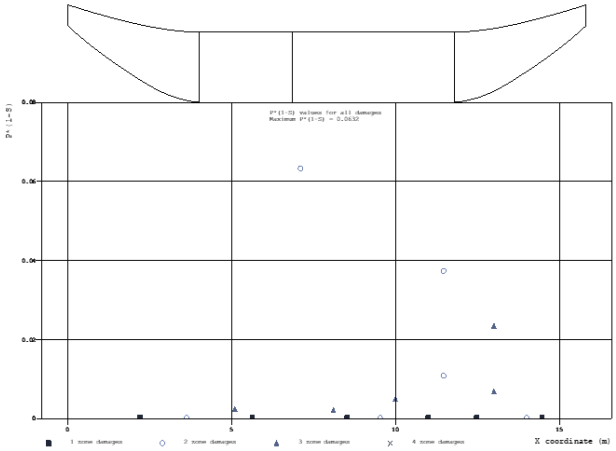

Figure 17: Updated Risk Profile

4.14 Risk Analysis & Calculation of RCO Cost-Effectiveness

4.14.1 PLL Calculation

The cost effectiveness of RCOs has been evaluated in relation to the reduction in PLL they yield relative to the value of statistical life within the Philippines. In estimating the cost of each RCO, the following assumptions have been made:

- Pontoon modifications - $1,500 per pontoon
- Passive Foam - $6 per kg installed.

The results of this process are provided within Table 9, where it can be observed that each RCO configuration has been found to be cost-effective. This serves to indicate that the RCOs explored hold great potential as a solution to many of the damage stability problems faced by this vessel type.

Table 9: Cost Effectiveness Calculation on the Basis of PLL, NPV & NCAF

Item	As-Built	RCOs 1 & 2	RCO 3	RCOs 1, 2 & 3
Attained Index	0.6741	0.7988	0.8215	0.874
PLL	0.003	0.0018	0.0016	0.0011
ΔPLL/ship-year	N/A	0.001	0.001	0.002
ΔPLL/ship-life	N/A	0.005	0.006	0.009
Costs for financing, insurance etc ($)	N/A	320	520	840
CAPEX ($)	N/A	2160	2700	4860
Net Present Value NPV ($)	N/A	2376	2970	5346
GCAF Limit ($)	N/A	4358	5151	6985
GCAF/NPV	N/A	1.83	1.73	1.31

4.14.2 Risk Acceptance Criteria - FN Diagram

An FN diagram has been produced in order to indicate if the flooding risk relating to the vessel falls

within tolerable limits. This diagram is provided in Figure 18 below, where we can observe that the as-built vessel design, shown in black, falls within the ALARP region. This may come as a surprise, given that the vessel's damage stability performance was inadequate. However, in the case of motor bancas, the collision frequency was found to be much lower than that of conventional passenger vessels. Furthermore, the limited passenger capacity of these vessels means that the people at risk is also low. Nevertheless, the implementation of RCOs has shown that the risk can be further reduced into the negligible region. This is a significant finding.

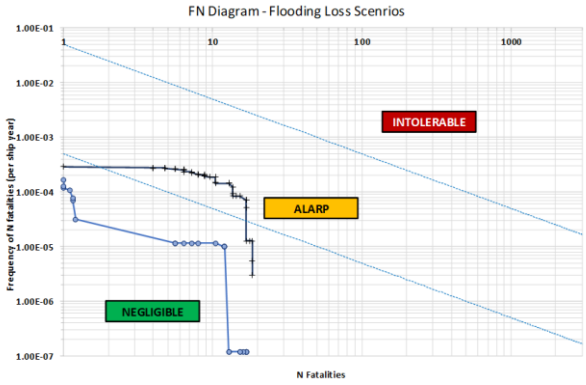

Figure 18: FN-Diagram Showing the Impact of RCOs

5. CONCLUSIONS / RECOMMENDATIONS

Concluding remarks pertaining to the ships being addressed in this paper, include the following:

There are some specific features in the design of the currently operating fleet of motor bancas in the Philippines that makes these boats susceptible to flooding risk, namely (a) lack of subdivision, (b) unprotected openings, (c) lack of adequate freeboard, (d) lack of adequate buoyancy in the outriggers; (e) distance of outriggers from the main hull. Most importantly, they also operate at distances from shore and in environmental conditions beyond their design envelope.

Moreover, considering the current state of enforcement and verification of damage stability standards (lack of fit for purpose regulations; gaps in enforcement and verification – frequency and rigor), ships must be made more robust to withstand this hazard by adopting risk control measures that are cost-effective to incentivise the operator to meet higher standards, which in turn will fuel a virtuous cycle for continuous safety enhancement.

Working with this incentive in mind, and armed with significant research findings and knowledge from a series of large-scale, EC and industry-funded projects on damage stability and flooding risk, the most-effective and practicable solutions have been selected and applied to the selected sample of ships, as described in this paper, enabling these most rudimentary means of transport to reach damage stability standards applicable to passenger ships engaged in any domestic or international voyages. This is unprecedented and exciting, enabling Philippines in the short-medium term to showcase the safety of their domestic fleet against the best in the world.

6. AKNOLEDGEMENTS

We should like to express our appreciation to the International Maritime Organisation and the Word Bank for their support in this project, financial and otherwise, as well as our collaborators from the World Maritime University, Prof Jens-Uwe Schroeder-Hinrichs, Dr Anish Hebbar and Dr Serdar Yildiz for their unfailing support and comradeship during this project. We should also like to express our gratitude to all the Authorities and maritime industry in the Philippines for making us feel at home and for their help in every phase and aspect of this project.

REFERENCES

Aven, T, 2012, "The risk concept – Historical and recent development trends.", Reliability Engineering and System Safety, 99, p. 33-42.

Aven, T., 2022, "A risk science perspective on the discussion concerning Safety I, Safety II and Safety III", Reliability Engineering and System Safety, 217, 108077.

Bulian, G., Lindroth, D., Ruponen, P., Zaraphonitis, G., 2016, "Probabilistic assessment of damaged ship survivability in case of grounding: Development and testing of a direct non-zonal approach", Ocean Engineering, 120, p. 331-338.

Cardinale, M., 2021, "Flooding risk calculations", FLARE Deliverable 7.1.

Goerlandt, F., Montewka, J., 2015, "Maritime transportation risk analysis: Review and analysis in light of some fundamental issues." Reliability Engineering and System Safety, 138, p. 115-134.

IMO, 2009, "International Convention for the Safety of Life at Sea (SOLAS)", Consolidated Edition as of 2009.

IMO, 2020, “International Convention for the Safety of Life at Sea (SOLAS)”, Consolidated Edition as of 2020.

Mauro, F., Vassalos, D., 2022, ”The influence of damage breach sampling process on the direct assessment of ship survivability”, Ocean Engineering, 250, 111008.

Puisa, R., McNay, J., Montewka, J., 2021, “Maritime Safety: Prevention versus Mitigation?” Safety Science, 136, 105151.Ruponen, P., Manderbacka, T., Lindroth, D., 2018, “On the calculation of the righting lever curve for a damaged ship.”, Ocean Engineering, 149, p. 313-324.

Vassalos, D., Atzampos, G., Paterson, D., Cichowicz, J., Boulougouris, E., Konovessis, D., 2019, “Intact stability of passenger ships: safety issue or design concern? Neither.”, 2019, Proceedings of the 17th International Ship Stability Workshop, Helsinki, Finland.

Vassalos, D., Paterson, D., Boulougouris, E., Mauro, F., 2021, “Life-cycle stability management for passenger ships”, Proceedings of the International Offshore and Polar Engineering Conference, ISOPE 2021, p. 2786-2793.

Vassalos, D., Paterson D., Mauro F., Murphy A., Mujeeb-Ahmed M.P., Michalec R., Boulougouris E., 2022a, “A multi-level approach to flooding risk estimation of passenger ships”, Proceedings of the SNAME 14th International Marine Design Conference, IMDC 2022, Vancouver, Canada.

Vassalos, D., Paterson, D., Mauro, F., Atzampos, G., Assinder, P., Janicek, A., 2022b, “High-Expansion Foam: A Risk Control Option to Increase Passenger Ship Safety during Flooding”, Applied Science, 12(10), 4949.

Vassalos, D., Paterson, D., Mauro, F., 2023, “Real-time flooding risk evaluation for ship-to-ship collisions based on first principles”, Ocean Engineering, 281, 114847.

Ship Vulnerability Assessment by Forensic Investigation of Critical Damage Scenarios

Donald Paterson, *Sharjah Maritime Academy, UAE,* donald.paterson@sma.ac.ae
Francesco Mauro, *Sharjah Maritime Academy, UAE,* francesco.mauro@sma.ac.ae
Dracos Vassalos, *Sharjah Maritime Academy, UAE,* dvassalos@sma.ac.ae

ABSTRACT

Forensic level flooding analysis offers the ability to gain a detailed understanding of the manner in which a vessel floods and the mechanisms through which a vessel may be lost. This is made possible through the use of numerical flooding simulations, which provide a wealth of information on the flooding process. However, difficulties arise in processing and handling this information in a manner that allows maximum utility to be gained from the results, without sacrificing time-efficiency. This drives the need to establish a clear and rational methodology for conducting flooding forensic analysis, which forms the focus of this paper. In order to demonstrate the methodology developed, a case study on a large modern cruise vessel is presented. The vessel is subjected to dynamic flooding vulnerability analysis, allowing critical damage scenarios to be identified. These scenarios are then subject to further scrutiny at the forensic level, leading to a comprehensive account of the manner in which the vessel may flood and ultimately be lost. The process culminates in the identification and ranking of critical openings and spaces, providing crucial input in the process of RCO implementation.

Keywords: *Damage Stability, Forensic Flooding Analysis, Passenger Vessel Safety*

1. BACKGROUND

Forensic level flooding analysis is traditionally rooted in accident investigation, where the ability to form a detailed understanding of the flooding process and the causal factors leading to vessel loss is of paramount importance. Pioneering examples of such work include the investigation made by Spouge into the loss of the European Gateway (Spouge 1986), the study performed by Dand following the Herald of Free Enterprise disaster (Dand, 1989), and the accident investigation conducted after the loss of Estonia (JAIC, 1994). Since then, a great deal of process has been made, with more contemporary examples including the work conducted in (Karolius et al., 2020), (Vassalos et al., 2021) and (Valanto, 2023).

Concurrently, such work has driven the development of advanced flooding simulation tools and tank testing techniques which, unlike hydrostatic analysis, are able to support forensic level analysis. Unfortunately, to date, such tools and techniques have not yet been adopted or utilised in any meaningful way within conventional ship design. Instead, most existing examples of forensic level flooding analysis relate to some form of accident investigation, where the aim is to understand what has gone wrong and why. However, it is the intension of this work to establish a methodology that can be applied during the design phase. As such, the focus shifts from determining what has gone wrong to what could go wrong. This presents a less constrained problem which, in turn, widens the area of investigation. It is here where difficulties can arise in ensuring the forensic analysis process is time-efficient, as one can end up with a lot of ground to cover.

Furthermore, the manner in which floodwater evolves following any given flooding event can be, and often is, a highly complex and stochastic process. This is particularly true in the case of large-scale breaches, where a significant portion of the vessel is affected by damage, thereby broadening the flooding landscape. This, in turn, increases the degree of randomness, complexity, and uncertainty in the flooding process, particularly in higher sea state conditions.

All of the aforementioned can make forensic level flooding analysis a difficult and arduous task. However, as will be demonstrated in this paper, it is possible to approach the analysis in such a way as to streamline the process and provide some clarity amidst the complexity.

2. METHODOLOGY

The methodology that has been developed for forensic level flooding analysis is detailed within Figure 1. In total, the approach consists of 9 distinct stages, which are elaborated upon in the following sections.

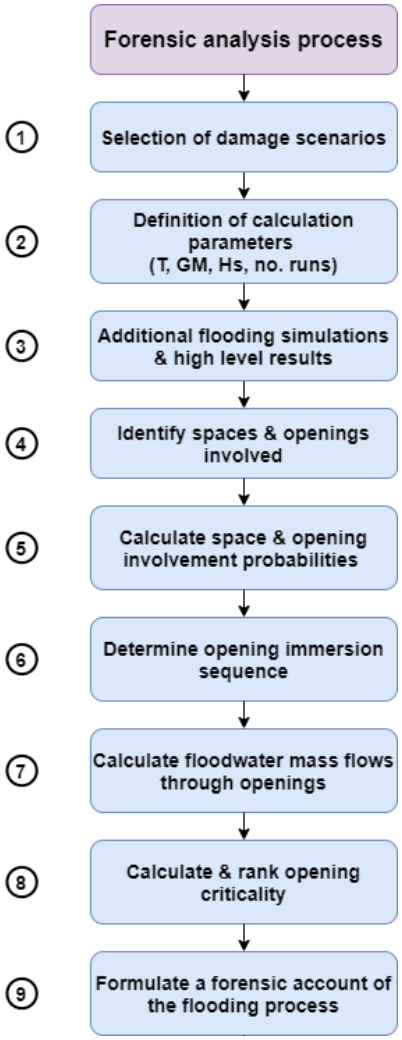

Stage 1: Selection of Damage Cases

The objective in conducting forensic level analysis, is to gain a greater understanding of the mechanisms by which a vessel may be lost as a result of flooding. This is generally undertaken with a view to resolving the underlying issues that have led to vessel loss, through the implementation of appropriate RCOs. Given the latter, it is of great importance that the forensic analysis is able to capture and identify as many sources of vulnerability within the vessel design as possible, thus ensuring that the process of implementing RCOs is well informed. In other words, the more information that can be fed into the design process from forensic analysis, the better the outcome is liable to be.

Ideally, forensic level analysis would be conducted with consideration of all loss scenarios identified following any given dynamic flooding vulnerability analysis. However, at present, this is simply not practical due to the time burden such an assessment would entail. Instead, a more efficient process is proposed, whereby a limited number of representative critical damage scenarios are selected for further scrutiny under forensic examination. This is made possible without fear of jeopardising the quality of the analysis as:

- Vulnerability to flooding is not generally found throughout the entire vessel design. Instead, there are typically concentrated areas of vulnerability found in only a handful of locations (generally one or two). In passenger vessels this is normally towards the fore and aft shoulders.
- Damage cases of a given of loss-modality, located around the same region of the vessel, will generally suffer from the same sources of vulnerability.

Given the above, it stands to reason that consideration of representative loss scenarios from areas demonstrating heightened flooding risk, would identify sources of vulnerability common to most, if not all, damage cases affecting that region. Further safeguarding the process, is the fact that the damage stability performance of the vessel is reassessed following the implementation of RCOs, so if any sources of vulnerability were “missed” in the initial forensic assessment, they would be highlighted here as residual loss scenarios.

Stage 2: Definition of Calculation Parameters

In determining the flooding simulation parameters that underpin the forensic analysis, it is important to ensure they reflect the general operation of the vessel and the environmental conditions it is likely to encounter. Only through doing so, can one ensure that all pertinent vulnerabilities are captured by the forensic examination. However, vessels can be subject to a wide range of variations in both loading and environmental conditions, leaving a rather large area to cover. This, in turn, poses problems as regards the time-efficiency of the calculation process and, ultimately, its applicability during the design process.

Ideally, it would be feasible to conduct simulations with respect to an extensive range of operational and environmental conditions, though this is simply not practical at present. Instead, it has been necessary to develop a more limited yet efficient approach, whereby a form of selective sensitivity analysis is conducted on key input parameters. This approach is described within the following:

- **Draft:** Only the vessel subdivision draft is considered within the calculations, as the work conducted within (Paterson et al., 2019), has indicated that passenger vessels operate predominantly towards the upper extremity of their draft range. Furthermore, the subdivision draft typically represents the most vulnerable loading condition, resulting from lower freeboard and reserve buoyancy. Therefore, this assumption is conservative in nature, and of a higher propensity to capture vulnerabilities within the vessel design.
- **Trim:** In line with current SOLAS assumptions, if the service trim of the vessel under subdivision draft conditions does not exceed ±0.5% of L, then a single level trim value should be considered. However, if this is not the case, then consideration should be given to assessing the vessel under service trim conditions.
- **Heel:** Level heel conditions are assumed, as the vessel is typically upright in the intact condition.
- **GM:** Two GM values are considered within the calculations, one reflecting the statutory subdivision draft loading condition, and the other relating to the limiting GM condition. Through doing so, it is possible to assess the vessel in a manner more reflective of its true operation and, also, with respect to the most adverse condition permitted by regulations.
- **No. of Realisations:** As the simulations are conducted within random waves, the manner in which the vessel floods and the final outcome is non-deterministic. For this reason, it is prudent to consider a number of simulations realisations, if one wishes to account for the stochastic nature of the flooding process. To this end, five simulation realisations have been considered for each of the assessed damage scenarios.
- **Vessel Heading:** Two vessel headings are considered (90 deg, 180 deg), such that the approaching wave train is always acting upon the vessel in the beam direction for both port and starboard damages.
- **Exposure Time:** An exposure time of 30 minutes has been considered, which is in line with current SOLAS standards. However, consideration could be given to extending this period for larger passenger vessels.
- **Wave Spectrum:** In selecting an appropriate wave spectrum, one must consider the area of operation of the vessel and the nature of the wave environment. As the vessel under consideration is an internationally operating cruise vessel, the Pierson-Moskowitz Spectrum has been selected. This spectrum assumes a deep sea and a fully developed sea state, which is appropriate for the operational environment of such vessels.
- **Significant Wave Height (Hs):** As the survivability of passenger vessels tends to be largely influenced by significant wave height, a more refined form of sensitivity analysis has been conducted on this parameter. In total, four Hs values have been considered ranging from still water conditions up to Hs = 7 m. This upper limit has been selected on the basis of global wave statistics, which is appropriate given that cruise vessels tend to operate on an international level. However, if the vessel under consideration was known to operate in a particular location, local statistics regarding significant wave height could easily be utilised instead.

Stage 3: Additional Flooding Simulations & High-Level Results

Within this stage, further flooding simulations are conducted on the damage scenarios selected within Stage 1, under the conditions outlined within the previous stage. This serves to provide the simulation results that will ultimately inform the subsequent forensic analysis process.

In addition, a high-level summary of the results is created at this stage, indicating for each damage scenario:

- TTC values for each simulation realisation and Hs condition considered.
- Mean TTC values for each damage scenario, conditional on Hs.
- Capsize probabilities for each damage scenario, conditional on Hs.

Stage 4: Identification of Spaces & Openings Involved

Here, with respect to all simulations conducted, the spaces and openings found to be involved within the flooding chain are catalogued. This is achieved by observing which rooms have been subject to water accumulation at any stage during the simulations, and also by observing which openings have been engaged in the passage of floodwater. By doing so, it is possible to assess:

- The total number of openings and rooms affected by each flooding scenario.
- The demographic of openings and rooms involved, including the total number of openings and rooms affected with respect to type/purpose, and the combined volume of affected rooms according to purpose.
- The location and properties of each room and opening involved.

Stage 5: Calculate Space & Opening Involvement Probabilities

Here, both room and opening involvement probabilities are calculated, which provides an important first indicator of criticality. This is conducted with respect to each damage scenario, accounting for involvement probabilities conditional on Hs, and in overall terms with respect to all simulated cases (mean values). The involvement probabilities are calculated by assessing the frequency with which a given opening or room was found to be involved with respect to the total number of simulation realisations. For example, if a certain opening featured in 3 out of 5 simulations, then the involvement probability would be 0.6 or 60%. The mean involvement probabilities have then been calculated with respect to all four of the Hs conditions assessed.

Further analysis conducted at this stage also includes the following:

- Investigating the number of openings/rooms found to have an involvement probability of 1, relative to the total number involved. This provides an indication of the degree of randomness present within the flooding process, with fewer openings/rooms possessing an involvement probability of 1 indicating a higher degree of randomness within the process.
- Analysing the impact of Hs on the number of openings/rooms with involvement probabilities of 1, allowing the influence of sea state on the degree of randomness within the flooding process to be observed.
- Determining the manner in which Hs impacts the total number of openings/rooms involved, and thus the scale and complexity of the floodwater evolution.

In the case of rooms, a further step is taken in which a heatmap is created, indicating each rooms respective involvement probability. An example of this diagram is provided in Figure 2**Hata! Başvuru kaynağı bulunamadı.**, where breached rooms are indicated in red, and progressively flooded spaces are colour coded in accordance with the probability scale shown at the bottom.

Such analysis can be highly useful in gaining a greater understanding of the nature and severity of the flooding process, in a format where this information is easily digestible.

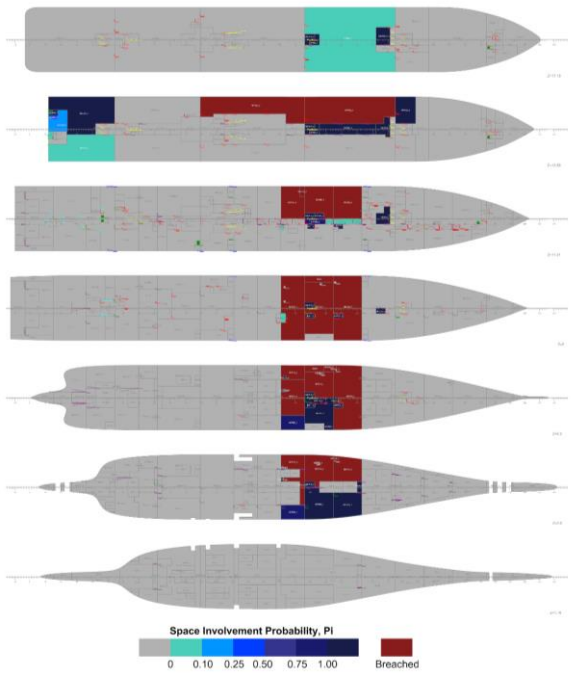

Figure 2: Example room involvement probability heat map

Stage 6: Determine Opening Immersion Sequence

At this stage, the flooding chain is evaluated by examining the immersion time of each opening, i.e., the point at which floodwater initially begins to flow through an opening. This provides important information on the sequence in which the vessel

floods, and also provides useful input as regards the implementation of RCOs which may be time sensitive. The opening immersion sequence is generated for each flooding scenario, firstly with respect to Hs, and secondly in average terms. Following this process, all openings are then ranked in relation to the immediacy of their immersion.

Stage 6: Calculate Floodwater Mass Flows Through Openings

Within this stage the net floodwater mass flowing through each opening is calculated, providing a second important indicator of opening criticality. The simulation results provide values relating to the floodwater mass transferred through each open for every time step, with inflow indicated by positive mass values, and outflow negative values. From this, the total floodwater mass flowing through each opening is calculated by summing up the floodwater mass values relating to each time step. This is conducted for individual damage scenarios, producing opening-specific floodwater mass quantities for each simulation realisation. From these, average mass values are then calculated with respect to each Hs condition, in addition to a global average value, derived with respect to all cases assessed. Openings have then been ranked in accordance with the average magnitude of floodwater found to pass through each.

Stage 7: Calculate and Rank Opening Criticality

During this stage opening criticality is determined on the basis of the involvement probability and net floodwater mass flow values associated with each opening. Specifically, the product of these two values is calculated in order to determine opening risk. The logic behind this approach is that likelihood will be captured by involvement probability, and consequence by the net floodwater mass passing through each opening, meaning that the product of these two values should provide some indication of risk.

Further analysis conducted at this stage include:

- Assessment of the distribution of risk across all openings involved.
- Assessment of risk by opening type.

Stage 8: Formulate A Detailed Forensic Account of Flooding

The final stage in the methodology involves the creation of a detail forensic account the manner in which the vessel floods. As part of this process, all elements of the previously conducted analysis are combined in order to give a complete picture of the flooding process for each damage case. The results are presented in the form of a general arrangement plot, Figure 3, which indicates various key components of the results in different ways. Specifically, the following is included:

- Information bubbles for each opening, colour coded in accordance with the magnitude of floodwater mass found to flow through each. In addition, the information bubbles indicate the opening ID, mean involvement probability and mean time of immersion.
- Initially breached compartments plotted in red.
- Progressively flooded compartments are coloured in accordance with their involvement probability.
- Unaffected compartments coloured in grey.
- The damage breach extent, including fore and aft extremities, in addition to damage length.

The impetus behind presenting the results in this fashion derives from the need to make the results easily interpretable, allowing the designer to gain a greater understanding of the flooding process in a time-efficient manner. In particular, such plots enable rapid assessment of the manner in which the vessel floods, while also indicating the causal factors leading to vessel loss. This, in turn, provides an indication which areas should be targeted for RCO implementation.

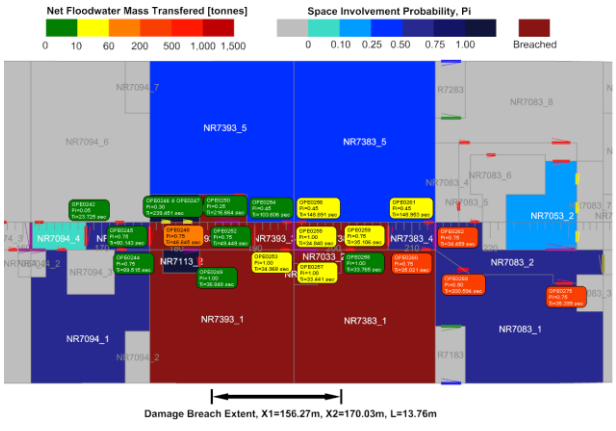

Figure 3: Example forensic analysis plot (bulkhead deck)

3. CALCULATION PARAMETERS

Within this section an overview of the calculation parameters and key inputs is provided.

3.1 Vessel Properties

The vessel under consideration, is a large cruise vessel with main particulars as specified in **Hata! Başvuru kaynağı bulunamadı.**. In addition, the internal ship arrangement is presented in **Hata! Başvuru kaynağı bulunamadı.**.

Table 1: Ship particulars

Parameter	Value
Length overall (LOA)	≃300 m
Length between perpendiculars	270.00 m
Subdivision Length	296.74 m
Beam (B)	35.20 m
Subdivision draft (HSD)	8.20 m
Height of the main deck	11.00 m
Number of Passengers	2,750
Number of Crew	1,000
Gross tonnage	95,900
Deadweight	8,500 t
No. of pax cabins	1,270

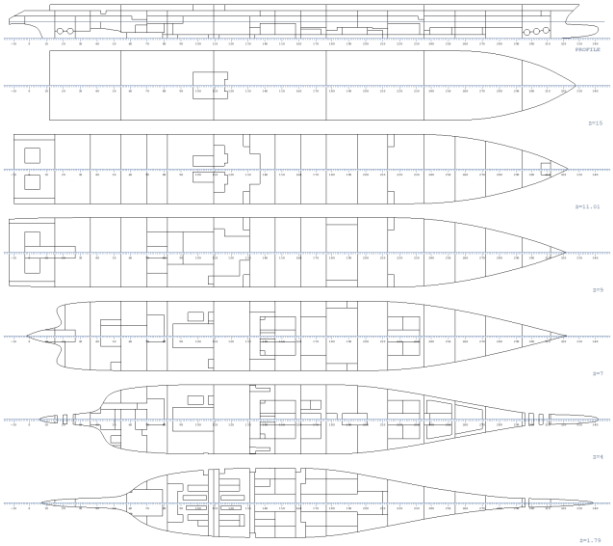

Figure 4: Vessel General Arrangement

3.2 Simulation Properties

An overview of the conditions evaluated in the flooding simulations is provided in **Hata! Başvuru kaynağı bulunamadı.**.

Table 2: Simulation input parameters

Parameter	Assumptions
Draft (m)	8.2
Trim (m)	0
Heel (deg)	0
GM (m)	2.114, 2.802
No. of Realisations (-)	5
Heading (deg)	90/270 (beam seas)
Exposure Time (min)	30
Wave Spectrum (-)	Pierson-Moskowitz
Hs (m)	(0, 2, 4, 7)

3.3 Damage Selection

In order to select the damage scenarios to be considered as part of this assessment, the results of an initial dynamic vulnerability screening have been used to inform the process. The results of this initial assessment are provided within Figure 5 and Figure 6, showing all loss scenarios and indicating their location, damage length, centre, and loss modality. From these results, two clear areas of concentrated loss scenarios can be identified towards the vessel fore and aft shoulders. In light of this, cases have been selected from these two areas, including examples of transient capsize and progressive flooding loss from each.

Furthermore, two criteria failing cases have also been selected in these areas, including one case failing ITTC capsize criterion and another failing the SOLAS final floating position heel criterion.

Within the figures, the selected cases are highlighted in red circles.

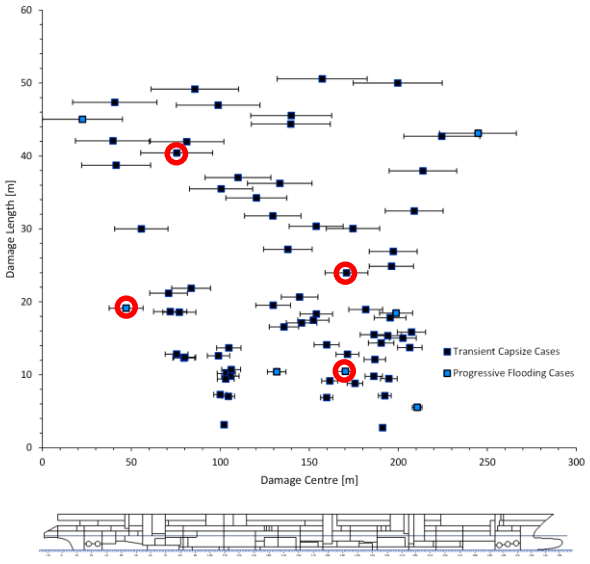

Figure 5: Transient & Progressive Flooding Capsize Cases

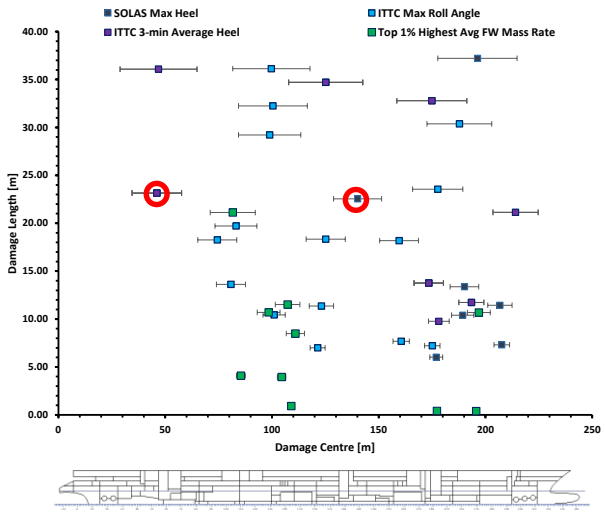

Figure 6: Criteria Failing Cases

It should be noted, that while the six scenarios have been selected and analysed as part of this study, for the sake of brevity only one transient and progressive flooding loss scenario are elaborated upon within this paper.

4. TRANSIENT CAPSIZE CASE

4.1 Description of Damage Case

The first case considered is a transient capsize scenario located on the vessel fore shoulder, see Figure 7. The breach is situated across two transverse bulkheads, thus affecting three compartments. The resultant damage is asymmetric in nature, which is exacerbated further as the three lower affected spaces each have restricted transverse channels connecting port and starboard sides. The vertical extent of the damage lies above the double bottom and extends to Deck 05 (one deck below the uppermost deck modelled).

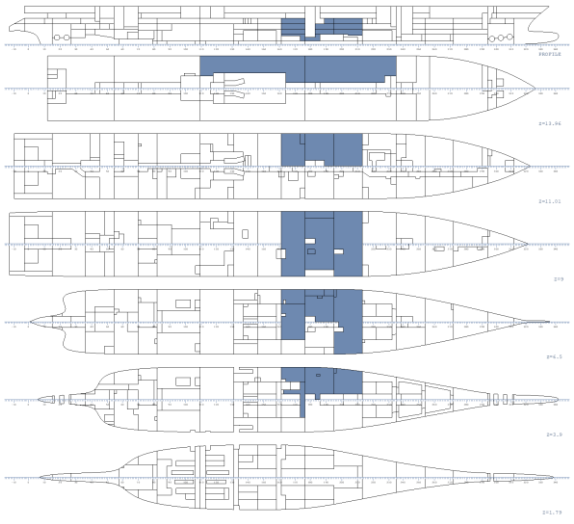

Figure 7: Transient capsize, initial breach plot

4.2 Additional Simulation High-Level Results

This section provides a summary of the additional flooding simulation that have been conducted on the damage case in question, under the conditions outlined within section 3. As no capsize scenarios were witnessed under the higher GM condition, only results pertaining to the lower GM simulations are presented. The results are provided within Table 3, indicating TTC values relating to each significant wave height (Hs) and simulation realization, along with mean TTC values and the resultant capsize probability.

Table 3: High-level results of additional simulations

	DMC0671 - Transient Capsize Case			
	TTC [sec]			
Realisation	Hs=7 m	Hs=4 m	Hs=2 m	Hs=0 m
1	47.8	60.3	67.3	52.5
2	64.2	63.6	67	52.5
3	53.4	63.6	70.8	52.5
4	48.7	61.3	67.9	52.5
5	64	64.1	68.6	52.5
Mean TTC [sec]	**55.6**	**62.6**	**68.3**	**52.5**
Pc [-]	**1**	**1**	**1**	**1**

4.3 Opening Involvement Probability

The results relating to the calculation of opening involvement probability are provided in Figure 8. From this, the following observations can be made:

- 61 openings (75%) were found to have an involvement probability of 1.00, with the remaining 20 openings (25%) having probabilities ranging from 0.05-0.95. This indicates only a marginal degree of randomness within the flooding process which is to be expected when considering a transient capsize case.
- To determine the effect of significant wave height on the degree randomness observed within the flooding process, the percentage of openings found to have involvement probabilities of 1.00 with respect to each significant wave height has been calculated, resulting in the following:
  - Hs=7m, 80% openings
  - Hs=4m, 87% openings
  - Hs=2m, 88% openings

- Hs=0m, 100% openings

These findings serve to demonstrate the tendency of increasing Hs to lead to a greater degree of randomness within the flooding process.

- An additional study has been performed looking into the impact of HS on the number of openings found to be involved within the flooding chain. As one would expect, there is a tendency for an increased number of openings to be involved at higher sea states, as shown in the following:
  - Hs=7m, 77 openings
  - Hs=4m, 76 openings
  - Hs=2m, 77 openings
  - Hs=0m, 67 openings

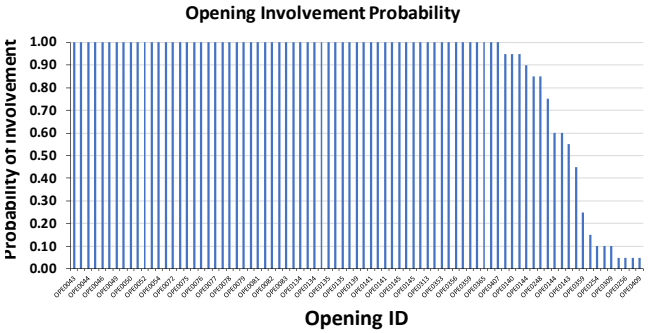

Figure 8: Opening involvement probabilities

4.4 Opening Immersion Time

The calculated opening immersion times are provided in Figure 9 and serve to indicate the flooding sequence. As can be observed, all openings involved are subject to rapid immersion (within 80 seconds or breach opening), which is typical of a transient capsize case.

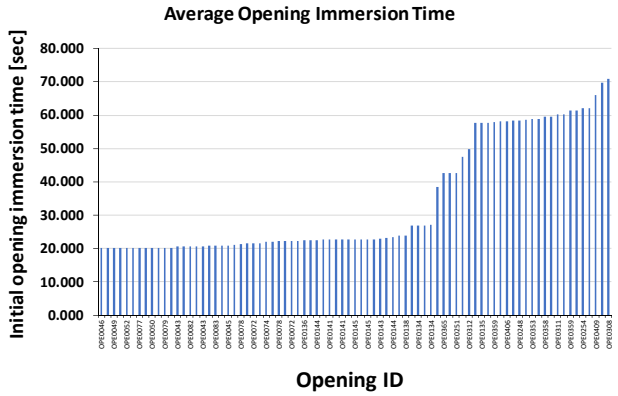

Figure 9: Opening immersion times

4.5 Net Floodwater Mass Flow Through Openings

The calculated net floodwater mass flow through each opening involved within the flooding sequence is provided within Figure 10. From these results the following high-level observations can be made:

- A total of 51 openings (63%) were found to have flood water mass flows less than 1 tonne.
- Furthermore, of the 81 openings involved, on average just 18 openings (22%) were found experience floodwater mass flows greater than 10 tonnes.
- In fact, it was found that the top 1% of highest ranked openings are responsible for a greater floodwater mass flow than all the remaining openings combined. This would indicate that there are only a limited number of openings that significantly contributing to the flooding process.

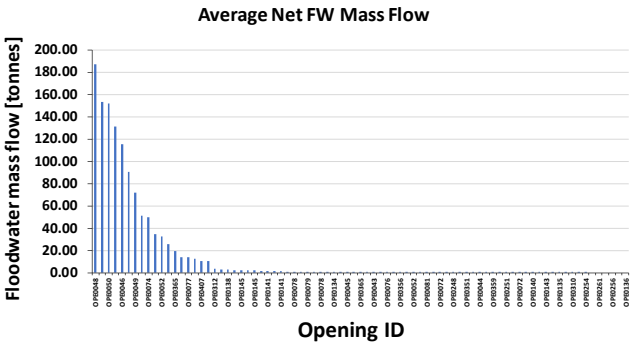

Figure 10: Net floodwater mass flows through openings

4.6 Room Involvement Probability

The calculated room involvement probabilities for the case in question are provided within Figure 11, leading to the following observations:

- Of the 28 rooms found to be affected, 17 (60%) were found to have an involvement probability of 1.00, indicating on a marginal degree of randomness within the flooding process.
- The remaining 11 rooms (40%) were found to have involvement probabilities ranging from 0.05-0.95.
- A to be expected, a tendency for a greater number of rooms to be involved at higher sea states was observed, as demonstrated in the following:

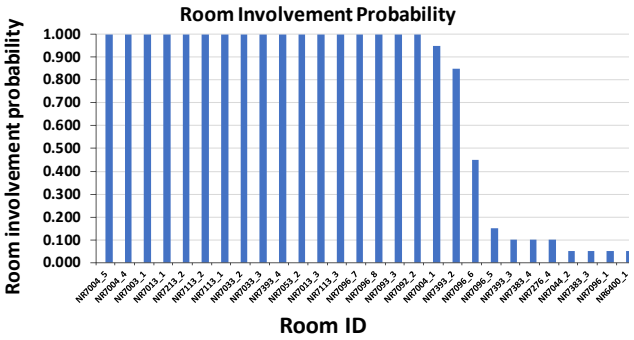

Figure 11: Room involvement probabilities

In addition, a heat map of the room involvement probabilities calculated across all case-specific simulations is provided within Figure 12**Hata! Başvuru kaynağı bulunamadı.**. Here, It can be observed that the flooding process is for the most part deterministic as far a room involvement is concerned. Only a limited degree of randomness has been observed within the flooding process, resulting from rare occurrences of progressive flooding in the aft of the vessel and up-flooding to Deck 06.

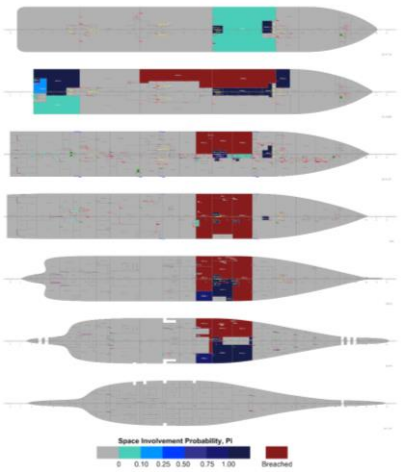

Figure 12: Room involvement probability heat map

4.7 Ranking of Openings by Criticality

The final opening criticality ranking, made on the basis of both involvement probability and the floodwater mass flow through each opening, is provided within Figure 13. Furthermore, information relating to the top ten highest risk openings is provided within Table 4. Based on these results, the following observations can be made:

- The top 5% most critical openings possess a higher combined risk than all other openings combined. This indicates that despite a rather large numbner of openings being involved, only a select few lead to significant flooding progression.
- The risk contribution deriving from each opening type has also been calculated as a percentage of the total risk, leading to the following results:
  - Holes: 58%
  - Hinged Double Fire Doors: 13%
  - Hinged Escape Doors: 11%
  - Sliding Lift Doors: 10%
  - Hinged Weathertight Doors: 3%
  - Hinged Fire Doors: 2.8%
  - Escape Hatches: 1%

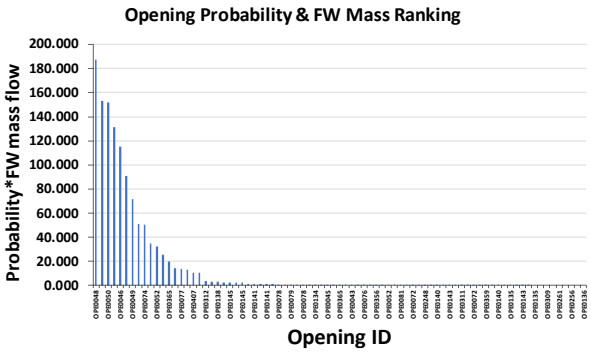

Figure 13: Opening criticality ranking

Table 4: Top ten highest criticality openings

Unique OPE ID	Opening Type	Immersion Time [sec]	Probability Pi	Net FW Mass Flow [tonnes]	Pi*FWM
56	Hole	20.287	1.00	187.078	187.078
64	Hole	20.289	1.00	153.005	153.005
59	Hole	20.289	1.00	151.764	151.764
96	Hinged Double Fire Door	20.289	1.00	131.446	131.446
54	Hole	20.284	1.00	115.317	115.317
63	Hole	20.608	1.00	90.719	90.719
57	Hinged Escape Door	20.284	1.00	71.657	71.657
89	Sliding Lift Door	22.087	1.00	51.166	51.166
88	Sliding Lift Door	22.064	1.00	50.115	50.115
489	Hinged Weathertight Door	38.508	1.00	34.676	34.676

4.8 Detailed Forensic Account of Flooding

The final stage in the process is to combine all the information previously outlined, in order to build up a clear picture of the way in the vessel may flood when subject to the damage scenario in question. As detailed within the methodology, this is achieved through the creation of a forensic level flooding diagram. To provide a flavour of the information one can readily deduce from such a diagram, a single deck example is provided within Figure 14, followed by the observations that can be made on the basis of this diagram.

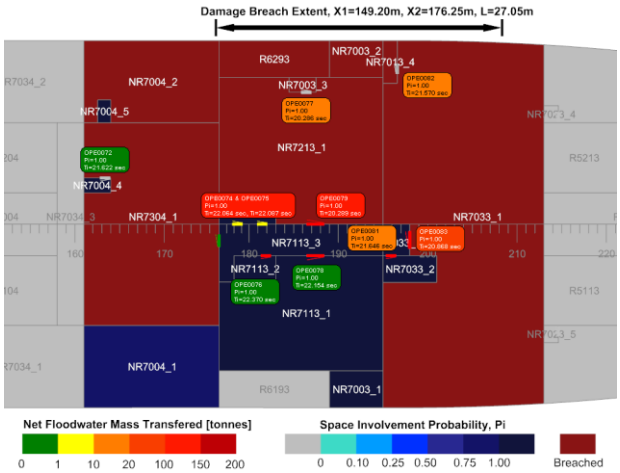

Figure 14: Forensic level flooding diagram

Observations:

- On Deck 02, floodwater almost immediately begins to equalise within the mid affected compartment, flowing transversely through double fire doors OPE0079 and OPE0078. However, the degree of floodwater delivered to NR7113_1 on the starboard side is minimal (< 1 tonne), indicating asymmetry within the flooding process.
- There are also signs of moderate up-flooding through openings OPE0074 & OPE0075, through the lift trunk NR7213_2.
- Further progressive flooding can be observed in the fore affected compartment through the double fire door OPE0083 and into stairwell NR7033_2 via OPE0081, however this is in fairly mild quantities (<20 tonnes)
- Within the aft breach compartment only minimal up-flooding can be observed through the escape trunk OPE0072 (< 1 tonne).

5. PROGRESSIVE FLOODING SCENARIO

5.1 Description of Damage Case

The damage case under consideration is a progressive flooding loss scenario, located on the vessel fore shoulder, as shown in Figure 15. The breach is situated across a single transverse bulkhead, thus affecting two compartments. The

vertical extent of the damage is significant and ranges from a position just below Deck 02 up until the uppermost deck.

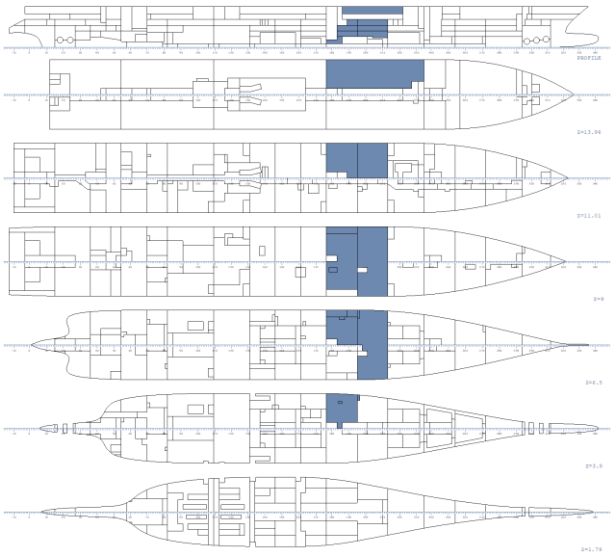

Figure 15: Prgressive flooding loss, initial breach plot

5.2 Additional Simulation High-Level Results

This section provides a summary of the additional flooding simulation that have been conducted on the damage case in question, under the conditions outlined within section 3. As no capsize scenarios were witnessed under the higher GM condition, only results pertaining to the lower GM simulations are presented. The results are provided within Table 3, indicating TTC values relating to each significant wave height (Hs) and simulation realization, along with mean TTC values and the resultant capsize probability.

Table 5: High-level results of additional simulations

Realisation	**DMC0671 - Transient Capsize Case**			
	TTC [sec]			
	Hs= 7 m	Hs= 4 m	Hs= 2 m	Hs= 0 m
1	708.1	1658.1	1820	1820
2	678.3	1384	1820	1820
3	797.1	1551.2	1820	1820
4	657.1	1587	1820	1820
5	830	1288.3	1820	1820
Mean TTC [sec]	**734.1**	**1493.7**	**N/A**	**N/A**
Pc [-]	**1**	**1**	**0**	**0**

5.3 Opening & Room Involvement

The following provides a summary of the openings and rooms found to be involved within the flooding sequences analysed. In total, 160 openings affecting 58 rooms were identified across all simulations conducted.

A short summary of the demographic of spaces involved is provided within the following:

- 35 crew spaces, totalling 9,873 m³ in volume.
- 12 passenger spaces, totalling 12,717 m³ in volume.
- 6 technical spaces, totalling 3,129 m³ in volume.
- 3 engine spaces, totalling 1,207 m³ in volume.
- 2 store spaces, totalling 44 m³ in volume.

In addition, a short summary of the opening types involved and their quantity is provided within the following:

- 34 hinged fire doors and 42 gaps.
- 21 holes
- 12 escape hatches (comprised of 4 openings each)
- 10 sliding lift doors
- 10 hinged double fire doors and 11 gaps.
- 5 hinged escape doors and gaps
- 4 hinged weathertight doors
- 3 sliding fire doors and gaps
- 5 sliding cold room doors

Of the openings involved 59 (37%) were found to lie below the bulkhead deck and 101 (63%) above. This is typical of a progressive flooding scenario, where floodwater tends to predominantly propagate along the bulkhead deck.

5.4 Opening Involvement Probability

Figure 15 summarises the calculated opening involvement probabilities. On the basis of these results, the following observations can be made:

- 36 openings (23%) were found to have an involvement probability of 1.00, with the remaining 124 openings (77%) having involvement probabilities ranging from 0.05-0.90, indicating a large degree of randomness in the flooding process.
- Generally speaking, it was observed that the number of openings involved within the flooding sequence increases with respect to significant wave height. For example, simulations at Hs=7 m were found to have four times as many openings involved relative to Hs=0m, thus signalling the importance of accounting for variations in sea state.

- To determine the effect of significant wave height on the degree randomness observed within the flooding process, the percentage of openings found to have involvement probabilities of 1.00 with respect to each significant wave height has been calculated, resulting in the following:
  - Hs=0m, 100%,
  - Hs=2m, 98%,
  - Hs=4m, 95%,
  - Hs=7m, 33%

  The above indicates that as sea states rises, so too does the randomness observed within the flooding sequence. In this instance, the impact is only slight in conditions up to Hs=4 m. However, there is a substantial increase in randomness under Hs=7 m conditions, with 67% of openings found to have involvement probabilities <1.00.

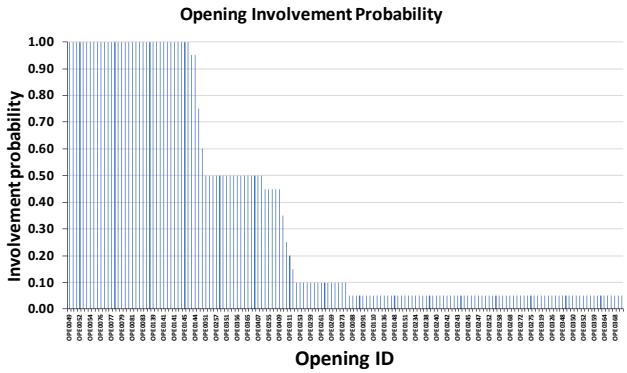

Figure 15: Opening Involvement Probabilities

5.5 Opening Immersion Time

The average opening immersion times, calculated in accordance with all simulated cases, is provided within Figure 16. This serves to illustrate the flooding sequence. On the basis of these results, the following observations can be made:

- On average, 125 openings (78%) were found to be immersed within the transient phase.
- The remaining 35 openings (22%) were immersed in the progressive flooding stage, with the last opening immersed following 24 minutes.

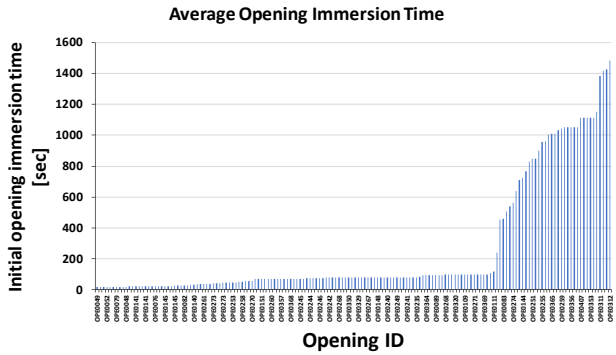

Figure 16: Opening Involvement Probabilities

5.6 Net Floodwater Mass Flow Through Openings

The calculated average net floodwater mass flow through each opening is presented within Figure 17. On the basis of these results, the following remarks can be made:

- Of the 160 openings involved, on average just 31 openings (19%) were found experience floodwater mass flows greater than 10 tonnes.
- Furthermore, 112 openings (70%) were found to have flood water mass flow rates less than 1 tonne. This demonstrates that, despite what can appear as a highly complex flooding event, there often exist only a limited number of openings that play a significant role in the flooding process.
- To further illustrate the above point, the top 5 highest ranked openings, out of the 160 found to be involved within the flooding sequence, are responsible for 60% of the total progressive floodwater mass.

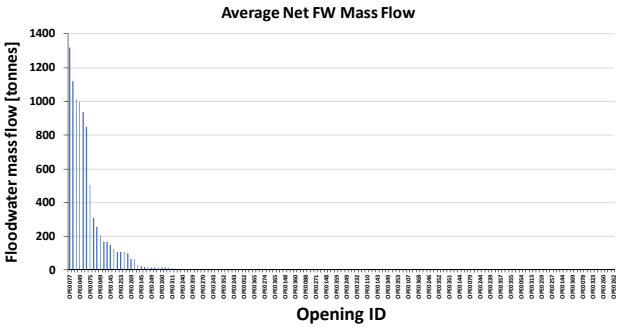

Figure 17: Opening Involvement Probabilities

5.7 Room Involvement Probability

The calculated room involvement probabilities are provided within Figure 18, from which the following observations can be made:

- Of the 58 rooms found to be affected, just 10 (17%) were found to have an involvement probability of 1.00.

- The remaining 48 rooms (83%) were found to have involvement probabilities ranging from 0.05-0.50. This is indicative of a large degree of randomness within the flooding process, which is to be expected from a progressive flooding scenario in a complex vessel.
- As in the previously examined cases, a tendency for a greater number of rooms to be involved at higher sea states was observed, as detailed in the following:
  - Hs=7m, 58 rooms
  - Hs=4m, 23 rooms
  - Hs=2m, 10 rooms
  - Hs=0m, 10 rooms

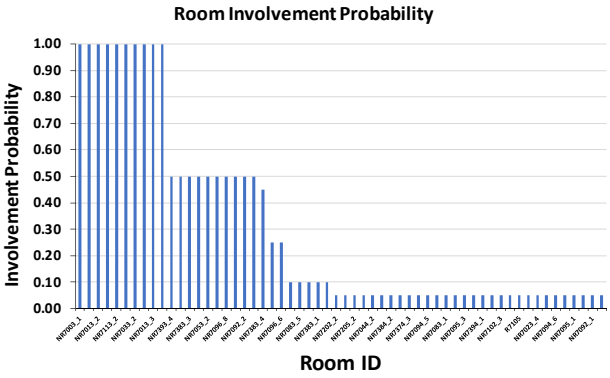

Figure 18: Room involvement probabilities

In addition, a heat map of the room involvement probabilities calculated across all case-specific simulations is provided within Figure 19**Hata! Başvuru kaynağı bulunamadı.**, where several instances of widespread progressive flooding can be observed.

This works to illustrate the potential scale of floodwater dispersion throughout the vessel, particularly when the upper decks become involved in the flooding sequence, where watertight integrity is marginal. Fortunatley, such widespread flooding was only realised in 5% of cases, though there are still signs of significant progressive flooding occurring within the upper decks in up to 50% of cases.

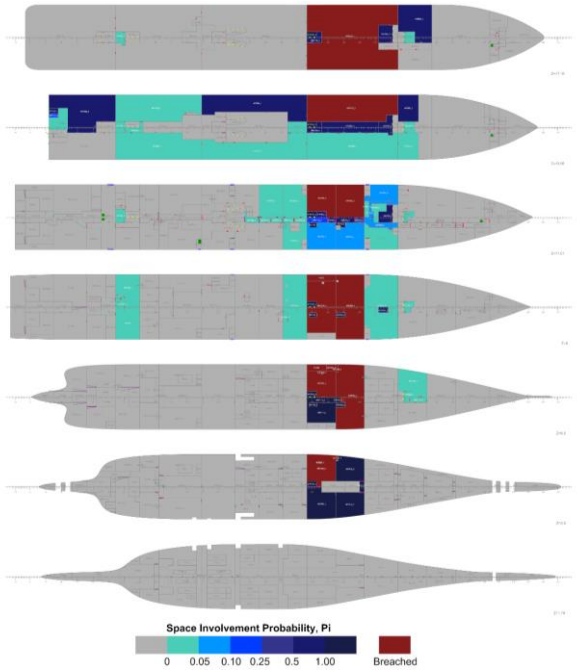

Figure 19: Room involvement probability heat map

5.8 Ranking of Openings by Criticality

As in the previous example, a final ranking of opening criticality has been made on the basis of involvement probability and floodwater mass flow. The results of this process are summarised within Figure 19. Furthermore, information relating to the top ten highest risk openings is provided within Table 6. Based on these findings, the following observations can be made:

- The upper 1% of critical openings are responsible for 28% of the risk, with the top 5% of critical openings representing 80% of the risk. This again serves to indicate that only a handful of openings hold a significant bearing on the severity of flooding.
- Once again, the risk contribution deriving from each opening type has also been calculated as a percentage of the total risk, leading to the following results:
  - Holes: 46%
  - Hinged Escape Doors: 29%
  - Hinged Double Fire Doors: 11%
  - Sliding Lift Doors: 5%
  - Escape Hatches: 5%
  - Hinged Fire Doors: 2%

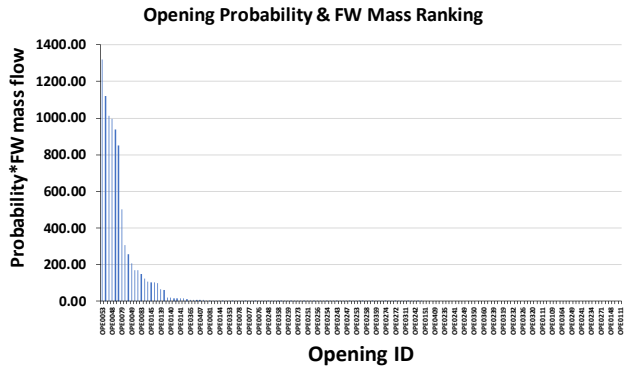

Figure 19: Opening criticality ranking

Table 6: Top ten highest criticality openings

Unique OPE ID	Opening Type	Immersion Time [sec]	Probability Pi	Net FW Mass Flow [tonnes]	Pi*FWM
63	Hole	55.689	1	1318.561	1318.56
61	Hinged Escape Door	20.291	1	1122.000	1122.00
101	Hinged Escape Door	28.014	1	1014.755	1014.76
56	Hole	20.411	1	997.709	997.71
64	Hole	30.622	1	937.870	937.87
59	Hole	20.408	1	849.185	849.18
96	Hinged Double Fire Door	20.339	1	503.990	503.99
94	Hinged Double Fire Door	24.608	1	308.092	308.09
92	Hinged Escape Door	20.342	1	255.418	255.42
57	Hinged Escape Door	20.284	1	205.609	205.61

5.9 Detailed Forensic Account of Flooding

As was conducted in the previous example, a detailed forensic account of the flooding process has been generated in graphical form. An example of the results of this process is provided for a single deck in Figure 20, followed by the observations that can be made.

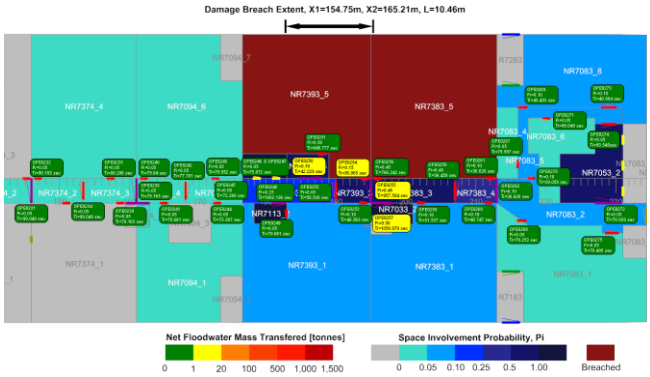

Figure 20: Forensic level flooding diagram

Observations:

- On Deck 04 the most widespread progressive flooding was observed which is typical given that there is generally a reduction in internal watertight integrity beyond the bulkhead deck, as the internal geometry begins to open up.
- However, it is interesting to note that the magnitude of progressive flooding and associated frequency of occurrence are both considerably low.
- The primary conduit for progressive flooding in this case is the service corridor, which allows floodwater to pass both forward and aft of the breached area and into several surrounding spaces. However, the mass of floodwater engaged in this progressive flooding was identified as less than 1 tonne on average. Furthermore, this occurred in only 10% of cases in relation to fore progressive flooding and in just 5% of cases regarding aft progressive flooding.
- Also present here are several signs of up-flooding, most significantly through stairwell NR7033_2 and opening OPE0257.
- Other examples of up-flooding include stairwell NR7113_2 and lift trunk NR7213_2, where negligible quantities of floodwater progression were identified (<1 tonne).

6. POST PROCESSING RESULTS FOR RCO IMPLEMENTATION

Ranking openings in terms of criticality provides an indication of which should be targeted for the implementation of RCOs. However, the question remains as to how many openings should be considered. In order to answer this, the cumulative opening risk has been evaluated as a function of the number of openings considered, as shown in Figure 21. This enables the point of diminishing returns to be identified, which represents the optimal number of openings to be considered for additional protection. This process is based on the combined results from all damage scenarios considered, in order to provide the overall optimal number of openings to be considered. The results of this process have indicated that the top 40 highest risk openings should be considered, though further filtering is required, as described in the following section.

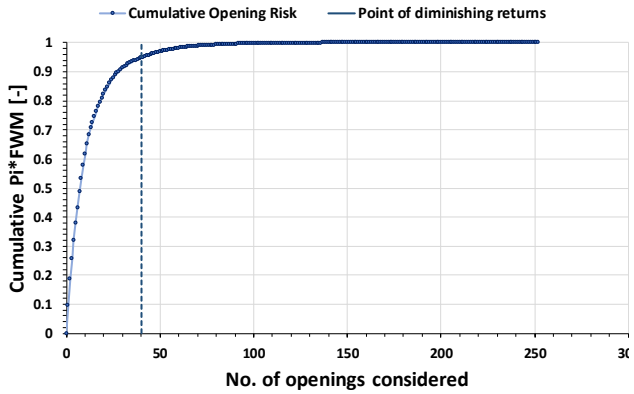

Figure 21: Cumulative Opening Risk

The final stage in the process is to filter out those openings engaged in positive forms of progressive flooding e.g., cross-flooding. Conducting this process leads to just 20 openings that should be considered for additional flooding protection through the implementation of suitable RCOs, see Table 7.

Table 7: Filtered critical openings to be considered for RCOs

OPE ID	Opening Type	Pi*FWM	Flooding Type
61	Hinged Escape Door	379.07	Up/Downflooding
24	Hinged Escape Door	103.97	Up/Downflooding
148	Hinged Escape Door	90.71	Up/Downflooding
103	Hinged Double Fire Door	86.68	Prog. flooding
90	Hinged Fire Door	76.36	Up/Downflooding
406	Hole	66.8	Prog. flooding
295	Hinged Escape Door	46.94	Up/Downflooding
484	Hinged Weathertight Door	31.49	Prog. flooding
403	Hinged Fire Door	30.82	Prog. flooding
426	Hinged Double Fire Door	28.3	Prog. flooding
402	Hinged Fire Door	28.06	Progressive flooding
204	Hinged Fire Door	26.24	Up/Downflooding
21	Hinged Escape Door	24.92	Up/Downflooding
382	Hole	20.58	Up/Downflooding
102	Hinged Escape Door	19.59	Up/Downflooding
413	Sliding Fire Door	18.74	Prog. flooding
400	Hinged Double Fire Door	17.29	Prog. flooding
563	Hinged Fire Door	14.13	Prog. flooding
77	Hinged Escape Door	11.89	Up/Downflooding
489	Hinged Weathertight Door	11.79	Prog. flooding

7. CONCLUSIONS

On the basis of the results presented in this paper, the following conclusions and recommendations can be made:

- A methodology has been developed, allowing one to obtain a detailed and comprehensive account of the manner in which the vessel may be lost due to flooding.
- The methodology created allows openings and rooms to be ranked in terms of involvement probability, immersion time, floodwater mass flow, and finally the risk they pose to flooding.
- It has be observed that of all rooms and openings within the vessel, only a limited number pose significant risk. As such, the results of the forensic analysis can be distilled in order to isolate only a handful of the most critical openings/rooms to be targeted for application of RCOs.
- It has been observed that higher Hs values, lead to a greater degree of complexity and randomness within the flooding sequence.
- No capsize scenarios were observed for the vessel under consideration with respect to operational GM values, as such it has been necessary to explore reduced GM values in order to produce capsize scenarios to inform the analysis undertaken.

- A process has been developed in order to create a detailed account of the flooding process at the forensic level, with recommendations made on how best to convey the results of the analysis, such that they are easily digested by the designer.
- Looking forward, further automation within the process would help aid in time-efficiency and the scale at which the analysis can be conducted.

8. REFERENCES

Dand, I., 1989, "Hydrodynamic Aspects of the Sinking of the Ferry 'Herald Of Free Enterprise'", Transactions of the Royal Institution of Naval Architects

Spouge, J., 1986, "The Technical Investigation of the Sinking of the Ro/Ro Ferry European Gateway", Transactions of the Royal Institution of Naval Architects

Joint Accident Investigation Committee (JAIC), 1995, "Concerning technical issues on the capsizing on 28 September 1994 in the Baltic Sea of the M/S Estonia"

Karolius, K., Chichowicz, J., Vassalos, D., 2020, "Risk-based, sensor-fused detection of flooding casualties for emergency response", Ships and Offshore Structures, 16(5):1-30

Vassalos, D., Paterson, D., 2021, "Towards Unsinkable Ships", Ocean Engineering, 232(No.2)

Valanto, P., 2023, "On Boundary Conditions for Damage Openings in RoPax-Ship Survivability Computations", Journal of Marine Science and Engineering 11(3), 643

Paterson, D., Vassalos, D., Atzampos, G., Boulougouris, E., Luhmann, H., 2019, "Impact of draft on the damage survivability of cruise ships", Ocean Engineering, 187

Ship Damage Stability Enhancement through Crashworthiness

Hongseok Bae, *Sharjah Maritime Academ, Khorfakkan, Sharjah, UAE,* hongseok.bae@sma.ac.ae
Dracos Vassalos, *Sharjah Maritime Academy , Khorfakkan, Sharjah, UAE,* dvassalos@sma.ac.ae
Donald Paterson, *Sharjah Maritime Academy, Khorfakkan, Sharjah, UAE,* donald.paterson@sma.ac.ae
Francesco Mauro, *Sharjah Maritime Academy , Khorfakkan, Sharjah, UAE,* Francesco.Mauro@sma.ac.ae

ABSTRACT

Crashworthiness as one of the Risk Control Options (RCOs) for damage stability enhancement has been around since the 1990s, potentially earlier. Yet, it has never managed to gain inroads for routine use in ship design and operation to enhance ship damage stability cost-effectively, more specifically targeting passenger ships. A key reason relates to lack of understanding of how the concept can be used in ship design or design upgrades to enhance damage stability, especially since this requires a complete risk assessment of this RCO adopting the Alternative Design and Arrangements methodology, which could be time-consuming and only possible through expert guidance. The latter is also linked to lack of efficient tools to undertake such analysis routinely as well as a lack of in-depth research and experiential knowledge on how best to benefit from this concept. This paper attempts to cover these gaps and provide proof of concept evidence by considering damage stability upgrade of a cruise ship through crashworthiness. Other risk control options are also evaluated, for comparative assessment of cost-effectiveness, leading to useful conclusions and guidelines on how to use the crashworthiness concept as a credible risk control option for damage stability enhancement.

Keywords: *Crashworthiness, Damage stability, Flooding Risk Assessment, RCOs, Ship Collision*

1 INTRODUCTION

After the Titanic accident, SOLAS regulations were established and strengthened to enhance ship safety pertaining to flooding risk. SOLAS 1948 introduced deterministic methods for ship stability criteria, and SOLAS 2009 probabilisitc methods with additional determinstc criteria based on the righting levers (GZ-curve) of the ship, residual metacentric height (GM), heeling angle range, heeling angle-righting arm area, and maximum righting arm (GZ). In particular, in SOLAS 2009, a new concept of damage stability assessment was introduced, which uses a probabilistic approach based on flooding occurrence probabilities for each longitudinal, transverse, side of damage, and vertical direction for each compartment zone. Both types of damage stability criteria have been widely applied to commercial vessels and passenger ships under different requirements in addition to SOLAS, such as MARPOL, ICLL, SPS code, Stockholm Agreement, etc.

Although the current SOLAS damage stability criteria have been effective in maintaining high standards of ship survivability against flooding accidents, many issues of concern are still embedded in these. The criteria assume that flooding occurs in all zones, which means that innovative structural designs, such as new structural arrangements and crashworthy material applications, are treated the same as a typical structure. Additionally, predetermined breach distributions (p-factors) lead to biased damage stability solutions that focus solely on ship survival improvement (s-factor), disregarding individual operating characteristics such as operating area and profiles.

To address crashworthy structure applications to ships, Germanischer Lloyd (IMO, 2003, Zhang et al., 2004) introduced a direct analysis as an approval procedure for alternative double-hull structure arrangements within the scope of the EU-funded project Crash Coaster, being suggested for adoption in the context of explanatory notes as contained in IMO Resolution A.684(17) (IMO, 1991). Unfortunately, this approval procedure has not been

successfully adopted as an IMO Resolution. Additionally, it only focused on physical crashworthiness analysis for ship-ship collision regarding collision energy and penetration using FE and no knowledge was introduced pertaining to ship damage stability for overall ship survivability.

This paper focuses on how to enhance overall ship survivability, petaining to p-factors, with the application of crashworthy structural designs as risk control options (RCOs). As a direct assessment, crashworthiness analysis is employed to identify actual damage extents. Section 2 suggests a quantitative risk assessment methodology that provides equivalent damage stability criteria to the current SOLAS regulations within the IMO framework in a cost-effective way. Section 3 describes a practical demonstration using a reference vessel as a case study, including vulnerable zone identification, application of RCOs, FE analysis, and cost-benefit analysis. Six crashworthy RCOs as passive measures were investigated and the optimum RCO was selected for the final decision-making of related stakeholders.

2 QUANTITATIVE RISK ASSESSMENT METHODOLOGY

This proposed methodology places focus on improving damage stability using crashworthiness analysis to enhance survivability. Through structural crashworthiness analysis from the FE method, it is possible to estimate the reduction in damage extents from the application of crashworthy structural design alternatives (Risk Control Options), as illustrated in Figure 1. This leads to updated damage breach distributions and an impact on ship survivability. The cost-effectiveness of these Risk Control Options can be analysed using the Gross Cost of Averting a Fatality (GCAF) for ship survivability enhancement, taking into account both cost and risk reduction.

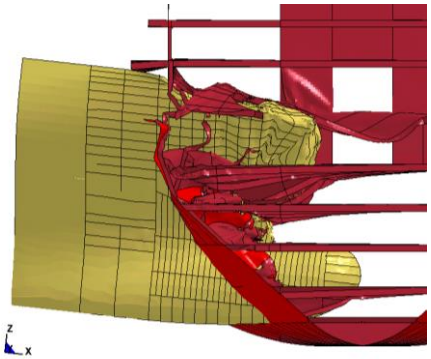

Figure 1 : Typical Crashworthiness Analysis on ship collisions

As a quantitative risk assessment, the proposed methodology consists of seven steps as follows;

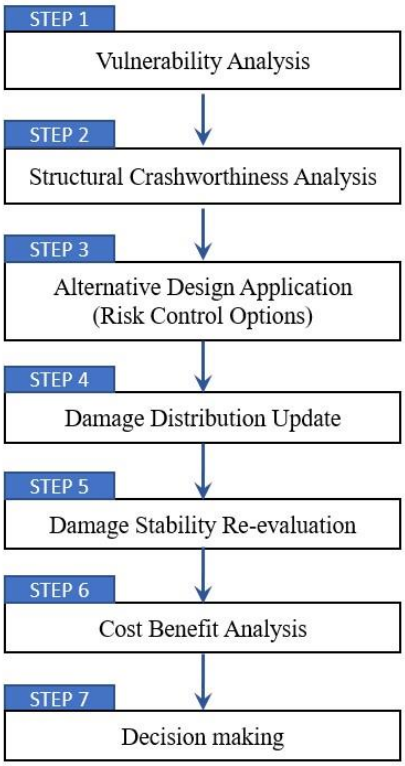

Figure 2 : Overall Methodology

Step 1: Vulnerability Analysis

The first step is to calculate the damage stability of the target ship using standard damage stability analysis according to current SOLAS 2020 regulations. Based on the calculation results, Equation (1) can be used to calculate the local Attained Index loss for the classification of high-risk zones. This enables the identification of the most vulnerable zone in the target ship.

$$Index\ Loss = \sum p_i \times (1 - s_i) \qquad (1)$$

Next, one or two high-risk zones can be selected for RCO application to improve overall ship risk. To achieve this, the permeability of each subdivision zone can be manually set to zero (i.e., no flooding condition) to determine how much the Index can be improved. However, this manual calculation for all relevant compartments requires additional effort and increased calculation time. To address these problems, this paper proposes a vulnerability

analysis method, suggesting a plurality approach with extension to adjacent zones.

Step 2: Structural Crashworthiness Analysis

The next step involves conducting ship collision simulations for the target vulnerable zone. Since the structural response in ship collisions involves crushing, buckling, plasticity, and rupture, which are highly nonlinear, this paper adopts the nonlinear finite element method (NLFEM). This method is also recommended in ADN 2009 for alternative structure procedures (UN, 2008). Unlike the FE analysis method in ADN 2009, which employs restraint in three transitional freedoms, the proposed methodology takes into account actual ship motions with surrounding water effects using MCOL solver, such as added mass effects, restoring and wave damping forces. This enables the reflection of actual external dynamics between the two ships and coupling dynamics with internal collision mechanics.

Collision Scenario Definition

The selection of collision scenarios is a crucial factor in crashworthiness analysis for ship collisions since it directly affects the damage breach size results. Typically, six aspects are taken into account for collision scenarios, including striking ship, collision location, collision speed, collision angle, draught, and trim. This paper proposes a reasonable worst-case scenario within the current SOLAS framework. However, the final collision scenario should be discussed and approved by the relevant Administration based on the target ship's operating areas and profiles.

Striking ship: The striking ship is primarily related to the initial kinetic energy, which is determined by its mass and speed. Additionally, the bow shape directly affects the damage breach results. Therefore, it is reasonable to select the actual target striking vessel instead of using generalised bow shapes and assumptions. This paper recommends selecting a ship with a high probability of encountering a target ship based on its actual operational profile history, such as the IAS data of the target vessel.

Collision Speed: the primary determinant of the initial kinetic energy during a collision is the collision speed of the striking vessel, which in turn significantly impacts the outcome of breach penetration. Numerous researchers have employed different collision speeds in their collision assessments. For instance, velocities ranging from 0.5 to 14 knots were used for a 179m Ropax ship (Schreuder et al., 2011), for a VLCC (Paik et al., 2017), for a 9,000 TEU container ship (Kim et al., 2021), for an Aframax (Zheng et al., 2007), and even as high as 19.44 knots (equivalent to 10 m/s) for a 310 LNG carrier (Ehlers et al., 2008). It is worth noting, however, that the kinetic energy at 19.44 knots is 15 times greater than that at 5 knots, leading to vastly distinct simulation outcomes. Therefore, in contrast to the previously used fixed collision speeds derived from accident databases, this paper introduces the concept of a "relative collision speed." This concept is defined as the specific speed that yields a B/2 penetration of the ship, as per the current SOLAS framework. This approach offers two main advantages. Firstly, the collision scenario aligns with the IMO framework, ensuring a collision case that is neither overly gentle nor excessively severe, adhering to the principle of regulation criteria of maximum penetration at B/2. Secondly, this concept could mitigate or harmonise discrepancies in damage extents resulting from uncertainties in simulation setups, encompassing variations in failure criteria and material behaviour. Consequently, the collision speed utilised in each analysis is adaptable to different collision scenarios and the crashworthiness analysis techniques employed by individual researchers. To determine the "relative collision speed" for achieving B/2 penetration, a series of preliminary simulations involving varying collision speeds were undertaken, as depicted in Figure 3.

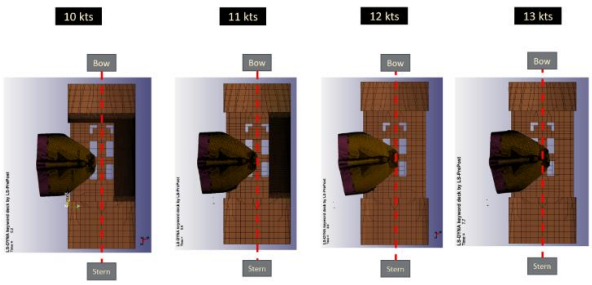

Figure 3 Collision Simulations to find the Relative Collision Speed

Collision Location: The middle of the vulnerable zone selected in STEP1 is determined as the

collision location. The RCOs will be applied on this target zone for damage stability improvement.

Collision Angle: A commonly recognised fact is that the highest internal energy materialises during a collision at a right-angle impact (Zheng et al., 2007, Hogstrom and Ringsberg, 2012), particularly when the impacted vessel is stationary. Therefore, to maintain a cautious and conservative stance, a collision angle of 90° is adopted.

Collision Draught and Trim: Differences in draught between the involved vessels can result in varying degrees of damage. Nonetheless, for the purposes of this paper, collisions are presumed to occur under even trim conditions at the designated design draught.

Step 3: Alternative Design Arrangements as RCOs

The third step involves the implementation of alternative design arrangements for (flooding) risk reduction, known as Risk Control Options (RCOs), to the target zones identified in the first step. These RCOs are not only intended to provide crashworthy arrangements, but also to reduce damage, especially transverse penetration, and increase buoyancy to improve the overall survivability of the ship. In order to assess the impact of RCOs on ship collisions, the crashworthiness analysis conducted in Step 2 with the use of RCOs should be repeated.

Step 4: Transverse Breach Distribution Update

After completing Step 3 and analysing the simulation results, the penetration reductions for each RCO arrangement can be determined. Using these reduced penetrations, the cumulative transverse breach distribution function of the target zone can be adjusted proportionally from a predetermined SOLAS CDF by shifting the point of 1 from the ship's centre (B/2) to the position of maximum penetration, as illustrated in Figure 12. This updated CDF can then be used to obtain the corresponding PDF for recalculating the damage stability.

Step 5: Damage Stability Re-evaluation

Once the new RCO arrangements and updated breach distribution have been established, the damage stability can be recalculated. This will enable the identification of the improvement in the Subdivision Attained Index resulting from each RCO.

Step 6: Cost-Benefit Analysis

The subsequent step involves conducting a cost-benefit analysis to determine the optimal RCO solution. In accordance with the FSA guidelines recommended by IMO (2018), the Gross Cost of Averting a Fatality (GCAF) is utilised to evaluate the cost-effectiveness of each RCO, as outlined below:

$$GCAF = \frac{\Delta Cost}{\Delta Risk} \quad (2)$$

The cost of each RCO encompasses both capital expenditure, such as material and labour costs, and operational costs, such as increased fuel consumption resulting from the added weight of RCO implementation. In terms of risk reduction, the reduction in expected fatalities (i.e., PLL) is utilised as a risk reduction factor. The EMSAIII (2013-2016) project risk models have been utilised for these calculations.

Step 9: Decision-Making

In the final step, the additional design, operation, maintenance aspects of the selected optimal RCOs must be thoroughly discussed and investigated by relevant decision-makers, including shipowners, shipbuilders, designers, class societies, and Administrations, to arrive at a final decision. Following this, an approval process may be initiated for the implementation of the selected RCOs in the construction or modification of the target ship.

3 CASE STUDY

To illustrate the application of this proposed methodology, a case study was undertaken using a reference cruise ship named FLOODSTAND SHIP B (Luhmann, 2009), simulating a collision scenario with a 45,000 GT RoPax vessel as the striking ship. The essential ship details are presented in Table 1.

Table 1 : Main Particulars of ships in the case study

	Target Ship	Striking Ship
LBP (m)	216.8	200.0
Breadth (m)	32.2	30.0
Displacement (tonne)	35,367	31,250
Pax Capaxity	2,400	-

3.1 STEP 1: Vulnerability Analysis

The assessment of damage stability was conducted according to the prevailing SOLAS regulatory framework to ascertain the vulnerability of the original design for the reference vessel. The achieved Subdivision Index was calculated as 0.8579, falling short of the mandated Required Subdivision Index of 0.8676. This outcome indicates non-compliance with SOLAS regulations, as outlined in Table 2.

Table 2 : As-Built Desgin Damage Stability Results

Draught (m)		Trim (m)	GM (m)	Attained Index A
Dl	6.890	0.120	2.670	0.1756
Dp	7.196	0.000	2.620	0.3429
Ds	7.400	0.000	2.720	0.3394
Attained Subdivision Index A				0.8579
Required Subdivision Index R				0.8676

Based on the outcomes of the damage stability analysis, the individual Attained Indices for each zone are compared to the maximum Index value. This maximum Index can be computed when the s-factor attains its highest value of 1 (i.e., the maximum local Subdivision Attained Index = $\sum p \times s_{max} = \sum p \times 1$). As highlighted within a black dashed rectangle in Figure 4, the zones between Z11 and Z18 exhibit lower local Indices for both the 3-zone and 4-zone damage scenarios. This signifies that the ship's survivability (s-factor) in case of damage occurring in these zones is relatively diminished, thereby classifying them as high-risk zones.

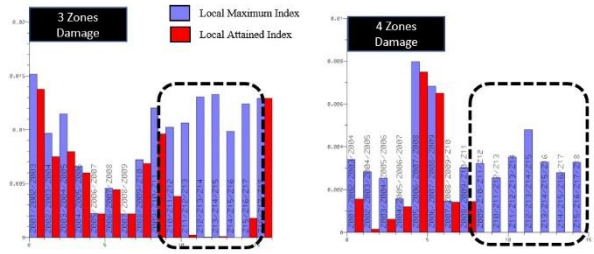

Figure 4 : Local Attained Index Loss

The quantification of these risks can be accomplished through the application of Equation (1), yielding the Index loss. However, a challenge arises in determining how much the Index loss of each zone contributes to the overall local Index loss in cases of multi-zone damage. To address this, the paper proposes a novel approach, an extension to adjacent zones, as a method for vulnerability analysis. This methodology assumes that the zone where the damage centre of each multi-damage case is located absorbs the entire Index loss, a concept sometimes referred to as a "winner-take-all" approach.

Furthermore, the adjacent zones' local Attained Indices also experience enhancement when the target zone exhibits heightened survivability. This implies that the risks of the adjacent zones are intertwined with the target zone. Consequently, the risk associated with the target zone is considered to result from the cumulative risk of three zones: the target zone itself and its two adjacent zones. Bae (2022) has substantiated this vulnerability analysis approach by comparing it to the individual enhancement outcomes of each zone under conditions of maximum survivability (i.e., zero permeability).

A comprehensive summary of the vulnerability analysis conducted on a reference vessel is presented in Figure 5.

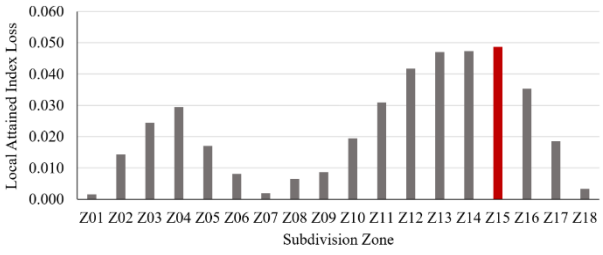

Figure 5: Local Risk of each Zone

3.2 STEP 2: Structural Crashworthiness Analysis

Subsequently, the collision simulations were executed utilising the ANSYS/LS-DYNA explicit code to address internal mechanics, complemented by the MCOL solver for external dynamics. A comprehensive breakdown of the specific parameters employed in these simulations, encompassing geometric modelling, material property characterisation, failure criteria, contact and friction considerations, as well as the delineation of hydrodynamic boundaries, is presented in the subsequent sections.

Geometry Modelling

The complete geometry of the reference ship was meticulously replicated, from zone 1 to zone 18. To achieve this, fine meshes serving as deformable regions were incorporated in the target zone 15 and its contiguous zones, namely Zone 14 and Zone 16. The remaining segments were configured with coarser meshes and identified as rigid components. Conversely, for the striking ship, solely the foremost 30.0 meters were considered for simulation, as this region is the only area undergoing deformation during collisions, as depicted in Figure 6. Furthermore, the Centre of Gravity (COG) and mass properties of the striking ship were factored into the MCOL solver, as elaborated in Table 3. In the simulation, the forepart of the striking ship was modeled using refined meshes and denoted as a deformable segment, while the end part was treated as rigid.

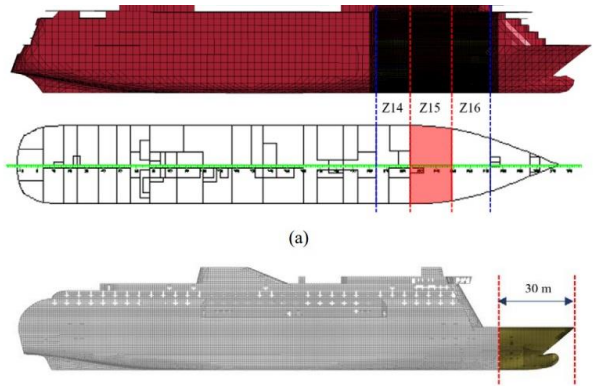

Figure 6: Geometric modellings with 2D shells

The fine meshes for the struck ship and the striking ship were designed with element sizes of 175 mm and 200 mm, respectively. These sizes were chosen as they are a quarter of the frame spacing for each respective ship, offering an economical yet reasonably accurate representation of the structural behaviour. Additionally, these mesh sizes adhere to the recommendation for fine meshing (i.e., less than 200 mm) as stipulated in AND 2009 guidelines.

For the simulation, Belytschko-Tsay 2D shell elements (LSTC, 2019) were employed. These elements incorporated a 5/6 shear factor and were integrated through the shell thickness with 5 integration points. This approach was implemented not only for the plate components but also for the stiffeners, ensuring a consistent modeling strategy across all geometries.

Material Property

Both vessels were considered to be constructed only from mild steel, and their material properties are outlined in Table 3. The collision simulations incorporated a Piecewise Linear Isotropic Plasticity material model (Hodge et al., 1956; LSTC, 2019). This model was applied to the contact areas constructed using fine meshes for both ships, enabling the observation of elastoplastic deformation resulting from collisions.

Table 3: Material properties for mild steel

Parameters	values
Density, ρ (kg/m3)	7850
Young's modulus, E (MPa)	205,800
Poisson's ratio	0.3
Yield stress, σY (Mpa)	235
Ultimate tensile strength (Mpa)	400

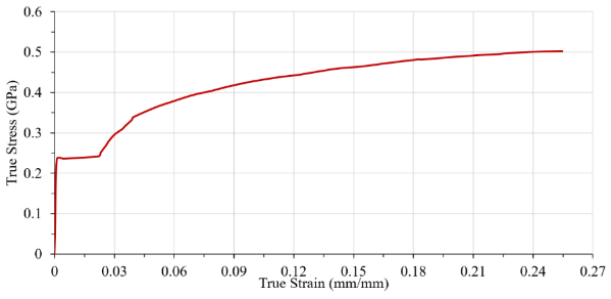

Figure 7 : Appied true stress/strain curve

In accordance with the given material properties, the simulation employed a true stress/strain curve as

described in Figure 7. This curve was extrapolated from experimental data (Paik, 2018) and was adjusted to be applicable within the simulation framework.

Failure Criteria and Dynamic Effects

The evaluation of structural response under impact loading is underpinned by the provided stress-strain curve established in the preceeding section. However, a pivotal concern is the estimation of fracture points in finite element analysis. Over time, various authors have investigated and proposed a range of failure criteria. These encompass traditional constant failure strain criteria, criteria dependent on element size following Barba's law (Barba, 1880), strain-based failure criteria utilising forming limit diagrams, stress state-based failure criteria encompassing stress triaxiality, and criteria that account for crack propagation.

Given the complexity in selecting an optimal failure criterion, which can vary based on material properties, geometries, and collision scenarios, this paper adopts the through-thickness strain criterion introduced by Vredeveldt (2001) as expressed in Equation (3). This criterion, commonly known as the "GL criterion," is renowned for its simplicity and frequent application in FE analysis. It takes into consideration element size dependence and has been deemed the most widely employed failure criterion in FE analysis, endorsed by organizations such as IMO (2003) and UN (2008).

$$\varepsilon_c = \varepsilon_g + \varepsilon_e \frac{t}{l_e} \tag{3}$$

where, ε_c denotes critical fracture strain represented as $\varepsilon_{3f} = \varepsilon_c / (1 + \varepsilon_c)$, thinning strain ε_{3f} may be obtained from $\varepsilon_{3f} = -0.5(\varepsilon_1 + \varepsilon_2)$ based on the incompressibility condition with the Poisson ratio of 0.5. Uniform strain ε_g of 0.056 and necking strain ε_e of 0.540 were used for 2D shell element types (Scharrer et al., 2002) used in these simulations.

In addition to the complexities of failure criteria, it's widely recognised that elevated strain rates can influence strain-stress curves by increasing dynamic yield stress. Strain rates are notably impacted by the initial collision energies, which in turn are contingent on variations in collision speeds. Consequently, for collision simulations involving relatively high speeds, the consideration of strain rate effects becomes imperative. To address this concern, the formulation presented by Cowper and Symonds (1957) has been implemented. This formulation serves to account for the effects of strain rates and is structured as follows;

$$\frac{\sigma_{Yd}}{\sigma_Y} = 1.0 + \left(\frac{\dot{\varepsilon}}{C}\right)^{1/q} \tag{4}$$

Where σ_{Yd} and σ_Y are dynamic and static yield stresses, $\dot{\varepsilon}$ is strain rate, C and q are coefficients determined on the basis of test data. For mild steel, C=40.4 and q=5 have been used.

Contact and Friction Definition

Contact definition was established using the node-on-segment penalty method. For this purpose, the "Automatic Single Surface" option available in LS-DYNA was employed to set up contact in the finite element analysis. In terms of friction between colliding bodies, the friction coefficient has a notable impact on simulation outcomes. This is due to the separation of the initial collision energy into both frictional and internal energy components. Consequently, a significant increase in friction energy can lead to a reduction in internal energy, and vice versa. Given these considerations, the selection of the friction coefficient demands careful attention. Engineering references suggest a range of 0.09 to 0.19 for lubricated mild steel surfaces and a coefficient of 0.57 for non-lubricated surfaces. In practice, industry standards and several works in the literature, including Sajdak and Brown (2005) and Paik (2007), advise adopting dynamic friction coefficients within the range of 0.1 to 0.3 for the sake of simplification.

Considering the typical conditions of vessel hull, which are often affected by biofouling, a value of 0.3 for the dynamic friction coefficient was thought to be a reasonable choic

Hydrodynamic Boundary Definition

Historically, numerous collision simulations have often limited the translational degrees of freedom. Nonetheless, the accurate representation of hydrodynamic boundary conditions in ship

collisions is pivotal, as it encompasses the external dynamics of both vessels. This includes factors like the restoring forces linked to ship mass and buoyancy, the added mass of both ships, and the damping forces induced by wave actions.

In this study, the MCOL solver, integrated within LS-DYNA, was harnessed to account for these intricate ship motions and added mass effects in the finite element analysis. The input parameters for this solver were computed using ANSYS AQWA (ANSYS, 2019), leveraging the ship characteristics detailed in Table 4. This approach enabled a comprehensive consideration of the complex hydrodynamic interactions in collision scenarios.

Table 4: Hydrodynamic input for ship motions

Parameters		Struck ship	Striking ship
Draft (m)		7.2	6.9
Displacement (tonne)		35,367	31,250
LCG (m)		99.29	85
KG (m)		15	14
Gyration radius (m)	Surge	10.95	11
	Sway	54.20	55
	Heave	56.37	55

Collision Scenario Definition

This phase involves the specification of a collision scenario that will be utilised in the finite element analysis. Six key parameters have been primarily considered for this purpose, including the striking ship, collision speed, collision location, collision angle, draft, and trim.

In this context, the 45,000 GT RoPax has already been assigned as the striking ship. As a result, the geometric configuration of its bow shape and the ship mass have been ascertained from the provided striking ship drawings and its main particulars, respectively. Zone 15 has been identified as the most vulnerable region of the reference vessel, as determined in STEP 1. The collision angle is set at 90° and the trim is assumed to be at the design draft. Given these considerations, the only remaining parameter is the collision speed, which will be the focal point of this scenario definition.

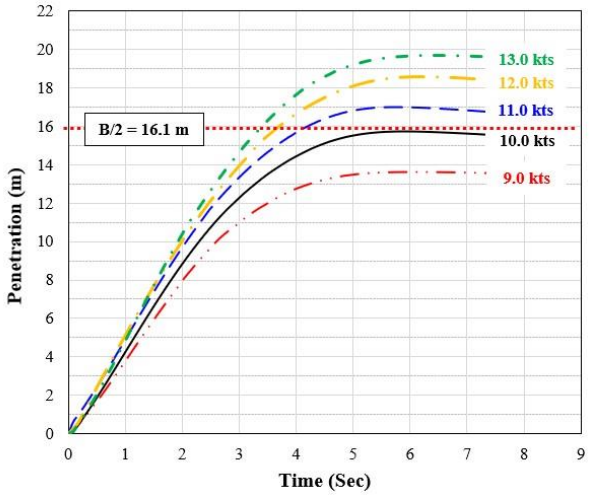

Figure 8 : Collision Simulations Results

To determine the relative speed that results in the maximum penetration of B/2, a sequence of simulations has been executed. It is important to emphasise that the simulation configuration used for the finite element analyses should also be maintained for these preliminary simulations. Figure 8 shows the variation in maximum penetration over time across different speeds. Notably, a collision speed of 10.14 knots yields transverse penetration closest to B/2. With this insight, the collision scenario for the simulations involving the reference ship and the striking ship can be succinctly summarised in Table 5.

Table 5 : Summary of Collision Scenario

Ships	speed (knots)	angle (˚)	From A.P. (m)	Draft (m)
Struck ship	0	0	0	7.2
Striking ship	10.14	90	165.8(*)	6.9

3.3 STEP 3: Risk Control Option Applications

To manage and mitigate damage stability risks, alternative design arrangements in the form of RCOs have been implemented. The RCOs considered in this case study are comprehensively outlined in Table 6. A total of 6 RCOs were thoroughly examined, falling under the categories of passive measures. These measures can be categorized into two distinct types: those involving a single longitudinal bulkhead at varying locations and measures that entail reinforcing the hull thickness.

Table 6 : Applied Risk Control Options

Name	Description
RCO1	Single LBHD at B/20
RCO2	Single LBHD at 2B/20
RCO3	Single LBHD at 3B/20
RCO4	Single LBHD at 4B/20
RCO5	20T hull + Single LBHD at 10.6m (*)
RCO6	30T hull + Single LBHD at 6.6m (*)

(*) Locations to be out of the maximum penetrations

This type of passive measure is referred to as the "double-hull concept," a concept already implemented in tankers and LNG carriers to mitigate environmental risks such as oil spills or gas leaks resulting from ship collisions. The single longitudinal bulkhead on each side is assumed to be installed from a double bottom on deck 1 to the embarkation deck on deck 5, as illustrated in Figure 9. These bulkheads are constructed using mild steel with a thickness of 10mm. Two wing compartments on each side, formed by each longitudinal subdivision, are connected to one another through cross-flooding arrangements.

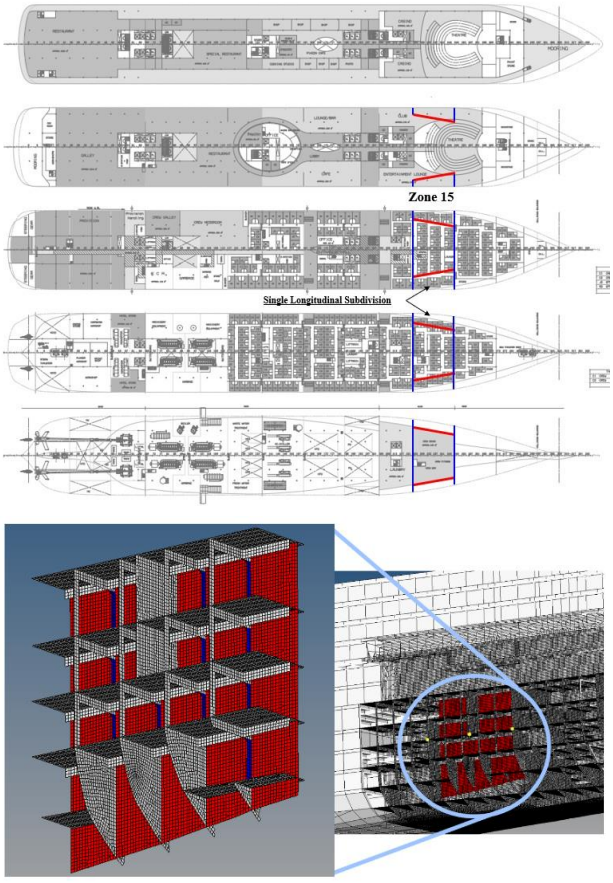

Figure 9 : Single LBHD Arrangements

Specifically, the RCOs were explored with four distinct plate installation positions: B/20, 2B/20, 3B/20, and 4B/20. Here, B/20 pertains to the criterion for the double bottom height. Additionally, B/10 serves as the position criterion not only for the maximum penetration as defined in the current SOLAS Reg.II-1/B-1/8 but also as one of the recommendations for maximum transverse penetration during the establishment of SRtP regulations. Furthermore, B/5 aligns with the criteria for maximum damage penetration for RoPax vessels in accordance with the Stockholm Agreement (EU, 2003). For tankers with fuel oil capacities exceeding 5,000m3, MARPOL regulations (IMO, 2004) stipulate requirements for a distance between the longitudinal bulkhead and the hull, ranging from 1.0m to 2.0m depending on the fuel oil capacity.

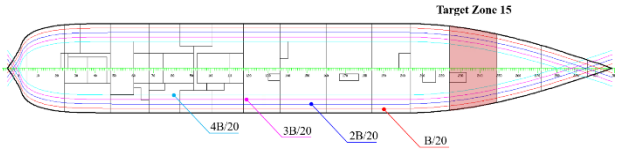

Figure 10 : Different Locations of LBHD

FE analysis results

Based on the established simulation configuration and the defined collision scenario, a series of simulations were conducted for each RCO, utilizing a collision speed of 10.14 m/s. Figure 11 provides an overview of the penetration results obtained from finite element analysis (FEA) for each RCO.

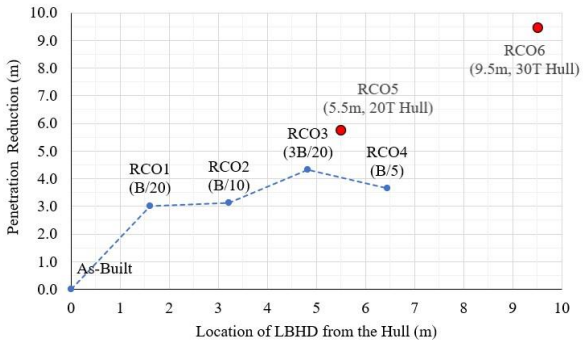

Figure 11 : Penetration Reductions for each RCO

For RCO1, RCO2, RCO3, and RCO4, transverse penetrations ranged from 3.3m to 4.3m depending on the Longitudinal Bulkhead Distance (LBHD) locations. Notably, these RCOs revealed a reduction in transverse penetrations, with the LBHD

effectively absorbing collision energy and contributing to a decrease in transverse penetration by approximately 3.5m. However, it's important to note that the specific location of each different RCO had a minimal impact on the penetration reduction.

In contrast, RCO5 and RCO6, which involve the reinforcement of the hull to 20T and 30T thickness, respectively, demonstrated more substantial improvements. These two measures led to explicit penetration reductions of 5.7m and 9.6m, highlighting their effectiveness in enhancing collision resistance.

3.4 STEP 4: Transverse Distribution Update

Utilizing the results from the finite element analysis conducted in STEP 3, adjustments can be made to the local transverse distribution associated with zone 15. The cumulative distribution function (CDF) can be updated by proportionally accounting for the reduction in penetration. This adjustment involves shifting the point of maximum penetration from the initial value of 16.1m (B/2) to the calculated actual transverse penetration measured from the hull of the struck ship.

Figure 12 visually illustrates the updated probability density function (PDF) and CDF for RCO6 in comparison to the original distribution stipulated in the current SOLAS regulation for the p-factor. Subsequently, the updated PDF can be deduced from the adjusted CDF. The new PDF, represented by the red culumn, can then replace the original PDF shown in the blue culumn (i.e., the old p-factor). As a consequence, the updated p-factor for damage cases will undergo an increase, achieved by multiplying it with the s-factors. This, in turn, leads to improvements in the local Attained Indices.

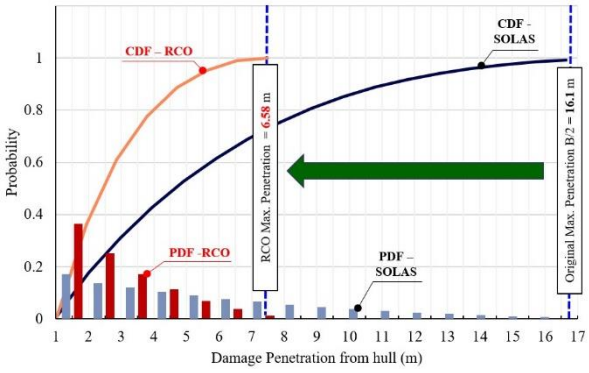

Figure 12 : Suggested Methodology for Transverse Distribution (p-factor) Update

If the RCO arrangement results in increased s-factors, then the enhancement in the Attained Index will be more pronounced, providing a substantial enhancement in damage stability performance.

3.5 STEP 5: Damage Stability Re-evaluation

Having integrated the RCO arrangement and adjusted local transverse breach distribution (p-factor) within the target zone 15, a comprehensive reassessment of the reference ship's damage stability was undertaken. This re-evaluation was conducted in adherence to the prevailing SOLAS regulations, with the primary objective of identifying the collective enhancement in the Attained Index, which serves as a measure of improved damage stability.

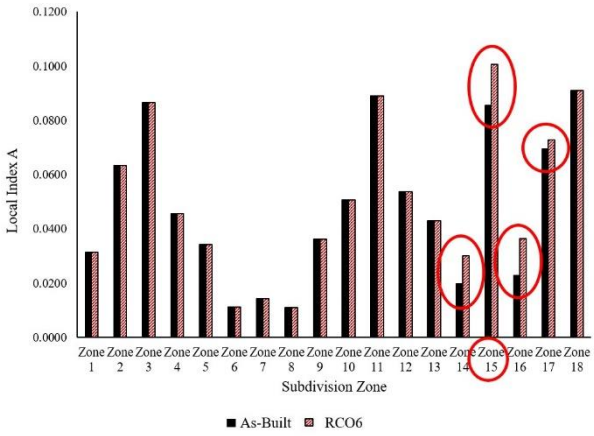

Figure 13 : RCO6 -Local Attained Index Improvement

With the updated breach distribution in Zone 15, the local p-factors within the range of transverse penetration have undergone changes. The new p-factors for damage cases within the transverse penetration zone have increased, attributed to the augmentation of the probability density function (PDF) in that range, as illustrated by the red column in Figure 12. However, the old p-factors between 6.58m and 16.1m (depicted by the blue column) have become irrelevant for calculation purposes since this region is free from damages (refer to Figure 12). Regarding s-factors in Zone 15, the local s-factors have experienced improvement through the application of the RCO arrangement. Consequently, the local Attained Indices (sum of p-factor × s-factor) of not only Zone 15 but also Zones 14, 16, and 17 have been elevated, as described in Figure 13. Interestingly, the impact of the RCOs extends beyond the target zone and influences adjacent

zones, introducing relevant risks to those zones as well, which is instrumental for the vulnerability analysis conducted in STEP 1. Especially, for RCO6, the overall Attained Index has been heightened by 3.46%, ascending from the original value of 0.8579 to 0.8925. The outcomes of the damage stability re-assessment for the other RCOs are succinctly presented in Table 7.

Table 7 : Summary of Damage Stability Recalculation for all RCOs

RCO	Attained Index	Increase (%)
As-Built	0.8579	-
RCO1	0.8590	+ 0.11
RCO2	0.8619	+ 0.41
RCO3	0.8692	+ 1.13
RCO4	0.8727	+ 1.48
RCO5	0.8816	+ 2.38
RCO6	0.8925	+ 3.46

3.6 STEP 6: Cost-Benefit Analysis

The final step involves the selection of an optimal solution or solutions among the RCOs, taking into account the costs associated with each RCO. This is accomplished through cost-benefit analysis employing the Gross Cost of Averting a Fatality (GCAF), defined as GCAF = ΔCost / ΔRisk. To estimate the costs of each RCO, the unit costs outlined in the EMSA III project have been adopted as followings;

- 6,600 USD/ton : Steel weight, including piping, ducting, painting
- 3,300 USD/m2 : Public areas, including ducting, cabling etc
- 2,750 USD/ m2 : Cabin and Service areas, including ducting, cabling
- 33,000 USD/pcs : Additional Watertight Sliding Door, including cabling (*)
- 275 USD/m2 : Cost for penetration watertight subdivision including ducting and cabling etc.(*)
- 418 USD/kW : Additional installed power of main engines, taking into account any discrete step in engine size

(*)An additional 20% of the door cost is included for penetrations of ducting and cabling on the subdivision.

These unit costs are considered based on an exchange rate of 1.1 between Euro and USD in 2015. Additionally, the increased fuel costs due to the additional weights of each RCO are evaluated. These increases are calculated using data from NAPA, and the assumption is made that the increase in wetted area directly impacts ship fuel consumption. This is because friction resistance, which constitutes a significant portion of total ship resistance, is influenced by the wetted surface area. The costs of various types of fuel, including 60% Heavy Fuel Oil (HFO), 20% Marine Gas Oil (MGO), and 20% low sulfur HFO, are presumed to be 600 USD/ton, 900 USD/ton, and 840 USD/ton, respectively, based on EMSA (2015) data.

The expected reduction of fatalities (ΔPLL) was defined as risk reduction ($\Delta risk$) and the same assumption in EMSAIII (2013-2016) was adopted for Potential Loss of Life (PLL) calculations:

$$PLL_{total} = PLL_{collision} + PLL_{grounding/contact} + PLL_{fire/explosion} \quad (5)$$

The risk models for both collisions and groundings, as defined in the EMSA III project, have been utilized for this analysis. However, there has been an update to the sinking probability in these modes. This update is based on the update final Attained Index calculated for each RCO in STEP 5, reflecting the enhanced damage stability achieved through the RCO arrangements.

The necessary cost and the corresponding PLL for each RCO are concisely summarized as following Table.

Table 8 : Cost and PPL Calculated for each RCO

RCO	Cost (Mil USD)	PPL	Δ PPL
As-Built	-	4.64	-
RCO1	0.55	4.59	- 0.05
RCO2	0.58	4.44	- 0.20
RCO3	0.62	4.09	- 0.55
RCO4	0.64	3.92	- 0.72
RCO5	1.22	3.48	- 1.16
RCO6	1.94	2.95	- 1.69

3.7 STEP 7: Decision Making

The outcomes of the cost-benefit analysis are visually summarized in Figure 14, which presents the Gross Cost Assessment Factor (GCAF) values corresponding to the improved Attained Index for all 6 RCOs applied to the reference ship. These GCAFs are derived from the detailed results obtained at each step of the analysis:

- Penetration reductions from Figure 11
- Attained Index improvements from Table 6
- RCO costs from Table 7
- Risk reduction (Δ PPL) from Table 7

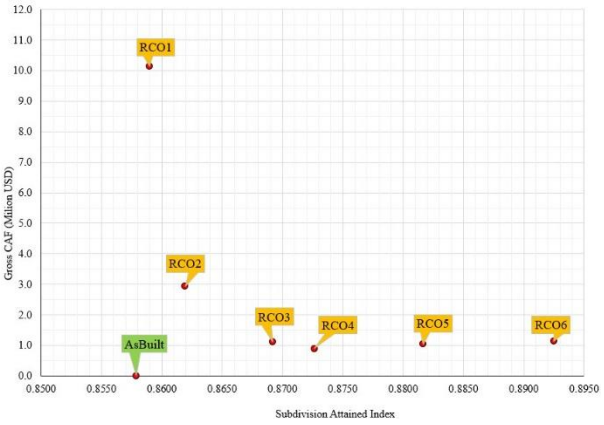

Figure 14: Summary of Cost Benefits Analysis

Based on the graph, it's evident that RCO6, characterized by a hull thickness of 30T and a single longitudinal bulkhead positioned 6.6m from the ship's centerline, emerged as the most effective measure. It obtained a GCAF of 1.09, thereby offering the highest survivability with an Attained Index of 0.8925. It's worth noting, however, that the placement of the single longitudinal bulkhead in RCO6 is relatively close to the ship's centerline compared to the other risk control options. This implies that the inner spaces confined by the two bulkheads might be constrained, potentially leading to reduced flexibility in terms of space utilization.

Given these considerations, the final decision-making process for the optimum solution should carefully weigh the advantages and disadvantages of RCO6. This entails a comprehensive evaluation of its potential benefits and drawbacks within the context of the ship's design and intended purpose.

4 CONCLUSIONS / RECOMMENDATIONS

This paper introduces a novel methodology for enhancing ship survivability through crashworthiness analysis, focusing on alternative designs not covered by the current SOLAS framework. The methodology, consisting of seven distinct steps, has been demonstrated using a 65,000 GT cruise ship as a case study. Within this context, six Risk Control Options (RCOs) were considered to either control or mitigate risks.

The process began with a vulnerability analysis utilizing a plurality approach with extension to adjacent zones. This analysis identified Zone 15 as the target zone and collision location. Subsequently, the collision scenario, involving a collision speed of 10.14 knots to yield maximum B/2 penetration, was defined. Collision simulations for each RCO followed, leading to the acquisition of penetration reduction results. The local transverse breach distribution of the target zone was updated for each RCO, enabling the re-assessment of damage stability and the computation of improved Attained Indices. cost-benefit analyses encompassing both CAPEX and OPEX for a ship's 30-year life cycle were conducted. This entailed calculating Potential Loss of Life (PLL) reduction for each RCO, using risk models from the EMSA III project and the results of damage stability re-assessment.

The culmination of the analysis is to quantify effects of each RCOs using crashworthiness anaysis, using penetration and attained index. Then, in turn, the design effects of each RCO were plotted with the GCAF and Attained Index, to identify the optimal solution among RCOs. The selected optimum RCO involves a double hull design with a single longitudinal subdivision positioned at 6.6m and strengthened hull thickness of 30mm. However, while RCO6 proves advantageous in terms of cost and risk reduction, associated limitations related to design, operation, and maintenance should be meticulously assessed by decision-makers prior to final implementation.

Based on this proposed quantitative risk assessment methodology and anaysis outcomes, it is recommended that the implementation of RCOs across adjacent zones and the target zone can lead to more versatile and spacious internal spaces. This potential innovation could pave the way for

significant design advancements in the future, fostering a new paradigm for ship design.

5 REFERENCES

ANSYS 2019. User's manual for ANSYS AQWA version 18. *In:* INC., A. (ed.). PA, USA.

BAE, H., VASSALOS, D., PATERSON, D., MUJEEB-AHMED, M. & BOULOUGOURIS, E. 2021. The Effectiveness of Crashworthiness as a Damage Stability Risk Control Option. Conference: 1st International Conference on the Stability and Safety of Ships and Ocean Vehicles (STAB&S 2021). Glasgow, UK

BARBA, M. 1880. Mémoires de la Société des Ingénieurs Civils. *Memoirs of the Society of Civil Engineers*, 22.

COWPER, G. R. & SYMONDS, P. S. 1957. Strain-hardening and strain-rate effects in the impact loading of cantilever beams. Brown Univ Providence Ri.

EHLERS, S., BROEKHUIJSEN, J., ALSOS, H. S., BIEHL, F. & TABRI, K. 2008. Simulating the collision response of ship side structures: a failure criteria benchmark study. *International Shipbuilding Progress*, 55**,** 127-144.

EMSA 2015. Risk Acceptance Criteria and Risk Based Damage Stability, Final Report, Part 2: Formal Safety Assessment.

EMSAIII 2013-2016. Study assessing the acceptable and practicable risk level of passenger ships related to damage stability ("EMSA 3"), undertaken by DNVGL. EMSA/OP/10/2013, http://emsa.europa.eu/damage-stability-study.html.

EU 2003. THE EUROPEAN PARLIAMENT AND OF THE COUNCIL of 14 April 2003 on specific stability requirements for ro-ro passenger ships. *DIRECTIVE 2003/25/EC*. Official Journal of the European Union.

HARDER 2000-2003. Harmonisation of Rules and Design Rationale. EC Contact No. GDRB-CT-1998-00028, Final Technical Report.

HODGE, P., HOPKINS, H. & LEE, E. 1956. The theory of piecewise linear isotropic plasticity. *Deformation and Flow of Solids/Verformung und Fliessen des Festkörpers*. Springer.

HOGSTRÖM, P. & RINGSBERG, J. W. 2012. An extensive study of a ship's survivability after collision–a parameter study of material characteristics, non-linear FEA and damage stability analyses. Marine structures, 27, 1-28.

IMO 1991. Expanatory notes to the SOLAS regulation on subdivision and damage stability of Cargo ships of 100 meters in length and over. Res.A.684(17). the Assembly, International Maritime Organisation, London, UK.

IMO 2003. DEVELOPMENT OF EXPLANATORY NOTES FOR HARMONIZED SOLAS CHAPTER II-1, Approval procedure concept for alternative arrangements, Submitted by Germany. SLF 46/INF.10. SUB-COMMITTEE ON STABILITY AND LOAD LINES AND ON FISHING VESSELS SAFETY, International Maritime Organisation, London, UK.

IMO 2004. Amendments to the Annex of the Protocol of 1978 relating to the International Convention for the Prevention of Pollution From Ships, 1973. Res.MEPC.117(52) Reg.19 & 20. Marine Environment Protection Committee, International Maritime Organisation, London, UK.

KIM, S. J., KORGERSAAR, M., AHMADI, N., TAIMURI, G., KUJALA, P. & HIRDARIS, S. 2021. The influence of fluid structure interaction modelling on the dynamic response of ships subject to collision and grounding. Marine Structures, 75, 102875.

LSTC 2019. LS-DYNA keyword user's manual. In: CORPORATION, L. S. T. (ed.). California, USA.

LUHMANN, H. 2009. Floodstand WP1 Deliverable D: Concept ship desing B.

PAIK, J. 2007. Practical techniques for finite element modeling to simulate structural crashworthiness in ship collisions and grounding (Part I: Theory). Ships and Offshore Structures, 2, 69-80.

PAIK, J. K. 2018. Ultimate limit state analysis and design of plated structures, Wiley Online Library.

PAIK, J. K., KIM, S. J., KO, Y. K. & YOUSSEF, S. A. Collision risk assessment of a VLCC class tanker. SNAME Maritime Convention, 23-28 October 2017 2017 Houston, USA. The Society of Naval Architects and Marine Engineers.

PATERSON, D. 2020. Reconfiguring the ship environment for damage stability enhancement. University of Strathclyde.

SAJDAK, J. & BROWN, A. 2005. Modeling longitudinal damage in ship collisions. SSC-437, Ship Structure Committee.

SCHARRER, M., ZHANG, L. & EGGE, E. 2002. Kollisionsberechnungen in schiffbaulichen entwurfssystemen (collision calculation in naval design systems). Bericht ESS 2002.183. Germanischer Lloyd.

SCHREUDER, M., HOGSTRÖM, P., RINGSBERG, J. W., JOHNSON, E. & JANSON, C. E. 2011. A method for assessment of the survival time of a ship damaged by collision. Journal of ship research, 55, 86-99.

UN 2008. European Agreement concerning the international Carriage of Dangerous Goods by Inland Waterways (ADN). ECE/TRANS/203 (Vol.I). United Nations, New York and Geneva.

VASSALOS, D., MUJEEB-AHMED, M., PATERSON, D., MAURO, F. & CONTI, F. 2022. Probabilistic damage stability for passenger ships—the p-factor illusion and reality. Journal of Marine Science and Engineering, 10, 348.

VREDEVELDT, A., FEENSTRA E 2001. Crashworthy side structures for improved collision damage survivability of coasters and medium sized Ro-Ro cargo ships.

ZHANG, L., EGGE, E.-D. & BRUHNS, H. 2004. Approval procedure concept for alternative arrangements, Germanischer Lloyd.

ZHENG, Y., AKSU, S., VASSALOS, D. & TUZCU, C. 2007. Study on side structure resistance to ship-ship collisions. Ships and Offshore Structures, 2, 273-293.

An improved method for dynamic assessment of survivability of damaged ships in waves

Jianwen Duan, *State Key Laboratory of Ocean Engineering, School of Naval Architecture, Ocean and Civil Engineering, Shanghai Jiao Tong University, Shanghai, China,* sjtudjw@sjtu.edu.cn

Ning Ma, *State Key Laboratory of Ocean Engineering, School of Naval Architecture, Ocean and Civil Engineering, Shanghai Jiao Tong University, Shanghai, China,* ningma@sjtu.edu.cn

Qiqi Shi, *State Key Laboratory of Ocean Engineering, School of Naval Architecture, Ocean and Civil Engineering, Shanghai Jiao Tong University, Shanghai, China,* graceshqq@sjtu.edu.cn

Xiechong Gu, *State Key Laboratory of Ocean Engineering, School of Naval Architecture, Ocean and Civil Engineering, Shanghai Jiao Tong University, Shanghai, China,* xcgu@sjtu.edu.cn

Xin Li, *State Key Laboratory of Ocean Engineering, School of Naval Architecture, Ocean and Civil Engineering, Shanghai Jiao Tong University, Shanghai, China,* doulammeng@sjtu.edu.cn

ABSTRACT

This study aims at the contribution to the improvement of current damaged stability regulations, and the enhancement of both accuracy and efficiency in evaluation of the Attained Survivability Index (A-index) for the damaged ships in waves. The probabilistic framework in Safety of Life at Sea (SOLAS) based on static assessment is not accurate enough for damaged ships in waves. In this paper, a probabilistic framework based on dynamic model for the survivability assessment of damaged ships in waves is proposed. The calculation of p-factor is based on "non-zonal" approach. The definition of s-factor is related to the short-term mean stability failure rate of damaged ships under design sea states. In addition, the pre calculation method and parameter model identification are used to improve the computational efficiency of the numerical model. Finally, the probabilistic framework is used for the survivability assessment of a frigate ship DTMB 5415 in beam seas at zero speed. The availability of Latin Hypercube sampling method for determining sampling numbers to calculate p-factor is shown.

Keywords: *Probabilistic framework, Dynamic survivability assessment, Damaged ships, A-index, Parameter model identification, Latin Hypercube sampling method.*

1. INTRODUCTION

The survivability of damaged ships is always focused on by designers. But the current regulations based on static assessment are not with good accuracy. Also, the calculation of damage stability in waves is needed to assess the survivability of ships at sea.

The damaged stability regulation Safety of Life at Sea (SOLAS) for damaged civil ships in still water is within the probabilistic framework (IMO, 2020a). The Attained Survivability Index (A-index) represented the survivability of damaged ships is calculated. There are two key points in calculating A-index: one called p-factor is calculating the probability of the occurrence of each damage case, the other called s-factor is probability to survive the flooding of each damage case.

The p-factor in SOLAS is calculated based on the dedicated marginal distribution functions of breaches in collision damage. The method used in SOLAS to calculate p-factor is commonly referred to as "zonal" method. In order to calculate the p-factor of different damage types, the "non-zonal" approach is proposed (Bulian et al., 2016; Mauro and Vassalos, 2022a). The so-called "non-zonal" approach relies on both the sampling method used and the number of samples collected.

The s-factor in SOLAS based on static assessment considers only ship stability residual parameters. But internal water motions need to be considered to effectively improve the accuracy of damage stability simulation. The hybrid two-level framework for the stability of damaged ships was proposed (Mauro et al., 2023): Level-1 assessment

based on static damage stability simulation and Level-2 assessment based on dynamic flooding simulation. However, it should be noted that Level-2 assessment is only applicable to a few dangerous damage conditions. The main reason is due to the computational speed limitations of dynamic numerical model.

In this paper, an improved method within probabilistic framework for assessing the survivability of damaged ships in waves is proposed. In this method, the p-factor is calculated based on the "non-zonal" approach. The Latin Hypercube sampling method is utilized, and the impact of varying sample sizes is discussed. The definition of s-factor is related to the short-term mean stability failure rate of damaged ships under design sea states. To calculate s-factor, this paper proposes a fast dynamic numerical model to compute the motion of damaged ships under design sea states. Finally, the improved method is used for the survivability assessment of a frigate ship DTMB 5415 which sustained collision damage in beam seas at zero speed.

2. PROBABILISTIC FRAMEWORK IN SOLAS

The SOLAS regulation is in the probabilistic framework and the safety level of a damage ship is represented by the Attained Survivability Index (A-index). The A-index for a certain draught is calculated by:

$$A = \sum_{j=1}^{N_{DC}} s_j p_j \quad (1)$$

Where N_{DC} is the number of damage cases. The "damage case" refers to a specific combination of the same damaged compartments. The p_j is the p-factor of the jth damage case and the s_j is the s-factor of the jth damage case.

The p-factor is based on the "zonal" method. There are some characteristics of collision damage breaches described in SOLAS (IMO, 2020a):

$X_C(m)$: longitudinal position of potential damage center; $L_{x,p}(m)$: longitudinal extent of the potential damage; $L_{y,p}(m)$: lateral penetration of the potential damage; $L_{zext,p}(m)$: vertical extension of the potential damage. I_{side}: flag distinguishing starboard and portside damage. The potential damage means that the range of the damage breach can be extended out of the ship. The "worst case approach" is proposed in SOLAS instead of lower vertical limit of the breach.

The marginal distribution functions of the above five characteristics are only for collision damage. In order to calculate the p-factor of other different damage types, "non-zonal" approach is needed.

The s-factor in SOLAS is based on the static method to calculate the residual parameters of damaged ships. However, the static method is not accurate enough to assess the survivability of damaged ships in waves.

3. IMPROVEMENT OF PROBABILISTIC FRAMEWORK FOR DYNAMIC ASSESSMENT

In this section, the improved method within probabilistic framework based on dynamic assessment is introduced. The purpose of the probabilistic framework is to evaluate the survivability of damaged ships in waves. And the framework provides a detailed description of the calculation process for both the p-factor and s-factor.

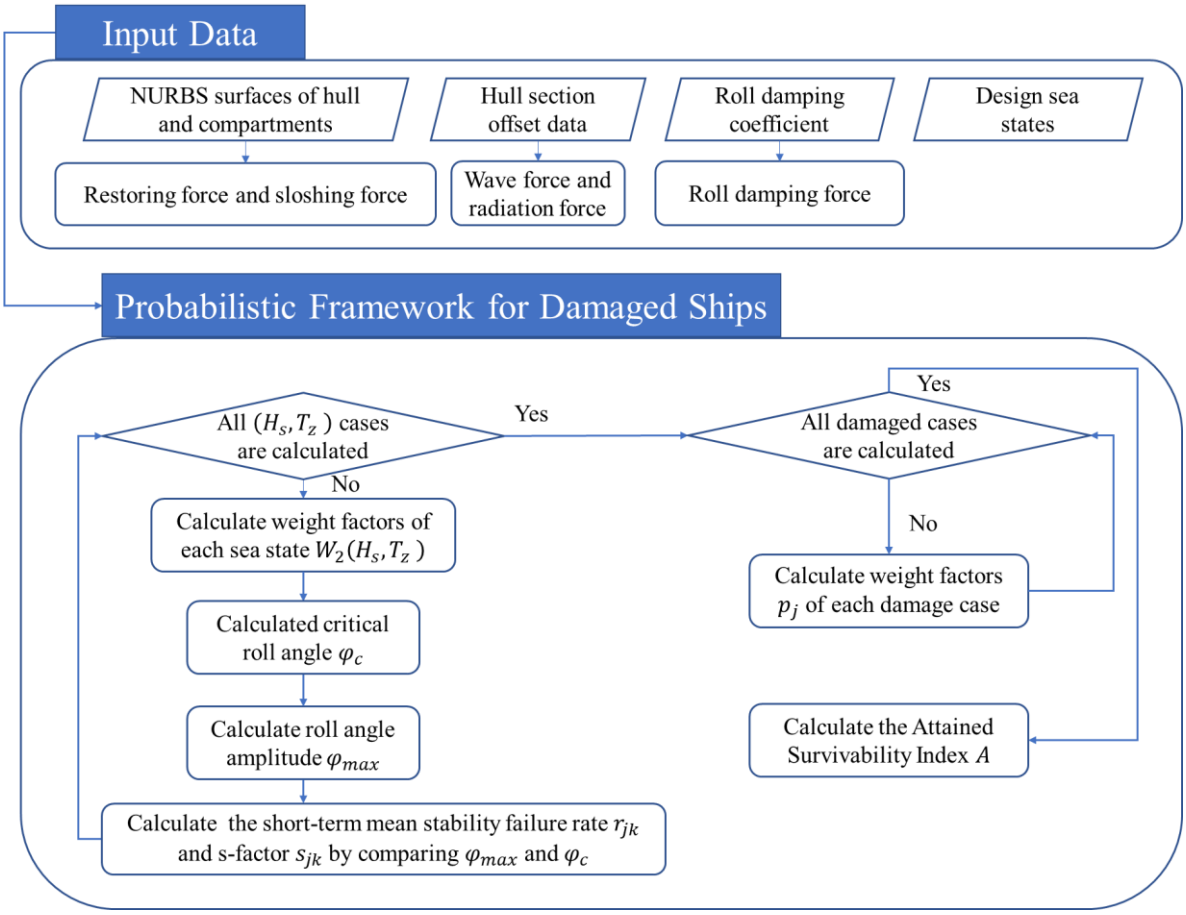

Figure 1: Probabilistic framework based on dynamic assessment for damaged ships in waves.

Improved probabilistic framework

The probabilistic framework is represented in Figure 1.

The input data includes the parameters of hull and compartments. The parameters of design sea states are also needed to calculate the motion of ships in waves.

In this probabilistic framework, the A-index also represents the safety level of a damage ship and it can be calculated through Eq. (1). The calculation process is as follow:

1) Generating models of hull and compartments. Generating the geometry models of breaches and calculating the probability of each breach. Grouping of breaches involving the same combination (represents one damage case) of damaged compartments and calculating the p-factor of each damage case.

2) For a specific damaged case, calculating the roll angle amplitude φ_{max} based on dynamic numerical model at design sea states. Calculating the critical roll angle φ_c according to the hull attitude.

3) Calculating the short-term mean stability failure rate r_{jk} for jth damage case and kth sea states based on direct counting procedure (IMO, 2020b). The s-factor for jth damage case and kth sea states can be calculated through:

$$s_{jk} = 1 - r_{jk} \quad (2)$$

4) If all the sea states are calculated, the s_j can be calculated through weighted sum of s_{jk} and $W_2(H_s, T_z)$.

5) If all damage cases are calculated, the A-index can be calculated through Eq. (1).

Calculation of the p-factor

The "non-zonal" approach is used to calculate the p-factor. Comparing to "zonal" method, "non-zonal" approach needs the marginal distribution functions of the lower vertical limit of the breach ($L_{ll,p}$) additionally. The cumulative distribution functions of lower vertical limit of the breach are proposed by Bulian et al (Bulian et al., 2019).

There are two points required attention in order to be consistent with SOLAS:

The first point is the correspondence between the longitudinal position of potential damage center X_C and the longitudinal extent of the potential damage $L_{x,p}$ at both ends of the hull. The relationship is represented in Figure 2. When the damage is within the range of the hull, the position of potential damage center and the longitudinal extent of the potential damage are not changed. But when the damage is outside the range of the hull, the position of potential damage center and the longitudinal extent of the potential damage are changed as shown in Figure 2.

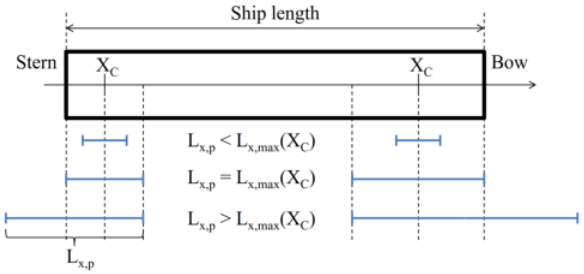

Figure 2: The relationship between X_C and $L_{x,p}$ at the end of the ship (Bulian et al., 2019).

The second point is the suitability of the generated lateral penetration of the potential damage $L_{y,p}$. The maximum value of $L_{y,p}$ is $B/2$ in SOLAS. Where B is the local breadth of the ship at the considered waterline. In the "non-zonal" approach, the maximum value of $L_{y,p}$ is defined associate with the subdivision length L_s and longitudinal extent of the potential damage $L_{x,p}$ empirically (Mauro and Vassalos, 2022b):

$$L_{y,pmax} = \begin{cases} 15B\dfrac{L_{x,p}}{L_s}\dfrac{L_s}{L_{x,p}} < 30 \\ \dfrac{B}{2} \qquad \dfrac{L_s}{L_{x,p}} \geq 30 \end{cases} \tag{3}$$

The Latin Hypercube sampling method is used. The six characteristics including X_C, $L_{x,p}$, $L_{y,p}$, $L_{zext,p}$, $L_{ll,p}$ and I_{side} are sampled based on the individual marginal distribution functions respectively. As SOLAS proposes " worst case approach" instead of the probabilistic model for lower vertical limit of the breach $L_{ll,p}$, the "non-zonal" approach needs additional marginal distribution functions of $L_{ll,p}$ to sample the breaches.

Calculation of the s-factor

In order to calculate s-factor, a fast 1-DOF time domain dynamic numerical model is proposed. The motion equation is as follow:

$$\begin{aligned}(I_{44} + a_{44}(\infty) + M_{44}^{w})\dot{v}_4(t) + B_v v_4(t) \\ + MgGZ(t) \\ = F_4^{FK}(t) + F_4^{dif}(t) \\ + F_4^{rad}(t) + F_4^{slosh}(t)\end{aligned} \tag{4}$$

Where the subscript "4" represents the roll degree of freedom; the superscript dot represents the derivative of time. I_{44} is the roll moment of inertia of intact ship; $a_{44}(\infty)$ is the infinite-frequency roll added moment of inertia of intact ship; M_{44}^{w} is roll moment of inertia caused by flooding water; $v_4(t)$ is the roll angular velocity; B_v is the roll damping coefficient of the damage ship; M is the mass of the damage ship; $GZ(t)$ is the restoring arm in still water; g is the gravitational acceleration ($9.81\ m/s^2$); $F_4^{FK}(t)$ is the roll Froude-Krylov moment; $F_4^{dif}(t)$ is the roll diffraction moment; $F_4^{rad}(t)$ is the roll radiation moment; $F_4^{slosh}(t)$ is the roll sloshing moment because of flooding water.

The calculation methods for some components in the motion equation are introduced as follow:

The restoring arm is a pre-computed parameter based on pressure integration over the instantaneous wetted surfaces at different heel angle. The calculation results are stored in database and will be called based on linear interpolation method.

The frequency domain roll add mass $a_{44}(\omega)$ and damping coefficient $b_{44}(\omega)$ are pre-calculated based on STF method. But when the frequency is high, the numerical errors will be occurred. In order to get time domain results, impulse response function is used. But the convolution term in impulse response function is not efficient in numerical simulation. The parametric model identification is proposed to improve computational efficiency (Pérez and Fossen, 2008). The parameter model of frequency domain retardation functions is used for calculate the damping coefficient at the high frequency. The equation of parameter model is as follow:

$$\begin{aligned}\widehat{K}(s) &= \frac{P(s)}{Q(s)} \\ &= \frac{p_m s^m + p_{m-1}s^{m-1} + \cdots + p_0}{q_n s^n + q_{n-1}s^{n-1} + \cdots + q_0}\end{aligned} \tag{5}$$

Where $\widehat{K}(s)$ is the fitting results of parameter model; $[p_m, \ldots p_0, q_n, \ldots, q_0]$ are the parameters to be fitted.

The parameter model of time domain retardation functions is used for calculating the convolution of

impulse response function. This parameter model is the state-space model represented by Eq. (6). The advantage of the state-space model is that the value of the state summaries all the past information of the system.

$$\begin{aligned} \dot{x} &= A'x + B'v_4 \\ F_4^{rad}(t) &= C'x \end{aligned} \tag{6}$$

Where A', B' and C' are the parameters matrixes to be fitted. x is the intermediate variable.

The frequency domain roll Froude-Krylov moment $F_4^{FK}(\omega)$ and roll diffraction moment $F_4^{dif}(\omega)$ are pre-calculated by STF method and the values at wave frequency are obtained by linear interpolation method. The time domain values can be calculated based on simplified formula (Shin and Chung, 2021; Gu et al., 2013):

$$\begin{aligned} F_4^{FK}(t) &= F_4^{FK}(\omega_0)\sin(\omega_0 t + \theta_0) \\ F_4^{dif}(t) &= F_4^{dif}(\omega_0)\sin(\omega_0 t + \theta_0) \end{aligned} \tag{7}$$

Where ω_0 is the wave frequency; θ_0 is the wave phase angle.

The lump mass method is used to calculate the sloshing force $F_4^{slosh}(t)$:

$$\begin{aligned} \boldsymbol{F^{slosh}} = M_{water}(&\dot{\boldsymbol{u}}_{\boldsymbol{h}} + \dot{\boldsymbol{\omega}}_{\boldsymbol{h}} \times \boldsymbol{r_w} + \boldsymbol{\omega_h} \\ &\times (\boldsymbol{u_h} + \boldsymbol{\omega_h} \times \boldsymbol{r_w}) \\ &+ \dot{\boldsymbol{u}}_{\boldsymbol{w}} + 2\boldsymbol{\omega_h} \times \boldsymbol{u_w}) \\ &+ \dot{M}_{water}(\boldsymbol{u_h} + \boldsymbol{u_w} \\ &+ \boldsymbol{\omega_h} \times \boldsymbol{r_w}) - \boldsymbol{F^G} \end{aligned} \tag{8}$$

Where M_{water} is the mass of water in the compartment; $\dot{M}_{water}$ is the velocity at which water flows in or out of a breach, and the value is zero in this paper; Where $\boldsymbol{u_h} = (u, v, w)^T$ and $\boldsymbol{\omega_h} = (p, q, r)^T$ are the translational speed and rotational speed of ship respectively; $\boldsymbol{r_w} = (x_w, y_w, z_w)^T$ is the coordinate of flooding water center in damaged compartment; Superscript dot means the derivative of time and $\boldsymbol{u_w} = \dot{\boldsymbol{r}}_{\boldsymbol{w}}$.

In this paper, the M_{44}^w of DTMB 5415 ship is set as the roll moment of inertia of flooding water at steady-flooding stage. This is because the results of motion with constant flooding water mass are similar to the results with variable flooding water (Acanfora and Balsamo, 2021). The large symmetrical damaged compartments may be a possible reason for similar calculation results. But for the universality of the numerical model, the modified Bernoulli equation for incompressible fluids can be used to calculate variable flooding water mass $M_{44}^w(t)$ in future research.

The 1-DOF numerical model is used to calculate the roll angle amplitude φ_{max} at the design sea states. Computational efficiency of the model is related to the number of damaged compartments. A simulation in irregular waves for four compartments damaged runs on average 120 times faster than real-time (using a regular laptop without parallel computing). The real-time refers to the time set by the simulation for the ship motion at the design sea states. And for one compartment damaged, the computational efficiency is increased to 240 times faster than real-time.

Different damage cases cause different hull attitudes. In order to measure the danger level of each damage case, the critical roll angle φ_c in this paper is set as the angle when the water is on the deck instead of a constant value.

The short-term mean stability failure rate r_{jk} for jth damage case and kth sea states is calculated based on the following direct counting procedure:

1) Simulating the motion of a ship under design sea state for 7200s (exposure time is set as 2h) repeatedly.

2) Estimating the mean time T when $\varphi_{max} > \varphi_c$.

3) Calculating short-term mean stability failure rate r_{jk} as Eq. (9) (IMO, 2020b):

$$r_{jk} = \begin{cases} 1 & T = 0s \\ 1 - e^{-\frac{7200}{T}} & 0s < T < 7200s \\ 0 & T = 7200s \end{cases} \tag{9}$$

Finally, the s-factor for jth damage case and kth sea states can be calculated through Eq. (2).

4. VALIDATION OF 1-DOF DYNAMIC NUMERICAL MODEL

Before the systematical survivability assessment, the 1-DOF time domain dynamic numerical model in section 3 should be validated. The frigate ship DTMB 5415 is selected because of the available experimental results in beam seas at zero speed.

DTMB 5415 ship

The main particulars of the intact ship (full scale) can be seen in Table 1.

Table 1: Main particulars of DTMB 5415 (full scale).

Items	Values
Length, Lpp/m	142.200

Breadth, B/m	19.082
Depth, D/m	12.470
Mean draught, T/m	6.150
Displacement, Δ/t,kg	8635
Metacentric height, GM/m	1.938
Height of COG, Z_G/m	7.555
Roll radius of inertia in water, kxx/m	6.932
Pitch radius of inertia in air, kyy/m	36.802
Yaw radius of inertia in air, kzz/m	36.802

The ship subdivision is presented in Figure 3. The definition of damaged compartments and distribution in the direction of ship length (positive direction: from stern to bow) are presented in Table 2.

Table 2: The damaged compartments definitions of DTMB 5415 (full scale).

Name	After end(m)	Forward end(m)
com1	-	30.86
com2	30.86	65.66
com3	65.66	76.15
com4	76.15	90.02
com5	90.02	108.63
com6	108.63	130.56
com7	130.56	-

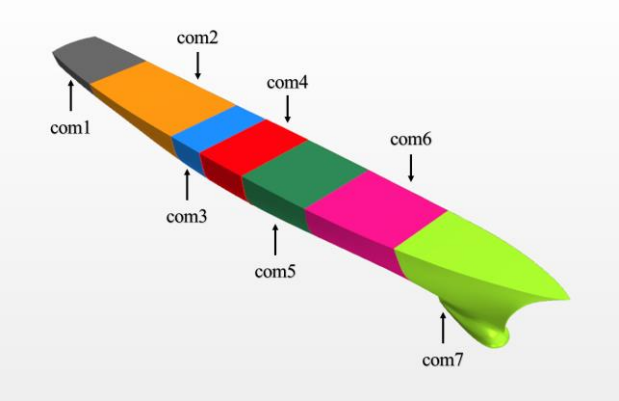

Figure 3: The subdivision of DTMB 5415.

Validation of model

Figure 4 shows the GZ curves of the frigate hull DTMB 5415 in still water with different flooding water mass when two compartments are damaged (com3 and com4). The blue dashed line represents the GZ curve when there is no flooding water in the damaged compartments. And the red dotted line represents the GZ curve when flooding water fully fills the damaged compartments. It has been qualitatively verified that as the flooding water mass increases, the restoring arm of the ship decreases.

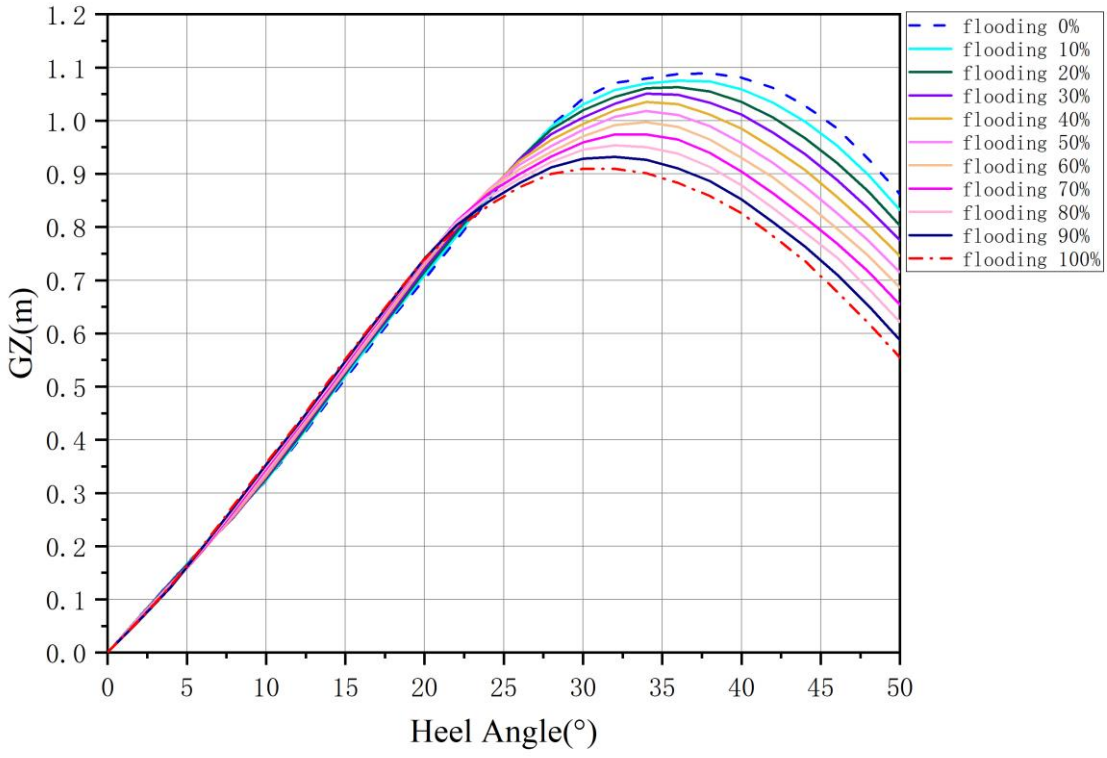

Figure 4: GZ curve of DTMB 5415 with different flooding water mass (damaged compartments: com3 and com4).

The results of frequency domain damping coefficient based on Eq. (5) are represented in Figure 5. The sample ship is DTMB 5415. In Figure 5, the red circle represents the calculation results based on STF method. And the blue dashed line represents the fitting results based on parameter model.

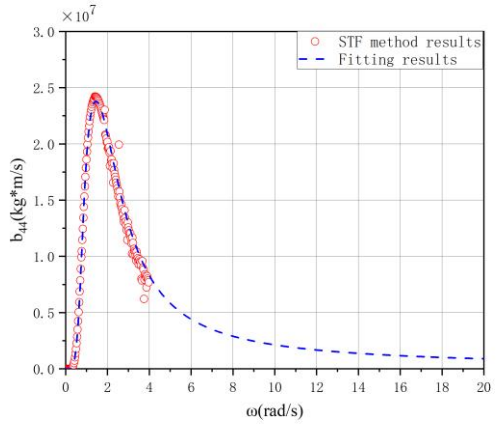

Figure 5: Comparison of $b_{44}(\omega)$ between the calculation results based on STF method and fitting results from parameter model.

The results of time domain retardation functions $K_{44}(t)$ are represented in Figure 6. The convolutional calculation results are from fitting data of $b_{44}(\omega)$. In Figure 6, the red circle represents the calculation results based on convolutional computation. And the blue dashed line represents the fitting results based on state-space model.

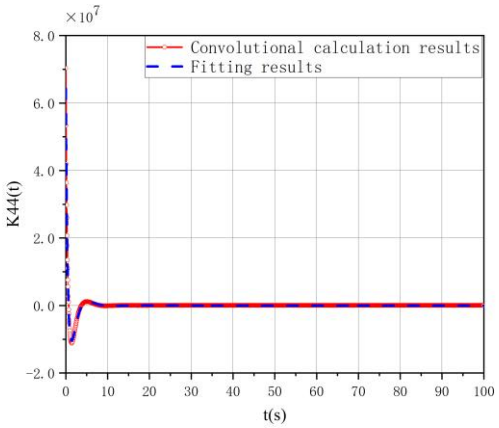

Figure 6: Comparison of $K_{44}(t)$ between the calculation results based on convolutional computation and fitting results from state-space model.

The calculation results based on the numerical model in this paper are compared with the results based on static model and full model (Acanfora and Balsamo, 2021) and experimental data (Begovic et al., 2017) for DTMB 5415 ship in beam regular waves. They are represented in Figure 7. The roll amplitude φ used for roll response calculation in regular beam waves is the amplitude at which the roll motion of the ship reaches a stable state within 7200s. The roll amplitude is nondimensionalized by dividing it by the wave steepness (kA, where k is the wave number and A is the wave amplitude). Red dashed line represents the results based on static model. Green double dot dash line represents the results based on full model (considering sloshing force and variable flooding water). Blue solid line represents the results based on 1-DOF dynamic model. Black triangle represents the experimental data. The results show that the roll motion values based on dynamic numerical model in this paper have better consistency with experimental data than static model. And the calculation results of the simplified method presented in this paper exhibit poor accuracy only when the wave period is below 9s, as compared to the full model (Acanfora and Balsamo, 2021).

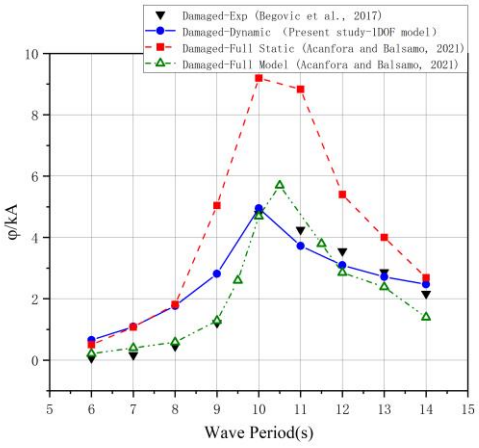

Figure 7: Comparison of roll responses in beam regular waves for DTMB 5415 ship (damaged compartments: com3 and com4).

5. SURVIVABILITY ASSESSMENT OF DTMB 5415 SHIP

In this section, the probabilistic framework in section 3 is used for the survivability assessment of a frigate ship DTMB 5415 in beam seas at zero speed. The damage type is only for collision damage. And the ship is simulated in steady flooding stage (the final equilibrium angle is reached but the ship may experience roll motions and flooding water will slosh due to wave excitation)

Survivability assessment

The survivability assessment for DTMB 5415 ship is evaluated by A-index. The p-factor and s-factor should be calculated first based on the parameters of ship and sea states.

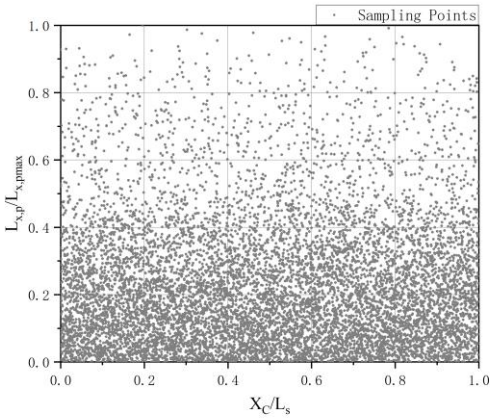

Figure 8: Non-dimensional damage length and position for DTMB 5415.

Because the compartments subdivisions are only along the direction of the ship length, the marginal distribution functions of X_C and $L_{x,p}$ are needed. The Latin Hypercube sampling method is used and the sampling points of non-dimensional damage position X_C/L_s and damage length $L_{x,p}/L_{x,pmax}$ are show in Figure 8 (10000 sampling points). Then the p-factor of each damage case is calculated. P-factor of a specific damage case is equal to the ratio of the corresponding number of sampling points to the total number of sampling points.

The calculation method for s-factor is introduced in section 3. Because there is no official statistical data of sea states when ships are sustained collision damage, the significant wave height H_s is equal to 6m and average zero crossing period T_z is equal to 9.6s. JONSWAP wave spectrum is used to simulate the long crest irregular wave. The time varying roll angle and critical roll angle of damaged DTMB 5415 ship in different damage cases are shown in Figure 9.

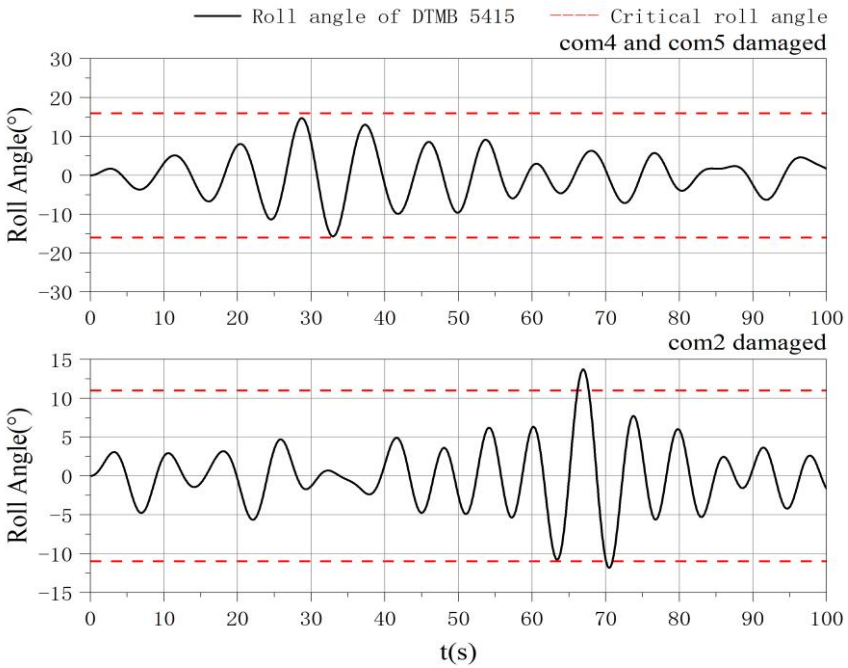

Figure 9: Roll motion for DTMB 5415 in different damage cases: com4 and com5 damaged (up), com2 damaged (down).

The A-index of DTMB 5415 ship at design sea states is calculated through Eq. (1):

$$A = \sum_{j=1}^{N_{DC}} s_j p_j = 0.7545 \tag{10}$$

Comparison of A-indexes under different sampling numbers

In order to compare the A-indexes under different sampling numbers N, the sampling numbers are set as 100,1000,10000 and 100000. The variation of A-index is shown in Figure 10.

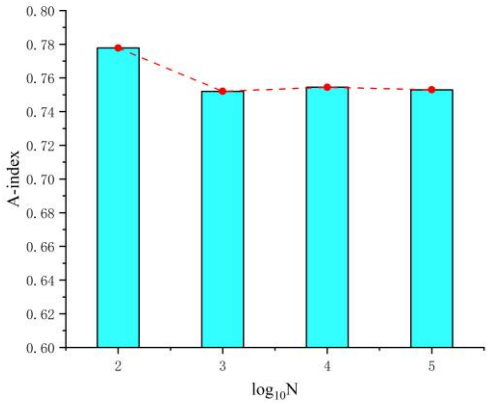

Figure 10: A-indexes for DTMB 5415 under different sampling numbers.

It shows that the A-index tends to be a constant value when the sampling numbers are greater than 1000 as in Figure 10. The results prove that the A-index under 10000 sampling points is reliable.

6. CONCLUSION

In this paper, a probabilistic framework based on dynamic simulation for the survivability assessment of damaged ships in waves is proposed.

S-factor in this probabilistic framework is defined related to the short-term mean stability failure rate which gives a probabilistic definition of the survival probability of damaged ships under sea states.

The calculation of s-factor in this paper is based on dynamic numerical model. In order to maintain the rapidity of the calculation model, the pre calculation method and parameter model identification are used. The results of simplified 1-DOF numerical model are verified by comparison with experimental data. The simulation time for DTMB 5415 damaged ships is at least 120 times faster than real-time.

Moreover, the probabilistic framework is used for the survivability assessment of a frigate ship DTMB 5415 in beam seas at zero speed. And the influence of sampling numbers to calculate p-factor based on Latin Hypercube sampling method is analyzed.

ACKNOWLEDGEMENTS

This study is financially supported by the Fundamental Research Funds for the Central Universities, the Foundation of National Key Laboratory of Hydrodynamics (JCKY2022201CA02).

REFERENCES

Acanfora, M., Balsamo, F, 2021, “On the development of fast numerical methods for the estimation of hull girder loads for a flooded ship in waves”, *Ocean Eng*, 233, 109213.

Begovic, E., Day, A. H., Incecik, A, 2017, “An experimental study of hull girder loads on an intact and damaged naval ship”, *Ocean Eng*, 133, 47-65.

Bulian, G., Lindroth, D., Ruponen, P., Zaraphonitis, G., 2016, “Probabilistic assessment of damaged ship survivability in case of grounding: development and testing of a direct non-zonal approach”, *Ocean Eng*, 120, 331-338.

Bulian, G., Cardinale, M., Dafermos,G., Eliopoulou, E., Francescutto, A., Hamann, R., Lindroth, D., Luhmann, H., Ruponen, P., Zaraphonitis, G., 2019, “Considering collision, bottom grounding and side grounding/contact in a common non-zonal framework”, In Proceedings of the 17th International Ship Stability Workshop, Helsinki, Finland, pp. 245-257.

Gu, M., Lu, J., Wang, T, 2013, “Experimental and numerical study on stability under dead ship condition of a tumblehome hull”, In Proceedings of the 13th International Ship Stability Workshop, Brest, France, pp. 23-26.

IMO, 2020a, “International convention for the safety of life at sea (SOLAS)”, Technical Report, IMO, Consolidated edition as of 2020.

IMO, 2020b, “MSC.1/Circ. 1627 - Interim Guidelines on the Second Generation Intact Stability Criteria”, International Maritime Organization, London, UK.

Mauro, F., Vassalas, D., 2022a. “The influence of damage breach sampling process on the direct assessment of ship survivability”, *Ocean Eng*, 250, 111008.

Mauro, F., Vassalos, D., Paterson, D., Boulougouris, E., 2022b, “Exploring smart methodologies for critical flooding scenarios detection in the damage stability assessment of passenger ships”, *Ocean Eng*, 262, 112289.

Mauro, D., Vassalos, D., Paterson, D., Boulougouris, E., 2023, “Evolution of ship damage stability assessment—Transitioning designers to direct numerical simulations”, *Ocean Eng*, 268, 113387.

Pérez, T., Fossen, T., 2008, “Time-vs. frequency-domain identification of parametric radiation force models for marine structures at zero speed”, *Modeling, Identification and Control*, 29(1), pp. 1-19.

Shin, D. M., Chung, J., 2021, “Application of dead ship

condition based on IMO second-generation intact stability criteria for 13K oil chemical tanker", *Ocean Eng*, 238, 109776.

Investigation on the capsizing probability of damaged ship in irregular seaway

Shu-xia, Bu, *China Ship Scientific Research Center* bushuxia8@163.com
Min, Gu, *China Ship Scientific Research Center* gumin702@163.com
Chen, Yang, *China Ship Scientific Research Center* yangchen@cssrc.com.cn
Pei-jie, Zhang, *China Ship Scientific Research Center* pjzhang@cssrc.com.cn

ABSTRACT

Serious incidents occurred from time to time as a result of collision and grounding, mainly resulting in ship damage and water ingress/egress. As a result, the direct assessment of damaged ship stability in a complicated environment is of great significance. This paper investigates the use of the direct stability procedure and direct counting method for the failure rate of damaged ships proposed by the IMO second generation intact ship stability criteria. One damaged passenger ship is chosen for the experimental test in order to first validate the accuracy of the prediction method in both regular and irregular waves. Second, the existing failure probability calculation method on intact ship stability provided by IMO is introduced. Third, a 15-hour simulation is run for each realization under different sea states, and four methods are used to obtain failure rate in different sea states: a piecewise linear method on the GZ curve, a probabilistic method with first stability failure occur, a probabilistic method with fixed specified exposure time, and a deterministic method. The comparison of different methods reveals that calculating the capsizing probability on damaged ships is highly dependent on the selection of criterion.

Keywords: *Failure rate, Damaged ship, Probabilistic method, Deterministic method*

1. INTRODUCTION

The majority of catastrophic ship accidents are closely related to the phenomena of failure caused by flooded water of damaged compartment due to a variety of reasons in waves, which has attracted the attention of the International Maritime Organization and academia. Flooding water changes ship`s inherent parameters and motion attitude, causing the flow to change. When the restoring moment of the ship is zero or negative during ship motions in waves, or when the ship`s dynamic stability is insufficient, the inclination angle of the damaged ship grows larger and larger, resulting in unstable motion. Consequently, the ship will capsize or sink, as illustrated in Figure 1. Figure 2 depicts the motion of a damaged ship in waves, which inculdes water flowing in and out of the damge entrance as well as the complex flow mechanism of water inside the cabin. There is a strong real-time coupling between motion, interal flow of water, and external transformation of wave. Therefore, the research on damaged ship stabiliy in waves is extremely complicated.

(a) Costa Concordia, 2012

(b) Sewol, 2014

Figure 1: Part of accidents about damaged ship

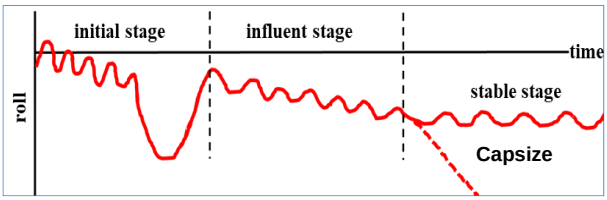

Figure 2: Three main stages in the flooding process of damaged ships

The survivability of the damaged ship is largely dependent on the ship`s residual stability and the damage-control efforts of the crew on board. Prediction of damaged ship motion in waves requires additional consideration of inflow and outflow at the damaged apertures, flooding inside the cabin, and sloshing and load generated by the flooding water, in addition to the basis of intact ship motion prediction. In terms of accuracy, it is necessary to describe the flooding process and flow impact as precisely as possible, which increases the calculation`s complexity and expense. However, it is more desirable for engineering applications to improve calculation speed as much as feasible based on a reduced model under the premise of certain accuracy.

Regarding the flow process of inflow and outflow water in damaged cabins, a quasi-static model was built on the basis of Bernoulli's equation(Vassalos et al., 1997), and was further developed into a dynamic hydraulic model (Lee, 2015). In most relevant investigations, the particle trajectory method (Qian et al., 2000) or shallow wave equation (Lorkowski et al., 2014) are used to describe slosing inside the tank. In the preliminary investigation, we used the hydraulic model to calculate floodwater and developed a damaged ship time-domain motion model based on potential theory, which was able to predict ship motion in the event of broadside damage (Bu et al., 2018).

This paper begins with a brief introduction to the motion assessment approach for damaged ships. The failure rate of one damaged passenger ship is then evaluated using the IMO approach for assessing the direct stability of intact ship.

2. PREDICTION METHOD

2.1 Governing equations

In order to reduce the model complexity without compromising calculation accuracy, a four-degree-of-freedom (4 DOF) sway-heave-roll-yaw coupled mathematical model is adopted in this article to investigate the motion of damaged ships in irregular seaway. At the same time, the influence on ship motion imposed by water flowing into and out of the damage opening is reflected in governing equations of motion concerning damaged ships, which are defined in terms of total influent mass and mass flow rate:

$$\{[M]+[M_w(t)]+[A_\infty]\}\{\ddot{Q}\}+\begin{cases}\{\dot{M}_w(t)+[B]_v\}\{\dot{Q}\} & \text{sway, heave, pitch}\\ \{\dot{M}_w(t)\}\{\dot{\phi}\}+N_1\dot{\phi}+N_2\dot{\phi}|\dot{\phi}| & \text{roll}\end{cases}$$
$$+\int_0^t K(t-\tau)\{\dot{Q}(\tau)\}\,d\tau=\{F\}_w+\{F\}_r+\{F\}_G \quad (1)$$

Where $[M_w(t)]$ denotes the mass matrix induced by floodwater inside the damaged ship and $[\dot{M}_w(t)]$ corresponds to the mass rate matrix equivalent to damping; x_w, y_w, z_w are barycentric coordinates of floodwater in the ship coordinate system. Definition of other physical parameters are consistent with governing equations of motion concerning unbroken ship, which can be derived by the conventional potential theory.

Because of the inherent significant nonlinearity, the flow at the damaged opening is quite complex, and it is affected by many parameters such as the shape, size, and position of the openings, the direction of the wave, and the shape of the wave surface. To cope with the inflow and outflow at the damaged orifice without significantly increasing the system's complexity, a simplified model for the ideal fluid based on Bernoulli's equation is used. The essential principle is that the instantaneous internal free surface is considered to be parallel to the mean external water surface and that there is no phase difference between the motion of flooding water and the hull, which is equivalent to the flow through a small hole and in an open channel, as shown in Figure 3. Based on the assumptions above, Equation 2 may be used to compute the mass flow rate, and the total mass of the flooded water can be simply obtained by integrating the flow rate over time.

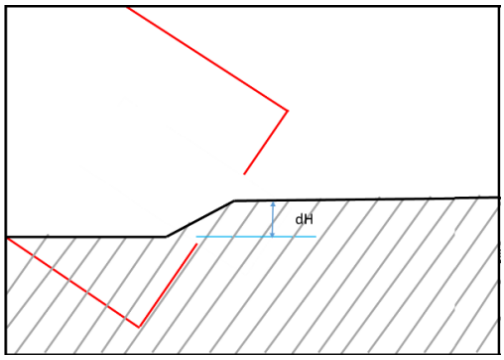

Figure 3: Sketch of the flooding model

$$\begin{aligned} \dot{M}_w(t) &= K\int_S \mathrm{sgn}(h_{out}-h_{in})\cdot\rho v_f \mathrm{d}A \\ v_f &= \sqrt{2g|h_{out}-h_{in}|} \\ M_w &= \int_0^t \dot{M}_w(t)\mathrm{d}t \end{aligned} \quad (2)$$

where K represents the outflow coefficient reflecting influence of factors, such as damage opening parameters and tank sloshing. It generally distributes in the range of 0.6~1.4, and 0.7 is used in this paper.

We have used the method described above to participate in the FLARE international benchmark study of one damaged curise ship (Ruponen et al., 2022).

2.2 Prediction method for the failure rate

Ship motion in a specific sea state should be calculated under random wave series thousands of times to ensure the accuracy of the results, which takes a lot of time. This article outlines the IMO's second generation intact ship stability criteria's recommended processes for the direct stability assessment of intact ship. According to IMO MSC.1/Circ.1627, 2020, the assessment for an intact ship can be carried out using any of the following similar alternatives::

.1 full probabilistic assessment;

.2 assessment in design situations using probabilistic criteria;

.3 assessment in design situations using deterministic criteria .

The direct counting procedure uses ship motions resulting from multiple independent realizations of an irregular seaway to estimate the rate of stability failure, *r*, and the failure rate *r* and associated confidence interval can be estimated:

.1 by carrying out a simulation for each realisation of an irregular seaway only until the first stability failure; or.

.2 on the basis of a set of independent simulations with fixed specified exposure time t_{exp} (s), under the assumption that the relation between the probability p of failure within t_{exp} and the failure rate r is $p = 1 – \exp(-r \cdot t_{exp})$.

The maximum effective duration of a single simulation procedure for the failure rate of a damaged ship is determined in this article using auto-correlation analysis on wave time series. It presents the groundwork for time-domain computation of ship motion within the effective duration, with governing equations of motion for damaged ships serving as the foundation. The simulation results should then be separated into n equal time interval sections in order to receive sufficient amplitude of motion in each time interval. The average significant value is calculated as a result of ship motion in a single effective duration period. Finally, it is possible to predict if failure phenomena will occur by comparing ship prediction data to a safety threshold value.

3. RESEARCH OBJECTIVE

A self-designed passenger ship with two propellers and two rudders is analyzed experimentally and mathematically in the article, and its basic dimensions are shown in Table 1 with a scale ratio of 1: 49.54.

Table 1. Principal particulars of the damaged ship model

name	symbol	unit	Full scale ship
length between perpendiculars	L_{PP}	m	247.7
breadth	B	m	35.5
Designed draft	D	m	8.3
Designed displacement volume	Vol	m^3	52218.67
height of gravitational center (above the baseline)	KG	m	16.409
initial stability height	GM	m	2.2
natural rolling period	T	s	17.474

As shown in Figure 4, the damaged cabin is divided into two compartments that are connected by a square hole in the wall. In calm water, the longitudinal and vertical positions of the center of gravity, the longitudinal moment of inertia, and the transverse moment of inertia are all determined prior to the case study. The inclination experiment confirms the initial metacentric height (Bu et al, 2022).

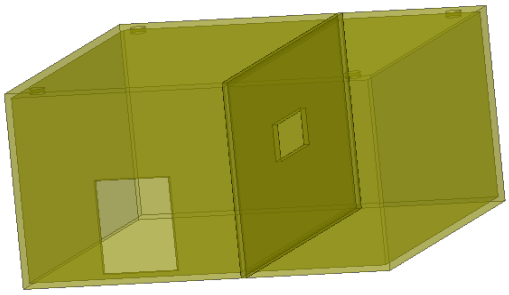

Figure 4: Type of damaged openings

4. RESULTS AND DISCUSSION

4.1 Verification of prediction method

The model was tested at the China Ship Scientific Research Center's seakeeping basin. For structural strength, the ship model employs a ribbed slab structure made from glass fiber reinforced plastic material in an integrated molding process. In the full-scale ship, the hull and appendage satisfy geometrical similarity. For the immediate production of openings in the damaged ship, a self-developed breakage controlling apparatus is used. Except for the damaged cabin, all other elements are sealed with a cover plate, waterproof viscose, and other watertight treatment techniques, as shown in Figure 5.

Figure 5: Photo of model test

The method employed in this article produces results that are compared to experimental values. Figures 6-7 compare model test and simulation results in regular waves with varying wave periods, and Table 2 compares results in irregular waves. Please see the author's work (Bu et al., 2023) for a more detailed analysis. These results demonstrate the accuracy of the method utilized in this study and provide an efficient method for calculating and analyzing this article.

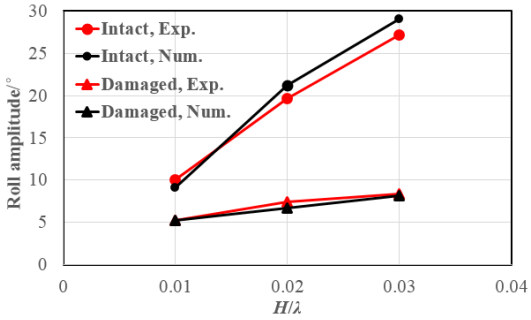

(*a*) *T*=17.478 s

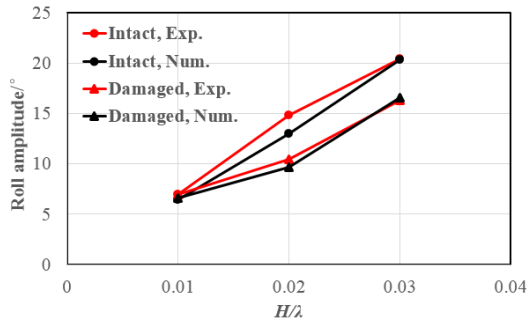

(*b*) *T*=19.349 s

Figure 6: Variation of ship's roll amplitude against wave steepness (Bu, et al., 2023)

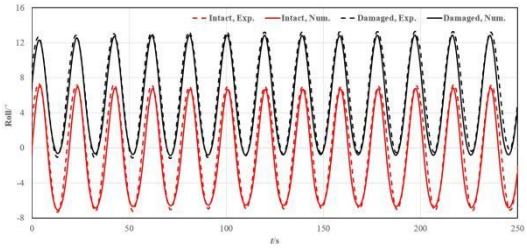

Figure 7: Time history of roll motion in regular wave (*T*=19.349 s, *H*=5.846 m, *λ*=584.59 m)

Table 2. Comparison of ship's roll motion in irregular waves (Bu, et al., 2023)

State	Average heeling angle/°			Maximum roll amplitude/°			Significant rolling angle/°		
	Exp.	Cal.	R. E.	Exp.	Cal.	R. E.	Exp.	Cal.	R. E.
Intact state	0	0	/	15.82	14.2	10.24%	7.63	6.49	14.94%
Damaged state	6.93	6.1	11.98%	10.77	11.21	4.08%	11.95	13.74	14.98%

4.2 Direct simulation under irregular seaway

The direct stability calculation is carried out in accordance with the most recent IMO regulation for intact ship. It is worth noting that the IMO provides significant wave height and zero-crossing period corresponding to the unrestricted service region for intact stability evaluation using various capsizing probability calculation methodologies. Related parameters are shown in Table 3, where the significant wave height reaches 16m, which is clearly unrealistic for damaged vessels. To make the procedure more rational and specifically applicable in the assessment of damaged ship stability, this study did not use the IMO's suggested wave conditions, but instead employed the generally used ITTC wavelength conditions, as indicated in Table 4.

Table 3. Significant wave height with probability criteria for unrestricted service (IMO MSC1/Cir.1627, 2022)

Tz(s)	4.5	5.5	6.5	7.5	8.5	9.5	10.5	11.5	12.5	13.5	14.5	15.5	16.5
10^{-5}	2.8	5.5	8.2	10.6	12.5	13.8	14.6	15.1	15.1	14.8	14.1	12.9	10.9

Table 4. Sea states used for simulation

Sea state	Significant wave height $H_{1/3}$ (m)	Mean period T_{01}(s)
2	0.5	5
3	1.25	5.5
4	2.5	7.3
5	4	8.2
6	6	9.6
7	9	11.6

Based on the aforementioned wave parameters, a 15-hour simulation is run in each sea state to determine the maximum roll amplitude. During a 15-hour simulation, no capsizing occurs in sea states 3 and 4. Table 5 displays the results of a 15-hour simulation in sea states 3-7, where 'cap' refers for capsizing. The maximum roll amplitude reaches 35 degrees at sea state 5. Capsize accidents occur 9 times at sea state 6, and 15 times at sea state 7. Different approaches are used to calculate the capsizing probability at sea states 5-7.

Table 5. Maximum roll angles of damaged ship in sea states 3-7

No.	Maximum roll angles (degree)				
	3	4	5	6	7
1	4.845	5.11	12.048	cap	cap
2	4.785	5.392	8.555	36.716	cap
3	4.66	6.439	10.268	27.891	cap
4	4.991	5.385	8.243	30.098	cap
5	4.721	5.731	8.356	28.745	cap
6	4.862	5.271	7.749	cap	cap
7	4.824	5.48	17.093	cap	cap
8	4.838	5.25	8.989	cap	cap
9	4.725	5.236	34.308	37.657	cap
10	4.834	5.372	7.711	17.6	cap
11	4.735	5.141	17.775	cap	cap
12	4.817	5.328	35.365	cap	cap
13	4.694	6.158	10.35	cap	cap
14	4.727	5.26	32.273	cap	cap
15	4.891	4.968	11.384	cap	cap

4.3 Calculation methods of capsizing probability

4.3.1 Method 1: Piecewise linear method

IMO proposed a piecewise linear approach on the GZ curve for the study of dead ship stability. The capsizing problem can be separated into non-rare and rare problems. The former refers to the phenomena in which a ship returns to its equilibrium position at a tiny angle below a certain value when roll motion exceeds the ϕ_{m0} threshold. The latter is associated with capsizing, when the roll motion exceeds the threshold and the roll angle diverges.

In accordance with the concept in the vulnerable criterion for dead ship stability, we set the angle corresponding to the maximum value ϕ_{m0} of the ship's GZ curve in calm water under damaged condition as the demarcation point (shown as Figure 8). It can be observed that under certain conditions (e.g. condition R=3), the ship can return to the safe range after exceeding this cut-off point. Down-crossing does not result in ship capsize in this circumstance. However, under certain conditions (e.g. condition R=5), the ship will not return to the prior state, and the capsizing of ship can be attributed to down-crossing.

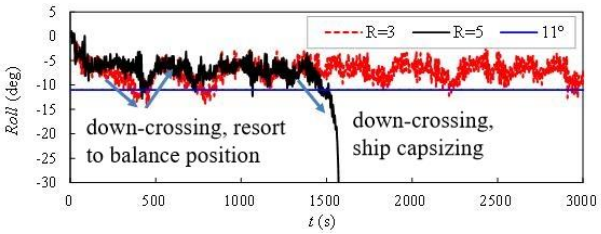

Figure 8: Sketch for down-crossing in irregular waves

In regard to the target ship, we set the demarcation point ϕ_{m0} as 30º for counting times of excess, which corresponds to the maximum value of the ship's GZ curve in calm water while damaged. Table 6 shows the computation results in different sea states when the value of capsizing times is divided by the frequency of down-crossing. From

the results, it can be seen that from sea state 5 to 7, the capsizing probability is increasing.

Table 6. Simulation results of ship capsizing in irregular waves

Sea state	Number of simulations	Number of down-crossing	Number of capsizing	Capsizing probability
5	15	19	3	15.79%
6	15	45	9	20.00%
7	15	23	15	65.22%

4.3.2 Method 2: Probabilistic method based on the time before first stability failure

In this article, we consider roll angle 40º as the critical point for stability failure. With the adoption of statistical criteria introduced in this part, it is of great significance to determine time before the first stability failure. The length time T_i of each simulation can be recorded after numerous instances of simulation, which stop until first stability failure. The average value of T_i acquired from each simulation is used to compute the failure rate of stability r:

$$r = \frac{1}{\left(\sum_{i=1}^{N} T_i \Big/ N\right)} \quad (3)$$

From results in Table 5, it can be judged that the maximum roll angle is not reach 40º at sea state 5, so that the ship is safe at sea state 5. The ship capsizes 9 times throughout the 15-hour simulation for sea state 6, and the relative cumulative simulation time T_i before first stability failure is presented in Table 7. Then the calculated average time T=3534.08s, and the failure rate r=2.8296E-04.

In accordance with latest IMO document for second generation intact ship stability criteria, the criterion should not exceed the threshold corresponding to one stability failure every 2 hours in full scale in designed sea states (7200 seconds) with the probability density 10^{-5} $(m \cdot s)^{-1}$. If we use this criterion to judge, we can assume that the ship is prone to lose stability at sea state 6.

Table 7. Cumulative simulation T_i before first stability failure at sea state 6

No.	1	2	3	4	5
T_i	14597.47	502.61	2012.21	7537.09	1557.14
No.	6	7	8	9	
T_i	555.35	1914.69	442.68	14597.47	

When it comes to the sea state 7, ship capsizes 15 times during the 15-hour simulation. The cumulative simulation time T_i before stability failure is listed in Table 8. The calculated average time of stability failure T=259.02s, and the failure rate r=3.86071E-03. It can be concluded that the ship is far from meeting the criterion at sea state 7.

Table 8. Cumulative simulation time T_i before first stability failure at sea state 7

No.	1	2	3	4	5
T_i	581.188	192.669	105.702	124.3	148.665
No.	6	7	8	9	10
T_i	261.006	337.485	284.2	286.505	476.085
No.	11	12	13	14	15
T_i	464.003	210.24	116.974	114.599	181.688

4.3.3 Method 3: Probabilistic method with fixed specified exposure time

In this strategy, the frequency of stability failure is given special consideration. During the statistical approach regarding the number of stability failure, independent simulation with the duration time of t_{exp} will be carried out for N times. The number of failures n_{fail} can be counted and the failure probability can be calculated as $p = \frac{n_{fail}}{N}$. Finally, the failure rate r can be obtained as:

$$r = -\ln(1-p)/t_{\exp} \quad (4)$$

From the results in Table 5, we can conclude that the ship is very safe at sea state 5 as there is no roll amplitude excess 40 degrees, and the number of stability failure is 0. In a 15-hour simulation, the ship capsizes 9 times for sea state 6, with a failure probability p=0.6 and a failure rate r= 2.54525E-04. The same conclusion can be drawn that the ship investigated in this paper is likely to lose stability at sea state 6.

In the case of sea state 7, the failure probability p=1.0. To put it another way, the ship capsizes 15

times in a 15-hour simulation, which does not meet the probability criterion requirements.

4.3.4 Method 4: Deterministic method

Applying deterministic criteria, such as the mean 3-hours maximum roll amplitude, may reduce the required simulation time and this may make it easier to use model test results with, or instead of, numerical simulation result (IMO MSC.1/Circ.1627, 2020). In this article, the result of the 15-hour simulation is divided into 5 groups for selecting the maximum roll angle respectively. After calculating the mean value, the average three-hour roll amplitude can be obtained.

In the case of sea state 5, the roll amplitudes for five groups are shown in Table 9. It can be seen that the average roll amplitude under this condition is 24.47°, more than half of the criterion value 40°. According to the requirement of this assessment, the ship is not safe at sea state 5, which differs from the judgment based on probability criterion.

Table 9. Average three-hour roll amplitude at sea state 5

Order	1	2	3	4	5	Average
Roll amplitude	12.05	8.36	34.31	35.37	32.27	24.47

As regard to the sea state 6, statistical results of five groups are listed in Table 10. Considering that the ship capsizes every three hours, it does not meet the criterion. The average three-hour roll amplitude at sea state 7 is shown in Table 11, which is exactly the same as that at sea state 6.

Table 10. Average three-hour roll amplitude at sea state 6

Order	1	2	3	4	5
Roll amplitude	cap	cap	cap	cap	cap

Table 11. Average three-hour roll amplitude at sea state 7

Order	1	2	3	4	5
Roll amplitude	cap	cap	cap	cap	cap

4.4 Comparison of results by means of different methods on capsizing probability

On the basis of the intact ship stability assessment method proposed by IMO, this article applies four methods to study the capsizing probability of a damaged passenger ship under different sea states. In the following table, factual data can be compared:

Table 12. Comparison of capsizing probability by means of different methods

Sea state	Method 1 Piecewise linear method on GZ curve	Method 2 Probability method based on the time before first stability failure	Method 3 Probabilistic method with fixed specified exposure time	Method 4 Deterministic method
3	safe	safe	safe	safe
4	safe	safe	safe	safe
5	0.1579	safe	safe	24.47
6	0.2	2.8296E-04	2.54525E-04	cap
7	0.6522	3.86071E-03	infinite	cap
Criterion for intact ship	-	10-5	10-5	20°

As seen in the table above, all four approaches used in this work can accurately predict the ship's capsize probability in extreme sea conditions. However, there is a gap between current judgment outcomes due to the differing criterion values of different approaches that are aimed at intact ships. For example, using the ‘Probability criterion’, the ship is safe at sea state 5. The ‘Deterministic method’, on the other hand, produces the opposite result. As a result, the study of the capsizing probability for damaged ship is closely related to the study of criteria.

5. CONCLUSIONS

This paper investigates the method for calculating the capsizing probability for damaged ships in irregular seaway. According to the research:

(1) The approach of capsizing probability for intact stability proposed by IMO can provide a certain reference for damaged ship. However, the range of significant wave height and zero-crossing period is not applicable to damaged ships.

(2) Four methods adopted in this work, including a piecewise linear method on the GZ curve, a probabilistic method with the first stability failure

occurring, a probabilistic method with a fixed specified exposure time, and a deterministic method, have a certain range of application for calculating the capsizing probability of damaged ships.

(3) Different capsizing probability calculation methods correspond to different criterion. Future work is required due to the lack of probability criterion aiming at damage stability.

Acknowledgments

The author would like to acknowledge the support from National Natural Science Foundation of China (Grand No.52001285, 52271336), Young Elite Scientists Sponsorship Program by CAST (YESS20200004).

References

Bu S., Gu M., Lu J., 2018, "Prediction of Damaged Ship Motions in Waves in Time Domain", Shipbuilding of China, vol 59, pp. 80-89.

Bu S., Gu M., Zhan J., Zhang P., 2022, "Experimental and numerical investigations on a damaged passenger ship motion in regular beam waves", 14th International Conference on Hydrodynamics, 2022

Bu S., Zhang P., Liu H., Shi Y., Gu M., 2023, "Researches on the motion and flooding process of a damaged passenger ship in regular and irregular beam waves", Ocean Engineering, 114927

IMO MSC.1/Circ.1627. Interim guidelines on the second generation intact stability criteira, 2022.

Lee G. J., 2015, "Flow Model for flooding simulation of a damaged ship", Proceedings of the 12th STAB, Glasgow, UK.

Lorkowski O., Dankowski H., Kluwe F., 2014, "An experimental study on progressive and dynamic damage stability scenarios", 33rd International Conference on Ocean, Offshore and Arctic Engineering, American Society of Mechanical Engineers Digital Collection.

Ruponen, P., van Basten Batenburg, R., van't Veer, R., Braidotti, L., Bu, S., Dankowski, H., Lee, G. J., Mauro, F., Ruth, E., & Tompuri, M., 2022, "International benchmark study on numerical simulation of flooding and motions of a damaged cruise ship", Applied Ocean Research, vol 129, 103403.

Qian K., Wang Y., Wang D., 2000, "Calculation of wave load encountered by damaged ships", Proceedings of the 7th STAB, Australia.

Vassalos D., Conception G., Letizia L., 1997, "Modelling the Accumulation of Water on the Vehicles Deck of a Damaged Ro-Ro Vessel", Third International Stability Workshop on Theoretical Advances in Ship Stability and Practical Impact, Greece.

Statistical approach of the most effective manoeuvre to undertake when parametric roll appears on a container ship in longitudinal seas

Vivien Luthy, *CMA CGM, France*, vivien.luthy@supmaritime.fr
François Grinnaert, *Ecole Nationale Supérieure Maritime*, francois.grinnaert@supmaritime.fr
Jean-Yves Billard, *Ecole navale*, jean-yves.billard@ecole-navale.fr

ABSTRACT

Parametric roll is a serious operational issue leading to undesired heavy roll motion. Merchant navy vessels consider weather routing in order to avoid the worst conditions. However, unexpected weather conditions may appear. Consequently, the conditions leading to its development as well as the ship motions are monitored in real time. Several methods to identify parametric roll based on the ship motions are available and provide alerts informing the officer of the watch of the existing danger. Following this alert, the officer of the watch may decide to manoeuvre to avoid heavy roll motions and secure cargo safely. This paper proposes to statistically assess the efficiency of different possible manoeuvres in real sea states after parametric roll is detected, such as course or speed modifications. Therefore, simulations in six degrees of freedom are conducted on the C11 class container ship, known for her vulnerability to parametric roll. When parametric roll is detected in a simulation, the simulation is rerun with a manoeuvre engaged after the parametric roll detection, with a slight delay corresponding to the reaction time of the officer of the watch. Simulations are compared and the efficiency of each manoeuvre is assessed. The results show that statistically a significant course alteration permits to reduce heavy roll motions.

Keywords: *Parametric roll, Time-domain simulation, Real sea state, Real-time evaluation, Manoeuvre*

1. INTRODUCTION

Parametric roll is a stability failure in waves which can lead to undesired heavy roll motions. Recent accidents on container ships have been or may be imputed to this phenomenon (France, 2003, Carmel, 2006, ATSB, 2020, MAIB 2020, Theillard 2020, DMAIB 2022). Those accidents hold the attention of the community, leading to extensive studies on this topic and to new intact stability criteria (IMO, 2020). The physic of the phenomenon is nowadays well understood. However, this phenomenon is hardly operationally avoided due to the complexity of the sea state estimation and to heavy operational constraints. Real-time detection methods of the appearance of parametric roll based on inertial unit data exist (Galeazzi et al., 2009a, Galeazzi et al., 2015, Luthy et al. 2022b). When such detection methods are implemented onboard (Acomi, 2016), they permit to inform the officer of the watch of the existing risk of parametric roll. However, most of the time the officer of the watch does not have the culture and sufficient information to execute the most adequate manoeuvre to reduce this risk. DNV reported that in case of heavy weather leading to heavy roll motions a prudent captain would come to head sea and reduce speed (DNV, 2005). However, it is in longitudinal seas (head and following seas) that parametric roll can appear. In fact, the Masters and the Officer Of the Watch often ask themselves “what would have happened if I had engaged another manoeuvre ?”. Simulations permit to reproduce several times the exact same conditions and provide an answer on the efficiency of different manoeuvres. Thus, it is possible to identify the most relevant manoeuvre to execute when unexpected heavy roll motions in head or following seas appear. Galeazzi et al. (2009b), Breu (2013) and Holden et al. (2012) conducted an evaluation based on frequency detuning with the aim to avoid large roll motions, consequence of both parametric and synchronous resonances. Such method permits to identify when the vessel is out of the resonance condition. However, it does not provide to the Officer Of the Watch the immediate first action to carry out.

This paper presents a statistical evaluation of the most relevant manoeuvre to undertake after

parametric roll detection, in order to avoid undesired roll motions in head and following seas. The study is conducted on a container ship in real sea state. First the time domain solver used to simulate the ship motions, the detection method and the vessel are briefly introduced. Then, the method used to evaluate the efficiency of the selected manoeuvres is presented and validated. Finally, the efficiency of each manoeuvre is presented and discussed. This study has been previously presented within the scope of the PhD thesis of Dr. Luthy (2023).

2. TIME DOMAIN SIMULATION

Time domain solver

The seakeeping and manoeuvring time-domain solver Fredyn Version 16 (MARIN, 2022), developed by the Cooperative Research Navies consortium (CRNav), is chosen to conduct this study. Such solver permits to realise simulations in 6 degrees of freedom in real sea state. Hydrodynamics forces acting on the hull are pre-computed using a partially non-linear strip theory. The diffraction forces are pre-calculated by Haskind method (MARIN, 2011) using linear strip theory. Excitation forces and motion response in waves are considered in detail and validated. Time domain simulations in 6 DoF permits to reproduce rare stability failures such as parametric roll. The propulsion forces are calculated in calm water based on the instantaneous water speed in the vicinity of the propeller. The forces applied on the appendages (rudder) are calculated at each time-step considering their shape and the local speed. Thus, the combination of the ship model and the 6-DoF solver provides a digital twin of the actual ship. Fredyn has been validated trough manoeuvring tests in calm water, in regular and irregular waves (Quadvlieg et al., 2019).

Vessel

The Post Panamax C11-class container ship (4800 TEU) selected for this study is qualified as vulnerable to the phenomenon of parametric roll. A ship of this class suffered in 1998 of unexpected extreme roll motions up to 40 degrees while sailing Eastwards North Pacific Ocean from Kaohsiung (Taiwan) to Seattle (USA). France et al. (2003) analyzed in detail this accident and concluded that it was due to parametric roll. The total cost was estimated over 50 million dollars, which was greater than the value of the vessel herself (Ginsberg, 1998).

Table 1 presents the full-scale particulars of the C11-class container ship. Figure 1 presents the body plan and a three-dimension representation of the vessel.

Table 1: C11-class container ship main particulars

Main particulars	Value	Unit
LBP	262	m
B	40	m
Draught	12	m
Displacement	73450	t
GM	1.5	m
Natural roll period	29.5	s
Maximum speed	25	knots

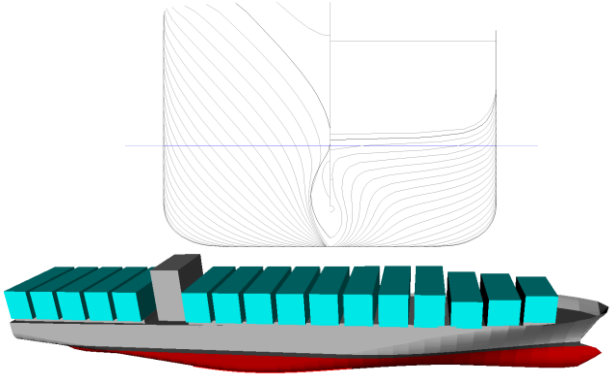

Figure 1: C11 container ship

Parametric roll detection method

The detection method selected in this study to determine if vessel motions may be leading to parametric roll is presented by Luthy et al. (2022b). This method provides an accurate detection of the parametric roll episodes for such type of vessel. Any other real-time detection method suitable to warn the officer of the watch of the immediate danger can be used, such as the one proposed by Galleazi (2009a, 2015) or the one implemented onboard in the Octopus system (Acomi, 2016).

3. AVOIDANCE MANOEUVRE

Manoeuvre mitigation

In heavy weather, Masters and Officers Of the Watch monitor the ship motions in real-time, and anticipate her behaviour based on weather forecast. DNV (2005) reported that the habit of Masters is to reduce speed and come to head sea when large roll motions appear. During both well-documented container losses consecutive to stability failures, involving firstly the C11-class container ship APL China (France, 2003) and secondly the Panamax G-class container ship Maersk Carolina (Carmel, 2006), the Masters reduced speed and altered course

towards head sea. However, in those conditions, the variation of the transverse stability in waves is important and leads to the largest probability of appearance of parametric roll. Reducing speed in head seas permits to reduce wave encounter frequency, which allows the Masters to assume that more time is available to select the most suitable heading. However, a reduction of the ship's speed causes a reduction of the roll damping, leading to a possible increase of the roll amplitude.

This study focuses on two types of manoeuvres, either a course alteration or a speed modification, with the aim to identify the most relevant manoeuvre to be executed when parametric roll appears. The simulations are conducted in 6 degrees of freedom in real sea states with course and speed autopilots. Each simulation is one hour long. The simulation begins with the autopilot set to head seas to maximise the probability of appearance of parametric roll. A first simulation without any manoeuvre is performed. When parametric roll is detected on this first simulation prior half an hour, then the initial conditions (environmental, loading, speed) are memorised. Hereafter, those simulations without manoeuvre are identified as reference simulations. The time at which the parametric roll alarm rises on the reference simulation is denoted by t_{Alarm}, then 20 seconds are left to the OOW to select and begin a manoeuvre at a time denoted hereafter by t_{start}, Equation 1. According to the authors, 20 seconds is an acceptable reaction time for an immediate first response of a trained OWW. The simulation is run again with identical initial conditions (same wave seed) several times to assess the effect of each manoeuvre. The simulations prior t_{start} are strictly identical to the one of reference. The comparison of the roll time series permits to identify the most relevant manoeuvre.

$$t_{start} = t_{Alarm} + 20s \quad (1)$$

Course alteration

A course alteration modifies the encounter period (Equation 2), which is a key parameter of the appearance of parametric roll. Indeed, the first mode of parametric roll appears when the natural roll period of the ship is twice the encounter period (IMO, 2020). According to Equation 2, modifying the ship course of few degrees will not significantly modify the encounter period. Operationally, the amplitude of a course alteration may be limited by the traffic and by nautical constraints. In this study, the vessel is considered to sail in open waters without traffic. Table 2 presents the four course alterations assessed in this study.

Table 2: Course alterations

Short Name	Course alteration [deg]
C+22.5	22.5
C+45	45
C+67.5	67.5
C+90	90

$$\omega_e = \omega_w + \omega_w{}^2 \frac{V}{g} \cos\beta \quad (2)$$

ω_e	[rad.s^{-1}]	Encounter frequency
ω_w	[rad.s^{-1}]	Wave frequency
V	[m.s^{-1}]	Ship speed
g	[m.s^{-2}]	Acceleration of gravity
β	[rad]	Encounter angle

The magnitude of the turn ratio is validated prior to simulate course alterations. The course alterations are carried out by modifying the heading setting in the auto pilot at t_{start}. In calm water the course alteration leads to a loss of speed which is compensated in a second time by the speed autopilot. As well, the course alteration in calm water leads to heel. Thus, this course alteration is not exactly representative of the reality since the OOW would have to increase the propeller rotational speed while altering course to keep speed. In the simulation, the action of the OOW on the engine is replaced by the speed autopilot. However, this permits to consider the efficiency of the course alteration independently of the speed modification.

Figure 2 provides an example of a 30-degree course alteration simulated on the C11-class container ship in calm water. It is observed that the course autopilot permits to realise efficiently the course alteration. The speed begins to decrease when the vessel alters her course, then the speed autopilot compensates the loss to resume the speed. During this manoeuvre the C11 rolls up almost to 2 degrees.

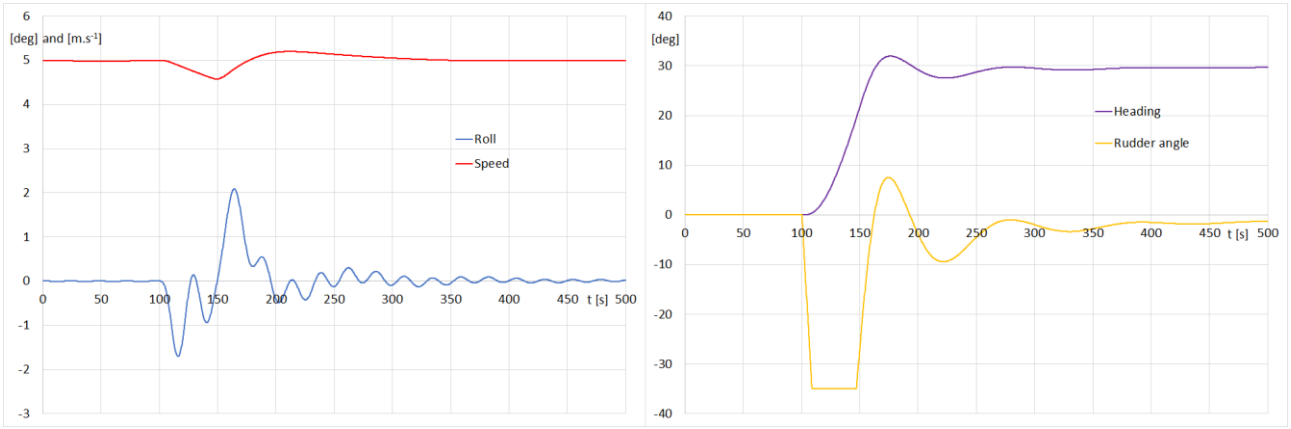

Figure 2: Course alteration in calm water

Speed modification

The ship speed directly influences the encounter period (Equation 2), especially when sailing in head or following seas. It also modifies the ship's roll damping. Thus, the speed has a direct impact on the parametric roll response. The speed modification is realised by modifying the speed setting in the autopilot at t_{start}. Consequently, the solver automatically adjust the propeller rotational speed (in revolutions per minute, denoted by RPM). Thus, the vessel maximum speed throught water is limited by the maximum RPM of the engine. The engine loading sequence is not considered in this study. However, the resistance curve triggers the speed variation. Table 3 presents the two speed modifications assessed in this study.

Table 3: Speed modifications

Short Name	Speed modification [m.s^{-1}]	Comments
V+2.5	+2.5	Increases roll damping
V-2.5	-2.5	Reduces roll damping

Assessment method, focus on a single case

The manoeuvre assessment method has been validated and preliminary results were provided on a naval vessel and published during the 18th International Ship Stability Workshop 2022 in Gdansk (Luthy et al., 2022a). Here, as an example, a focus is realised on a single case obtained on the C11 class container ship. The ship's roll damping coefficients are calculated using Ikeda's method (Ikeda, 1978, Kawahara, 2009). For this single case, the simulations are conducted on a fully-developed sea state modelled with a Pierson Moskowitz spectrum of significant height equal to 8 metres and of zero-up-crossing period equal to 12 seconds (peak period 16.9 seconds). A "cos^8" spreading function and a spreading angle of ±90 degrees are considered to simulate real sea state (BV, 2019a, 2019b). The assessed manoeuvres are the one presented in Table 2 and 3.

In this single case the simulations are 5000 seconds long and begin with the autopilot set to head seas and the speed set at 7.5 m.s^{-1}. A first reference simulation without any manoeuvre is performed. At 1328.8 seconds a parametric roll detection alarm is raised (t_{Alarm}), using the method described by Luthy et al., (2022b). The OOW reaction time is added to calculate the time of the beginning of the manoeuvre (1348.8 s). The simulation is run again several times to assess the effects of all manoeuvres presented in Table 2 and Table 3.

Figure 3 presents the reference simulation and two manoeuvres with a course alteration of respectively 22.5 and 45 degrees. Figure 4 presents the reference simulation and two manoeuvres with larger course alterations of respectively 45 and 90 degrees. Figure 5 presents the reference simulation and two manoeuvres with a speed modification of respectively +2.5 and –2.5 m.s^{-1}.

Table 4 presents results of the roll amplitudes reached during each simulation. Three roll amplitudes are presented. The first roll amplitude represents the maximum roll amplitude reached during the entire simulation and denoted by ΦSim. The second one represents the roll amplitude reached around t_{start} and denoted by ΦPR. The third one is the maximum roll amplitude reached once the manoeuvre is completed on the final part of the simulation and denoted by Φ2ndPart. On the reference time series ΦSim, ΦPR and Φ2ndPart are respectively denoted ΦSimRef, ΦPRRef, Φ2ndPartRef and are illustrated in Figure 3.

For each manoeuvre, the comparison of those roll amplitudes with the ones observed on the reference simulation is provided in Table 5. The

results are provided as a fraction of the amplitude observed on the roll time series of the reference simulation during the same time interval. The right column of Table 5 compares the roll amplitude reached during the final part of the simulation Φ2ndPart) with the roll amplitude reached around t_{start} on the reference time series (PRRef).

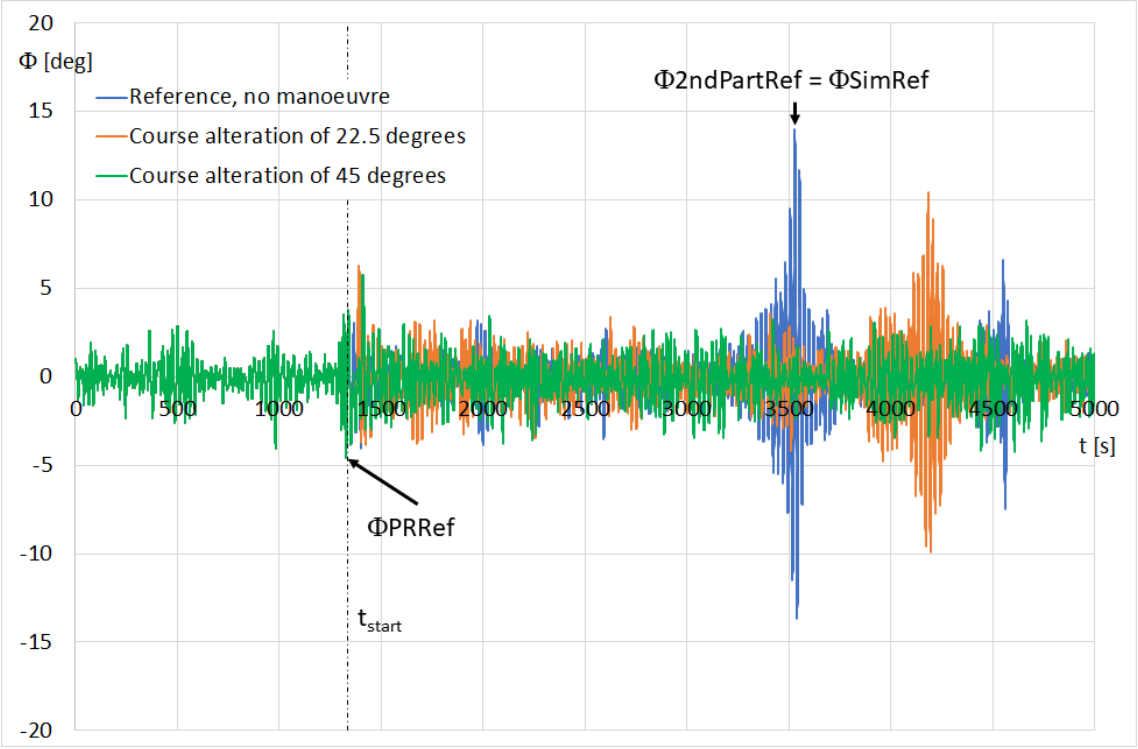

Figure 3: Effect of limited course alterations on the roll motion

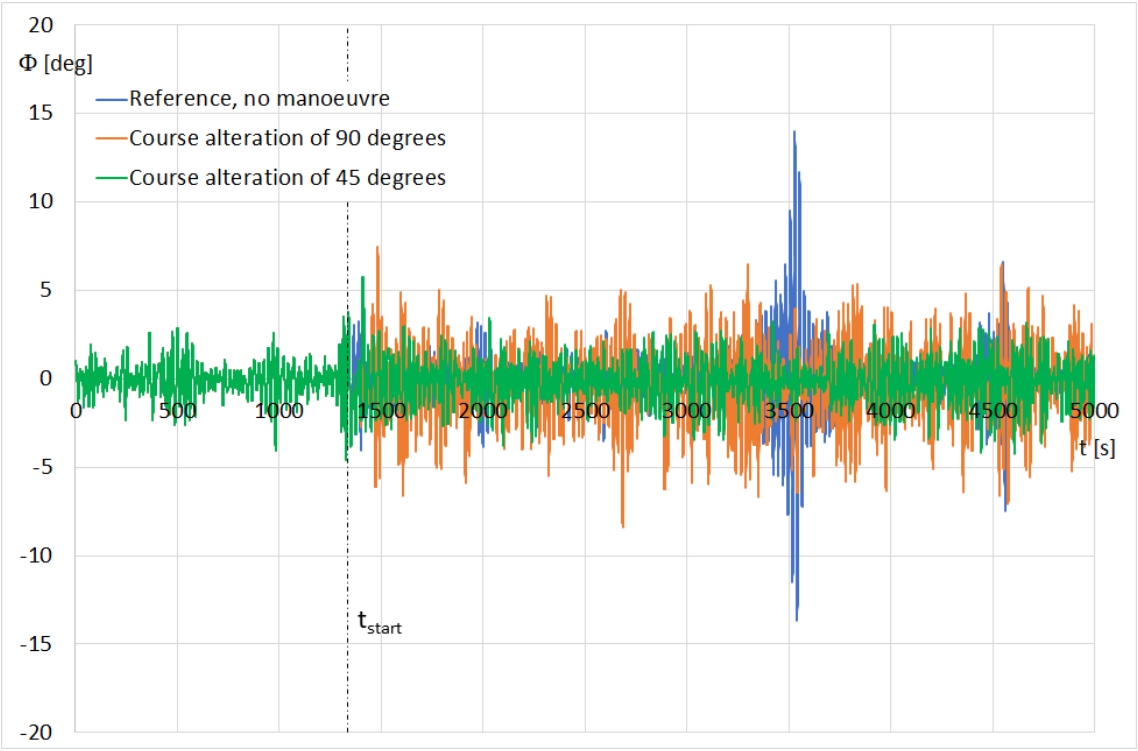

Figure 4: Effect of large course alterations on the roll motion

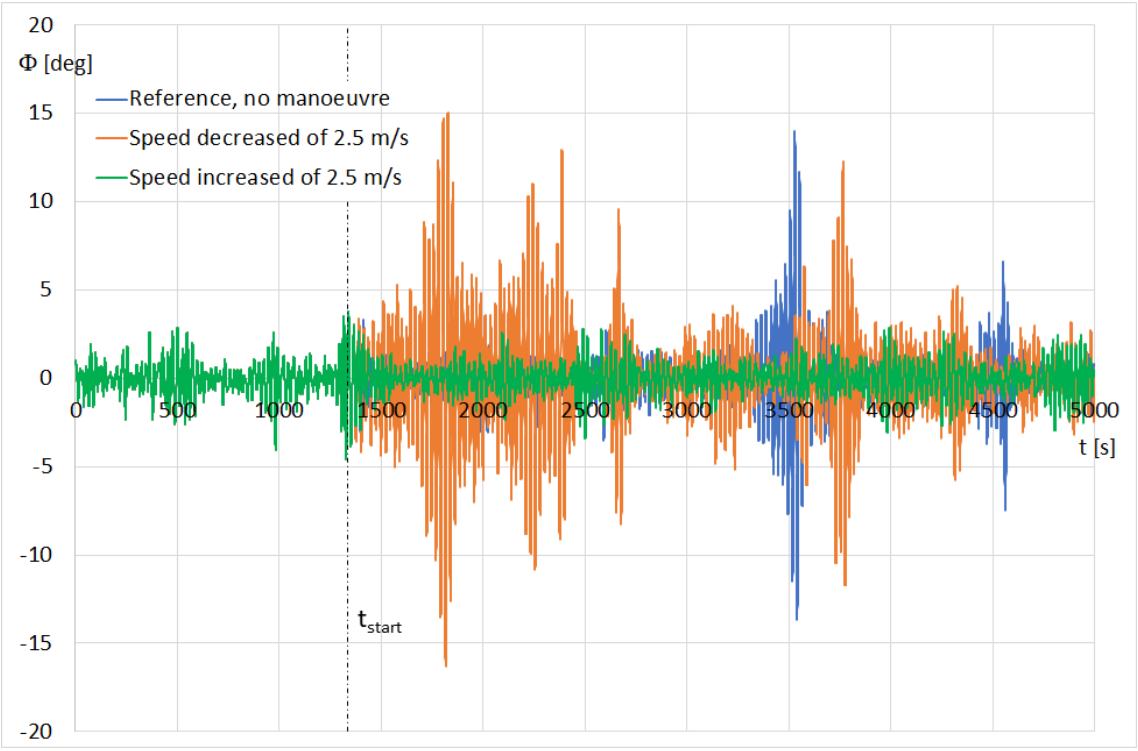

Figure 5: Effect of speed modifications on the roll motion

Table 4: Roll amplitudes

Sim	ΦSim [deg]	ΦPR [deg]	Φ2ndPart [deg]
Ref	13.97 = ΦSimRef	4.52 = ΦPRRef	13.97 = Φ2ndPartRef
C+22.5	10.46	6.24	10.46
C+45	5.73	5.73	4.20
C+67.5	6.91	4.52	6.91
C+90	8.36	4.52	8.36
V-2.5	16.26	4.52	16.26
V+2.5	4.52	4.52	3.43

Table 5: Roll amplitudes relative to the ones of reference

Sim	ΦSim / ΦSimRef	ΦPR / ΦPRRef	Φ2ndPart / Φ2ndPartRef
Ref	100%	100%	100%
C+22.5	75%	138%	75%
C+45	41%	127%	30%
C+67.5	49%	100%	49%
C+90	60%	100%	60%
V-2.5	116%	100%	116%
V+2.5	32%	100%	25%

It is observed in Figure 3, Figure 4 and Table 4 that the roll amplitude reached at the time of the manoeuvre (ΦPR) is large when a limited course alteration is realised. This may be due to the rapid modification of the rudder position.

Figure 3 shows that a course alteration of 22.5 degrees is not sufficient to avoid parametric roll to appear after manoeuvre is engaged, since another parametric roll episode is observed between 4000 and 4500 seconds. This parametric roll episode leads to roll amplitude more than twice larger than the one reached around t_{start}. However, the roll amplitude reached after the manoeuvre is 15 % smaller than the one reached on the reference simulation.

In this example, a course alteration of 45 degrees permits to avoid the appearance of severe roll motion due to parametric roll. The roll amplitude reached after the course alteration decreases significantly and no roll amplitude larger than the one reached at the time of the manoeuvre is observed. The roll amplitude reached after the manoeuvre is 70 % smaller than the one observed if no manoeuvre is engaged (Table 5).

Figure 4 shows that a course alteration of 90 degrees leads to larger roll motions than the ones observed after a course alteration of 45 degrees. A slight modification of the roll period is observed. Therefore, those heavy roll motions are not a consequence of parametric roll since the ship is sailing in beam sea. They may be due to the phenomenon of synchronous roll. A course alteration of 67.5 degrees (not displayed) leads as well to larger roll amplitudes than the one observed after a course alteration of 45 degrees (Table 4 and Table 5). This may be due to synchronous roll since the sea state is defined with spreading.

In this case, a course alteration may permit to avoid large roll amplitudes. A limited course alteration does not permit to avoid the appearance of parametric roll and a large course alteration may lead to synchronous roll.

Figure 5 shows that a speed reduction of 2.5 $m.s^{-1}$ leads to larger roll amplitudes than the ones of the reference (without manoeuvre). Even if the speed reduction alters the encounter period, the phenomenon of parametric roll still appears and leads to large roll motions, probably due to the roll damping reduction. In this case, when the ship increases her speed, no more unacceptable parametric roll is encountered. The maximum roll amplitudes are significantly lower than the one of reference (Table 4 and Table 5).

A modification of 2.5 $m.s^{-1}$ does not seem sufficient to alter the encounter period sufficiently to avoid the appearance of parametric roll. When the ship speed is reduced, the roll damping decreases, amplifying the roll motion. Thus, a speed reduction should be avoided. When the ship speed is increased, the roll damping increases consequently, limiting the roll motion. These results should be handled with care since the speed modifications are simulated faster than in reality. Therefore, in reality, this speed increase would present a longer transient state, during which the roll motion may be closer to the one of the reference simulation.

The effects of each manoeuvre have been separately assessed for this specific case in real sea state. This concludes that for this specific case the most effective manoeuvre is a course alteration of 45 degrees.

Probability of avoiding large roll amplitudes

A single case, such as the one presented previously, is not sufficient to state that a course alteration of 45 degrees is the most adequate manoeuvre to execute when parametric roll appears. Thus, a statistical study is conducted to assess the efficiency of each manoeuvre with regard to parametric roll based on simulations conducted on a C11-class container ship. The simulations include a wide spectrum of environmental and loading conditions presented in Table 6. The loading conditions consider a draught of 12 metres.

Table 6: Assessed loading and environmental conditions

	From	To	Step	Unit
GM	1.25	4.25	3/45	m
Wave height	5	12	1	m
Wave period	7	16	1	s
Ship speed	4	10	0.5	$m.s^{-1}$

The environmental conditions presented in Table 6 are modelized with a Pierson-Moskowitz spectrum. Three spreading angles are considered (0, ± 30 degrees and ± 90 degrees). All combinations are not assessed; the combinations are selected to obtain a relevant probability of appearance of parametric roll. This selection is conducted with regards to the encounter frequency calculated from the peak wave period. Thus, 50000 simulations are performed, within which 1703 present a parametric roll detection in the first half of the simulation and are consequently identified as reference simulations. The 1703 reference simulations are rerun with the manoeuvres executed 20 seconds after the parametric roll alarm (t_{start}). The 4 course alterations and the 2 speed modifications presented respectively in Table 2 and Table 3 are executed, representing 10218 additional simulations.

Statistical results are presented as the percentage of time spent above several roll amplitude thresholds after the beginning of the manoeuvres (t_{start}), Table 7. Each percentage is calculated by dividing the total time of the 1703 simulations where roll amplitude exceeds the selected threshold after t_{start} by the total time of the 1703 simulations after t_{start}. The first line in Table 7 presents the results for the reference simulations. Those results without manoeuvre are considered to assess the global efficiency of each manoeuvre.

As presented in Table 7, a course alteration of 22.5 degrees reduces the time spent above the roll amplitude threshold of 25 degrees by about 30 %. The efficiency of this manoeuvre reduces as the considered roll amplitude threshold decreases. A course alteration of 45 degrees reduces significantly the time spent above all roll amplitude thresholds. The time spent above 5 degrees remains above 15 %. A course alteration of 67.5 degrees provides the best statistical results, reducing significantly the time spent above all roll amplitude thresholds. A course alteration of 90 degrees provides statical results equivalent to the ones observed for a course alteration of 45 degrees. t_{start} is also considered to calculate these percentage in the reference simulations even if no manoeuvre is engaged.

Speed modifications also lead to significant results. When the speed is reduced by 2.5 $m.s^{-1}$, the time spent above 25 degrees is multiplied by almost 8, and by more than 3 above 15 degrees. Reducing the speed statistically increases the parametric roll

amplitude in head seas. When the speed is increased by 2.5 $m.s^{-1}$, the parametric roll is significantly reduced. The time spent above 25 degrees is divided by 30, and by almost 12 above 15 degrees. A speed modification of 2.5 $m.s^{-1}$ significantly modifies both the encounter period and the roll damping, and therefore the parametric roll response. It is observed that a speed reduction should be avoided since it statistically increases the roll amplitude. It is observed that a speed increase permits to significantly reduce statistically the roll amplitude. However, it should be noted that this study does not consider the engine loading sequence, which can last 10 to 30 minutes for such a large container ship. Therefore, the speed increase should be considered as a long-term option since it is expected that its statistical results considering the engine loading sequence would be closer to the one without manoeuvre due to the longer transient state.

In addition to this first part of the statistical study, ΦSim, ΦPR and Φ2ndPart are identified on the 1703 reference simulations in which parametric roll has been detected prior 1800 seconds. This permits to compute statistical results considering each simulation independently from each other. In 38 % of the reference simulations, the maximum roll angle observed during the roll episode where parametric roll is detected is the maximum roll amplitude observed in the whole simulation (ΦSimRef = ΦPRRef). In 43 % of the reference simulations, the maximum roll amplitude reached after the time of the manoeuvre is lower than the one observed when parametric roll is detected (Φ2ndPartRef < ΦPRRef). Thus, for those cases, the manoeuvres cannot reduce the maximum roll amplitude of the whole simulations. However some may be counterproductive.

Table 8 presents statistical results based on ΦSim, ΦPR and Φ2ndPart observed for each manoeuvre. In the first column, Φ2ndPart observed in each manoeuvre is compared to the one of its reference simulation (Φ2ndPartRef). As in the first part of the statistical study, it is observed that the most efficient course alteration to reduce the roll motion is the one of 67.5 degrees. As well, a course alteration of 45 and 90 degrees present results equivalent to the ones of the first part of the statistical study. Thus, in the opinion of the authors, the most relevant course alteration which can operationally be engaged is to alter course of 45 degrees since it presents interesting statistical results and it deviates the ship from her original course less than 67.5 degrees. Indeed, a course alteration of 67.5 degrees is not operationally acceptable most of the time. A speed reduction reduces the maximum roll angle observed after the manoeuvre in only 7.6 % of the cases, while a speed increase reduces this angle in 91.7 % of the cases. Thus, it is statistically undeniable that a speed increase is a more relevant option than a speed reduction to counter parametric roll.

In the second column of Table 8, Φ2ndPart observed for each manoeuvre is compared to the roll amplitude reached around t_{start} on the reference simulations (Φ2PRRef). This permits to observe the probability of not encountering roll motions larger than the ones observed at the time of the detection of parametric roll. It is observed that a course alteration of 67.5 degrees permits to avoid to encounter larger roll motions than the one encountered at the time of the detection in 76 % of the cases. Course alterations of 45 and 90 degrees permit to avoid to encounter larger roll motions than the one encountered at the time of the detection in 59 % of the cases. Those statistical results have to be considered related to the 43 % of the reference simulations for which the maximum roll amplitude in the second half of the simulation were lower than the ones at the time of the detection. Thus, course alterations of 45 and 90 degrees permit to avoid roll amplitudes larger than the ones at the time of the detection in 16 % additional cases. As well, a course alteration of 67.5 degrees permits to avoid roll amplitudes larger than the ones at the time of the detection in 33 % additional cases. However, it has to be noticed that a course alteration of 22.5 degrees may be counterproductive since the roll amplitudes reached after the manoeuvre are lower than the ones observed at the time of the detection in only 40 % of the cases. In other words, in 3 % of the cases altering course of 22.5 degrees leads to roll episodes larger than the ones observed when no manoeuvre is engaged. This result is masked in the first part of the statistical study where it is observed that this course alteration provides encouraging results. Speed modifications of +2.5 $m.s^{-1}$ and -2.5 $m.s^{-1}$ permit avoiding larger roll motions than the ones encountered at the time of the detection in 87.1 % and 13.8 % of the cases, respectively. Reducing speed leads to larger roll amplitudes than without

manoeuvre in 29.2 % of the cases (43 % - 13.8 %). Thus, this manoeuvre should be avoided. Increasing speed permits to avoid roll amplitudes larger than the ones at the time of the detection in an additional 4.1 % of the cases (47.1 % - 43 %). Thus, statistically, a speed increase is recommended to avoid large roll motions due to parametric roll.

Finally, in the last column of Table 8, Φ2ndPart is compared to the maximum roll amplitude observed during the whole simulation (ΦSim). The largest roll amplitude reached after course alterations of 45 and 90 degrees are lower than the one of whole simulation in 61 % of the cases. As well, the largest roll amplitude reached after a course alteration of 67.5 degrees is lower than the one of whole simulation in 80.1 % of the cases. Thus, those course alterations allow to statistically reduce the appearance of large roll episodes. Statistical results observed for the speed modifications confirm the conclusions previously formulated.

Table 7: Percentage of time spent above the thresholds after manoeuvres

	%t > 25 deg	**%t > 20 deg**	**%t > 15 deg**	**%t > 10 deg**	**%t > 5 deg**
Reference simulation	0.30%	1.06%	3.09%	8.14%	21.78%
Course alteration of 22.5 deg	0.19%	0.67%	2.15%	6.74%	22.95%
Course alteration of 45 deg	0.07%	0.17%	0.52%	2.28%	15.59%
Course alteration of 67.5 deg	0.05%	0.12%	0.26%	0.91%	8.42%
Course alteration of 90 deg	0.05%	0.15%	0.45%	2.08%	15.75%
Speed reduction of 2.5 $m.s^{-1}$	2.35%	5.80%	12.51%	24.74%	47.20%
Speed increase of 2.5 $m.s^{-1}$	0.01%	0.05%	0.26%	1.13%	5.10%

Table 8: Percentage of simulations for which the manoeuvre provided an improvement

	Φ2ndPart < Φ2ndPartRef	**Φ2ndPart < ΦPRRef**	**Φ2ndPart < ΦSim**
Ref	-	43.0%	45.7%
C+22.5	46.8%	40.0%	41.9%
C+45	62.7%	59.1%	61.4%
C+67.5	70.7%	76.0%	80.1%
C+90	61.0%	59.0%	61.2%
V-2.5	7.6%	13.8%	17.6%
V+2.5	91.7%	87.1%	85.9%

This study also comes as an additional validation of the parametric roll detection method presented by Luthy et al. (2022b). In the 1703 reference simulations without manoeuvre, the maximum roll amplitude is observed during the roll episode where parametric roll is detected or later in 92 % of the cases (ΦPRRef = ΦSimRef or Φ2ndPartRef = ΦSimRef). This shows that parametric roll is identified by the method before or at the time of the worse roll episode, with an acceptable relevance in the opinion of the authors. The maximum roll angle is observed prior the parametric roll detection in only 8 % of the reference simulations.

4. CONCLUSION

The aim of this study was to assess the relevance of several manoeuvres to counter parametric roll after a first real-time detection, throughout a large number of simulations conducted in 6-DoF and in real sea-state on a container ship selected for her well-known vulnerability to this phenomenon.

This study permits to state that the most relevant manoeuvre considering both statistical and operational aspects to undertake when parametric roll is detected is to come to 45 degrees of the main wave direction and to increase simultaneously the engine load to reduce as much as possible the speed loss due to the course alteration. As well this study permits to state that no speed reduction should be executed when parametric roll occurs. The habit of prudent Masters to reduce speed when encountering heavy weather, reported by DNV (2005), statistically leads to larger motions in case of parametric roll.

This conclusion should be consolidated by conducting the study on other container vessels. Additionally, the study should be improved by simulating the engine loading sequence in order to reproduce the operational transient states with a better accuracy. Finally, the efficiency of the manoeuvres could be assessed for several reaction time of the OOW.

REFERENCES

Acomi, N., Ancuta, C., Andrei, C., Bostina, Al., Bostina, A., 2016, “Avoiding the parametric roll”, Advanced Topics in Optoelectronics, Microelectronics, and Nanotechnologies VIII.

Australian Transport Safety Bureau, 2020, “Loss of container overboard involving APL England”, Australia.

Breu, D., 2013, "Frequency Detuning of Parametric Roll

Resonance", PhD thesis, Norwegian University of Science and Technology.

Bureau Veritas., 2019a, "Guidance for Long-term Hydro-structure Calculations", Rule Note NI 638 DT R00 E.

Bureau Veritas., 2019b, "NR 667 DT R00 E. Parametric Roll Assessment", France, Bureau Veritas.

Carmel, S.M., 2006, "Study of parametric rolling event on a panamax container vessel", Journal of the Transportation Research Board, Vol. 1963.

DMAIB, 2022, "MAERSK ESSEN Marine accident report on loss of cargo 16 JANUARY 2021", Danish Maritime Accident Investigation Board, Denmark

DNV., 2005, "Parametric rolling - a concern for container ships?" Paper series 2005-P011

France, W.N., Levadou, M., Treakle, T.W., Paulling, J.R., Michel, R.K., Moore, C., 2003, "An Investigation of Head Sea Parametric Rolling and its Influence on Container Lashing Systems", Marine Technology¸ Volume 40, pp 1-19.

Galeazzi, R., Blanke, M., Kjølstad Poulsen, N., 2009a, "Parametric Roll Resonance Detection using Phase Correlation and Log-likelihood Testing Techniques", IFAC Proceedings, Volume 42, Issue 18, Pages 316-321, ISBN 9783902661517.

Galeazzi, R., Christian, H., Mogens, B., Fossen, T.I., 2009b, "Stabilisation of parametric roll resonance bycombined speed and fin stabiliser control", Proceedings of the European Control Conference, 4895-4900, Budapest, Hungary.

Galeazzi, R., Blanke, M., Falkenberg, T., Poulsen, N.K., Violaris, N., Storhaug, G., Huss, M., 2015, "Parametric roll resonance monitoring using signal-based detection", Ocean Engineering, 109, pp. 355–371.

Ginsberg S., 1998, "Lawsuit rock APL's boat", San Francisco Business Times, November 22nd 1998.

Holden, C., Breu, D.A., Fossen, T.I., 2012, "Frequency Detuning Control by Doppler Shift", In: Fossen, T., Nijmeijer, H. (eds) "Parametric Resonance in Dynamical Systems", Springer, New York, NY. ISBN 978-1-4614-1042-3.

Ikeda, Y., Himeno, Y., Tanaka, N., 1978, "Components of roll damping of ship at forward speed" Department of Naval Architecture University of Osaka Prefecture, Report No 404.

IMO, 2020, MSC.1/Circ.1627, "Interim Guidelines On The Second Generation Intact Stability Criteria", pp 29, London.

Kawahara, Y., Maekawa, K., Ikeda, Y., 2009, "A Simple Prediction Formula of Roll Damping of Conventional Cargo Ships on the Basis of Ikeda's Method and Its Limitation", Proceedings of the 10th International Conference on Stability of Ships and Ocean Vehicles, (STAB2009), St. Petersburg, Russia, pp. 387-398.

Luthy, V., Grinnaert, F., Billard, J.Y., 2022a, "Mitigation manoeuvres to reduce parametric roll on a naval ship", Proceedings of the 18th International Ship Stability Workshop, pp 195-200, Gdańsk, Poland.

Luthy, V., Grinnaert, F., Billard, J.Y., Rapp, J., 2022b, "Real Time Identification of Parametric Roll", Journal of Ship Research, SNAME.

Luthy V., 2023, "Probability of occurrence of parametric roll on a predefined sea state", PhD thesis, Ecole Nationale Supérieure d'Arts et Métiers.

Marine Accident Investigation Branch, 2020, "Report on the investigation into the loss of 137 containers from the container ship, CMA CGM G. Washington, in the North Pacific Ocean on 20 January 2018", Report 02.2020.

MARIN., 2011, "Fredyn - A computer program for the simulation of a steered ship in wind and waves", MARIN, Netherlands, Maritime Research Institute Netherlands.

MARIN, 2022, "Fredyn V16", Maritime research Institute of Netherland"

Quadvlieg, F., Rapuc, S., 2019, "A pragmatic method to simulate maneuvering in waves", SNAME Convention.

Theillard, T., 2020, "One : 1816 conteneurs perdues dans le pacifique. Le Marin", 02 of December 2020, updated the 09 of December.

Development of an on-board system to monitor and estimate lateral accelerations

Rosano Gennaro, *University of Naples Federico II, Department of Industrial Engineering Via Claudio 21, 80125 Naples (Italy),* gennaro.rosano@unina.it

Begovic Ermina, *University of Naples Federico II, Department of Industrial Engineering Via Claudio 21, 80125 Naples (Italy),* begovic@unina.it

Boccadamo Guido, *University of Naples Federico II, Department of Industrial Engineering Via Claudio 21, 80125 Naples (Italy),* guido.boccadamo@unina.it

Míguez González Marcos, *Grupo Integrado de Ingeniería, CITENI, Campus Industrial, Universidade da Coruña, C/ Mendizábal S/N, Ferrol, 15403, Ferrol (Spain),* marcos.miguez@udc.es

Rinauro Barbara, *University of Naples Federico II, Department of Industrial Engineering Via Claudio 21, 80125 Naples (Italy),* barbara.rinauro@unina.it

Santiago Caamaño Lucía, *Grupo Integrado de Ingeniería, CITENI, Campus Industrial, Universidade da Coruña, C/ Mendizábal S/N, Ferrol, 15403, Ferrol (Spain),* lucia.santiago.caamano@udc.es

ABSTRACT

An on-board system developed to monitor the lateral accelerations based on measured data is presented. The system informs the crew on the actual situation of the vessel by calculating the root mean square (*RMS*) of accelerations in given time windows. The calculated *RMS* value is compared with the limiting values from the seakeeping operability criteria. Additionally, the system estimates the extreme values of accelerations that could occur in the short-term, based on the extreme value theory.

The application of the system has been performed on a fishing vessel model. Fishing vessels are potentially vulnerable to dangerous dynamic phenomena in waves being relatively small ships, with a peculiar operational profile, characterized by a variability of the loading condition during operations.

Simulated data from a weakly non-linear time domain software ShipX® and experimental data have been used to analyse the performance of the system. Experiments were conducted at the University of A Coruña (Spain) towing tank in irregular beam waves. Results have shown that the estimated extreme values are close to the to the observed ones, for both numerical and experimental time series.

Keywords: *On-board decision support system, Excessive acceleration, Extreme value, Fishing vessel.*

1. INTRODUCTION

A ship sailing in waves can experience large ship motions and/or accelerations that can be a source of risk for people on-board and cargo. A verification at the design stage is of paramount importance to assess the ship behaviour in waves and to identify potentially dangerous sailing or environmental conditions (Begovic et al. 2022; Petacco et al. 2021) but has the drawback that only a limited number of theoretical scenarios can be considered, including combinations of environmental conditions (sea and wind spectra) and standard loading conditions. In real operations, environmental and loading conditions can significantly differ from the theoretical ones, limiting the applicability of the results obtained at the design stage. Real time measurements of waves and/or ship motions can be a way to integrate the theoretical findings and to provide useful information to assist the crew in handling the vessel. Measurements of wind and waves can be used as input data for a physical model that identifies in real time the level of safety associated with the actual sailing condition through the calculation of ship responses. Alternatively, the measurement of ship responses can provide an insight into the actual state of the vessel and to forecast probable responses in the short-term, allowing the crew or automatic systems to readily act and avoid unsafe situations (Míguez González et al. 2011; Galeazzi et al. 2015; Santiago Caamaño et al. 2019).

In the present work, an on-board system that monitors the actual condition of the vessel from

measured data is described. The system compares the root mean square (*RMS*) of the lateral acceleration in a given time window with the typical limits of seakeeping operability criteria. Additionally, the system performs estimation of the extreme values that could occur in a given time based on the extreme value theory. The performance of the system is verified using simulated data by ShipX®, a weakly non-linear simulation software, and results from an experimental campaign conducted at the University of A Coruña (Spain).

2. ON-BOARD SYSTEM DESCRIPTION

On-board systems can support the crew in the decision-making process by measurement and analysis of accelerations at selected points along the ship. The proposed system is designed to perform two tasks, based on real time data:

- monitoring of the actual condition of the vessel by calculating the *RMS* of the lateral acceleration and comparing it with the seakeeping operability limits;
- estimation of the extreme values of acceleration that could be experienced in a specified time.

Time windows of 20 minutes length are considered to provide statistically accurate samples for the evaluation of the parameters necessary to perform the designed tasks. Two thresholds have been selected for the first task, respectively equal to 0.1g (severe risk level) and 0.2g (extreme risk level), Graham (1990). The condition is considered safe if the *RMS* is below the lowest limit; an alert is provided if it is in between the two limit values; an alarm is given if the *RMS* is higher than 0.2g.

The second task consists in the estimation of the extreme value of the lateral acceleration, according to the extreme value theory, Ochi (1973). The method requires the estimation of the mean zero-crossing period T_{z,a_y} and the *RMS* of the lateral acceleration in the last time window. The extreme values in a time T can be defined, under the assumptions that the lateral acceleration time series is a Gaussian random process, stationary in the analysed time window, and that the peaks of the initial distribution are independent and identically distributed. In the time T, the most probable extreme value, corresponding to the modal value of the probability distribution function of the extremes, is defined as:

$$\bar{a}_{y,T} = \sqrt{2ln\left(\frac{T}{T_{z,a_y}}\right)} \cdot RMS \tag{1}$$

The probability of exceeding the most probable extreme is, by definition, high. A preassigned probability of exceedance α can be defined. Then, the extreme acceleration exceeded with a probability α in the period T is:

$$\hat{a}_{y,T} = \sqrt{2ln\left(\frac{T}{\alpha T_{z,a_y}}\right)} \cdot RMS \tag{2}$$

Equations (1) and (2) are valid for any bandwidth parameter, i.e. for narrow and wide band processes. The time T is defined by the user (20 minutes, 30 minutes, 1 hour etc.). In this work, it has been set to 20 minutes to have information in the short-term.

For the second task, the most probable extreme has been assumed as reference for raising an alert or an alarm; g/2 and g/3 have been selected as threshold values. The highest threshold comes from Section 4.5.5.3 of the Interim guidelines on the Second Generation Intact Stability Criteria, (IMO, 2020), that set it as limit value in the development of deterministic operational guidance for the excessive acceleration failure mode. It has been lowered to g/3 to provide a reference value to provide an alert. The system provides an alert if the estimation is in between the two limit values and an alarm if it is higher than the highest limit.

This limit values are summarized in Table 1.

Table 1: Summary of the limit values.

	Monitoring	**Estimation**
	RMS (m/s²)	$\bar{a}_{y,T}$ (m/s²)
ALERT	0.1g	g/3
ALARM	0.2g	g/2

3. TEST CASE

A mid-sized stern trawler typical of the fleet of Galicia (Spain) is considered as test case for the verification of the performance of the on-board system. The vessel has already been object of research in Míguez González and Bulian (2018), Santiago Caamaño et al. (2019). The vessel was found vulnerable to the excessive acceleration failure mode, one of the Second Generation Intact Stability Criteria, in Rosano et al. (2023).

The choice of a fishing vessel is due to the expected vulnerability of this ship type in terms of lateral accelerations since many operations are conducted at low speed and eventually in beam waves. Additionally, the loading condition can change during operations, making appropriate the adoption of a system that monitors the ship motions and accelerations in real-time, providing information to the crew.

Among all the available loading conditions (Santiago Caamaño et al., 2019), the selected one is characterised by the largest initial stability, specifically "*Departure from the fishing ground with full catch and fishing gear, 35% of fuel oil and stores and no ice*", which is the most vulnerable in terms of lateral accelerations.

The main ship characteristics are listed in Table 2; the body plan is shown in Figure 1.

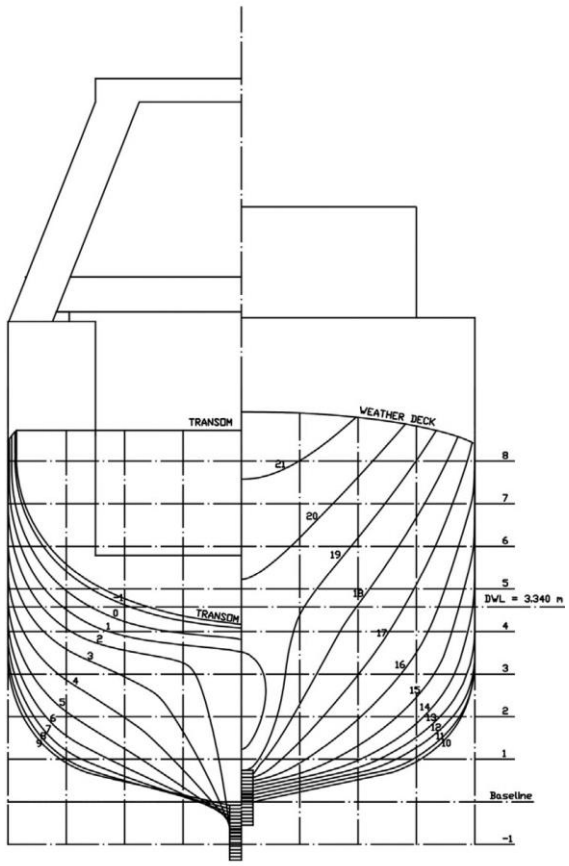

Figure 1: Fishing vessel body plan.

Table 2: Ship main characteristics.

Parameter	Units	
Length overall, L_{OA}	(m)	34.5
Length between perpendiculars, L_{BP}	(m)	29.0
Breadth, B	(m)	8.0
Draught, d	(m)	3.48
Displacement, Δ	(t)	489
Trim, θ	(°)	0.0
Longitudinal position of the centre of gravity, LCG	(m)	14.0
Vertical position of the centre of gravity, VCG	(m)	3.43
Metacentric height, GM	(m)	0.659
Natural roll frequency, ω_φ	(rad/s)	0.804
Natural roll period, T_r	(s)	7.81
Longitudinal distance of the calculation point of lateral acceleration from AP, x_{AP}	(m)	23.5
Height of the calculation point of lateral acceleration from BL, H_{BL}	(m)	10.20

4. NUMERICAL AND EXPERIMENTAL TIME SERIES

The performance of the system has been verified on simulated and experimental data, assuming the wheelhouse as the calculation point for lateral acceleration. The vessel has been considered at zero speed in beam waves, under the action of irregular beam waves, described by the Bretschneider wave energy spectrum. Sea states having a significant wave height in a range between 0.5 m and 3.5 m and zero up-crossing period between 5.5 s and 8.5 s have been considered to study the ship response in terms of lateral acceleration. The selected zero-crossing periods are close to the ship's natural roll period.

Numerical simulations

Numerical simulations have been performed by ShipX® software by SINTEF Ocean. The Froude-Krylov roll moment and the restoring moment are calculated accounting for the instantaneous wetted surface.

Damping has been modelled by an equivalent linear representation, via a stochastic linearization (Kaplan, 1966). An iterative procedure to calculate the equivalent linear roll damping coefficient has been performed for different wave heights and zero-crossing periods, to account for the effect of the sea state on the roll damping. The obtained damping coefficients are represented in Figure 2, showing an expected increase with the significant wave height, and local maxima around the natural roll frequency.

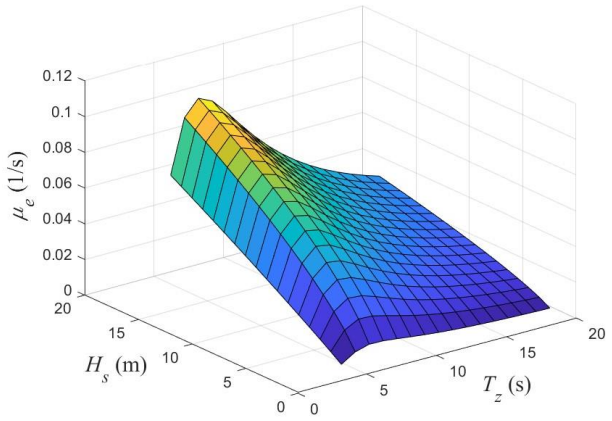

Figure 2: Equivalent linear roll damping as a function of the sea state.

Experimental tests

An experimental campaign was conducted at the University of A Coruña, to provide an additional source of data to test the system. The towing tank, shown in Figure 3, is 56 m long, 4.20 m wide and 1.80 m deep. A unidirectional wave-maker generates regular and irregular waves. A long acquisition time is allowed by active force feedback mode and a specifically designed beach that limits the wave reflection.

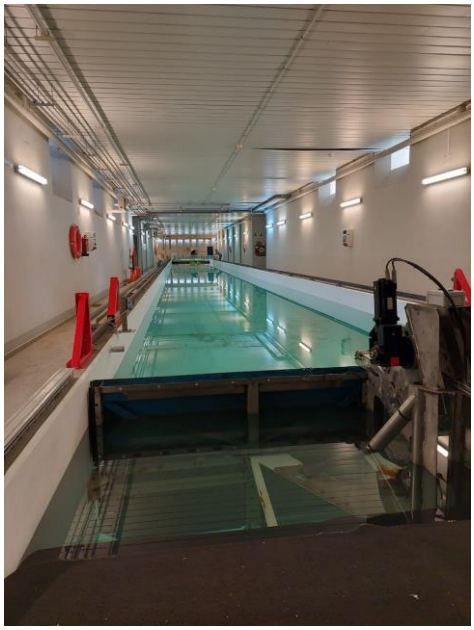

Figure 3: University of A Coruña towing tank.

Tests in irregular beam waves were conducted on a 1/30 geosim fiberglass model of the fishing vessel, Figure 4. The model was ballasted to reach the ship displacement in model scale and the position of the weights was adjusted to obtain the required zero trim condition and the roll radius of gyration. Inclining and roll decay tests were performed to measure the metacentric height *GM* and the roll radius of gyration.

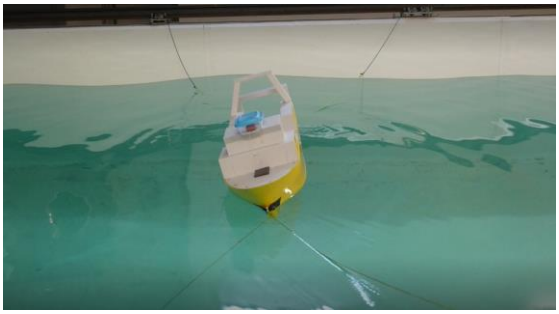

Figure 4: Fishing vessel model.

A series of roll decay tests were performed following the guidelines for the alternative assessment of the weather criterion (IMO, 2006). The roll motion was measured by an Inertial Motion Unit (IMU) with a sampling frequency of 100 Hz. The tests started from an initial heel angle greater than 25° and the motion was recorded until the rolling angle was less than 0.5°.

The roll damping has been modelled using a quadratic function approach. The linear μ and quadratic β damping coefficients have been calculated considering the linear decrement of roll decay and fitting the decay curve through a second-degree polynomial. The obtained coefficients, in full scale, are reported in Table 3.

Table 3: Roll damping coefficients.

μ	(1/s)	0.0025
β	(1/rad)	0.343

Two wave gauges located on the paddles of the wave maker were used to measure the wave elevation and perform an active calibration of the wave generator. Checks were performed by comparing the theoretical wave spectra with those from the experiments.

An IMU was used to measure the roll motion and lateral accelerations at the wheelhouse. The model was restrained to the tank walls using four semi-elastic ropes, to limit sway and yaw motions.

5. RESULTS

The developed on-board system uses the real time measurement of the lateral acceleration to perform its tasks, i.e. monitoring the actual vessel

condition and the estimation of the extreme values in the short-term.

Data are collected considering a time interval of 20 minutes. An overlapping of 87.5% among consecutive time windows is introduced, allowing the system to provide information every 2.5 minutes. For the estimation stage, a time of 20 minutes is considered.

The application of the system has been performed on simulated and experimental time series. Time series of almost 1 hour have been generated for all the analysed sea states. Then, the time series have been merged to simulate a change in the sea state and to verify the capability of the system to recognize these changes. Two situations have been considered:

- the zero-crossing period is kept constant, and the significant wave height is increased almost every hour;
- the significant wave height is kept constant, and the zero-crossing period is increased almost every hour.

Three cases, corresponding to the situations described above are summarised in Table 4.

Table 4: Combinations of sea states used to test the system.

	H_s (m)	T_z(s)		
Case 1	0.5	6.5	Simulated	Figure 5
	1.5	6.5		
	2.5	6.5		
Case 2	1.5	5.5	Simulated	Figure 6
	1.5	6.5		
	1.5	7.5		
	1.5	8.5		
Case 3	1.5	5.5	Experimental	Figure 7
	1.5	6.5		
	1.5	7.5		
	1.5	8.5		

For each case, a figure with three graphs is provided. In each graph, the vertical dashed lines represent the time instant that corresponds to the start of a change in the sea state is introduced. The first graph represents the lateral acceleration time series. The *RMS* of the lateral acceleration in the considered time intervals is given in the second graph. The first value is provided at minute 20 once the first estimation is performed. In the graph, two horizontal lines are included, corresponding to the lower ($0.1g$) and upper ($0.2g$) limits of the monitoring task of the system. Three different colours have been selected to draw the markers: green to identify the safe condition; orange and red for the critical conditions. In the lower graph, the most probable extreme value and the extreme value that is exceeded with a probability α=0.10 are represented, to show what could occur in the next 20 minutes. The most probable extreme is used as reference value for the estimation task and the markers are coloured in green, orange, or red depending on the assumed value. The extreme exceeded with a probability α = 0.10 is always represented in black and provides an insight into the worst scenario that could occur in the assumed time. The information provided by this second task gives information in the short-term about potentially dangerous situations, allowing the crew to take corrective actions, if necessary.

For Case 1, three simulated time series of the lateral acceleration have been merged, see Figure 5. Accelerations are generated under the action of irregular beam waves having a zero-crossing period equal to 6.5 s. The *RMS* increases with the significant wave height, exceeding the lower limit $0.1g$ after 75 minutes and the threshold $0.2g$ after 150 minutes. The most probable extreme $\bar{a}_{y,T}$ remains lower than the first limit value $g/3$ for the first 75minutes. During the second hour, it is very close to the second threshold $g/2$, trespassing it many times. It exceeds $g/2$ after 140 minutes, raising an alarm all the time. From the graphs it can be observed that the system needs around 5 minutes to identify the change in the sea state.

For Case 2, four simulated time series have been merged, Figure 6, generated by irregular beam waves having significant wave height of 1.5m and different zero-crossing periods. The *RMS* is in the orange zone between $0.1g$ and $0.2g$ all the time. The most probable extreme $\bar{a}_{y,T}$ exceeds few time the highest limit value $g/2$ during the second and third hours, while the extreme $\hat{a}_{y,T}$is many times above it.

For Case 3, four experimental time series have been merged, Figure 7. The considered sea states are the same used for Case 2. The *RMS* is in the orange zone between $0.1g$ and $0.2g$ all the time (the highest threshold is exceeded only two times in the first minutes), assuming almost constant values for the four considered sea states. A moderate reduction develops with the increase of the mean-zero crossing period. The most probable extreme $\bar{a}_{y,T}$ exceeds most of the time the highest limit value $g/2$: the ship is experiencing all the time dangerous conditions,

and based on the provided alarm the crew is expected to take corrective actions, as an increase of ship speed to introduce additional roll damping, or a change in the wave heading to reduce the external excitation due to the waves.

Referring to all the simulated and experimental data, a check on the estimations based on the extreme value theory has been performed. For each time series, the first 20 minutes have been considered to collect data to perform the estimations. Therefore, the most probable extreme $\bar{a}_{y,T}$ and the extreme $\hat{a}_{y,T}$ that is exceeded with a probability 0.10 have been calculated referring to a period of 20 minutes. Finally, a comparison has been performed between the estimations and the greatest acceleration recorded in the 20 minutes immediately after, corresponding to the period to which the estimations refer. The results of this comparison are summarized in Table 5, showing that:

- in the case of simulated data, the most probable extreme is exceeded in nine sea states over fourteen while the extreme exceeded with a probability 0.10 is exceeded two times;
- in the case of experimental data, the most probable extreme is exceeded in three sea states over ten while the extreme exceeded with a probability 0.10 is exceeded only one time.

Table 5: Comparison between the estimations and the observed extreme ($\bar{a}_{y,T}$most probable extreme; $\hat{a}_{y,T}$ extreme exceeded with a probability 0.10; $a_{y,max}$ observed extreme).

		Simulated			Experimental		
H_s	T_z	$\bar{a}_{y,T}$	$\hat{a}_{y,T}$	$a_{y,max}$	$\bar{a}_{y,T}$	$\hat{a}_{y,T}$	$a_{y,max}$
(m)	(s)	(m/s^2)	(m/s^2)	(m/s^2)	(m/s^2)	(m/s^2)	(m/s^2)
0.5	5.5	2.02	2.44	2.38	-	-	-
0.5	6.5	1.75	2.13	1.83	-	-	-
0.5	7.5	2.26	2.74	2.06	-	-	-
0.5	8.5	1.71	2.06	1.83	-	-	-
1.5	5.5	4.16	5.03	4.18	6.34	7.65	4.90
1.5	6.5	4.69	5.67	5.90	5.79	6.99	6.39
1.5	7.5	4.41	5.34	4.69	4.90	5.91	4.53
1.5	8.5	3.37	4.09	4.06	4.95	5.98	4.24
2.5	5.5	5.73	6.92	5.42	8.13	9.79	7.56
2.5	6.5	7.72	9.34	5.93	7.44	8.96	7.20
2.5	7.5	7.07	8.57	5.95	7.52	9.08	6.28
2.5	8.5	5.73	6.95	8.07	6.91	8.34	6.02
3.5	6.5	8.41	10.17	8.90	9.61	11.6	10.07
3.5	7.5	8.46	10.24	7.80	7.72	9.31	9.97

In Figure 8, a series of four experimental time series is analysed, to have a better insight on how many times the most probable extreme value is exceeded. In the lower graph, the blue line represents the largest acceleration (observed extreme) experienced in the 20 minutes that follow each prediction. It must be noted that to perform the comparison the observed maximum values are not represented at their exact time; they should be plotted 20 minutes later than the corresponding prediction. The same maximum value is often repeated on subsequent intervals due to the overlapping among consecutive intervals. The results in Figure 8 show that the most probable extreme value $\bar{a}_{y,T}$ is often exceeded, which is coherent with its own definition, being defined as the modal value of the probability distribution function of the extreme values. In detail, it is exceeded 60% of the time. The extreme value $\hat{a}_{y,T}$ exceeded with a probability 0.10 is exceeded 16% of the time.

6. CONCLUSION

In the present paper, a decision support system for the monitoring and estimation of lateral acceleration experienced on-board has been proposed. Results from the application of the system on a mid-sized stern trawler have been shown.

Based on time intervals of 20 minutes and including an overlapping among consecutive intervals, the developed on-board system performs two tasks. The first task is the monitoring of the actual condition of the vessel, performed by comparison of the *RMS* of lateral acceleration in each time interval with the typical limit values of the seakeeping operability criteria. For the second task, the extreme values that could be experienced in a preassigned time T are calculated based on the extreme value theory. The most probable extreme and the extreme value exceeded with a probability 0.10 are calculated and compared with two limit values, respectively equal to half and one-third of the acceleration due to gravity.

Numerical simulations and experimental tests have been performed to obtain different source of data to test the system, confirming its capability to discriminate between safe and unsafe conditions. The extreme value in the short-term has been predicted with good accuracy.

The proposed system can be used for monitoring of any other ship responses, such as roll motion or vertical accelerations; in the same way, the corresponding extreme values could be calculated and compared with assigned thresholds.

Real voyage data should be used to further analyse the system. Some of the assumptions, as the hypothesis that the lateral acceleration is a Gaussian and stationary process in the analysed time window, could be violated due to the increased variability in real operations. Changes in the magnitude and the characteristics of the response caused by variations in heading angle, ship velocity, fishing nets, the water on deck and the variation of the loading condition during operations should be included in the analysis of the time interval. Finally, the adopted limited values for the monitoring and estimation stages should be carefully analysed and calibrated to correctly inform the crew on actual dangerous situations.

REFERENCES

Begovic, E., Boccadamo, G., Rinauro, B., Rosano G., "Excessive acceleration simplified Operational Guidance", *International Journal of Naval Architecture and Ocean Engineering*, Vol. 14, 2022, 100473, https://doi.org/10.1016/j.ijnaoe.2022.100473

IMO 2006, "MSC.1/Circ.1200 - Interim Guidelines for Alternative Assessment of the Weather Criterion", 24 May.

IMO 2020, "MSC.1/Circ.1627 - Interim Guidelines on the Second Generation Intact Stability Criteria".

Galeazzi, R., Blanke, M., Falkenberg, T., Poulsen, N.K., Violaris, N., Storhaug, G., Huss, M., 2015. "Parametric roll resonance monitoring using signal-based detection". *Ocean Engineering* 109, 355–371. doi:https://doi.org/10.1016/j.oceaneng.2015.08.037.

Graham, R., 1990, "Motion-Induced Interruptions as Ship Operability Criteria", *Naval Engineers Journal* 102, 65–71. doi:https://doi.org/10.1111/j.1559-3584.1990.tb02556.x.

Kaplan, P., 1966, "Lecture notes on nonlinear theory of ship roll motion in a random seaway", *Webb Institute of Naval Architecture*.

Míguez González, M., Peña, F.L., Díaz Casás, V., Neves, M.A.S., 2011, "Large Amplitude Roll Motion Forecasting through an Artificial Neural Network System", *Proceedings of the 12th International Ship Stability Workshop*, Washington D.C., USA. pp. 219–224

Míguez González, M., Bulian, G., 2018, "Influence of ship dynamics modelling on the prediction of fishing vessels roll response in beam and longitudinal waves", *Ocean Engineering* 148, 312–330. doi:10.1016/j.oceaneng.2017.11.032.

Ochi, M.K., 1973, "On prediction of extreme values", *Journal of Ship Research* 17, 29–37

Petacco, N., Pitardi, D., Podenzana Bonvino, C., Gualeni, P., "Application of the IMO Second Generation Intact Stability Criteria to a Ballast-Free Containership", *J. Mar. Sci. Eng.* 2021, 9, 1416. https://doi.org/10.3390/jmse9121416

Rosano, G., Begovic, E., Boccadamo, G., Míguez González, M., Rinauro, B., Santiago Caamaño, L. 2023, "On-board monitoring and estimation of lateral accelerations through extreme value theory", *Ocean Engineering 284,* https://doi.org/10.1016/j.oceaneng.2023.115177.

Santiago Caamaño, L., Galeazzi R., Nielsen U.D., Míguez González M., Díaz Casás V., 2019, "Real-time detection of transverse stability changes in fishing vessels", *Ocean Engineering* 189, doi:10.1016/j.oceaneng.2019.106369

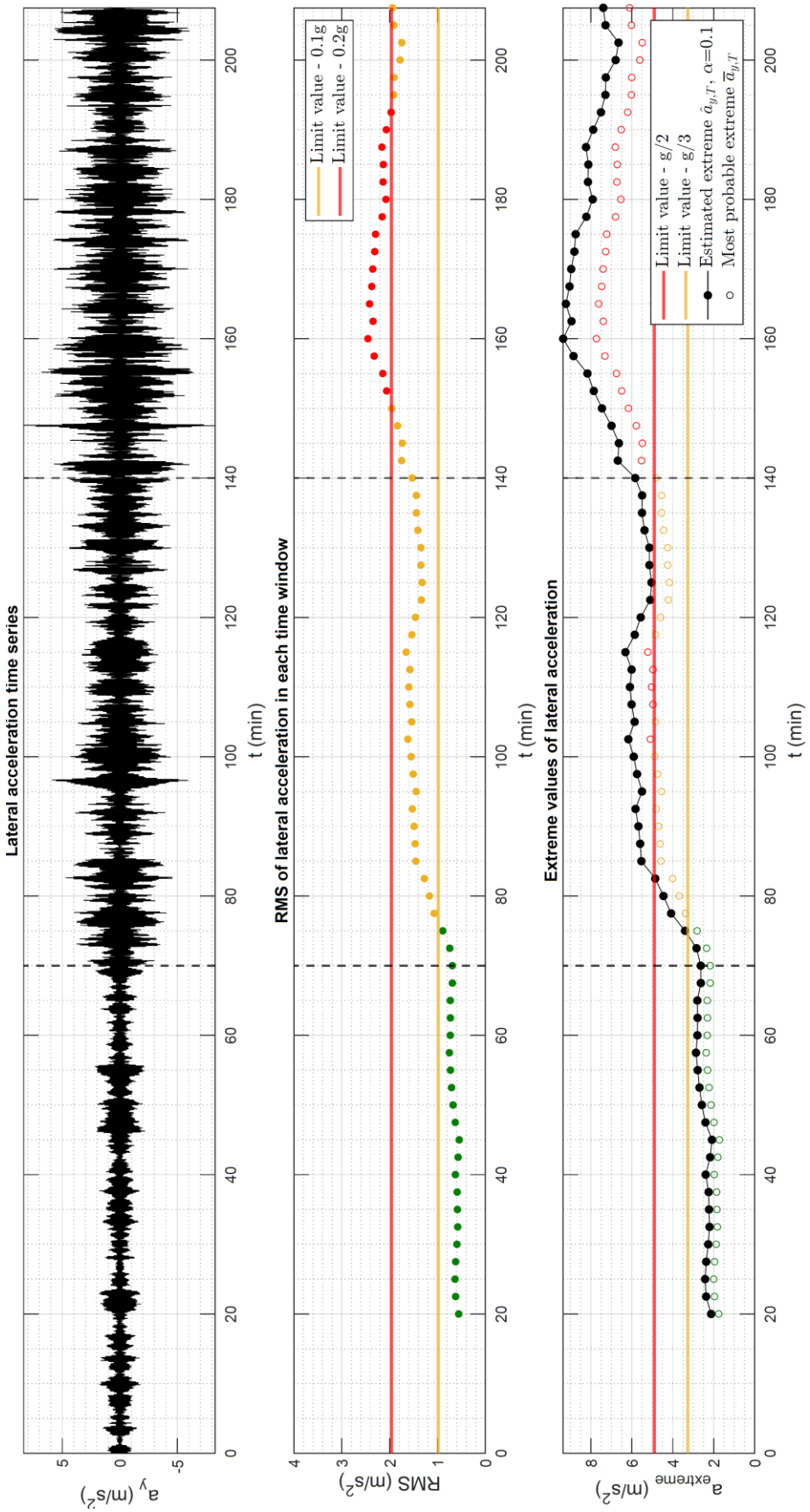

Figure 5: From top to bottom. Simulated lateral acceleration time series for T_z=6.5s and H_s=0.5m, 1.5m and 2.5m, *RMS* values, and extreme value.

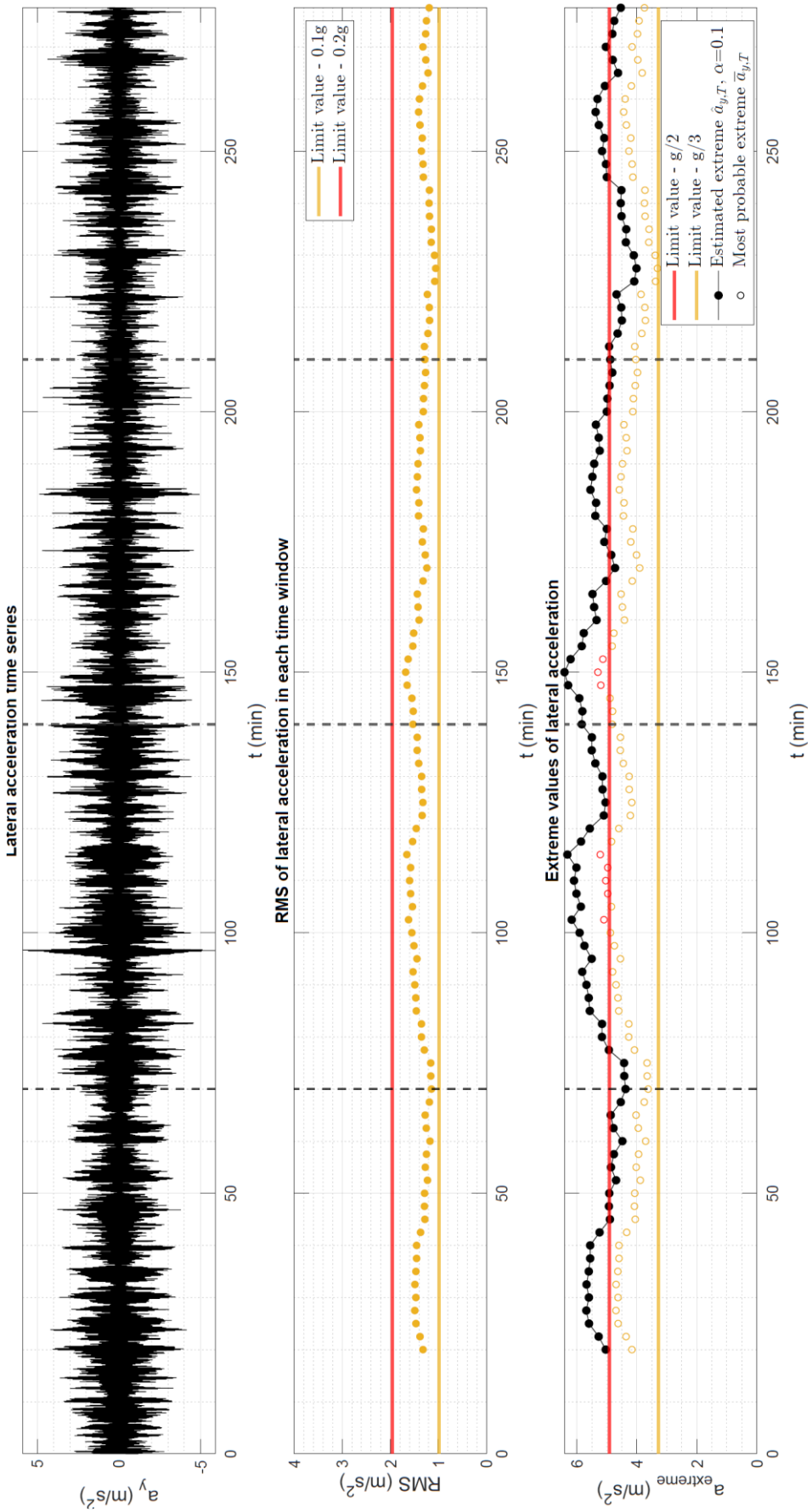

Figure 6: From top to bottom. Simulated lateral acceleration time series for T_z=5.5s, 6.5s, 7.5s and 8.5s and H_s=1.5m, *RMS* values, and extreme value.

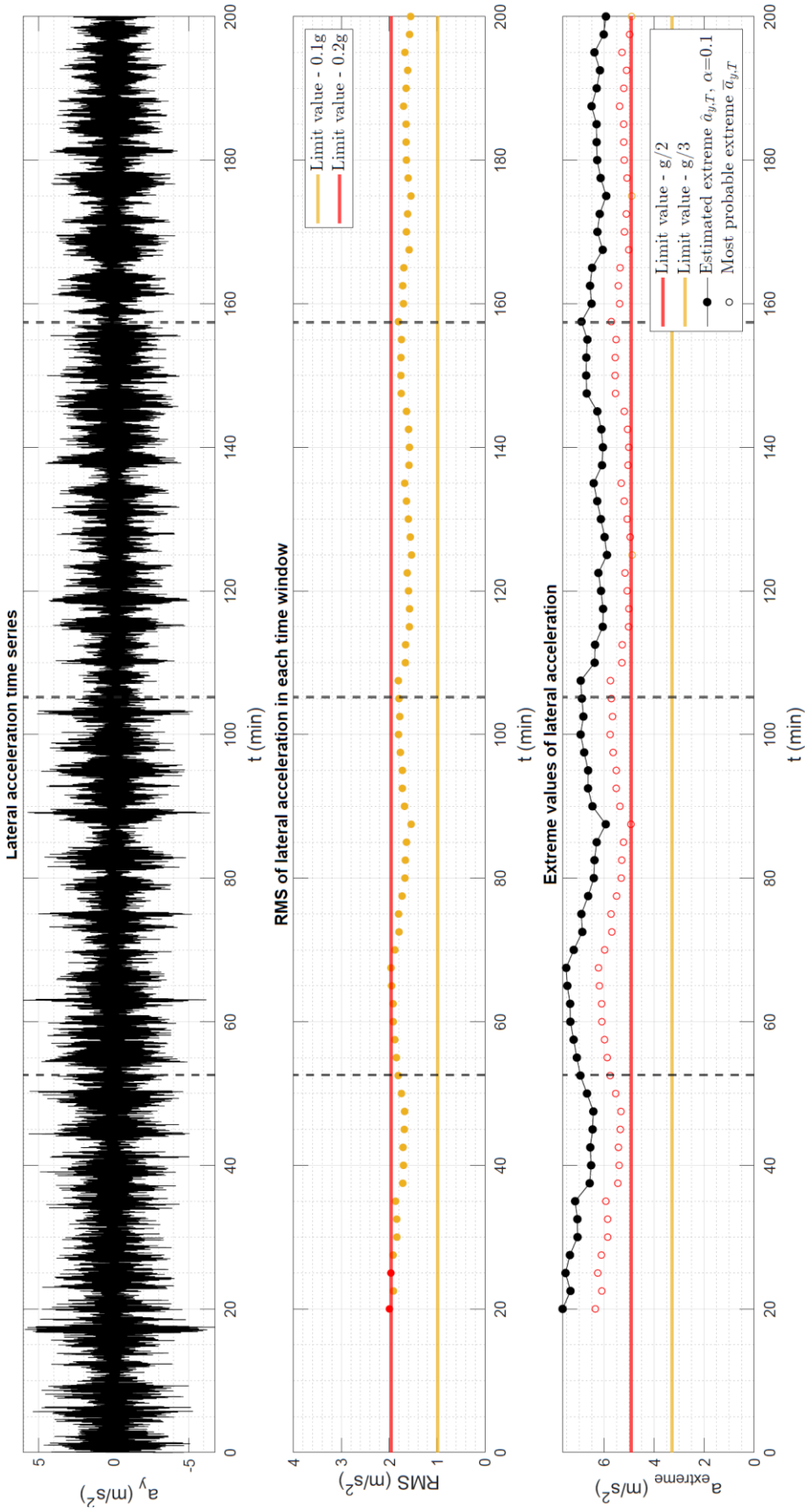

Figure 7: From top to bottom. Experimental lateral acceleration time series for T_z=5.5s, 6.5s, 7.5s and 8.5s and H_s=1.5m, *RMS* values, and extreme value.

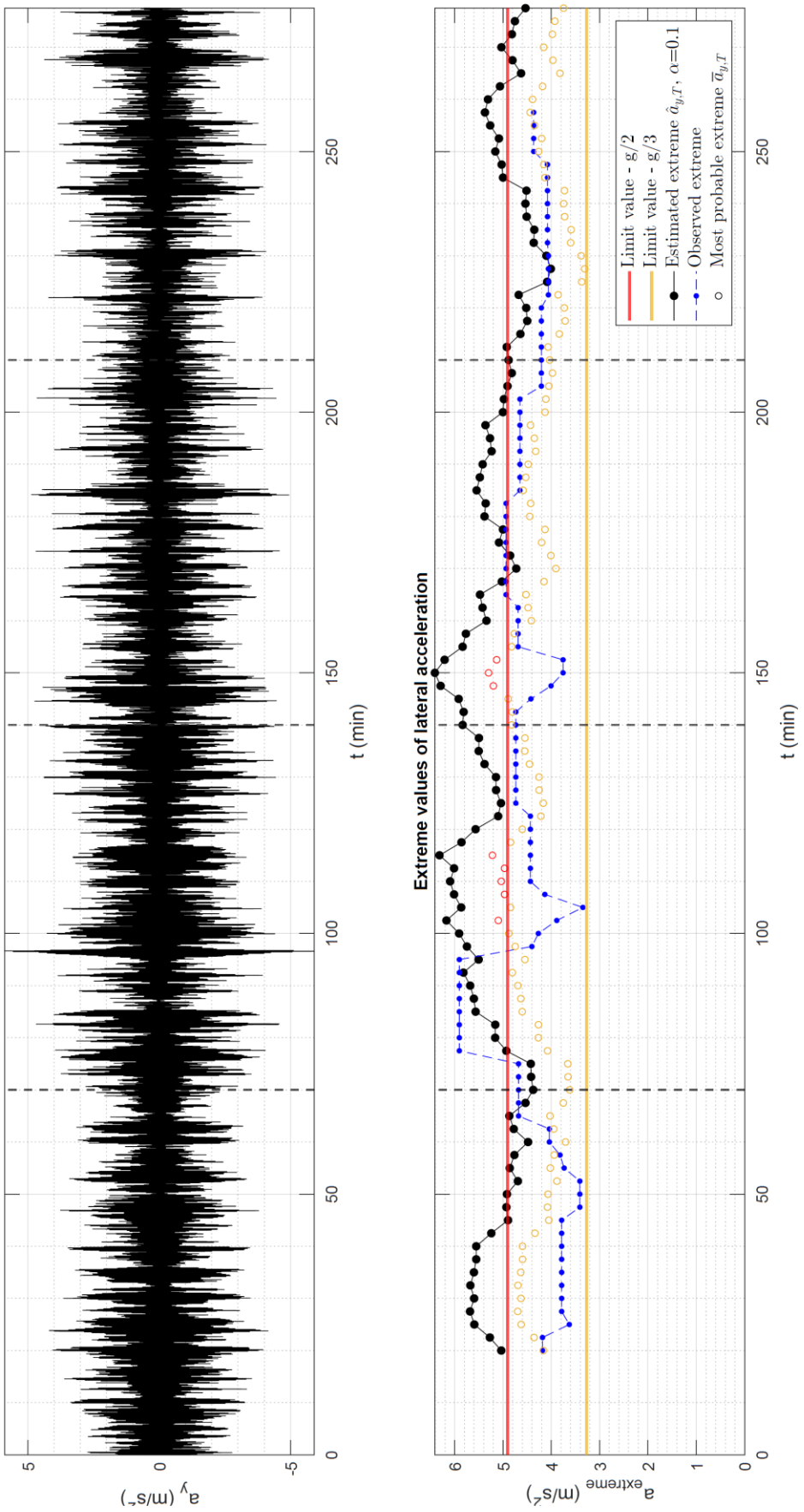

Figure 8: From top to bottom. Simulated lateral acceleration time series for T_z=5.5s, 6.5s, 7.5s and 8.5s and H_s=1.5m and estimated and observed extreme .

An improved method for operational guidance in bimodal seas

Samuel J. Edwards, *David Taylor Model Basin (NSWCCD),* samuel.j.edwards33.civ@us.navy.mil
Michael Levine, *David Taylor Model Basin (NSWCCD),* michael.d.levine2.civ@us.navy.mil
Justin Harler, *David Taylor Model Basin (NSWCCD),* justin.m.harler.civ@us.navy.mil

ABSTRACT

The safe operation of a ship in heavy weather and high sea states requires accounting for the risk of extreme ship motion responses in stochastic ocean waves. To address this risk, operational guidance can employ a pre-computed database or lookup table of ship motions responses covering a range of potential ocean conditions. A simplified approach typically assumes a unidirectional seaway. However, realistic conditions often encompass both wind and swell components characteristic of bidirectional seaways. In this study, data-adaptive Long Short-Term Memory (LSTM) neural networks are investigated as part of a multi-fidelity approach incorporating Large Amplitude Program (LAMP), and a reduced-order model known as SimpleCode. An assessment of this multi-fidelity approach focuses on prediction of ship motion responses in bidirectional waves with bimodal spectra

Keywords: *Operational guidance, hydrodynamic simulations, machine learning*

1. INTRODUCTION

The safety of a ship and its crew in heavy weather requires careful attention to seakeeping and operational guidance. Operational guidance is an important consideration in the survival of a ship, and has been the focus of International Maritime Organization (IMO) publications (IMO 1995, IMO 2007, IMO 2020). Recommendations for ship-specific operational guidance have been developed and addressed in the interim guidelines of the Second Generation Intact Stability Criteria by IMO (2020). While these guidelines are useful in ship design and operations, they are not comprehensive.

Seakeeping typically entails selection of ship speed and heading, based on prediction of ship motions in response to a given seaway. On-board operational guidance can employ a pre-computed database or lookup table of ship motions responses covering a range of potential conditions. Operational limits can be applied based on maximum acceptable response levels.

Generating a database covering a comprehensive set of potential ship speeds, headings, loading and wave conditions can potentially provide a robust operational guidance capability. However, since the ocean environment is random and complex, a pre-computed database cannot completely capture all wave conditions inevitably encountered. Consequently, a computationally feasible approach is needed to estimate ship responses for a range of realistic conditions.

A simplified approach for ship motion response predictions typically assumes a unidirectional seaway with a unimodal wave spectrum. However, realistic seaways typically encompass both wind and swell components that are can be delineated in terms of wave directionality and modal frequencies. Bi-directionality and bimodal spectra are common wave characteristics that are suitable for consideration in predictive ship response models.

In a recent effort, Levine et al. (2022) described a data-adaptive model to evaluate predicted ship motions in unidirectional waves with a unimodal spectrum. Data-adaptive Long Short-Term Memory (LSTM) neural networks were investigated as part of a multi-fidelity approach incorporating Large Amplitude Motion Program (LAMP) (Shin et al. 2003) , and a reduced-order model known as SimpleCode. LSTM networks were trained and tested with three degree-of-freedom (3-DOF) LAMP simulations as a target, and 3-DOF SimpleCode simulations and wave time-series as inputs. LSTM networks were shown to improve the fidelity of SimpleCode seakeeping predictions relative to LAMP, while retaining the computational efficiency of a reduced-order model. The method was expanded to bidirectional seaways in Howard et. al. (2022). The LSTM network showed improvement of

SimpleCode relative to LAMP but was still restricted to the 3-DOF SimpleCode and LAMP.

In this paper, this data-adaptive approach employing LAMP, SimpleCode and LSTM neural networks is evaluated for prediction of heave, roll and pitch motions in response to bidirectional waves and bimodal spectra. Simulations are performed based on the David Taylor Model Basin (DTMB) Model 5415. LAMP and SimpleCode simulations are configured for generation of 6-DOF motions, which provides improved accuracy as compared to a simpler 3-DOF vertical motion configuration (heave, roll and pitch) with horizontal motions (surge, sway and yaw) constrained.

2. METHODOLOGY

SimpleCode and LAMP

SimpleCode is a reduced order seakeeping code that can quickly produce acceptable results (Smith et al. 2019). One of the key simplifications is in the local variation of wave pressure, where the hydrostatic and Froude-Krylov equations can instead use volume integrals rather than integrating over the surface of the ship (Weems and Wundrow 2013). With pre-computed Bonjean curves, the instantaneous submerged volume and geometric center are easily accessed, therefore, sectional hydrostatic and Froude-Krylov forces can be calculated quickly.

LAMP is a higher fidelity code that considers the forces and moments acting on the ship in the time-domain in 6-DOF via a 4th-order Runge-Kutta solver (Shin et al. 2003). Central to the code is the solution to the 3-D wave-body interaction problem. Within LAMP, the complexity of this solution can be altered based on the version of the code. In this study, the version is LAMP-3. In LAMP-3, the pertubation velocity potential is solved over the mean wetted hull surface, and hydrostatic and Froude-Krylov forces are solved over the instantaneous wetted hull surface. Additionally, LAMP-3 allows for large lateral motions that may be induced by forces acting on the sides of the ship.

SimpleCode can produce an approximation of LAMP, especially with tuned radiation and diffraction forces included (Weems and Belenky 2018, Pipiras 2022). However, a fidelity gap exists, especially when considering a bimodal wave spectrum.

In this study, the 6-DOF versions of SimpleCode LAMP has effectively estimated motions comparable to model tests (Lin et al. 2007), but is significantly more computationally expensive than SimpleCode. Though some parameters such as the number of wave frequency components, free surface panel definition, and hull offsets can be adjusted, LAMP-3 runs in nearly real time. In contrast, SimpleCode can run much faster than real-time.

Long Short-Term Memory

A Long Short-Term Memory (LSTM) neural network (Hochreiter and Schmidhuber 1997) is a recurrent neural network that incorporates both long- and short-term effects that are learned and developed during the training process. These memory effects are stored in weight matrices where with other operations, transform input to the target output. Equations 1-6 describe the operations that occur in a LSTM layer.

$$f_1 = \sigma\left(W_{f_1} x^{[t]} + U_{f_1} h^{[t-1]} + b_{f_1}\right) \quad (1)$$

$$f_2 = \sigma\left(W_{f_2} x^{[t]} + U_{f_2} h^{[t-1]} + b_{f_2}\right) \quad (2)$$

$$f_3 = tanh\left(W_{f_3} x^{[t]} + U_{f_3} h^{[t-1]} + b_{f_3}\right) \quad (3)$$

$$f_4 = \sigma\left(W_{f_4} x^{[t]} + U_{f_4} h^{[t-1]} + b_{f_4}\right) \quad (4)$$

$$c^{[t]} = f_1 \odot c^{[t-1]} + f_2 \odot f_3 \quad (5)$$

$$h^{[t]} = f_4 \odot \tanh\left(c^{[t]}\right) \quad (6)$$

where:

- W weight matrix
- U weight matrix
- b bias vectors
- $x^{[t]}$ input vector at time *t*
- $h^{[t]}$ hidden state vector at time *t*
- $c^{[t]}$ cell state vector at time *t*
- σ sigmoid function
- *tanh* hyperbolic tangent function
- $\odot$ Hadamard product.

The input vector $x^{[t]}$ is standardized by the respective means and standard deviations for each input channel. The output or target at time *t* is equal to the hidden state vector $h^{[t]}$. The weight matrices and bias vectors are progressively adjusted during

the training process to minimize the specified loss between the training and test data.

The present work uses the mean-squared error in Equation 7 to quantify the error between the training and test sets.

$$MSE = \frac{1}{N}\sum_{i=1}^{N}\left(y_T(t_i) - y_L(t_i)\right)^2 \quad (7)$$

where N is the number of points in the time series, y is the response matrix which contains the time series of heave, roll, and pitch, subscript T is the target time series, subscript L is the LSTM produced time series, and t_i is the *i-th* time instant in the time series.

The input time series are the heave, roll, and pitch quantities provided from 6-DOF SimpleCode as well as the input wave elevation at the ship's center of gravity generated from the LAMP simulations. The target time series are the heave, roll, and pitch quantities from 6-DOF LAMP. The LSTM architecture consisted of two layers of size 50.

Numerical Experimental Set-up

The hullform used for this study was the David Taylor Model Basin (DTMB) Model 5415. Figure 1 is a rendering of the DTMB Model 5415 and Table 1 provides the particulars for the vessel.

Figure 1: 3-dimensional rendering of the DTMB Model 5415.

Table 1: Particulars for the DTMB Model 5415.

Particular	Symbol	Value
Length between perpendiculars	L_{PP}	142.0 m
Beam	B	19.1 m
Draft	T	6.2 m
Radius of gyration about X-axis	k_{xx}	7.1 m
Radius of gyration about Y-axis	k_{yy}	35.5 m
Vertical center of gravity (w.r.t baseline)	KG	7.5 m
Longitudinal center of gravity (w.r.t midships)	L_{cg}	-0.9 m
Displacement mass	Δ_m	8424 t

For this case study, a primary International Towing Tank (ITTC) spectrum (ITTC 2002) characterizing wind-generated waves was applied with wave height of 4.0 meters and model period of 9.0 seconds for relative wave heading at stern-quartering seas of 45 degrees. This corresponds to NATO (1983) Standard Sea State 5 at most probable modal period. The secondary ITTC spectrum for the swell component was wave height of 2.0 m, modal period of 15 s, and relative wave heading varied from 0 to 330 degrees. The primary ship speed was set to 10 knots.

A single network was trained to include all secondary wave headings. Due to the difference in ship dynamics between SimpleCode and LAMP, the effect of the heading controller and therefore ship position in space differed. Since the overall dynamics solved for by SimpleCode and LAMP differ (i.e., the inclusion of diffraction and radiation by LAMP,) the corresponding action by the rudder differs between LAMP and SimpleCode simulations. The range of secondary headings resulted in varying levels of drift between the SimpleCode and LAMP model geospatial locations but given that the rest of the parameters such as primary heading, sea state, and ship speed were fixed, the LSTM framework could compensate for all secondary headings. The addition of the wave elevation at the ship's center of gravity time series from LAMP aided in improving the network's performance as well. There is the caveat that ship's path in LAMP is an unknown and would not be known in practice. However, by showing improvement in the process through adding this additional knowledge to the input, the issue in differing geospatial locations between LAMP and SimpleCode can be decoupled.

A total of 15 realizations were generated in LAMP and SimpleCode for each of the 12 secondary headings. The duration of each realization was 30-minutes. The LSTM network utilized seven realizations from each secondary heading for training, three realizations for validation, and five for testing. In total, 84 realizations were included in the training set, 36 realizations for validation, and 60 for testing.

The average standard deviations for heave, roll, and pitch from the five test realizations generated using SimpleCode, LAMP, and the LSTM framework were compared. In addition, the absolute percentage error, ϵ, was used to compare SimpleCode and the LSTM to LAMP. The equation for absolute percentage error is as follows:

$$\epsilon = \frac{|\hat{X}_L - \hat{X}_E|}{\hat{X}_L} \quad (8)$$

where $\hat{X}_L$ represents the standard deviation of LAMP data and $\hat{X}_E$ represents the standard deviation of the LSTM estimate or SimpleCode.

In addition to the standard deviation statistic, the estimations of peaks between mean up-crossings were compared. The peaks between mean up-crossings from each of the test SimpleCode, LAMP, and LSTM time series were tabulated and pdfs were generated. Furthermore, visual comparison of time series behavior near large LAMP peaks was performed.

3. RESULTS

Statistical Comparison

Obtaining a statistical representation of ship dynamics is a key enabler for performance analysis of seakeeping predictions. The performance of the LSTM-based approach was assessed relative to LAMP and SimpleCode based on comparison of the respective motion responses of heave, roll, and pitch. The average standard deviation was computed for the ensemble of each motion response type and speed-heading combination, which provided the ship motion response statistics for this study. Comparison of the standard deviations of the LAMP, SimpleCode, and LSTM-based method predictions for heave, roll and pitch as function of secondary heading are in Figures 2, 3 and 4.

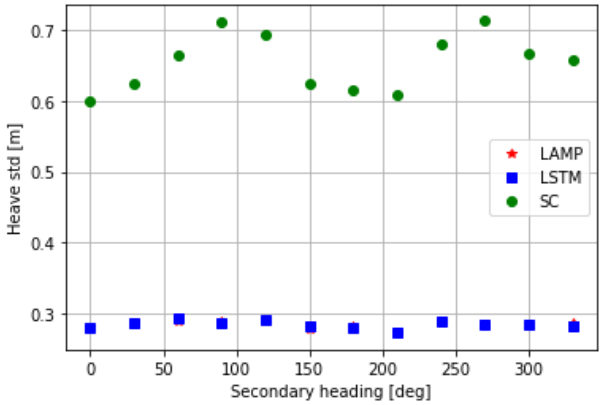

Figure 2: Comparison of heave standard deviation for the different secondary headings between LAMP, the LSTM, and SimpleCode.

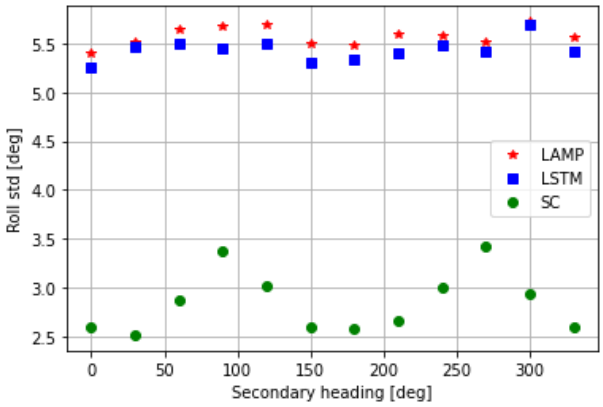

Figure 3: Comparison of roll standard deviation for the different secondary headings between LAMP, the LSTM, and SimpleCode.

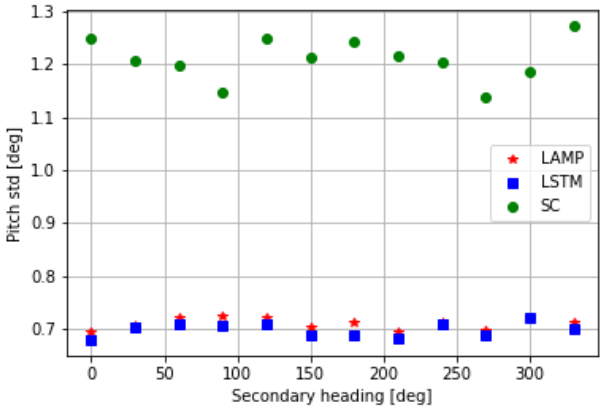

Figure 4: Comparison of pitch standard deviation for the different secondary headings between LAMP, the LSTM, and SimpleCode.

In Figures 2-4, the LSTM network greatly improves in the estimation of heave, roll, and pitch standard deviation in each secondary heading relative to LAMP compared to SimpleCode. Aside from the sunk cost of training, the generation of additional LSTM realizations is a minimal computational cost in addition to SimpleCode and is still much faster than generating ensembles of LAMP runs.

Table 2 provides a more in-depth look at the absolute error percentage of the standard deviation estimation of SimpleCode and the LSTM compared to LAMP.

Table 2: Comparison of absolute error percentage between SimpleCode (SC), the LSTM, and LAMP across the three examined degrees of freedom and 12 secondary headings.

DOF	β_s [deg]	SC	LSTM
Heave	0	1.165	0.008
	30	1.203	0.012
	60	1.296	0.011
	90	1.455	0.006
	120	1.404	0.006
	150	1.244	0.013
	180	1.183	0.008
	210	1.245	0.011
	240	1.377	0.011
	270	1.497	0.007
	300	1.341	0.002
	330	1.286	0.017
Roll	0	0.520	0.028
	30	0.544	0.009
	60	0.490	0.026
	90	0.404	0.039
	120	0.470	0.036
	150	0.528	0.035
	180	0.531	0.026
	210	0.524	0.033
	240	0.463	0.017
	270	0.379	0.016
	300	0.486	0.006
	330	0.533	0.025
Pitch	0	0.803	0.022
	30	0.709	0.005
	60	0.664	0.016
	90	0.587	0.023
	120	0.734	0.019
	150	0.732	0.020
	180	0.747	0.031
	210	0.753	0.016
	240	0.689	0.007
	270	0.637	0.011
	300	0.654	0.002
	330	0.787	0.019

The estimation of the heave, roll, and pitch standard deviations by the LSTM network greatly improve compared to SimpleCode. The largest error in standard deviation estimation by the LSTM framework is less than 4%, while many of the errors by SimpleCode exceed 50%, with the *lowest* error is about 38%. However, it is known that SimpleCode generally does not capture the quantitative nature of LAMP, but can generally reproduce the results in a qualitative respect. One such measure would be identifying large motions, or peaks. The following section investigates peak distribution and the time series behavior near large peaks.

Peak Comparison

In Howard et. al (2022), the peaks generated by the LSTM were underpredicting the corresponding peaks in LAMP. With additional data and different training techniques, the gap between LAMP and the LSTM has reduced. To examine the peak behavior, the maximum values between mean up-crossings were used. A mean up-crossing is defined as when a time series changes from less than the mean value to more than the mean value. Figure 5 illustrates a number of up-crossing points and the corresponding maximum values that would be considered peaks.

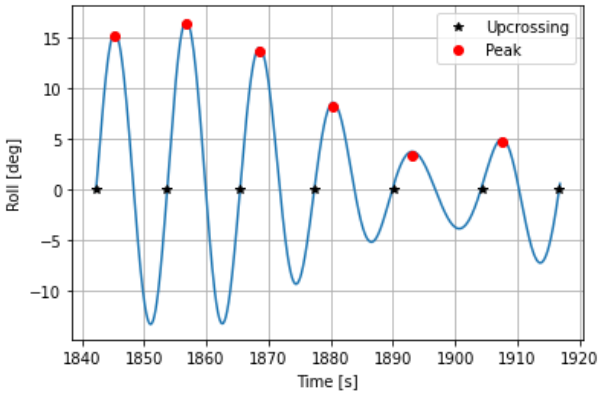

Figure 5: Example of roll up-crossings and the peak values that are considered for this study.

To compare the peak behavior between LAMP, SimpleCode, and the LSTM, the peaks between mean up-crossings were gathered from each of the test time series. Figures 6,7 and 8 show the pdfs of the peaks between mean up-crossings for heave, roll, and pitch generated by SimpleCode, LAMP, and the LSTM. The pdfs shown for each degree of freedom are from the secondary heading that resulted in the largest average standard deviation.

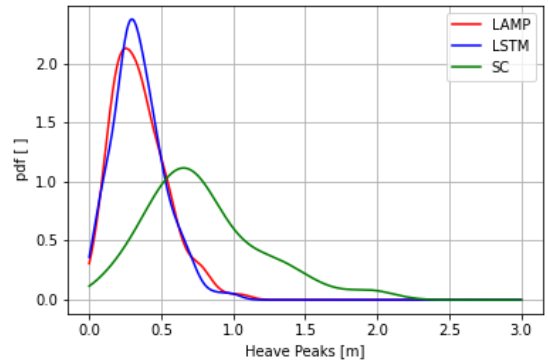

Figure 6: Comparison of heave up-crossing peak pdf for a secondary heading of 0° between LAMP, the LSTM, and SimpleCode.

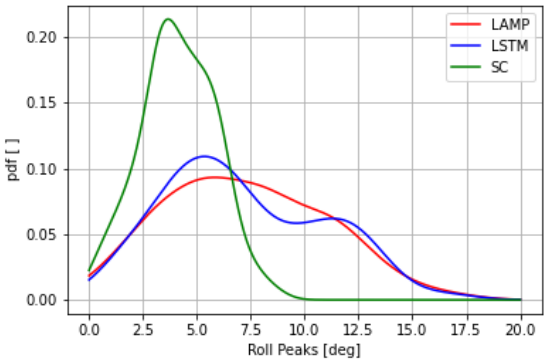

Figure 7: Comparison of roll up-crossing peak pdf for a secondary heading of 300° between LAMP, the LSTM, and SimpleCode.

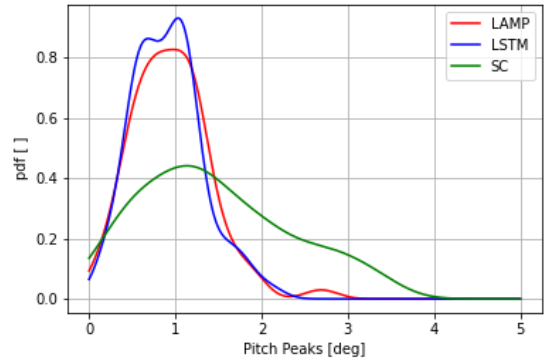

Figure 8: Comparison of pitch up-crossing peak pdf for a secondary heading of 90° between LAMP, the LSTM, and SimpleCode.

The estimation of the peak pdf for each degree of freedom is greatly improved by applying the LSTM network to the SimpleCode results. Furthermore, the reproduction near the tails of the distribution appear to follow similar behavior compared to LAMP. Of course, these pdfs were only drawn from five realizations containing a total of 130-160 peaks depending on secondary heading, degree of freedom, and realization. An increased number of peaks is needed to further examine tail behavior.

Another metric for comparison of peak PDFs known as the match distance (MD) is applied, where

$$MD = \frac{1}{N}\sum_{x=1}^{N} F_L(x) - F_E(x) \tag{9}$$

The match distance is the average difference between the cumulative density function (cdf) of the peaks generated by the higher fidelity tool, $F_L(x)$, and the lower fidelity tools, $F_E(x)$, over the number of queried points, N. Table 3 provides the match distance between the peaks pdfs from each degree of freedom and secondary heading.

Table 3: Comparison of match distance between SimpleCode (SC), the LSTM, and LAMP across the three examined degrees of freedom and 12 secondary headings.

DOF	β_s [deg]	SC	LSTM
Heave	0	0.104	0.003
	30	0.114	0.001
	60	0.135	0.002
	90	0.159	0.006
	120	0.129	0.003
	150	0.138	0.001
	180	0.130	0.001
	210	0.130	0.001
	240	0.114	0.002
	270	0.154	0.003
	300	0.129	0.007
	330	0.143	0.002
Roll	0	0.167	0.017
	30	0.177	0.015
	60	0.183	0.018
	90	0.162	0.015
	120	0.143	0.027
	150	0.149	0.021
	180	0.194	0.024
	210	0.176	0.017
	240	0.145	0.020
	270	0.129	0.013
	300	0.156	0.016
	330	0.175	0.024
Pitch	0	0.113	0.003
	30	0.105	0.008
	60	0.105	0.004
	90	0.102	0.007
	120	0.106	0.007
	150	0.135	0.005
	180	0.111	0.003
	210	0.116	0.003
	240	0.128	0.007
	270	0.079	0.002
	300	0.068	0.004
	330	0.130	0.004

For the behavior near large peaks, Figures 9, 10, and 11 show the ship response near the largest LAMP heave, roll, and pitch responses in the test dataset along with the corresponding LSTM and SimpleCode time series. These largest peaks identified in the dataset are characterized as "rare events".

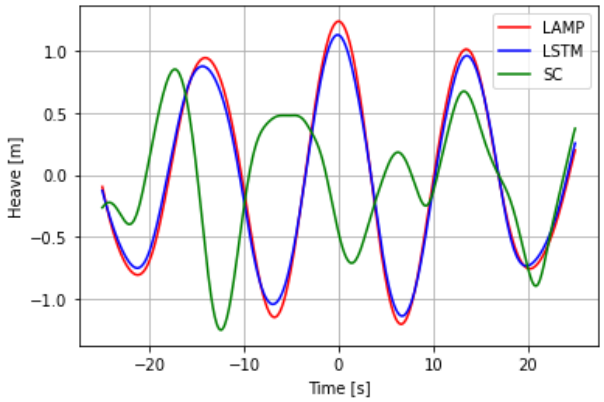

Figure 9: Comparison of heave time series at the largest LAMP heave event which occurred at a secondary heading of 120°.

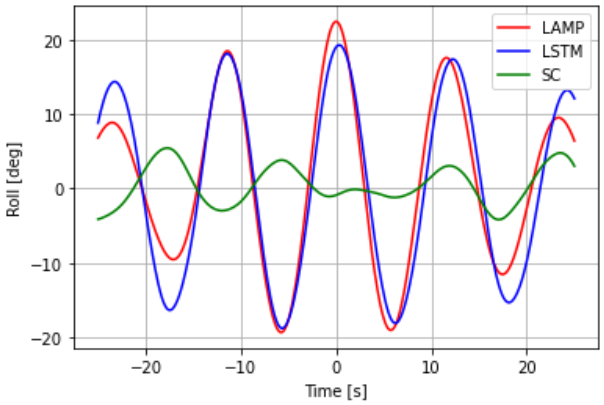

Figure 10: Comparison of roll time series at the largest LAMP roll event which occurred at a secondary heading of 180°.

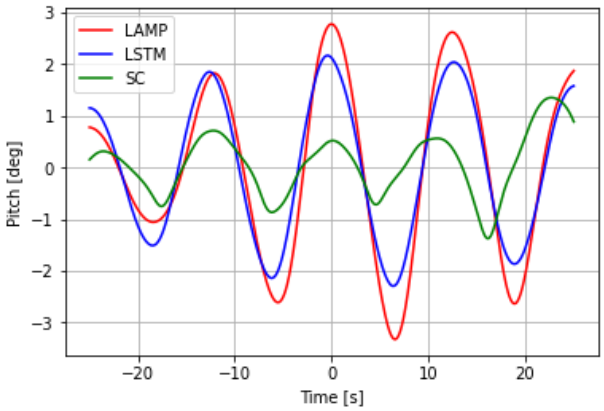

Figure 11: Comparison of pitch time series at the largest LAMP pitch event which occurred at a secondary heading of 180°.

Relative to LAMP, the LSTM network provided a noted improvement compared to SimpleCode in both the phase relationship and magnitude of the largest peaks at time t = 0 s. However, some difference is observed. A larger amount of training data would likely further strenghten the results.

4. CONCLUSION

In this paper, a method to correct low-fidelity 6-DOF ship response time series to the level of higher-fidelity 6-DOF time series was examined. An LSTM network was trained to correct 6-DOF SimpleCode time series to achieve operational guidance statistics and peak distributions on the level with those from LAMP across a range of secondary wave headings.

One major assumption made in this study was having the wave elevation at the ship's center of gravity as determined by LAMP. This input could not be provided without the accompanying LAMP simulations. However, by introducing this framework, it decouples the problem of the differing geospatial locations of LAMP and SimpleCode. An additional network could be trained to estimate the path of the simulated ship as determined by LAMP given the planned path and the wave field so that the wave elevation of the ship's center of gravity as determined by LAMP could be estimated.

The LSTM-based approach demonstrated significant improvement relative to SimpleCode. The largest error in standard deviation for LSTM was less than 4%, while many of the errors by SimpleCode exceeded 50%, with smallest error of approximately 38%.

Furthermore, the LSTM approach appears to be able to predict peak behavior. The overall peak distribution and time series behavior near peaks improved as compared to a previous study by Howard et. al. (2022). Increasing the size of the training dataset could help further improve the performance of LSTM for peak prediction.

Future work could include expanding the parameter space to enhance robustness and utility of the framework. A more comprehesnsive approach could incorporate other ship response types including structural loads and accelerations. Employment of larger training sets has the potential to increase fidelity of predictions of extreme motions associated with the tail of the distribution.

REFERENCES

Hochreiter, S., and Schmidhuber, J., "Long Short-Term Memory," *Neural Computation*, Vol. 9, No. 11, 1997, pp. 1735–1780.

Howard, D., Edwards, S.J., Levine, M.D., Sapsis, T., Weems, K., and Pipiras, V. "A Method for Operational Guidance in Bimodal Seas," Proceedings of the 18th International Ship Stability Workshop, Gdansk, Poland, 2022.

IMO, "MSC.1/Circ. 1627 - Interim Guidelines on the Second Generation Intact Stability Criteria," Maritime Safety Committee, International Maritime Organization, London, 2020.

IMO, "MSC.1/Circ. 1228 - Revised Guidance to the Master for Avoiding Dangerous Situations in Adverse Weather and Sea Conditions" Maritime Safety Committee, International Maritime Organization, London, 2007.

IMO, "MSC/Circ. 707 - Guidance to the Master for Avoiding Dangerous Situations in Following and Quartering Seas" Maritime Safety Committee, International Maritime Organization, London, 1995.

ITTC, "The Specialist Committee on Waves – Final Report and Recommendations for the 23rd ITTC," Proceedings of the 23rd International Towing Tank Conference, Venice, Italy, 2002.

Lin, W.-M., Collette, M., Lavis, D., Jessup, S., & Kuhn, J., "Recent Hydrodynamic Tool Development and Validation for Motions and Slam Loads on Ocean-Going High-Speed Vessels", Practical Design of Ships and Offshore Structures (PRADS) 2007.

Moelgaard, A. "PMM-tests with a model of a frigate class DDG-51," DMI 2000071, Report No. 1, 2000.

NATO, "Standardized Wave and Wind Environments and Shipboard Reporting of Sea Conditions," NATO Standardization Agreement, STANAG 4194, North Atlantic Treaty Organization, Brussels, Belgium, 1983.

Pipiras, P., Howard, D., Belenky, V., Weems, K., and Sapsis, T., "Multi-Fidelity Uncertainty Quantification and Reduced-Order Modeling for Extreme Ship Motions and Loads", Proceedings of the 34th Symposium of Naval Hydrodynamics, Washington, D.C., 2022.

Shin, Y. S., Belenky, V., Lin, W. M., and Weems, K. M., "Nonlinear Time Domain Simulation Technology for Seakeeping and Wave-Load Analysis for Modern Ship Design," *SNAME Transactions*, Vol. 111, pp. 557–578, 2003.

Smith, T. C., "Validation Approach for Statistical Extrapolation," Chapter 34 of *Contemporary Ideas on Ship Stability, Risk of Capsizing*, Belenky, V., Neves, M., Spyrou, K., Umeda, N., van Walree, F., eds., Springer, ISBN 978-3-030-00514-6, pp. 573- 589, 2019.

Weems, K, and V. Belenky, "Extended Fast Ship Motion Simulations for Stability Failures in Irregular Seas," Proceedings of the 13th International Conference on Stability of Ships and Ocean Vehicles, Kobe, Japan, 2018.

Weems, K. M., and Wundrow, D., "Hybrid Models for the Fast Time-Domain Simulation of Stability Failures in Irregular

Waves with Volume based Calculations for Froude-Krylov and Hydrostatic Forces," Proceedings of the 13th International Ship Stability Workshop, Brest, France, 2013.

Yano, T., Hirayama, K., Baba, M., & Sakai, M. "Wave radar application to the simplified parametric roll operational guidance at actual sea," Proceedings of the 17th International Ship Stability Conference, Helsinki, Finland, 2019

Errors induced by wind fluctuations during inclining test

Jean-François Leguen, *DGA Techniques Hydrodynamiques*, jean-francois.leguen@intradef.gouv.fr
Jean-Yves Billard, *Ecole navale*, jean-yves.billard@ecole-navale.fr
François Grinnaert, *Ecole Nationale Supérieure Maritime, IRENav*, francois.grinnaert@supmaritime.fr

ABSTRACT

In the present work the effect of wind fluctuations during an inclining test are investigated. For a given accuracy chosen by the surveyor, a maximum value of the mean wind is calculated. Moreover, the interest of an alternative method to determine *KG* value is proved to be efficient to allow a larger wind speed during the experiment.

Keywords: *Inclining test, Wind fluctuation, Metacentric Height, Cross Curves*

1. INTRODUCTION

Different authors have described the traditional inclining test (IT) as early as the XVII and XVIII centuries (Hoste, 1697, Bouguer, 1746) with a hypothesis concerning the position of the metacentre or the linearity of the stability curve for small heel angles. The goal of this experiment consists in the determination of the vertical position of the ship's centre of gravity. The previously mentioned hypothesis has been raised recently in various papers (Dunworth, 2015, Karolius & Vassalos, 2018a, Karolius & Vassalos, 2018b, Ozayan & Taylan, 2019, Taylan, 2020) leading to a better accuracy in the determination of the vertical position of the centre of gravity (*KG*) thanks to alternative methods.

Nevertheless, numerous parameters, listed in table 1, are necessary to determine hydrostatic data and ship's displacement. These data are degraded by inaccuracies that have been analysed by many authors (Woodward, et al., 2016, Wilczynski, et al., 1998, Grinnaert, et al., 2015, Grinnaert & Billard, 2021). At our knowledge in these studies the wind gust effect has not been taken into account but by a requirement that the mean wind does not be greater than 10 kts (IACS 2004, ITTC 2012) during the experiment regardless of the ship displacement or windage. That will be the scope of this paper.

The evaluation of the *KG* is usually the result of 8 measurements of inclining angles realized by movement of weight *w* over a transverse distance *y*. A linear regression is then performed using, for example, the method described by Dunworth (2015) to avoid effects of non-linearity of the ship's stability curve that have been studied previously (Leguen, et al., 2023).

If the mean wind value has no effect on the result of the IT and can be easily accounted for, variations of wind during the set of measurements introduce a new source of error and the goal of this paper is an analyse of the wind gust effect for a mean wind supposed to be only in the transverse direction. For that purpose, we will first use bibliographical information to obtain the gust effect that must be associated with a given mean wind speed. Second, we will use a previously determined value of the maximum mean wind speed that can be sustained to respect a given accuracy[1] on the position of the ship's vertical centre of gravity. And finally we will propose a validation of the results by Monte Carlo simulations of a large set of experiments.

Table 1: Parameters required in the determination of KG

Geometrical parameters	
∇ [m^3]	Displacement volume
KN [m]	Cross curves
KM [m]	Vertical position of transverse metacentre
Experiment parameters	
w [N]	Weight used for the experiment
y [m]	Distance of weight displacement
φ_{weight} [rad]	Heel angle associated with weight displacement
τ [s]	Duration of measure
Physical parameters	
g [m.s^{-2}]	Acceleration due to gravity

[1] Accuracy can be imposed by different actors and taken into account by our procedure.

ρ_{air} [kg.m^{-3}]	Mass density of air
ρ_{water} [kg.m^{-3}]	Mass density of seawater
Wind parameters	
V [m.s^{-1}]	Nominal transverse wind speed during experiment (averaged on 10 minutes at 10 metres high)
σ [-]	Standard deviation of wind due to gusts
φ_{wind} [rad]	Added heel angle due to wind effect
A [m^2]	Area of windage
Z [m]	Inclining lever of wind
C_y [-]	Drag coefficient of transverse wind

2. WIND CHARACTERISTICS DURING THE INCLINING TEST

This part is based on Durst's work (1960) who studied wind characteristics of hurricanes. His data have been re analysed by Krayer & Marshall (1992) and then by Vickery & Skerlj (2005). They show that for mean winds used in these analyses (from 15 to 50 kts) the wind is supposed to be gaussian with a standard deviation that is proportional to the mean value of the wind speed. As far as these data have been used by IMO for the establishment of the weather criterion (see for example IMO, 2008), it has seemed logical for us to use the same set of data to develop our analysis of the uncertainty introduced by wind during an IT.

It is assumed that wind characteristics remain stationary during the measurement, which has been performed for a duration of one hour. For shorter durations, it is possible to estimate the standard deviation by use of Vickery's data presented in Table 2. These data can be approximated using a linear regression shown in Figure 1.

Table 2: Excerpt of table 1 in [15]

τ [s]	σ [-]	Gust factor [-]
600	0.065	1.09
60	0.115	1.24
30	0.132	1.32
10	0.15	1.42
5	0.159	1.48

These data are dimensionless and can be approximated by the relation:

$$\sigma = 0.1966 - 0.02 \ln(\tau) \quad (1)$$

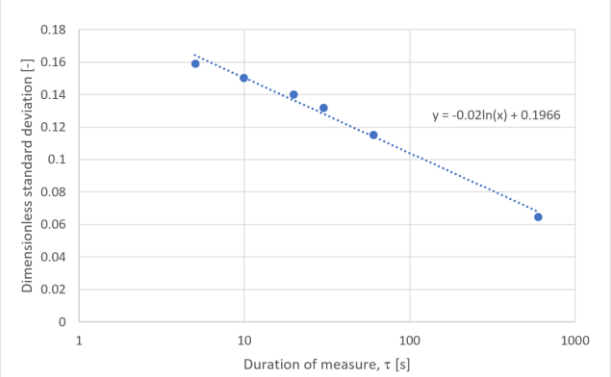

Figure 1: Standard deviation of wind versus measure duration

The original paper mentioned wind speeds encountered in storms, but the experimental data used show that this law remains valid for lower wind speeds. Davenport's studies (summarised by Isyumov, 2012) used in MSC.1/Circ. 1627 (IMO, 2020) describing the spectral representation of wind speed also show that the standard deviation of wind variations during gusts is constant with wind speed (if we keep the same definition of mean wind speed). The comparison of standard deviations from Durst or Davenport results show a maximum difference less than 2%.

3. WIND SPEED LIMIT GIVEN BY INCLINING ANGLE AND REQUIRED PRECISION

To avoid difficulties associated with the non-linearity of the *GZ* curve the speed limit has been determined on *GM* from a choice of both the maximum angle imposed during IT and the required precision on the result. As far as wind effects do not affect the hydrostatics (in other words, the influence of gust wind on draft measurements is neglected), the uncertainty due to the wind effect is the same on the *GM* or *KG*. In the present work, the position of the transverse metacentre is slightly perturbed by non-linearity and, after validation, we will verify that this perturbation remains of small amplitude compared to the required precision. This will be the goal of the Monte Carlo simulations. Some cases presented by Leguen, et al. (2023) showed more influence of the non-linearities (traditional or alternative post-treatment of the IT gave different results) but the effect of the gust wind on uncertainties is similar.

Assuming a linear *GZ* up to an angle φ, the sum of the angle due to weight displacement, φ_{weight},

required by the experiment and the angle due to the wind effect, φ_{wind}, the value of *GM* is given by:

$$GM = \frac{wy + \frac{1}{2}\rho_{air} S V^2 Z C_y}{\rho_{water} g \nabla \varphi} \quad (2)$$

Here, *V* denotes the mean value of the wind speed during one measurement of the IT, assumed to have a duration of 10 natural roll periods.

The angle due to wind effect can be evaluated by the relation:

$$\frac{1}{2}\rho_{air} S V^2 Z C_y = \rho_{water} g \nabla GM \varphi_{wind} \quad (3)$$

Where the inclining and righting effects are equated. With the hypothesis that the only term to be uncertain is the wind, the derivative of (2) gives (details of the calculation are given in appendix):

$$dGM_{wind} = \frac{\rho_{air} S V Z C_y}{\rho_{water} g \nabla \varphi} dV \quad (4)$$

Leading to:

$$\frac{dGM_{wind}}{GM} = 2 \frac{\varphi_{wind}}{\varphi_{wind} + \varphi_{weight}} \frac{dV}{V} \quad (5)$$

The value of dGM_{wind} must be lower than the maximum allowed value, $dGM_{wind.max}$, set by the surveyor. Thus, this relation allows the determination of the maximum wind speed that fulfil the requirements first on φ_{wind}:

$$\varphi_{wind} \leq \frac{1}{2\frac{\lambda}{\delta} - 1} \varphi_{weight} \quad (6)$$

Where δ denotes the dimensionless value of the maximum error on *GM*:

$$\delta = \frac{dGM_{wind.max}}{GM} \quad (7)$$

Replacing φ_{wind} by its value determined by (3) leads to:

$$V \leq \sqrt{\frac{GM}{2\frac{\lambda}{\delta} - 1} \frac{2\rho_{water} g \nabla}{\rho_{air} S Z C_y} \varphi_{weight}} \quad (8)$$

Where λ is the wind relative uncertainty:

$$\lambda = \frac{dV}{V} \quad (9)$$

The value of λ is chosen as equal to twice the wind standard deviation to fulfil the requirement on the precision of δ in 95% of the cases.

4. MONTE CARLO RESULTS

The analytical study with linear *GZ* presented in Section 3 is extended by a numerical study of the IT with non-linear *GZ* throughout a Monte Carlo approach. Ships are modelled using a stability software, Calcoque, presented by Grinnaert, et al. (2015). The results given by the code are only degraded by numerical errors and will be referred as "actual". A large number of IT (N = 10000) will be simulated using the same ship characteristics. However, the 8 measurements included in one IT are obtained with a different wind of same mean value but with a gaussian distribution of standard deviation σ around the mean value. The same procedure is repeated *N* times given rise to *N* values of *KGi*. The mean value of *KG* is very closed to the exact value and the distribution of the *KGi* is very closed to a Gaussian distribution. We verify that with the wind *V* determined by (8) the required value of δ is correctly evaluated in 95% of the cases. The *KN* value required to follow the procedure is determined from a *GZ* curve of the ship computed in the vicinity of the loading condition of the IT by the addition of $KG.sin\varphi$ to avoid a modification of the ship's trim and the corresponding additional error. For some other ships with a more complex flotation surface, the use of an iterative hydrostatic with Calcoque remains possible in order to take into account the actual position of the centre of gravity.

The results of the Monte Carlo procedure are presented in Figure 2 for a polar patrol vessel. The blue dots represent the histogram of the 10000 values of *KG* resulting from 10000 IT. The red cross represents the results of the Monte Carlo process. The green cross represents the actual value of the *KG* set in the hydrostatic simulator. The vertical bar represents the value of *KG* (actual in green and estimated by the mean of 10000 IT in red). The horizontal bar represents the requirement δ in green and 2 times the standard deviation of the 10000 values of *KG* in red.

It can be seen that the accuracy is slightly lower than expected (16.2 mm vs. 15 mm) with a probability of success (accuracy in the requirement) a little lower than 95%, but the differences are small enough to be acceptable.

The same computations have been realized for different French Navy ships. Half of them are following a civilian regulation. The results are presented in table 3. It can be seen from the results that:

- The acceptable wind is mostly lower than the 10 knots generally allowed for an IT
- The angle of inclination must be larger to allow a larger mean wind value without a significant loss of accuracy;
- The level of confidence of a single IT is of about 93 %, slightly lower than the 95 % expected for the determination of the maximum wind value.

5. CONCLUSION

The proposed methodology provides a maximum wind speed for an inclining test, taking into account the characteristics of the ship and a targeted accuracy on the resulting value of *KG*.

It shows that the resulting acceptable wind speed is lower than 10 kts, which value is generally set as maximum allowed speed in the IT procedures. It also shows the resulting acceptable wind speed can vary largely from a ship to another, depending on her characteristics.

The effectiveness of alternative methods of the IT greatly improves the accuracy of measurements. This study also points out that, due to the possibility of increased imposed heeling lever, such methods allow a wind speed to be more severe than the one required by the traditional method for an equivalent accuracy.

6. PERSPECTIVES

Using other Davenport's parameters of the spectrum will allow other effects, such as the nature of the environment of the place of the experience and the wind profile in relation with the windage of the ship.

In order to have the total uncertainty of an inclining test, the Monte Carlo methodology used in this paper could be generalised to other effects such as the uncertainty associated with draft measurements, hydrostatics errors induced by geometry or the uncertainty due to hull deformation.

REFERENCES

Bouguer, P., 1746, Traité du navire, de sa construction et de ses mouvements, Paris : Jombert.

Dunworth, R., 2015, Beyond the wall, Proceedings of STAB2015 14-19 June, Glasgow, United Kingdom.

Durst, C. S., 1960, Wind speeds over short periods of time, The meteorological magazine, Vol 89, pp 181-186.

Grinnaert F., Billard J.-Y., Laurens J.-M., 2015, Calcoque: a fully 3D Ship Hydrostatic Solver. Proceedings of the 12th International Conference on the Stability of Ships and Ocean Vehicles, Glasgow, UK.

Grinnaert, F., Billard, J.-Y., 2021, Towards a Better Accuracy in the Draught Survey, Proceedings of the 1st International Conference on the Stability and Safety of Ships and Ocean Vehicles, 7-11 June 2021, Glasgow, Scotland, UK.

Hoste, P., 1697, Théorie de la construction des vaisseaux, Lyon : Anisson & Posuel.

IACS REC-31, 2004, Inclining test unified procedure

International Maritime Organization, 2008, MSC.1/Circ.1281, Explanatory notes to the international code on Intact Stability, 2008.

International Maritime Organization, 2008, Res. MSC.267(85). Adoption of the International Code on Intact Stability, 2008 (2008 IS CODE).

International Maritime Organization, 2020, MSC.1/Circ.1627. Interim Guidelines on the Second Generation Intact Stability Criteria

Isyumov N., 2012, Alan G. Davenport's mark on wind engineering, Journal of Wind Engineering and Industrial Aerodynamics, Vol. 104–106, May–July 2012, pp 12-24

ITTC Procedure 7.5-02-07-04.7, 2012, Inclining test

Karolius, K.B., Vassalos, D., 2018, Second generation calculation method for use in the inclining test, Proceedings of STAB2018 16-21 September, Kobe, Japan.

Karolius K.B. and Vassalos, D., 2018, Tearing down the wall – The inclining experiment, Ocean Engineering, Vol 148, pp 442-475.

Krayer, W. R., and Marshall, R. D., 1992, Gust factor applied to hurricane winds, Bulletin of American Meteorological Society, Vol 73, n° 5, pp 613-617.

Leguen, J-F., Billard, J-Y., Grinnaert, F., Analyse des erreurs liées au vent lors d'une expérience de stabilité, ATMA, 2023, Paris, France.

Ozayan, S., and Taylan, M., 2019, Another blow on the torn down wall – The inclining experiment, Brodogradnja, Vol 70, n°2, pp 135-153.

Taylan, M., 2020, Reliability analysis of GM and KG of ships from the inclining experiment, Journal of Engineering for the Maritime Environment, Proc IMechE part M, pp 1-7.

Vickery, P. J., and Skerlj, P. F., 2005, Hurricane gust factors revisited, Journal of Structural Engineering, Vol 131, n° 5, pp 825-832.

Wilczynski, V., Knowles, P. H., Diehl, W. J., 1998, Uncertainty

analysis of a vessel's metacentric height, Proceedings of the probabilistic safety assessment and management conference, New York.

Woodward; M.D., Rijsbergen, M.V., Hutchinson, K.W. and Scott, A., 2016, Uncertainty analysis procedure for the ship inclining experiment, Ocean Engineering, Vol 114, pp 79-86.

Table 3: Monte Carlo results for a set of naval vessels

		φ_{weight}=1°, δKG=10mm, N=10000				φ_{weight}=4°, δKG=10mm, N=10000			
Vessel	KG (exact) [m]	KG (estim) [m]	2σ	% of KGi	V_{wind} [ms^{-1}]	KG (estim) [m]	2σ	% of KGi	V_{wind} [ms^{-1}]
Polar patrol vessel	6.367	6.367	10.68	93.5	3.9	6.367	10.74	93.4	6.7
Training ship	3.1	3.1	10.65	93.6	2.81	3.1	10.65	93.5	5.62
Mine hunter	3.84	3.84	10.83	93.1	4.8	3.84	10.9	92.9	9.6
Service boat	1.954	1.954	10.01	95.07	3.2	1.954	9.07	97.02	6.1
Helicopter carrier	9.00	9.0	10.67	93.52	3.33	9	10.73	93.4	6.67
76-m Frigate	4.44	4.44	10.84	93.02	3.07	4.44	10.78	93.2	6.1
129-m Frigate	6.04	6.037	10.81	93.2	2.9	6.037	10.71	93.4	5.8
Scientific vessel	6.70	6.70	10.74	93.4	2.55	6.7	10.74	93.4	4.83
Large naval vessel #1	12.34	12.34	10.45	94.1	0.85	12.34	10.26	94.55	2.48
Large naval vessel #2	14.03	14.03	10.6	93.7	3.6	14.03	10.7	93.32	7.3

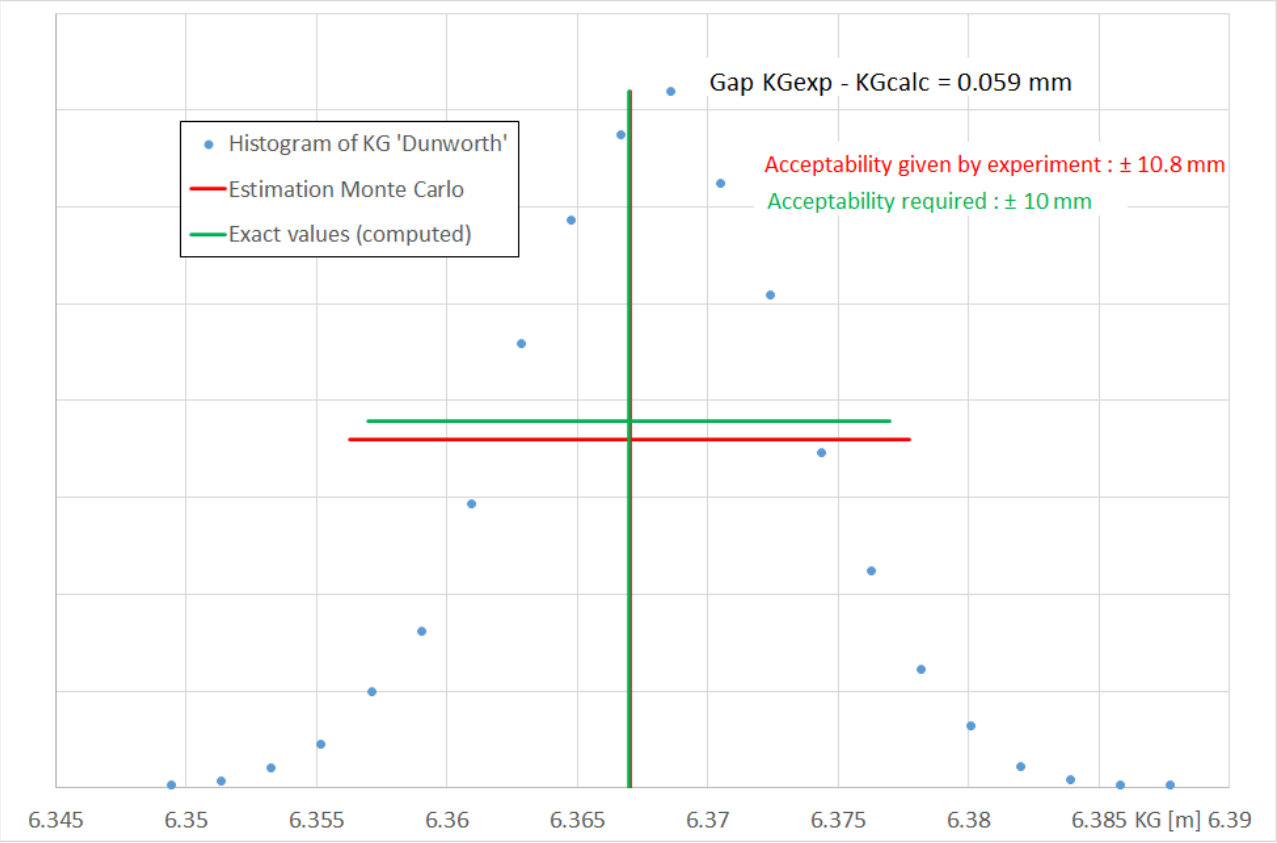

Figure 2: Monte Carlo results for the Polar Patrol Vessel

APPENDIX

$$GM \sim \frac{w.y.g + \frac{1}{2}\rho_{air}.S.V^2.Z.C_y}{\rho_{water}.g.\nabla.\varphi}$$

By differentiating this relationship with respect to the measured parameters, the expression of the uncertainty associated with each one can be determined analytically:

$$dGM \sim \frac{d\left[w.y.g + \frac{1}{2}\rho_{air}.S.V^2.Z.C_y\right]\rho_{water}.g.\nabla.\varphi - \left(w.y.g + \frac{1}{2}\rho_{air}.S.V^2.Z.C_y\right).d[g.\rho_{water}.\nabla.\varphi]}{{\rho_{water}}^2.g^2.\nabla^2.\varphi^2}$$

$$dGM \sim \frac{1}{{\rho_{water}}^2.g^2.\nabla^2.\varphi^2}.\left(\left(d[w.y.g] + \frac{1}{2}d\left[\rho_{air}.S.V^2.Z.C_y\right]\right)\rho_{water}.g.\nabla.\varphi - \left(w.y.g + \frac{1}{2}\rho_{air}.S.V^2.Z.C_y\right).g.(\rho_{water}.\nabla.d[\varphi] + \rho_{water}.\varphi.d[\nabla] + \nabla.\varphi.d[\rho_{water}])\right)$$

$$dGM \sim \frac{1}{{\rho_{water}}^2.g^2.\nabla^2.\varphi^2}.\left(\left(g.y.d[w] + g.w.d[y] + \frac{S.V^2.Z.C_y}{2}.d[\rho_{air}] + S.\rho_{air}.V.Z.C_y.d[V] + \frac{\rho_{air}.V^2.Z.C_y}{2}.d[S] + \frac{\rho_{air}.S.V^2.C_y}{2}.d[a] + \frac{\rho_{air}.S.V^2.Z}{2}.d\left[C_y\right]\right)\rho_{water}.g.\nabla.\varphi - \left(w.y.g + \frac{1}{2}\rho_{air}.S.V^2.Z.C_y\right).g.(\rho_{water}.\nabla.d[\varphi] + \rho_{water}.\varphi.d[\nabla] + \nabla.\varphi.d[\rho_{water}])\right)$$

This paper takes only into account the term depending on the uncertainty due to the wind speed:

$$dGM_{wind} \sim \frac{1}{{\rho_{water}}^2.g^2.\nabla^2.\varphi^2}.\left(\rho_{water}.g.\nabla.\varphi\left(S.\rho_{air}.V.Z.C_y.d[V]\right)\right)$$

$$dGM_{wind} \sim \frac{S.\rho_{air}.V.Z.C_y.\rho_{water}.g.\nabla.\varphi.d[V]}{{\rho_{water}}^2.g^2.\nabla^2.\varphi^2}$$

$$dGM_{wind} \sim \frac{S.\rho_{air}.V.Z.C_y}{\rho_{water}.g.\nabla.\varphi}d[V]$$

$$dGM_{wind} \sim \frac{\rho_{air}}{\rho_{water}}.\frac{S.V.Z.C_y}{\mathrm{g}.\nabla.\varphi}d[V]$$

Recent results on wind and wave generation, stability of parametric rolling, method of moment equation and maneuvering stability for ship dynamics in irregular seas

Atsuo Maki, *Osaka University,* maki@naoe.eng.osaka-u.ac.jp
Yuuki Maruyama, *Osaka University,* yuuki_maruyama@naoe.eng.osaka-u.ac.jp
Masahiro Sakai, *Osaka University,* sakai@naoe.eng.osaka-u.ac.jp
Leo Dostal, *Hamburg University of Technology,* dostal@tuth.de

ABSTRACT

This paper addresses the recent progress in wave generation, stability of parametric rolling, moment method for ship dynamics, and maneuvering stability in irregular seas. In the estimation of the ship motion in irregular seas by the theory of stochastic process, the system must be represented by SDE (Stochastic Differential Equation). Therefore, first, the authors introduce the research to generate the time history of wind and waves in SDE is presented. Second, the authors introduce the research to analytically estimate wave conditions that cause parametric rolling by the method of Arnold-Dostal. Third, the authors introduce the research to estimate the parametric rolling with the use of the Moment method. Finally, the authors introduce a study on the stochastic stability of ship maneuvering systems under random disturbance from the aspect of the theory of Lyapunov stability.

Keywords: *Theory of Stochastic Process; Parametric Rolling; Lyapunov stability.*

1. INTRODUCTION

The theory of stochastic process is a powerful tool to conduct research on ship motion in irregular wind and waves. In this research, the authors introduce the recent research progress on several topics.

In order to analyze the ship motion in a random disturbance with the use of the theory of stochastic process, the wind and wave time histories must be generated by SDE (Stochastic Differential Equation). The pioneering study on these topics can be found in the work of e.g. Spanos (1983 and 1986), Flower and Vijeh (1983 and 1985), Thampi and Niedzwecki (1992). Dostal et al. (2012) is also using a CARMA filter to generate the Grim's effective wave in the form of the SDE. Recently, the authors conducted the work on the wind and wave generation by the SDE, then we proposed the coefficient list of the SDE for the nondimensional wave spectrum (Maki et al., 2023a and 2023b). Therefore, the user can use for any combination of mean wave period T_{01} and significant wave height $H_{1/3}$.

The research history of the estimation of roll motion in irregular seas is long e.g. Price (1964), Haddara (1975), Muhuri (1980), and Roberts (1982a). Particularly, concerning parametric rolling in irregular seas, we can find the pioneering work conducted by Roberts (1982b). In recent five years, the authors have conducted works on the estimation of parametric rolling in irregular seas based on the work of Dostal et al. (2011 and 2012). In this report, the authors introduce the recent work of Maruyama et al. for the estimation of the parametric rolling and the acceleration acting on the container due to parametric rolling with the use of the moment method (Maruyama et al., 2022a and 2023b).

Parametric rolling in irregular seas is triggered off by the loss of the stability of the origin (upright position). This mechanism is almost the same as the parametric rolling in regular seas. Ariaratnam and Tam (1979) presented the pioneering work on this topic, and Roberts (1982b) also applied this approach to the ship's parametric rolling motion. Recently, Dostal et al. (2012) conducted the approach of Lyapunov stability based on Arnold's

approach (Arnold et al., 1986). In this report, the author introduces the recent progress conducted by the authors (Maki et al., 2023b).

The stability of the ship's maneuvering motion was stabilized or destabilized due to random external disturbance (Maki et al., 2023c). The change in the stability of the system can be assessed with the use of the theory of the Lyapunov stability. In this study, the authors introduce the recent research of the authors.

2. WIND GENERATION

The ship maneuverability in low-speed operation is strongly affected by wind. Therefore, it is important to assess the safety of a ship in random wind by numerical simulations. Now, mean wind velocity $\bar{u}$ and direction $\bar{\gamma}$ are given. The variations of wind velocity and direction from $\bar{u}$ and $\bar{\gamma}$ are represented as $\tilde{u}(t)$ and $\tilde{\gamma}(t)$, respectively. In the research of the authors, the systems of $\tilde{u}(t)$ and $\tilde{\gamma}(t)$ were represented by the 1D (dimensional) SDE as follows: 。

$$\begin{cases} \mathrm{d}\tilde{u} = m_u(t,\tilde{u})\mathrm{d}t + \sigma(t,\tilde{u})\mathrm{d}W(t) \\ \mathrm{d}\tilde{\gamma} = m_u(t,\tilde{\gamma})\mathrm{d}t + \sigma(t,\tilde{\gamma})\mathrm{d}W(t) \end{cases} \quad (1)$$

In our recent works (Maki et al. (2022), Maki et al. (2023a)), the coefficients were obtained based on the work of Kuwajima and Kobayashi (1977 and 1979). In our framework, these coefficients can be estimated only from the mean speed $\bar{u}$. The comparative result between the observation and the present theory are shown in Fig.1.

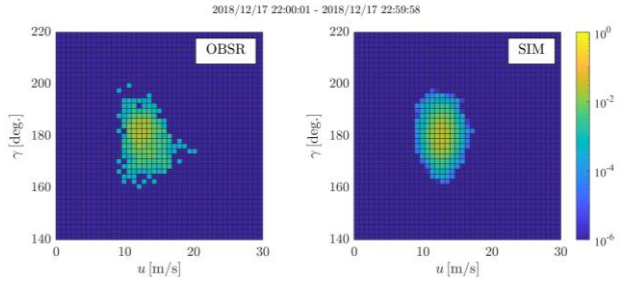

Fig.1 Example of comparison joint PDF of wind direction and speed between the observed data and simulated data.

The left panel in Fig.1 shows the observed joint PDF of wind velocity and direction whereas the right panel does the simulated joint PDF. As can be seen in this plot, both are well correlated. Finally, it was concluded that the time histories of wind velocity and direction can be well estimated by the proposed theory.

3. WAVE GENERATION

In order to numerically calculate the ship motion in waves, it is necessary to generate waves numerically. If a stochastic process is to be used, the generation of waves must also be performed using SDE. In previous studies by Spanos (1983 and 1986), Flower and Vijeh (1983 and 1985), and Thampi and Niedzwecki (1992), Dostal et al. (2012), and Maruyama et al. (2022c). wave generation using the CARMA filter has been investigated. The main scope of these studies was focused on demonstrating the methodology of wave generation itself. On the other hand, the method which is applicable to the arbitral combination of mean wave period T_{01} and significant wave height $H_{1/3}$ has not been proposed. Therefore, the authors used a global optimization method to find the coefficients of the SDEs that fit the nondimensional wave spectrum well (Maki et al., 2023b).

The ITTC spectrum is now used as the wave spectrum, as follows.

$$S_{\mathrm{ITTC}}(\omega) = 172.8\frac{H_{1/3}^2}{T_{01}^4\omega^5}\exp\left(-691.2\frac{1}{T_{01}^4\omega^4}\right) \quad (1)$$

Here, the authors use the following 6D SDE.

$$\begin{aligned} \frac{\mathrm{d}x_1}{\mathrm{d}t} &= x_2 - \alpha_1 x_1 \\ \frac{\mathrm{d}x_2}{\mathrm{d}t} &= x_3 - \alpha_2 x_1 \\ \frac{\mathrm{d}x_3}{\mathrm{d}t} &= x_4 - \alpha_3 x_1 \\ \frac{\mathrm{d}x_4}{\mathrm{d}t} &= x_5 - \alpha_4 x_1 + \Gamma\sqrt{\pi}\frac{\mathrm{d}W(t)}{\mathrm{d}t} \\ \frac{\mathrm{d}x_5}{\mathrm{d}t} &= x_6 - \alpha_5 x_1 \\ \frac{\mathrm{d}x_6}{\mathrm{d}t} &= -\alpha_6 x_1 \end{aligned} \quad (2)$$

The spectrum which corresponds to the above SDE is written as $S_{\mathrm{ITTC}}^{(6,2)}(\omega)$.

We now define a nondimensional ITTC spectrum corresponding to the dimansional ITTC spectrum. Note that the dimensionless frequency $\hat{\omega}$ is used here.

$$\begin{cases} \hat{S}_{\mathrm{ITTC}}(\hat{\omega}) = \dfrac{S_{\mathrm{ITTC}}(\omega)}{H_{1/3}^2 T_{01}} \\ \hat{S}_{\mathrm{ITTC}}^{(6,2)}(\hat{\omega}) = \dfrac{S_{\mathrm{ITTC}}^{(6,2)}(\omega)}{H_{1/3}^2 T_{01}} \\ \hat{\omega} = \omega T_{01} \end{cases} \quad (1)$$

In accordance with this non-dimensionalization, the coefficients of SDE will also be non-dimensionalized as follows:

$$\begin{cases} \hat{\alpha}_0 = 1 \\ \hat{\alpha}_k = \alpha_k T_{01}^k \\ \hat{\Gamma}^2 = \Gamma^2 \dfrac{T_{01}^{4\bar{n}-2m-1}}{H_{1/3}^2} \end{cases} \quad (1)$$

Due to the non-dimensionalization, the obtained coefficients are applicable for arbitrary given the arbitral combination of mean wave period T_{01} and significant wave height $H_{1/3}$. Then, the coefficients of the filter equation described by SDE that fits the given ITTC spectrum were obtained as shown in Table 1.

Table 1 Coefficient list of $\hat{S}_{\mathrm{ITTC}}^{(6,2)}(\hat{\omega})$

item	value	item	value
Γ^2	$7.708 \cdot 10^3$	α_3	$8.231 \cdot 10^2$
α_0	$1.000 \cdot 10^0$	α_4	$6.720 \cdot 10^3$
α_1	$8.739 \cdot 10^0$	α_5	$1.375 \cdot 10^4$
α_2	$1.741 \cdot 10^2$	α_6	$6.010 \cdot 10^4$

Simulation results using the coefficients obtained from the theory of the authors are shown in Fig. 2. This figure shows not only the amplitude of the wave but also the effective wave slove and Grim's effective wave (1961). These were generated simultaneously from the same random source.

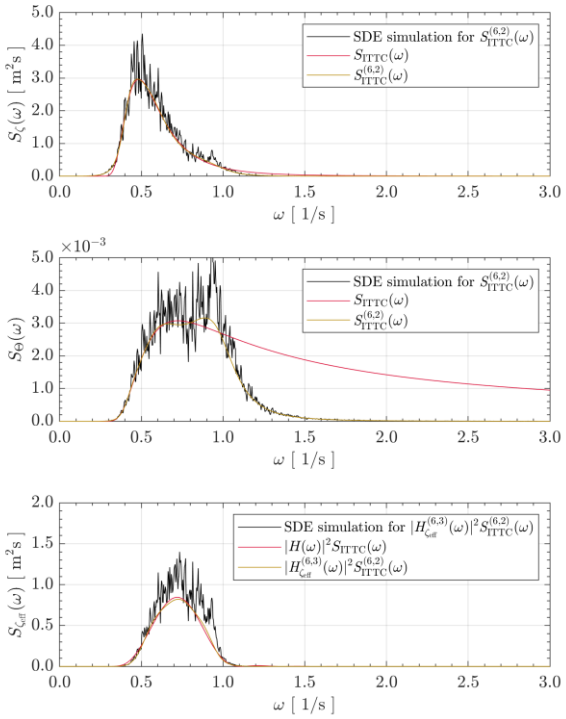

Fig.2 Comparison of wave amplitude, wave slope, and Grim's effective wave spectra.

4. STABILITY OF PARAMETRIC ROLLING

There have been many studies on the stochastic estimation of roll motion due to the parametric rolling using the SDE approach. On the other hand, there have been many attempts to estimate the threshold of wave conditions that trigger off parametric rolling.

Parametric rolling in regular seas is caused by instability of the upright position due to variations in the restoring force. Similarly, parametric rolling in irregular waves is also caused by instability of the right position due to stochastic disturbance. It is known that such stability associations can be estimated using the Lyapunov stability theory.

Here, the authors tackled the following equation of motion. In this equation, $f(t)$ means the restoring variation.

$$\ddot{x}_1(t) + 2\zeta \dot{x}_1(t) + (c_1 + f(t))x_1(t) = 0 \quad (1)$$

In the results of Dostal et al. (2012) based on the work of Arnold et al. (1986), they finally shows the threshold of parametric rolling as follows:

$$-\zeta + \frac{\pi}{4(c_1 - \zeta^2)} S_{f_t f_t}\left(2\sqrt{c_1 - \zeta^2}\right) = 0 \qquad (1)$$

Here, $S_{f_t f_t}(\omega)$ represents the value of $f(t)$ att frequency ω.

This result seems to be very simple but the result well correlates with the numerically obtained result as shown in the work of Maki et al. (2023c). Fig.3 shows the comparison of the boundary of parametric rolling between the results of MCS and theory.

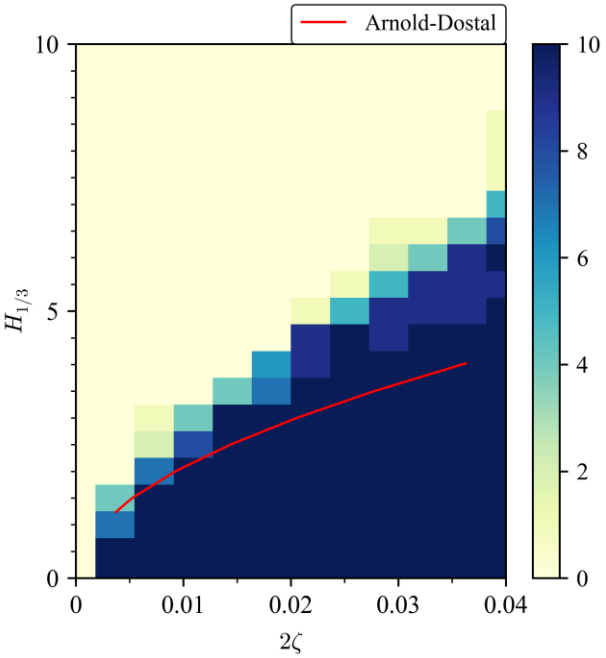

Fig.3 Comparison of the stability diagram between 'Arnold-Dostal's approach and numerical simulation for C11 container ship parameters and forcing due to a ITTC spectrum with mean period $T_{01} = 10$ [s].

5. MOMENT EQUATION

Recently, Maruyama et al. have been extensively conducting analyses using the moment equation. The moment equation is an ordinary differential equation derived from the stochastic differential equation. By solving this equation, the moments of roll angle and roll angular velocity can be obtained. In obtaining the steady-state solution, it is common to set the left-hand side of the moment equation (d/dtE[x]) to zero and solve the simultaneous equations. On the other hand, a method such as that proposed by Maruyama et al. (2022a) can also be used to obtain steady-state moment values. In this method, the moment equations, which are ordinary differential equations, are solved numerically by usual numerical schemes such as the Runge-Kutta method, and the obtained moments at a steady state in the time series are regarded as the steady-state moments obtained from the moment equations. This way of computation prevents computational complexity or instability due to the increase in the number of moment equations.

Also, if the SDE is nonlinear, the moment equation does not become a closed form. Therefore, an infinite number of equations are required. Therefore, it is necessary to truncate the higher-order moments in order to make the moment equations closed. To solve this issue, Maruyama et al. (2022a, 2023b) applied the cumulant neglect closure method. By applying this method, higher-order moments can be expressed in terms of lower-order moments. This method is based on the theory of the relationship between cumulants and moments. As a result, the moment equations are in closed form and moment values can be successfully obtained.

On the other hand, by solving the moment equation numerically, moment values can be obtained, but the probability density function of the roll response is still unknown. Maruyama et al. proposed a method to determine the coefficients in the function by assuming the shape of the probability density function and using the moment value obtained from the moment equation as a constraint condition. This method showed that the probability density function for the angle of rollover can be estimated accurately by using accurate moment values and an appropriate shape of the function as proposed.

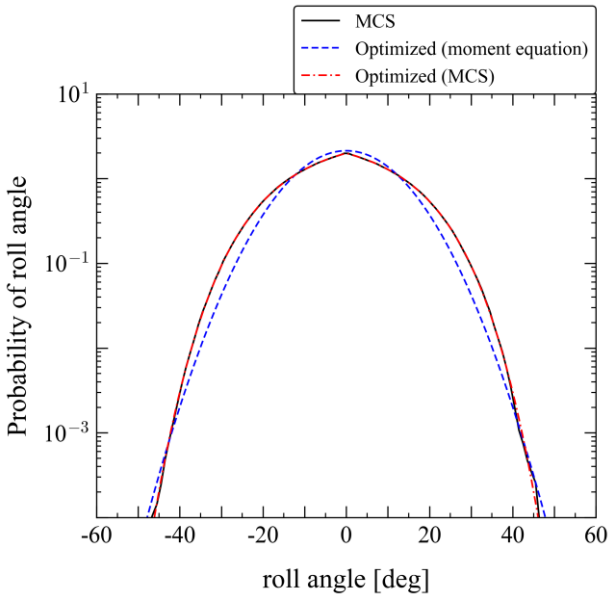

Fig.4 Comparison of the roll angle's PDFs among the MCS result, optimized result by using moment values obtained from solving the moment eqations, and optimized result by using moment values obtained from the MCS result, with Fn=0.0

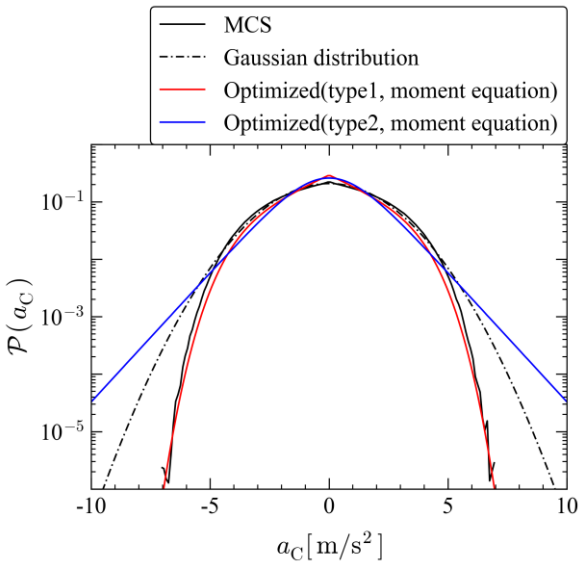

Fig.5 Comparison of the roll angluler acceletarion PDFs among the MCS result, optimized result by using moment values obtained from solving the moment eqations, and optimized result by using moment values obtained from the MCS result, with Fn=0.0

6. MANEUVERING STABILITY

As Tsubokawa et al. (1982) have shown, if irregular disturbance noise are added to a ship's maneuvering motion system, the stability of the ship could change. In the case of regular disturbance noize, the state equation becomes a Mathew-type differential equation, and such a problem has been already analyzed by Spyrou (1997). Adding such disturbance noise may destabilize the maneuvering system, but in some cases it may also stabilize it. Maki et al. (2023d) have recently studied such matters based on the work of Kozin (1971), and the results of their study are presented here.

In this section, the SDE dealt with is as follows:

$$\begin{cases} \mathrm{d}x_1(t) = x_2(t)\mathrm{d}t \\ \mathrm{d}x_2(t) = -\big(2\zeta x_2(t) + c_1 x_1(t)\big)\mathrm{d}t \\ \qquad\qquad +\Gamma x_1(t)\mathrm{d}W(t) \end{cases} \tag{1}$$

Here, $x_1(t)$ measns yaw angle whereas $x_2(t)$ does yaw angular velocity. Then, Maki et al. (2023d) showed that the above system becomes stable if $\mathcal{J} = 0$ is satisfied. Now, $\mathcal{J}$ is defined as:

$$\mathcal{J} = 2C\int_{-\frac{\pi}{2}}^{\frac{\pi}{2}} (\& \cos 2\varphi - \frac{4\zeta}{\Gamma^2}\tan^2\varphi + (1-c_1)\frac{2}{\Gamma^2}\tan\varphi\Big)\eta_\zeta(\varphi)\mathrm{d}\varphi \tag{1}$$

where $\eta_\zeta(\varphi)$ can be defined as:

$$\eta_\zeta(\varphi) = \exp\left[-\frac{2}{3\Gamma^2}\tan\varphi \cdot (3c_1 + 3\zeta\tan\varphi + \tan^2\varphi)\right] \cdot \int_{-\pi/2}^{\varphi} \exp\left[\frac{2}{3\Gamma^2}\tan\theta(3c_1 + 3\zeta\tan\theta + \tan^2\theta)\right]\sec^2\theta\mathrm{d}\theta \tag{1}$$

The results are shown in Fig.6. The left panel is the theoretical result whereas the right panel is the numerical result. As can be seen in these plot, the threshold of the maneuvering stability can be represented by the used theory.

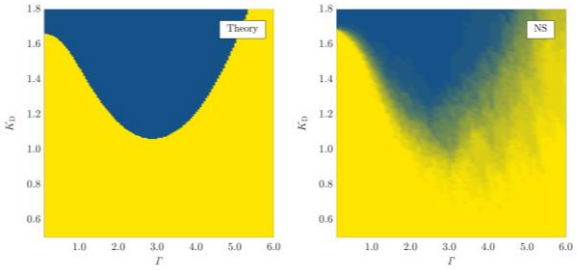

Fig.6 Theoretically obtained stability diagram for an unstable system. The yellow region means $\mathcal{J} > 0$ (unstable), whereas the blue region indicates $\mathcal{J} < 0$ (stable)

7. CONCLUDING REMARKS

In this paper, the authors briefly present the results of their recent research on the application of SDE to ship and ocean engineering. However, as shown in this paper, various theories on SDE can be used to estimate hull response, stability bounds, and much more. The authors intend to continue to advance such research.

ACKNOWLEDGEMENTS

This work was supported by a Grant-in-Aid for Scientific Research from the Japan Society for Promotion of Science (JSPS KAKENHI Grant Number 22H01701).

REFERENCES

Ariaratnam, S., Tam, D., 1979, "Random vibration and stability of a linear parametrically excited oscillator", Zeitschrift Angewandte Mathematik und Mechanik, vol.59, pp.79

Arnold, L. Papanicoaou, V. Wihstutz, 1986, "Asymptotic analysis of the Lyapunov exponent and rotation number of

the random oscillator and application", Siam Journal on Applied Mathematics, vol.46, pp.427-450.

Dostal, L. and Kreuzer, E., 2011, "Probabilistic approach to large amplitude ship rolling in random seas", Proceedings of the Institution of Mechanical Engineers, Part C: Journal of Mechanical Engineering Science, vol.225, No.10, pp.2464.

Dostal, L., Kreuzer, E. and Namachchivaya N.S., 2012, "Non-Standard Stochastic Averaging of Large-Amplitude Ship Rolling in Random Seas", Proceeding of the Royal Society of London A: Mathematical, Physical and Engineering Sciences, Vol.468, pp.4146-4173.

Dostal, L. and Kreuzer, E., 2014, "Assessment of extreme rolling of ships in random seas", ASME 2014 33rd international conference on ocean, offshore and arctic engineering. American Society of Mechanical Engineers, p. V007T12A-VT12A, 2014.

Flower, J., Vijeh, N., 1983, "A note on ratio-of-polynomials curve fitting of seawave spectra", International Shipbuilding Progress, Vol. 30, No. 341, pp. 10–12.

Flower, J., Vijeh, N., 1985, "Further considerations of the ratio of polynomials form fit of seawave spectra", International Shipbuilding Progress, Vol. 32, No. 365, pp. 2–5.

Thampi, S. K., Niedzwecki, J. M. 1992, "Filter approach to ocean structure response prediction", Applied Ocean Research, Vol. 14, No. 4, pp. 259–271.

Grim, O., 1961, "Beitrag zu dem problem der sicherheit des schiffes in seegang", Schiff und Hafen 6 pp. 490–497.

Haddara, M.R., 1974, "A Modified Approach for the Application of Fokker-Plank Equation to the Nonlinear Ship Motion in Random Waves", International Shipbuilding Progress, Vol.21, No.242, pp.283-288.

Haddara, M.R.,1975, "A study of stability of the mean and variance of rolling motion in random waves", Proceedings, International Conference on the Stability of Ships and Ocean Vehicles, University of Strathclyde, Glasgow, U.K.

Kozin, F., Prodromou, S., 1971, "Necessary and sufficient conditions for almost sure sample stability of linear Ito equations", SIAM Journal on Applied Mathematics, vol.21, No.3, pp.413

Kuwajima, S., Kobayashi, H., 1977, "Wind turbulence and its effect on ship's motion I", The Journal of Japan Institute of Navigation, Vol.58, pp.51-60.

Kuwajima, S., Kobayashi, H., 1979, "Wind turbulence and its effect on ship's motion II", The Journal of Japan Institute of Navigation, Vol.60, pp.73-82.

Maki, A., Umeda, N., Shiotani, S and Kobayashi, E., 2011, "Parametric rolling prediction in irregular seas using combination of deterministic ship dynamics and probabilistic wave theory", Journal of Marine Science and Technology, Vol.16, No.13, pp.294-310.

Maki A, 2017, "Estimation method of the capsizing probability in irregular beam seas using non-Gaussian probability density function". Journal of Marine Science and Technology, Vol. 22, No. 2, pp.351–360.

Maki, A, Sakai, M. and Umeda, N., 2018, "Estimating a non-Gaussian probability density of the rolling motion in irregular beam seas", Journal of Marine Science and Technology, doi.org/10.1007/s00773-018-0606-7 (First Online).

Maki, A, Umeda, N., Miino, Y., Sakai, M. and Ueta, T., 2019, "Estimating a non-Gaussian probability density of the rolling motion in irregular beam seas Part 2", Journal of Marine Science and Technology (to be submitted).

Maki, A., Maruyama, Y., Dostal, L., Sakai, M., Sawada, R., Sasa, K., Umeda, N., 2022, "Practical method for evaluating wind influence on autonomous ship operations", Journal of Marine Science and Technology, vol.27, No.4, 1302-1303.

Maki, A., Maruyama, Y., Dostal, L., Sasa, K., Sawada, R., Wakita, K., 2023a, "Practical method for evaluating wind influence on autonomous ship operations (2nd Report)", Journal of Marine Science and Technology, under review.

Maki, A., Maruyama, Y., Akimoto, Y., Dostal, L., 2023b, "Filter method for generating wave, wave slope, Grim's effective wave", Journal of Marine Science and Technology, under review.

Maki, A., Maruyama, Y., Liu, Y., Dostal, L., 2023c, "Comparison of stochastic stability boundaries for parametrically forced systems with application to ship rolling motion", Journal of Marine Science and Technology, under review.

Maki, A., Hoshino, K., Dostal, L., Maruyama, Y., Hane, F., Yoshimura, Y., 2023d, "Stochastic Stabilization and Destabilization of Ship Maneuvering Motion by Multiplicative Noise, Journal of Marine Science and Technology, under review.

Maruyama, Y., Maki, A., Dostal, L. and Umeda, N., 2022a, Application of Linear Filter and Moment Equation for Parametric Rolling in Irregular Longitudinal Waves, Journal of Marine Science and Technology, Vol.27, pp.1252-1267.

Maruyama, Y., Maki, A., Dostal, L. and Umeda, N., 2022b, "Improved stochastic averaging method using hamiltonian for parametric rolling in irregular longitudinal waves", Journal of Marine Science and Technology, Vol.27, pp.186-202.

Maruyama, Y., Maki, A., Dostal, L., Umeda, N., 2022c, "Stochastic Assessment Using Moment Equation Method for Parametric Rolling of Ships in Random Seaways", Proceedings of the 18th International Ship Stability Workshop, Technical University of Gdansk,177-183.

Maruyama, Y., Maki, A. and Dostal, L., 2023, "Stochastic Assessment of Acceleration Probability Density Function for Parametric Rolling Using Moment Method", Journal of Marine Science and Technology, under review.

Maruyama, Y., Maki, A., Dostal, L., Umeda, N., 2023b, "Estimation of Acceleration Probability Density Function for Parametric Rolling Using PLIM", Ocean Engineering, vol. 280.

Muhuri, P.K., 1980, "A study of the stability of the rolling motion of a ship in an irregular seaway", International Shipbuilding Progress, Vol.27, pp.139-142.

Price, W.G., 1964, "A stability analysis of the roll motion of a ship in an irregular seaway", International Shipbuilding Progress, Vol.11, p103-112.

Roberts, J.B., 1982a, "A Stochastic Theory for Nonlinear Ship Rolling in Irregular Seas", Journal of Ship Research, Vol.26, No.4, pp.229-245, 1982.

Roberts, J.B., 1982b, "Effect of Parametric Excitation on Ship Rolling Motion in Random Waves", Journal of Ship Research", Vol.26. No. 4, p.246-253.

Spanos, P.T.D., 1983, ARMA Algorithms for Ocean Wave Modeling, Journal of Energy Resources Technology, Vol. 105, pp. 300–309.

Spanos, P.T.D. 1986, Filter approaches to wave kinematics approximation, Applied Ocean Research, Vol. 8, No. 1, pp. 2–7.

Spyrou, K.J., Dynamic Instability in Quartering SeasPart III, 1997, Nonlinear Effects on Periodic Motions, Journal of Ship Research, vol.41, No.3, pp.210

Tsubokawa, T. Uemura, K. Nomoto, 1982, "Power loss related to automatic course-keeping", Journal of the Society of Naval Architects of Japan, Vol.151, pp.101-114.

Longuet-Higgins Wave Model And ARMA Representations

Vladas Pipiras, University of North Carolina, Chapel Hill, pipiras@email.unc.edu
Arthur Reed, Naval Surface Warfare Center Carderock Division
Themistoklis Sapsis, Massachusetts Institute of Technology
Kenneth Weems, Naval Surface Warfare Center Carderock Division

ABSTRACT

ARMA models were proposed previously to represent the spatio-temporal Longuet-Higgins model for irregular ocean waves, as means to address some of its shortcomings. It is argued here that the spatio-temporal Longuet-Higgins model does not admit (infinite-order) AR/MA representations. This is an immediate consequence of the so-called Wold decomposition of general stationary random fields, which also implies that the Longuet-Higgins model is deterministic in the sense that it can be predicted perfectly from its "past" values. The latter point is also argued more directly from newly derived ARMA-like representations of the spatio-temporal Longuet-Higgins model.

Keywords: Longuet-Higgins wave model; Stationary processes and fields; Spectral representations; Spectral measures; Wold decompositions; ARMA models; Predictability.

1 INTRODUCTION AND MOTIVATION

The Longuet-Higgins (LH) model is used widely to describe ocean wave height over spatial domain and across time. We are interested here in the LH model for irregular (random) waves. For 1-D space for simplicity,[1] the LH model postulates that the wave height $\zeta(t,x)$ at location $x \in \mathbb{R}$ and time $t \in \mathbb{R}$ is expressed as

$$\zeta(t,x) = \sum_{\ell=1}^{L} c_\ell \cos(k_\ell x - w_\ell t + \phi_\ell), \qquad (1)$$

where the integer $L \geq 1$ indicates the number of wave components (typically, in the order of a few hundreds), ϕ_ℓ are independent random variables uniformly distributed on $(0, 2\pi)$, w_ℓ are (positive) discrete frequencies typically equally spaced at discretization step $\Delta w_\ell = w_{\ell+1} - w_\ell$,

$$c_\ell = \sqrt{2\Delta w\, S(w_\ell)} \qquad (2)$$

are amplitude coefficients with some (e.g. Bretschneider spectrum) $S(w)$ and k_ℓ are the so-called wave numbers related to frequencies w_ℓ through a dispersion relation. We shall assume the deep water dispersion relation

$$k_\ell = \frac{w_\ell^2}{g}, \qquad (3)$$

where g is the gravitational acceleration constant, though the finding below extend to other dispersion relations as well. The expression (1) is viewed as discretizing the analogous model (7) below with the sum replaced by an integral in the limit $L \to \infty$. The present study will concern this limiting form of the LH model.

Introduced by Longuet-Higgins [12], the LH model has been used extensively in naval architecture (e.g. Lewis [11]) and other fields such

[1] We work in 1-D space for simplicity. The findings of the paper extend to the more common 2-D setting without additional technical difficulties.

as oceanography, marine engineering, and others. The corresponding wave velocity potential can be computed through a closed-form expression akin to (1), making the LH model particularly appealing for computer programs simulating ship motions (e.g. Large Amplitude Motion Program; Shin et al. [15]).

The LH model has some shortcomings as well. As noted in Weems et al. [17], these include its necessarily Gaussian nature, self-repeating effects (Belenky [1]) and the need to take a large number of frequencies L, and slow convergence to expected limiting quantities. As a way to resolve some of these issues, several authors (Degtyarev and Reed [4], Weems et al. [17], Gankevich and Degtyarev [7], Degtyarev et al. [5]) have suggested using AutoRegressive (AR) and/or Moving Average (MA) processes to represent the LH model. For example, the AR model postulates in discrete space x_r and time t_n that

$$\zeta(t_n, x_r) = \sum_{(i,j)\in S} \phi_{(i,j)}\zeta(t_{n-i}, x_{r-j}) + \epsilon(t_n, x_r), \quad (4)$$

where $\epsilon(t_n, x_r)$ are error terms, $\phi_{(i,j)}$ are the AR parameters and S represents some set of "past" index values.[2] Several potential advantages of the AR model are that it can be propagated indefinitely based on its "past" values and that the error terms can be taken non-Gaussian. See Section 3 for more information on AR/MA processes and the notions of "past" and associated index sets. For fixed x and across time t, AR/MA representations of the LH model were considered by Spanos [16] and others.

In this study, we revisit the LH model and its ARMA representations with the following main objectives in mind:

- We question the basis of (or at least raise issues about) AR/MA representations of the spatio-temporal LH model. In view of the so-called Wold decomposition of stationary spatio-temporal process, we argue that the LH model does not have (possibly infinite-order) AR/MA representations. Indeed, the LH model is deterministic (in the terminology of the decomposition) in that it can be perfectly predicted in terms of its "past" values.
- We derive (to our best knowledge) new ARMA-like representations of the LH model which make the statements of the previous point much more evident. The representations are of independent interest, shed further light on the LH model, address some of the shortcomings of the representation (1) and are related to other models for ocean waves.

The rest of the paper is organized as follows. In Section 2, we provide the limiting form of the LH model where the sum in (1) is replaced by an integral, and argue that it is a special case of a general representation of a stationary (spatio-temporal) process in the spectral domain. Section 3 concerns AR/MA processes and the notions of "past." The Wold decompositions, their implications for the LH model and AR/MA representations are discussed in Section 4. The aforementioned ARMA-like representations of the LH model can be found in Section 5. Conclusions are in Section 6.

2 SPECTRAL REPRESENTATIONS OF STATIONARY RANDOM FIELDS

We shall first replace the sum in (1) by an integral in the limit $L \to \infty$. We do so to show in part that our findings are not due to the discrete nature of the LH model (1). Note that (1) can be expressed as

$$\zeta(t, x) = \sum_{\ell=1}^{L} \cos(k_\ell x - w_\ell t)\sqrt{S(w_\ell)}\eta_{1,\ell} - \sum_{\ell=1}^{L} \sin(k_\ell x - w_\ell t)\sqrt{S(w_\ell)}\eta_{2,\ell}, \quad (5)$$

[2] The quotation marks around "past" are meant to indicate that this notion can be defined in several ways in the spatio-temporal context.

where $\eta_{1,\ell} = \sqrt{2}\cos(\phi_\ell)$, $\eta_{2,\ell} = \sqrt{2}\sin(\phi_\ell)$ satisfy

$$\begin{aligned} &\mathbb{E}\,\eta_{i,\ell} = 0,\ \mathbb{E}\,\eta_{i,\ell}^2 = \Delta w, \\ &\mathbb{E}\,\eta_{i,\ell}\eta_{i',\ell'} = 0,\ (i,\ell) \neq (i',\ell'), \end{aligned} \tag{6}$$

and $\mathbb{E}$ denotes the expectation (in this case, with respect to $\phi_\ell, \phi_{\ell'}$). As $L \to \infty$, the limit of (5) can be written as

$$\begin{aligned} \zeta_c(t,x) = &\int_0^\infty \cos(kx - wt)\sqrt{S(w)}Z_1(dw) \\ &- \int_0^\infty \sin(kx - wt)\sqrt{S(w)}Z_2(dw), \end{aligned} \tag{7}$$

where $k = k(w) = w^2/g$ and $Z_i(dw)$, $i = 1, 2$, are random measures satisfying

$$\begin{aligned} &\mathbb{E}\,Z_i(dw) = 0,\ \mathbb{E}\,Z_i(dw)^2 = dw, \\ &\mathbb{E}\,Z_i(dw)Z_{i'}(dw') = 0,\ (i,dw) \neq (i',dw') \end{aligned} \tag{8}$$

(cf. Eq. (6)).[3] When $Z_(dw)$, $i = 1, 2$, are Gaussian measures, the resulting spatio-temporal process $\zeta_c(t,x)$ is Gaussian. We shall refer to (7) as the LH model as well.

For later reference, we note that Eq. (7) can also be written as

$$\zeta_c(t,x) = \int_{-\infty}^\infty e^{\mathrm{i}(kx-wt)}\sqrt{S(w)}Z(dw), \tag{9}$$

where $k(w) = \mathrm{sign}(w)w^2/g$, $S(-w) = S(w)$ by assumption and $Z(dw)$ is a complex-valued random measure defined as

$$Z(dw) = \frac{1}{2}(Z_1(dw) + \mathrm{i}Z_2(dw)) \tag{10}$$

for $dw \subset (0,\infty)$, and

$$Z(dw) = \frac{1}{2}(Z_1(-dw) - \mathrm{i}Z_2(-dw)) \tag{11}$$

for $dw \subset (-\infty, 0)$. (As usual, i is the imaginary unit, $\mathrm{i}^2 = -1$.) The definitions of complex-valued quantities in (9) are such that $\overline{Z(dw)} = Z(-dw)$ and $\overline{e^{\mathrm{i}(k(w)x-wt)}} = e^{\mathrm{i}(k(-w)x-(-w)t)}$, so that the process in (9) is indeed real-valued. (Hereafter, the bar indicates the complex conjugation.)

AR/MA models are for processes in discrete space/time. We turn to an analogue of the LH model (7) in such setting, which we define for locations $x_m = \Delta x \cdot r$, $r \in \mathbb{Z}$, and times $t_n = \Delta t \cdot n$, $n \in \mathbb{Z}$, and index by r, n as

$$\zeta_d(n,r) = \int_{-\frac{\pi}{\Delta t}}^{\frac{\pi}{\Delta t}} e^{\mathrm{i}(k(w)\Delta x r - w\Delta t n)}\sqrt{S(w)}Z(dw), \tag{12}$$

where the truncation of the integral in (7) follows Spanos [16].[4] After a change of variables, the representation (12) can be expressed as

$$\zeta_d(n,r) = \int_{-\pi}^{\pi} e^{\mathrm{i}(k_d(w)r - wn)}\sqrt{S_d(w)}Z(dw), \tag{13}$$

where $Z(dw)$ has the same properties as in (12) (and as in (7)), and $k_d(w) = k(\Delta t \cdot w)$, $S_d(w) = S(\Delta t \cdot w)\Delta t$. We shall still refer to (13) as the LH model and it will be the focus of our analysis.

The representation (13) is a special case of a general spectral representation of a zero mean, (second-order) stationary random field $Y(\vec{m})$, $\vec{m} = (m_1, m_2) \in \mathbb{Z}^2$. Stationarity refers to the property that $\mathbb{E}[Y(\vec{m} + \vec{h})Y(\vec{m})] = \mathbb{E}[Y(\vec{h})Y(\vec{0})]$ depends only on the shift $\vec{h} \in \mathbb{Z}^2$ for any $\vec{m} \in \mathbb{Z}^2$. It is known (e.g. Mandrekar and Redett [13]) that such random field can be represented as

$$Y(\vec{m}) = \int_{-\pi}^{\pi}\int_{-\pi}^{\pi} e^{\mathrm{i}(\vec{m}\cdot\vec{w})}Z(d\vec{w}), \tag{14}$$

where $\vec{w} = (w_1, w_2)$, $\vec{m}\cdot\vec{w} = m_1w_1 + m_2w_2$, $Z(d\vec{w}) = Z_1(d\vec{w}) + \mathrm{i}Z_2(d\vec{w})$ is a complex-valued random measure satisfying $\overline{Z(d\vec{w})} = Z(-d\vec{w})$, $\mathbb{E}\,Z(d\vec{w}) = 0$,

$$\mathbb{E}\,Z(d\vec{w})\overline{Z(d\vec{w}')} = 0, \tag{15}$$

$$\mathbb{E}\,|Z(d\vec{w})|^2 = F(d\vec{w}), \tag{16}$$

where $F(d\vec{w})$ is a deterministic spectral measure. Note that the LH model (13) admits

[3] The subscript c in $\zeta_c(t,x)$ refers to the continuous nature of the representation (7).

[4] The subscript d in $\zeta_d(n,r)$ refers to the discrete setting.

the representation (14) with $m_1 = n$, $m_2 = r$ and

$$F(d\vec{w}) = S_d(w_1)dw_1\delta_{\{-k_d(w_1)\}}(dw_2), \quad (17)$$

where $\delta_{\{a\}}(dw)$ indicates a point mass at $w = a$.

Remark. For a univariate stationary process $Y(m)$, $m \in \mathbb{Z}$, its spectral domain representation reads

$$Y(m) = \int_{-\pi}^{\pi} e^{imw} Z(dw), \quad (18)$$

where a complex-valued random measure $Z(dw)$ satisfies $\overline{Z(dw)} = Z(-dw)$, $\mathbb{E}\, Z(dw) = 0$, $\mathbb{E}\, Z(dw)\overline{Z(dw')} = 0$ and, with a deterministic spectral measure $F(dw)$,

$$\mathbb{E}\,|Z(dw)|^2 = F(dw). \quad (19)$$

3 ARMA MODELS AND NOTIONS OF PAST

We shall consider below AR/MA models. The AR models, in particular, assume that the current value of the process can be expressed in terms of its "past." The notion of "past" can be defined in several ways in the spatial or spatio-temporal context, and is associated with a set of indices. One choice in the literature (with references given in Section 4 below) has been the (non-symmetrical) half-space "past" associated with the set of indices given by

$$S = \{(j_1, j_2) : j_1 > 0 \text{ or } j_1 = 0, j_2 > 0\}. \quad (20)$$

Another choice is that of the quarter-plane "past" associated with the set

$$S = \{(j_1, j_2) : j_1, j_2 \geq 0, (j_1, j_2) \neq (0, 0)\}. \quad (21)$$

Let also

$$S_0 = S \cup \{(0, 0)\}. \quad (22)$$

Our discussion in the following two sections will focus on the half-space "past" and the sets (20) and (22).

For any of the "past" sets S and S_0, the corresponding (infinite-order) AR model is defined as a stationary field $\{Y(\vec{m})\}$, $\vec{m} \in \mathbb{Z}^2$, satisfying

$$Y(\vec{m}) = \sum_{\vec{i} \in S} \phi_{\vec{i}}\, Y(\vec{m} - \vec{i}) + \epsilon(\vec{m}), \quad (23)$$

where $\phi_{\vec{i}}$ are the AR coefficients and $\{\epsilon(\vec{m})\}$ is white noise, that is, $\mathbb{E}\,\epsilon(\vec{m}) = 0$, $\mathbb{E}\,\epsilon(\vec{m})\epsilon(\vec{m}') = 0$, $\vec{m} \neq \vec{m}'$, $\mathbb{E}\,\epsilon(\vec{m})^2 = \sigma^2$. In practice, the AR model has a finite number of non-zero AR coefficients.

The MA model corresponding to (23) is defined as

$$Y(\vec{m}) = \sum_{\vec{j} \in S_0} \theta_{\vec{j}}\, \epsilon(\vec{m} - \vec{j}), \quad (24)$$

where $\theta_{\vec{i}}$ are the MA coefficients with $\theta_{\vec{0}} = 1$. In practice, the MA model has a finite number of non-zero MA coefficients. The AR and MA models can be combined into an ARMA model.

4 WOLD DECOMPOSITION AND ARMA REPRESENTATIONS

It is instructive to start with stationary processes (18) in the univariate case. The Wold decomposition in this case states (e.g. Brockwell and Davis [2]) that a stationary process $\{Y(m)\}$ can be decomposed into two uncorrelated components as

$$Y(m) = Y_1(m) + Y_2(m), \quad m \in \mathbb{Z}\,. \quad (25)$$

Here, $\{Y_1(m)\}$ has a (possibly infinite-order) MA or AR representation as

$$\begin{aligned} Y_1(m) &= \sum_{j=0}^{\infty} \theta_j \epsilon(m - j) \\ &= \sum_{i=1}^{\infty} \psi_i Y_1(m - i) + \epsilon(m) \end{aligned} \quad (26)$$

with a white noise series $\{\epsilon(m)\}$, and is called purely non-deterministic. The second component $\{Y_2(m)\}$, on the other hand, is called

deterministic,[5] in the sense that $Y_2(m)$ can be predicted perfectly in terms of the past values $Y_2(m')$, $m' < m$.

Finite-order AR, MA and ARMA models account in practice for the purely non-deterministic components of the Wold decomposition. Necessary and sufficient conditions for a process to be purely non-deterministic are well-known (e.g. Brockwell and Davis [2]), namely,

$$\frac{dF}{dw} = f(w), \ \int_{-\pi}^{\pi} \log f(w) dw > -\infty. \quad (27)$$

That is, the spectral measure (19) needs to have a spectral density satisfying the integrability condition (27). The condition is mild (assuming the density exists). For example, for the LH model (13) as a process in n for fixed r, the spectral density exists, is given by $S_d(w)$ and is expected to satisfy (27) for commonly considered spectrum models of ocean waves.

Wold decompositions have been studied for stationary random fields as well by many authors, starting with Helson and Lowdenslager [9] and then many others (e.g. Mandrekar and and Redett [13], Section 3 and references therein). An issue specific to this setting as noted above is the notion of "past." Much of the original work on Wold decompositions concerned results for the half-space "past" discussed in Section 3. For this type of the "past," the Wold decomposition postulates similarly (Helson and Lowdenslager [9]) that

$$Y(\vec{m}) = Y_1(\vec{m}) + Y_2(\vec{m}), \quad \vec{m} \in \mathbb{Z}^2. \quad (28)$$

Here, the purely non-deterministic component $Y_1(\vec{m})$ has (possibly infinite-order) MA and AR representations as

$$\begin{aligned} Y_1(\vec{m}) &= \sum_{\vec{j} \in S_0} \theta_{\vec{j}} \epsilon(\vec{m} - \vec{j}) \\ &= \sum_{\vec{i} \in S} \phi_{\vec{i}} Y_1(\vec{m} - \vec{i}) + \epsilon(\vec{m}) \end{aligned} \quad (29)$$

with $\theta_{\vec{0}} = 1$, the "past" sets S, S_0 given by (20) and (22), and white noise error terms $\epsilon(\vec{m})$. The deterministic component $Y_2(\vec{m})$ is such that is value at $\vec{m}$ can be predicted perfectly from its "past" values at $\vec{m} - \vec{i}$, $\vec{i} \in S$. The condition analogous to (27), that is,

$$\frac{dF}{d\vec{w}} = f(\vec{w}), \ \int_{-\pi}^{\pi} \int_{-\pi}^{\pi} \log f(\vec{w}) d\vec{w} > -\infty, \quad (30)$$

is known to be necessary and sufficient for a random field to be purely non-deterministic.

An immediate consequence of the condition (30) is that the LH model (13) does *not* have (possibly infinite-order) AR/MA representations,[6] since its spectral measure F in (17) does *not* have a density with respect to the Lebesgue measure $d\vec{w}$. Furthermore, by the Wold decomposition, the LH model (13) is *deterministic*.

5 ARMA-LIKE REPRESENTATIONS OF LONGUET-HIGGINS MODEL

Our goal here is to derive new representations of the LH model (13) that will make the above point quite evident and that should be of independent interest. We focus on AR-like representations but MA- or ARMA-type representations can be derived similarly.

Consider the LH model (13) for fixed $r = 0$, that is,

$$\zeta_d(n) = \int_{-\pi}^{\pi} e^{-inw} \sqrt{S_d(w)} Z(dw), \quad n \in \mathbb{Z}. \quad (31)$$

By the Wold decomposition, we expect that it has an (infinite-order) AR representation

$$\zeta_d(n) = \sum_{i=1}^{\infty} \phi_i \zeta_d(n-i) + \epsilon_0(n), \quad (32)$$

where $\{\epsilon_0(n)\}$ is a white noise series. In practice, a finite-order AR approximation and its

[5] "Deterministic" does not mean non-random. A typical example of a deterministic process is $Y_2(m) = Z_1 \cos(cm) + Z_2 \sin(cm)$ with zero mean, uncorrelated, equal variance, random Z_1, Z_2.

[6] If the LH model does not have (infinite-order) AR/MA representations for the half-space "past", then it does not have such representations for the more restrictive quarter-space "past."

AR coefficients ϕ_i can be obtained as, e.g., in Spanos [16]. Setting

$$\Phi(z) = 1 - \sum_{i=1}^{\infty} \phi_i z^i \tag{33}$$

and letting B denote the backward shift operator (i.e., $BX(n) = X(n-1)$ and, more generally, $B^s X(n) = X(n-s)$, $s \in \mathbb{Z}$) in the time dimension, the representation (32) can be written formally as

$$\Phi(B)\zeta_d(n) = \epsilon_0(n) \tag{34}$$

and also $\zeta_d(n) = \Theta(B)\epsilon_0(n)$ with $\Theta(z) = \Phi(z)^{-1}$.

We shall use the following consequence of (32). As $\{\epsilon_0(n)\}$ is white noise, its spectral representation is

$$\epsilon_0(n) = \int_{-\pi}^{\pi} e^{-\mathrm{i}nw} Z_0(dw), \tag{35}$$

where $Z_0(dw)$ is a complex-valued random measure satisfying $\overline{Z_0(dw)} = Z_0(-dw)$, $\mathbb{E}\, Z_0(dw) = 0$, $\mathbb{E}\, Z_0(dw)\overline{Z_0(dw')} = 0$, and having the spectral measure

$$\mathbb{E}\,|Z_0(dw)|^2 = \frac{\sigma_0^2}{2\pi}. \tag{36}$$

(We use $e^{-\mathrm{i}nw}$ instead of $e^{\mathrm{i}nw}$ in (35) for convenience below.) The representation (34) can then be written as

$$\int_{-\pi}^{\pi} e^{-\mathrm{i}nw} \Phi(e^{\mathrm{i}w}) \sqrt{S_d(w)} Z(dw) = \int_{-\pi}^{\pi} e^{-\mathrm{i}nw} Z_0(dw). \tag{37}$$

Since (37) holds for all n, it implies that

$$\Phi(e^{\mathrm{i}w}) \sqrt{S_d(w)} Z(dw) = Z_0(dw). \tag{38}$$

Turning back to the LH model (13), the relation (38) implies that

$$\Phi(B)\zeta_d(n,r) = \int_{-\pi}^{\pi} e^{-\mathrm{i}wn} e^{\mathrm{i}k_d(w)r} Z_0(dw). \tag{39}$$

Note that the right-hand side of (39) has the same form as (31), where $\sqrt{S_d(w)}$ is replaced by $e^{\mathrm{i}k_d(w)r}$, the latter depending on r. We can similarly expect as going from (31) to (37) that another AR operation would remove the component $e^{\mathrm{i}k_d(w)r}$ of the representation. To do so, we proceed slightly differently from above by considering the Fourier series as

$$e^{-\mathrm{i}k_d(w)r} = \sum_{j=-\infty}^{\infty} \phi_{r,j} e^{\mathrm{i}jw} =: \Phi_r(e^{\mathrm{i}w}), \tag{40}$$

where

$$\phi_{r,j} = \frac{1}{2\pi} \int_{-\pi}^{\pi} e^{-\mathrm{i}k_d(w)r} e^{-\mathrm{i}jw} dw \tag{41}$$

are the Fourier coefficients. Then, in view of (39) and (40), we obtain the following AR-type representation of the LH model,

$$\begin{aligned} &\Phi_r(B)\Phi(B)\zeta_d(n,r) \\ &\quad = \int_{-\pi}^{\pi} e^{-\mathrm{i}nw} \Phi_r(e^{\mathrm{i}w}) e^{\mathrm{i}k_d(w)r} Z_0(dw) \\ &\quad = \int_{-\pi}^{\pi} e^{-\mathrm{i}nw} Z_0(dw) = \epsilon_0(n), \end{aligned} \tag{42}$$

that is,

$$\Phi_r(B)\Phi(B)\zeta_d(n,r) = \epsilon_0(n). \tag{43}$$

Setting

$$\Psi_r(z) = \Phi_r(z)\Phi(z) = \sum_{i=-\infty}^{\infty} \psi_{r,i} z^i, \tag{44}$$

the representation (43) reads

$$\begin{aligned} &\ldots + \psi_{r,1}\zeta_d(n-1,r) + \psi_{r,0}\zeta_d(n,r) \\ &\quad + \psi_{r,-1}\zeta_d(n+1,r) + \ldots = \epsilon_0(n). \end{aligned} \tag{45}$$

It is notable that $\epsilon_0(n)$ are the *same* in the representation (43) or (45) for all r.

The MA-type representation corresponding to (43) is

$$\zeta_d(n,r) = \Theta_r(B)\Theta(B)\epsilon_0(n), \tag{46}$$

where $\Theta_r(z) = \Phi_r(z)^{-1}$, $\Theta(z) = \Phi(z)^{-1}$. Setting

$$\Pi_r(z) = \Theta_r(z)\Theta(z) = \sum_{j=-\infty}^{\infty} \pi_{r,j} z^j, \tag{47}$$

the representation (46) reads

$$\zeta_d(n,r) = \ldots + \pi_{r,1}\epsilon(n-1) + \pi_{r,0}\epsilon(n) + \psi_{r,-1}\epsilon(n+1) + \ldots. \quad (48)$$

Remark. Note that the representation (48) is similar in character to the so-called "effective wave" models. An example is the Grim sinusoidal wave with random amplitude as

$$\zeta_d(n,r) = \cos\left(\frac{2\pi\Delta x \cdot r}{L}\right)\epsilon_1(n) + \sin\left(\frac{2\pi\Delta x \cdot r}{L}\right)\epsilon_2(n), \quad (49)$$

where L is the ship length and $\{\epsilon_i(n)\}$, $i = 1, 2$, are independent white noise series (Grim [8]). Extensions of this model can be found in Bulian [3], Dostal and Kreuzer [6].

An immediate consequence of the above ARMA-like representations is that $\zeta_d(n,r)$ can be expressed in terms of its "past" values. For example, when $r = 0$, note by (34) that

$$\zeta_d(n,0) = \Theta(B)\epsilon_0(n), \quad (50)$$

where $\Theta(z) = \Phi(z)^{-1}$. It follows by (43) with $r = -1$ that

$$\zeta_d(n,0) = \Theta(B)\Phi_{-1}(B)\Phi(B)\zeta_d(n,-1) = \Phi_{-1}(B)\zeta_d(n,-1), \quad (51)$$

since $\Theta(z)\Phi(z) = 1$. That is, $\zeta_d(n,0)$ can be expressed in terms of the "past" values $\zeta_d(n',-1)$, $n' \in \mathbb{Z}$.

Remark. Note the special character of the filter $\Phi_r(e^{\mathrm{i}w})$ in (40), which satisfies

$$|\Phi_r(e^{\mathrm{i}w})|^2 = 1. \quad (52)$$

The filters satisfying (52) are known as allpass filters. See, e.g., Regalia et al. [14], Lang [10].

6 CONCLUSIONS

This study explored certain connections between the Longuett-Higgins and ARMA models for ocean waves. Several avenues for future research remain open, including numerical work (e.g., around the AR/MA-type representations (43) and (46)), closer examination of the case of the quarter-plane "past" and implications on the previous ARMA approximations of the Longuett-Higgins model.

Acknowledgments

This work was facilitated and funded by the NSWCCD Summer Faculty Program, managed by Dr. Jack Price, and the Office of Naval Research grant N00014-23-1-2176 under Dr. Woei-Min Lin.

References

[1] V. Belenky. On long numerical simulations at extreme seas. In *Proceedings of the 8th International Ship Stability Workshop*, Istanbul, Turkey, 2005.

[2] P. J. Brockwell and R. A. Davis. *Time Series: Theory and Methods*. Springer science & business media, 2009.

[3] G. Bulian. On an improved Grim effective wave. *Ocean Engineering*, 35(17):1811–1825, 2008.

[4] A. Degtyarev and A. M. Reed. Synoptic and short-term modeling of ocean waves. In *Proceedings of the 29th Symposium on Naval Hydrodynamics*, Gothenburg, Sweden, 2012.

[5] A. Degtyarev, A. M. Reed, and V. Mareev. Modeling of incident waves near the ship's hull (Application of autoregressive approach in problems of simulation of rough seas). In V. L. Belenky, K. J. Spyrou, F. van Walree, M. Almeida Santos Neves, and N. Umeda, editors, *Contemporary Ideas on Ship Stability: Risk of Capsizing*, pages 25–35. Springer International Publishing, 2019.

[6] L. Dostal and E. Kreuzer. Probabilistic approach to large amplitude ship rolling

in random seas. *Proceedings of the Institution of Mechanical Engineers, Part C: Journal of Mechanical Engineering Science*, 225(10):2464–2476, 2011.

[7] I. Gankevich and A. Degtyarev. Simulation of standing and propagating sea waves with three-dimensional ARMA model. In M. G. Velarde, R. Y. Tarakanov, and A. V. Marchenko, editors, *The Ocean in Motion: Circulation, Waves, Polar Oceanography*, pages 249–278. Springer International Publishing, 2018.

[8] O. Grim. Beitrag zu dem Problem der Sicherheit des Schiffes im Seegang. *Schiff und Hafen*, 6:490–497, 1961.

[9] H. Helson and D. Lowdenslager. Prediction theory and Fourier series in several variables. *Acta Mathematica*, 99:165–202, 1958.

[10] M. Lang. Allpass filter design and applications. *IEEE Transactions on Signal Processing*, 46(9):2505–2514, 1998.

[11] E. Lewis. *Principles of Naval Architecture Second Revision, Volume III (Motions in Waves and Controllability)*. The Society of Naval Architects and Marine Engineers, Jersey City, NJ, 1989.

[12] M. S. Longuet-Higgins. The statistical analysis of a random, moving surface. *Philosophical Transactions of the Royal Society of London. Series A, Mathematical and Physical Sciences*, 249(966):321–387, 1957.

[13] V. S. Mandrekar and D. A. Redett. *Weakly Stationary Random Fields, Invariant Subspaces and Applications*. CRC Press, 2017.

[14] P. A. Regalia, S. K. Mitra, and P. P. Vaidyanathan. The digital all-pass filter: A versatile signal processing building block. *Proceedings of the IEEE*, 76(1):19–37, 1988.

[15] Y. Shin, V. Belenky, W. Lin, K. Weems, and A. Engle. Nonlinear time domain simulation technology for seakeeping and wave-load analysis for modern ship design. authors' closure. *Transactions os the Society of Naval Architects and Marine Engineers*, 111:557–583, 2003.

[16] P.-T. D. Spanos. ARMA algorithms for ocean wave modeling. *Transactions of the American Society of Mechanical Engineers*, 105:300–309, 1983.

[17] K. Weems, A. M. Reed, A. Degtyarev, and I. Gankevich. Implementation of an autoregressive wave model in a numerical simulation code. In *Proceedings of the 31st Symposium on Naval Hydrodynamics*, Monterey, CA, USA, 2016.

Considerations for a free-running implementation of the critical wave groups method

Kevin M. Silva, David Taylor Model Basin (NSWCCD), kevin.m.silva14.civ@us.navy.mil
Kevin J. Maki, University of Michigan, kjmaki@umich.edu

ABSTRACT

Vessels experience a wide range of wave groups throughout their lifetime that can lead to extreme ship response events. Previous research in the observation and quantification of extreme events has involved simplifications such as only considering zero speed or constant speed and heading, and has mainly neglected free-running vessels traveling with 6 degrees of freedom (6-DoF), where surge, sway, and yaw motions in conjunction with propeller and rudder forces can lead to extreme events and failures. This work aims to survey previous efforts in their ability to observe extreme events of free-running vessels and formally outlines a methodology of observing deterministic wave groups with prescribed encounter states through a methodology referred to as the natural initial condition.

Keywords: *Extreme Events, Critical Wave Groups, Free-Running, Initial Conditions.*

1. INTRODUCTION

The observation and probabilistic quantification of extreme ship responses is paramount in the design and operational of naval vessels. These extreme response events can include capsizing, broaching, and large loads that can lead to catastrophic failures and possible loss of vessels, equipment, and personnel. Analysis must not only quantify the probability of occurrence of extremes but also produce observations of specific extreme events to understand the physical underlying mechanisms causing them. Analysis with either model testing or numerical hydrodynamic analysis typically focuses on assessments of the dynamical response of ships in random waves with exposure time only sufficient to quantify mean, standard deviation, and low-order peak statistics. However, quantification of extremes requires long exposure windows that are impractical to realize through a Monte Carlo-type approach

Several methodologies exist for quantifying the probability of extremes including extrapolation methods such as the Peaks Over Threshold (POT) (Campbell and Belenky, 2010a) and the Envelope Peaks Over Threshold (EPOT) (Campbell and Belenky, 2010b; Belenky and Campbell, 2011) methods. In addition to the extrapolation methods is the split-time method which utilizes a *distance to danger* methodology to identify extreme events (Belenky, 1993; Belenky et al., 2010; Weems et al., 2020).

However, traditional extreme event probabilistic methods do not actually provide physically realizable events and are more concerned with the probabilistic calculation. Wave group and wave episode methods are more focused on the observation of extreme events and the probabilistic quantification is a by-product of observing a sufficient amount of tailored events.

These methods include the Design Loads Generator (DLG) developed in Alford (2008), Alford et al. (2011), and Kim (2012) which utilizes a calculated response spectrum to predict the Extreme Value Distribution (EVD), then generates random non-uniform phases that match the distribution, and finally maps the phases to a wavemaker that generates the waves that lead to the response.

Another methodology is the reduced-order wave group sequential sampling methods of Gong et al. (2020), Mohamad and Sapsis (2018), and Sapsis (2021). The sequential sampling methods reduce wave fields into simplified group descriptions and then build surrogate models with Gaussian Process Regression (GPR) to map the maximum response of the vessel to the wave group that caused it. The

parametrized wave groups have an associated probability and the wave group space is sampled to bias toward low probability and large responses to resolve the tail of the probability density function (PDF).

Additionally, the work by Guth and Sapsis (2022) utilizes Gaussian Process Regression (GPR) and a Karhunen-Loève (KL) expansion description of the random wave field to generate wave episodes and surrogate models of the ship response to produce PDFs.

Lastly, is the critical wave groups (CWG) method first developed in Themelis and Spyrou (2007) for regular waves and then further extended to irregular waves and explored in Anastopoulos et al. (2016); Anastopoulos and Spyrou (2016, 2017, 2019).). The CWG method aims at identifying a series of deterministic wave groups and corresponding initial conditions that produce a desired maximum response. Through a systematic exploration of deterministic wave groups of different shapes and initial conditions, the probability of the series of combinations that produce the same desired maximum response can be compiled into a probability of exceedance calculation for a maximum response threshold of interest.

The sequential sampling, GPR/KL wave episode, and CWG methods all produce both observations and probabilistic quantifications of extreme ship responses but the work of Guth and Sapsis (2022) with GPR/KL and Silva (2023) and Silva et al. (2022) with CWG have shown the greatest applicability towards generalized extreme events for free-running vessels.

The objective of this paper is to summarize recent research of applying wave group and wave episode methods towards the prediction of extreme events for free-running vessels for a holistic characterization of extreme event responses. The paper will focus on the CWG method as an example case but the concepts and methodologies could be extended to other deterministic wave group methodologies.

2. BACKGROUND

The application of wave group and wave episode methods to free-running vessels has been limited due to the main challenge of ensuring that the vessel encounters the correct waves at the precise instance in space and time such that the events are consistent across the parameterization of waves and initial conditions.

Knight et al. (2020) applied the DLG method to a self-propelled ship in head seas that was constrained in sway, roll, and yaw. The ship was constrained to a constant speed leading up to the target wave sequence and then was released in surge such that the extreme event was experienced in a self-propelled state. The consequences of constraining and then releasing degrees of freedom (DoF) is not well understood and likely has a negative consequence on the ability to produce realistic extreme events due to the generated transients.

Guth and Sapsis (2022) only considered constant speed and heading in the application of their wave episode method. Unlike wave group methods, the wave episode method of Guth and Sapsis (2022) is more generating random wave sequences where the impact of KL coefficients on the waves is much more intuitive than utilizing the superposition of sinusoidal waves sampled from a wave spectrum with random phasing. Because the wave episodes and their associated stochastic preludes are essentially spectrum-consistent random waves, it is possible that precisely encountering the wave episode in space and time for free running vessels may not be as important as it is in wave group methods. However, Guth and Sapsis (2022) only considered vertical bending moment (VBM) and the method would have to be applied to a quantity like extreme roll to confirm the method is applicable to free-running vessels for cases where initial conditions have a strong impact on the resulting maximum response.

Silva et al. (2022) and Silva (2023) developed a methodology to implement the CWG method for free-running vessels, where the deterministic wave groups generated within the CWG method are embedded into an irregular wave train with a known corresponding ship response such that the ship state at the moment the wave group is encountered is essentially prescribed. The utilization of an irregular wave train to produce encounter conditions at the wave group is referred to as the *natural initial condition*, in that the encounter conditions are achieved naturally and not artificially by constraining DoF. This methodology is described in detail in Section 3.

Out of the reviewed methodologies, the natural initial condition methodology provides the best avenue for producing physically realizable extreme events with prescribed encounter conditions and desired deterministic wave groups.

3. NATURAL INITIAL CONDITION

The natural initial condition was originally introduced in Silva and Maki (2021, 2023) and Silva et al. (2021) for implementing the CWG method with computational fluid dynamics (CFD) for the extreme roll of a two-dimensional (2D) midship section. Previous implementations with the CWG method were with 1-DoF ordinary differential equation (ODE) models of roll where the entire dynamic state when encountering the wave group can be easily defined through an initial condition but in reality the entire dynamical state of the vessel and the surrounding fluid cannot be prescribed instantaneously with an initial condition. Therefore, the natural initial condition idea was introduced where they are achieved by embedding deterministic wave groups into an ensemble of previously observed irregular seaways that will naturally produce different encounter conditions as a ship reaches the wave group of interest. This methodology avoids the issues associated with explicitly prescribing initial conditions, and instead allows for the fluid flow and ship responses to develop naturally. Additionally, prescribing the encounter conditions in this manner preserves the integrity of the CWG methodology developed for an ODE, while making the method accessible for higher-fidelity numerical hydrodynamic tools and physical experiments.

Consider a single realization of a free-running vessel starting traveling through a random seaway that evolves in space and time. Throughout the realization, a specific encounter condition of interest occurs at time t_e. The waves experienced by the vessel in the encounter frame can be approximated as the wave elevation function $\eta_{IP}^{(E)}(t)$, which up until time t_e is referred to as the irregular prelude. The ship speed $U_e = x_e/t_e$ can also be estimated based on the ship traveling a distance x_e in time t_e. The deterministic wave groups are defined in the earth-fixed frame through Fourier components which results in a wave group elevation time-history at the origin $(x, y = 0{,}0)$:

$$\eta_{WG}(t) = \sum_f a_{g_f} \cos\left(\omega_{g_f} t + \phi_{g_f}\right) \quad (1)$$

where a_{g_f}, ω_{g_f}, and ϕ_{g_f} are the Fourier amplitudes, frequencies, and phases describing the deterministic wave group. See Anastopoulos and Spyrou (2019) and Silva (2023) for a more detailed description of how deterministic wave groups are constructed for the CWG method with Markov chains. Figure 1 shows the wave elevation at the origin described by the Fourier components representing a wave group. Since the Fourier components only correspond to the wave group, the wave group repeats continuously in time.

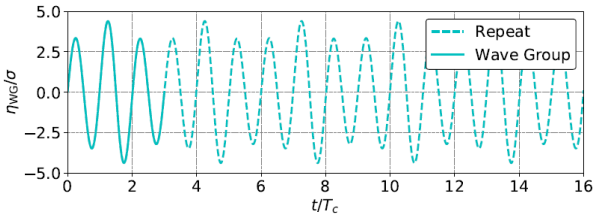

Figure 1. Representation of a repeating deterministic wave group at the origin with Fourier components.

An estimate of encountering the wave group in a constant moving frame can be made by utilizing the deep water dispersion relation for the wavenumber, $k_{g_f} = \omega_{g_f}/g$, along with U_e to transform the wave group time-history at a single point into a wave train that repeats in space and time. g here refers to the acceleration due to gravity. This modifies Equation (1) to describe the wave group in the estimated encounter frame:

$$\eta_{WG}^{(E)}(t) = \sum_f a_{g_f} \cos\left(\omega_{g_f} t - k_{g_f}(\cos(\mu) U_e) + \phi_{g_f}\right) \quad (2)$$

where μ is the wave heading defined such that 180 deg is head seas, 0 deg is following seas, and 90 deg is starboard beam seas. Figure 2 shows the encountered wave field as a vessel travels through the origin at $t = 0$ with constant speed and heading.

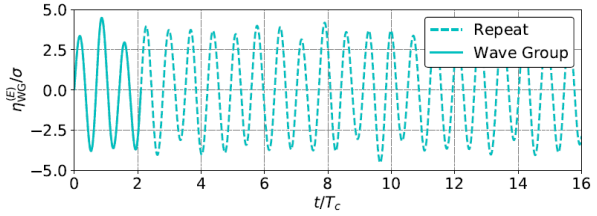

Figure 2. Encountered wave elevation traveling through the repeating wave group wave field with constant speed and heading.

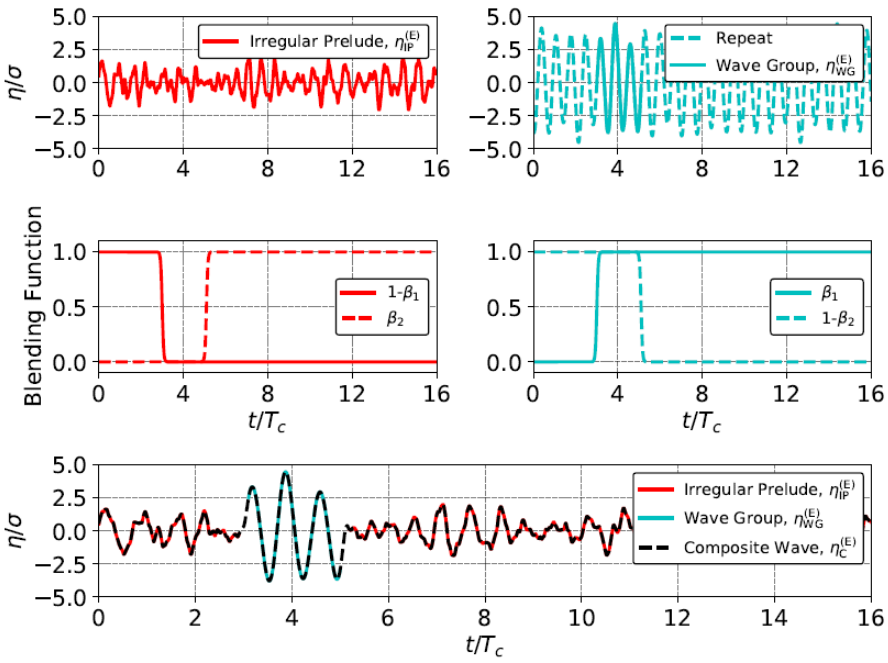

Figure 3. Formation of a composite wave by embedding a deterministic wave group into the irregular prelude in the estimated encounter frame.

The wave group of interest is encountered over a different time-interval due to the forward speed of the vessel. Like the wave group elevation at the origin, the encountered wave group is repeated in time with the Fourier representation.

To create a physically realizable extreme event, the deterministic wave group in the encounter frame $\eta_{WG}^{(E)}(t)$ is embedded into the encountered irregular prelude $\eta_{IP}^{(E)}(t)$. The encountered wave group $\eta_{WG}^{(E)}(t)$ is shifted by t_e such that the group starts at location x_e, thus ensuring that the encountered wave group $\eta_{WG}^{(E)}(t)$ will start directly at t_e. The new composite seaway in the estimated encounter frame $U_e t$ is formed with the blending functions β_1 and β_2 as:

$$\eta_C^{(E)}(t) = (1-\beta_2)\left[(1-\beta_1)\eta_{IP}^{(E)}(t) + \beta_1\eta_{WG}^{(E)}(t-t_e)\right] + \beta_2\eta_{IP}^{(E)}(t) \quad (3)$$

where each blending function is defined as:

$$\beta = \frac{1}{2}\left(1 + \tanh\left(\frac{t-t_e}{t_o}\right)\right) \quad (4)$$

The functions β_1 and β_2 correspond to the blending at the start and end of the wave group, respectively. Figure 3 shows the blending process for embedding the wave group into an irregular wave train to create a single composite wave train. The wave elevation and time in Figure 3 are non-dimensionalized by the standard deviation of the height from specified wave spectrum σ and the period of the largest wave in the group T_c, respectively.

The time scale t_o is selected with Equation (5) where the factor of 0.9 corresponds to approximately 95% of the first signal at the start of the interval and 95% of the second signal at the end. Equation (5) results in a composite wave, where the majority of the blending process occurs within two time intervals of duration $T_p/5$. To form the full composite wave train, t_o is the same for β_1 and β_2, while t_e depends on the start and end of the wave group. The portion of the composite wave train after the wave group is not considered when assessing the extreme ship response, but is required for the wave generation to ensure that the wave group sequences of interest are not repeated in the observed time.

$$t_o = \frac{T_p}{10\ \tanh^{-1}(0.9)} \quad (5)$$

The blending procedure outlined in **Hata! Başvuru kaynağı bulunamadı.** produces a description of the composite wave train in the estimated encounter frame $\eta_C^{(E)}(t)$. To generate the necessary waves for a simulation or experiment, a full spatial and temporal description of the wave field is required. Therefore, $\eta_C^{(E)}(t)$ must be transformed to the earth-fixed frame. In beam to head seas (90- 180 deg/180-270 deg), the transformation is straight forward utilizing

the relationship $\omega_e = \omega_o - \Psi\omega_o^2$, where $\Psi = \cos(\mu)U_e/g$. With the conversion of the frequencies to the absolute frame and calculation of the wavenumber through the dispersion relation, the resulting composite wave train $\eta_C^{(E)}(x,t)$ is a function of both space and time. However, in beam to following seas (0-90 deg, 270-360 deg), the Doppler effect causes the transformation to be multi-valued due to do the movement of the ship relative to the direction of the waves. Figure 4 illustrates the 3-to-1 mapping problem, where under the right conditions, an encounter frequency ω_e can correspond to three separate absolute frequencies ω_o . Nielsen (2017) introduced an algorithm to address this issue. In cases where this multi-valued problem exists, the encounter frequency can be mapped to the three separate absolute frequencies. A scale factor is then applied to the original corresponding amplitude Fourier components, based on a nominal wave spectrum estimated from the Fourier components in the encounter frame.

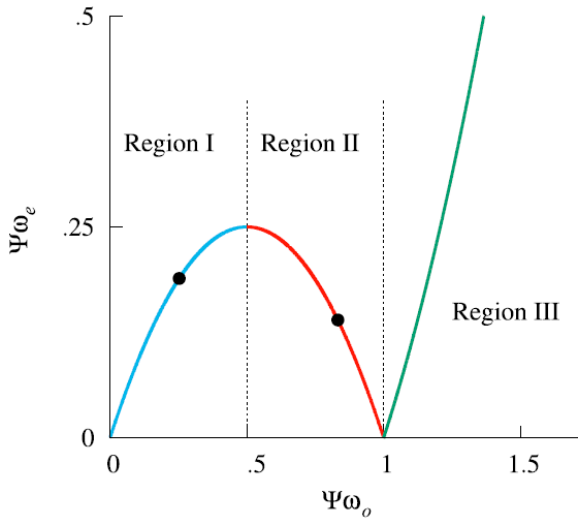

Figure 4. Relationship between encounter and absolute frequencies (Xu et al., 2020).

The natural initial condition method allows for enforcement of the encounter conditions of interest and generation of the wave group in a natural manner without intrusive and nonphysical measures or mechanisms (physical or virtual). All of the necessary information needed for the observation is contained within the composite wave train. Figure 5 reflects an ensemble of composite waves that possess the same wave group with different irregular preludes. The time-histories in Figure 5 have been shifted such that the peak of the largest wave in the group occurs at the same time for the composite wave trains to illustrate the methodology. All of the irregular preludes must account for the ramping up of the wave generation and the vessel reaching it's target speed. This logic ensures that vessel will reproduce the previously observed results that led to the encounter condition.

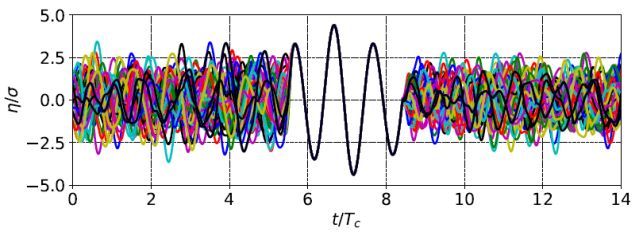

Figure 5. Ensemble of various waves with corresponding different irregular preludes for the same wave group that is shifted in time such that the largest wave in the group's peak occurs at the same time.

An added benefit of the natural initial condition method is that a separate set of irregular wave trains that satisfy the same encounter condition can be determined. This identification allows for the construction of an ensemble of composite wave trains that can be studied to further understand sensitivity to encounter conditions. For instance, if only roll and roll velocity are considered for the encounter condition, but sway velocity contributes significantly, then irregular preludes with different sway velocities can be found to assess the importance of sway. Conversely, if unfavorable encounter conditions are selected such as heave motion and surge velocity when considering large roll, recognition of unsuitable quantities would be simple. Significant differences would occur in the ship response for the same encounter condition and wave group. This aspect of the natural initial condition methodology yields greater utility with more complicated failure mechanisms like capsizing due to broaching-to, where the quantities considered for the encounter conditions are not evident.

4. UNCERTAINTY QUANTIFICATION

The natural initial condition methodology enables the enforcement of prescribed encounter conditions through an irregular prelude and produces physically realizable wave trains with embedded deterministic wave groups. If the entire body and fluid states were captured in the encounter condition, then the response to the deterministic wave group would be deterministic. However, this is impractical

and requires discretization of the high-dimensional combination of the flow field and body state.

It is important to quantify the uncertainty due to different irregular preludes that lead to the same

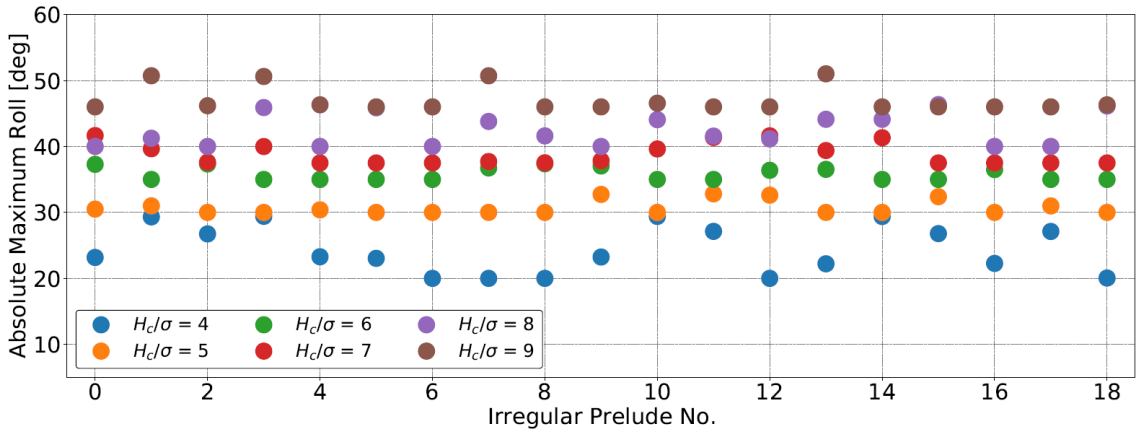

Figure 6. Example absolute maximum roll for different irregular preludes of the same encounter condition for wave groups with different H_c but the same shape.

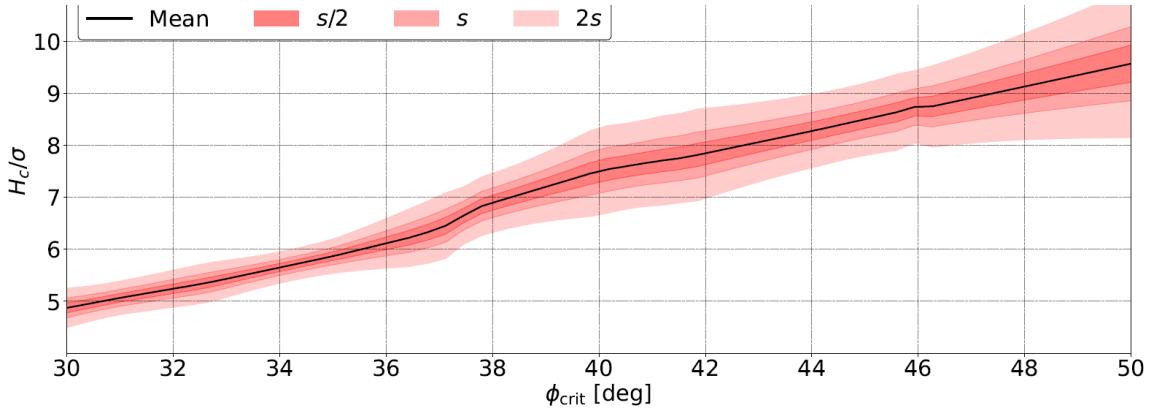

Figure 7. Illustration of quantification of the uncertainty due to the irregular preludes through the identification of critical wave groups.

Therefore, the encounter condition is a reduced-order series of quantities that attempts to summarize the dominating contributions of both the state of the body and the fluid.

In the example of extreme roll, the encounter conditions are typically the roll and roll velocity. The roll and roll velocity attempt to capture all of the body dynamics and hydrodynamics into two simplified quantities. In the context of the natural initial condition, an infinite number of combinations of body and fluid states can lead to the same encounter condition for a free-running vessel. The irregular prelude only ensures that the prescribed encounter condition occurs, but it does not guarantee that the resulting ship response will be identical for different irregular preludes with the same encounter condition. Therefore, an uncertainty estimate is required to quantify the variation due to different irregular preludes.

encounter condition and understand how it propagates through the different calculations into the probability of exceedance calculations. In the case of the CWG method, the uncertainty from the irregular preludes is easily defined in the identification of critical wave groups. Figure 6 illustrates example observations of the absolute maximum roll for 18 different irregular preludes of the same encounter condition for wave groups with different heights of the maximum wave in the group H_c but the same overall shape in time. The variation of the maximums across different irregular preludes with the same encounter condition can vary across all observations with the same H_c.

A critical wave group can be identified for each irregular prelude at the various critical roll angle thresholds ϕ_{crit}, through the interpolation of H_c and the absolute maximum roll predictions in Figure 6. Figure 7 demonstrates the mean and uncertainty in the prediction of height of the critical wave group

H_c, from the different irregular preludes for the same encounter condition. Different levels of uncertainty are shown in terms of the standard deviation s of the H_c predictions across all the irregular preludes. Overall, the uncertainty due to the irregular preludes increases as the critical roll angle threshold increases and there is more variation in the roll response.

Once the critical wave groups are identified as shown in Figure 7, they can be evaluated probabilistically for the mean, as well as a lower and upper bound, individually. The only difference between the probability calculations would be that the mean, lower bound, and upper bound, all of their own set of unique critical wave groups for each encounter condition and wave group shape. The probability of encounter conditions remains the same and is independent of this irregular prelude variation.

Currently, the same wave trains are used to develop irregular preludes for multiple encounter conditions and may introduce bias into the probability calculations. This section describes a methodology for quantifying the uncertainty due to the irregular prelude through identifying a different set of critical wave groups for a mean response as well as an upper and lower bound.

5. EXPERIMENTAL CONSIDERATIONS

Previous research of Anastopoulos et al. (2016) discussed implementing the CWG method and wave group methods in general experimentally. They proposed a mechanism like that shown in Figure 8 to release the ship at a desired encounter condition. While restraining a model in a desired orientation and then releasing it at a prescribed time is difficult but possible, releasing the model with a desired velocity is much more difficult. To arrive at a velocity from rest, acceleration is necessary. The manner in which the model accelerates will influence the radiation force and wave field, and hence, influence the hydrodynamic response. The fact that such a release mechanism requires the selection of an acceleration profile now introduces an additional parameter that must be selected. Also, it is not clear how to distinguish phenomena associated with the encounter conditions from that which is caused by the release method of the ship model. All of these experimental drawbacks also arise in application of the CWG in hydrodynamic simulation tools. Even though a great deal of control exists within simulations to prescribe encounter conditions explicitly (like in ODE models), the impact of the acceleration or impulsive start of the body motion on its subsequent response is of concern.

The natural initial condition presented in Section 3 is generalized for both simulations and experiments. Previous research with initial conditions and wave group methods discussed experimental implementations that required intrusive dynamic mechanisms that would lead to unrealistic events. The natural initial condition enables, for the first time, the observation of curated extreme events with initial conditions in an experimental setting. The one caveat is that a mechanism or methodology is required to ensure that the model is started from rest in a consistent location and time relevant to the wavemaker initializing the wave field. This is a much easier task than a mechanism providing a precise encounter condition at speed in large amplitude waves at the start of the wave group. Even with controls to start the observations the same way repeatedly, there will be slight variations that must be encountered for in the uncertainty experimentally that is not present in simulations.

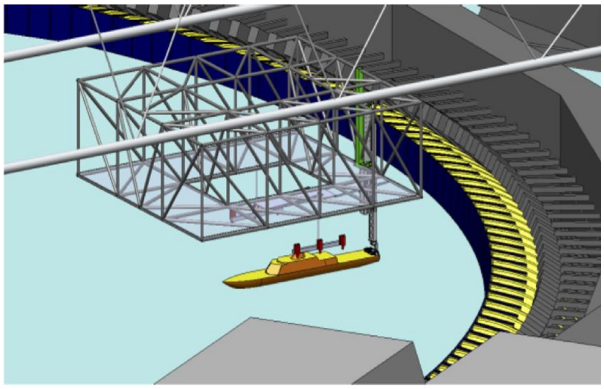

a.) Carriage

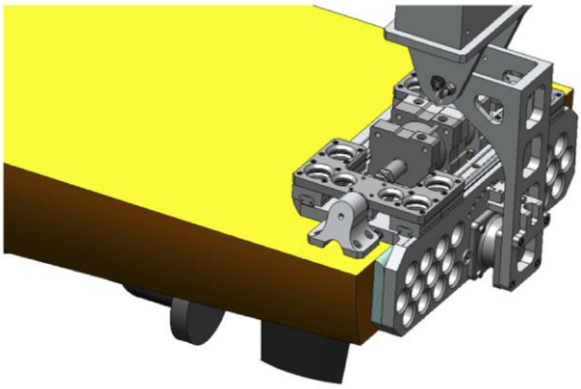

b.) Mechanism

Figure 8. Illustration of a proposed initial condition enforcement mechanism from Anastopoulos et al. (2016).

6. CONCLUSION

This paper surveyed different wave group and wave episode methods to understand their applicability to observing extreme events for free-running vessels. The natural initial condition methodology of embedding deterministic wave groups into random irregular wave trains was formalized for free-running vessels and the implications of the method in terms of uncertainty were outlined.

Future research will take the natural initial condition methodology outlined in this paper and perform a statistical validation for free-running vessels combining the CWG method with a numerical hydrodynamic simulation tool. Application of the natural initial condition to experiments was also discussed and should also be a part of future work in stages, starting from a vessel at zero speed, then constant speed and heading, and then finally completely free-running.

ACKNOWLEDGEMENTS

This work is supported by the Department of Defense (DoD) Science, Mathematics, and Research for Transformation (SMART) scholarship, and the NSWCCD Naval Innovative Science and Engineering (NISE) programs. The authors would also like to acknowledge and thank the Office of Naval Research for the support of this work under contracts N00014-20-1-2096 by the program manager Woei-Min Lin.

REFERENCES

Alford, L., 2008, “Estimating Extreme Responses Using a Non-Uniform Phase Distribution”, Ph.D. Thesis, The University of Michigan, Ann Arbor, MI.

Alford, L.K., Kim, D.H., Troesch, A.W., 2011, “Estimation of extreme slamming pressures using the non-uniform Fourier phase distributions of a design loads generator”, Ocean Engineering Vol. 38, pp. 748–762.

Anastopoulos, P.A., Spyrou, K.J., 2016, ”Ship dynamic stability assessment based on realistic wave group excitations”, Ocean Engineering Vol. 120, pp. 256–263.

Anastopoulos, P.A., Spyrou, K.J., Bassler, C.C., Belenky, V., 2016, “Towards an improved critical wave groups method for the probabilistic assessment of large ship motions in irregular seas”, Probabilistic Engineering Mechanics Vol. 44, pp. 18–27.

Anastopoulos, P.A., Spyrou, K.J., 2017. “Evaluation of the critical wave groups method for calculating the probability of extreme ship responses in beam seas”, In: Proceedings of the 16th International Ship Stability Workshop, Belgrade, Serbia. pp. 131–138.

Anastopoulos, P.A., Spyrou, K.J., 2019, “Evaluation of the critical wave groups method in calculating the probability of ship capsize in beam seas”, Ocean Engineering Vol. 187, pp. 106213.

Belenky, V., 1993, “A capsizing probability computation method”, Journal of Ship Research Vol. 37, pp. 200–207.

Belenky, V., Campbell, B., 2011, “Evaluation of the Exceedance Rate of a Stationary Stochastic Process by Statistical Extrapolation Using the Envelope Peaks Over Threshold (EPOT) method”, Technical Report NSWCCD-50-TR-2011/032, Naval Surface Warfare Center Carderock Division, Hydromechanics Dept, West Bethesda, MD.

Belenky, V., Weems, K.M., Lin, W., Spyrou, K.J., 2010, “Numerical evaluation of capsizing probability in quartering seas with split time method”, Proceedings of the 28th Symposium on Naval Hydrodynamics.

Campbell, B., Belenky, V., 2010a, “Statistical extrapolation for evaluation of probability of large roll”, Proceedings of the 11th International Symposium on Practical Design of Ships and other Floating Structures.

Campbell, B., Belenky, V., 2010b, “Assessment of short-term risk with Monte-Carlo method”, Proceedings of the 11th International Ship Stability Workshop.

Gong, X., Zhang, Z., Maki, K., Pan, Y., 2020, “Full Resolution of Extreme Ship Response Statistics”, Proceedings of the 33rd Symposium on Naval Hydrodynamics.

Guth, S., Sapsis, T.P., 2022, ”Wave episode based Gaussian process regression for extreme event statistics in ship dynamics: Between the Scylla of Karhunen–Loève convergence and the Charybdis of transient features”, Ocean Engineering Vol. 266, Part 1, pp. 112633.

Kim, D.H., 2012, “Design Loads Generator: Estimation of Extreme Environmental Loadings for Ship and Offshore Applications”, Ph.D. Thesis, The University of Michigan, Ann Arbor, MI.

Knight, B.G., Xu, W., Maki, K.J., 2020, “Numerical Prediction of Self-Propulsion in Extreme Head Seas”, Proceedings of the 33rd Symposium on Naval Hydrodynamics.

Mohamad, M.A., Sapsis, T.P., 2018, “Sequential sampling

strategy for extreme event statistics in nonlinear dynamical systems", Proceedings of the National Academy of Sciences Vol. 115, pp. 11138-11143.

Nielsen, U.D., , 2017, "Transformation of a wave energy spectrum from encounter to absolute domain when observing from an advancing ship,", Applied Ocean Research Vol. 69, pp. 160-172.

Sapsis, T. P., 2021, "Statistics of Extreme Events in Fluid Flows and Waves," Annual Review of Fluid Mechanics, Vol. 53:85-111.

Silva, K.M., Maki, K.J., 2021, "Towards a Computational Fluid Dynamics implementation of the critical wave groups method", Ocean Engineering, Vol. 235, pp. 109451.

Silva, K.M., Xu, W., Maki, K.J., 2021, "Critical Wave Group Implementation with Computational Fluid Dynamics and Neural Networks," Proceedings of the 1st International Conference on the Stability and Safety of Ships and Ocean Vehicles (STAB&S 2021), Virtual.

Silva, K.M., Knight, B.G., Maki, K.J., 2022, "Numerical Prediction of Extreme Roll of a Free-Running Ship with Computational Fluid Dynamics and Neural Networks", Proceedings of the 34rd Symposium on Naval Hydrodynamics.

Silva, K.M., 2023, "A Computational Fluid Dynamics Driven Machine-Learning Framework for Observation and Quantification of Extreme Ship Responses", Ph.D. Thesis, The University of Michigan, Ann Arbor, MI.

Silva, K.M., Maki, K.J., 2023, "Implementation of the Critical Wave Groups Method with Computational Fluid Dynamics and Neural Networks", *Under Review* in Ocean Engineering.

Themelis, N., Spyrou, K.J., 2007, "Probabilistic assessment of ship stability", SNAME Transactions, Vol. 115, pp. 181–206.

Weems, K., Belenky, V., Spyrou, K., Aram, S., Silva, K., 2020, "Towards numerical estimation of probability of capsizing caused by broaching-to", Proceedings of the 33rd Symposium on Naval Hydrodynamics.

Xu, W., Filip, G.P., Maki, K.J., 2020, "A Method for the Prediction of Extreme Ship Responses Using Design-Event Theory and Computational Fluid Dynamics", Journal of Ship Research Vol. 64, pp. 48-60.

Testing and benchmarking of direct counting methods

Cleve Wandji, *Bureau Veritas, Paris, France*, cleve.wandji@bureauveritas.com
Vladimir Shigunov, *DNV GL SE Maritime, Hamburg, Germany*, vladimir.shigunov@dnv.com
Vadim Belenky, *David Taylor Model Basin, W. Bethesda, Maryland, USA*, vadim.belenky@navy.mil

ABSTRACT

Benchmarking and comparative testing of three approaches for direct counting of stability failures are described. These approaches are based on the estimation of the failure rate from sample data using exponential distribution of time to failure, statistical frequency of failures and binomial distribution. All three approaches were included in the draft Explanatory Notes for the Second-Generation International Maritime Organization (IMO) Intact Stability Criteria. The benchmarking is performed with results of numerical simulations of ship motions in beam waves. A practical issue of decision making, based on direct counting, is discussed and the influence of the sample size is analyzed.

Keywords: *IMO Second-generation intact stability criteria, Direct Stability Assessment; Direct Counting, Decision Making, Failure rate.*

1. INTRODUCTION

Significant progress, achieved in the last two decades (reviews by Beck and Reed, 2001 and by Reed and Beck, 2016) opens a practical opportunity to apply time-domain numerical simulations for dynamic stability assessment and operational measures. Once a set of time histories has been generated, the rate of stability failures needs to be estimated from these data. If a simulation tool is fast enough, such as *rolls* (Söding, 1982, Söding et al., 2013), *HydroStar++* (Wandji, 2018, Kapsenberg et al. 2020) or SimpleCode (Weems et al., 2023), the dataset is large enough to observe a sufficient number of stability failures. For the simulation tools with higher fidelity and slower computational speed or for moderate sea conditions, extrapolation methods are available (e.g., Shigunov, 2023, Campbell et al., 2023, Belenky et al., 2023, and Wandji, 2022). However, even if extrapolation methods are applied, estimation of the rate of exceedance (or upcrossing events) is still required.

Thus, the estimation of the rate of events from observations, commonly referred to as *direct counting* is one of the basic problems of dynamic stability assessment with time-domain numerical simulations of ship motions in waves.

The Guidelines on the second-generation intact stability criteria, published by IMO for a trial use as MSC.1/Circ.1627 (2020), contain a provision for the application of state-of-the-art numerical simulations for stability assessment (methods referred to as Direct Stability Assessment, DSA) or for operational measures. Requirements for DSA are detailed in the Explanatory Notes, which were finalized at the 8-th session of the Ship Design and Construction Subcommittee of IMO and approved by the IMO Maritime Safety Committee (MSC) in 2022, MSC.1/Circ.1652.

DSA allows probabilistic or deterministic criteria (MSC.1/Circ.1627, paragraph 3.5.3.1.4). A probabilistic criterion is formulated in terms of the rate of stability failures, i.e., the number of failures per time unit. Three direct counting procedures are described in sections 3.3, 3.4 and 3.5 of the Appendix 4 of the Explanatory Notes. All these procedures assume the Poisson process model to relate the probability of stability failure to the time of exposure. A brief overview of a Poisson process is given in the next section.

Since the application of the Poisson process model requires that the data satisfy certain assumptions, the first part of this work (Shigunov et al., 2022) applies the three direct counting procedures to data that are synthesized to follow a Poisson distribution with a known rate parameter. For this purpose, the data in the benchmarking were generated in such a way that they satisfy the Poisson process assumptions.

The objective of this paper is to apply the direct counting procedures to results of numerical simulations of ship motions in waves. The rate estimate and the confidence intervals are computed with the three methods and compared. The second objective is to discuss practical decision making, based on direct counting, and the influence of the sample size on the decision.

2. DIRECT COUNTING PROCEDURES

Poisson process is a model of a memoryless process, i.e. the process for which future outcomes do not depend on past outcomes. For a Poisson process, the number of random events that occur within a specified time interval satisfies the Poisson distribution (e.g., Hayter, 2012, or Ryan, 2007),

$$f(k) = p\{N(t) = k\} = (rt)^k \cdot e^{-rt}/k! \qquad (1)$$

which expresses the probability of occurrence of $k = 0, 1, \ldots$ events during a time interval t. Here, $N(t)$ is the number of events in a time interval of the length t and the constant rate $r > 0$ is the *rate* parameter, which is equal to the expected number of events per unit time. The application of the Poisson distribution for stability failures is described by Shigunov (2019). A summary of useful properties of a Poisson process is provided here.

A special case of eq. (1) is when $k = 0$, which corresponds to the probability that no failures occur during the time interval t:

$$p \equiv p\{N(t) = 0\} = e^{-rt} \qquad (2)$$

From eq. (2), the probability that at least one failure happens during time interval T, i.e., $k > 0$, (loosely formulated: "probability of stability failure during time t") is

$$p^* \equiv p\{N(t) > 0\} = 1 - p\{N(t) = 0\} = 1 - p = 1 - e^{-rt} \qquad (3)$$

The mean of a Poisson process, i.e., the mean number of events per time interval t, is

$$\mu_N(t) = \sum_{k\geq 0} k \cdot f(k) = rt \qquad (4)$$

Thus, the rate r is equal to the expected number of events per time unit:

$$r = \mu_N(t)/t \qquad (5)$$

A useful property of a Poisson process is that the time intervals between events are independent random variables, exponentially distributed with the rate r (and vice versa: if the time intervals between events are not exponentially distributed, the process will not be a Poisson process). If T_j denotes the time to the next event with the index j, eq. (2) leads to

$$p\{t < T_j\} = e^{-rt} \quad \text{for } t > 0 \qquad (6)$$

The independence of stability failures can be violated in practice by self-dependence of wave elevations and ship motions. The result of this self-dependence is observed as a clustering of large roll amplitudes: large roll amplitudes tend to appear in groups. The direct counting techniques have to include a way to decluster large roll amplitudes. The three methods, described in the Explanatory Notes (section 3 of Appendix 4 to MSC.1/Circ.1652), differ by the techniques by which they implement such declustering.

The method described in section 3.3 of Appendix 4 to MSC.1/Circ.1652 (further referred to as M1 for brevity) is based on the estimation of the failure rate from sample data using exponential distribution of time intervals between failures, eq. (6). In this method, each simulation is conducted for an arbitrary simulation time but not longer than the occurrence of the first stability failure (The duration of simulation is limited in any case due to self-repetition effects).

Denote the time intervals to failures as T_j, $j = 1, \ldots, N$, where N is the total number of the encountered stability failures. Then the total simulation time is $t_t = \sum_{j=1}^{N} T_j$ and the sample mean time to failure is $\bar{T} = t_t/N$. The likelihood function for the rate parameter r, according to eq. (2), is

$$L(r) = \prod_{j=1}^{N} r e^{-rT_j} = r^N e^{-rN\bar{T}} \qquad (7)$$

and the derivative of its logarithm is

$$\mathrm{d}\{\ln L(r)\}/\mathrm{d}r = N/r - N\bar{T} \qquad (8)$$

Thus, the maximum likelihood estimate of the rate parameter, which corresponds to the condition $d\{ln\, L(r)\}/dr = 0$, is

$$\hat{r} = 1/\bar{T} = N/t_\mathrm{t} \qquad (9)$$

The $\hat{r}$ is a biased estimator of the rate parameter r, with the relative bias equal to

$$\frac{\mathbb{E}(\hat{r}) - r}{r} = \frac{1}{N-1} \qquad (10)$$

Instead of the rate parameter, the *scale* parameter is sometimes employed, which is equal to the reciprocal of the rate parameter and to the expected time between events, $\mu_T = 1/r$. The sample mean time between events $\bar{T} = 1/\hat{r}$ is an unbiased

minimum variance maximum likelihood estimator of the mean time to failure.

For exponentially distributed intervals T_j, $j = 1, \dots, N$ with the scale parameter equal to μ_T, the distribution of the sum $\sum_{j=1}^{N} T_j$ is a Gamma-distribution with the shape parameter equal to N and the scale parameter equal to μ_T, Ibe (2014). If $X \sim \Gamma(\alpha, s)$ and $c > 0$, then $cX \sim \Gamma(\alpha, cs)$ and substituting $X = \sum_{j=1}^{N} T_j$ and $c = 1/N$ leads to the following distribution for the sample mean time interval: $\bar{T} \sim \Gamma(N, \mu_T/N)$. This expression is rewritten as $2N\bar{T}/\mu_T \sim \Gamma(N, 2)$, and $\Gamma(\nu/2,2) = \chi^2_\nu$, the χ^2-distribution with ν degrees of freedom leads to

$$2N\bar{T}/\mu_T \sim \chi^2_{2N} \tag{11}$$

From Shigunov (2023), equation (11) is exact for exponential time intervals T_j.

According to eq. (11), the two-sided $100 \cdot (1-\alpha)\%$-confidence interval for the scale parameter μ_T is given by

$$2N\bar{T}/\chi^2_{1-\alpha/2,2N} = \mu_{T\mathrm{L}} < \mu_T < \mu_{T\mathrm{U}} = 2N\bar{T}/\chi^2_{\alpha/2,2N} \tag{12}$$

which can be rewritten for the rate parameter r as

$$0.5\hat{r}\chi^2_{\alpha/2,2N}/N = r_\mathrm{L} < r < r_\mathrm{U} = 0.5\hat{r}\chi^2_{1-\alpha/2,2N}/N \tag{13}$$

In the expressions for $\mu_{T\mathrm{L}}$, eq. (12), and r_U, eq. (13), the number of stability failures N is increased by 1 if the last simulation did not end with a stability failure.

The method described in section 3.4 of Appendix 4 to MSC.1/Circ.1652 (further referred to as M2) is based on the estimation of the failure rate from the statistical frequency of failures. Numerical simulations are carried out for a constant simulation duration Δt and considered as independent Bernoulli trials. The only parameter describing such trials is the probability p of encountering at least one event in a single simulation. The maximum likelihood estimator of this probability is calculated as

$$\hat{p} = N_*/M \tag{14}$$

where N_* is the number of simulations in which at least one stability failure was encountered, and M is the total number of simulations. Thus, in this method any stability failure encountered in a simulation after the first one does not affect the estimate. The boundaries of the confidence interval of the probability p are computed by the Clopper–Pearson method, Agresti and Coull (1998), as

$$\frac{\nu_{\mathrm{L}1}F(\alpha/2,\nu_{\mathrm{L}1},\nu_{\mathrm{L}2})}{\nu_{\mathrm{L}2}+\nu_{\mathrm{L}1}F(\alpha/2,\nu_{\mathrm{L}1},\nu_{\mathrm{L}2})} = p_\mathrm{L} < p < p_\mathrm{U} = \frac{\nu_{\mathrm{U}1}F(1-\alpha/2,\nu_{\mathrm{U}1},\nu_{\mathrm{U}2})}{\nu_{\mathrm{u}2}+\nu_{\mathrm{U}1}F(1-\alpha/2,\nu_{\mathrm{U}1},\nu_{\mathrm{U}2})} \tag{15}$$

where $F(\alpha, \nu_1, \nu_2)$ is the α-quantile from F-distribution with ν_1 and ν_2 degrees of freedom, $\nu_{\mathrm{L}1} = 2N_*$, $\nu_{\mathrm{L}2} = 2(M - N_* + 1)$, $\nu_{\mathrm{U}1} = 2(N_* + 1)$ and $\nu_{\mathrm{U}2} = 2(M - N_*)$.

The probability p of encountering at least one event in a single simulation of duration Δt, according to eq. (1), is equal to

$$p = 1 - p\{N(\Delta t) = 0\} = 1 - e^{-r\Delta t} \tag{16}$$

Thus, the rate parameter can be calculated from the probability p as $r = -\ln(1-p)/\Delta t$; therefore, the boundaries of the confidence interval for the failure rate in method M2 are defined as

$$r_{\mathrm{L,U}} = -\ln\left(1 - p_{\mathrm{L,U}}\right)/\Delta t \tag{17}$$

where $p_{\mathrm{L,U}}$ are given by eq. (15).

The method described in section 3.5 of Appendix 4 to MSC.1/Circ.1652 (further referred to as M3) is based on the estimation of the rate from sample data with binomial distribution (Leadbetter et al., 2019). In this method, numerical simulations are carried out for arbitrary duration. All stability failures are recorded; however, to achieve independence of events, only one failure is counted during the *decorrelation time* of roll motion. The decorrelation time is defined as the time for the envelope of the autocorrelation function of roll motion to decrease to a specified threshold level (set to 0.05 in section 3.8 of Appendix 4 to MSC.1/Circ.1652).

To relate the Poisson process, specified by eq. (1), to the binomial distribution, the time interval $t = \delta t$ is considered sufficiently small, so that, first, the exponential function in eq. (1) can be linearized and, second, the number of events during the interval δt cannot be greater than 1, i.e., $k = 0$ or $k = 1$. In the problems considered here, the latter condition is satisfied even for a relatively large time intervals δt since to encounter more than one excessive roll event is not possible during a time interval that is shorter than half of a roll period. To satisfy the first condition, the time interval δt should be rather small, e.g., like in method M3, equal to the time step used in the integration of the motion equations of the

ship. Under these assumptions, $e^{-r\delta t} \approx 1 - r\delta t$ and $k! = 1$, therefore, eq. (1) becomes

$$f(k) = p\{N(\delta t) = k\} = (r\delta t)^k \cdot e^{-rt} \approx (r\delta t)^k \cdot (1 - r\delta t)^{1-k} = \delta p^k (1 - \delta p)^{1-k} \quad (18)$$

Eq. (18) is the Bernoulli distribution, where k is either 0 or 1 and $\delta p = r \cdot \delta t$ is the probability of "success", here the probability that at least one event occurs during the exposure time δt. The number of "successes" in n independent Bernoulli trials is a binomial random variable, with the following probability distribution (Ross, 2009):

$$p\{N(n\delta t) = k\} = \frac{n!\,\delta p^k (1 - \delta p)^{n-k}}{k!\,(n-k)!} \quad (19)$$

which is equal to the probability that k events occur in n trials with the probability of "success" in each trial equal to δp. In method M3, $n = N_\mathrm{a}$ is the total number of time steps in all simulations and $k = N$ is the total number of the counted stability failures,

$$N \sim \mathcal{B}(N_\mathrm{a}, \delta p) \quad (20)$$

Equation (20) requires large computational time, when the number of simulations is large; therefore, method M3 uses a normal approximation of this distribution,

$$N \sim \mathbb{N}\{N_\mathrm{a}\delta\hat{p}, \sqrt{N_\mathrm{a}\delta\hat{p}(1 - \delta\hat{p},)}\} \quad (21)$$

where $\delta\hat{p} = N/N_\mathrm{a}$ is the unbiased maximum likelihood estimator of δp. Then, the confidence interval for the number of stability failures is

$$\mathbb{N}_{\alpha/2}\left(N_\mathrm{a}\delta\hat{p}, \sqrt{N_\mathrm{a}\delta\hat{p}}\sqrt{1 - \delta\hat{p}}\right) < N < \mathbb{N}_{1-\alpha/2}\left(N_\mathrm{a}\delta\hat{p}, \sqrt{N_\mathrm{a}\delta\hat{p}}\sqrt{1 - \delta\hat{p}}\right)$$

and $N = N_\mathrm{a} r\delta t$,

$$\delta\hat{p} \cdot \mathbb{N}_{\alpha/2}\left(1, \sqrt{1 - \delta\hat{p}}/\sqrt{N}\right)/\delta t = r_\mathrm{L} < r < r_\mathrm{U} = \delta\hat{p} \cdot \mathbb{N}_{1-\alpha/2}\left(1, \sqrt{1 - \delta\hat{p}}/\sqrt{N}\right)/\delta t \quad (22)$$

The corresponding step by step procedures for the three approaches are described in MSC.1/Circ.1652 and in Shigunov et al. (2022).

3. INPUT DATA AND CALCULATIONS

The objective of this study was to test the direct counting methods in "real" conditions, where the data were obtained from numerical simulations of ship motions in waves.

The roll motion time series were obtained by performing time domain simulations for the containership ITTC-A1, (Umeda et al., 2000, Spanos and Papanikolaou, 2009). The ship main dimensions and particulars are listed in Table 1 and the hull geometry is in Fig. 1.

Table 1: Main particulars of ITTC A-1 container ship.

Particulars	Value
Length between perpendiculars	150.0 m
Breadth	27.20 m
Depth	13.50 m
Mean draught	8.50 m
Trim	0.0 m
Block coefficient	0.667
Metacentric height	1.38 m
Natural roll period	19.2 s

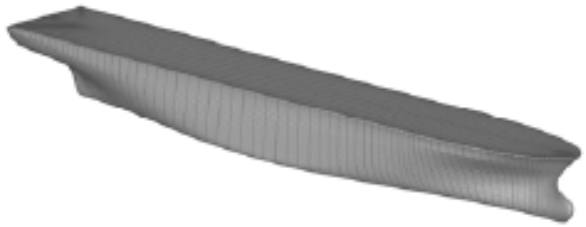

Figure 1: Geometry of container ship ITTC-A1.

Numerical simulations were performed with the 6 degree-of-freedom seakeeping simulation tool *rolls* (Söding, 1982, Söding et al., 2013) in irregular long-crested beam waves at zero forward speed, mean wave period 12.49 s and significant wave heights 10.5 to 16.5 m with the step 1.0 m. The mean wave period was selected to maximize the exceedance rate (i.e. corresponds to the synchronous resonance). For each sea state, several realizations were computed. For each realization a different set of random phases and frequencies of the harmonic wave components composing the JONSWAP ($\gamma = 3.3$) wave energy spectrum (Hasselman et al. 1973) was generated. Each simulation was conducted for 0.5 hours simulation time to avoid self-repetition effects but not longer than the occurrence of the first stability failure. The stability failure event corresponded to the exceedance of the roll angle 40 degrees.

A summary of results is provided in Table 2. These results are already cleaned from the initial transients, which were set equal to 20 natural roll periods in calm water. In Table 2, H_s represents the significant wave height, N is the total number of the encountered stability failures, t_t is the total simulation time (equal to the sum of all times to stability failure), $\hat{T}$ the sample mean time to event,

and r the maximum likelihood estimate of the failure rate.

Table 2: Summary of all results of numerical simulations of ship motions in waves.

H_s, m	N	t_t, s	$\widehat{T}$, s	r, 1/s
10.5	2170	9.530e10	4.392e7	2.277e-8
11.5	2578	8.920e9	3.460e6	2.890e-7
12.5	4940	2.555e9	5.173e5	1.933e-6
13.5	8805	1.016e9	1.154e5	8.665e-6
14.5	5595	2.143e8	3.830e4	2.611e-5
15.5	8993	1.379e8	1.533e4	6.521e-5
16.5	8837	6.476e7	7.329e3	1.364e-4

4. ANALYSIS OF TIME TO FAILURE

Before applying the direct counting procedures to the data collected from numerical simulations of ship motions in waves, it was checked whether the time to stability failure follows the exponential distribution. Since the simulations were conducted following the declustering technique of method M1 in section 2, the stability failures are independent, whereas the exponential distribution of time to failure should verify the memorylessness property of the Poisson process.

Fig. 2 has quantile plots (Q-Q plots) of the time to event, i.e., the cumulative distribution function of the times to event obtained from numerical simulations vs. exponential cumulative distribution function. The bisect line means exact agreement. The results indicate no systematic deviations of the empirical data from the exponential distribution.

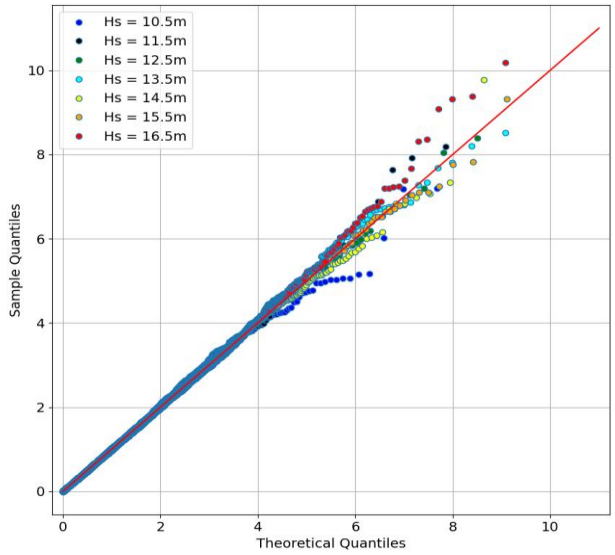

Figure 2: Q-Q plots: theoretical vs. empirical time to failure, hours, for H_s equal to 10.5, 11.5, 12.5, 13.5, 14.5, 15.5 and 16.5 m.

To quantify the deviations of the empirical data from the exponential distribution, the χ^2 and Kolmogorov-Smirnov goodness-of-fit tests were applied. In the χ^2 goodness-of-fit test, the number of bins K was varied as 10, 20, 50, 100, 200, 500, 1000 and 2000. The critical values were calculated as $\chi^2_{\alpha,f}$ with the significance level $\alpha = 0.05$ and the number of degrees of freedom $f = K - 1$. The χ^2 test statistic divided by the critical value vs. K, separately for each significant wave height is in Fig. 3. The zero hypothesis that the empirical data were drawn from an exponential distribution cannot be rejected when the test statistic is less than the critical value. With the increasing number of bins (i.e. increasing accuracy of the test), the results increasingly support the exponentiality of the data for each significant wave height (i.e. for each failure rate). The χ^2 goodness-of-fit test is considered very strict when the amount of data is large, which is the case here.

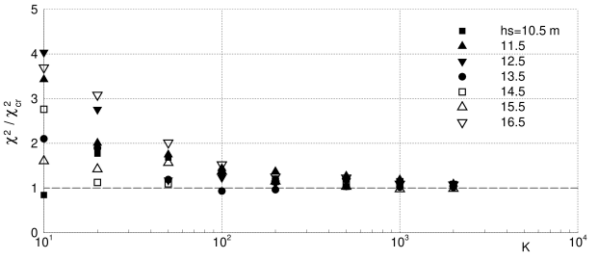

Fig. 3. Ratio χ^2 test statistic critical value vs. K for each significant wave height. Ratio corresponding to critical value is shown by dashed line.

The Kolmogorov-Smirnov goodness-of-fit test is based on the calculation of the maximum deviation of the empirical cumulative probability distribution from the assumed one. To account for the fact that the parameters of the exponential distribution are unknown and are estimated from the sample, the critical values were taken according to the Lilliefors' test correction for the exponential distribution, Edgeman and Scott (1987). The critical values are in Fig. 4 according to Lilliefors for the confidence level $\alpha = 0.05$ and the Kolmogorov-Smirnov test statistics vs. the sample size N for all significant wave heights.

The zero hypothesis that the empirical data were drawn from an exponential distribution cannot be rejected when the test statistic is less than the critical value, which is satisfied with an expressive margin

for all significant wave heights (i.e. for all failure rates), which confirms the exponentiality of the data.

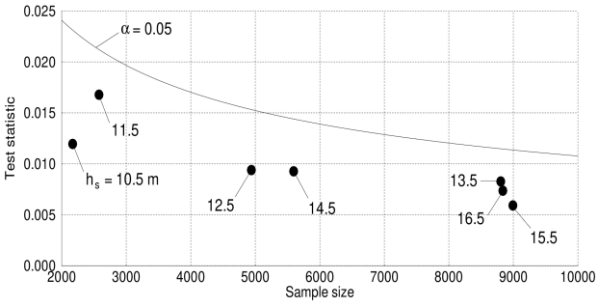

Fig. 4. Critical values for Kolmogorov-Smirnov test per Lilliefors for confidence level $\alpha = 0.05$ (line) and Kolmogorov-Smirnov test statistics (dots) vs. sample size N for all significant wave heights.

5. DIRECT COUNTING RESULTS

The aim of direct counting is to provide the boundaries of the 95 % confidence interval of the stability failure rate (especially the upper boundary, which is for acceptance decision). In this section, the sample estimates of the failure rate and its 95 %-confidence interval, obtained with the three methods, were compared.

For the M1 method, the duration of a simulation is arbitrary, and the result does not depend on the duration of individual simulations. The maximum length of a simulation, here set to 1800 s, is defined by self-repetition effects. The results for the complete datasets are presented in Table 3, which lists the total number of stability failures N, the maximum likelihood estimate of the failure rate $\hat{r}$ and the upper r_U and lower r_L boundaries of the 95 % confidence interval of the failure rate. For the complete dataset, the maximum likelihood estimates of the failure $\hat{r}$ agree with the benchmark estimates in all sea states.

Table 3: Application of M1 procedure to full datasets.

H_S, m	N	$\hat{r}$, 1/s	r_U, 1/s	r_L, 1/s
10.5	2170	2.277e-8	2.374e-8	2.182e-8
11.5	2578	2.890e-7	3.003e-7	2.780e-7
12.5	4940	1.933e-6	1.987e-6	1.880e-6
13.5	8805	8.665e-6	8.847e-6	8.485e-6
14.5	5595	2.611e-5	2.680e-5	2.543e-5
15.5	8993	6.521e-5	6.657e-5	6.387e-5
16.5	8837	1.364e-4	1.393e-4	1.336e-4

For method M2, the simulations were assumed to be of the same length 1800.0 s for comparison. The results for the complete datasets, presented in Table 4, indicate that the maximum likelihood estimates of the failure rate $\hat{r}$ agree with the benchmark estimates in all sea states.

Table 4: Application of M2 procedure to full datasets.

H_S, m	N	$\hat{r}$, 1/s	r_U, 1/s	r_L, 1/s
10.5	2170	2.277e-8	2.375e-8	2.182e-8
11.5	2576	2.889e-7	3.002e-7	2.778e-7
12.5	4932	1.933e-6	1.988e-6	1.880e-6
13.5	8731	8.660e-6	8.843e-6	8.479e-6
14.5	5462	2.609e-5	2.680e-5	2.541e-5
15.5	8486	6.522e-5	6.662e-5	6.384e-5
16.5	7884	1.370e-4	1.404e-4	1.344e-4

For method M3, a constant simulation duration of 1800 s was applied, and the time step δt was set to the one for the integration of the equations of motion, i.e., 0.5 s. The decorrelation time was set to 0 s since the data were already declustered. The results for the complete datasets, presented in Table 5, demonstrate that the maximum likelihood estimates of the failure rate $\hat{r}$ agree with the benchmark estimates in all sea states.

Table 5: Application of M3 procedure to full datasets.

H_S, m	N	$\hat{r}$, 1/s	r_U, 1/s	r_L, 1/s
10.5	2170	2.277e-8	2.373e-8	2.181e-8
11.5	2578	2.890e-7	3.002e-7	2.778e-7
12.5	4940	1.933e-6	1.987e-6	1.879e-6
13.5	8805	8.664e-6	8.846e-6	8.484e-6
14.5	5595	2.611e-5	2.680e-5	2.543e-5
15.5	8993	6.521e-5	6.562e-5	6.387e-5
16.5	8837	1.363e-4	1.393e-4	1.336e-4

Fig. 5 compares the estimates of the failure rate and the upper and lower boundaries of its 95 % confidence interval between the three methods for the full dataset for the significant wave heights 10.5, 11.5, …, 15.5 m. Here, the rate estimates and the upper and lower boundaries of the confidence interval agree well between the three procedures.

Fig. 6 compares the estimates of the failure rate and the upper and lower boundaries of its 95 % confidence interval between the three methods for the full dataset for the significant wave height 16.5 m, i.e. for the greatest failure rate. Here, the results obtained with the M2 method slightly differ from those obtained with the M1 and M3 procedures, whereas the results of the M1 and M3 procedures are almost identical.

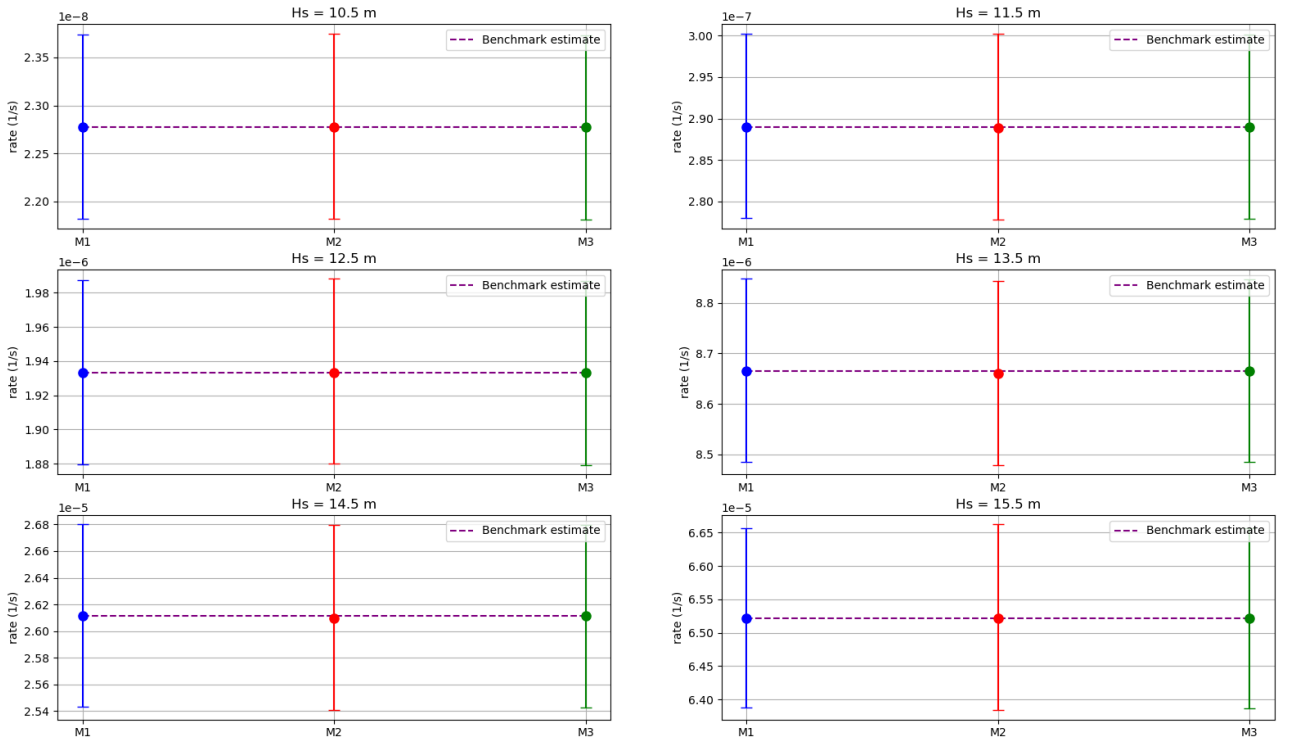

Figure 5: Estimate of failure rate and upper and lower boundaries of its 95 % confidence interval for significant wave heights (from left to right, then top to bottom) 10.5, 11.5, 12.5, 13.5, 14.5 and 15.5 m.

The method M2 considers only the first stability failure in a simulation; therefore, not all failures may be considered if the simulation length is insufficiently small.

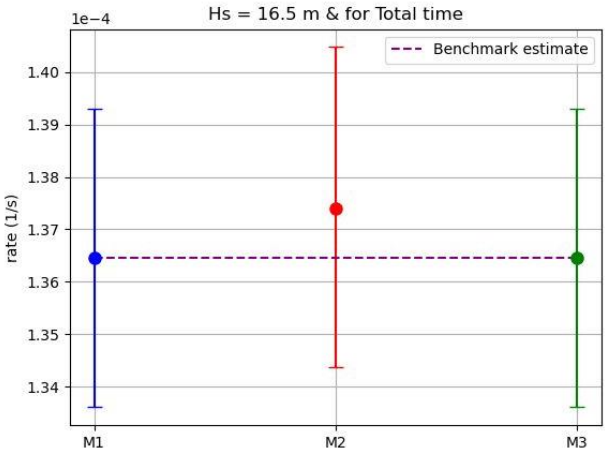

Figure 6: Estimate of failure rate and upper and lower boundaries of its 95 % confidence interval for significant wave height 16.5 m.

For $H_s = 16.5$ m, the M2 procedure has accounted for only 7884 stability failures out of the total of 8837 failures in Table 4. Another reason is that the rate in the M2 method is estimated as $r = -\ln(1 - N/M)/\Delta t$, where Δt is the simulation length and M is the total number of simulations. This estimate converges to the maximum likelihood estimate when $\Delta t \to 0$ while $M\Delta t = \text{const} = t_t$, i.e., in the zero-limit exposure time, Shigunov et al. (2022).

Fig. 7 compares the estimates of the failure rate and the upper and lower boundaries of its 95 % confidence interval between the three methods as a function of the number of events for the significant wave heights 10.5, 11.5, …, 15.5 m. The rate estimates and the upper and lower boundaries of the confidence interval agree well between the three procedures for large number of failure events. For small numbers of failure events the upper boundary of the confidence interval obtained with method M2 is higher than those obtained from methods M1 and M3, while the lower boundary obtained from method M3 is lower than those obtained from methods M1 and M2.

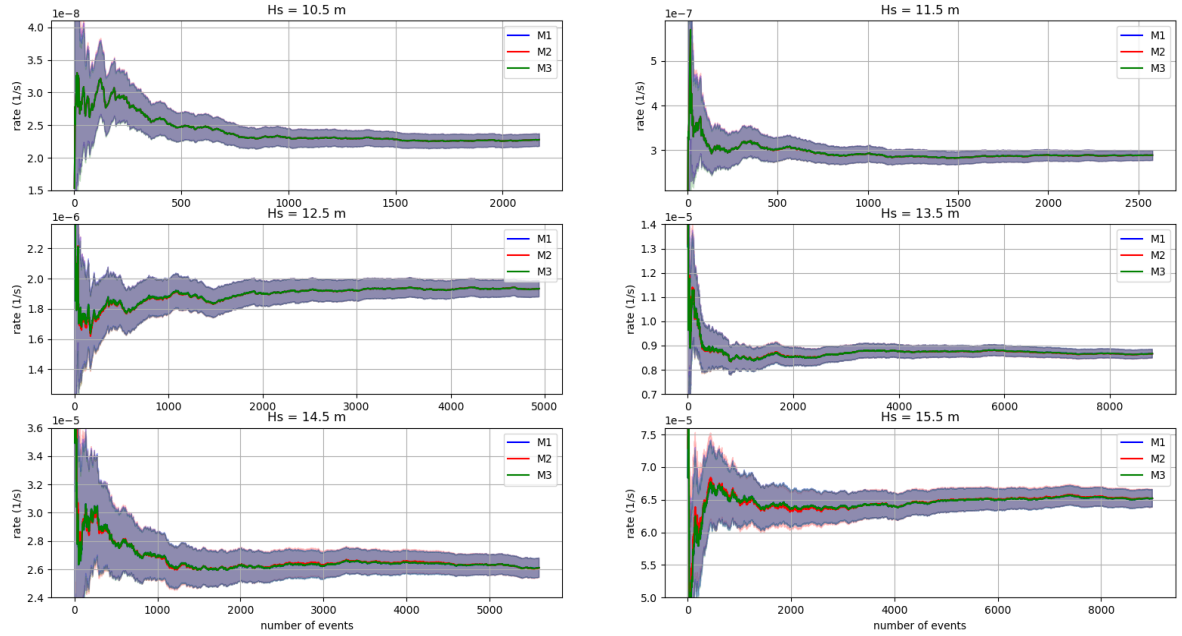

Figure 7: Estimate of failure rate and upper and lower boundaries of its 95 %-confidence interval for significant wave heights (from left to right, then top to bottom) 10.5, 11.5, 12.5, 13.5, 14.5 and 15.5 m vs. number encountered of events.

Fig. 8 compares the estimates of the failure rate and the upper and lower boundaries of its 95 % confidence interval between the three methods as a function of the number of failures for the greatest significant wave height 16.5 m. Here, the results obtained with the M2 method slightly differ from those obtained with the M1 and M3 procedures. In addition, the upper boundary of the confidence interval obtained with procedure M2 is always higher than those obtained from procedures M1 and M3.

To validate the confidence interval constructed by the three direct counting methods, all data for each significant wave height were divided into 200 independent samples. The resulting number of simulations M of 0.5 hour duration in each such sample is in Table 6.

Table 6: Number of simulations vs. significant wave height.

H_S, m	M
10.5	264725
11.5	24778
12.5	7098
13.5	2822
14.5	595
15.5	383
16.5	179

The procedures were applied for the number of simulations varied from 1 to the maximum number of simulations in Table 6. The percentage of the samples was counted where the "true" rate, computed from all data (Table 2), was above the upper boundary of the 95 % confidence interval or below its lower boundary.

The results for M1 and M2 methods are shown in Fig. 9 for the significant wave heights 13.5, 14.5, 15.5 and 16.5 m: the left-hand side plots have the percentage of cases where the "true" value of the rate is above the upper boundary of the 95 % confidence interval, and the right-hand side plots show the percentage of cases where the "true" value of the rate is below its lower boundary. Each row corresponds to one significant wave height. In general, the results deviate from the expected value 2.5 % (more than for the synthesized data (Shigunov et al., 2022). A study of these deviations for M3 method is ongoing.

The horizontal pieces at small numbers of simulations in the left-hand side plots for methods M1 and M2 correspond to the situations, when no stability failures were observed in the initial simulations. In such cases, the upper boundary is defined conservatively, so that the true rate is never above the estimated upper boundary.

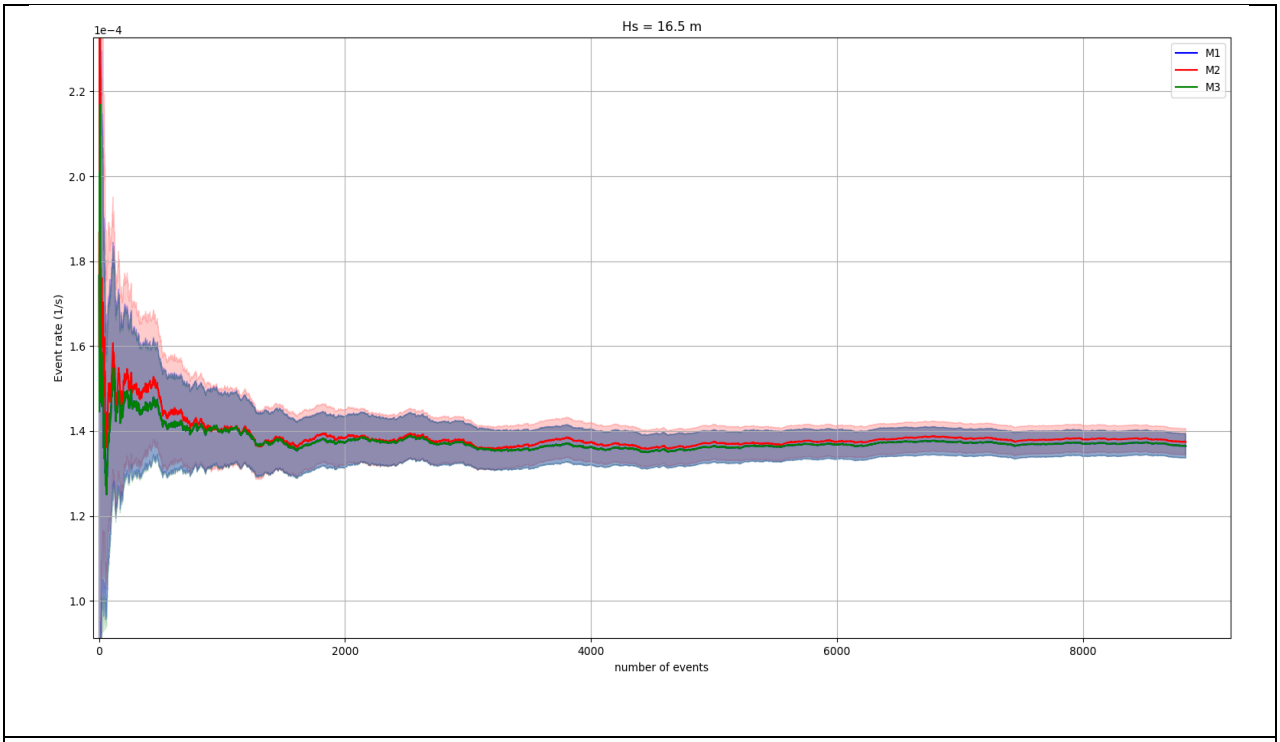

Figure 8: Estimate of failure rate and upper and lower boundaries of its 95 % confidence interval for significant wave height 16.5 m vs. number of events.

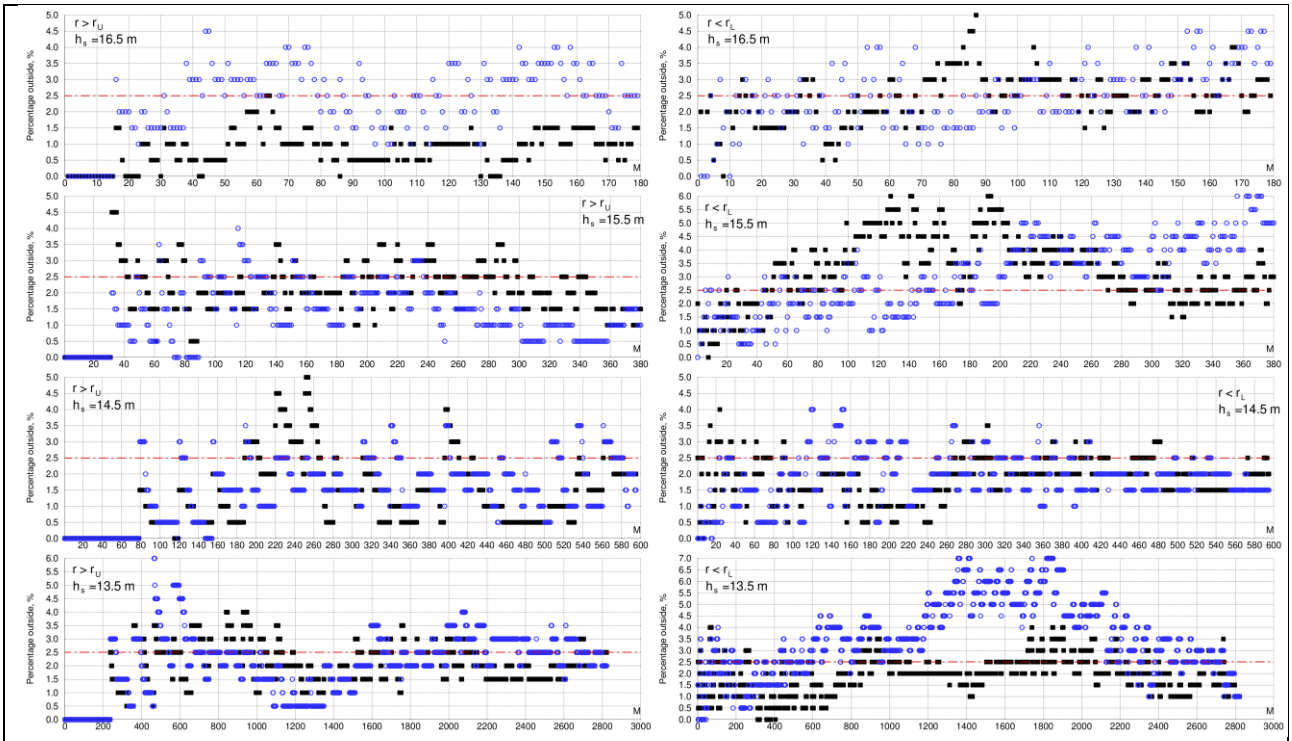

Figure 9 Percentage of cases when "true" value of rate is above upper boundary of 95 %-confidence interval (left) and below its lower boundary (right) for significant wave heights (from top to bottom) 16.5, 15.5, 14.5 and 13.5 m vs. number of simulations for methods M1 (■) and M2 (○)

6. PRATICAL CONSIDERATIONS

The upper r_U and lower r_L boundaries of the 95 % confidence interval of the failure rate can be computed after each (i.e., even already after the first) numerical simulation or model test run. If r_U is less than the acceptance standard, the considered loading condition is judged as acceptable in the considered situation, whereas if r_L exceeds the acceptance standard, as unacceptable. Thus, the decision can be effectively achieved "on the fly", without performing further unnecessary simulations. If, however, after a simulation the acceptance standard happens to be between r_L and r_U, the data gathered from the simulations so far are not sufficient to make an acceptance or unacceptance decision. Such case is "undecided" only from the mathematical point of view: from the approval point of view, it is treated as unacceptance.

In such cases, the designer has two choices: either to admit the unacceptance outcome and render the considered loading condition (in the direct stability assessment) or situation (in the operational guidance) as unacceptable or, alternatively, to proceed with further simulations or model tests to collect more data. Further numerical simulations will narrow down the width of the confidence interval of the failure rate, in general decreasing r_U and increasing r_L. Thus, after a certain number of simulations, either r_U will get below the acceptance standard (which will lead to acceptance) or r_L will get above the standard (which will lead to unacceptance).

Therefore, the designer has a trade-off between reducing the number of numerical simulations (or model tests) and increasing the number of acceptable loading condition (in the direct stability assessment) or situations (in the operational guidance). This is illustrated in Figures 10 and 11. Figure 10 contains the percentage of acceptance cases (denoted as "positives"), unacceptance cases ("negatives") and "undecided" cases depending on the specified ratio of the true value of the failure rate to the acceptance standard ("Rate/Standard", x-axis) and the number of stability failures encountered in the simulations ($N = 1,\ 10,\ 25,\ 50,\ 100,\ 250,\ 500$ and 1000, different plots).

These results were obtained by method M1 with 10000 samples of randomly generated exponentially distributed times to failure. The acceptance cases are denoted as "true positives" for the ratio $\mathrm{Rate}/\mathrm{Standard} < 1$ (i.e., when the acceptance decision is correct) and "false positives" when $\mathrm{Rate}/\mathrm{Standard} > 1$ (i.e., when the acceptance decision is wrong). Similarly, "false negatives" denote wrong unacceptance cases, i.e., unacceptance when $\mathrm{Rate}/\mathrm{Standard} < 1$, and "true negatives" denote correct unacceptance cases, i.e., those corresponding to $\mathrm{Rate}/\mathrm{Standard} > 1$. The cases denoted as "undecided" are those for which the acceptance standard is between r_L and r_U, i.e., those for which the available data are not sufficient yet to make a decision in the "mathematical" sense (from the point of view of approval, such cases are treated as unacceptance).

For the sample size $N = 1$, the number of conclusive cases, both "positives" and "negatives", is low, whereas the number of "undecided" cases is, expectedly, large (more than 90 % for most values of the $\mathrm{Rate}/\mathrm{Standard}$ ratio). With the increasing number of the simulated stability failures, the number of "positives" to the left from the vertical line $\mathrm{Rate}/\mathrm{Standard} = 1$ increases, as well as the number of "negatives" to the right from this line, whereas the number of the "undecided" cases reduces and their range narrows towards this line. For a large sample size, e.g., $N = 1000$, the correct decision is made in 100 % of cases far from the line $\mathrm{Rate}/\mathrm{Standard} = 1$, whereas on this line, the number of wrong decisions increases to about 25 % of "false positives" and about 25 % of "false negatives"; about 50 % of cases remain "undecided".

The same data as the percentage of the acceptance cases are in Figure 11, depending on the ratio $\mathrm{Rate}/\mathrm{Standard}$ for the number of simulated stability failures $N = 1,\ 10,\ 25,\ 50,\ 100,\ 250,\ 500$ and 1000 (different lines). For the ratio $\mathrm{Rate}/\mathrm{Standard} = 0.5$, the number of accepted cases is close to 100 % for the sample sizes greater than about 50, whereas closer to the line $\mathrm{Rate}/\mathrm{Standard} = 1$, approaching 100 %-acceptance requires an increasing number of simulations.

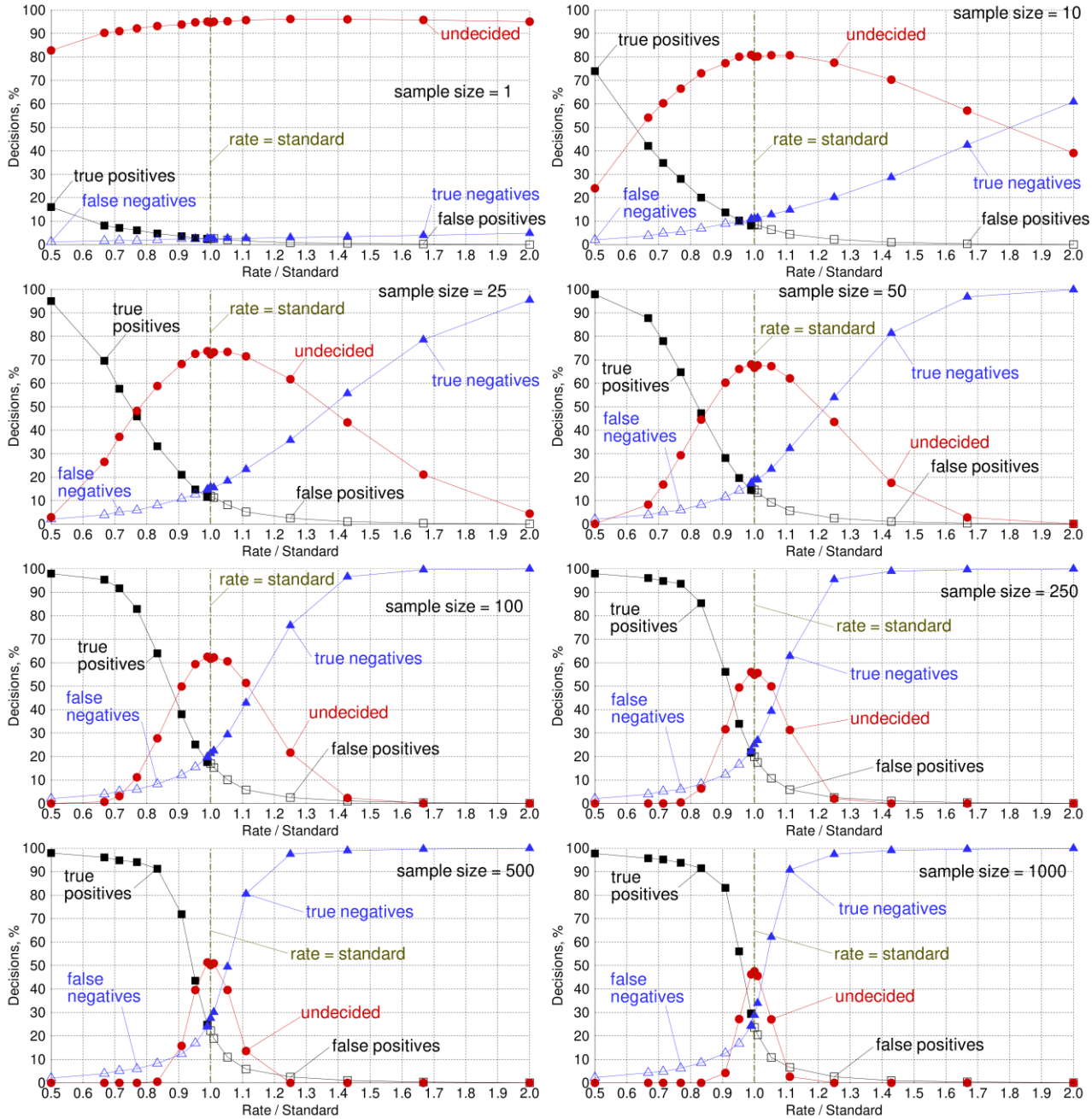

Figure 10: Percentage of outcomes ("positives", "negatives" and "undecided") vs. specified ratio of failure rate to acceptance standard for sample sizes $N = 1,\ 20,\ 25,\ 50,\ 100,\ 250,\ 500$ and 1000.

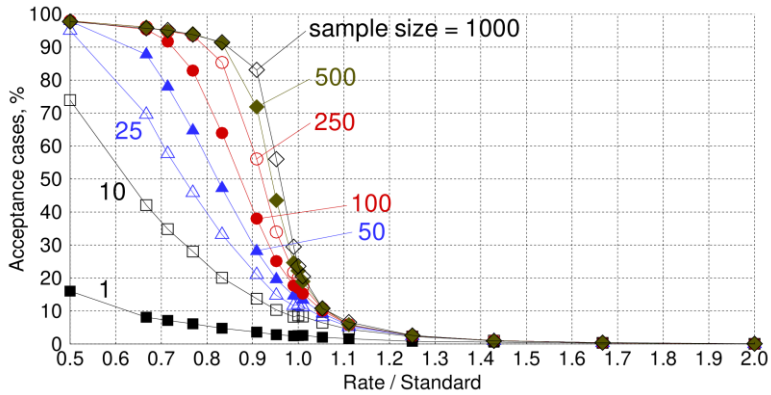

Figure 11: Percentage of acceptance cases vs. ratio of actual rate to acceptance standard for $N = 1, 10, 25, 50, 100, 250, 500$ and 1000.

The presence of acceptance cases for the ratio Rate/Standard ≥ 1 (i.e. "false positives"), which occur due to the probabilistic nature of the assessment, may seem concerning. However, the probabilistic assessment leads to about the same amount of "false negatives", i.e., unacceptance cases for the ratio Rate/Standard < 1. Besides, both "false positives" and "false negatives" occur in a very narrow segment of the ratio Rate/Standard around 1. For example, "false positive" decisions are made in not more than 5 % of all such cases, for which the true value of the failure rate exceeds the acceptance standard by up to about 15 %. However, the errors in the estimation of the failure rate from numerical simulations or model tests due to other sources of uncertainty significantly exceed 15 %.

7. CONCLUSIONS

The aim of the described effort was to compare three approaches for direct counting that are included in the draft Explanatory Notes for the IMO Second-generation intact stability criteria, MSC.1/Circ.1652. These approaches are based on the estimation of the failure rate from the sample data assuming exponential distribution of time to failure, on the estimation of the statistical frequency of failures per simulation, and on the binomial distribution of the observations of roll angle.

A comparison of these approaches was performed with data gathered from numerical simulations of ship motions in irregular long-crested beam waves. The collected datasets were found to fulfill the Poisson process assumptions. The ability of method M1 to de-cluster has been verified, whereas the declustering ability of methods M2 and M3 was not addressed.

The results in terms of the estimate of the failure rate and the upper and lower boundaries of its 95 % confidence interval obtained for seven sea states were very close between the three methods.

In practice, using a probabilistic assessment procedure based on the construction of the confidence interval can be combined with a technique that allows making the decision effectively "on the fly", i.e., during numerical simulations or model tests, taking into account the decreasing width of the confidence interval with the increasing amount of data. Such a technique allows deciding whether the decision can be already done, or further simulations are necessary. The acceptance decision depends on the sample size and the ratio of the failure rate to the acceptance standard, thus the designer has a choice whether to admit unacceptance or to continue numerical simulations or model tests to achieve, potentially, an acceptance.

This study applied numerical simulations of ship motions in beam waves. Further study should use data derived from numerical simulations of ship motions in longitudinal (head or following) waves, when the ship experiences such nonlinear phenomena as parametric roll. Another characteristic to compare is the practicability of the three methods in the actual assessment, addressing declustering of large roll motions, initial transients, and the practically relevant failure rates.

ACKNOWLEDGEMENTS

The participation of the third author in the described effort was partially supported by the US Office of Naval Research under the supervision of Dr. Woei-Min Lin.

The authors are also grateful to Mr. William Peters of the US Coast Guard and Dr. Vladas Pipiras of the University of North Carolina for fruitful discussions and encouragement.

REFERENCES

Agresti, A., Coull, B. A., 1998, "Approximate is better than 'exact' for interval estimation of binomial proportions," *The American Statistician,* 52(2) 119–126.

Beck, R, and Reed, A., 2001 "Modern Computational Methods for Ships in Seaway," *SNAME Transactions*, Vol. 109, 2001, pp. 1–51.

Belenky, V., Weems, K., Lin, W. M, Pipiras, V., and Sapsis, T., 2023, "Estimation of Probability of Capsizing with Split-Time Method," *Ocean Engineering*, Special Issue on Extreme Stochastic Dynamics Ships (to appear).

Campbell, B., Belenky, V., Pipiras, V., Sapsis, T. and Weems, K., 2023, "Estimation of Probability of Large Roll Angle with Envelope Peaks over Threshold Method," *Ocean Engineering*, Special Issue on Extreme Stochastic Dynamics Ships (to appear).

Edgeman, R. L., Scott, R. C., 1987, "Lilliefors's test for transformed variables," *Braz. J. Probability Stat*. 1, 101–112.

Hasselman, K., Barnett, T. P., Bouws, E., Carlson, H., Cartwright, D. E., Enke, K., Ewing, J. A., Gienapp, H., Hasselmann, D. E., Kruseman, P., Meerburg, A. Muller, P. , Olbers, D. J., Richter, K., Sell, W., and Walden, H., 1973,

"Measurements of Wind-Wave Growth and Swell Decay during the Joint North Sea Wave Project (JONSWAP)," Deutsches Hydrographisches Institut, Hamburg, Germany.

Hayter, A., 2012, *Probability and Statistics for Scientists and Engineers*, 4th edition, Brook/Cole, ISBN 978-1111827045, pp.173-178.

Ibe, O. C., 2014, *Fundamentals of applied probability and random processes,* (2nd ed.), Academic Press, p. 128.

IMO MSC.1/Circ. 1627, "Interim Guidelines on the Second Generation Intact Stability Criteria", London, 2020,

IMO MSC.1/Circ.1652, "Explanatory Notes to the Interim Guidelines on the Second Generation Intact Stability Criteria", May 19, London, 2023

Kapsenberg, G., Wandji, C., Duz, B. and Kim, S., P., 2020, "A Comparison of Numerical Simulations and Model Experiments on Parametric Roll in Irregular Seas," *Journal of Marine Science and Engineering*, 8(7), 474.

Leadbetter, M. R., Rychlik, I. and Stambaugh K., 2019, "Estimating Dynamic Stability Event Probabilities from Simulation and Wave Modeling Methods," *Chapter 22 of Contemporary Ideas on Ship Stability. Risk of Capsizing*, Belenky, V., Spyrou, K., van Walree F., Neves, M.A.S, and N. Umeda, eds., Springer, ISBN 978-3-030-00514-6, pp. 381-391.

Reed, A. M and Beck, R. F., 2016, "Advances in the Predictive Capability for Ship Dynamics in Extreme Waves," *Trans. SNAME*, Vol. 124, pp. 2-39.

Ross, S. M., 2009, *Introduction to Probability and Statistics for Engineers and Scientists*, 4th Edition, Academic Press, ISBN 978-0123704832.

Ryan, T., P., 2007, *Modern Engineering Statistics*, Widley-Interscience, ISBN 978-0-47008187-7, pp 1-586.

Shigunov, V., 2019, "Direct Counting Method and its Validation," *Proceeding to 17th International Ship Stability Workshop*, Helsinki, Finland, pp 119-128.

Shigunov, V., Wandji, C., A., and Belenky, V., 2022, "Benchmarking of Direct Counting Approaches," *Proceedings of 18th International Ship Stability Workshop*, pp. 167-175.

Shigunov, V., 2023, "Extrapolation of Failure Rate over Wave Height", *Ocean Engineering*, Volume 272, ISSN 0029-8018.

Söding, H., 1982, "Leckstabilität im Seegang". Report No. 429, Institut für Schiffbau, Hamburg, Germany, 69 p.

Söding, H., Shigunov, V., Zorn, T., and Soukup, P., 2013, "Method rolls for Simulating Roll Motions of Ships," *Ship Technol. Research – Schiffstechnik*, Vol.60, Nr. 2.

Spanos, D. and Papanikolaou, A., 2009, "Benchmark Study on Numerical Simulation Methods for the Prediction of Parametric Roll of Ships in Waves," *Proceeding of the 10th International Conference Stability of Ships and Ocean Vehicles*, St. Peterburg, Russia, pp. 627-636.

St Denis, M. and Pierson Jr., W., J., 1953, *On the Motions of Ships in Confused Seas*, New York University Bronx School of Engineering and Science.

Umeda, N., Munif, A., and Hashimoto, H., 2000, "Numerical Prediction of Extreme Motions and Capsizing for Intact Ships in Following/ Quartering Seas," *Proceeding of the 4th Osaka Colloquium on Seakeeping Performance of Ships*, Osaka, Japan, pp. 368-373.

Wandji, C., 2018, "Investigation on IMO Second Level Vulnerability Criteria of Parametric Rolling," *Proceedings of 13th International Conference on the Stability of Ships and Ocean Vehicles*, pp. 202-212.

Wandji, C., 2022, "Application of Statistical Extrapolation Techniques to Dynamic Stability," *Proceedings of 18th International Ship Stability Workshop*, pp. 137-147.

Weems, K., Pipiras, V. and Belenky, V., 2023, "Multifidelity Fast Code for Direct Stability Assessment," *Proceeding of 19th International Ship Stability Workshop*, Istanbul, Turkey.

A unified mathematical model for direct stability assessments of surf-riding/broaching and pure loss of stability in stern quartering waves

Jiang, Lu, *China Ship Scientific Research Center* lujiang1980@aliyun.com

Min, Gu, *China Ship Scientific Research Center* gumin702@163.com

ABSTRACT

The second-generation intact stability criteria and their explanatory notes were finalized by the IMO in 2022. However, due to their complexity, the direct stability assessments of surf-riding/broaching and pure loss of stability still need to be made easier to realize for the users. Therefore, the mathematical models for surf-riding/broaching and pure loss of stability in stern quartering waves are studied. Firstly, a time-domain surge-sway-heave-roll-pitch-yaw coupled mathematical model named 6 DOF is established combined seakeeping and maneuvering mathematical models based on an MMG standard method for ship maneuvering predictions and existing mathematical models for broaching, pure loss of stability and parametric rolling predictions. Secondly, the heave and pitch motions, the diffraction forces, added mass, and damping coefficients are obtained by an enhanced strip method with the upright hull under different speeds in the frequency domain. Then their time-domain values are transferred from their frequency-domain values with the speed variation considered. Thirdly, the 6 DOF motions are used to determine the simultaneous relative position of the ship to waves in the time domain. Then the nonlinear Froude-Krylov force and hydrostatic force in the directions of the surge, sway, roll, and yaw are calculated by integrating the wave pressure up to the wave surface. Fourthly, the rudder exposure and the wave-particle velocity are considered for predicting broaching. Finally, the numerical results are compared with the published experimental results. The results show that the 6 DOF surge-sway-heave-roll-pitch-yaw coupled mathematical model can be unified for direct stability assessment of surf-riding/broaching and pure loss of stability in stern quartering waves.

Keywords: *Surf-riding, Broaching, Pure loss of stability, Second generation stability criteria, Stability in Waves, IMO*.

LIST OF SYMBOLS

A_{ij}, B_{ij}, C_{ij} coupling seakeeping coefficients

$A_{Hij}(x), B_{Hij}(x)$ coupling seakeeping coefficients at the x section

a_H Rudder force increase factor

AE, FE After section and forward section

A_R Rudder area

A_{RP}, A_{RS} The port and starboard rudder area

$B(x)$ Sectional breadth

C_T Total resistance coefficient in calm water

C_W Wave celerity

d Ship draft

$d(x)$ Sectional draught

D_P Propeller diameter

$D(p)$ Roll damping moment

F_j^{FK} Froude-Krylov force in the j direction

F_j^{DF} Diffraction force in the j direction

F_j^B Hydrostatic force in the j direction

F_N Rudder normal force

F_n Froude number based on ship length

I_{xx}, I_{yy}, I_{zz} Inertia moments in roll, pitch, and yaw direction, respectively

N_{vrr}, Y_{vrr} The derivative of yaw moment and sway force corresponding to squared yaw rate and sway velocity, their non-dimensional are N'_{vrr}, Y'_{vrr}

N_{vvr}, Y_{vvr} The derivative of yaw moment and sway force corresponding to squared yaw rate and sway velocity, their non-dimensional N'_{vvr}, Y'_{vvr}

N_v, Y_v The derivative of yaw moment and sway force corresponding to sway velocity, their non-dimensional N'_v, Y'_v

N_{vvv}, Y_{vvv} The derivative of yaw moment and sway force corresponding to cubic sway velocity, their non-dimensional N'_{vvv}, Y'_{vvv}

k Wave number

K_ϕ, N_ϕ, Y_ϕ The derivative of roll moment, yaw moment, and sway force corresponding to roll angle, their non-dimensional $K'_\varphi, N'_\varphi, Y'_\varphi$

K_P Rudder gain

K_T Thrust coefficient of the propeller

L_{PP} Ship length between perpendiculars

L Ship length for integration

ℓ_R' Correction factor for flow-straightening due to yaw

m Ship mass

n_P Propeller revolution number

OG The vertical distance between the center of gravity and waterline

p Roll rate

r Yaw rate

R Ship resistance

$S(x)$ Sectional area

S_F Wetted hull surface area

S_H Sectional line for sectional integration

t_P Thrust deduction factor

t_R Steering resistance deduction factor

T Propeller thrust

T_E The time constant for the steering gear

T_D The time constant for differential control

T_φ Natural roll period

u, v Surge and sway velocity

u_R, v_R Longitudinal and lateral inflow velocity components to the rudder, respectively

U Ship forward velocity

w_P Wake fraction at propeller position

w_R Wake fraction at rudder position

W Ship weight

x_{HR} The longitudinal position of additional sway force due to the rudder

x_R The longitudinal position of the rudder

X_H, Y_H, N_H, K_H Surge force, sway force, yaw moment, and roll moment around the center of ship gravity acting on the ship hull

X_P Surge force due to the propeller

X_R, Y_R, N_R, K_R Surge force, sway force, yaw moment, and roll moment around the center of ship gravity by steering

X_W, Y_W, N_W, K_W Surge force, sway force, yaw moment, and roll moment around the center of ship gravity acting on the ship hull induced by waves

Z_H The vertical position of the center of sway force due to sway motion

z_{HR} The vertical position of additional sway force due to the rudder

z_R The vertical position of the center of the rudder

α The linear roll-damping coefficient

α_R Effective inflow angle to the rudder

β Hull drift angle

δ Rudder angle

δ_j The initial phase of the *j* mode ship motion

η The ratio of propeller diameter to rudder span

ε The ratio of wake fraction at the propeller and rudder position

κ Propeller-induced flow velocity factor

λ Wavelength

Λ Ruder aspect ratio

Λ_P Port ruder aspect ratio

Λ_S Starboard ruder aspect ratio

φ Roll angle

φ_0 Potential of incident waves

φ_j Potential of radiation waves in the *j* direction

φ_7 Potential of diffraction waves

γ The cubic nonlinear roll damping coefficient

γ_R Flow-straightening effect coefficient

θ Pitch angle

χ Instantaneous ship heading angle considering the yaw motion

χ_c Autopilot course or constant ship heading

ρ Water density

ω Wave frequency

ω_e Averaged encounter frequency

ξ_G The longitudinal position of the center of ship gravity from a wave trough

(ξ_G, η_G, ζ_G) Position of center of ship gravity in the space-fixed coordinate system

ζ_w Wave amplitude

j 1: surge; 2: sway; 3: heave; 4: roll; 5: pitch; 6: yaw

1. INTRODUCTION

After 20 years of efforts by worldwide researchers on stability in waves, the interim guideline on the second-generation intact stability criteria was approved by the International Maritime Organization (IMO) on 10 December 2020 (IMO, Msc.1/Circ.1627,2020). Her explanatory notes were finalized in 2022 (IMO, SDC 8/WP.4, 2022). Five stability failure models with Level 1 and 2 vulnerability criteria and direct stability assessment are included in the second-generation intact stability criteria. For evaluating the second-generation intact stability criteria, a software named HydroSTAB-CSSRC is developed by the stability group in CSSRC. Based on the methods of predicting parametric rolling guided by Prof. Naoya Umeda, the first author develops numerical methods for surf-riding/broaching and pure loss of stability at CSSRC. In addition, the documents on direct assessment methods of pure loss of stability (IMO 2023, SDC 9/INF.7) and surf-riding/broaching (IMO 2022, SDC 8/INF.4) were submitted to IMO by the authors in the Chinese Delegation. However, both surf-riding/broaching and pure loss of stability are extreme nonlinear motions in waves related to the ship's maneuvering force, the body's exact roll-restoring force, zero-encounter problem, the rudder force, and the rudder exposure in waves. Therefore, the numerical results in these documents could depend on selecting some crucial elements, and the introductions in these documents need to be more detailed. Predicting broaching and pure loss of stability accurately is still tricky at this stage. Hence, this paper tries to give detailed introductions and first unify the mathematical model of surf-riding/broaching and pure loss of stability in stern quartering waves.

The opinions expressed herein are those of the authors for academic exchange and do not reflect the views of the Chinese Delegation in IMO.

2. BACKGROUND

Surf-riding occurs when a ship is captured by a wave from the stern and forced to run with wave celerity. During surf-riding, the ship is often unstable and turns uncontrollably despite keeping a maximum rudder angle in the opposite direction, defined as broaching. Broaching is considered one of the most dangerous phenomena in following and stern-quartering waves for high-speed ships, such as destroyers and fishing vessels. For the numerical simulation of surf-riding and broaching, the numerical approach is required at least a 4 DOF mathematical model of surge-sway-roll-yaw motion in the second-generation intact stability criteria.

Prof. Umeda studied the mechanical of surf-riding in a regular wave and its probability in irregular waves in his Ph.D. thesis, and a 4 DOF mathematical model for broaching prediction (Umeda, 1999) is investigated. To provide an accurate mathematical model for broaching prediction, Umeda and Hashimoto investigated essential terms in the 4 DOF mathematical model one by one by utilizing fishing vessels. Nonlinear maneuvering forces in calm water (Umeda & Hashimoto, 2002), wave effect on linear maneuvering forces, roll restoring, and rudder forces (Umeda et al., 2003) are studied. Several nonlinear factors are further investigated, such as nonlinear wave forces, nonlinear sway-yaw coupling, wave effect on propeller thrust, heel-induced hydrodynamic forces for large heel angle in calm water (Hashimoto et al., 2004), and wave effect on heel-induced hydrodynamic forces for large heel angle(Hashimoto et al., 2011a). A simplified mathematical model is proposed for more practical use (Hashimoto et al., 2011a). Finally, the existing 4 DOF mathematical model is used for broaching predictions of the ONR tumblehome vessel, and a fair quantitative prediction is realized (Hashimoto et al., 2011b).

It is still difficult to accurately predict broaching using the ONR tumblehome with twin rudder and propellers by personal academic exchange with Prof. Hashimoto. The twin rudder forces could be one crucial factor for predicting broaching. The twin rudder normal forces are investigated by a free-running model experiment to improve a broaching numerical model (Umeda et al., 2014). Broaching is a nonlinear phenomenon related to ship maneuvering in the wave, and the above 4 DOF mathematical models are based on a Maneuvering Modeling Group (MMG) model. However, simulation methods without standard expressions could not be used in general. Therefore, an MMG standard method for ship maneuvering predictions was introduced (Yasukawa & Yoshimura, 2015). A 4 DOF mathematical model is refined for broaching prediction of the ONR flare topside vessel (Umeda et al., 2016). The effect of the above-waterline hull

shape on the broaching-induced roll was studied. The broaching probability of the tumblehome with the flare's rudder parameters is given out (Htet et al., 2019a), and the experiment of broaching in irregular waves using the tumblehome with the flare's rudder at the same wave condition was done in the new seakeeping basin (170m length, 40m width, 6m depth) of CSSRC in March 2023. The results could be discussed at STABS2024. The measured wave-induced forces and moments could be more significant than those in simulations and were used to estimate the broaching probability(Htet et al., 2019b).

It is also reported that surf-riding and broaching-to produced by the hydrodynamic code LAMP is used for evaluating probability with a split-time formulation, and its time-domain method of broaching is not published (Belenky et al., 2016a).

Once the crest of a large wave passes the midship section of the ship with a slightly higher speed than the ship speed, stability loss at the crest may exist long enough to evolve a large heel angle or even capsizing. Several freely running experiments also prove that coupling with maneuvring sway and yaw motion is essential for explaining the forward speed effect on pure loss of stability in stern-quartering waves (IMO SDC 3，2016).

In the early stage, pure loss of stability is considered as a static capsizing mode of the ship losing static restoring in waves (Paulling, 1961; Paulling et al., 1975). The study focuses on the method to calculate the GZ curve in regular and irregular waves (Kuo et al., 1986； Hamamoto & Nomoto, 1982). With the development of hydrodynamics and improved human cognition, stability loss is considered a capsizing mode of significant time-domain roll motion due to the lost roll-restoring arm at the crest and the staying time at the crest. However, the difficulty of developing criteria for pure loss of stability is not limited to calculating the GZ curve in waves (Bassler et al., 2011). The latest methods for predicting the occurrence of pure loss of stability are reviewed by Neves (Neves, 2016). The significant roll motion, even capsizing in the time domain due to the lost roll restoring at the crest and the staying time at the crest, is confirmed by comparing the mathematical roll and surge-roll coupled models in following seas (Hashimoto, 2009). This phenomenon is further confirmed with a surge-heave-roll-pitch coupled model. However, the significant roll motion may not be reproduced in the simulation and experiment in following seas without initial heel moments (Lu et al., 2019). Therefore, the time-domain simulation is focused on pure loss of stability in the second stage.

With the improvement of human cognition, stability loss is considered not "pure" in astern waves. Umeda first pointed out that pure loss of stability in stern quartering waves could not be pure, and the maneuvering sway and yaw motions could be the reason for the large rolling in stern quartering waves (Kubo et al., 2012; Umeda et al., 2019). On the other hand, the Japanese Delegation (IMO SLF55, 2013) notes that predicting pure loss of stability with their newly-developed 4 degrees of freedom (DOF) mathematical model (Kubo et al., 2012) is more accurate than the 2 DOF mathematical model (Hashimoto, 2009). Therefore, at least 4 DOF for predicting pure loss of stability is requested at this stage (IMO, SDC 8/WP.4, 2022).

A surge-sway-roll-pitch (4 DOF) standard mathematical model for pure loss of stability in stern quartering waves is tried to be established and further confirmed that the ship maneuvering motions, such as sway and yaw are also a key reason for capsizing during pure loss of stability in stern quartering waves (Lu et al., 2017a; 2018). Furthermore, a 6 DOF mathematical model is further intended to be established for pure loss of stability in stern quartering waves by using time-varied amplitude and phase of heave and pitch to calculate the restoring variation in waves, and rudder force is an essential factor for the large rolling during pure loss of stability (Lu et al., 2020, 2023).

It is also reported that pure loss of stability produced by the hydrodynamic code LAMP is used for evaluating the probability of capsizing with a split-time method. However, its time-domain method does not consider the effect of the surge, sway, yaw, and rudder. (Belenky et al., 2016b).

Both surf-riding/Broaching and pure loss of stability in astern waves are related to the ship's maneuvering force, the rudder force, and the body's exact roll-restoring force in waves. This paper intends to establish a unified numerical method in which the body's exact Froude-Krylov and hydrostatic forces are based on an existing method for parametric rolling prediction (Lu et al., 2011a, 2011b, 2016, 2017b; Umeda et al., 2008, 2015), and

maneuvering sway and yaw motions are considered. In addition, the rudder exposure and the wave-particle velocity are considered for predicting broaching.

3. MATHEMATICAL MODEL

3.1 Coordinate systems

A space-fixed coordinate system $O-\xi\eta\zeta$ with the origin at a wave trough, a body-fixed system $G-x'y'z'$ with the origin at the center of gravity of the ship, and a horizontal body coordinate system(Hamamoto & Kim, 1993) $G-xyz$ which has the exact origin with the body-fixed system but does not rotate around the x-axis and y-axis are adopted as shown in Fig.1.

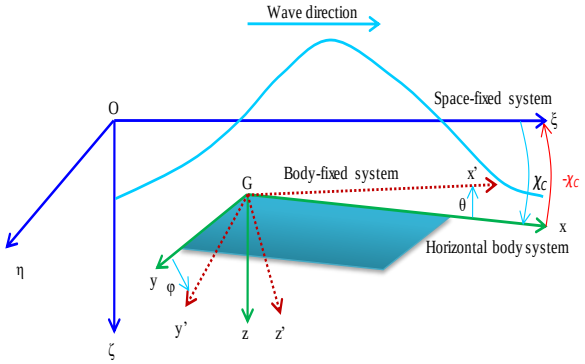

Figure 1: Coordinate systems

The ship autopilot heading angle is χ_C, and the heading angle of the incident wave is $-\chi_C$. The instantaneous heading angle χ takes the yaw motion into account.

The relationships between the horizontal body coordinate system $G-xyz$, the body-fixed system $G-x'y'z'$ and the space-fixed system $O-\xi\eta\zeta$ are shown in Eq. (1) and Eq. (2), respectively.

$$\begin{bmatrix} x \\ y \\ z \end{bmatrix} = \begin{bmatrix} \cos\theta & \sin\phi\sin\theta & \cos\phi\sin\theta \\ 0 & \cos\varphi & -\sin\varphi \\ -\sin\theta & \sin\varphi\cos\theta & \cos\varphi\cos\theta \end{bmatrix} \begin{bmatrix} x' \\ y' \\ z' \end{bmatrix} \quad (1)$$

$$\begin{bmatrix} \xi-\xi_G \\ \eta-\eta_G \\ \zeta-\zeta_G \end{bmatrix} = \begin{bmatrix} \cos\theta\ \cos\chi & \sin\varphi\ \sin\theta\ \cos\chi & \cos\varphi\ \sin\theta\ \cos\chi \\ & -\cos\varphi\ \sin\chi & +\sin\varphi\ \sin\chi \\ \cos\theta\ \sin\chi & \sin\varphi\ \sin\theta\ \sin\chi & \cos\varphi\ \sin\theta\ \sin\chi \\ & +\cos\varphi\ \cos\chi & -\sin\varphi\ \cos\chi \\ -\sin\theta & \sin\varphi\ \cos\theta & \cos\varphi\ \cos\theta \end{bmatrix} \begin{bmatrix} x' \\ y' \\ z' \end{bmatrix} \quad (2)$$

3.2 Mathematical model

The weak 6 DOF mathematical model is expressed by the surge, sway, roll, yaw, heave, and pitch motions. The surge, sway, and yaw motions are shown in Eq (3), (4), and (6), respectively, while the seakeeping model is used for the roll motion as shown in Eq. (5). The heave and pitch motions are expressed in Eq. (7) and (8), respectively. The amplitudes and phases of the heave and pitch motions in the frequency domain are calculated at each constant forward speed applied to an upright hull by a strip method using an enhanced integrating method of direct line integral to solve the velocity potential (Kashiwagi et al., 2010). The time-domain heave and pitch motions are calculated according to the ship's relative position to waves, as shown in Eq. (9) and (10), respectively. The amplitudes and phases of the heave and pitch motions do not consider the yaw angle. However, the instantaneous heading angle is considered in the time domain, as shown in Eq. (11).

The control equation for keeping course by steering is added in the weak 6 DOF mathematical model, as shown in Eq. (12).

$$\begin{aligned}&(m+A_{11})\dot{u}-(m+A_{22}(u))vr = X_H + X_P + X_R(\delta) \\ &+F_1^{FK}(\xi_G/\lambda,\zeta,\varphi,\theta,\chi)\end{aligned} \quad (3)$$

$$\begin{aligned}&(m+A_{22}(u))\dot{v}+(m+A_{11})ur = Y_H + Y_R(\delta) \\ &+F_2^{FK}(\xi_G/\lambda,\zeta,\varphi,\theta,\chi)+F_2^{DF}(\xi_G/\lambda,\chi_C,u)\end{aligned} \quad (4)$$

$$\begin{aligned}&(I_{xx}+A_{44})\dot{p}+D(p)+A_{42}(u)\dot{v}+B_{42}(u)v+A_{46}(u)\dot{r} \\ &+B_{46}r+C_{46}(\chi-\chi_C) = K_H + K_R(\delta) \\ &+F_4^{FK+B}(\xi_G/\lambda,\zeta,\varphi,\theta,\chi)+F_4^{DF}(\xi_G/\lambda,\chi_C,u)\end{aligned} \quad (5)$$

$$\begin{aligned}&(I_{zz}+A_{66}(u))\dot{r} = N_H + N_R(\delta) \\ &+F_6^{FK}(\xi_G/\lambda,\zeta,\varphi,\theta,\chi)+F_6^{DF}(\xi_G/\lambda,\chi_C,u)\end{aligned} \quad (6)$$

$$\begin{aligned}&(m+A_{33}(u))\ddot{\zeta}+B_{33}(u)\dot{\zeta}+C_{33}\zeta+A_{35}(u)\ddot{\theta} \\ &+B_{35}(u)\dot{\theta}+C_{35}\theta = F_3^{FK}(u)+F_3^{DF}(u)\end{aligned} \quad (7)$$

$$\begin{aligned}&(I_{yy}+A_{55}(u))\ddot{\theta}+B_{55}(u)\dot{\theta}+C_{55}\theta+A_{53}(u)\ddot{\zeta} \\ &+B_{53}(u)\dot{\zeta}+C_{53}\zeta = F_5^{FK}(u)+F_5^{DF}(u)\end{aligned} \quad (8)$$

$$\zeta_G(t) = \zeta_{Ga}(u)\cos[2\pi\cdot(\xi_G/\lambda)-\delta_3(u)] \quad (9)$$

$$\theta(t) = \theta_a(u)\cos[2\pi\cdot(\xi_G/\lambda)-\delta_5(u)] \quad (10)$$

$$\xi_G/\lambda = (u(t)\times\cos(\chi(t))-v(t)\sin(\chi(t))-C_W)\cdot t/\lambda \quad (11)$$

$$\dot{\delta} = \{-\delta-K_P(\chi-\chi_C)-K_PT_Dr\}/T_E \quad (12)$$

The subscripts H, R, and P refer to the hull, rudder, and propeller. Eq. (4) and (6) are the time-domain

maneuvering mathematical models of sway and yaw motions. Eq. (5) is the time-domain seakeeping mathematical model of the roll motion. Eq. (7) and (8) are the frequency-domain seakeeping mathematical models of heave and pitch motions.

3.3 Hydrodynamic forces acting on a ship hull

Hydrodynamic forces acting on a ship hull of an MMG standard method (Yasukawa & Yoshimura, 2015) is referenced with the roll motion and heel-induced hydrodynamic forces considered.

The hull forces in still water X_H, Y_H, K_H and N_H are expressed as follows referring to the references (Yasukawa & Yoshimura, 2015; Umeda et al., 2016):

$$X_H = -R(u) \tag{13}$$

$$\begin{aligned} Y_H = \frac{1}{2}\rho L_{pp} d U^2 (&Y_v' \cdot v' + Y_r' \cdot r' + Y_\varphi' \cdot \varphi \\ &+ Y_{vvv}' \cdot v'^3 + Y_{vvr}' \cdot v'^2 r' + Y_{vrr}' \cdot v' r'^2 + Y_{rrr}' \cdot r'^3) \end{aligned} \tag{14}$$

$$K_H = \frac{1}{2}\rho L_{pp} d^2 U^2 (K_\varphi' + Y_\varphi' \frac{OG}{d}) \cdot \varphi \tag{15}$$

$$\begin{aligned} N_H = \frac{1}{2}\rho L_{pp}^2 d U^2 (&N_v' \cdot v' + N_r' \cdot r' + N_\varphi' \cdot \varphi \\ &+ N_{vvv}' \cdot v'^3 + N_{vvr}' \cdot v'^2 r' + N_{vrr}' \cdot v' r'^2 + N_{rrr}' \cdot r'^3) \end{aligned} \tag{16}$$

where v', r' denote non-dimensional sway velocity, and yaw rate, respectively, and are expressed as follows:

$$v' = \frac{v}{U} \quad , r' = \frac{r L_{pp}}{U} \tag{17}$$

3.4 Propeller thrust and the hull resistance in still water

The surging force due to propeller thrust X_P with twin propellers is expressed as follows, and the wave-particle velocity at the position of port propeller and starboard propeller u_{PP}^W, u_{PS}^W is considered for broaching.

$$X_P = (1-t_P)(T_P + T_S) \tag{18}$$

$$\begin{aligned} T_P &= (1-t_p)\rho n_P^2 D_P^4 K_T(J_{PP}) \\ T_S &= (1-t_p)\rho n_P^2 D_P^4 K_T(J_{PS}) \end{aligned} \tag{19}$$

$$\begin{aligned} J_{PP} &= \frac{(1-w_P)u - u_{PP}^W}{n_P D_P} \\ J_{PS} &= \frac{(1-w_P)u - u_{PS}^W}{n_P D_P} \end{aligned} \tag{20}$$

$$\begin{aligned} u_{PP}^W &= -\zeta_a \omega_e \cos\chi \exp(-kz_{PP}) \\ &\quad \cdot \cos[2\pi \cdot (\xi_G / \lambda) + kx_P \cos\chi - ky_{PP} \sin\chi] \\ u_{PS}^W &= -\zeta_a \omega_e \cos\chi \exp(-kz_{PS}) \\ &\quad \cdot \cos[2\pi \cdot (\xi_G / \lambda) + kx_P \cos\chi - ky_{PS} \sin\chi] \end{aligned} \tag{21}$$

The hull resistance in still water R in the surge motion is expressed as follows:

$$R = \frac{1}{2}\rho S_F u^2 C_T(\frac{u}{\sqrt{gL_{PP}}}) \tag{22}$$

3.5 Hydrodynamic force by steering

Hydrodynamic forces acting on a ship hull of an MMG standard method (Yasukawa & Yoshimura, 2015) are referenced with the heeling effect added.

The steering rudder forces components X_R, Y_R, N_R and K_R with twin rudders (Khanfir, et al., 2011) are referred to and expressed as follows (S: starboard; P: port). The average values of $\overline{\gamma_R}$, $\overline{\ell_R'}$ are used in this paper.

The rudder exposure and the wave-particle velocity at the position of port rudder and starboard rudder u_{RP}^W, u_{RS}^W are considered for broaching.

$$X_R = -(1-t_R)(F_{NP} + F_{NS})\sin\delta \tag{23}$$

$$Y_R = -(1+a_H)(F_{NP} + F_{NS})\cos\delta \cdot \cos\varphi \tag{24}$$

$$N_R = -(x_R + a_H x_{HR})(F_{NP} + F_{NS})\cos\delta \cdot \cos\varphi \tag{25}$$

$$K_R = (z_R + a_H z_{HR})(F_{NP} + F_{NS})\cos\delta \tag{26}$$

where

$$\begin{aligned} F_{NP} &= \frac{1}{2}\rho A_{RP}(u_{RP}^2 + v_R^2) f_{\alpha P} \sin\alpha_{RP} \\ F_{NS} &= \frac{1}{2}\rho A_{RS}(u_{RS}^2 + v_R^2) f_{\alpha S} \sin\alpha_{RS} \end{aligned} \tag{27}$$

$$\begin{aligned} u_{RP} &= \varepsilon\left(1-w_p\right)(u - y_{RP} \cdot r) \\ &\quad \cdot \sqrt{\eta\left\{1+\kappa\left(\sqrt{1+\frac{8K_T(J_{PP})}{\pi J_{PP}^2}}-1\right)\right\}^2 + 1 - \eta} \\ &\quad - u_{RP}^W \\ u_{RS} &= \varepsilon\left(1-w_p\right)(u - y_{RS} \cdot r) \\ &\quad \cdot \sqrt{\eta\left\{1+\kappa\left(\sqrt{1+\frac{8K_T(J_{PS})}{\pi J_{PS}^2}}-1\right)\right\}^2 + 1 - \eta} \\ &\quad - u_{RS}^W \end{aligned} \tag{28}$$

$$v_R = \bar{\gamma}_R U(\beta - \bar{\ell}'_R r') \tag{29}$$

$$\alpha_{RP} = \delta - \bar{\gamma}_R \frac{U}{u_{RP}}(\beta - \bar{\ell}'_R r') \tag{30}$$
$$\alpha_{RS} = \delta - \bar{\gamma}_R \frac{U}{u_{RS}}(\beta - \bar{\ell}'_R r')$$

$$\bar{\gamma}_R = \frac{1}{2}(\gamma_{R(s)} + \gamma_{R(P)}) \tag{31}$$

$$\bar{\ell}'_R = \frac{1}{2}(\ell'_{R(s)} + \ell'_{R(P)}) \tag{32}$$

$$f_{\alpha P} = \frac{6.13\Lambda_P}{2.25 + \Lambda_P} \tag{33}$$
$$f_{\alpha S} = \frac{6.13\Lambda_S}{2.25 + \Lambda_S}$$

$$\varepsilon = \frac{1 - w_R}{1 - w_P} \tag{34}$$

$$\eta = \frac{D_P}{H_R} \tag{35}$$

$$\beta = \arctan(\frac{-v}{u}) \tag{36}$$

$$U = \sqrt{u^2 + v^2} \tag{37}$$

$$\begin{aligned}
\zeta_{W_RP} &= \zeta_W \cos k[\xi_G + x_R \cos\chi\cos\theta \\
&\quad + y_{RP}(\cos\chi\sin\theta\sin\varphi - \sin\chi\cos\varphi) \\
&\quad + z_{RP_top}(\cos\chi\sin\theta\cos\varphi + \sin\chi\sin\varphi)] \\
\zeta_{Ship_RP} &= \zeta_G - x_R\sin\theta + y_{RP}\cos\theta\sin\varphi + z_{RP_top}\cos\theta\cos\varphi \\
D_{RP-W} &= \zeta_{Ship_RP} - \zeta_{W_RP}
\end{aligned} \tag{38}$$

$$\begin{aligned}
\zeta_{W_RS} &= \zeta_W \cos k[\xi_G + x_R \cos\chi\cos\theta \\
&\quad + y_{RS}(\cos\chi\sin\theta\sin\varphi - \sin\chi\cos\varphi) \\
&\quad + z_{R_top}(\cos\chi\sin\theta\cos\varphi + \sin\chi\sin\varphi)] \\
\zeta_{Ship_RS} &= \zeta_G - x_R\sin\theta + y_{RS}\cos\theta\sin\varphi + z_{R_top}\cos\theta\cos\varphi \\
D_{RS-W} &= \zeta_{Ship_RS} - \zeta_{W_RS}
\end{aligned}$$

$$A_{RP} = A_R + D_{RP-W} \cdot \sqrt{\frac{A_R}{\Lambda}} \quad (if\ D_{RP-W} < 0) \tag{39}$$
$$A_{RS} = A_R + D_{RP-W} \cdot \sqrt{\frac{A_R}{\Lambda}} \quad (if\ D_{RS-W} < 0)$$

$$\Lambda_P = [\sqrt{A_R\Lambda} + D_{RP-W}]/\sqrt{A_R/\Lambda} \quad (if\ D_{RP-W} < 0) \tag{40}$$
$$\Lambda_S = [\sqrt{A_R\Lambda} + D_{RS-W}]/\sqrt{A_R/\Lambda} \quad (if\ D_{RS-W} < 0)$$

3.6 Excited wave force

The wave-induced forces, including the Froude-Krylov force (F_j^{FK}), and the diffraction force (F_j^{DF}) are rewritten as follows referring to the reference (Kashiwagi,1995; Kashiwagi et al.,2010).

A ship advances with a constant speed u and oscillates with a circular frequency ω_e in deep water. With the assumption of linearized potential flow, the velocity potential and the excited wave forces F_j^{FK} and F_j^{DF} are given out by Kashiwagi et al. in the reference (Kashiwagi,1995; Kashiwagi et al.,2010) and their seakeeping book according to the slender ship theory. The excited wave forces F_j^{FK} and F_j^{DF} are re-obtained detailed as follows, according to the reference (Kashiwagi,1995; Kashiwagi et al.,2010). n_j denotes the $j-th$ component of the unit normal vector, and $s_{H(x)}$ is the sectional contour at station x . The method of subsection integration is used from step 2 to step 3 in Equation (40)

$$\begin{aligned}
F_j^{FK}(\xi_G/\lambda,u,\zeta,\theta,\chi) &= \frac{\rho g\zeta_w}{i\omega}\int_L\left\{\int_{S_H} n_j(i\omega_e - u\frac{\partial}{\partial x})\varphi_0 d\ell\right\}dx \\
&= \frac{\rho g\zeta_w}{i\omega}\int_L\left\{\int_{S_H}\left[(i\omega_e + iku\cos\beta)n_j e^{-kz-ik[x\cos\chi+y\sin(-\chi)]}\right]d\ell\right\}dx \\
&= \rho g\zeta_w\int_L e^{-ikx\cos\chi}\left\{\int_{S_H} e^{-kz-ik[x\cos\chi+y\sin(-\chi)]}n_j d\ell\right\}dx \\
&(j = 2,3,4,5,6)
\end{aligned} \tag{41}$$

$$\begin{aligned}
F_j^{FK}(t) &= \left|F_j^{FK}(\xi_G/\lambda,u,\zeta,\theta,\varphi,\chi)\right|\cdot\cos\left\{2\pi\cdot(\xi_G/\lambda) - \delta_j^{FK}\right\} \\
&\quad (j = 2,3,4,5,6) \\
F_1^{FK}(t) &= -\rho g\zeta_w k\cos\chi\int_{AE}^{FE} C_1(x)S(x)e^{-kd(x)/2}\sin k(\xi_G + x\cos\chi)dx \\
C_1 &= \frac{\sin(k\sin\chi\cdot B(x)/2)}{k\sin\chi\cdot B(x)/2}
\end{aligned} \tag{42}$$

$$\begin{aligned}
F_j^{DF}(u,\chi) &= \frac{\rho g\zeta_w}{i\omega}\int_L\left\{\int_{S_H} n_j(i\omega_e - u\frac{\partial}{\partial x})\varphi_7 d\ell\right\}dx \\
&= \frac{\rho g\zeta_w}{i\omega}\int_L\left\{\int_{S_H}(i\omega_e n_j\varphi_7 - u\cdot n_j\frac{\partial\varphi_7}{\partial x})d\ell\right\}dx \\
&= \frac{\rho g\zeta_w}{i\omega}\int_L\left\{\int_{S_H}(i\omega_e n_j\varphi_7 + u\varphi_7\frac{\partial n_j}{\partial x})d\ell\right\}dx \\
&= \frac{\rho g\zeta_w}{i\omega}\int_L\left\{\int_{S_H}\left[i\omega_e n_j k_0 e^{-k_0 z - ik_0 x\cos\chi}(i\sin(-\chi)\varphi_2 + \varphi_3)\right]d\ell\right\}dx \\
&\quad + \frac{\rho g\zeta_w}{i\omega}\int_L\left\{\int_{S_H}\left[uk_0 e^{-k_0 z - ik_0 x\cos\chi}(i\sin(-\chi)\varphi_2 + \varphi_3)\frac{\partial n_j}{\partial x}\right]d\ell\right\}dx \\
&= -\zeta_w\omega\omega_e\int_L e^{-k_0 z - ik_0 x\cos\chi}\left\{-\rho\int_{S_H}\left[(i\sin(-\chi)\varphi_2 + \varphi_3)(n_j + \frac{u}{i\omega_e}\frac{\partial n_j}{\partial x}\right]d\ell\right\}dx \\
&(j = 2,3,4,5,6)
\end{aligned} \tag{43}$$

$$F_2^{DF}(u,\chi)=-\zeta_w\omega\omega_e\int_L e^{-k_0z-ik_0x\cos\chi}\left\{-\rho\int_{S_H}\left[(i\sin(-\chi)\varphi_2+\varphi_3)(n_2+\frac{u}{i\omega_e}\frac{\partial n_2}{\partial x}\right]d\ell\right\}dx$$
$$=-\zeta_w\omega\omega_e\int_L e^{-k_0z-ik_0x\cos\chi}\left\{-\rho\int_{S_H}\left[(i\sin(-\chi)\varphi_2n_2+\varphi_3n_2)\right]d\ell\right\}dx$$
$$=-\zeta_w\omega\omega_e\int_L e^{-k_0z-ik_0x\cos\chi}\left\{i\sin(-\chi)(-\rho\int_{S_H}\varphi_2n_2d\ell)+(-\rho\int_{S_H}\varphi_3n_2d\ell)\right\}dx$$
$$=-\zeta_w\omega\omega_e\int_L e^{-k_0z-ik_0x\cos\chi}\left\{i\sin(-\chi)\left[A_{H22}(x)+\frac{1}{i\omega_e}B_{H22}(x)\right]+\left[A_{H23}(x)+\frac{1}{i\omega_e}B_{H23}(x)\right]\right\}dx \quad (44)$$

$$F_3^{DF}(u,\chi)=-\zeta_w\omega\omega_e\int_L e^{-k_0z-ik_0x\cos\chi}\left\{-\rho\int_{S_H}\left[(i\sin(-\chi)\varphi_2+\varphi_3)(n_3+\frac{u}{i\omega_e}\frac{\partial n_3}{\partial x}\right]d\ell\right\}dx$$
$$=-\zeta_w\omega\omega_e\int_L e^{-k_0z-ik_0x\cos\chi}\left\{-\rho\int_{S_H}\left[(i\sin(-\chi)\varphi_2n_3+\varphi_3n_3)\right]d\ell\right\}dx$$
$$=-\zeta_w\omega\omega_e\int_L e^{-k_0z-ik_0x\cos\chi}\left\{-\rho\int_{S_H}\varphi_3n_3d\ell+i\sin(-\chi)(-\rho\int_{S_H}\varphi_2n_3d\ell)\right\}dx$$
$$=-\zeta_w\omega\omega_e\int_L e^{-k_0z-ik_0x\cos\chi}\left\{\left[A_{H33}(x)+\frac{1}{i\omega_e}B_{H33}(x)\right]+i\sin(-\chi)\left[A_{H23}(x)+\frac{1}{i\omega_e}B_{H23}(x)\right]\right\}dx \quad (45)$$

$$F_4^{DF}(u,\chi)=-\zeta_w\omega\omega_e\int_L e^{-k_0z-ik_0x\cos\chi}\left\{-\rho\int_{S_H}\left[(i\sin(-\chi)\varphi_2+\varphi_3)(n_4+\frac{u}{i\omega_e}\frac{\partial n_4}{\partial x}\right]d\ell\right\}dx$$
$$=-\zeta_w\omega\omega_e\int_L e^{-k_0z-ik_0x\cos\chi}\left\{-\rho\int_{S_H}\left[(i\sin(-\chi)\varphi_2n_4+\varphi_3n_4)\right]d\ell\right\}dx$$
$$=-\zeta_w\omega\omega_e\int_L e^{-k_0z-ik_0x\cos\chi}\left\{i\sin(-\chi)(-\rho\int_{S_H}\varphi_2n_4d\ell)+(-\rho\int_{S_H}\varphi_3n_4d\ell)\right\}dx$$
$$=-\zeta_w\omega\omega_e\int_L e^{-k_0z-ik_0x\cos\chi}\left\{i\sin(-\chi)\left[A_{H24}(x)+\frac{1}{i\omega_e}B_{H24}(x)\right]+\left[A_{H34}(x)+\frac{1}{i\omega_e}B_{H34}(x)\right]\right\}dx \quad (46)$$

$$F_5^{DF}(u,\chi)=-\zeta_w\omega\omega_e\int_L e^{-k_0z-ik_0x\cos\chi}\left\{-\rho\int_{S_H}\left[(i\sin(-\chi)\varphi_2+\varphi_3)(n_5+\frac{u}{i\omega_e}\frac{\partial n_5}{\partial x}\right]d\ell\right\}dx$$
$$=-\zeta_w\omega\omega_e\int_L e^{-k_0z-ik_0x\cos\chi}\left\{-\rho\int_{S_H}\left[(i\sin(-\chi)\varphi_2+\varphi_3)(-xn_3-\frac{u}{i\omega_e}n_3)\right]d\ell\right\}dx$$
$$=-\zeta_w\omega\omega_e\int_L e^{-k_0z-ik_0x\cos\chi}\left\{-\rho\int_{S_H}\left[(-1)(x+\frac{u}{i\omega_e})(i\sin(-\chi)\varphi_2+\varphi_3)n_3\right]d\ell\right\}dx$$
$$=\zeta_w\omega\omega_e\int_L e^{-k_0z-ik_0x\cos\chi}(x+\frac{u}{i\omega_e})\left\{-\rho\int_{S_H}\varphi_3n_3d\ell+i\sin(-\chi)(-\rho\int_{S_H}\varphi_2n_3d\ell)\right\}dx$$
$$=\zeta_w\omega\omega_e\int_L e^{-k_0z-ik_0x\cos\chi}(x+\frac{u}{i\omega_e})\left\{\left[A_{H33}(x)+\frac{1}{i\omega_e}B_{H33}(x)\right]+i\sin(-\chi)\left[A_{H23}(x)+\frac{1}{i\omega_e}B_{H23}(x)\right]\right\}dx \quad (47)$$

$$F_6^{DF}(u,\chi)=-\zeta_w\omega\omega_e\int_L e^{-k_0z-ik_0x\cos\chi}\left\{-\rho\int_{S_H}\left[(i\sin(-\chi)\varphi_2+\varphi_3)(n_6+\frac{u}{i\omega_e}\frac{\partial n_6}{\partial x}\right]d\ell\right\}dx$$
$$=-\zeta_w\omega\omega_e\int_L e^{-k_0z-ik_0x\cos\chi}\left\{-\rho\int_{S_H}\left[(i\sin(-\chi)\varphi_2+\varphi_3)(xn_2+\frac{u}{i\omega_e}n_2)\right]d\ell\right\}dx$$
$$=-\zeta_w\omega\omega_e\int_L e^{-k_0z-ik_0x\cos\chi}\left\{-\rho\int_{S_H}\left[(x+\frac{u}{i\omega_e})(i\sin(-\chi)\varphi_2+\varphi_3)n_2\right]d\ell\right\}dx$$
$$=-\zeta_w\omega\omega_e\int_L e^{-k_0z-ik_0x\cos\chi}(x+\frac{u}{i\omega_e})\left\{i\sin(-\chi)(-\rho\int_{S_H}\varphi_2n_2d\ell)-\rho\int_{S_H}\varphi_3n_2d\ell\right\}dx$$
$$=-\zeta_w\omega\omega_e\int_L e^{-k_0z-ik_0x\cos\chi}(x+\frac{u}{i\omega_e})\left\{i\sin(-\chi)\left[A_{H22}(x)+\frac{1}{i\omega_e}B_{H22}(x)\right]+\left[A_{H32}(x)+\frac{1}{i\omega_e}B_{H32}(x)\right]\right\}dx \quad (48)$$

The lift force of the after and forward sections is also considered based on the strip theory.

The added mass (A_{ij}), the wave damping coefficient (B_{ij}), and the restoring coefficient (C_{ij}) used in this paper are given by the following formulas. The divergence at a low encounter frequency is checked by referring to STFM and OSM strip theory. Some formulas of radiation forces in the STFM are the same as those in the OSM, and some of those of radiation forces are not the same. (OSM, STFM) means the formulas of radiation forces are identical in the STFM and OSM. The OSM formulas of A_{22} and A_{66} are used because the STFM formulas of A_{22} and A_{66} are divergent with a low-encounter frequency. Eq. (54) is used for A_{46} and B_{46} to avoid divergence with a low-encounter frequency. The radiation forces are divergent with a near zero-encounter frequency, but an interpolation method is used for the radiation forces with a near zero-encounter frequency avoiding directly calculating these values with a near zero-encounter frequency.

$$A_{22}=\int A_{H22}dx \quad (OSM) \quad (49)$$

$$A_{33}=\int M_{33}dx+\frac{u}{\omega_e^2}[N_{33}]_{AE}^{FE} \quad (STFM)$$
$$B_{33}=\int N_{33}dx-U[M_{33}]_{AE}^{FE} \quad (STFM) \quad (50)$$
$$C_{33}=\rho g\int\{y_S(x)-y_P(x)\}dx \quad (STFM)$$

$$A_{35}=-\int x\cdot A_{H35}dx-\frac{u}{\omega_e^2}\int B_{H33}dx-\frac{u}{\omega_e^2}[x\cdot B_{H33}]_{AE}^{FE}+\frac{u^2}{\omega_e^2}[x\cdot A_{H33}]_{AE}^{FE} \quad (STFM)$$
$$B_{35}=-\int x\cdot B_{H33}dx+u\int A_{H33}dx+u[x\cdot A_{H33}]_{AE}^{FE}+\frac{u^2}{\omega_e^2}[B_{H33}]_{AE}^{FE} \quad (STFM) \quad (51)$$
$$C_{35}=-\rho g\int x\cdot\{y_S(x)-y_P(x)\}dx \quad (STFM)$$

$$A_{42}=A_{24}=\int A_{H42}dx \quad (OSM, STFM)$$
$$B_{42}=B_{24}=\int B_{H42}dx-U[M_{H42}]_{AE}^{FE} \quad (OSM, STFM) \quad (52)$$
$$C_{42}=0.0$$

$$I_{xx}+A_{44}=m\cdot g\cdot GM\cdot(\frac{T_\varphi}{2\pi})^2 \quad (53)$$

$$A_{46}=\int x\cdot A_{H42}dx+\frac{u}{\omega_e^2}\int B_{H42}dx-\frac{u}{\omega_e^2}[x\cdot B_{H42}]_{AE}^{FE} \quad (STFM\ without\ \frac{u^2}{\omega_e^2}[A_{H42}]_{AE}^{FE})$$
$$B_{46}=\int x\cdot B_{H42}dx-u\int A_{H42}dx-u[x\cdot A_{H42}]_{AE}^{FE} \quad (STFM\ without\ \frac{u^2}{\omega_e^2}[B_{42}]_{AE}^{FE}) \quad (54)$$
$$C_{46}=-u\int B_{H42}dx+u^2[A_{H42}]_{AE}^{FE}$$

$$A_{55}=\int x^2\cdot A_{H33}dx+\frac{U^2}{\omega_e^2}\int A_{H33}dx+\frac{U}{\omega_e^2}[x^2\cdot B_{H33}]_{AE}^{FE}-\frac{U^2}{\omega_e^2}[x^2\cdot A_{H33}]_{AE}^{FE} \quad (STFM)$$
$$B_{55}=\int B_{H33}dx+\frac{U^2}{\omega_e^2}\int B_{H33}dx-U[x^2\cdot A_{H33}]_{AE}^{FE}-\frac{U^2}{\omega_e^2}[x\cdot B_{H33}]_{AE}^{FE} \quad (STFM) \quad (55)$$
$$C_{55}=\rho g\int x^2\cdot\{y_S(x)-y_P(x)\}dx \quad (STFM)$$

$$A_{66}=\int x^2\cdot A_{H22}dx \quad (OSM) \quad (56)$$

3.7 Roll restoring force variation.

Pure loss of stability is one of the problems related to the roll restoring force variation. The discussion on the forces in the roll direction for pure loss of stability can be referred to in the reference (Lu et al., 2023).

3.8 Roll damping moment

Roll damping is one of the essential terms for predicting significant amplitude roll motion. The roll damping moment is calculated by linear and cubic nonlinear roll damping coefficients, as shown in the reference (Lu et al., 2023).

4. EXPERIMENTS

The free-running experiment with a 1/40.526 scaled model of the ONR (The Office of Naval Research in USA) tumblehome vessel was conducted in the seakeeping basin (length: 69m, breadth: 46m, depth: 4m) of China Ship Scientific Research Center according to the test guidelines in the ITTC.

The principal particulars and the lines of the ONR tumblehome vessel are shown in Table 1 and Fig.2, respectively. The system parameters of the ONR tumblehome used in this mathematical model, as shown in Table 2. The maneuvering coefficients used in this paper referring to the reference (Araki et al., 2012) are not given out here.

Note: BR is broaching, and PL is pure loss of stability in Table 1.

Table 1 Principal particulars of the ONR tumblehome

Items	Ship-BR	Ship-PL
Length:L_{PP}	154.000m	154.000m
Draft:d	5.494m	5.494m
Breadth:B	18.800m	18.800m
Depth:D	14.5m+top	14.500m
Displ.:W	8507ton	8507ton
C_B	0.535	0.535
GM	2.068m	1.480m
OG	-2.178m	-2.767m
L_{CB}	-2.569m	-2.569m
T_φ	12.380s	14.000s
κ_{xx}/B	0.472	0.451
κ_{yy}/L_{pp}	0.250	0.250
κ_{zz}/L_{pp}	0.250	0.250
$2\times A_R$	2×28.639m^2	2×23.740 m^2
$x_{R\ from\ middle}$	-70.110m	-70.110m
y_R	±3.090m	±3.090m
$z_{R\ from\ waterline}$	4.691m	4.691m
$x_{HR\ from\ middle}$	-66.211m	-66.211m
$z_{HR\ from\ waterline}$	4.691m	4.691m
z_{R_top}	1.602m	1.602m
D_p	5.220m	5.220m
$x_{P\ from\ middle}$	-66.211m	-66.211m
y_P	±4.093m	±4.093m
$z_{P\ from\ waterline}$	5.490m	5.490m
$\delta_{\max}$	35degrees	35degrees

Table 2 System parameters of the ONR tumblehome used in this mathematical model

Items	Ship-BR	Ship-PL
m_x/m	0.015	0.015
K_P	3.000	3.000
T_D	0.000	0.000
T_E	0.100	0.100
t_P	0.250	0.250
w_P	0.150	0.150
z_H/d	0.852	0.852
Λ	1.180	1.180
κ	0.647	0.647
ε	0.932	0.932
t_R	0.677	0.677
a_H	-0.157	0.250
$x_R+a_H x_{HR}$	-57.5m	83.4m
$z_R+a_H z_{HR}$	5.790m	5.790m
$\overline{\gamma_R}$	0.472	0.472
$\overline{\ell'_R}$	-1.000	-1.000

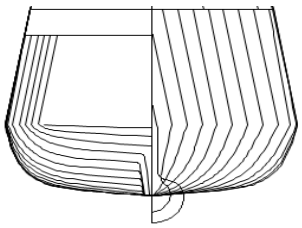

Fig.2: The ONR Tumblehome lines

The ship model was free running in astern waves with twin propellers and rudders. During the free-running tests, the 6 DOF optical fiber gyroscope was placed on the ship model to measure the roll, pitch, and yaw angle. An onboard system was connected to an onshore control computer by wireless data transfer to record the roll, pitch, yaw, rudder angles, and propeller rotation speed. A servo-needle wave height sensor was attached to a steel bridge which is 78 m in length and spans over the basin to measure the wave elevation at the middle of the basin. A total station system is used to record the position of the ship model with a specified propeller rate in calm water, and then one specified propeller rate corresponding to one nominal speed in calm water is obtained. The same specified propeller rate in calm water is used to achieve the same nominal speed in the free-running experiments in astern waves.

First, two workmen keep the model with a zero forward speed and an initial heading angle near the wave maker. Next, the waves are generated by the wave-making system. Then, the propeller rate is increased up to the specified value after receiving the order from the onshore control computer. Finally, the ship model is released near one wave crest with its initial heading when the wave train propagates far enough, and then the model automatically runs in astern waves with its specified propeller rate and autopilot course.

A PD control system is used for course keeping which reacts according to the bias between the instantaneous heading angle measured by the gyroscope and the autopilot course, and the yaw velocity measured by the gyroscope. The rudder gain is set based on experience according to the reaction of course keeping in calm water.

The ship model in the free-running experiment is shown in Figs. 3 and 4.

Fig.3: The free-running experiment of broaching with the tumblehome in CSSRC

Fig.4: The free-running experiment of pure loss of stability with the tumblehome in CSSRC

5. SIMULATIONS AND DISCUSSIONS

5.1 Validation of the MMG in calm water

The mathematical model is based on the framework of MMG, and the maneuvering coefficients and the rudder parameters are significant for predicting broaching. For testing the MMG in calm water, the following mathematical model is used for the roll motion.

$$\left(I_{xx}+A_{44}\right)\dot{p}-m_x z_H u r-m_y z_H \dot{v}=Y_H\cdot Z_H+K_R(\delta) \quad (57)$$
$$-D(p)-m\cdot g\cdot GZ(\varphi)$$

The manoeuvring coefficients of the ONR tumblehome were obtained from model tests by Umeda (Umeda et al., 2008). The manoeuvring coefficients and the rudder coefficients were used in one system-based model by Araki et al. (2012). However, the manoeuvring coefficients and the rudder coefficients used by Araki et al. (2012) with a standard MMG model could not produce a good agreement of turning circles in calm water with both rudder angel 25 degrees and 35 degrees. The CFD methods are also checked that producing a good agreement of turning circles in calm water with both rudder angel 25 degrees and 35 degrees is challenging.

Some sensitivity rudder coefficients are adjusted, as shown in this paper, such as $a_H, \overline{\gamma_R}, \overline{\ell_R}$. The a_H value is -0.157 for the ONR flare topside vessel, and the a_H value is 0.0879 for the ONR tumblehome vessel in the reference (Umeda et al.,2014). The a_H value is usually about 0.3, according to empirical. The a_H value of -0.157 is used here.

Before predicting broaching, the effectiveness of the mathematical model in calm water should be checked. By comparing the experimental results from the references (Araki et al.,2012; Sanada et al., 2013), the maneuvering coefficients (Araki et al., 2012) and the rudder coefficients in this mathematical model for broaching which are given out in the Table 2 can produce agreement results of surge velocity, sway velocity, yaw rate, heeling angle and trajectories of turning circle for rudder angle 25 degree and 35 degrees, respectively, as shown in Figs.5 and 6. That means the rudder with the a_H value of -0.157 and other coefficients used in this paper can produce a balancing force with the manoeuvring force of the ship.

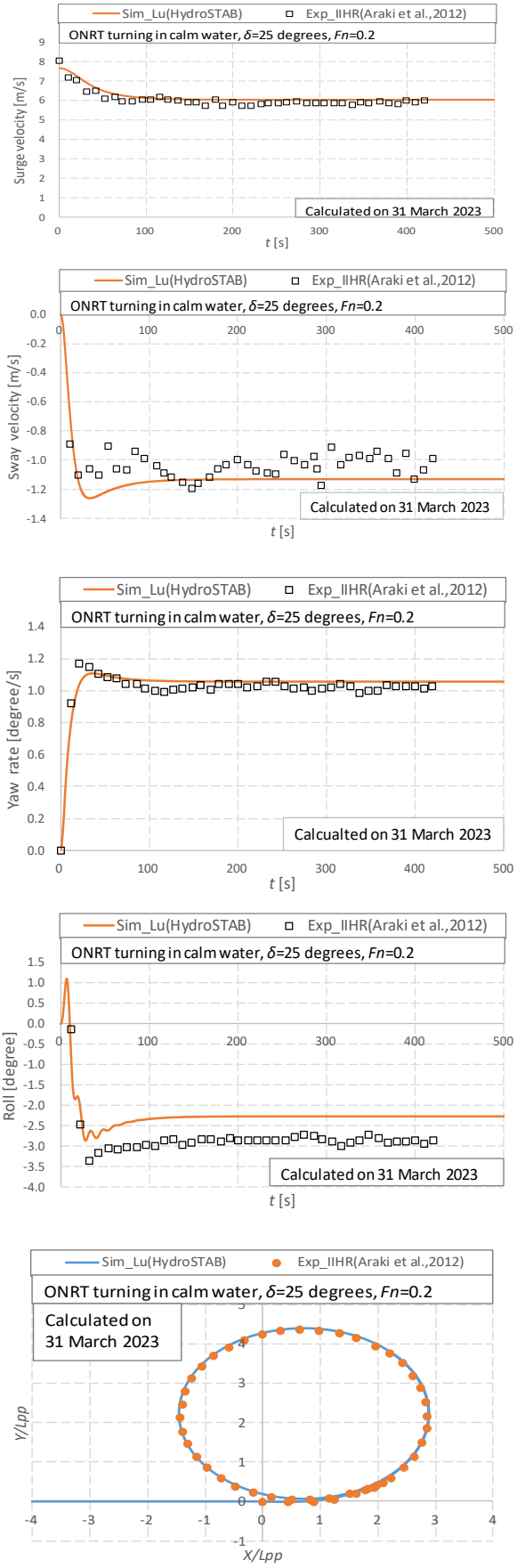

Figure 5: ONRT turning in calm water with δ=25 degrees and *Fn*=0.2.

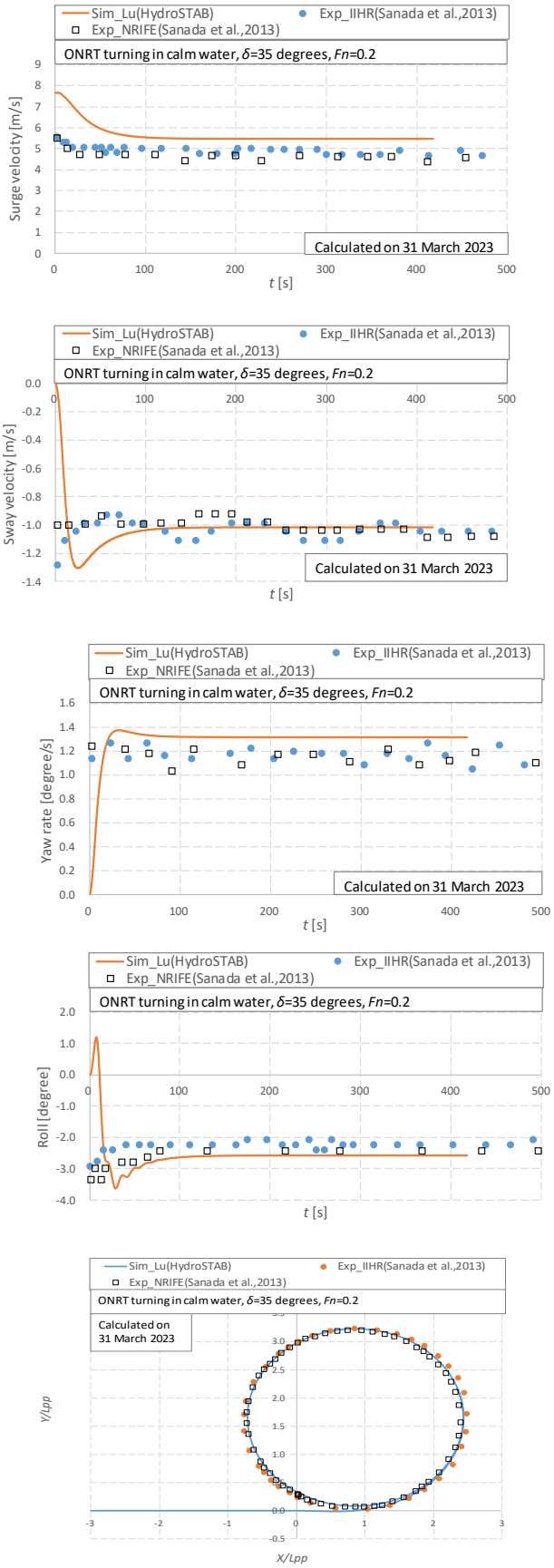

Figure 6: ONRT turning in calm water with δ=35 degrees and *Fn*=0.2.

5.2 Validation of the seakeeping motions

The time-domain heave and pitch motions obtained by a nonlinear strip method applied to an upright hull are used to determine the simultaneous relative position of the ship to waves in the time domain for predicting parametric roll, which is recommended by Prof. Umeda. The method is further utilized by using time-varied amplitude and phase of heave and pitch to calculate the restoring variation in waves for predicting pure loss of stability by Jiang Lu (Lu et al., 2019;2020,2023).

Surf-riding/broaching and pure loss of stability are related to a low encounter frequency of seakeeping motions. For validating the seakeeping motions, the authors calculated sway, heave, roll, pitch, and yaw motions with OSM and STF strip methods using an enhanced integrating method of direct line integral (Kashiwagi et al., 2010) to solve the velocity potential named EStrip in this paper, and then compare the numerical results with the experimental results published by 14th ITTC. Both EStrip_OSM and EStrip_STF can produce reasonable results in stern quartering waves with *Fn*=0.275, as shown in Fig.7. EStrip_STF method is used to calculate heave and pitch motions at each constant forward speed applied to an upright hull while the non-uniform forward speed is considered by an interpolation method in this paper. The yaw amplitude by potential theory is generally smaller than that by tests, as shown in Fig.7. The reference (Htet et al., 2019b) reported that the measured wave-induced yaw moments could be more significant than those in simulation. The wave-induced yaw moments are crucial for predicting broaching, and the theory of calculating wave-induced yaw moments should be further studied.

The RAO of the sway motion calculated in the frequency domain shall diverge at the zero-encounter frequency, as shown in Figure 7. It is due to the absence of restoring term in the sway direction in the frequency domain. The time-domain manoeuvring mathematical model of the sway motion overcomes the frequency domain divergence.

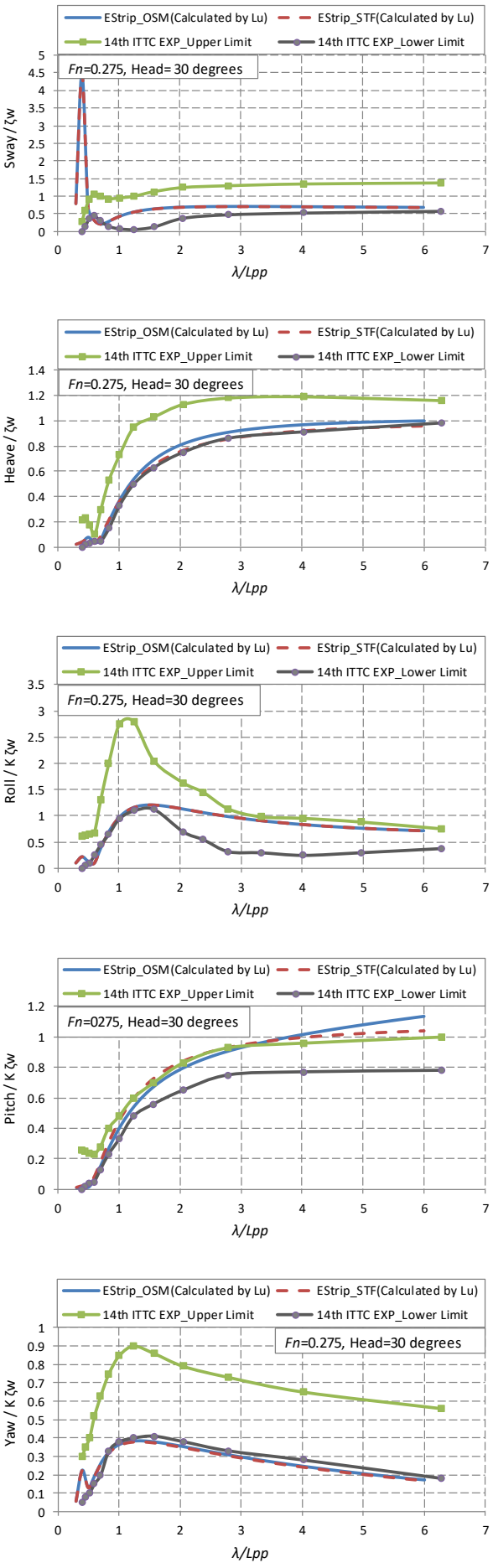

Figure 7: Seakeeping motions of S175 ship with χ=30 degrees and *Fn*=0.275.

5.3 Validation of surf-riding/broaching

Prof. Umeda carried out free-running model experiments with the tumblehome hull in astern waves (Umeda et al., 2008) to examine their mathematical model for surf-riding/broaching, and some experimental results were submitted to IMO by Prof. Umeda for developing the second-generation intact stability criteria. The free-running experiments for surf-riding and broaching with the ONR tumblehome vessel were conducted in regular following, and stern-quartering waves at the manoeuvring and seakeeping basin (length: 69 m, breadth: 46 m, depth: 4 m) of China Ship Scientific Research Center, and four types of ship motions with periodic motion, stable surf-riding, broaching without capsizing and broaching with capsizing were observed (Gu et at., 2017). The time-domain broaching in the experiment with λ/Lpp=1.25, H/λ=0.05, χ=30 degrees is shown in Fig. 8. Broaching is observed two times in one wave case. Broaching in regular waves could lead to unstable roll motions and uncertainty in the maximum roll or capsizing in the experiments.

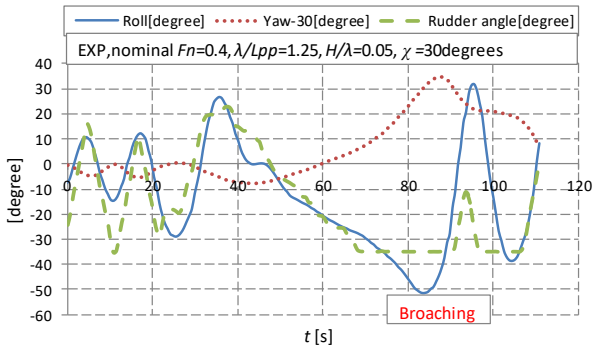

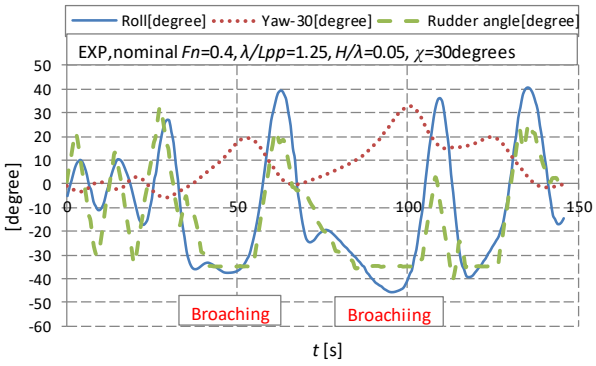

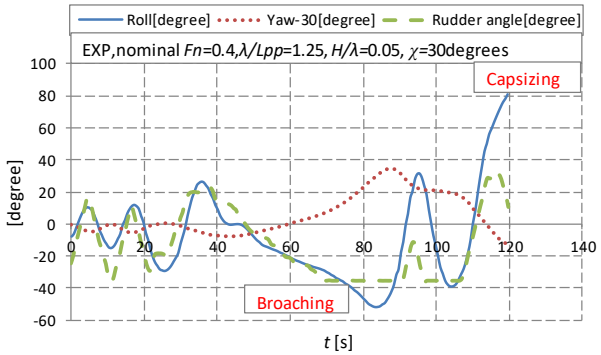

Figure 8: Time-domain experimental results of surf-riding/broaching with λ/Lpp=1.25, H/λ=0.05, χ=30 degrees, and *GM*=2.068m.

Time-domain numerical results of ship motion modes with λ/Lpp=1.25, H/λ=0.05 are shown in Fig.9. Four types of ship motions with periodic motion, surf-riding, broaching without capsizing, and broaching with capsizing can be produced by numerical simulations.

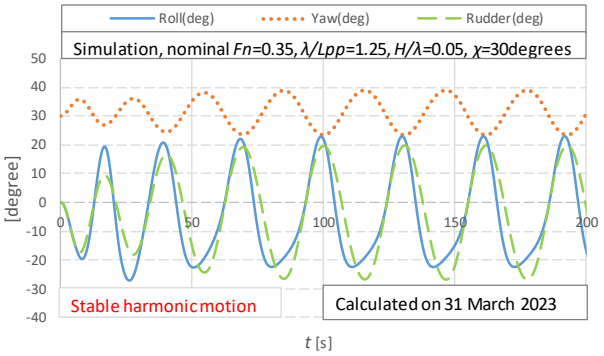

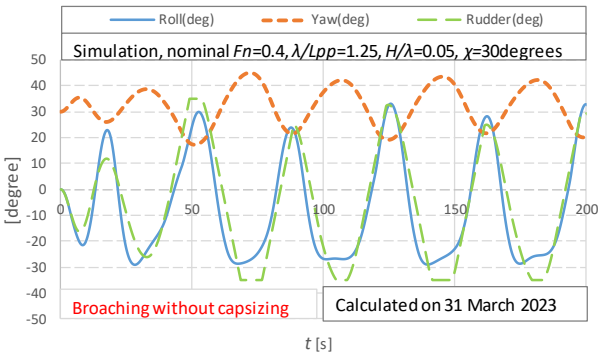

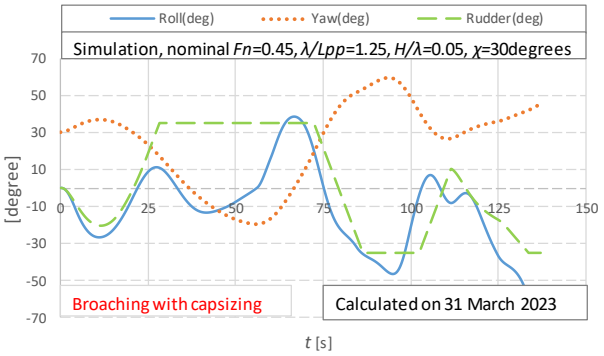

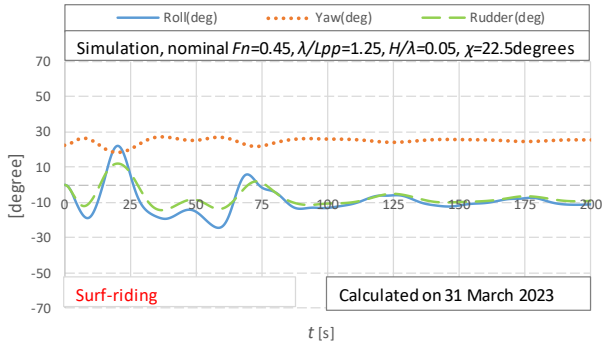

Figure 9: Time-domain numerical results of ship motion modes with λ/Lpp=1.25, H/λ=0.05, and GM=2.068m.

Time-domain numerical results of broaching with λ/Lpp=1.25, H/λ=0.05, χ=30degrees, Fn=0.45 are shown in Fig.10. The rudder exposure is significant during broaching, and the instantaneous wave profile, heave, pitch and roll motions affect the instantaneous rudder exposure.

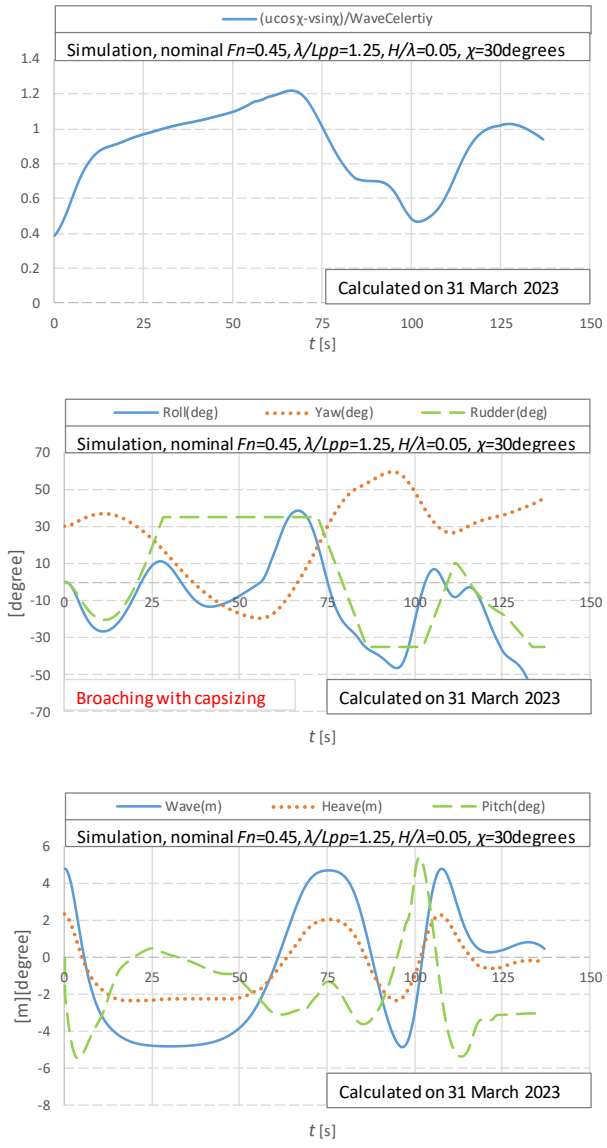

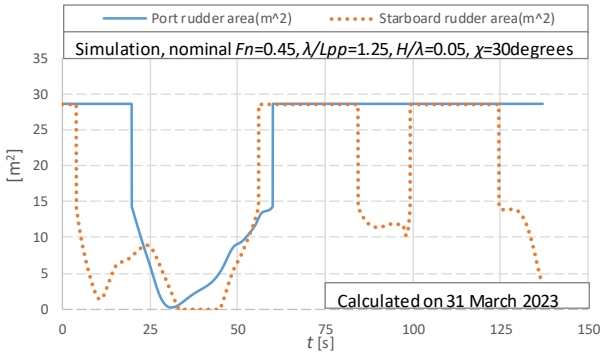

Figure 10: Time-domain numerical results of broaching with λ/Lpp=1.25, H/λ=0.05, χ=30degrees, Fn=0.45, and GM=2.068m.

The 6 DOF mathematical model for pure loss of stability in stern quartering waves (Lu et al., 2023) is further developed with the rudder exposure and the wave-particle velocity considered for surf-riding/broaching. The ship motion modes by the 6 DOF mathematical model with λ/Lpp=1.25, H/λ=0.05, different autopilot courses, and nominal Froude numbers are compared with the existing free-running model experiments (Umeda et al., 2008; Gu et al., 2017), and a good agreement can be realized except for the case with autopilot courses 22.5 degrees and nominal Froude numbers 0.45, as shown in Fig.11. The exposure of starboard rudder is significant during enormous rolling to port, as shown in Fig.10.

The wave excited surge force of Froude-Krylov component FK_1 is defined in Eq.(42). The sectional area $S(x)$ can be calculated with the draft in calm water named the mean wet hull. The sectional area $S(x)$ can be calculated with the time-varied draft in waves named the instantaneous wet hull.

The wave excited surge forces FK_1 with instantaneous wet hull and with mean wet hull are significantly different (Araki et al., 2010). The wave-excited surge force could affect the surge motion and the relative state between the ship and the wave. Therefore, the ship motion modes by the 6 DOF mathematical model with the mean wet hull for wave excited surge force are compared with the experimental results (Umeda et al., 2008； Gu et al., 2017), as shown in Fig. 12. The difference between Figs. 11 and 12 exists only at the case of Fn=0.4 and the autopilot course of 22.5 degrees, and the state becomes surf-riding in Fig.12. Surf-riding/Broaching is sensitive to the ship speed at the critical speed. The amplitude and the phase of FK_1

with the mean wet hull and the instantaneous wet hull are different, and the time-domain surge force and the time-varied speed are changed. The relative position between the ship to the wave is changed. The time-varied yaw moment and rudder angle could also be changed. Surf-riding is the pre-condition of broaching, and surf-riding is also an unstable state. Therefore, a small disturbance during surf-riding could change the unstable state to broaching.

For unifying the mathematical model for surf-riding/broaching and pure loss of stability, the mathematical model for pure loss of stability (Lu et al., 2023) in which the rudder exposure, the wave-particle velocity, and the instantaneous wet hull for wave excited surge force, are not taken into account. The ship motion modes with periodic motion and surf-riding can be numerically calculated. Still, some cases of broaching cannot be evaluated accurately，as shown in Fig.13. The rudder exposure is significant in severe waves. The rudder force in the yaw direction becomes tiny when the rudder is significantly exposure. Therefore, the rudder force is a crucial factor for broaching.

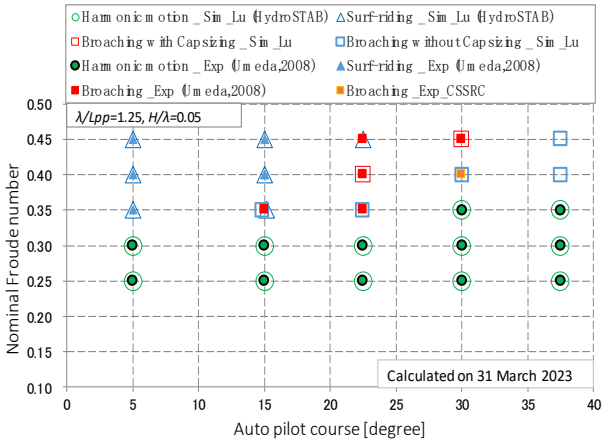

Figure 11: Ship motion modes with *λ/Lpp*=1.25, *H/λ*=0.05, *GM*=2.068m, and *FK₁* with the instantaneous wet hull.

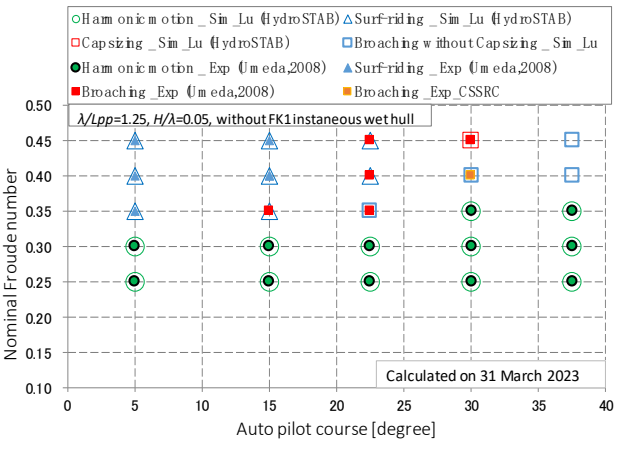

Figure 12: Ship motion modes with *λ/Lpp*=1.25, *H/λ*=0.05, *GM*=2.068m, and *FK₁* with the mean wet hull.

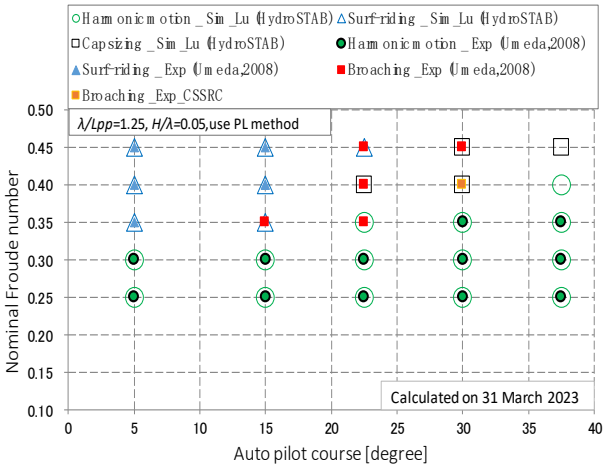

Figure 13: Ship motion modes with *λ/Lpp*=1.25, *H/λ*=0.05 and *GM*=2.068m, *FK₁* with the mean wet hull, and without considering the rudder exposure and the wave-particle velocity.

5.4 Validation of pure loss of stability

Pure loss of stability may occur in astern waves at high speed, and it is related to seakeeping problems of the high speed and low encounter frequency. The methods for pure loss of stability are mostly based on a static balance assumption for heave and pitch motions (Kubo et al., 2012; Hashimoto, 2009； Lu et al., 2018). The nonlinear Froude-Krylov roll restoring variation is calculated according to the ship's relative position to waves determined by the heave and pitch motions calculated by a strip method, as discussed by the authors in the reference (Lu et al., 2019;2020,2023).

The time-domain rolling, pitching, yawing motions, and rudder angle in the tests with *λ/Lpp*=1.25, *H/λ*=0.05, χ=30 degrees are shown in Fig. 14. An unstable rolling motion, subharmonic rolling with two times the encounter period, and capsizing due to yaw-roll coupling with loss of stability are observed in the time-domain experimental data, as shown in 14.

The 6 DOF time-domain ship motions are calculated with the numerical method in the reference (Lu et al., 2023), as shown in Fig.15. The 6 DOF numerical method can predict the maximum rolling angles, as given out in Fig. 16. The numerical simulations with a_H =0.25, -157 are carried out, and the simulations with a_H = -157 could underestimate the large roll at the critical speed. The reason is that the rudder forces in the roll direction are crucial for the large roll during pure loss of stability (Lu et al.,

2023). There is a significant yaw angle during pure loss of stability in stern quartering waves, and the rudder angle is significant to keep the course (Lu et al., 2023). When *GM* is small, Z_{HR} becomes large from the gravity of the ship, and then $a_H \cdot Z_{HR}$ also becomes significant. If a_H = -157, the rudder force in the roll direction, as shown in Eq. (26) is reduced, and then the roll angle becomes smaller than that with a_H =0.25.

The wave excited surge force with the instantaneous wet hull is further considered, and the numerical results with a_H =0.25, -157 underestimate the large roll at the critical speed, as shown in Fig.17. The reason is that the surging force is a crucial reason for the large roll during pure loss of stability. Pure loss of stability is sensitive to the ship speed at the critical speed. The amplitude and the phase of FK_1 with the mean wet hull and the instantaneous wet hull are different, and the time-domain surge force and the time-varied speed are changed. The state at the crest could be changed. And then, the roll angle could be affected during pure loss of stability.

For unifying the mathematical model for surf-riding/broaching and pure loss of stability, the mathematical model considering the rudder exposure, the wave-particle velocity, and wave excited surge force with the instantaneous wet hull is used to predict pure loss of stability, and the results are smaller than the experimental results as shown in Fig.18. The reason is that the rudder forces in the roll direction are a crucial reason for the large roll during pure loss of stability (Lu et al., 2023). Therefore, when the rudder exposure is considered, the rudder force in the roll direction is reduced, and the roll angle could become small.

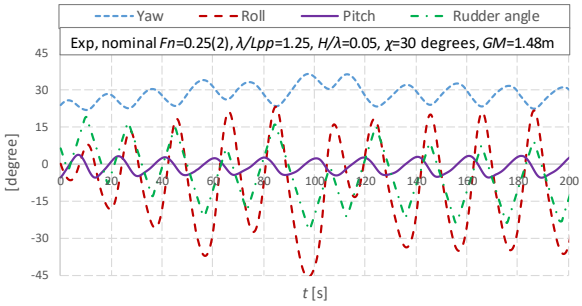

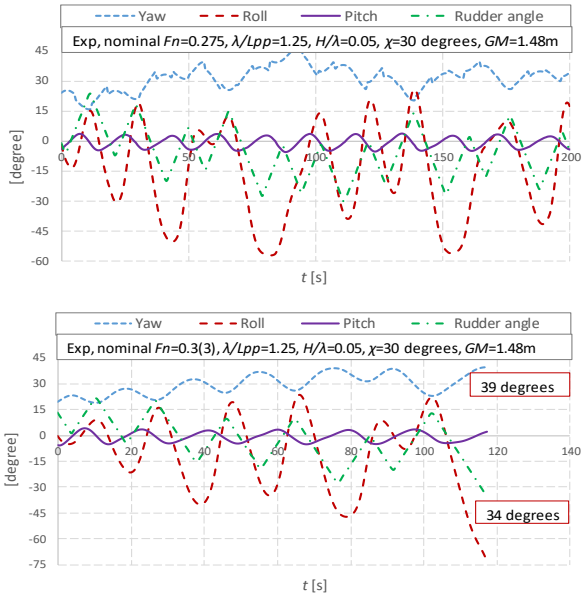

Figure 14: Yaw, roll, pitch motions, and rudder angle in the free-running experiment with λ/Lpp=1.25, H/λ=0.05, χ=30 degrees, and *GM*=1.48m.

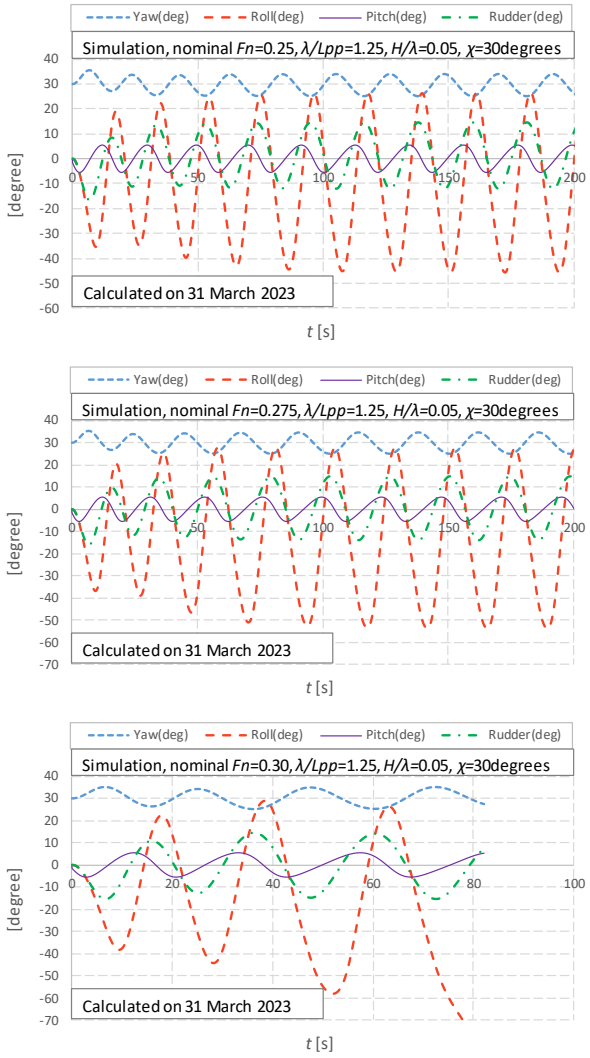

Figure 15: Yaw, roll, pitch motions, and rudder angle in the simulation with the 6 DOF mathematical model with

***λ/Lpp*=1.25, *H/λ*=0.05, *χ*=30 degrees, *GM*=1.48m, and** $a_H = 0.25$.

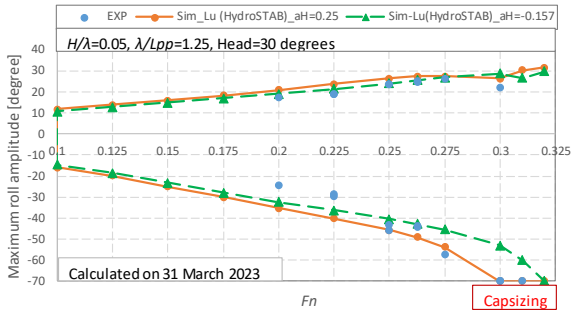

Figure 16: Comparison of maximum roll angle as a function of the nominal Froude number between the experimental results and calculated results with the 6 DOF mathematical model with *λ/Lpp*=1.25, *H/λ*=0.05, and *χ*=30 degrees, $a_H = 0.25, -0.157$ **, and *FK1* with the mean wet hull.**

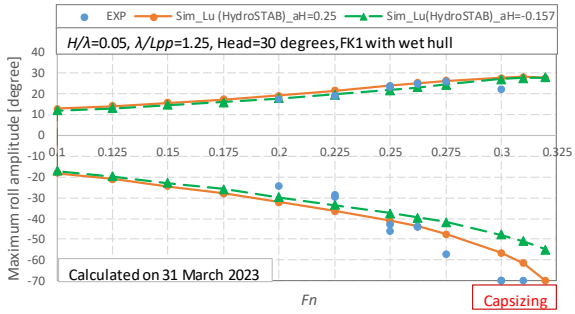

Figure 17: Comparison of maximum roll angle as a function of the nominal Froude number between the experimental results and calculated results with the 6 DOF mathematical model with *λ/Lpp*=1.25, *H/λ*=0.05, *χ*=30 degrees, $a_H = 0.25, -0.157$ **and *FK1* with the instantaneous wet hull.**

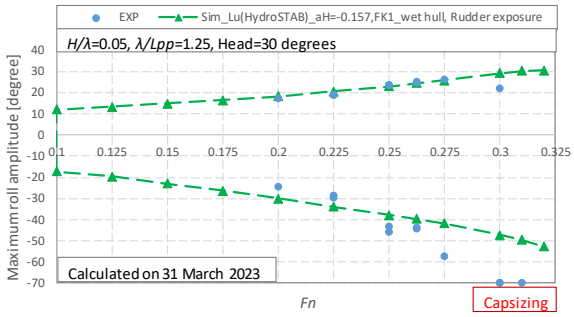

Figure 18: Comparison of maximum roll angle as a function of the nominal Froude number between the experimental results and calculated results with the 6 DOF mathematical model with *λ/Lpp*=1.25, *H/λ*=0.05, *χ*=30 degrees, $a_H = -0.157$ **, *FK1* with the instantaneous wet hull, and with considering the rudder exposure and the wave-particle velocity.**

The large rolling can be predicted by the 6 DOF mathematical model for pure loss of stability. The mathematical model with rudder exposure and instantaneous wetted surface for surge force seems perfect. However, the results for pure loss of stability are not better than that without rudder exposure and instantaneous wetted surface for surge force. The phenomena of significant rolling during pure loss stability, such as the unstable rolling motion and subharmonic rolling with two times the encounter period, are more complicated than our previous cognition, and cannot be captured by the simulations at this stage.

6. CONCLUSIONS

Based on the study of a unified mathematical model for surf-riding/broaching and pure loss of stability in stern quartering waves with the ONR tumblehome vessel, the following remarks can be made:

1) Both rudder and surging forces are very important for surf-riding/broaching and pure loss of stability.

2)The rudder exposure should be considered for surf-riding/broaching, while that should not be considered for pure loss of stability.

3) The wave-excited surging force with instantaneous wet hull should be considered for surf-riding/broaching , while that should not be necessary for pure loss of stability.

4) The 6 DOF mathematical model can be utilized for predicting surf-riding/broaching and pure loss of stability in stern quartering waves by selecting the rudder exposure and the wave-excited surging force.

During the review process, the authors identified the following issues to be further discussed at the workshop and in the future.

1) The effect of diffraction surge force on broaching and pure loss of stability should be further investigated.

2) The “weak 6 DOF model” should be defined.

3) A way to avoid duplication of hydrodynamic lift components in seakeeping and manoeuvring models, such as B_{22} and Y_v, should be established.

4) Effect of the initial condition on broaching should be further clarified.

5) Effect of heave motion on broaching and pure loss of stability should be experimentally identified.

Acknowledgments

Some contents used in this research were once guided by Prof. Naoya Umeda during the first author's Ph.D course at Osaka University supported by China Scholarship Council [No.2008606031]. The research is supported by Ministry of Industry and Information Technology of China (No. [2016] 25, 26; [2017]614). These supports are gratefully acknowledged.

References

Araki M., Sadat-Hosseini H., Sanada Y., Tanimoto K., Umeda N., 2012, "Estimating Maneuvering Coefficients Using System Identification Methods with Experimental, System-based, and CFD Free-running Trial Data", Ocean Engineering, 2012(51), pp. 63-84.

Araki M., Umeda N., Hashimoto H., Matsuda A., 2010, "Broaching Prediction Using an Improved System-based Approach", Proceedings of the 28th Symposium on Naval Hydrodynamics, Pasadena, Califrnia, 12-17 September 2010.

Belenky V., Weems K., Spyrou K., 2016a, "On Probability of Surf-riding in Irregular Seas with a Split-time Formulation", Ocean Engineering, 2016(120), pp. 264-273.

Belenky V., Weems K., Lin W.M., 2016b, "Split-time Method for Estimation of Probability of Capsizing Caused by Pure Loss of Stability", Ocean Engineering, 2016(122), pp. 333-343.

Bassler, C., Belenky, V., Bulian G., Francescutto A., Spyrou K., Umeda N., "Review of Available Methods for Application to Second Level Vulnerability Criteria". Contemp. Ideas Ship Stab. Capsizing Waves 2011, *97*, 3–23.

Hamamoto M., and Nomoto K., 1982, "Transverse Stability of Ships in a Following Sea", Proceeding of the 2nd International Conference on Stability of Ships and Ocean Vehicles, Sasakawa Hall, Tokyo, 24–29 October 1982; pp. 215–224.

Hamamoto M., Kim Y.S., 1993, "A New Coordinate System and the Equations Describing Manoeuvering Motion of a Ship in Waves", Journal of the Society of Naval Architects of Japan, Vol. 173, pp. 209-220.

Hashimoto H., Umeda N., Matsuda A., 2004, "Importance of Several Nonlinear Factors on Broaching Prediction", Journal of Marine Science and Technology, Vol.9, pp. 80-93.

Hashimoto H., 2009, "Pure Loss of Stability of a Tumblehome Hull in Following Seas", Proceedings of the 19th International Offshore and Polar Engineering Conference Osaka, Japan, June 21-26.

Hashimoto H., Umeda N. and Matsuda A.,2011a, "Model Experiment on Heel-Induced Hydrodynamics Force in Waves for Realising Quantitative Prediction of Broaching", M.A.S. Neves et al. (eds.), Contemporary Ideas on Ship Stability and Capsizing in Waves, Fluid Mechanics and Its Application 96, pp. 379-397.

Hashimoto H., Umeda N. and Matsuda A., 2011b, "Broaching Prediction of a Wave-piercing Tumblehome Vessel with Twin screws and Twin Rudders", Journal of Marine Science and Technology, Vol. 16, pp. 448-461.

Htet T.Z., Umeda N., Maki A, Matsuda A. And Terada D., 2019a, "Effect of Above-waterline Hull Shape on Broaching-induced roll in irregular Stern-quartering Waves", Journal of Marine Science and Technology, Vol. 24, pp. 166-173.

Htet T.Z., Umeda N., Maki A, Matsuda A. And Terada D., 2019b, "Estimation of Broaching Probability using Wave-induced Forces and Moment Measured in Captive Model Tests", Journal of Marine Science and Technology, Vol. 24, pp. 317-327.

IMO 2020, Interim Guidelines on the Second Generation Intact Stability Criteria, Msc.1/Circ.1627.

IMO 2022, SDC 8/WP.4. Development of Explanatory Notes to the Interim Guidelines on Second Generation Intact Stability Criteria[R]. Report of the Drafting Group, London.

IMO 2022, SDC 8/INF.4. The Mathematical Model and Its Validation for the Direct Stability Assessmentof Surf-riding/Broaching. Submitted by China.

IMO 2023, SDC 9/INF.7. The Mathematical Model and Its Validation for the Direct Stability Assessment of Pure Loss of Stability in the Application of MSC.1/Circ.1627. Submitted by China.

IMO 2016, Finalization Second Generation Intact Stability Criteria, SDC 3/WP.5.Annex 3

IMO 2013, Development of Second Generation Intact Stability Criteria, SLF 55/INF.15.Annex 12.

Gu M., Chu J., Han Y., and Lu J., 2017, "Study on Vulnerability Criteria for Surf-riding/Broaching with a Model Experiment", Proceeding of the 16th International Conference Stability Workshop, Belgrade, Serbia, 5–7 June 2017.

Kashiwagi M., 1995, "Prediction of Surge and Its Effect on Added Resistance by Means of the Enhanced Unified Theory", Trans West-Japan Soc Nav Arch, No.89, pp. 77-89.

Kashiwagi M., Ikeda T. Sasagawa T., 2010, "Effect of Forward Speed of a ship on Added Resistance in waves", International Journal of Offshore and Polar Engineering, 20(2):1 -8.

Khanfir S., Hasegawa K., Nagarajan V., Shouji K. and Lee S.K.,2011, "Maneuvering Characteristics of Twin-rudder systems: Rudder-hull Interaction Effect on the Maneuverability of Twin-rudder Ships", Journal of Marine Science and Technology, Vol. 16, pp. 472-490.

Kubo H., Umeda N., Yamane K., Matsuda A.,2012, "Pure Loss of Stability in Astern Seas -Is It Really Pure?", Proceedings of the 6th Asia-Pacific Workshop on Marine Hydrodynamics, pp. 307-312.

Kuo C., Vassalos D., Alexander JG., 1986, "Incorporating Theoretical Advances in Usable Ship Stability Criteria", In Proceedings of the RINA International Conference on the Safeship Project—Ship Stability and Safety, London, UK.

Lu J., Umeda N. and Ma K., 2011a, "Theoretical Study on the Effect of Parametric Rolling on Added Resistance in Regular Head Seas"., Journal of Marine Science and Technology, Vol. 16(3), pp. 283-293.

Lu J., Umeda N. and Ma K., 2011b, "Parametric Rolling Prediction in Irregular Head Seas with Added Resistance Taken Into Account", Journal of Marine Science and Technology, Vol. 16(4), pp. 462-471.

Lu J., Gu M. and Umeda N., 2016, "A Study on the Effect of Parametric Rolling on Added Resistance", Ocean Engineering, 2016(122), pp. 288-292.

Lu J., Gu M. and Umeda N., 2017b, "Experimental and Numerical Study on Several Crucial Elements for Predicting Parametric Roll in Regular Head Seas", Journal of Marine Science and Technology, Vol. 22, pp. 25-37.

Lu J., Gu M.,2017a, "Study on Standard Mathematical Model of Pure Loss of Stability in Stern-quartering Waves",16th International Ship Stability Workshop,5-7June 2017, Belgrade, Serbia.

Lu J., Gu M., Wang TH., Shi C., 2018, "Experimental and Numerical Study on Standard Mathematical Model for Pure Loss of Stability", Proceeding of the 13th International Conference on Stability of Ships and Ocean Vehicles,16-21 September 2018, Kobe, Japan

Lu J., Gu M. and Boulougouris E, 2019, "Model Experiments and Direct Stability Assessments on Pure Loss of Stability of the ONR Tumblehome in Following Seas", Ocean Engineering, 194 (2019) 106640

Lu J., Gu M. and Boulougouris E, 2020, "Model Experiments and Direct Stability Assessments on Pure Loss of Stability in Stern Quartering Waves", Ocean Engineering, 216 (2020) 108035

Lu J., Gu M. and Boulougouris E, 2023, "Further Study on One of the Numerical Methods for Pure Loss of Stability in Stern Quartering Waves", Journal of Marine Science and Enginering, 2023, 11, 394.

Neves M., "Dynamic stability of ships in regular and irregular seas—An overview", Ocean Engineering, 2016, *120*, 362–370.

Paulling, J.R. "The Transverse Stability of a Ship in a Longitudinal Seaway", J. Ship Res. 1961, *44*, 37–49.

Paulling, J.R.; Oakley, O.H.; Wood, P.D. Ship capsizing in heavy seas: The correlation of theory and experiments. In Proceedings of the 1st International Conference on Stability of Ships and Ocean Vehicle, Glasgow, UK, 24-27 March, 1975.

Sanada Y., Tanimoto K., Takagi K., Gui L., Toda Y. and Stern F., 2013, "Trajectories for ONR Tumblehome maneuvering in calm water", Ocean Engineering, 2013(72), pp. 45-65.

Umeda N., 1999, "Nonlinear Dynamics of Ship Capsizing due to Broaching in Following and Quartering Seas", Journal of Marine Science and Technology, Vol. 4, pp. 16-26.

Umeda N. and Hashimoto H., 2002, "Qualitative Aspects of Nonlinear Ship Motions in Following and

Quartering Seas with High Forward Velocity", Journal of Marine Science and Technology, Vol. 6, pp. 111-121.

Umeda N., Hashimoto H. and Matsuda A., 2003, "Broaching Prediction in the Light of an Enhanced Mathematical Model, with Higher-order Terms Taken Into Account", Journal of Marine Science and Technology, Vol. 7, pp. 145-155.

Umeda N., Furukawa T., Matsuda A., and Usada S., 2014, "Rudder Normal Force during Broaching of a Ship in Stern Quartering Waves", 30th Symposium on Naval Hydrodynamics, Hobart, Tasmania, Australia, 2-7 November 2014.

Umeda N., Usada S., Mizumoto K., and Matsuda A., 2016, "Broaching Probability for a Ship in Irregular Stern-quartering Waves: Theoretical Prediction and Experimental Validation", Journal of Marine Science and Technology, Vol. 21, pp. 23-37.

Umeda N., Hashimoto H., Frederick S., Nakamura S., Seyed H S H., Matsuda A. and Pablo C., 2008, "Comparison Study on Numerical Prediction Techniques for Parametric Roll", Proceedings of the 27th Symposium on Naval Hydrodynamics, Seoul, 2008, 5-10.

Umeda N., Fujita N., Morimoto A., Sakai M., 2015, "N Terada D., "Numerical Prediction of Parametric Roll Resonance in Oblique Waves", Proceeding of 12th International Conference on Stability of Ships and Ocean Vehicle. Glasgow.

Umeda N., Osugi M., Ikenaga Y., Matsuda A., 2019, "Pure Loss of Stability in Stern Quartering Waves: Revisited with Numerical Simulations Reproducing Accidents",17th International Ship Stability Workshop, 10-12 June 2019, Helsinki, Finland.

Umeda N., Yamamura S., Matsuda A., Maki A., Hashimoto H., 2008, "Model Experimental on Extreme Motions of a Wave-piercing Tumblehome Vessel in Following and Quartering Waves", Journal of the Society of Naval Architects of Japan.

Yasukawa H. and Yoshimura Y., 2015, "Introduction of MMG Standard Method for Ship Maneuvering Predictions", Journal of Marine Science and Technology, Vol. 20, pp. 37-52.

Filling gaps in Direct Stability Assessment procedures

Naoya Umeda, *Osaka University,* umeda@naoe.eng.osaka-u.ac.jp
Yuki Maruyama, *Osaka University,* yuuki_maruyama@naoe.eng.osaka-u.ac.jp
Soichiro Okamoto, *Osaka University,* soichiro_okamoto@naoe.eng.osaka-u.ac.jp
Akihiro Oka, *Osaka University,* akihiro_oka@naoe.eng.osaka-u.ac.jp
Shinya Masamoto, *Osaka University,* shinya_edo@naoe.eng.osaka-u.ac.jp
Akihiko Matsuda, *Japan Fisheries Research and Education Agency,* amatsuda@fra.affrc.go.jp

ABSTRACT

The following items were investigated to fill the gaps in the direct stability assessment. Firstly, a mathematically guaranteed method for generating a wave signal without self-repetition is proposed to establish the direct counting technique without any trial and error. Secondly, an example of quantitative validation of a numerical code for pure loss of stability with a model experiment in short-crested irregular waves is presented to demonstrate feasibility of assessment using realistic seas. Thirdly, an example of almost validation of a numerical code for parametric rolling with a model experiment in short-crested irregular waves is also shown to realize more realistic phenomenon than the long-crested irregular waves.

Keywords: *avoiding self-repetition effect, short-crested irregular waves, validation, pure loss of stability, parametric rolling*.

1. INTRODUCTION

Responding to Section 1.2 of the 2008 Intact Stability (IS) Code, the International Maritime Organization (IMO) approved the interim guidelines of the second generation intact stability criteria as MSC.1/Circ. 1627 (IMO,2020) and its explanatory notes as MSC.1/Circ. 1652 (IMO, 2022). These new criteria include the direct stability assessment using a time domain numerical simulation code for extreme ship motions leading to capsizing in irregular waves.

In the interim guidelines, the direct counting method is a standard technique for executing the probabilistic direct stability assessment, developing the probabilistic operational guidance and validating the extrapolation methods. The main drawback of the direct counting method is that it could require a very long duration to be simulated if the stability failure rate is close to the standard, i.e. one failure per two hours. During such a long duration, if the self-repetition effect of irregular time series exists, the stability failure rate could be unreasonably underestimated (Shigunov, 2019). Thus, the explanatory notes provide ways to avoid the self-repetition effect, which requires to conform whether the results of the first passage time can be regarded as the exponential distribution in the light of the Q-Q plot or whether the calculated autoregression function (Belenky, 2011) is sufficiently small. At the ISSW 2022, some of the authors (Maruyama et al., 2022) showed numerical examples in that the self-repetition does not exist in the inverse Fourier transformation using non-uniform frequency sampling and in the linearly filtered white noise. Further, Tsoumpelis and Spyrou (2023) proposed a scheme for capturing repeating portions in time series. These results are beneficial in practice but are not exactly guaranteed for avoiding self-repetition with mathematical proof. Thus, more theoretical work is required.

The used code should be quantitively validated with model experiments, which are executed following the ITTC recommended procedures (ITTC, 2008). If the assessment uses short-crested waves, the experiment should be conducted preferably in short-crested irregular waves. If it is not feasible, the experimental validation at least in long-crested irregular waves with many different wave headings can be regarded as the alternative.

In the explanatory notes (IMO, 2022), the examples of the experimental validation of numerical codes in short-crested irregular waves are not included, except for the excessive acceleration

mode (Kuroda et al. 2019). Only an experimental validation example in long-crested irregular waves (Hashimoto and Umeda, 2019) is available for parametric rolling in the explanatory note and no examples for pure loss of stability. Matsubarta et al. (2023) published their validation study using short-crested irregular waves for the broaching failure mode. Thus, it is highly expected to publish the experimental validation for other failure modes, i.e. pure loss of stability, parametric rolling and dead ship stability, in short-crested irregular waves. It is important to demonstrate that the stochastic experimental validation in short-crested irregular waves is feasible.

To resolve these drawbacks, the authors propose a mathematically proven method for avoiding self-repetition and provide examples of experimental validation for pure loss of stability and parametric rolling in short-crested irregular waves.

2. WAVE SIGNAL GENERATION METHOD WITHOUT SELF-REPETITION

Proposal of method

Irregular wave elevation, $\zeta_{\mathrm{w}}(t)$, can be generated as the sum of many cosine waves having different frequencies with random phases, as shown in Eq. (1)

$$\begin{aligned}\zeta_{\mathrm{w}}(t) &= \int_0^\infty \sqrt{2S_{\mathrm{w}}(\omega)d\omega}\cos(\omega t+\delta)\\ &= \sum_{n=1}^{N}\sqrt{2S_{\mathrm{w}}(\omega_n)\Delta\omega_n}\cos(\omega_n t+\delta_n)\end{aligned} \tag{1}$$

Here, ω_n, $\Delta\omega_n$ and δ_n describe the wave frequency, the frequency interval and the phase of the wave. *N* denotes the number of elements. Suppose the ratio of the frequencies of two different component waves is rational. In that case, the sum of these two waves shall be periodic so that the possibility of self-repetition of the time series shall exist. On the other hand, if the ratio of any combination of two different waves in the spectrum is irrational, the possibility of self-repetition of the time series shall not exist. Therefore, for avoiding the self-repetition effect it is sufficient to select the ratio of any combinations of two different waves in the spectrum as irrational (Hino, 1977).

To realize such requirements, a method to sample the frequencies of component waves, ω_n, can be proposed as follows:

$$\omega_n = \frac{z^{\frac{n}{m}}}{y} \tag{2}$$

where *z* is a prime number, *y* and *m* are natural numbers, and *m* is larger than n. As proved in Appendix, a prime number to the power of a non-integer rational number is irrational. The ratio of an irrational number to a rational number is irrational. Therefore, the ratio of two different component wave frequencies, $\rho_{i,j}$, should be selected as follows;

$$\rho_{i,j} = \frac{\omega_i}{\omega_j} = \frac{z^{\frac{i}{m}}}{z^{\frac{j}{m}}} = z^{\frac{i-j}{m}} \tag{3}$$

Since $i - j < m$ and $\rho_{i,j}$ is a prime number to the power of a non-integer rational number, it shall be irrational. Thus, if we sample the component wave frequencies this way, the generated waves shall not be repeated even partially.

Application examples

To demonstrate the feasibility of the proposed method, we examine the time series generated by the method. The wave elevation is computed based on the Bretschneider spectrum of the significant wave height of 5m and the mean wave period of 9.99s. We executed 30 realizations and analysed these realizations separately, and the duration of each realization is 9 hours. Then the ensemble average of the outcomes of individual realizations is shown here.

The wave energy spectra and the autoregression functions calculated from the time series for different numbers of component waves are shown in Figs.1-3. While the smoothed power spectrum generated with 1000 component waves well represents the target spectrum, even the raw spectrum generated with 10000 waves well represents the target spectrum, as shown in Fig.1. Here smoothing spectra were executed with a triangular filter (Rikiishi and Mitsuyasu, 1973). The calculated autoregression functions quickly converged to zero if the number of component waves is larger than 1000. It is noteworthy here that even the time series free from the self-repetition effect shows a certain value of the autoregression functions

if the number of component waves is not so large. Because each component wave itself is periodic, many component waves are required to reduce such periodic nature. In other words, the judgement of self-repetition of the time series using the autoregression functions has limitation even when the number of component waves is not so large. Figs. 4 and 5 indicate the accuracy of realizing the wave energy spectrum and the probability density function, respectively, by calculating the mean square errors from the target ones. Precisely realizing the energy spectrum is more difficult than the probability density function. Using 10000 waves is sufficient for accurately representing the wave energy spectrum. In the examples shown here, we used z=23, y=5 and m=N. Since N indicates the number of sample frequencies, in the case of 1000 frequencies as an example, m=1000.

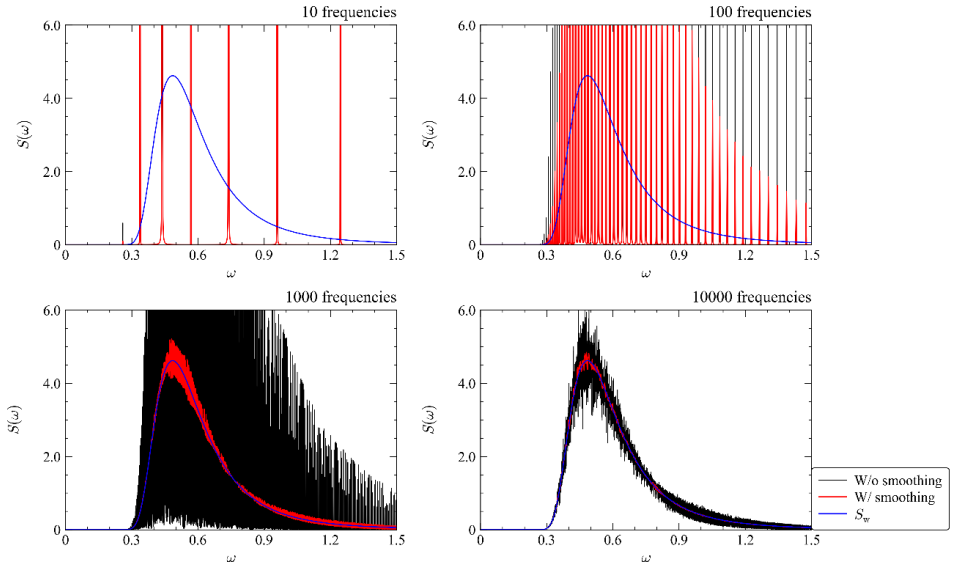

Fig. 1 Wave energy spectra obtained from the signal generated by the present method.

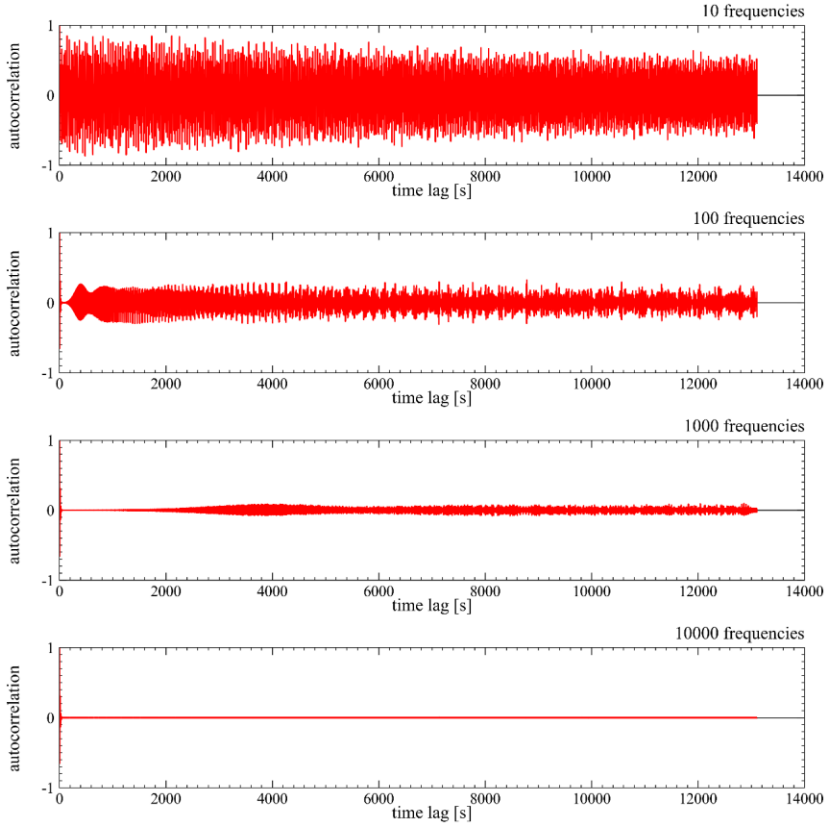

Fig. 2 Autoregression function obtained from the signal generated by the present method.

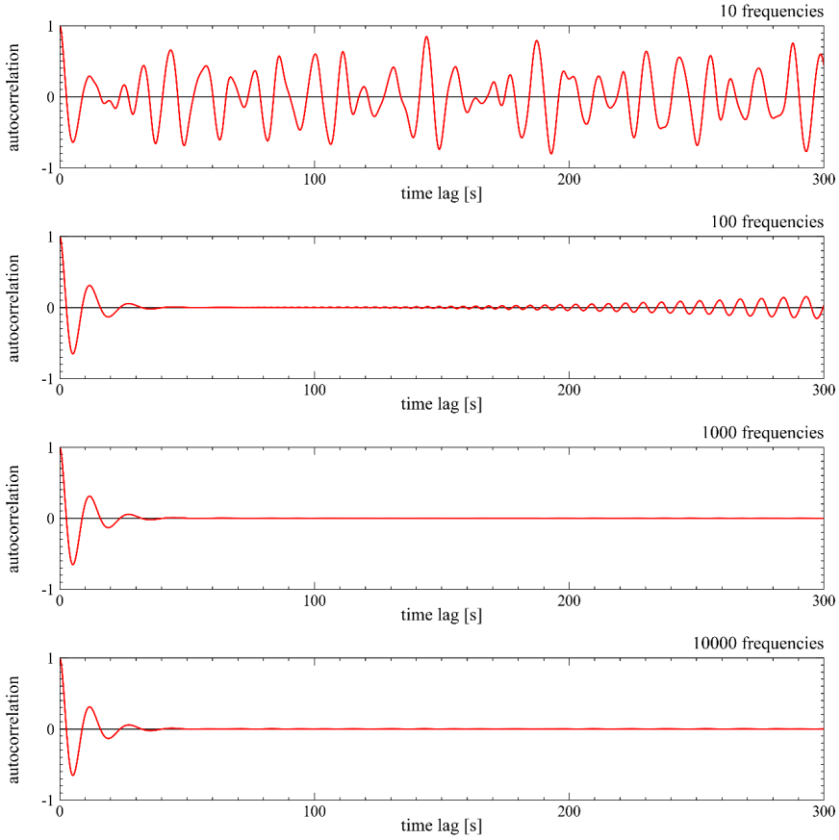

Fig. 3 Enlargements of the initial part of Fig. 2

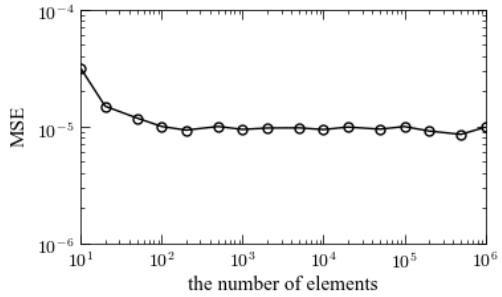

Fig. 4 Mean square error of the simulated probability density functions

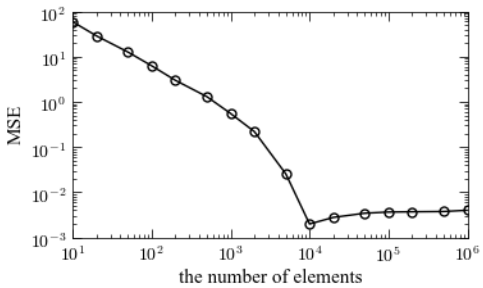

Fig.5 Mean square error of the simulated wave energy spectra

3. VALIDATION OF NUMERICAL SIMULATION CODES WITH MODEL EXPERIMENTS IN SHORT-CRESTED WAVES

Pure loss of stability

A model experiment was executed for a RoPax ship running in short-crested irregular stern quartering waves at the model basin of the National Research Institute of Fisheries Engineering, following the ITTC recommended procedure for intact stability model tests (ITTC, 2008). The model basin is 60m in long, 25m in wide and 3.2m in deep. The subject ship capsized due to loss of transverse stability in 2009 when she ran in stern quartering waves off the Japanese Isles in the North Pacific (Ueno et al., 2012). The ship length between perpendiculars is 150m and its 1/42.86 scalded model was used here. The Froude number was 0.33, and the autopilot course was 20 degrees from the

main wave direction. The rudder gain was 2.0. The waves used for the experiment have the Bretschneider spectrum of the mean wave period of 1.29s in model scale with cosine-squared wave energy spreading function. The natural roll period is 2.04 s and the pitch gyro radius is 0.889m. The wave signal was generated by the inverse Fourier transformation using non-uniformly sampled 200 frequencies and uniformly sampled 71 directions for the duration of 300s for each realisation excluding the transient stage. The waves were generated with 80 segmented plungers in a short side of the model basin and side-wall reflections at the long sides was positively utilised (Takezawa et al., 1988). Although the duration of model runs with high speed in astern waves is short, the ship meets more than 200 waves in total for each wave condition by repeating many model runs with different wave realisations. An example of the measured wave spectrum is shown in Fig. 6. The verification results were for the failure modes shown in Fig. 7. When the roll angle exceeds 25 degrees, the pitch angle shows zero up-crossing, corresponding to the wave crest amidship. In addition, the local roll period is almost equal to the local pitch period. Thus, this large heel could be regarded as an event due to a pure loss of stability in stern quartering waves.

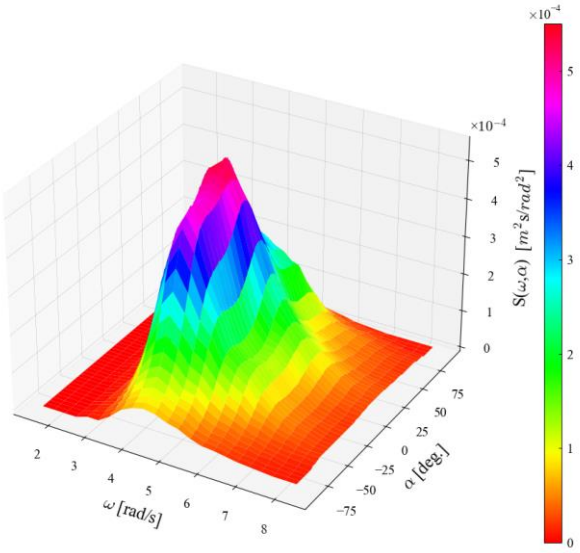

Fig. 6 An example of the measured wave spectrum in model scale (1/42.86 of the full scale).

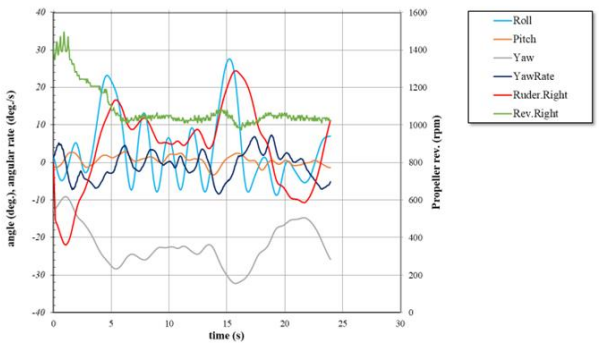

Fig. 7 Time series of measured ship behaviours including the roll angle exceeding 25 degrees under the significant wave height of 0.231m in model scale (1/42.86 of the full scale).

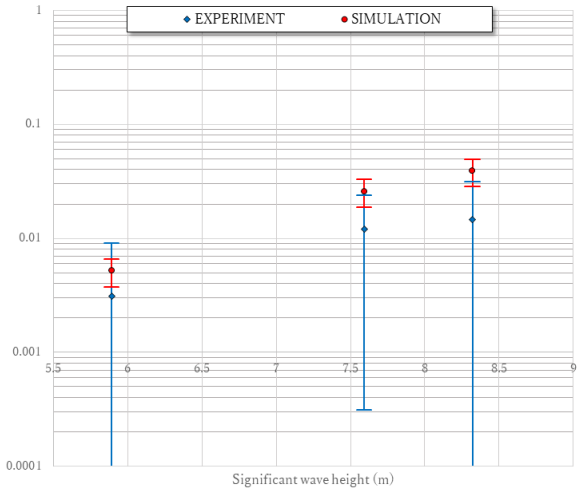

Fig. 8 Comparison in the probability of roll amplitude exceeding 25 degrees between the model experiment and the numerical simulation for pure loss of stability failure mode of a RoPax ship in short-crested failure mode. The symbols indicate the simple estimates, and the bars do their 95% confidence intervals.

The simulation model used was a surge-sway-roll-yaw model (Kubo et al., 2012): the heave and pitch motions are approximated to trace their static equilibrium because their natural frequencies are much larger than the wave encounter frequency (Umeda, 1996). It is based on a modular-type manoeuvring model with horizontal wave forces. Circular motion tests obtained the manoeuvring coefficients, and the wave forces were estimated by a slender body theory for low encounter frequency (Umeda et al., 1995) and assimilated with the captive

model tests. The restoring variation was hydrostatically calculated with Grim's effective wave concept (Grim, 1961).

The conditional probabilities of the roll amplitude exceeding the critical value, i.e. 25 degrees, when the ship meets a zero-cross wave for three different significant waves were plotted in Fig.8 together with the 95% confidence intervals. The simple estimate is the mean of the ratio of the number of the critical value up crossing of roll amplitude to the number of the encounter waves and the confidence intervals are calculated assuming the Gaussian distribution of the ratio. Because of the logarithmic scale, the lower confidence intervals are shown longer than the upper ones. The simulated probability is slightly more conservative than the measured values, and the confidence intervals overlapped. Thus, the qualitative requirement in the interim guidelines for the validation was satisfied.

Parametric rolling

A model experiment was executed for the C11 class containership running in short-crested irregular head and bow quartering waves at the model basin of the National Research Institute of Fisheries Engineering, following the ITTC recommended procedure for intact stability model tests (ITTC, 2008). The ship length between perpendiculars is 262m and its 1/100 scalded model was used here. As well known, the subject ship suffered a container loss accident due to parametric rolling in 1998 in the North Pacific. The natural roll period was 2.37s and the pitch gyro radius is 0.715m in the experiment. The rudder gain was 5.0. The waves used for the experiment have the Bretschneider spectrum of the significant wave height of 0.145m and the mean wave period of 1.12s with cosine-squared wave energy spreading function. The wave signals were generated by the inverse Fourier transformation using non-uniformly sampled 200 frequencies and uniformly sampled 71 directions for the duration of 300s for each realisation excluding the transient stage. The waves were generated with side-wall reflection (Takezawa et al., 1988). The verification results were for the failure mode shown in Fig. 9. When the roll angle exceeds 25 degrees, the local roll period is nearly equal to twice the local pitch period and is nearly equal to the natural roll period. Thus, this large heel could be regarded as an event due to parametric rolling.

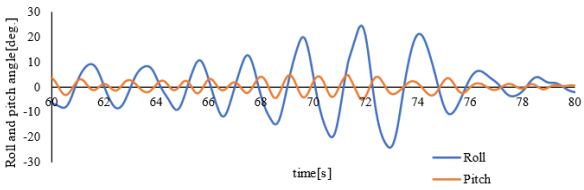

Fig. 9 Time series of the measured roll and pitch angles in short-crested irregular head waves in model scale (1/100 of the full scale).

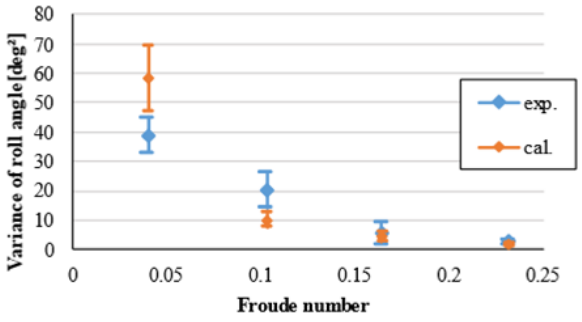

Fig. 10 Comparison in the roll angle variance between the experiment and the simulation in the short-crested irregular waves with a heading angle of 180 degrees from the main wave direction.

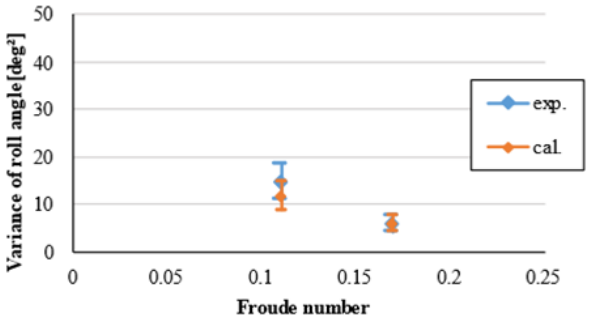

Fig. 11 Comparison in the roll angle variance between the experiment and the simulation in the short-crested irregular waves with the heading angle of 150 degrees from the main wave direction.

The simulation model used was a sway-heave-roll-pitch-yaw model (Umeda et al, 2016). It is based on a nonlinear strip theory. Regarding the Froude-Krylov forces, the hydrostatic pressure was integrated over the submerged hull up to the relative incident wave surface and the wave pressure

represented by the exponential function was done up to the calm-water level but taking account of the heave and pitch motions. The radiation forces were linearly calculated with the natural roll frequency and the peak wave frequency for the lateral and vertical motions, respectively. The diffraction forces were linearly calculated with the Salvesen-Tuck-Faltinsen method (Salvesen et al., 1970). The manoeuvring forces were nonlinearly estimated with a low-speed modular-type model.

As shown in Figs. 10-11, the numerical simulation provides a slightly conservative estimation of the roll angle variance measured by the model experiment not only in head waves but also bow quartering waves, except for one case, i.e., the Froude number of 0.1 with the heading angle of 180 degrees. The 95 % confidence intervals overlapped, except for two cases, i.e. the Froude numbers of 0.04 and 0.1 with the heading angle of 180 degrees. Thus, the qualitative requirement in the interim guidelines for the validation was not exactly but almost satisfied.

4. CONCLUSIONS

To fill the gaps in the direct stability assessment, we obtained the following points.

1) A mathematically-guaranteed method for generating a wave signal without self-repetition is proposed with its application example.

2) An example of quantitative validation of a numerical code for pure loss of stability in short-crested irregular waves is presented.

3) An example of almost quantitative validation of a numerical code for parametric rolling in short-crested irregular waves is presented.

The details of two validation examples of the numerical codes for direct stability assessment are planned to be separately published with their application in future.

ACKNOWLEDGEMENTS

This work was supported by a Grant-in-Aid for Scientific Research from the Japan Society for Promotion of Science (JSPS KAKENHI Grant Number 19H02360). It was partly carried out as a research activity of the Goal-based Stability Criteria Project of the Japan Ship Technology Research Association in the fiscal years 2021 and 2022, funded by the Nippon Foundation. The authors are grateful to Prof. Atsuo Maki and Dr. Masahiro Sakai for their valuable comments, and Dr. Sreenath Maniyappan, Messer Hiroaki Koike, Norifumi Segawa and Ms. Mayu Takaya for their effective assistance during the model experiments.

REFERENCES

Belenky, V., 2011, “On Self-Repeating Effect in Reconstruction of Irregular Waves”, in Neves, M.A.S., Belenky, V., deKat, J., Spyrou, K. and Umeda, N. (eds), *Contemporary Ideas on Ship Stability and Capsizing in Waves*., Fluid Mechanics and Its Applications, 97, 589-597.

France, W. N., Levadou, M., Treakle, T.M., Paulling, J.R., Michel, R W.K and Moore, C., 2003, "An Investigation of Head-Sea Parametric Rolling and its Influence on Container Lashing Systems", Marine Technology, 40(1):1-19.

Grim, O., 1961, “Beitrag zu dem Problem der Sicherheit des Schiffes im Seegang, Schiff und Hafen, 6, 490-497.

Hashimoto, H., Umeda, N., 2019, “Prediction of Parametric Rolling in Irregular Head Waves" Chapter 16 of *Contemporary Ideas on Ship Stability. Risk of Capsizing*, Belenky, V., Spyrou, K., van Walree F., Neves, M.A.S., and N. Umeda, *eds*., Springer, ISBN 978-3-030-00514-6, 275-289.

Hino, M., 1977, “Spectrum analysis (in Japanese)”, Asakura Publishing (Tokyo).

IMO, 2020, “Interim guidelines on the second generation intact stability criteria”, MSC.1/Circ.1627, 1-60.

IMO, 2022, “Explanatory Notes to Interim guidelines on the second generation intact stability criteria”, MSC.1/Circ.1652.

ITTC, 2008, “Recommended Procedures, Model Tests on Intact Stability”, 7.5-02-07-04.

Kubo. H., Umeda. N., Yamane. K., Matsuda. A., 2012.” Pure Loss of Stability in Astern Seas–Is it Really Pure?”. Proceedings of the 6th Asia-Pacific Workshop on Marine Hydrodynamics, University of Technology Malaysia, Johor, 307-312.

Kuroda T., Hara S., Houtani H. and Ota D., 2019, “Direct Stability Assessment for excessive acceleration failure mode and validation by model test”, Ocean Engineering, 187, 106137.

Maruyama, Y, Umeda, N, Maki, A, 2022, “Measures for avoiding self-repetition effect in the direct stability assessment”, Proceedings of the 18th International Ship Stability Workshop, Technical University of Gdansk,177-

183.

Matsubara, K., Umeda, N., Matsuda, A., 2023, "Probabilistic estimation of the large heel due to broaching associated with surf-riding for a ship in short-crested irregular waves and its experimental validation", Ocean Engineering, 269, 113540.

Rikiishi, K., Mitsuyasu, H., 1973, "On the Methods of Computing Power Spectrum", Bulletin of Research Institute for Applied Mechanics, 39, 77-104, (in Japanese).

Salvesen, N., Tuck, E.O., Faltinsen, O., 1970, "Ship Motions and Sea Load", Transaction of the Society of Naval Architects and Ocean Engineers, 78, 250–287.

Shigunov, V., 2019, "Direct Counting Method and its Validation", Proceedings of the 17th International Ship Stability Workshop, NAPA and Aalto University, 119-128.

Takezawa, S., Kobayashi, K., Kasahara, A., 1988. "Directional Irregular Waves Generated in a Long Tank", Naval Architecture and Ocean Engineering, 27, 51-62.

Tsoumpelis, D., Spyrou, K., 2023, "Identification of recurring patterns and repetitions in time-series, with application to pseudo-stochastic ship rolling", Ocean Engineering, 271, 113717.

Ueno, M., Miyazaki, H.,Taguchi, H.,Kitagawa, Y., Tsukada, Y., 2012, "Model experiment reproducing an incident of fast ferry", Journal of Marine Science and Technology, Springer, 18(2), 192-202.

Umeda, N, Y. Yamakoshi, S. Suzuki, 1995, "Experimental study for wave forces on a ship running in quartering seas with very low encounter frequency", Proceedings of the Sevastianov Symposium, Tech Univ Kaliningrad, 1(14) 1-18.

Umeda, N., 1996, "Some Remarks on Broaching Phenomenon", Proceedings on 2nd International Workshop on Stability and Operational Safety, Osaka Univ., 10-23.

Umeda, N., Sakai, M., Fujita, N., Morimoto, A., Terada, D., Matsuda, A., 2016, "Numerical prediction of parametric roll in oblique waves", Ocean Engineering, 120, 212-219.

APPENDIX PROOF OF THE FACT THAT A PRIME NUMBER TO THE POWER OF A NON-INTEGER RATIONAL NUMBER IS IRRATIONAL

A positive non-integer rational number is represented as *n/m* where *n* and *m* are coprime natural numbers. Here m≠1.

We assume that $z^{\frac{n}{m}}$ is rational, where z is a prime number. If we use coprime natural numbers, *p* and *q*, it can be represented as follows:

$$z^{\frac{n}{m}} = \frac{q}{p} \tag{4}$$

If we multiply both sides of this equation by *p* and raise them to the power of *m*, we obtain

$$z^n p^m = q^m \tag{5}$$

Since the left side is a multiple of *z*, *q* shall be a multiple of *z*. Thus,

$$q^m = r z^{km} \tag{6}$$

where *k* and *r* are natural numbers.

On the other hand, since *p* and *q* are coprime, *p* shall not be a multiple of *z*. Thus, *n=km* so that *n* shall be a multiple of m. However, this is a conflict because *n* and *m* are coprime natural numbers.

Therefore, the assumption that $z^{\frac{n}{m}}$ is rational shall be denied so that $z^{\frac{n}{m}}$ shall be irrational.

Multifidelity fast code for Direct Stability Assessment

Kenneth Weems, *David Taylor Model Basin NSWCCD,* kenneth.m.weems2.civ@us.navy.mil
Vladas Pipiras, *University of North Carolina at Chapel Hill,* pipiras@email.unc.edu
Vadim Belenky, *David Taylor Model Basin NSWCCD,* vadim.belenky.civ@us.navy.mil

ABSTRACT

A rapid time-domain seakeeping code incorporates a volume-based evaluation of the body-nonlinear incident wave and hydrostatic restoring forces along with simplified models of hydrodynamic forces. The code has 3-DOF (heave-roll-pitch) and 6-DOF simulation options and has been described in a series of previous publications. The tool was originally intended for the statistical validation of extraction methods and is very fast while preserving the nonlinear effects of stability in waves. To make this tool applicable to direct stability assessment, better approximations for diffraction and radiation forces need to be added in order to provide quantitative rather than qualitative results. This approximation is carried out using regression of LAMP calculation results. For the 6 DOF version, an option for soft springs has been added to complement previously implemented maneuvering derivatives.

Keywords: *IMO, Second Generation Intact Stability Criteria, Direct Stability Assessment*

1. INTRODUCTION

Direct stability assessment is a set of numerical procedures described in Section 3 of Interim Guidelines for the Second Generation Intact Stability Criteria MSC.1 / Circ. 1627, cited simply as IMO Interim Guidelines from here on. This set of procedures is intended to employ the latest simulation technology available, while remaining feasible for existing computational infrastructure of the maritime industry (paragraph 3.1.3 of the cited reference).

The highest-fidelity of numerical simulation technology for seakeeping problems that would be available to Naval Architects at this time involves numerical solution of Navier-Stokes equation using either Reynolds Averaging Navier-Stokes (RANS) or Large Eddy Simulation (LES) approaches (Reed and Beck, 2016). While providing a predictive capability with sufficient accuracy, these numerical technologies require considerable expertise and large computational resources, and become impractical when working with realistic (i.e. irregular) waves because of the volume of simulation data required.

Numerical simulation tools incorporating a potential-flow solution of the wave-body hydrodynamics, polynomial approximations of the viscous forces and appendage force models are considered to be more practical candidate tools for direct stability assessment. Peters et al. (2011) provides a list of such tools, which include TEMPEST (Belknap and Reed, 2019) and LAMP (Large-Amplitude Motion Program, Shin et al., 2003). These tools are sometimes referred as "hybrid" codes, but the term "multifidelity" would be more precise as the data for the approximation of viscosity forces would typically come from a RANS calculations or a model test.

Most of those simulation tools provide computational speeds close to real time when run on a single-core CPU. Some of the tools, including rolls [1] (Söding, 1982; Söding et al., 2013) and FREDYN (de Kat et al., 1994), are faster as they use lookup tables for diffraction and radiation rather than computing these forces during time-domain simulation run.

Faster computational speeds are attractive as they provide a flexibility to use the full probabilistic assessment (subsection 3.5.3.2 of the IMO Interim

[1] While "rolls" is the name of a simulation tools, its authors have chosen not to capitalize any letters in the name. This paper follows the authors of the tool.

Guidelines) along with assessment in design situations with probabilistic (subsection 3.5.3.3) or deterministic criteria (subsection 3.5.3.4).

The fastest computational speed is required for the statistical validation of extrapolation procedures (section 3.5.6 of the IMO Interim Guidelines), where rare stability failures in realistic conditions need to be observed. However, the simulation tools for statistical validation need to be only qualitatively correct (Smith 2019), meaning being able to reproduce a phenomenon of interest, but not necessarily being able to characterize its correct conditions and parameters. For example, being able to simulate a capsizing as a transition to another stable equilibrium, but not necessary able to correctly predict when it can occur.

One of these "statistical validation" tools is SimpleCode, which applies a body-nonlinear formulation for hydrostatic and Froude-Krylov forces computed from instantaneously submerged volume, coefficient-based radiation and no diffraction. Some ideas are described on how this tool can be made quantitatively correct and used for direct stability assessment.

2. DEVELOPMENT OF SIMPLECODE

The motivation for the development of the volume-based body-nonlinear formulation for hydrostatic and Froude-Krylov forces came from an unpleasant discovery of the very complex probabilistic properties of stability variation in waves (Belenky and Weems, 2008). This complexity does not leave much hope for a reasonable model of stability variation in irregular seas beyond Grim's effective wave (Grim, 1961; Umeda and Yamakoshi, 1986, 1994; Bulian, 2008). Lacking an effective probabilistic model, a direct evaluation of stability in waves is required. The instantaneous submerged volume (and its centroid) can provide the combined hydrostatic and Froude Krylov force, including a restoring moment that characterizes the stability variation in irregular waves.

The first description of SimpleCode was presented by Weems and Woodrow (2013) at the International Ship Stability Workshop 10 years ago. It was essentially a numerical model of ship motion in waves with 3 degrees of freedom:

$$\begin{aligned} &(m + A_{33})\ddot{\zeta} + B_{33}\dot{\zeta} + F_z(\zeta, \phi, \theta, t) = 0 \\ &(I_x + A_{44})\ddot{\phi} + M_r(\dot{\phi}) + M_x(\zeta, \phi, \theta, t) = 0 \\ &(I_y + A_{55})\ddot{\theta} + B_{55}\dot{\theta} + M_y(\zeta, \phi, \theta, t) = 0 \\ &M_r(\dot{\phi}) = B_{44}\dot{\phi} + B_{r1}\dot{\phi} + B_{r2}\dot{\phi}|\dot{\phi}| \end{aligned} \quad (1)$$

where m is a ship mass, I_x and I_y are mass moments of inertia about longitudinal and transversal axis, A_{33}, A_{44} A_{55} are added masses and B_{33}, B_{44} B_{55} are wave damping coefficients in heave, roll and pitch, respectively, while B_{r1} and B_{r2} are coefficient of viscous and vortex roll damping moments. F_Z, is vertical projection of the difference between hydrostatic and Froude-Krylov force and gravity, M_x and M_y are the transversal and longitudinal moments of this difference. Applying Gauss theorem's relationship between surface and volume integrals, these forces are computed through an instantaneous submerged volume and its centroid. The submerged volume and centers are computed by a section-based scheme which is very efficient and captures the effect of the longitudinal variation in relative motions, as shown in Figure 1.

The added mass and damping coefficients were treated as user input in the original version. The option to add the cross-terms for added mass and damping was included in the current version.

The first systematic theoretical justification of the computing hydrostatic and Froude-Krylov forces with volume integration was presented by Weems and Belenky (2015). Two main assumptions are in the calculation: neglecting the incident wave pressure decay with depth (the e^{kz} term) and small curvature of the wave surface over the beam of the ship. The second statement is equivalent to the assumption that the wave is long in comparison with ship breadth.

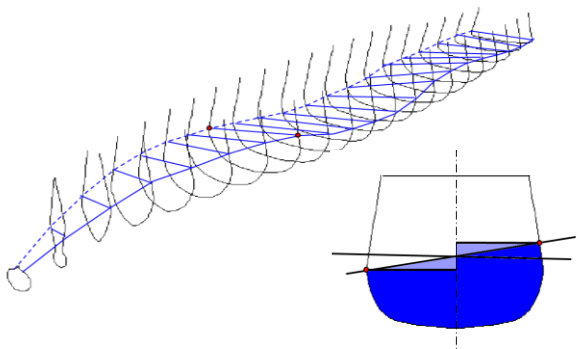

Figure 1. Station/incident wave intersection points for the ONR Tumblehome hull in stern quartering seas and sample sectional volume calculation (Weems and Belenky 2015).

Weems and Belenky (2018) describe the extension of SimpleCode to 6 DOF including the addition of the MMG (Maneuvering Modeling Group) maneuvering model (Yasukawa and Yoshimura, 2015). The volume-based calculation Froude-Krylov was extended for all 6 DOF, providing consistent body-nonlinear coupling between all of the degrees of freedom.

Weems and Belenky (2018) also describe a verification between SimpleCode and LAMP-0 (LAMP with the potential-flow hydrodynamics calculation turned-off). LAMP also has an option to switch off the incident wave pressure decay with depth, an option which allows the LAMP-0 integration of Froude-Krylov pressure to match SimpleCode's volume-based calculation.

SimpleCode's 6-DOF solver can be an implementation of the multifidelity approach, as the coefficient for maneuvering forces can be computed with RANS (Aram and Silva, 2019).

Three solvers are in SimpleCode. The "original" 3-DOF vertical plane (heave-roll-pitch) solver (Eq. 1), which has been employed extensively for statistical validation of extrapolation methods, e.g. Weems et al. (2023); Campbell et al. (2023). The 3-DOF horizontal plane (surge-sway-yaw) solver provides a maneuvering simulator and simplified model of surf-riding and broaching, see e.g. Belenky et al. (2023).

The 6-DOF solver provides the most general model and has been applied as a reduced-order model for the study of surf-riding, broaching-to and capsizing caused by broaching, e.g. Weems et al. (2020). A more complete description of the models and options of SimpleCode can be found in Weems and Belenky (2023).

Per the requirements of the IMO Interim Guidelines (Section 3.3.3), the simulation tool should have at least 4-DOF to be used for dead ship condition (sway-heave-roll and pitch), pure loss of stability and surf-riding broaching (surge, sway, roll and yaw). The 6-DOF solver may be used for these four failure modes. The 3-DOF solver may be applied for parametric roll and excessive acceleration failure modes.

3. TOWARDS QUANTITATIVE APPLICATION

To consider SimpleCode for a quantitative application such as Direct Stability Assessment or as a predictor for extreme events (Reed, 2021), a model of diffraction forces is needed. For the 3-DOF model (Eq. 1), this model is:

$$\begin{aligned} F_{d3}(t) &= \sum_{i=1}^{N} f_i^{c3} \cos \omega_i t + f_i^{s3} \sin \omega_i t \\ F_{d4}(t) &= \sum_{i=1}^{N} f_i^{c4} \cos \omega_i t + f_i^{s4} \sin \omega_i t \\ F_{d5}(t) &= \sum_{i=1}^{N} f_i^{c5} \cos \omega_i t + f_i^{s6} \sin \omega_i t \end{aligned} \quad (2)$$

where $f_i^{c3}, f_i^{s3}, f_i^{c4}, f_i^{s4}, f_i^{c5}$ and f_i^{s5} are amplitudes of cosine (identified with superscript *c*) and sine (identified with superscript *s*) components of frequency ω_i computed for heave, roll and pitch and identified with the superscripts 3, 4 and 5, respectively. Radiation forces are already included in the equation (1), so accounting for diffraction and radiation is a matter of effectively estimating the coefficients A_{jk}, B_{jk}, $B_{r1,2}$ and f_i; indices indicate modes of motion and take values 3, 4 and 5.

The roll damping coefficients B_{44}, B_{r1} and B_{r2} are traditionally estimated from roll decay tests or RANS simulations. If the logarithm of the roll decrement between peaks is plotted versus the roll amplitude, the linear roll damping coefficient $(B_{44} + B_{r1})$ is an intercept of the plot, while the quadratic coefficient is a slope.

Pipiras et al. (2021, 2022) formulated a regression approach to estimating the diffraction and radiation force coefficients. The idea is to extract the information on diffraction and radiation forces from potential-flow simulations in a similar way to how viscous forces can be extracted from a RANS simulation. The algorithm includes the following steps:

1. Run the potential-flow simulation tool for one or more records of the wave conditions.
2. Use the motions from these records to run forced motion simulations in calm water. Output the potential flow hydrodynamic forces and regress them against acceleration and velocities. The slope coefficients of accelerations are added masses, while the slope coefficients of velocities are damping coefficients.
3. Fix the ship and run "wave-pass" simulations in the same waves. The potential-flow forces represent diffraction. The diffraction coefficients f_i are estimated by regressing these forces against

the cosine and sine components of wave elevation representation (Eq. 2).

This approach has been implemented with LAMP, which has options for performing both the prescribed motion and wave-pass simulations and a capability to output hydrodynamic forces separately from Froude-Krylov forces.

The estimation of radiation with regression of potential flow data is carried out for pitch and heave only, as roll is set separately based on CFD or model test data. To estimate diagonal and cross-terms for radiation, the prescribed motions are simulated separately: only heave ζ_3 and only pitch θ_5:

$$\begin{aligned} F_{33} &= -\left(A_{33}\ddot{\zeta}_3 + B_{33}\dot{\zeta}_3\right) \\ F_{53} &= -\left(A_{53}\ddot{\zeta}_3 + B_{53}\dot{\zeta}_3\right) \\ F_{55} &= -\left(A_{55}\ddot{\theta}_5 + B_{55}\dot{\theta}_5\right) \\ F_{35} &= -\left(A_{35}\ddot{\theta}_5 + B_{35}\dot{\theta}_5\right) \end{aligned} \quad (3)$$

where F_{33} is heave radiation force due to heave, F_{53} is pitch radiation moment due to heave, F_{55} is pitch radiation moment due to pitch, F_{35} is heave radiation force due to pitch.

The radiation coefficients $\vec{c}_{jk} = (A_{jk} \quad B_{jk})^T$ are computed through a standard linear regression approach (*e.g.* Faraway, 2005):

$$\vec{c}_{jk} = \left(\boldsymbol{X}_j^T \boldsymbol{X}_j\right)^{-1} \boldsymbol{X}_j^T \vec{F}_{jk} \quad (4)$$

where $\vec{F}_{jk}$ is a response vector representing a time history of hydrodynamic force, superscript 'T" indicates transposition and $\boldsymbol{X}_j$ is a 2 by N_t matrix of predictors, while N_t is a number of data points generated by numerical simulation:

$$\begin{aligned} \boldsymbol{X}_3 &= \begin{pmatrix} \ddot{\zeta}_{31} & \dot{\zeta}_{31} \\ \dots & \dots \\ \ddot{\zeta}_{3N_t} & \dot{\zeta}_{3N_t} \end{pmatrix} \\ \boldsymbol{X}_5 &= \begin{pmatrix} \ddot{\theta}_{51} & \dot{\theta}_{51} \\ \dots & \dots \\ \ddot{\theta}_{5N_t} & \dot{\theta}_{5N_t} \end{pmatrix} \end{aligned} \quad (5)$$

It has been observed that the radiation heave-pitch cross-terms may have a little influence on the results in the considered cases. Neglecting these cross-term makes calculations a bit simpler as a single fixed motion run is required with heave ζ_{35} and pitch θ_{35} together:

$$\begin{aligned} F_{33} &= -\left(A_{33}\ddot{\zeta}_{35} + B_{33}\dot{\zeta}_{35}\right) \\ F_{55} &= -\left(A_{55}\ddot{\theta}_{35} + B_{55}\dot{\theta}_{35}\right) \end{aligned} \quad (6)$$

The accelerations and velocity of this combined run are used in equation (5), while regression formulae (4) stay the same.

Diffraction was computed for heave, roll and pitch. The diffraction coefficients for *j*-th degree of freedom $\vec{f}^j = \left(f_1^{cj}, \dots f_N^{cj}, f_1^{sj}, \dots f_N^{sj}\right)^T$ are estimated as:

$$\vec{f}^j = (\boldsymbol{Y}^T\boldsymbol{Y})^{-1}\boldsymbol{Y}^T\vec{F}_{dj} \quad (7)$$

where $\vec{F}_{dj}$ is a response vector representing a time history of hydrodynamic force for the *j*-th degree of freedom and $\boldsymbol{Y}$ is a 2*N* by N_t matrix of predictors that includes all the frequency components :

$$\boldsymbol{Y} = \begin{pmatrix} \cos\omega_1 t_1 \dots \cos\omega_N t_1 & \sin\omega_1 t_1 \dots \cos\omega_N t_1 \\ \dots \\ \cos\omega_1 t_{N_t} \dots \cos\omega_N t_{N_t} & \sin\omega_1 t_{N_t} \dots \cos\omega_N t_{N_t} \end{pmatrix} \quad (8)$$

As the matrix of predictors $\boldsymbol{Y}$ may be large, the calculation in equation (7) may become unstable. A penalization scheme described by Pipiras et al. (2022) and Kim et al. (2023) helps to obtain more stable regression estimates.

Essentially the regression (7, 8) is an equivalent for Fourier transformation. In principle, the diffraction coefficients could be taken from a frequency domain code, but the described regression scheme is needed for consistency with LAMP.

Further details of the regression approach and results are described in Kim et al. (2023).

As was mentioned above, the roll added mass and damping coefficients were computed from roll decay data. Setting up roll damping for a potential flow solver requires certain care to avoid double counting of the wave-making component of roll damping. The latter is present in roll decay data from model test and in any RANS result (unless the RANS configuration was double-body). The error due to duplication ("double counting") of the wave component of roll damping may be not insignificant (France et al. 2003).

To avoid duplication of the wave component of roll damping, the coefficients B_{44} and B_{r1} need to be separated. This can be done by performing roll decay tests with the potential-flow simulation and fitting roll damping coefficients to match experimental or RANS data, following the approach in Belenky et al. (2011). The necessity to avoid duplication is mentioned in paragraph 3.3.2.2.3 of the Interim Guidelines (MSC.1/ Circ. 1627) and at the end of subsection 2.4 of ITTC Recommended Procedure 7.5-02-07-04.5.

Added mass in roll A_{44} can also be estimated from roll decay test, usually by matching the periods of the free roll oscillations. If model test or RANS data is used to correct the roll added mass in a potential-flow solver, care must be taken to avoid double counting there as well.

4. APPLICATION AND COMPARISON

A numerical study was performed which compared SimpleCode results with an advanced potential flow solver in order to see if SimpleCode is viable for direct stability assessment. SimpleCode results were used "as is" without any post-calculation correction described by Levine et al. (2022).

The numerical study was performed for ITTC-A1 ship (Umeda et al., 2000), whose principal particulars are summarized in Table 1. This configuration was used in the ITTC benchmarking (ITTC, 2005) and SAFEDOR project (e.g. Spanos and Papanikolaou 2009). Roll decay data were available from the latter reference.

Table 1. Principal Particulars of ITTC-A1 Ship.

Parameter	Value	Parameter	Values
Length BP, m	150	GM, m	1.38
Breadth, m	27.2	CB	0.667
Draft, m	8.5	CM	0.959
KG, m	10.24	CW	0.786

LAMP provides a basis for comparison. LAMP simulations were carried out for three degrees of freedom (heave-roll-pitch) with the body-nonlinear formulation for the Hydrostatic and Froude-Krylov forces. Diffraction and radiation forces were computed using a body-linear potential-flow solution with Rankine singularities on the hull and free surface and a damping beach condition. In this formulation, the diffraction and radiation potential is calculated on the mean wetted hull surface with the instantaneous ship motion. This set of LAMP options is referred to as LAMP-2.

To evaluate the assumption of SimpleCode's volume-based force calculations, which are long waves and the neglecting of the exponential decay of the incident wave pressure, all the calculations are repeated with LAMP without diffraction and radiation. LAMP has an option to replace the potential-flow hydrodynamics calculations with diffraction and radiation coefficients like those in SimpleCode. This set of LAMP options is referred to as LAMP-0. LAMP-0 also has an option to switch off the exponential wave pressure decay, so the long wave assumption of SimpleCode can be tested separately.

Figure 2 compares of roll decay test data with the results of LAMP-2 calculation tuned to match the model test. The phase difference is apparently caused by a mismatch of natural period, which probably resulted from the difference in added mass. Numerical results are in Table 2

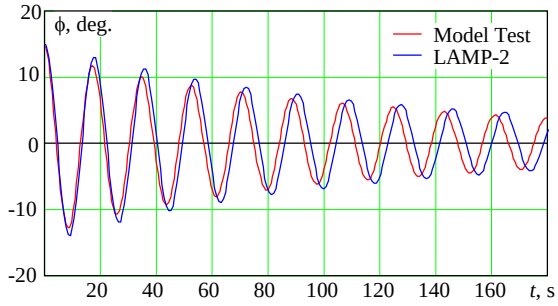

Figure 2. Roll decay comparison: model test and calibrated LAMP-2 simulation.

Table 2. Results of LAMP-2 roll damping calibration.

Parameter	Value
Linear coefficient (as fraction of critical)	0.018
Quadratic coefficient B_{r2}, kNm /(deg/s)^2	100

This damping calibration was carried out by visually checking the responses, so "double counting" can be avoided but the accuracy of the results in Table 2 is limited. These roll damping results generated a single record of ship motions in irregular waves from which diffraction and radiation coefficients were found. The ship is operating at 10 knots in quartering waves. Parameters of the irregular wave and results of radiation calibrations are in Table 3. A total of 1440 diffraction coefficients (240 cosine and sine components for three degrees of freedom) resulted (not shown here).

Table 3. Calibration for diffraction and radiation.

Parameter	Value
Significant wave height, m	5
Modal period, s	14
Duration of the record, s	940
Number of frequency components	240
Added mass in heave A_{33}/m	1.810
Added mass in pitch A_{55}/I_y	1.046
Damping coefficient in heave B_{33}, kN s/m	18300
Damping coefficient in pitch B_{55} kN m /(deg/s)	306000

The next step is roll decay calibration with LAMP-0 and SimpleCode, with the heave and pitch radiation data from Table 3. The difference with the

LAMP-2 roll decay calibration is that added mass in roll is also determined by trying to match natural period of roll. The resulting time histories are in Figure 3, while numerical results are in Table 4.

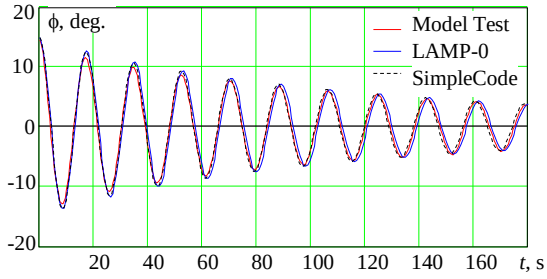

Figure 3. Roll decay comparison: model test and calibrated LAMP-0 and SimpleCode.

Table 4. Results of SimpleCode roll damping calibration.

Parameter	Value
Linear coefficient (in terms of critical)	0.015
Quadratic coefficient B_{r2}, kNm /(deg/s)^2	100.0
Added mass in roll A_{44}/I_x	0.1

The added mass in roll is part of the calibration, the LAMP-0 and SimpleCode results are closer to the model test data than those of LAMP-2 in Figure 2. As the calibration is done visually and the wave component of roll damping for the current configuration is not large, the LAMP-2 and SimpleCode damping coefficients are nearly the same.

Figure 4 compares sample irregular wave responses (wave parameters are given in Table 4) for LAMP-2, which is considered to be high-fidelity result in this context, SimpleCode and LAMP-0 and LAMP-0 without wave pressure decay. The right side of the figure contain zoomed in time histories from 800 s to 900 s.

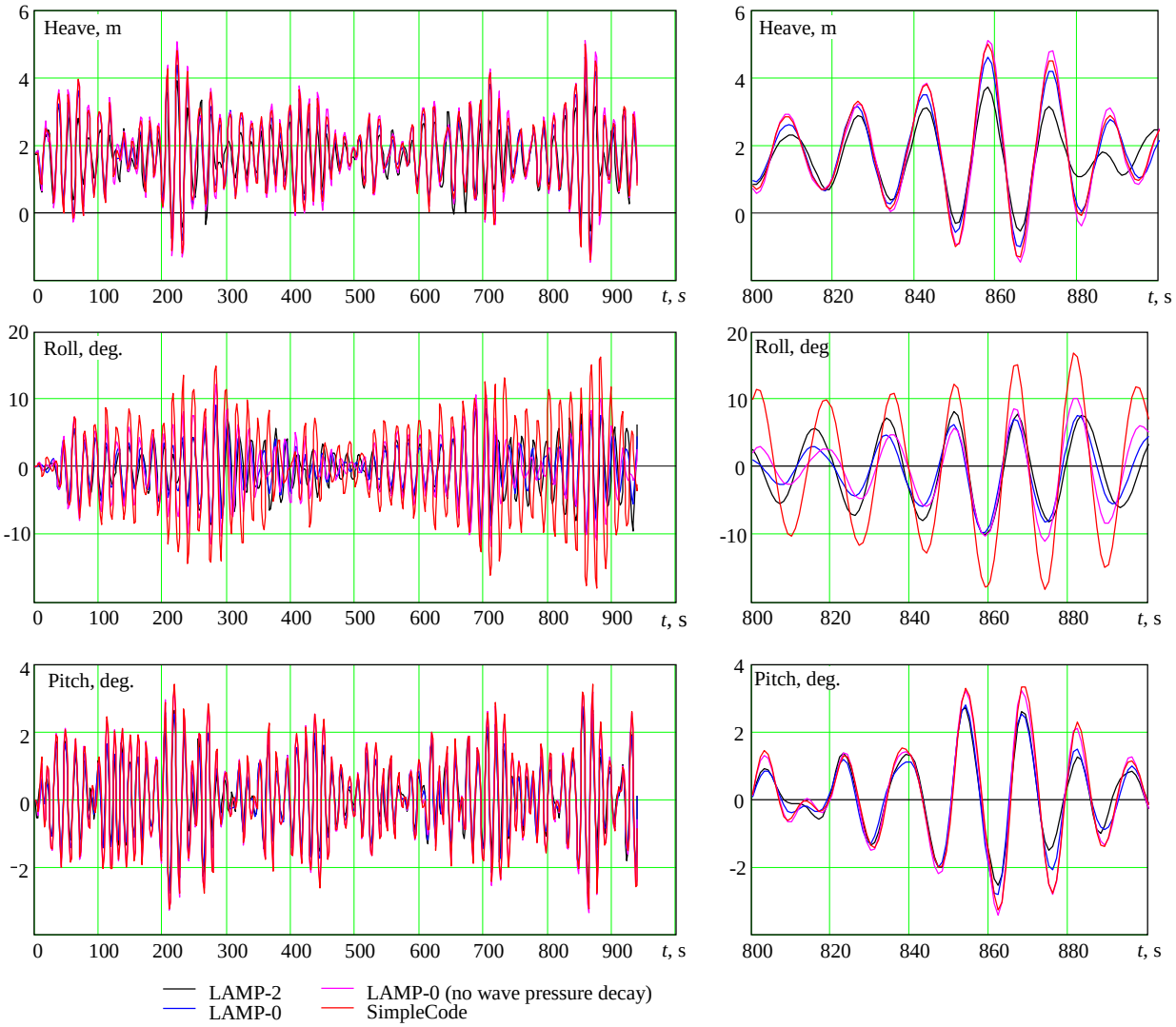

Figure 4. Irregular wave (10 knots, quartering seas) simulation results for LAMP-2 and LAMP-0 and SimpleCode with calibrated diffraction and radiation.

The overall visual impression is that heave and pitch compare favorably. SimpleCode seems to capture the phase well and slightly overestimate amplitudes of pitch and heave. The difference in pitch seems be driven by the assumption of wave pressure decay, while the approximation of diffraction and radiation seems to be behind the observed difference in heave amplitude.

The LAMP-2 versus SimpleCode difference in roll amplitude is significant and seems to be only partially a result of the wave pressure decay assumption; as the LAMP-0 result without the pressure decay is closer to LAMP-2 and LAMP-0 with the pressure decay than to SimpleCode result. That makes the long wave assumption the prime suspect for the difference.

To test this hypothesis, calculations were repeated with narrower bandwidth: from circular frequency 0.2 to 0.8 rad/s, eliminating shorter wave components. Other parameters (including number of frequencies) remains the same. Regression calculation for diffraction and radiations were repeated, but the added masses and damping coefficients (Table 5) did not change much.

Comparison between the time histories is shown in Figure 5. The difference in roll amplitude seems to decrease significantly, supporting the idea that the assumption of long wave is behind the difference.

Table 5. Calibration for diffraction and radiation.

Parameter	Value
Added mass in heave A_{33}/m	1.87
Added mass in pitch A_{55}/I_y	1.09
Damping coefficient in heave B_{33}, kN s/m	16200
Damping coefficient in pitch B_{55} kN m /(deg/s)	292000.

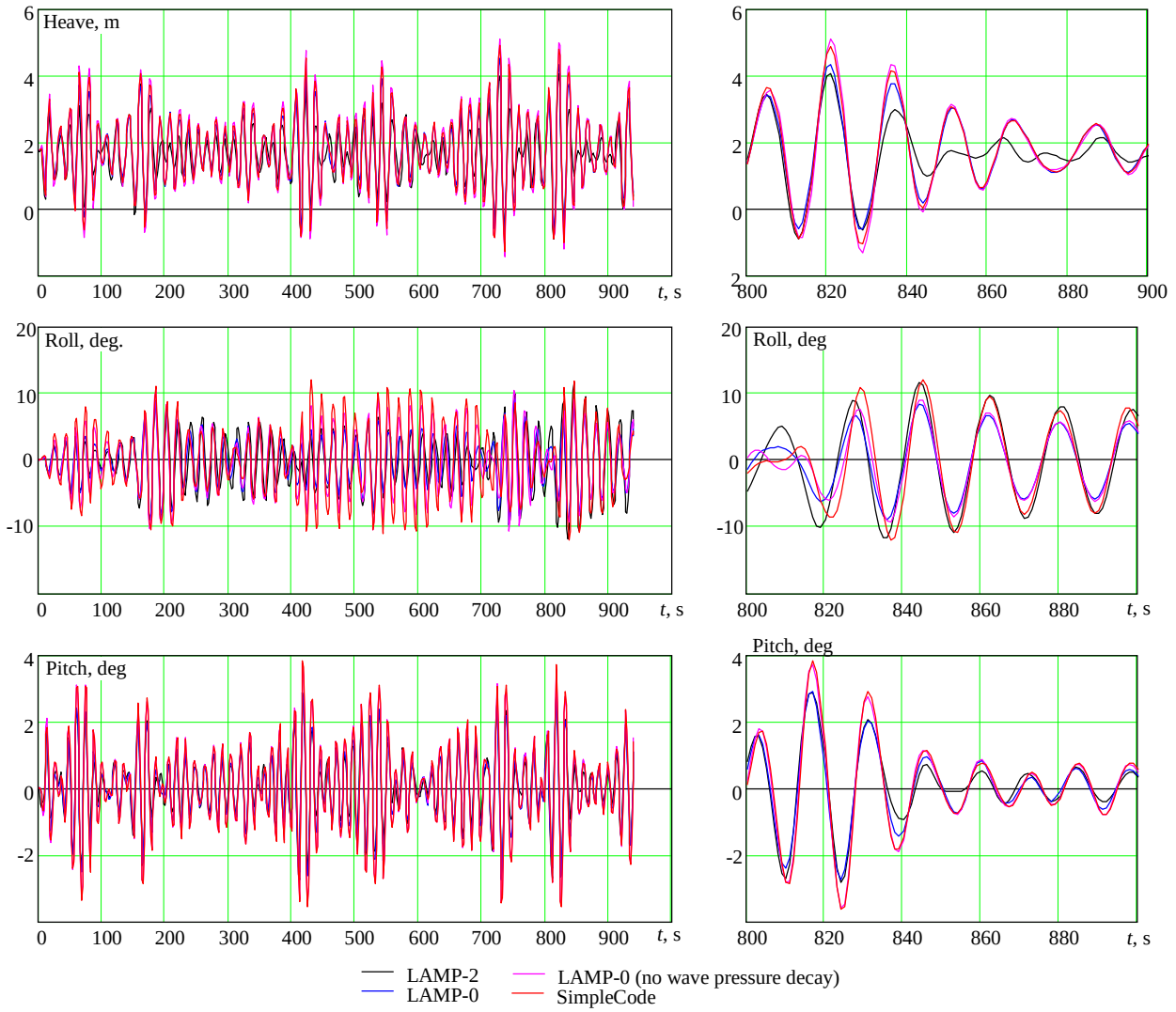

Figure 5. Irregular wave (10 knots, quartering seas) simulation results for LAMP-2 and LAMP-0 and SimpleCode calibrated with diffraction and radiation, with wave frequency limited to 0.2–0.8 1/s.

5. SUMMARY AND CONCLUSIONS

The paper considers the application of SimpleCode, which is simplified seakeeping simulation tool incorporating a volume-based body-nonlinear formulation for hydrostatic and Froude-Krylov forces, for Direct Stability Analysis within the framework of the Second Generation Intact Stability Criteria (MSC.1/Circ. 1627 and MSC.1/Circ. 1652). As SimpleCode was originally intended for the validation of statistical extrapolation, its computational speed makes it an attractive tool, but it needs to be quantitatively correct to be applied for this purpose.

To achieve this, a more accurate model of the diffraction and radiation forces is required. This is accomplished by computing ship and seaway-dependent diffraction and radiation coefficients to the hydrodynamic forces from potential flow seakeeping simulations. The radiation coefficients are computed by regression of forced-motion hydrodynamic forces against acceleration and velocities. Diffraction coefficients are computed by regression of wave-pass hydrodynamic forces to cosine and sine components of the wave presentation. The current implementation uses the regression approach for radiation in heave and pitch and for diffraction in all degrees of freedom. Roll Added mass and damping are estimated by fitting roll decay data.

There are two main assumptions in the volume-based body nonlinear formulation for hydrostatic and Froude-Krylov forces: waves are relatively long compared to the ship's beam and wave pressure decay can be neglected. These two assumptions provide a significant saving in computational costs. The number of evaluations of the wave field, which can be quite expensive for an irregular wave field, is reduced to a single elevation per station, rather than elevation and pressure at thousands of hull panel. These evaluations can be further economized via interpolation in space and/or time.

A comparison between potential-flow simulation using LAMP with potential flow hydrodynamics, LAMP with coefficient-based hydrodynamics and SimpleCode have indicated that the long wave assumption may be a limiting factor for roll, while neglecting wave pressure decay may be a limiting factor for pitch.

These limitations may be overcome with introduction of an attenuation function to mitigate the effect of these assumption (both wave pressure decay and long waves). The implementation of such a function remains for future work as well as more formal comparison between the results of numerical simulation of ship motions.

ACKNOWLEDGEMENTS

The development of the multifidelity reduced-order models and associated simulation tools have been funded by the Office of Naval Research (ONR) under Dr. Woei-Min Lin, including a NSWCCD research project managed by Dr. Art Reed. Participation of Prof. Pipiras was partially facilitated by the NSWCCD Summer Faculty and Sabbatical Programs, managed by Dr. Jack Price.

REFERENCES

Aram, S. and K. M. Silva, 2019, "Computational fluid dynamics prediction of hydrodynamic derivatives for maneuvering models of a fully-appended ship," *Proc. 17th Intl. Ship Stability Workshop*, Helsinki, Finland, pp. 57-66.

Belenky, V. and K.M. Weems, 2008, "Probabilistic Qualities of Stability Change in Waves," *Proc. 10th Intl. Ship Stability Workshop*, Daejon, Korea, pp. 95-108.

Belenky, V., H. Yu and K. M. Weems, 2011, "Numerical Procedures and Practical Experience of Assessment of Parametric Roll of Container Carriers," Chapter 16 of "*Contemporary Ideas on Ship Stability,*" Neves, M.A.S., Belenky, V., de Kat, J. O., Spyrou, K. and N. Umeda, eds., Springer, ISBN 978-94-007-1481-6, pp. 295-396.

Belenky, V., Weems, K. M, Spyrou, K., Pipiras, V. and T. Sapsis (2023) "Modeling Broaching-to and Capsizing with Extreme Value Theory," in *Contemporary Ideas on Ship Stability – From Dynamics to Criteria*, Spyrou, K., Belenky, V., Katayama, T., Bačkalov, I., Francescutto, A., eds., Springer, ISBN 978-3-031-16328-9, pp. 435- 457.

Belknap, W. F. and A. M. Reed, 2019, "TEMPEST: A New Computationally Efficient Dynamic Stability Prediction Tool," Chapter 1 of *Contemporary Ideas on Ship Stability. Risk of Capsizing*, Belenky, V., Spyrou, K., van Walree F., Neves, M. A. S., and N. Umeda, eds., Springer, ISBN 978-3-030-00514-6, pp. 3-21.

Bulian, G., 2008, "On an improved Grim effective wave". *Ocean Engineering*, vol. 35, pp. 1811-1825.

Campbell, B., K. Weems, V. Belenky, V. Pipiras, and T. Sapsis, 2023, "Envelope Peaks over Threshold (EPOT) Application and Verification," in *Contemporary Ideas on Ship Stability*

– *From Dynamics to Criteria*, Spyrou, K., Belenky, V., Katayama, T., Bačkalov, I., Francescutto, A., eds., Springer, ISBN 978-3-031-16328-9, pp. 265-289.

de Kat, J. O., R. Brouwer, K. McTaggart and W. L. Thomas, 1994, "Intact Ship Survivability in Extreme Waves: New Criteria from Research and Navy Perspective". *Proc. 5th Intl. Conf. Stability of Ships & Ocean Vehicles (STAB '94)*, Vol. 1, Melbourne, FL, 26 p.

France, W.M, Levadou, M, Treakle, T.W., Paulling, J. R., Michel, K. and C. Moore, 2003, "An Investigation of Head-Sea Parametric Rolling and its Influence on Container Lashing Systems," *Marine Technology,* Vol. 40, No. 1, pp. 1-19

Grim, O., 1961, "Beitrag zu dem Problem der Sicherheit des Schiffes im Seegang," Schiff und Hafen, 6:491–201.

IMO MSC.1/Circ. 1627, "Interim Guidelines on the Second Generation Intact Stability Criteria", London, December 2020

IMO MSC.1/Circ.1652, "Explanatory Notes to the Interim Guidelines on the Second Generation Intact Stability Criteria", London, April 2023

ITTC, 2021, "Estimation of Roll Damping," Recommended Procedure 7.5-02-07-04.5.

ITTC, 2005, "The Specialist Committee on Stability in Waves, Final Report and Recommendations to the 24th ITTC," *Proceedings of the 24th International Towing Tank Conference*, Vol. II, pp. 369-407.

Kim, M., Pipiras, V., Reed, A. and K. Weems, 2023, "Calibration of low-fidelity ship motion codes through regressions of high-fidelity forces," *Ocean Engineering, Special Issue on Extreme Stochastic Dynamics of Ships* (submitted).

Levine, M. D., Edwards, S. J., Howard, D., Sapsis, T., Weems, K., Pipiras, V. and V. Belenky, 2022, "Data-Adaptive Autonomous Seakeeping" *Proc. 34th Symp. Naval Hydrodynamics,* Washington, D.C., USA

Peters, W., Belenky, V., Bassler C., Spyrou, K., Umeda, N., Bulian, G. and B. Altmayer, 2011. "The Second Generation of Intact Stability Criteria an Overview of Development," *SNAME Trans.* 119**.** pp. 225-264.

Pipiras, V., Belenky, V., Weems, K., Brown, B., Frommer, A. and G. Ouimette, 2021, "Calibrating Multifidelity Ship Motion Codes Through Regression," *Proc. 1st Intl. Conf. on Stability and Safety of Ships and Ocean Vehicles STABS 2021*, Glasgow, Scotland, UK.

Pipiras, V., Howard, D., Belenky, V., Weems, K. and T. Sapsis, 2022, "Multi-Fidelity Uncertainty Quantification and Reduced-Order Modeling for Extreme Ship Motions and Loads," *Proc. 34th Symp. Naval Hydrodynamics,* Washington, D.C., USA.

Reed, A.M., 2021, "Predicting Extreme Loads and the Processes for Predicting Them Efficiently," *Proc. 1st Intl. Conf. on Stability and Safety of Ships and Ocean Vehicles STABS 2021*, Glasgow, Scotland, UK.

Reed, A. M and Beck, R. F., 2016, "Advances in the Predictive Capability for Ship Dynamics in Extreme Waves" *Trans. SNAME*, Vol. 124, pp. 2-39.

Smith, T. C., 2019, "Validation Approach for Statistical Extrapolation", Chapter 34 of *Contemporary Ideas on Ship Stability. Risk of Capsizing*, Belenky, V., Neves, M., Spyrou, K., Umeda, N., van Walree, F., eds., Springer, 2019 ISBN 978-3-030-00514-6, pp. 573-589.

Shin, Y. S, Belenky, V. L., Lin, W.-M., Weems, K. M., and A. H. Engle, 2003, "Nonlinear Time Domain Simulation Technology for Seakeeping and Wave-Load Analysis for Modern Ship Design," *Trans. SNAME*, Vol. 111, pp. 557-578.

Söding, H., 1982, "Leckstabilität im Seegang". Report No. 429, Institut für Schiffbau, Hamburg, Germany, 69 p

Söding, H., Shigunov, V., Zorn, T., and Soukup, P., 2013, "Method rolls for Simulating Roll Motions of Ships", Ship Technol. Research – Schiffstechnik, Vol.60, Nr. 2.

Spanos, D. and A. Papanikolaou, 2009 "Benchmark Study on Numerical Simulation Methods for the Prediction of Parametric Roll of Ships in Waves." *Proc. 10th Intl. Conf. Stability of Ships and Ocean Vehicles*, St. Petersburg, Russia, pp. 627–36.

Umeda, N. and Y. Yamakoshi, 1986, "Experimental Study on Pure Loss of Stability in Regular and Irregular Following Seas," *Proceedings 3rd Intl. Conf. on Stability of Ships and Ocean Vehicles*, Gdansk, Poland, Vol. 1, pp .93–99.

Umeda, N. and Y. Yamakoshi, 1994, "Probability of Ship Capsizing due to Pure Loss of Stability in Quartering Seas." *Naval Architecture and Ocean Engineering*, Vol. 30, pp. 73–85

Umeda, N., A. Munif and H. Hashimoto, 2000, "Numerical Prediction of Extreme Motions and Capsizing for Intact Ships in Following/ Quartering Seas," *Proceedings of the 4th Osaka Colloquium on Seakeeping Performance of Ships*, Osaka, Japan, pp. 368-373.

Weems, K. and V. Belenky, 2015, "Fast Time-Domain Simulation in Irregular Waves With Volume-Based Calculations for Froude-Krylov and Hydrostatic Force," *Proc. 12th Intl. Conf. on Stability of Ships and Ocean Vehicles (STAB 2015)*, Glasgow, UK, pp. 891-901.

Weems, K, and V. Belenky, 2018, "Extended Fast Ship Motion Simulations for Stability Failures in Irregular Seas," *Proc.*

13th Intl. Conf. on Stability of Ships and Ocean Vehicles STAB 2018, Kobe, Japan.

Weems, K., Belenky, V., Spyrou, K., Aram, S. and K. Silva, 2020, "Towards Numerical Estimation of Probability of Capsizing Caused by Broaching-to," *Proc. 33rd Symp. Naval Hydrodynamics,* Osaka, Japan.

Weems, K., V. Belenky, B. Campbell, and V. Pipiras, 2023, "Statistical Validation of the Split-Time Method with Volume-Based Numerical Simulation", in *Contemporary Ideas on Ship Stability – From Dynamics to Criteria*, Spyrou, K., Belenky, V., Katayama, T., Bačkalov, I., Francescutto, A., eds., Springer, ISBN 978-3-031-16328-9, pp. 225-243.

Weems, K., and V. Belenky, 2023, Volume-base Reduced-Order Model for ship motions. *Ocean Engineering, Special Issue on Extreme Stochastic Dynamics of Ships* (submitted).

Weems, K., and D. Wundrow, 2013, "Hybrid Models for Fast Time-Domain Simulation of Stability Failures in Irregular Waves with Volume-Based Calculations for Froude-Krylov and Hydrostatic Force," *Proc. of 13th Intl. Ship Stability Workshop*, Brest, France, pp. 130-137.

Yasukawa, H. and Y. Yoshimura, 2015, "Introduction of MMG standard method for ship maneuvering predictions," *Journal of Marine Science and Technology,* Vol. 20, pp. 37-52. DOI 10.1007/s00773-014-0293-y.

Current ITTC work to support Direct Stability Assessment

Vadim Belenky, *David Taylor Model Basin NSWCCD,* vadim.belenky@navy.mil
Evangelos Boulougouris, *University of Strathclyde* evangelos.boulougouris@strath.ac.uk
Shuxia Bu, *China Ship Scientific Research Centre*, bushuxia8@163.com
Taeyoung Kim, *Samsung Heavy Industries*, ty103.kim@samsung.com
Jean-François Leguen, *DGA Hydrodynamics,* jean-francois.leguen@intradef.gouv.fr
Yi Liu, *Marine Design and Research Institute of China*, liuyi3511@maric.com.cn
Akihiko Matsuda, *National Research Institute of Fisheries Engineering,* amatsuda@fra.affrc.go.jp
Claudio A. Rodríguez, *LabOceano - Federal University of Rio de Janeiro*, claudiorc@oceanica.ufrj.br

ABSTRACT

The paper describes current work of the Stability in Wave Committee (SiW) of the 30th International Towing Tank Conference. Development of recommended procedures for Direct Stability Assessment (DSA) under the Second Generation IMO Intact Stability Criteria. The following ITTC-recommended procedures are being developed: Avoiding Self-Repeating Effect, Estimation of Frequency of Random Events (direct counting) and Statistical Validation of Extrapolation Methods. The paper also covers the development and update of other relevant recommended procedures.

Keywords: *Second generation intact stability criteria, Direct Stability Assessment*.

1. INTRODUCTION

As stated on the ITTC website (https://www.ittc.info/), the International Towing Tank Conference (ITTC) is a worldwide association of organizations that provides guidelines and recommended procedures for the prediction of the hydrodynamic performance of ships and marine installations based on the results of physical experiments and numerical simulations.

Moreover, ITTC is recognized as a Non-Governmental Organization (NGO) with observer status to the International Maritime Organization (IMO), participating actively in discussions concerning safety and performance, such as in ship stability.

The Full Conference, comprising representatives of all member organizations, is held every three years and constitutes the highest authority of the ITTC. The Executive Committee is responsible for the day-to-day operation of the ITTC, assisted by the Advisory Council on technical matters. Several permanent and specialist technical committees perform assigned work tasks between Full Conferences and report to the Full Conference.

The structure of the technical committees includes General Committees, Specialist Committees and Groups. The Stability in Waves (SiW) Committee is one of the six General Committees. The SiW Committee covers the stability of intact and damaged ships in waves. The Terms of Reference (TOR) for each committee are proposed by the Advisory Council and approved by the Full Conference.

Since 1996, the Stability in Waves Committee has a strong link with the STAB conference community (e.g., Vassalos et al., 1997). This paper continues the tradition.

Some of the main tasks of TOR assigned in 2021 to the current SiW committee are:

- Task 2: “Review ITTC Recommended Procedures relevant to stability. A) Identify any requirements for changes in the light of current practice, and, if approved by the Advisory Council, update them. B) Identify the need for new procedures and outline the purpose and contents of these”,
- Task 4: “Develop new ITTC recommended procedures in support of direct stability assessment within 2nd generation IMO intact stability criteria”,

• Task 5: "Develop a new procedure, Computational procedure for instantaneous GZ curve during time-domain simulation in irregular waves",

• Task 7: "Continue the identification of benchmark data for validation of stability-in-waves predictions".

Complete terms of references, other details and more information are available at the ITTC website: https://www.ittc.info/.

This paper is specifically focused on the description of the development of new procedures and updating the existing procedures. It reports the committee's view on their scope, methodology and main references. Other activities of the SiW committee such as literature review and recommendation of further research will be included in the SiW Committee report to the 30th International Towing Tank Conference and are not covered in this paper.

2. NEW AND UPDATED PROCEDURES IN SUPPORT OF DIRECT STABILITY ASSESSMENT

The committee has been assigned, under Task 4 of the Terms of Reference, to develop three new procedures in support of direct stability assessment (DSA) within the 2nd generation IMO intact stability criteria. These new procedures aim to provide recommendations on avoiding self-repeating effects, estimation of the frequency of random events by direct counting, and statistical validation of extrapolation methods for time domain simulations of ship motions.

The ITTC-recommended procedures in support of direct stability assessment are meant to complement the Explanatory Notes for the Interim Guidelines. Like any other ITTC-recommended procedure, the audience is mainly the ITTC membership. The ITTC procedures are specifically geared towards capabilities and skill sets, available to ITTC members that are expected to participate in trial application of the DSA.

The ITTC-recommended procedures may be updated at a Conference i.e., every three years. That is a perfect opportunity for documenting DSA application experience. These updates may serve as a compliment to the submissions to IMO Subcommittee on Design and Construction (SDC) under the agenda item "any other business".

Self-repeating effect

The new procedure, as a part of Task 4A of the Terms of Reference, is being developed under the title of "Avoiding Self-Repeating Effect in Time-Domain Numerical Simulation of Ship Motions". The purpose of this procedure is to formulate a process for verification of absence of self-repetition effect and statistical validity of irregular waves and ship motions in a numerical simulation. Especially, the procedure targets providing specific guidelines to check the self-repetition effect in the direct stability assessment defined in Interim Guidelines on the Second Generation Intact Stability criteria.

The self-repeating effect is a result of the accumulation of integration error when evaluating wave elevation with the Longuett-Higgins model, resulting in the appearance of an artificial self-dependence of generated records.

The basic idea is to utilize the property of the auto-correlation function for irregular waves. If the time series has self- repetition effect, the auto-correlation function, computed from spectrum, tends to increase after some time (Belenky, 2011). The self-repetition effect is considered present if the envelope of the autocorrelation function up-crosses a level of significance (set to 0.05).

The procedure will contain a very brief section on the background of the self-repeating effect based on (Belenky 2011), where the accumulation of an integration error in the autocorrelation function is shown. The section extends this demonstration onto the calculation of wave elevation itself, which was not previously published. An abridged description is available in Appendix 1.

Direct Counting

A new draft procedure, titled "Estimation of Frequency of Random Events", has been developed by the Committee under Task 4B of the Terms of Reference. The draft procedure addresses post-processing of numerical simulation of roll motions or lateral accelerations, described in section 3 titled "Direct Counting" of Appendix 4 of MSC.1 /Circ.1652.

The objective of the post-processing is an estimation of the rate of failures, observed in the output of time-

domain numerical simulation, using the Poisson model of random events to relate probability and time. The draft procedure covers three methods of the rate estimations described in the Explanatory Notes. These methods offer different ways of addressing the independence of failures – the critical requirement of the Poisson model. The two other requirements – that the rate of events over time is constant and the events cannot occur simultaneously – are satisfied automatically for a stationary process of ship motions.

One method is based on the exponential distribution of the time interval before the event occurs (subsection 3.3 of Appendix 4 of MSC.1/Circ. 1652). The other method extracts the rate from an estimate of the probability of at least one failure during a record length (subsection 3.4 of the cited Appendix). The third method uses decorrelation time to identify the independent failure events (subsection 3.5 of the cited Appendix).

The draft procedure is focused on practical aspects of applications of these methods, while its theoretical background is described in Wandji et al. (2023a). A calculation example, accompanying the draft procedure, is a follow-up of the study presented by Shigunov et al. (2022) and Wandji et al. (2023b).

Statistical validation

This procedure is part of task 4C of the Terms of Reference and is being developed under the title "Statistical Validation of Extrapolation Methods for Time Domain Numerical Simulation of Ship Motions". The purpose of the procedure is to describe a process for the validation of extrapolation methods used for direct stability assessment for the stability failure modes described in section 3.5.6 MSC.1/Circ. 1627. The validation is considered successful if an extrapolation method (including those described in the ITTC Recommended Procedure 7.5-02-07-04.6) captures a "true" value. The percentage of these "successes" should be about accepted confidence probability.

The formulation of the procedure and the acceptance criteria for validation will be based on the work of Smith (2019), i.e., the three-tier (parameter, condition, and set) acceptance criteria will be adopted. The application to the split-time method described in Weems et al. (2023) and to the Envelope Peak Over Threshold (EPOT) method described in Campbell et al. (2023) will be referenced as examples, together with the ones presented in Smith (2019) and in the sub-section 5.4.4 of Appendix 4 to the Explanatory Notes for the Interim Guidelines MSC.1/Circ.1652.

Extrapolation

The committee proposes to update ITTC Recommended Procedure 7.5-02-07-04.6 "Extrapolation for Direct Stability Assessment in Waves". The original procedure with the effective date of 2021 described the application of envelope peak-over-threshold (EPOT) for estimation of the rate of roll motions failures when none of these failures were observed in the output of numerical simulation (subsection 4.5 of Appendix 4 of MSC.1 /Circ. 1652). The procedure also described the application of the split-time method for the estimation rate of total stability failures (capsizing). As the Explanatory Notes uses the split-time method for estimation of rates of partial stability failure (exceedance of 40 degrees roll), the respective update of the ITTC procedure is being proposed by the Committee.

The specific recommendations and examples for the extrapolation over wave height and critical wave method will be included in the further update of the procedure.

3. OTHER RELEVANT PROCEDURES

Roll damping

The committee proposes to update ITTC Procedure 7.5-02-07-04.5 "Estimation of Roll Damping". For this section, equation numbers refer to the 29th ITTC version of the procedure (2021). Typographical errors in Equations (13), (49) and (57) have been identified and corrected. Also, Equation (43) is corrected for the error identified in Ikeda's paper (1978) by Katayama et al. (2022), and the lower part of Equation (44) has been changed to a modified version of Ikeda's method. In Equation (29), a note has been included to stress that both φ_a and N-coefficient must be analyzed using the same units. For instance, the N-coefficient in Motora (1964) paper is analyzed using [deg]: φa must be [deg] and 180 should be in place of π.

Formulae affected by the changes are placed in Appendix 2.

Intact stability

The committee also proposes to update ITTC Procedure 7.5-02-07-04.1 "Model Tests on Intact Stability". Three references are being added to the procedure. For instance, if wind forces need to be included in the model tests, the projected areas need to be correct (Umeda et al., 2023). Also, roll decay tests carefully performed by manual handling can be sufficiently accurate as reported by Hashimoto et al. (2019). Finally, standard uncertainty analysis can be applied to all measured basic quantities and motions. Capsizing could be a different situation due to the extreme phenomenon involved. However, a properly designed experimental system is reproducible for strongly nonlinear phenomena (to the extent allowable by an indeterminism caused by the physics of the nonlinear system) as reported in Matsuda et al. (2016).

GZ curve in waves

Under task 5 of the Terms of Reference, the committee develops a new procedure titled "Computational procedure for instantaneous GZ curve during time-domain numerical simulation in irregular wave". As follows from the title, the objective of the procedure is the instantaneous GZ curve in irregular waves.

The instantaneous GZ curve in waves is an extension of the calm-water GZ curve concept to waves. The current restoring moment is a single point at the instantaneous GZ curve.

The instantaneous GZ curve reflects stability variation in waves and is used for assessing the Level 2 vulnerability criteria for pure loss of stability and parametric roll (Sections 2.4 and 2.5 of MSC.1 /Circ.1627) as well as qualitative validation in direct stability assessment (see Section 2.3 of Appendix 4 of MSC.1 /Circ.1652)

The GZ curve in waves is important for assessing the stability of the vessel in waves and for understanding the mechanisms of stability failure. Factors such as wave conditions, ship geometry, loading conditions, and others are reflected in the instantaneous GZ curve.

Calculation of the GZ curve in regular waves is included in commercially available hydrostatic software. Such functionality can also be useful in ship motion simulation tools, as either on-the-fly or post-processing capability. While these calculations are straight-forward, there are technical details, specific for time domain simulation. These details include (but are not limited to) treatment of inertial diffraction and radiation forces, and balancing (in terms of degrees of freedom to maintain instantaneous equilibria).

The draft procedure describes the role that the instantaneous GZ curve and its elements play in predicting ship stability failure. A calculation example is included with the draft procedure, following Belenky et al. (2008) and Bu et al (2019, 2021).

China Ship Scientific Research Center (CSSRC) conducted constrained model experiments for a container ship at a fixed heeling angle for the computation of the GZ curve in waves. This experiment provides benchmark data for different wave heights and lengths and may be used for validation of the calculation of the GZ curve in waves, see also Section 4.

Parametric Roll

The committee proposes to update the ITTC recommended procedure 7.5-02-07-04.3 "Predicting the Occurrence and Magnitude of Parametric Rolling" with the recent references mostly in relation publications of the Second Generation IMO stability criteria. Including references to recent Bureau Veritas (2019) and ClassNK (2023) documents were also part of the committee proposal.

Single Significant Amplitude and Confidence Intervals

The committee proposes to update the ITTC recommended procedure 7.5-02-01-08 "Single Significant Amplitude and Confidence Intervals for Stochastic Processes". The proposed update is mostly focused on the evaluation of the variance of the mean and variance estimate where latest information becomes available. Other updates are proposed for the inclusion of new references and improvement of readability.

Damage stability

The committee proposes to update the ITTC recommended procedure 7.5-02-07-04.2 "Model Tests on Damage Stability in Waves" incorporating feedback received from area experts from MARIN and HSVA, partners in EU project FLARE (2022) and recent benchmark data (see also Section 4).

4. BENCHMARK DATA

The collection of benchmark data has always been a very important work of ITTC. Previous SiW committees collected the benchmark data as described in the 28th and the 29th ITTC conference proceedings. As directed by task 7 of TOR and in continuation of the previous work, the following data has been identified.

The GZ curve in wave for an intact ship is provided by the CSSRC. The test cases include a change of the GZ curve in different wave conditions under a fixed heel angle for a container ship.

The second benchmark dataset is on damage stability. FLARE is a project funded by the European Union. Rupponen et.al. (2022a, 2022b) present the international benchmark study on the simulation of flooding and motions of damaged Ropax and cruise vessels that was conducted within the project. The ITTC recommended procedure 7.5-02-07-04.4 "Simulation of Capsize Behavior of Damaged Ships in Irregular Beam Seas" contains relevant details.

The committee plans to finalize a dataset for validation of extrapolation and other procedures related to the post-processing of numerical or experimental data.

SUMMARY AND DISCUSSION POINTS

The paper describes the current work of the 30th ITTC Stability in Waves Committee on the development and update of the ITTC recommended procedures in support of direct stability assessment under the second generation of IMO stability criteria. The following procedures are being developed or updated by the committee:

- Avoiding self-repeating effect
- Estimation of Frequency of Random Events (direct counting)
- Statistical validation of extrapolation procedures
- Extrapolation procedures (update)

Other relevant procedures briefly described in the paper include:

- Calculation of instantaneous GZ curve in waves
- Estimation of roll damping
- Model Tests on Intact Stability
- Predicting the Occurrence and Magnitude of Parametric Rolling
- Single Significant Amplitude and Confidence Interval.
- Damage stability model tests and numerical simulation.

The following issues may be worth further discussion, bearing in mind the future development of ITTC guidelines and recommended procedures:

- The techniques mentioned in the Explanatory Notes which should be developed next.
- The inclusion of elements related to the qualitative validation of the simulation tools. Candidates may include but are not limited to (references are made to Appendix 4 of MSC.1/Circ. 1652):
    - Backbone curve (Subsection 2.1)
    - Response curve for synchronous and parametric roll (Subsection 2.2 and 2.4)
- The development of an ITTC procedure for the qualitative validation of surf-riding, including presentation of behaviour in phase space.
- The rationale for the development of a large dataset for statistical validation and benchmarking statistical extrapolation by ITTC.
- The readiness of the stability community for running another benchmark study of the numerical simulation tools and in such a case, the modes of failure that should be considered first.

REFERENCES

Belenky, V., Weems, K.M., 2008, “Probabilistic qualities of stability change in waves”, Proceedings of the 10th International Ship Stability Workshop.

Belenky, V., 2011, “On Self-Repeating Effect in Reconstruction of Irregular Waves”, Contemporary Ideas on Ship Stability and Capsizing in Waves, Vol. 97.

Bu, S. X., Gu, M., Abdel-Maksoud, M., 2019. Study on roll restoring arm variation using a three-dimensional hybrid panel method, Journal of Ship Research. 63(2), pp. 94-107.

Bu, S. X., Lu, J., Gu, M., 2021. Study on the effects of radiation and diffraction forces on roll restoring arm with flared and tumblehome vessels. Ocean engineering. (239-Nov.1).

Bureau Veritas, 2019, Parametric Roll Assessment, Rule Note NR 667 DT R00 E.

Campbell, B., Weems, K., Belenky, V., Pipiras, V., Sapsis, T., 2023, "Envelope Peaks Over Threshold (EPOT): Application and Verification", Contemporary Ideas on Ship Stability. From Dynamics to Criteria. Springer, pp 265–290. ISBN 978-3-031-16328-9.

ClassNK, 2023, Guidelines on Preventive Measures against Parametric rolling (Edition 1.0).

EU FLARE, 2022, FLooding Accident Response (FLARE), https://cordis.europa.eu/project/id/814753 (accessed on 15 June 2023).

Hashimoto, H., Omura, T., Matsuda, A., Yoneda, S., Stern, H., Tahara, Y., 2019, "Several remarks on EFD and CFD for ship roll decay", Ocean Engineering, 186, pp. 371-382.

Ikeda Y., Himeno Y., Tanaka N., 1978, "Components of Roll Damping of Ship at Forward Speed", Journal of the Society of Naval Architects of Japan, Vol.143, pp.113-125 (in Japanese).

IMO, 2023, Explanatory Notes to the Interim Guidelines on the Second Generation Intact Stability Criteria, International Maritime Organization, MSC.1/Circ.1652.

ITTC, 2023, International Towing Tank Committee, www.ittc.info, (accessed on 15 July 2023).

Katayama, T., Yoshida, N., Yamamoto, Y., Kashiwagi, M., Ikeda, Y., 2022, "Correction of Eddy Making Component of Ikeda's method and its Modification for Shallow Draught Effects", Proceedings of the 18th International Ship Stability Workshop, Poland.

Matsuda, A., Hashimoto, H., Terada, D. and Taniguchi, Y., 2016, "Validation of Free running Model Experiments in Heavy Seas", Proceedings of 3rd International Conference on Violent Flows (VF-2016), Osaka, Japan.

Motora, S, 1964, Theory of Ship Motions, Kyoritsu Shuppan Book Co. (in Japanese)

Ruponen, P., Valanto, P., Acanfora, M., Dankowski, H., Lee, G.J., Mauro, F., Murphy, A., Rosano G., van't Veer R., 2022a, "Results of an international benchmark study on numerical simulation of flooding and motions of a damaged ropax ship", Applied Ocean Research, Volume 123.

Ruponen, P., Batenburg, R. van B., van't Veer, R., Braidotti, L. Bu, S., Dankowski, H., Lee, G. J., Mauro, F., Ruth, E., Tompuri, M., 2022b, "International benchmark study on numerical simulation of flooding and motions of a damaged cruise ship", Applied Ocean Research, Volume 129.

Shigunov, V., Wandji, C. W. and V. Belenky 2022 "Benchmarking of Direct Counting Approaches", *Proc. 18th Intl. Ship Stability Workshop*, Gdansk, Poland, pp. 167-175.

Smith, T., 2019, "Validation Approach for Statistical Extrapolation", Ch. 34. In: Contemporary Ideas on Ship Stability: Risk of Capsizing. Springer, Berlin, pp 573–589. ISBN 978-3-030-00514-6.

Umeda, N., Kawaida, D., Ito, Y., Tsutsumi, Y., Matsuda, A., Terada, D., 2023, "Overview of Model Test Procedures for Stability under Dead Ship Condition and Pure Loss of Stability in Astern Waves", Contemporary Ideas on Ship Stability, pp. 609-623.

Vassalos D., Renison M., Damsgaard A., Francescutto A., Gao H. Q., Hamamoto M., de Kat J. O., Matusiak J., Molyneux D. Papanikolaou A., 1997, "Numerical and Physical Modeling of ship Capsize in Heavy Seas: State of the art", *Proc. of 6th Intl. Conf. on Stability of Ships and Ocean Vehicles STAB-97*, Varna, Bulgaria.

Wandji, C., Shigunov, V., Belenky, V., V. Pipiras, 2023a "Benchmarking of Direct Counting Approaches", *Ocean Engineering, Ocean Engineering*, Special Issue on Extreme Stochastic Dynamics Ships (submitted).

Wandji, C., Shigunov, V. and V. Belenky 2023b, "Testing and Benchmarking of Direct Counting Methods" *Proc. 19th Intl. Ship Stability Workshop*, Istanbul, Turkey.

Weems, K., Belenky, W., Campbell, B., Pipiras, V., 2023. "Statistical Validation of the Split-Time Method with Volume-Based Numerical Simulation", In: Contemporary Ideas on Ship Stability: From Dynamics to Criteria. Springer, pp 225–243. ISBN 978-3-031-16328-9

APPENDIX 1

Consider calculation of autocovariance function from spectrum discretized with the constant-increment frequency set ω_i

$$R(\tau) = 0.5 \sum_{i=1}^{N} a_i^2 \cos(\omega_i \tau) \quad \text{(A1)}$$

where a_i is an amplitude of i-th component

Expand trigonometric functions Longuett-Higgins model of wave elevation at a point:

$$\zeta(t) = \sum_{i=1}^{N} (a_i \cos(\omega_i t) \cos(\varphi_i) - a_i \sin(\omega_i t) \sin(\varphi_i)) \quad \text{(A2)}$$

where φ_i is a random phase of i-th component

Note that both cosine and sine component of the integrand have a random terms: $\cos(\varphi_i)$ and $\sin(\varphi_i)$, and deterministic terms: $a_i \cos(\omega_i t)$ and $a_i \sin(\omega_i t)$, respectively. These random terms are shown as stems in Figures A1 and A2, while deterministic parts are shown as lines discretized by rectangles.

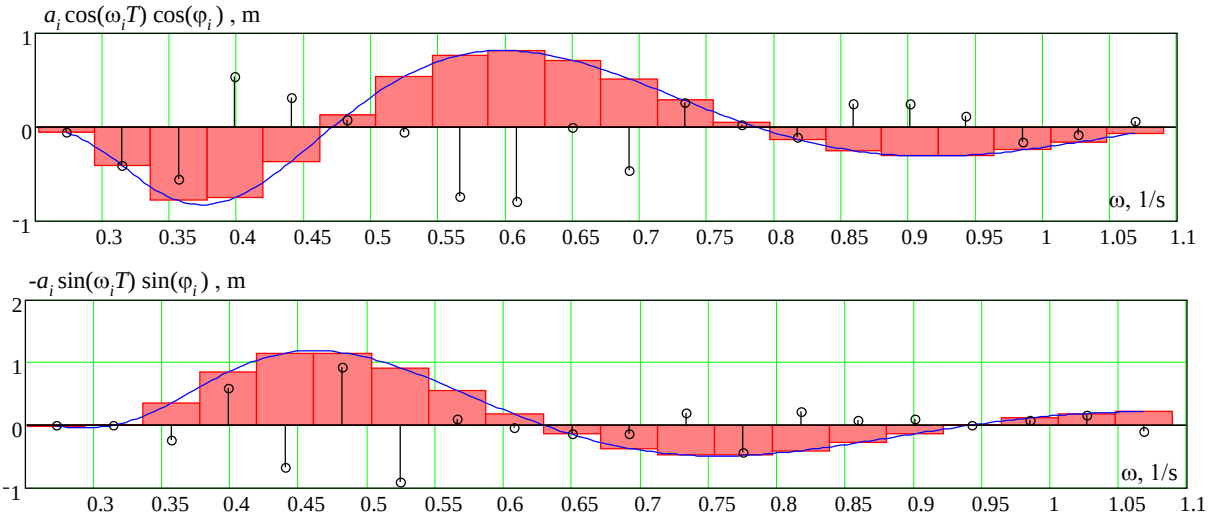

Figure A1. Rectangular Numerical Integration for the Inverse Fourier Transformation for Short Time Duration

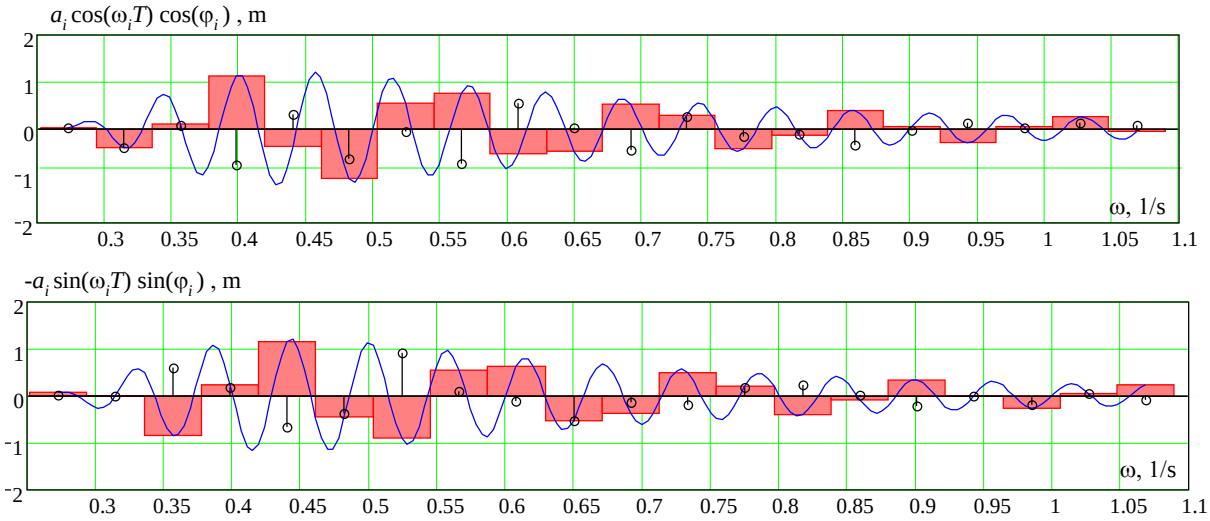

Figure A2. Rectangular Numerical Integration for the Inverse Fourier Transformation for Long Time Duration

The deterministic part can be considered as some sort of an envelope for the cosine of sine component of the integrand part. Thus, if the frequency discretization is sufficient, for accurate representation of the deterministic part, it should be good enough for the entire integrand, see Figure A1. The opposite is shown in Figure A2, where frequency discretization is not sufficent, so some laps of the integrand are going to be missed.

This illustrates that the mechanism of accumulation of integration error is similar for autocovariance function and wave elevation itself.

APPENDIX 2

List of proposed corrections for formulae in the ITTC recommended procedure 7.5-02-07-04.5 “Estimation of Roll Damping”. Note that these changes have not been approved by ITTC yet, so the 2021 revision of the procedure is still in effect.

Equations where typographical errors were identified (numbers of equations are given as in the 2021 revision of the procedure) are given below. Corrected typographical error are shown in bold:

$$\begin{cases} \mu_{eq}(\varphi_a) = \mu + \frac{4}{3\cdot\pi}\cdot\beta\cdot(\omega_E(\varphi_a)\cdot\varphi_a) + \\ \qquad + \frac{3}{8}\cdot\delta\cdot(\omega_E(\varphi_a)\cdot\varphi_a)^2 \\ \omega_E(\varphi_a) = \sqrt{\omega_{x,eq}^2(\varphi_a) - \mu_{eq}^2(\varphi_a)} \end{cases} \quad (13)$$

$$C_D = 0.\mathbf{4}7\cdot\ln(Ke)^2 - 4.94\cdot\ln(Ke) + 13.75 \quad (49)$$

$$R = \begin{cases} 2d\sqrt{\frac{H_0(\sigma-1)}{\pi-4}}, R < d \quad \& \quad R < \frac{B}{2} \\ d \ , \ H_0 \geq 1 \quad \& \quad \frac{R}{d} > 1 \\ \frac{B}{2} \ , \ H_0 \leq \mathbf{1} \quad \& \quad \frac{R}{d} > H_0 \end{cases} \quad (57)$$

Corrected formula for C_R in the equation (43) is given below (corrected paer is given in bold):

$$C_R = \begin{Bmatrix} \left(1 - f_1\frac{R}{d}\right)\left(\mathbf{1} - \frac{\mathbf{3}}{\mathbf{2}}\frac{\overline{OG}}{d} - \boldsymbol{f_1}\frac{\boldsymbol{R}}{\boldsymbol{d}}\right) \\ + f_2\left(H_0 - f_1\frac{R}{d}\right)^2 \end{Bmatrix} C_p\left(\frac{r_{max}}{d}\right)^2 \quad (43)$$

Corrected formulae for ψ_1 and ψ_2 in the equation (44) are given below:

$$\psi_1 = 0$$

$$\psi_2 = \begin{cases} \frac{1}{2}cos^{-1}\frac{a_1(1+a_3)}{4a_3} & \left(\left|\frac{a_1(1+a_3)}{4a_3}\right| \leq 1\right) \\ \tan^{-1}H_0 & \left(\left|\frac{a_1(1+a_3)}{4a_3}\right| > 1\right) \end{cases} \quad (44)$$

The challenges of Wind Turbine Installation Jack-ups within the regulatory stability framework

René van den Heuvel, GustoMSC, the Netherlands, rene.vandenheuvel@nov.com

ABSTRACT

This paper gives a brief overview on the background of Wind Turbine Installation (WTI) Jack-ups, the application of the regulatory stability framework is discussed, and the discussions on the application of the current regulatory framework considering the environmental limits of WTI jack-up operations are illustrated. Finally, the results of an optimization study to improve the damage stability of an existing WTI jack-up are presented, showing how larger compartments can lead to improved stability characteristics. It is advocated to expand the 2008 IS Code part B, to include weather-restricted criteria for WTI jack-ups. Also, further investigations should be made on how the damage penetration and survivability criteria should be applied to WTI jack-ups when applying the SPS probabilistic damage stability criteria. And finally, it should be defined more clearly in the 2008 IS Code if and how the weather criterion is to be applied to SPS vessels.

Keywords: Stability, Wind Turbine Installation, WTI, Jack-up, MODU code, SPS code.

1. INTRODUCTION

In 1958 the jack-up Seashell was built by Shipyard Gusto in the Netherlands. It was the first jack-up that was designed and built outside the USA. Since then, GustoMSC has designed many jack-ups for various purposes and in many shapes and sizes. Initially mainly for oil & gas drilling purposes, later also for civil construction and accommodation. With the onset of the offshore wind industry, a stable mobile platform was required to install the wind turbines. Initially jack-ups designed for the civil construction market were used. However, the development of the offshore wind industry continued rapidly and led to an increase in wind turbine size and a requirement for a higher installation efficiency in order to reduce cost. As a result, larger and more dedicated jack-ups were required to do the wind turbine installation work. This has led to the extensive development of the NG series of jack-ups at GustoMSC of which examples are presented in Figures 1 and 2.

The shape and size of WTI jack-ups is quite different from conventional vessels. WTI jack-ups are characterized by a large breadth over depth ratio. This causes high righting lever arms leading to good initial and dynamic stability, but a limited range of stability. To comply with the regulatory stability framework, which consists mainly out of the MODU and SPS code (IMO, 2009, 2008a), can therefore be challenging for WTI jack-ups and in most cases exemptions from flag states are required, taking into account the operational profile of a WTI jack-up. The regulatory stability framework is for severe environmental conditions, while the majority of the operations performed by a WTI jack-up are with environmental restrictions. Taking the environmental restrictions into account in the exemptions, will therefore not lead to a lower level of safety, compared to conventional vessels. Also, it must be noted that trying to comply with the regulatory framework shows that for example a higher level of compartmentation in a WTI jack-up is not always advantageous, especially if that leads to higher static heeling angles after flooding.

Figure 1: NG-14000XL transiting.

2. DESIGN PRINCIPLES OF A WTI JACK-UP

When installing WTGs (Wind Turbine Generator) at sea, a WTI jack-up can be used for both the foundation installation, which is most commonly either a monopile or a jacket, as well as the installation of the WTG itself, which consists out of a tower, nacelle and three blades. It must be noted that both are not installed at the same time. First all the foundations will be installed, after that all the WTG's will be installed. Although a WTI jack-up can be used for both phases, there are some differences in requirements. For foundations it is important that the crane has sufficient lifting capacity, but lifting height is less important, while for WTG installation lifting height becomes more important.

A typical operation can be described as follows:

- The WTI jack-up is in port elevated where it loads several sets of foundations or WTGs with its own crane.
- The WTI jack-up will jack down into the water and transits to the installation location.
- At the first installation site, it will jack out of the water and start with the installation of the components.
- After that it will jack down again, move to the second installation location, and jack up and will continue until all loaded components are installed.
- After that it will return to port and load the next set of components.

To be able to install WTGs at sea a WTI jack-up has the following requirements:

- Large crane: To install the components.
- Four legs: To be able to jack up above the water and quickly preload.
- Sufficient deck space: To carry the components.
- Sufficient spacing between the legs: To have a stable platform when elevated.
- Low lightship weight: To be able to elevate sufficient payload.
- Self-propelled: Easy transit from port to installation site and in between installation sites.

Figure 2: NG-20000X installing a WTG.

These requirements drive the design of WTI jack-ups. The requirements of sufficient distance between the legs and the low light ship weight, are the main causes that WTI jack-ups have a large B/D ratio. Table 1 shows the main dimensions of generic NG designs.

Table 1: Main dimensions generic NG designs.

	Length [m]	Breadth [m]	Depth [m]	B/D ratio [-]
NG-5500C	81.0	41.0	7.0	5.9
NG-5500X	87.5	42.0	8.0	5.3
NG-9000C	131.7	39.0	9.0	4.3
NG-9800C	124.0	45.0	10.0	4.5
NG-14000X	139.0	50.0	11.0	4.6
NG-14000XL	142.0	50.0	11.0	4.6
NG-16000X	148.0	56.0	11.5	4.9
NG-20000X	151.0	58.0	13.0	4.5

This large B/D ratio in connection with the high VCG caused by the legs and deck load drive the stability characteristics of a WTI jack-up. The typical GZ curve of a WTI jack-up has only a limited range, due to the early immersion of the deck edge in the water, however the area below the GZ curve is much larger compared to conventional ships. Figure 3 shows some typical GZ curves of various ship types in our portfolio compared to each other, where a drill ship comes the closest to a conventional ship design with respect to the stability range.

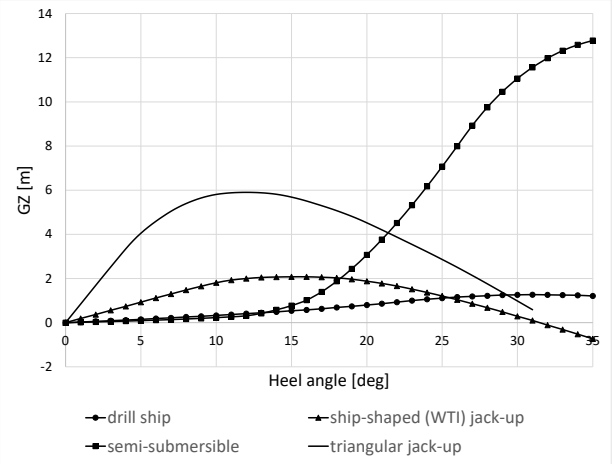

Figure 3: Generic GZ curves of various ship types.

The difference in GZ curve characteristics is quite obvious. However, as parts of the regulatory framework are based on conventional ships, this leads to challenges.

3. REGULATORY FRAMEWORK

MODU code

A major industry where jack-ups have been utilized the last few decades is the offshore oil & gas industry. A jack-up provides a well-suited stable platform for exploration drilling, maintenance and even production. Within the offshore oil & gas industry the MODU code (IMO, 2009) plays an important role in the field of statutory stability requirements. It even has dedicated stability requirements for self-elevating units. The MODU code has been around since 1979 and the latest update on the stability requirements for self-elevating units is from 2009.

The MODU code contains both intact as well as damage stability requirements. The intact criteria are based upon sufficient area under the GZ curve, based on the wind heeling moment and a positive GZ curve over the full range between upright and second intercept. In Figure 4 and Table 2, these criteria are presented.

The damage criteria are based on positive stability when subjected to wind for side (waterline) damages (with 1.5 m penetration in between watertight bulkheads) and on the minimum range of stability for single compartment flooding without wind load.

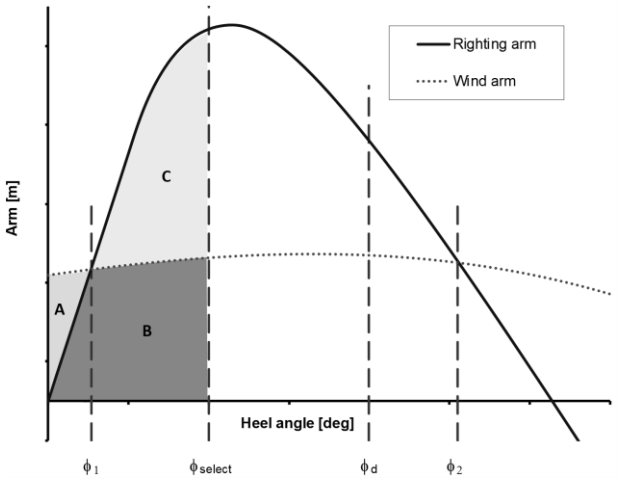

Figure 4: MODU code Intact stability criteria.

Table 2: MODU code Intact stability criteria.

Criterion no.	Description
1	(Area B + area C) ≥ 1.4 x (area A + area B) at or before the minimum of (φd or φ2)
2	Watertight up to φ1
3	Righting arm ≥ 0 m for any angle between 0 and φ2
4	GM0 ≥ 0 m
φd:	Angle of down flooding
φ1:	First intercept with wind
φ2:	Second intercept with wind
φselect:	selected angle at which requirements are evaluated
GM0:	GM value at upright position

It must be pointed out that the wind loads are determined based on the actual Cd values of the exposed areas, height above the sea level and three wind speeds: 100 knots for ocean transits, 70 knots for field moves and 50 knots for damaged conditions.

As WTI jack-ups are self-elevating units and only the IMO MODU code has dedicated stability criteria for self-elevating units, WTI jack-ups are designed according the MODU code. Although that may be a bit ambiguous, as the “D” in MODU stands for drilling and WTI jack-ups are there to expand the renewable energy production.

However, the mode of operation between a drilling jack-up and a WTI jack-up are quite different. Even such that it may be questionable for a WTI jack-up to only comply to the MODU code. A drilling jack-up is moved approximately once a year to a location, where in elevated condition it stands for a longer period. During moves, the drilling jack-up is normally not self-propelled and only a limited amount of crew is on board to help tow the drilling jack-up. A WTI jack-up is installing a WTG

in approximately a day, so this unit is transiting almost daily under its own power. Either from the port to the wind farm (or vice versa) or in between installation locations within the wind farm. It has a full complement of crew on board. But besides the ship's crew also a team of people is on board that are installing the actual WTG's. Considering these differences of mode of operation and number of people on board, several flag states do not find it sufficient to only comply to the MODU code. They therefore require that WTI jack-ups also comply to the Code of Safety for Special Purpose Ships, the so called SPS code (IMO, 2008a).

SPS code

The SPS code (IMO, 2008a) has been set up for vessels that carry besides crew a number of "special personnel". Special personnel are expected to be able-bodied with a fair knowledge of the layout of the ship and to have received some training in safety procedures and the handling of the ship's safety equipment before leaving port.

From stability point of view the SPS code describes both intact and damage stability criteria. For intact stability, section 2.5 of part B of the 2008 IS code (IMO, 2008b) is applicable. Which in turns directs us to section 2.2 of part A (for ships longer than 100 m). Here it is stipulated that the top of the GZ curve should be at a minimum of 25 degrees. For vessels with the large B/D ratios (>2.5) as indicated in Table 1, this is not practical and in line with the explanatory notes (IMO, 2008c) alternative criteria based on an equivalent level of safety are used. These are listed in Table 3.

It must be noted that in the SPS code no reference is made to comply to the IS code weather criterion. Also, in the IS code chapter 1.1 it is stated that special purpose ships are not required to comply to the weather criterion, but compliance to equivalent alternative criteria shall be demonstrated. The mentioned footnote to this statement in chapter 1.1 of the IS code however is not correct and should be reviewed by the authors of the IS code.

Application of the weather criterion would not be correct as the B/D ratio of WTI jack-ups is well above the limit of 3.5 as indicated in section 2.3 of part A of the IS code. The alternative proposed model testing to determine the roll back angle due to waves for vessels with larger B/D ratio, is not practical as this is costly and time consuming in the early design stages. As a WTI jack-up also complies to the wind criteria of the MODU code, this is seen as the required compliance to alternative criteria.

Table 3: Intact stability criteria for vessels with large B/D ratio.

Criterion no.	Description
1	Area under the GZ curve up to the lesser of φd and 40 deg ≥ 0.090 m*rad
2	Area under the GZ curve from 30 deg up to the lesser of φd and 40 deg ≥ 0.030 m*rad
3	GZ should be at least 0.2 m at an angle of heel ≥ 30 deg
4	GM0 ≥ 0.15 m
5	Area under the GZ curve up to 15 deg ≥ 0.070 m*rad if φGZmax = 15 deg
6	Area under the GZ curve up to 30 deg ≥ 0.055 m*rad if φGZmax ≥ 30 deg
7	Area under the GZ curve up to φGZmax ≥ 0.055 + 0.001 x (30 - φGZmax) m*rad if 15 deg < φGZmax < 30 deg
8	φGZmax ≥ 15 deg
φGZmax: Angle of maximum GZ	

For damage stability the SPS code refers to the probabilistic damage stability approach as described in SOLAS chapter II-1 (IMO, 1974), where the ship is considered as a passenger ship and the special personnel are considered passengers. Based on the total number of persons on board, the R-value can be reduced. Up to 60 persons on board 80% of R can be used, while for 240 or more 100% of R must be used. Between 60 and 240 persons, the percentage can be linearly interpolated. When the 2008 SPS was published, a reference was made to the 2009 SOLAS rules for the formula of the R-value. With later amendments, the R-value formula was incorporated directly into the SPS-code and is still the same as the R-value formula from the 2009 SOLAS, while the R-value formula in the 2020 SOLAS has been updated for conventional vessels.

Together with the probabilistic damage stability calculation also a deterministic double bottom damage stability calculation must be performed for those areas of the vessel that lack a double bottom structure in line with the rules.

Besides the described regulatory framework, consisting of the IMO MODU code and the IMO SPS code, in some cases also flag-specific stability criteria are being applied, like the ones mentioned in the Stability research report 387 from the Health and Safety Executive of the United Kingdom (HSE, 2005), or the stability regulations 878/91 of the

Norwegian Maritime Authority (NMA, 1991). However, that will be outside the scope of this paper.

4. COMPLIANCE TO THE REGULATORY FRAMEWORK

In the previous chapter the regulatory framework has been explained, however compliance of a WTI jack-up to these criteria is not straightforward and poses some challenges, in particular compliance to the SPS code. While the MODU code catches most of the stability characteristics of a WTI jack-up, the rules in the SPS code are more written for conventional ship shapes and not for WTI jack-ups.

Operational profile

The MODU code takes into account the kind of operation that is executed, by differentiating the used wind speed. For the SPS code all criteria are applied for unrestricted service. However, the operating profile of a WTI jack-up is quite different. Ocean transits are done in general with no or very limited deck load. Due to the characteristics of a WTI jack-up, an ocean transit cannot be done in unlimited significant wave height. During ocean transits the significant wave height is in general limited to between 5 and 7 m, depending on wave direction. Leg strength and lifeboat immersion (such that stored lifeboats are not damaged by waves) are in general the limiting factors.

Due to the fact that the VCG is limited due to the absence of deck load, compliance to the criteria is not an issue. However, the IS code requirement of having a minimum GZ curve area of 0.030 mrad between 30 degrees and down flooding angle, results in having very high unprotected openings for engine room air intakes: as high as 10-13 m above main deck depending on location and vessel shape. The resulting down flooding angle will only be slightly above 30 degrees (about 1-2 degrees) as the area under the curve is very high and reaches the area requirement very quickly.

When transporting WTG components, the VCG of the loading condition can be quite high. Towers with lengths of 100-130 m with a weight of 1,000-1,200 t are not uncommon nowadays. In the future these weights will still increase. These towers are transported upright and have a diameter of around 8 m. It can be imagined that the supporting grillage on the main deck must take up high loads due to vessel motions. To limit these loads, the sea state in which these transports take place is restricted. Also, when a WTI jack-up installs itself there is a phase that the legs impact the bottom due to wave induced motions of the WTI jack-up. To stay within the structural capabilities of the legs and jack-up the installation condition is in general limited to significant wave heights of around 2-2.5 m. So, sailing out to the installation site with a high significant wave height makes no sense, because on arrival the wave height should be below the installation limits. Due to the characteristics of sea fastening design and installation limits these so-called field moves are in general limited to a significant wave height of max 3.5 m and a wind speed of 25 m/s.

Alternative intact stability criteria

Compliance to the IS code criteria would make transporting sets of WTGs, especially the larger ones, nearly impossible. However, as these transports are done in a controlled environment, DNV has developed in close operation with GustoMSC a set of alternative criteria as guidance as described in DNV-OS-C301, chapter 2, section 1.6 (DNV, 2021), as reported in Table 4.

Table 4: Alternative intact stability criteria for WTI Jack-ups with weather limitations.

Criterion no.	Description
1	GM0 ≥ 0.5 m
2	Area under the GZ curve up to φGZmax ≥ 0.055 + 0.001 x (30 - φGZmax) m*rad if φGZmax ≤ 30 deg
3	Area under the GZ curve up to 30 deg ≥ 0.055 m*rad if φGZmax > 30 deg
4	Maximum GZ in range φs to φd ≥ 0.2 m
φs:	Angle of static equilibrium (without wind)

The range of stability is no longer required to be above 30 degrees heel, as long as the area below the GZ curve is sufficient. Also, the minimal GM value has increased from 0.15 m to 0.50 m.

Using this alternative set of criteria, the Allowable Vertical Centre of Gravity (AVCG) curve shifts upward, in such a manner that this criteria set is no longer governing. Other criteria sets, like damage criteria become governing. It must be noted that to apply these alternative criteria, an exemption by flag is required. Several flag states have already provided such an exemption. However, there is still a risk with flag states that do not have yet provided these exemptions. It would be therefore beneficial if these alternative criteria became part of part B of the IS code.

If the alternative intact stability criteria is applied, compliance to the SPS damage stability criteria becomes governing. As mentioned, there are two parts. The deterministic double bottom damages can be avoided as long as the double bottom arrangement is according to the rules. That leaves us with the probabilistic damage stability calculations as the limiting criteria.

Probabilistic damage stability

The application of the SOLAS probabilistic damage stability criteria can be questionable for WTI vessels. As already discussed, the ratios of overall dimensions, like B/D differ from conventional cargo and passenger vessels that have been used in the statistics to determine the p-factor (probability of a certain damage). When determining the p-factor it is assumed that the vessel under consideration is damaged with a penetration of B/2. However, a WTI vessel is much wider in general compared to general cargo and passengers vessels of the same length. Also, the construction is much different. While for a conventional vessel the longitudinal strength is based on the buoyancy and wave loads, the longitudinal strength of a WTI jack-up is dictated by the elevated and preload conditions. This requires that the side shell and the longitudinal bulkheads as indicated in figure 5 have increased plate thickness and stiffener dimensions than compared to a conventional vessel. It is therefore very unlikely that during a collision, a WTI jack-up has a damage penetration of B/2. We therefore advocate to use a reduced penetration like B/3 for example. This will still include damages to the centre compartment, but the probability of those damages becomes lower, while for minor damages the probability becomes higher. However, this application is still under consideration.

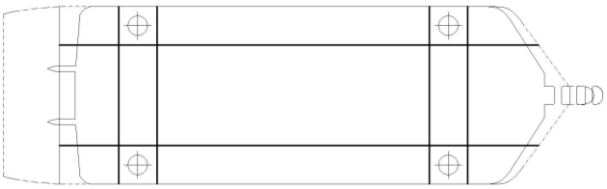

Figure 5: Main constructional bulkheads of a WTI jack-up.

Not only the determination of the p-factor is questionable for WTI jack-ups, also the calculation of the s-factor (if a certain damage is survived) poses with some challenges. In the calculation of the s-factor, range of stability and max GZ arm are only evaluated. As indicated a WTI jack-up has limited range, but a large area under the GZ arm. This area is not taken into account in the s-factor. Applying these criteria to WTI jack-ups is therefore questionable. We would advocate to have a separate set of criteria to calculate the s-factor for vessels with a large B/D ratio. How that separate set of criteria looks like, should be the outcome of a separate study.

5. STUDY CASE

As wind turbine generators are increasing in size and weight, existing WTI jack-ups need to be able to carry payloads with a higher VCG. In some cases, the foreseen VCG is above the limit curves, and the limit curves need to be improved. In this specific case, the probabilistic damage stability criteria were governing. With a few simple modifications to the watertight subdivision, significant improvements were seen in the allowable VCG curves.

WTI jack-ups of the NG type are in general outfitted with a double bottom and this double bottom is mostly filled with void spaces. For this specific case the double bottom voids were watertight divided by the centre and side girders as indicated with the dashed crosses in Figure 6.

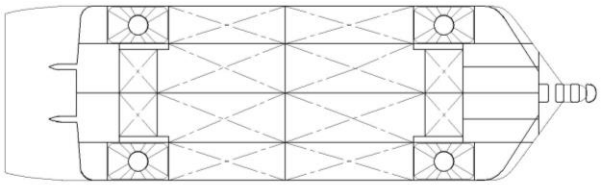

Figure 6: Double bottom voids original.

This arrangement leads to asymmetric flooding when damaged. As the range of stability is one of the leading criteria in determining the s-factor, and these kind of vessels with a large B/D ratio have a limited range of stability, it is important to keep the heeling angle after flooding as low as possible. Therefore, it was investigated what the effects are if these voids would be joined in transverse direction as indicated in Figure 7.

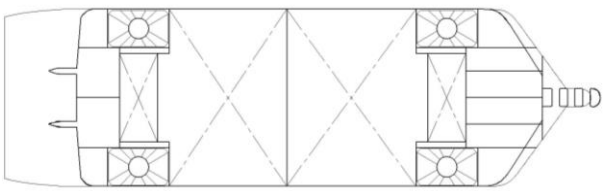

Figure 7: Joined double bottom voids.

The results are presented in Figure 8. No axis values are presented as this is considered

commercial sensitive information. The vertical axis (AVCG) grid spacing is 2 m and the horizontal axis (draught) grid spacing is 0.2 m. As can be seen the probabilistic damage AVCG curve for the joined double bottom is improved with around 1 m for the deeper draughts. As modifications to the watertight subdivision can also have a consequence on the other damage stability criteria, the AVCG curves based on the MODU code are therefore also presented. For single compartment (comp) damage, no changes in AVCG occur. For water line (WL) or side damages, the AVCG also improves with the joined double bottom voids.

It can therefore be concluded that a higher level of compartmentation does not always lead to better stability characteristics, especially if the compartmentation leads to asymmetric flooding. In this specific case the joining of the voids can be executed easily by cutting holes in the centre and side girders.

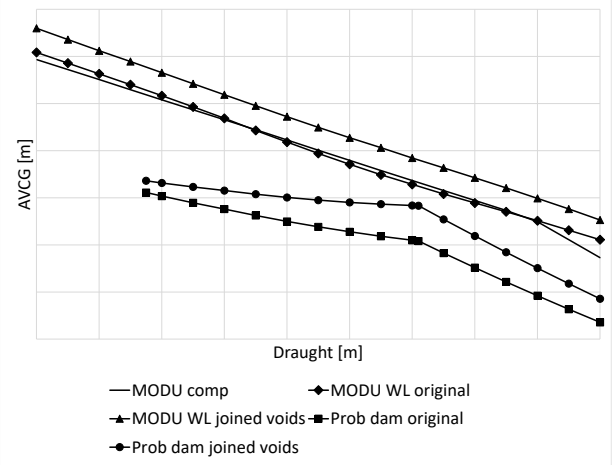

Figure 8: AVCG curves.

6. CONCLUSION

In this paper a short introduction is given on the basic principles of a Wind Turbine Installation (WTI) jack-up, what drives the design and the dimensions. The applicable regulatory stability framework consists mainly out of the IMO MODU code and the SPS code. Especially the application of the SPS code proves challenging for these kind of vessels as the B/D ratio is quite large (more than 4) and is not similar to the "conventional" ship types that serve as inspiration for the SPS code. Also, the operational limitations of a WTI jack-up are not taken into account in the SPS stability regulations. With a flag exemption it is possible to apply alternative intact stability criteria as stated in the guidance note in DNV OS-C301 for restricted conditions. However, it is advocated to include the alternative criteria from this guidance note as alternative criteria for WTI vessels in part B of the 2008 IS Code. Such that flag exemption is no longer required and the design risk is reduced.

The application of the probabilistic damage stability criteria on WTI jack-ups is questionable for both the determination of the p-factor as well as the s-factor. It is advocated to reduce the maximum damage penetration from B/2 to B/3 and to have a better look at the stability criteria used for determining the s-factor and take the large B/D ratio into account in these criteria. This can be the subject of further research.

Finally, it must be noted that chapter 1.1 of the 2008 IS Code contains a conflicting footnote regarding the exemption of the weather criterion for special purpose ships. This should be reviewed by the authors of the IS code.

REFERENCES

IMO, 2009, 2009 MODU Code, Code for the Construction and Equipment of Mobile Offshore Drilling Units, *Resolution A.1023(26)* (*see also A 26/Res.1023/Corr.1, 17 January 2011)*

IMO, 2008a, Code of Safety for Special Purpose Ships, *Resolution MSC.266(84) – As amended*

IMO, 2008b, The International Code on Intact Stability, *Resolution MSC.267(85) – As amended*

IMO, 2008c, Explanatory notes to the International Code on Intact Stability, *Circular MSC.1/Circ.1281*

IMO, 1974, International Convention for the Safety of Life at Sea – *As amended*

HSE, 2005, Stability, *Research Report 387*

NMA, 1991, Regulations Concerning Stability, Watertight Subdivision and Watertight/Weathertight Closing Means on Mobile Offshore Structures, *878/91 – As amended*

DNV, 2021, Stability and Watertight Integrity, *DNV-OS-C301*

Stability of inland vessels in extremely low water levels

Milica Vidić
University of Belgrade, Faculty of Mechanical Engineering, Department of Naval Architecture
Grupo Integrado de Ingeniería, CITENI, Campus Industrial, Universidade da Coruña
mvidic@mas.bg.ac.rs
Nathalie Reinach
Development Centre for Ship Technology and Transport Systems (DST e. V.)
reinach@dst-org.de
Igor Bačkalov
Development Centre for Ship Technology and Transport Systems (DST e. V.)
backalov@dst-org.de

ABSTRACT

The paper addresses the assessment of intact and damage stability of Western European inland dry cargo vessels equipped with "additional buoyancy bodies". Additional buoyancy bodies, such as the "pipe-based buoyancy" examined in this study, are intended for increase of buoyancy and, thus, cargo-carrying capacity of inland vessels sailing at low draughts in extremely low water levels. The use of additional buoyancy bodies, however, may imply an increased risk of stability-related hazards atypical for navigation in regular water levels. On the other hand, neither low water levels nor additional buoyancy bodies are considered by the present stability regulations. The analysis presented in the paper shows that compliance with the applicable intact and damage stability rules may be achieved with the standard loading practices, but that this may be insufficient to avoid grounding in particularly low water. The loss of one additional buoyancy body may be exceptionally dangerous, as it could lead to a total stability failure, grounding of the vessel, loss of cargo, and obstruction of navigation. The paper, thus, investigates the stability-related operational measures which could be employed to counter the risks triggered by navigation in extremely low water levels.

Keywords: *Inland vessels, Additional buoyancy bodies, Low water levels, NOVIMOVE.*

1. INTRODUCTION

The droughts in the summer of 2018 severely disrupted supply chains in Western Europe, which resulted in serious negative economic consequences: it is estimated that the losses of the manufacturing industry in Germany alone amounted to 4.7 billion EUR (Schweighofer et al., 2022). Recent research suggests that such extreme low-water events will be more frequent in the future. In fact, even more extreme low water levels were recorded on the Western European inland waterways already in 2022. In response, the creation of regional and national strategies addressing the problem of inland navigation in extremely low water levels was intensified. Such strategies consider different logistics, waterway management, and ship technology measures (see, for instance, Friedhoff et al., 2022). This paper focuses on technical solutions examined within the Horizon 2020 project NOVIMOVE (Novel inland waterway transport concepts for moving freight effectively), intended for improvement of efficiency of existing inland dry cargo / container vessels on the Rhine, and on the related implications for intact and damage stability performance of such vessels in extreme low-water conditions.

Some of the proposed technical solutions imply the increase of buoyancy (and, thus, cargo-carrying capacity) of ships sailing at low draughts by means of the so-called "additional buoyancy bodies" which would be temporarily deployed in shallow-water sectors. This idea is not entirely new: additional buoyancy bodies were used in the Netherlands already in the 17th century to assist ships in sailing over the shallows of the nowadays Ijsselmeer, see Boven & Hoving (2009). Iqbal et al.

(2008) considered the use of additional inflatable buoyancy to improve intact stability of small passenger ferries in Bangladesh. An overview of the contemporary solutions and patents intended for increase of buoyancy is given in Friedhoff et al. (2020).

One of the concepts of additional buoyancy bodies is the "pipe-based buoyancy" (PBB) consisting of fully rigid, steel cylindrical bodies with conical ends temporarily connected to the ship hull sides, see Figure 1. This paper addresses intact and damage stability of a standard inland container vessel of CEMT Class Va[1] (the so-called Large Rhine vessel) equipped with PBB.

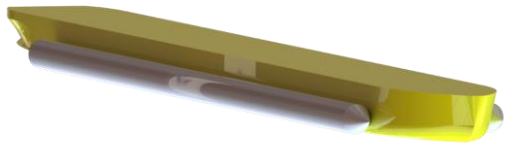

Figure 1. Principal arrangement of the pipe-based buoyancy (PBB)

Operational conditions in extremely low water levels may imply sailing with under-keel clearance as little as 0.3 m and in reduced fairway width, which increases the likelihood of grounding, collision, and allision. Therefore, stability failures may not be limited to large heel angles; for instance, even the relatively small angles of heel may cause the vessel grounding and subsequent suspension of traffic on the waterway. Neither the low-water operational conditions, nor the additional buoyancy bodies are specifically addressed by the current safety regulations for inland navigation.

Therefore, the paper investigates the "operational measures" for a sample vessel with additional buoyancy bodies from the ship stability point of view, with reference to the applicable regulations and the specific navigation conditions. In addition to calculating the maximum vertical center of gravity KG_{max} / the minimum metacentric height GM_{min} in compliance with the applicable stability regulations, it is examined if there are scenarios in which the safety of the sample ship equipped with PBB may be jeopardized even though the stability rules are formally being complied with.

[1] For CEMT classification of inland vessels in Europe see CEMT (1992).

2. APPLICABLE REGULATIONS

Intact stability of inland container vessels in Western Europe should conform to the requirements of ES-TRIN ("European Standard Laying Down Technical Requirements for Inland Navigation Vessels"), Chapter 27, see CESNI (2023). The standards (related to minimum metacentric height) differ depending on whether the ship transports "non-secured" or "secured" containers. The minimum metacentric height GM_{min} must not be below 1 m (in case the ship carries non-secured containers) or 0.5 m (in case the ship carries secured containers). When exposed to the simultaneous action of heeling moments due to turn (M_{dr}) and beam wind (M_w), the static angle of heel should not be greater than either the angle at which the deck edge enters the water (φ_{deck}) or 5°, whichever is less (Figure 2). Since inland container vessels have a large open cargo hold, it is required to conduct intact stability calculations assuming the presence of rainwater in cargo hold. Additionally, all intact stability calculations are carried out with 50% of supplies (in practice, mainly fuel and fresh water).

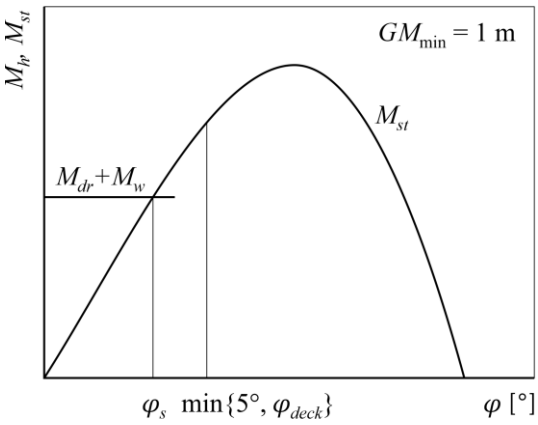

Figure 2. Intact stability requirements for inland container vessels carrying non-secured containers according to ES-TRIN (CESNI, 2023)

Damage stability assessment for this type of vessels is not mandatory unless:

- they carry dangerous cargo, in which case they are subject to the ADN ("European Agreement concerning the International Carriage of Dangerous Goods by Inland Waterways") rules, Chapter 9 (see UNECE, 2023), or
- they are longer than 110 m, in which case they are subject to ES-TRIN, Chapter 28 (CESNI, 2023).

This means that inland container vessels up to 110 m in length, which do not carry dangerous goods, do not have to comply with the damage stability requirements. The damage stability rules of both ADN and ES-TRIN contain deterministic requirements which should be satisfied in the final stage of flooding and in the relevant intermediate stages of flooding following assumed bottom and side damages whose dimensions are prescribed.[2] Considering inland container vessels, the requirements again differ depending on the securing of the containers. The ADN requirements applicable to container vessels carrying non-secured containers are given in Figure 3. Static angle of heel in the final stage of flooding should not be greater than 5°. The area under the righting lever beyond the static equilibrium and up to the angle at which the first unprotected opening enters the water (φ_{fl}) or 10° (whichever is less) should not be less than 0.0065 mrad. Two-compartment standard applies in the longitudinal direction, except in the case of the main engine room which is subject to one-compartment standard only. Bottom damages also imply flooding of adjacent athwartships compartments.

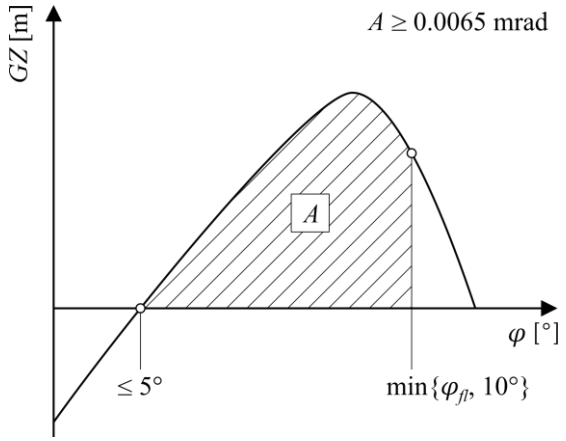

Figure 3. Damage stability requirements for inland container vessels carrying non-secured containers according to ADN (UNECE, 2023)

3. SAMPLE SHIP AND PBB BODIES

The sample ship used in the study is a standard Western European Class Va inland container vessel. The main dimensions of the sample ship and the pipe-based buoyancy bodies are given in Table 1. The body plan of the sample ship is given in Figure 4; the cross sections are equally spaced at 1 m distance, whereby "0" represents the aftmost station. Such vessels typically load containers in up to four tiers. It is assumed that the ship would carry non-secured containers which may contain dangerous goods. Furthermore, it is assumed that the PBB bodies would be deployed at low water levels when the fully loaded ship would sail at d_1 = 1.8 m and d_2 = 1.2 m. For the purpose of this study, the PBB bodies are considered to be cylindrical bodies of length L_{PBB} and diameter D_{PBB} (i.e., the conical ends are disregarded for the sake of simplicity of the analysis).

Table 1. Main dimensions of the sample ship without the pipe-based buoyancy (PBB) bodies and the free-floating PBB body

length overall, L_{OA} [m]	109.7
length of the waterline, L_{WL} [m]	109.4
beam, B [m]	11.44
design draught, d [m]	3.2
depth, D [m]	3.68
displacement, Δ [t]	3623.5
maximum ship speed, v [km/h]	18
maximum number of containers, n_{TEU}	208
length of the PBB body, L_{PBB} [m]	80
diameter of the PBB body, D_{PBB} [m]	3
draught of the PBB body, d_{PBB} [m]	0.3
mass of the PBB body, m_{PBB} [t]	30.1

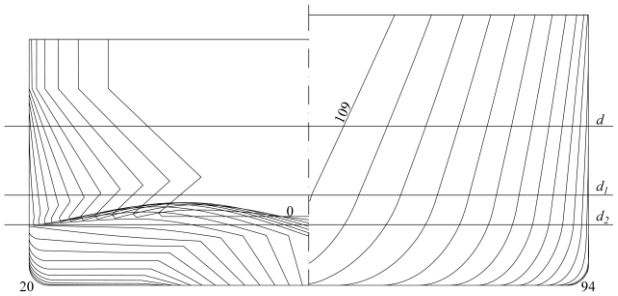

Figure 4. Body plan of the sample ship; d = 3.2 m is the design draught of the vessel, while d_1 = 1.8 m and d_2 = 1.2 m are the operational draughts at which the additional buoyancy bodies would be deployed

The practical benefits of using PBB on the sample ship are summarized in Table 2. At low draughts, the sample ship would be capable of carrying 39% (at d = 1.8 m) and 13% (at d = 1.2 m) of its cargo capacity at design draught; in addition, in latter case, the ship would not be able to carry the maximum number of containers. After the deployment of PBB, the cargo-carrying capacity of the sample vessel at low draughts increases by 63%

[2] Curiously, although the damage stability standards for container vessels of ADN and ES-TRIN are the same, the assumed damages differ.

(at d = 1.8 m) and by 102% (at d = 1.2 m) in comparison to the possible capacity of the same vessel at given draughts without the added buoyancy bodies.

Table 2. Cargo-carrying capacity of the sample ships without and with the pipe-based buoyancy (PBB) bodies

d	m_{cargo} [t]	
	without PBB	with PBB
3.2	2707.6	/
1.8	1046.5	1701.5
1.2	358.8	726.3

4. STABILITY ASSESSMENT

Intact and damage stability assessment of the sample ship equipped with the PBB bodies was carried out at draughts d = 1.753 m and d = 1.149 m (which correspond to draughts d = 1.8 m and d = 1.2 m with 50% of supplies) in two-tier and four-tier container arrangement.

Intact stability

The parameters necessary for intact stability calculations which change with the changes of draught and container arrangement are given in Table 3.

Table 3. Parameters necessary for intact stability assessment which depend on the draught and the container arrangement: lateral area exposed to wind A_W and the distance of the centroid of A_W from the waterline l_W

d	tiers	A_W [m^2]	l_W [m]
1.753	4	872.9	4.392
1.149	4	938.1	4.669
1.753	2	450.6	2.159
1.149	2	515.8	2.452

The maximum vertical center of gravity $KG_{\max}$ and the minimum metacentric height $GM_{\min}$, calculated in compliance with ES-TRIN regulations for the considered cases are given in Table 4. The results indicate that the sample ship equipped with the PBB bodies would fulfill intact stability requirements with a considerable margin. In all the cases, the limiting values of KG and GM are attained when the vertical center of gravity of the cargo, KG_{cargo}, is very high, outside of the physical boundaries of the cargo.

Therefore, the static angle of heel of the sample ship with the vertical center of gravity corresponding to uniform vertical distribution of cargo, exposed to the heeling moments defined by the ES-TRIN regulations, is calculated for all cases considered. The results reported in Table 5 show that the heeling angles are negligible. Such results could have been expected; the question is, however, if a ship satisfying intact stability standards could be considered as safe with reference to possible hazards in low water levels.

Table 4. Maximum vertical center of gravity and minimum metacentric height of the sample ship equipped with PBB, and the corresponding vertical center of gravity of the cargo, determined in compliance with the intact stability regulations of ES-TRIN (CESNI, 2023)

d	tiers	$KG_{\max}$	$GM_{\min}$	KG_{cargo}
1.753	4	12.738	2.607	18.531
1.149	4	18.814	4.219	39.966
1.753	2	13.063	2.281	19.029
1.149	2	19.351	3.681	41.173

Table 5. Static angle of heel of the sample ship equipped with PBB, due to heeling moments defined by the intact stability regulations of ES-TRIN (CESNI, 2023), corresponding to uniform vertical distribution of the cargo

d	tiers	KG	GM	KG_{cargo}	φ_s
1.753	4	4.41	10.934	5.782	0.6°
1.149	4	3.589	19.444	5.782	0.5°
1.753	2	2.718	12.626	3.191	0.3°
1.149	2	2.435	20.598	3.191	0.3°

Namely, while calculating the $GM_{\min}$ values given in Table 4, the condition that the static angle of heel should not be greater than 5° (Figure 2) proved to be the most stringent requirement in all the cases considered. Nevertheless, in extremely low water levels, even the very small angles of heel could lead to a contact with the riverbed and possible grounding. The minimum under-keel clearance (hereinafter marked by *ukc*) is not restricted by safety regulations (though it is typically considered that *ukc* = 0.3 m is sufficient to avoid contact with the riverbed, considering also the expected squat); it is at discretion of Master to decide whether to sail or not, whereby such decision is typically based on economy considerations (costs associated with inefficient propulsion vs. a business opportunity on the spot market). Indeed, if the sample vessel sailing at d = 1.753 m is inclined to 5°, the lowest point (at the bottom of the fore part of the PBB body) is 2.395 m below the waterline; if the sample vessel sails at d = 1.149 m, the lowest point corresponding to the 5°

heeling angle is 1.786 m below the waterline. Thus, at both draughts considered, the sample vessel equipped with the PBB bodies could avoid contact with the bottom only if the under-keel clearance is greater than ≈ 0.64 m, if its metacentric height corresponds to $GM_{\min}$ determined in compliance with ES-TRIN intact stability requirements. Otherwise, to prevent grounding at low water levels, the minimum metacentric heights should be greater than the values reported in Table 4. The minimum metacentric heights necessary to maintain a desired under-keel clearance (in different water depths, w_d), if the sample ship equipped with PBB is subjected to the heeling moments prescribed by the ES-TRIN rules, are given in Figure 5. With metacentric heights corresponding to uniform vertical distribution of cargo (given in Table 5) it would be (marginally) possible to avoid grounding even at the lowest water depths considered. (It should be, however, taken into account that the analysis is based on the loading conditions with 50% of supplies; thus, a certain margin should be accounted for when using the charts in Figure 5).

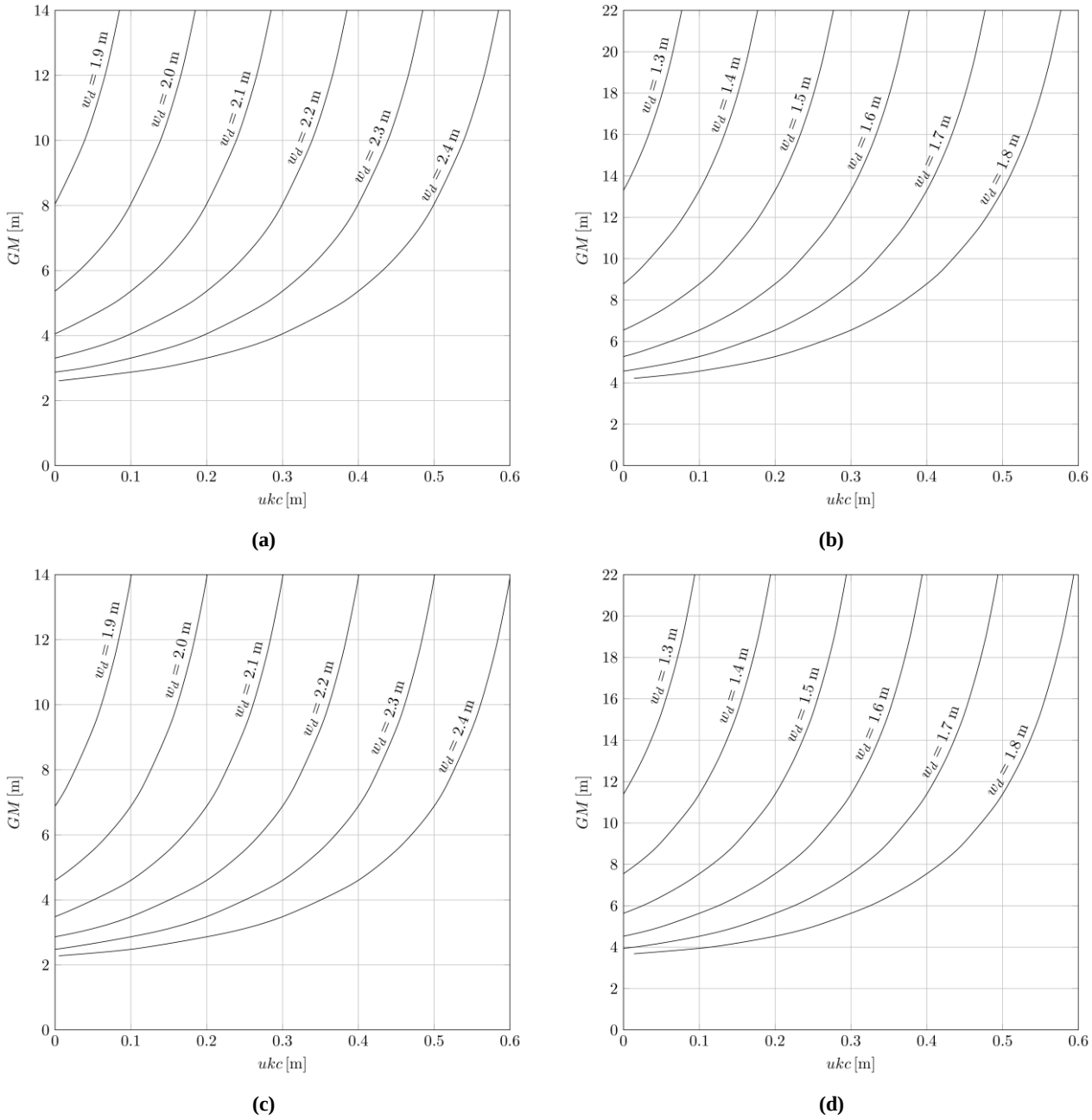

Figure 5. Minimum metacentric heights required to attain a certain under-keel clearance in case the sample ship subjected to heeling moments prescribed by the rules sails: (a) at *d* = 1.753 m with four container tiers, (b) at *d* = 1.149 m with four container tiers, (c) at *d* = 1.753 m with two container tiers, (d) at *d* = 1.149 m with two container tiers.

Another scenario which may be relevant in view of increased overall beam of the vessel and decreased width of the fairway is the stability of the vessel in case of a loss of one of the PBB bodies in intact condition. Such a loss may occur due to an allision with the fairway infrastructure or a bridge pillar, or a collision with another vessel. The calculations show that if the sample vessel sails with KG_{max}/GM_{min} reported in Table 4, the loss of one PBB body would lead to a total stability failure, in all the cases considered. Capsize and (partial) sinking in the shallow water would be followed by sliding and loss of non-secured containers.

Nevertheless, it was already emphasized that the values given in Table 4 comprise a considerable margin; in practice, the vertical center of gravity would be much lower. Thus, as a next step, the static angle of heel of the sample ship with the vertical center of gravity corresponding to uniform vertical distribution of cargo after the loss of one PBB body is calculated for all cases considered and reported in Table 6. If the sample ship sails at d = 1.753 m, the obtained values are well above the limiting 5° even prior to action of heeling moments prescribed by the rules, which could lead to the loss of non-secured cargo and subsequently, obstruction of navigation on the fairway.

Finally, it is examined which values of KG_{max}/GM_{min} would be sufficient to prevent the ship subjected to heeling moments defined by the rules from heeling for more than 5° after the loss of one PBB body. The results are reported in Table 7. The ship sailing at d = 1.753 m with one PBB body could not comply with the stability regulations with any positive value of KG because the heeling angles would be higher than the prescribed ones.

Table 6. Static angle of heel of the sample ship equipped with PBB, due to the loss of one PBB body, corresponding to uniform vertical distribution of the cargo; the draught corresponds to the floating position prior to the loss of a PBB body

d	tiers	KG	GM	KG_{cargo}	φ_s
1.753	4	4.444	5.31	5.782	10.7°
1.149	4	3.628	10.889	5.782	4.9°
1.753	2	2.732	7.023	3.191	8.2°
1.149	2	2.452	12.065	3.191	4.4°

In case that the examined ship sails at d = 1.149 m, generally it would be possible to limit the heeling angle to 5° after the loss of a PBB body in the two-tier arrangement; as for the four-tier arrangement, the required KG_{max}/GM_{min} values are theoretically possible, but could not be practically attained with any vertical distribution of cargo mass reported in Table 2. It follows that the loss of one PBB body could be very dangerous and that the risk mitigation apparently could not be achieved with the stability-related operational measures (i.e., a favorable cargo distribution). Instead, it seems that the probability of loss of a PBB body should be reduced by suitable design measures.

Table 7. Maximum vertical center of gravity and minimum metacentric height of the sample ship equipped with PBB, and corresponding vertical center of gravity of the cargo, after the loss of one PBB body, determined in compliance with intact stability regulations of ES-TRIN (CESNI, 2023)

d	tiers	KG_{max}	GM_{min}	KG_{cargo}
1.753	4	/	/	/
1.149	4	1.997	12.520	2.188
1.753	2	/	/	/
1.149	2	2.541	11.977	3.386

Damage stability

Damage stability considerations bring forward the issue of subdivision of the PBB bodies. According to the procedure for deployment of PBB, the PBB bodies would have to be ballasted prior to being connected to the ship, so as to attain (at least) the operational draught of the ship (d_1 or d_2). In course of ballasting, however, an interesting phenomenon may take place: the loss of static longitudinal stability ("flipping") of a cylindrical body with a free surface. It is found that the effective longitudinal metacentric height of the PBB body, which is not subdivided by means of transverse watertight bulkheads, would reach zero value during the ballasting at approximately d_{PBB} = 1.563 m. Considering that this draught is lower than d_1 = 1.8 m, it follows that the PBB body would have to be subdivided in the longitudinal direction. If the PBB body is divided into two watertight compartments by a single bulkhead placed lengthwise in the middle of the cylinder, the loss of the static longitudinal stability would not take place (almost) until the PBB body sinks, provided that the compartments are simultaneously ballasted. Nevertheless, such a simple subdivision would not be effective from the point of view of the damage stability of the ship equipped with PBB. Namely, in the application of the two-compartment standard, the damage of the single bulkhead would lead to

flooding of the entire PBB body. It follows that a higher degree of subdivision of the PBB bodies should be implemented. Therefore, in this study, the position of the transverse watertight bulkheads corresponds to the longitudinal subdivision of the ship, see Figure 6.

The outcomes of the damage stability calculations are reported in Table 8. It should be noted that number of container tiers does not affect the assessment of the KG_{max}/GM_{min} values from the damage stability point of view, which reduces the number of considered cases to two. Comparing the KG_{max}/GM_{min} values reported in Table 8 with the ones given in Table 4, it follows that the damage stability requirements are more stringent than the intact stability rules in all cases considered. Nevertheless, the required KG_{max}/GM_{min} values are practically attainable, as the minimum metacentric heights are still lower than the values which can be achieved by the uniform vertical distribution of the cargo (see Table 5).

Table 8. Maximum vertical center of gravity and minimum metacentric height of the sample ship equipped with PBB, and the corresponding vertical center of gravity of the cargo, determined in compliance with the damage stability regulations of ADN (UNECE, 2023)

d	tiers	KG_{max}	GM_{min}	KG_{cargo}
1.753	4/2	7.224	8.121	10.089
1.149	4/2	13.583	9.450	28.221

Finally, it is investigated if the flooding due to damage could lead to grounding. Metacentric heights necessary to maintain a targeted under-keel clearance following the most critical damage are reported in Figure 7. If the sample ship sails at d = 1.753 m, grounding would be inevitable in all examined water depths except in w_d = 2.4 m. The prospects slightly improve at d = 1.149 m, when grounding could be avoided with realistic metacentric heights in w_d > 1.6 m.

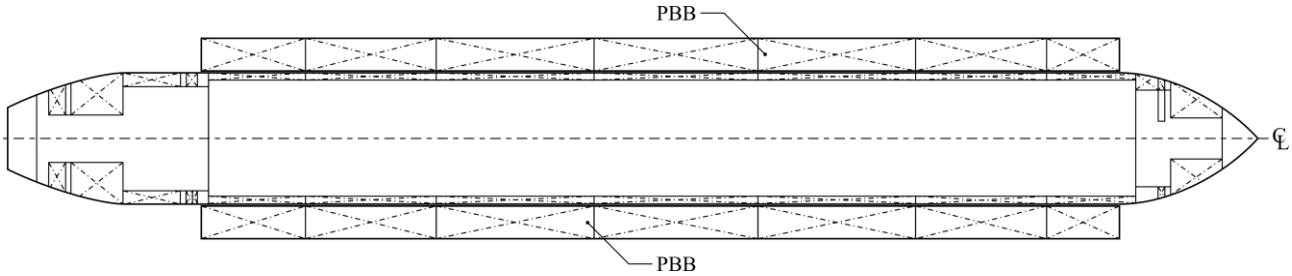

Figure 6. Subdivision of the PBB bodies

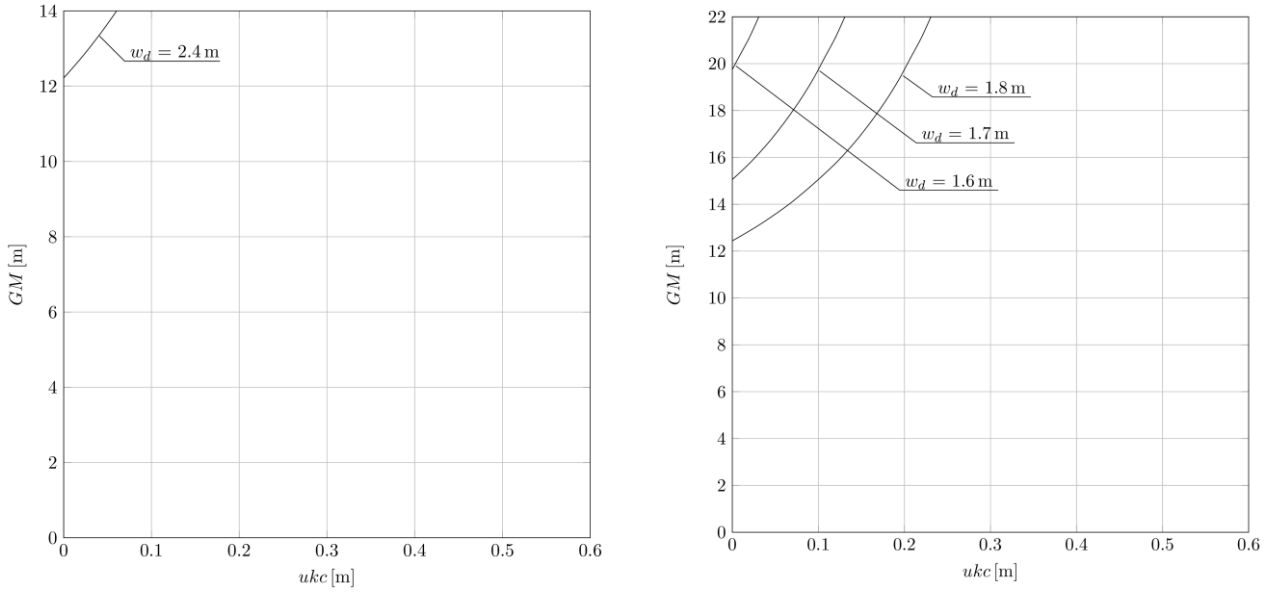

(a) **(b)**

Figure 7. Minimum metacentric heights required to maintain a certain under-keel clearance after the most critical damage in case the sample ship sails: (a) at d = 1.753 m, (b) at d = 1.149 m

As stated previously, the positive influence of PBB on intact stability could have been expected. The influence of PBB on stability in damaged condition, however, is not that straightforward. Namely, due to prescribed transverse extent of damage, the bottom damage cases may comprise both the compartments in the double bottom and the PBB body. These damage cases prove to be the critical ones and, as such, form the primary drivers of the damage stability assessment. At the same time, bottom damages are precisely the ones which are more likely to happen in extreme low-water conditions.

5. CONCLUSIONS

In extremely low water levels, the cargo-carrying capacity and the propulsive efficiency of inland vessels are decreased, freight rates are increased and the reliability of the whole supply chain is questioned. Additional buoyancy bodies may improve some of these aspects, but their use is intrinsically related to hazards atypical for regular navigation conditions. To get an insight into the potential safety issues of inland container vessels equipped with additional buoyancy bodies in extremely low-water navigation conditions, intact and damage stability assessment of a standard Large Rhine container ship equipped with the pipe-based buoyancy (PBB) bodies was performed following the requirements of the applicable stability regulations: ES-TRIN (CESNI, 2023) and ADN (UNECE, 2023).

As it may have been expected, the sample ship with the PBB bodies could fulfill the intact stability requirements of the applicable regulations with a considerable margin. The damage stability requirements were more stringent than intact stability rules in all the investigated cases; yet the required KG_{max}/GM_{min} values are attainable with the standard cargo loading practices. Nevertheless, as the water depth is not considered in the stability rules of ES-TRIN and ADN, the minimum metacentric heights determined in compliance with these regulations provide no guarantee against contact with the river bottom / grounding in low water levels. On the other hand, considering that the value of under-keel clearance is not formally restricted, it is up to the Master to decide whether to sail or not in given environmental and loading conditions. An analysis akin to defining "operational limitations", presented in this paper (see Figure 5 and Figure 7) could assist the Masters in a "risk-informed" planning of the voyage. The requirement to perform the damage stability calculations seems to be particularly relevant, in specific because the ships, such as the one examined in this paper, are not subject to mandatory damage stability assessment unless they carry dangerous goods.

Depending on the draught and the loading condition of the ship equipped with PBB, the loss of one PBB body (in intact condition), could lead to a total stability failure, partial sinking and grounding of the vessel, loss of cargo, and consequently, obstruction of navigation. The analysis presented in the paper indicates that the loss of a PBB body cannot be satisfactorily solved by stability-related operational measures.

Considering that more frequent and more extreme low-water navigation conditions could be expected in the future, it seems that the applicable regulatory framework should be updated as well, and the underlying risks should be reexamined.

6. ACKNOWLEDGMENTS

The research presented herein has been conducted within the project NOVIMOVE (Novel inland waterway transport concepts for moving freight effectively) and received funding from the European Union Horizon 2020 Programme under grant agreement n° 858508.

The first author was partly supported by Ministry of Education, Science and Technology Development of Republic of Serbia, Contract No. 451-03-47/2023-01/200105, and by TED2021-129756B-C33 project, funded by MCIN/AEI/10.13039/501100011033 and by European Union NextGenerationEU/PRTR

REFERENCES

Boven, G., Hoving, A., 2009, "Scheepskamelen & waterschepen: 'Eene ellendige talmerij, doch lofflijk middel'", Walburg Pers, Zutphen.

CEMT, 1992, "Resolution No. 92/2 on New Classification of Inland Waterways", Athens.

CESNI, 2023, "European Standard Laying Down Technical Requirements for Inland Navigation Vessels (ES-TRIN)", European Committee for drawing up Standards in the field of Inland Navigation, Strasbourg.

Friedhoff, B., Martens, S., Samuel, L., van Hassel, E., Ramne, B., Pot, H., 2020, "NOVIMOVE Deliverable 4.1: Detailed requirements for innovative vessel and cargo handling concepts", Duisburg, https://novimove.eu/downloads/.

Friedhoff, B., Ramne, B., Alias, C., van Hassel, E., Martens, S.E., zum Felde, J., Samuel, L., 2022, "Elevating the logistics resilience of the Rhine-Alpine Corridor with the help of innovative vessel and cargo handling concepts", Proceedings of the Transport Research Arena, (TRA 2022), Lisbon, Portugal.

Iqbal, K.S., Bulian, G., Hasegawa, K., Karim, M.M., Awal, Z.I., 2008, "Possible remedies for intact stability hazards involving contemporary small inland passenger ferries in Bangladesh." *Journal of Maritime Science and Technology* 13(3), pp. 282–290.

Schweighofer, J., Fraunhofer, S., Weissenburger, V., Kempmann, K., Florescu, R., Rafael, R., Quispel, M., Seitz, M., Gebraad, J., 2022, "PLATINA 3 Deliverable 4.1: Climate change adaptation strategies – information package for European inland waterway and port infrastructure managers", Vienna, https://platina3.eu/climate-change-adaptation-strategies/.

UNECE, 2023, "European Agreement concerning the International Carriage of Dangerous Goods by Inland Waterways (ADN)", United Nations Economic Commission for Europe, Committee on Inland Transport, New York and Geneva.

Vulnerability assessment of excessive acceleration of an offshore support vessel with moonpool

Fei Duan, *State Key Laboratory of Ocean Engineering, Shanghai Jiao Tong University, Shanghai, China,* feiduan@sjtu.edu.cn

Ning Ma, *State Key Laboratory of Ocean Engineering, Shanghai Jiao Tong University, Shanghai, China,* ningma@sjtu.edu.cn

Qiqi Shi, *State Key Laboratory of Ocean Engineering, Shanghai Jiao Tong University, Shanghai, China,* graceshqq@sjtu.edu.cn

Xiechong Gu, *State Key Laboratory of Ocean Engineering, Shanghai Jiao Tong University, Shanghai, China,* xcgu@sjtu.edu.cn

Yaohua Zhou, *Rules & Technology Center of China Classification Society, Shanghai, China*, yhzhou@ccs.org.cn

ABSTRACT

Numerous studies show that the existence of moonpool will reduce the hull damping. The risk of ship instability will be increased if the moonpool damping is not considered in the safety assessment of ship. In the five stability failure modes of the second generation intact stability criteria, the assessment of the excessive acceleration vulnerability criteria is directly related to the equivalent linear roll damping coefficient of the ship. Therefore, this study focuses on the Level 1 and Level 2 excessive acceleration vulnerability criterion assessment of an OSV. Based on simplified Ikeda method, the moonpool damping is attempted to be expressed as an independent part. In Level 1 vulnerability criteria, a supplementary method for estimating ship roll amplitude related to roll damping coefficient is proposed. The verification results on Level 1 and level 2 vulnerability criteria show that it is necessary to consider the moonpool damping in the assessment of excessive acceleration for ships with moonpool. The equivalent linear roll damping coefficient for a rolling amplitude of 10 deg is suggested to be used in the Level 2 vulnerability evaluation of the excessive acceleration for the ship with moonpool and lower weather deck.

Keywords: *Vulnerability criteria, Offshore supply/support vessel, Excessive acceleration, Moonpool damping.*

1. INTRODUCTION

Due to operation requirements, the moonpool i.e. a vertical well in the hull, is frequently found in drilling ships and in offshore supply/support vessels (OSVs). The sloshing and piston motion of fluid in the moonpool will affect the motion of the ship.

Wei et al. (2011) studied the influence of the size variation of a rectangular moonpool of an FDPSO on the additional mass and damping coefficient in heave direction by WADAM software and model test, respectively. In their research, 180 deg and 135 deg were taken for the wave incoming angles. The results show that the oscillation intensity of the water in the moonpool mainly depends on the size of the moonpool rather than the draft of the ship, but the natural frequency of the oscillation decreases with the increase of the draft of the ship. The smaller the size of the moonpool, the larger the resonance frequency and the higher the peak value of the hydrodynamic coefficient. Guo et al. (2016) and Liu et al. (2022) evaluated the influence of different moonpool sizes and shapes on the drillship's motion response based on the 3D potential flow theory. Different size and shape of the moonpool lead to different draft of the ship in the case of a constant displacement. The results show that the size of the moonpool would affect the ship's roll natural period and the amplitude of roll RAO. With the increase of the moonpool size, the ship's roll natural period increased. The research results of Yao et al. (2017) show that, compared with the drillship without the moonpool, the peak value of roll RAO of the drillship with the moonpool is significantly increased. The opening and closing of moonpool have little effect on the pitch RAO and yaw RAO. Based on SESAM software and model tests, Liu et

al. (2013) and Song et al. (2018) analyzed the effect of a vertical rectangular moonpool and a rectangular moonpool with a step on the motion performance of a drillship. The results of both studies show that the existence of a moonpool would significantly increase the heave and roll motion in beam waves and oblique waves. Through AQWA software and model test, Zhang et al. (2016) compared the influence of rectangular, circular and square moonpools with the same area on the roll RAO of drillship. The research results show that the existence of the moonpool reduced the natural roll period of drillship, but the peak value of the roll RAO increased significantly. The peak value of roll RAO of the drillship with circular moonpool is the lowest compared with the drillship with the square and rectangular moonpool. Chen et al. (2018) also used AQWA software to compare the 6-DOF motion of the drillship. In their research, the moonpools have the same wetted surface area. The results showed that the heave RAO, roll RAO and pitch RAO of the drillship with different moonpools are very close. Zhang et al. (2018) used HydroStar software to calculate the roll RAO of a drillship under the condition of the opening and closing of the moonpool. Different from other studies, in this research, the free surface effect still exists after closing the moonpool. The closed state of the moonpool is simulated by adding 0.04 artificial damping in the moonpool free surface. The comparison results show that the roll RAO of the drillship with the moonpool open and closed are almost the same after adding the artificial damping coefficient. Based on the CFD method, Sun et al. (2013) studied the influence of the moonpool on the heave and pitch motion of the hull in head waves. The results show that the piston motion of the fluid in the moonpool will increase the heave motion of the ship.

In ship stability assessment, the delegation of Japan (IMO, 2015a) provided model experiments of an offshore supply vessel in astern waves. They pointed out that it is not appropriate to apply the criteria for pure loss of stability to a ship having at least the freeboard of 0.02L for the extended low weather deck. The delegation of Norway (IMO, 2015b) assessed the Level 1 and level 2 vulnerability criteria for pure loss of stability, parametric rolling and surf-riding/broaching of 8 sample vessels. The sample vessels include 5 OSVs, 2 small Ro-pax and a double-ended ferry. The evaluation results show that the inconsistency for the vulnerability criteria of Level 1 and level 2 for pure loss of stability occurred on 3 OSVs. Liu et al. (2021) took the drillship as the research object and evaluated the influence of different moonpool shapes and sizes on the Level 1 and Level 2 vulnerability criteria of the parametric roll and the excessive acceleration. The results show that, as the size of the moonpool increases, the draft of the hull increases, and the lateral acceleration of the measuring point evaluated by the Level 1 vulnerability criteria and the long-term failure probability evaluated by the Level 2 vulnerability criteria both increase. In their study, the damping of the moonpool was not considered. Duan et al. (2023) proposed a supplementary calculation method for the Level 1 and Level 2 vulnerability criteria of excessive acceleration by considering the square moonpool damping of an OSV. The effectiveness of the method was verified by comparing with model test results.

A large number of studies on different types of ships with moonpool through different numerical prediction methods and model tests all show that the existence of moonpool will affect the roll motion, and the ship roll amplitude increases obviously at roll natural frequency. The risk of ship stability related failure may be wrongly assessed, and possibly underestimated, if the moonpool damping is not considered. In the pure loss of stability failure mode, OSVs do have the inconsistency for the Level 1 and Level 2 vulnerability criteria assessment. Consequently, further vulnerability criteria assessment for vessels with moonpool are necessary to identify possible inconsistencies and problems with the application of the criteria.

In the five stability failure modes of the second generation intact stability criteria, the assessment of the excessive acceleration vulnerability criteria is directly related to the equivalent linear roll damping coefficient of the ship. In addition, the vulnerability criteria of excessive acceleration was not proposed until 2015, the research on its principle is not as accurate and detailed as the other four failure modes. In the process of studying excessive acceleration, there is also the problem of insufficient number of calculations on sample ships. Therefore, this study focuses on the Level 1 and Level 2 excessive acceleration vulnerability criterion assessment of an OSV. In Level 1 vulnerability criteria, the influence

of bilge keel is considered in the estimation of roll amplitude, but the damping of moonpool cannot be considered in this equation for ships with moonpool. In order to consider the damping of the moonpool, this paper proposes to use the roll amplitude in regular beam waves of unit amplitude, multiplied by the wave amplitude standard deviation of the irregular wave, to represent the ship's characteristic roll amplitude. In Level 2 vulnerability criteria, based on simplified Ikeda method, the moonpool damping is attempted to be expressed as an independent part. By comparing the long-term failure probability of lateral acceleration, some suggestions on ships with moonpool and low weather deck are obtained.

2. VESSEL DETAILS AND TEST CONDITIONS

As a special type of ship, the examined OSV not only has an extended low weather deck, but also has a moonpool. The OSV model for the test is shown in Fig. 1. There are steps on all sides of the moonpool, the dimensions are shown in Fig. 2. The scale ratio is 1/42. The main dimensions of the ship and bilge keels are shown in Table 1.

Figure 1 The model photos of the OSV

Table 1: Particulars of the offshore support vessel (Ballast condition)

Particular		Unit	Full scale	Model scale
Length between perpendiculars	L_{PP}	m	126.1	3.00
Breadth	B	m	27.5	0.6545
Height of main deck	D	m	11.88	0.2827
Mean draught	$\bar{d}$	m	7.297	0.1737
Trim angle	θ	deg	0.166	0.166
Mass	m	kg	18518017.8	243.85
Height of center of gravity	Z_g	m	10.42	0.2481
Roll natural period	T	s	12.28	1.895
Roll moment of inertia	I_{xx}	kg·m^2	2340255219	17.47
Metacentric height	GM	m	3.74	0.089
Moonpool Length/breadth	L_{pool}	m	10.55	0.2513
Bilge keel length	L_{BK}	m	37.6	0.8953
Bilge keel height	H_{BK}	m	0.66	0.0157
Water density	ρ	Kg/m^3	1025	1000

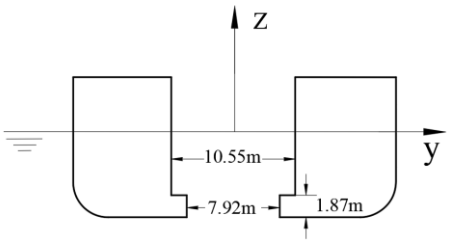

Figure 2 Shape of cross section of ship with moonpool (x=48.6m)

The model tests were carried out in the Multiple Function Towing Tank at Shanghai Jiao Tong University. In the test, a flexible rope constraint was used to limit the slow drift motion of the ship in the horizontal plane. The arrangement of soft moorings is shown in Fig. 3.

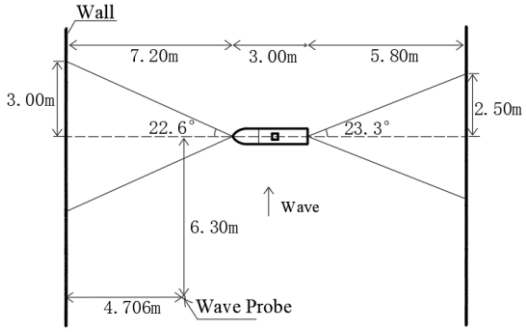

Figure 3 Arrangement of soft moorings of the ship model

According to the occurrence condition of excessive acceleration, beam wave conditions are adopted. Table 2 shows the regular wave test conditions. In the test, the wave steepness is 0.02. The wavelength ship length ratio λ / L_{PP} is from 0.7 to 2.5.

Table 2: Wave conditions

λ / L_{PP}	Full scale		Model scale	
	Wave frequency (rad/s)	Wave height (m)	Wave frequency (rad/s)	Wave height (m)
0.7	0.836	1.764	5.420	0.042
0.9	0.738	2.268	4.780	0.054
1.1	0.667	2.772	4.324	0.066
1.3	0.614	3.276	3.977	0.078
1.5	0.571	3.780	3.702	0.090

1.6	0.553	4.032	3.585	0.096
1.7	0.537	4.284	3.478	0.102
1.8	0.522	4.536	3.380	0.108
1.9	0.508	4.788	3.290	0.114
2	0.495	5.040	3.206	0.120
2.05	0.489	5.166	3.167	0.123
2.1	0.483	5.292	3.129	0.126
2.15	0.477	5.418	3.093	0.129
2.25	0.466	5.670	3.023	0.135
2.5	0.443	6.300	2.868	0.150

The bridge height position is chosen as the acceleration measurement point, the coordinates are shown in Table 3. The definition of the coordinate system is shown in Fig. 4.

Table 3: Location of measuring point (bridge house)

Coordinate	Full scale	Model scale
X (m)	98.95	2.356
Y (m)	13.74	0.327
Z (m)	33.09	0.788

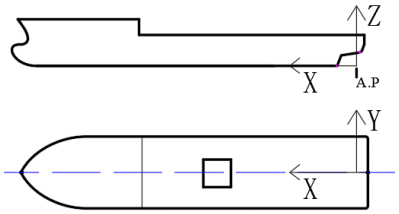

Figure 4 The coordinate system for location of measuring point

3. RESULTS OF ROLL DAMPING COEFFICIENTS OF AN OSV

The roll decay motion as well as the harmonic excited roll motion are established techniques to estimate roll damping for ships. The research of Kristiansen et al. (2014) and Wassermann et al. (2016) showed that the slight phase delays (in the order of ms) in the experiment of forced roll motion would lead to miscalculation of damping coefficient and that the roll decay motion has advantages to estimate roll damping if the ship has no forward speed. Therefore, taking into account the evaluation conditions of excessive acceleration (beam wave and zero-speed), the roll damping coefficient will be determined by roll decay motion in this paper.

Fig. 5 shows the comparison of time history curve of roll decay at different initial amplitude in calm water. The hull models include the bow thruster tunnel, moonpool and bilge keels. It can be seen that the CFD calculation results are in good agreement with the model test results. The ship roll natural period of model test 1, model test 2 and CFD method is 1.988 s, 1.986 s and 1.983 s, respectively, and the difference is less than 0.5%.

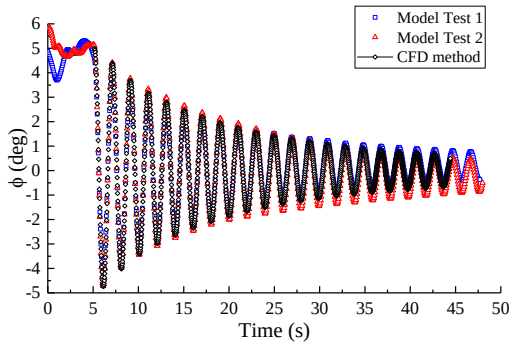

(a) Initial amplitude of the decay: 5 deg

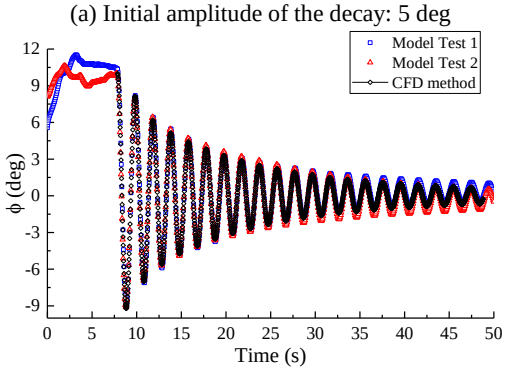

(b) Initial amplitude of the decay: 10 deg

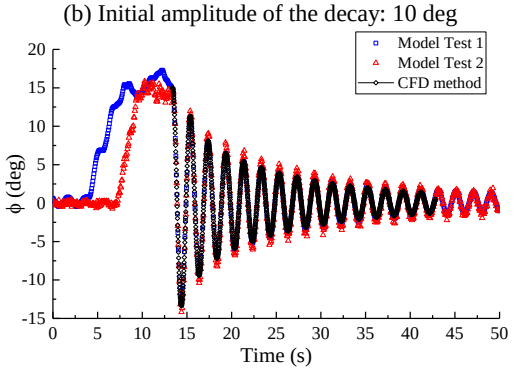

(c) Initial amplitude of the decay: 15 deg

Figure 5 Comparison of time history curve of roll decay in calm water (ballast condition)

In time domain simulation, polynomial expansion of roll angular velocity is usually used to approximate equivalent roll damping. The linear damping coefficients and nonlinear damping coefficients are obtained by quadratic polynomial fitting and cubic polynomial fitting, respectively. In the assessment of vulnerability criteria, the linear damping coefficients and nonlinear damping coefficients are expressed as equivalent linear roll damping coefficients B_ϕ by energy conservation principle (Himeno, 1981).

$$B_\phi = a\frac{mg\cdot GM\cdot T}{\pi^2} + b\frac{mg\cdot GM\cdot T}{\pi^2}\cdot\phi_a\cdot\left(\frac{180}{\pi}\right)$$

$$B_\phi = c\frac{mg\cdot GM\cdot T}{\pi^2} + d\frac{mg\cdot GM\cdot T}{\pi^2}\cdot\phi_a^2\cdot\left(\frac{180}{\pi}\right)^2 \quad (1)$$

where, a [-], b [1/deg], c [-], d [1/deg^2] are roll extinction coeffcients (Himeno, 1981), ϕ_a [rad] is the roll amplitude, m [kg] is the ship mass, GM [m] is the metacentric height and T [s] is the roll natural period.

With different definitions of roll amplitude ϕ_{ai}, the equivalent linear roll damping obtained by the extinction curve will have a great difference. Different roll amplitudes are defined as shown in Fig. 6. In Eq. 2, $\phi_{ai}=\phi_i$ takes all peaks into account for analysis, while $\phi_{ai}=\phi_{2i}$ and $\phi_{ai}=\phi_{2i+1}$ consider positive peaks and negative peaks respectively for analysis.

$$
\begin{aligned}
&(1)\quad \phi_{ai}=|\phi_i| \\
&(2)\quad \phi_{ai}=|\phi_{2i}| \\
&(3)\quad \phi_{ai}=|\phi_{2i+1}| \\
&(4)\quad \phi_{ai}=\frac{\phi_{D,i}}{2}=\frac{|\phi_i|+|\phi_{i+1}|}{2} \\
&(5)\quad \phi_{ai}=\frac{\phi_{D,i}+\phi_{D,i+2}}{4}=\frac{|\phi_i|+|\phi_{i+1}|+|\phi_{i+2}|+|\phi_{i+3}|}{4}
\end{aligned}
\tag{2}
$$

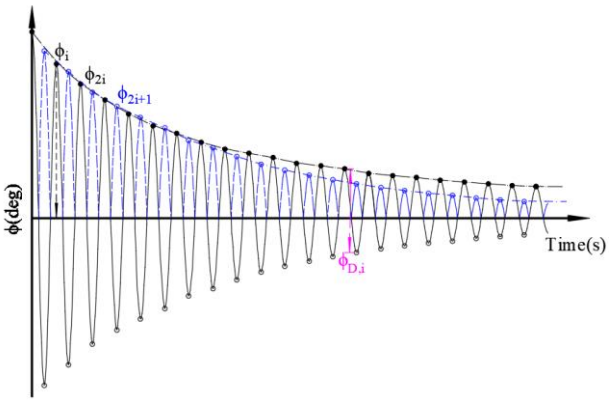

Figure 6 Different definitions of roll amplitude for free roll decay motion

In SDC3/WP.5 (IMO, 2016), an equivalent linear roll damping coefficient corresponding to a rolling amplitude of 15 deg is recommended for conventional ships. Fig. 7 compares roll damping coefficients obtained by different definition methods of roll amplitude for a rolling amplitude of 15 deg on ballast condition. It can be seen that the minimum value and maximum value of equivalent linear roll damping coefficients calculated by ϕ_i are 6.9245 (Nms) and 9.5310 (Nms), with a difference of 27.35%. The difference between the maximum and minimum values of equivalent linear roll damping coefficients calculated by $(\phi_{D,i}+\phi_{D,i+2})/4$ is the smallest, which was 7.1977 (Nms) and 8.0436 (Nms), respectively, and the difference is only 10.52%. The damping components of the OSV are mainly due to nonlinear damping, and the proportion of nonlinear damping in the total damping gradually increases with the increase of the roll amplitude. When the roll amplitude is 5 deg, 10 deg and 15 deg, the proportion of nonlinear damping is about 55.69%, 65.43% and 75.67%, respectively. It can be seen from Fig. 6 that the roll decay trend of ϕ_{2i} is quite different from that of ϕ_{2i+1}. The use of $\phi_{D,i}/2$ can effectively reduce this difference. Therefore, it is suggested to use $\phi_{D,i}/2$ as the roll amplitude to calculate the roll damping coefficient of ships when nonlinear damping accounts for a large proportion.

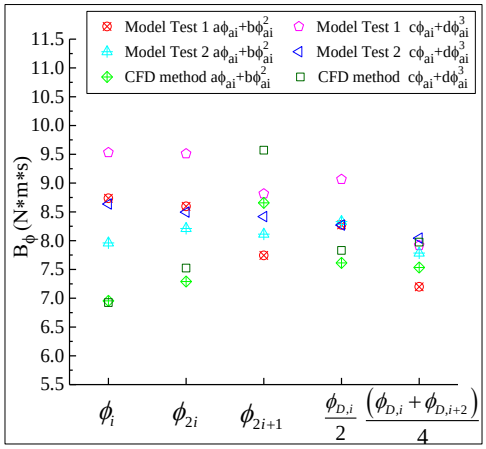

Figure 7 Comparison of equivalent linear roll damping coefficients at 15 deg, as obtained by different definitions of roll amplitude for the analysis of data (ballast condition)

The influence of the steps in moonpool on roll damping coefficients

As it may be seen from Fig. 1 and Fig. 2, there are steps on all sides of the moonpool. In the process of ship rolling, new vortices will be generated at the steps, leading to the increase of hull damping. Fig. 8 shows the comparison of equivalent linear roll damping coefficients of OSV with or without moonpool steps based on CFD method. It can be seen that when the rolling amplitude is 5 deg, 10 deg and 15 deg, the existence of steps in the moonpool leads to the ship's roll damping coefficients increasing by 13.59%, 8.62% and 8.26%, respectively. With the increase of rolling amplitude, the damping ratio of moonpool step decreases.

The calculation results based on CFD method considers moonpool damping and bilge keel damping, while the calculation result based on

simplified Ikeda method only considers bilge keel damping. Therefore, when there are no steps in the moonpool, the rolling damping coefficients calculated by CFD method are all smaller than those calculated by simplified Ikeda method (Kawahara et al., 2011), and the difference between the two results is greater with the increase of initial roll angle. When the rolling amplitude is 15deg, the difference is 22.2%.

In the Ikeda method, the bilge keel damping coefficient accounts for 83.13% of the total damping coefficient. The component is created by shedding vortices from the sharp edges of bilge keels due to roll motion, which can be divided into two components, the normal force component and the hull pressure component, each of which accounts for about 50% (Zhang et al., 2021). Both components are created by the same vortices from the edge of a bilge keel. The former one is created by the force acting a bilge keel, and the latter by the pressure on the hull surfaces in front of and behind the bilge keel. Due to the opening of the moonpool, the dynamic pressure on the hull surface decreases, the edge of the moonpool also generates vortices, but because it is perpendicular to the bottom of the ship and near the middle of the ship, this part of damping is not as large as the damping caused by the reduction of hull dynamic pressure. Therefore, the hull damping decreases because of the existence of the moonpool.

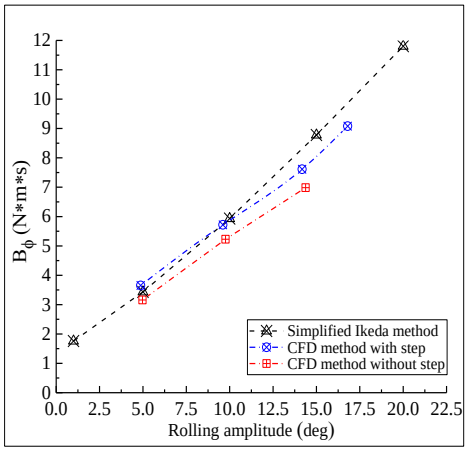

Figure 8 Comparison of equivalent linear roll damping coefficients of ship with or without moonpool step under ballast condition

The supplementary method for square moonpool damping calculation

Within the SGISC framework, the simplified Ikeda's method for roll damping assessment is recommended in absence of experimental data (SDC 8/WP.4/Add. 2, IMO, 2022). The simplified Ikeda's method divides the roll damping into the wave, friction, eddy and bilge keel components at zero forward speed. This study attempts to add moonpool damping on the basis of simplified Ikeda method for ships with moonpool, which is shown as follow:

$$B_{\phi NEW} = B_{\phi Ikeda} + B_{Pool} \tag{3}$$

It is assumed that moonpool damping is not correlated with the other five damping components, and can be solved separately. Suppose that the moonpool damping B_{Pool} (Nms) is:

$$B_{Pool} = C_1 \frac{L_{moonpool}}{B} + C_2 \frac{B}{\bar{d}} + C_3 \frac{A_{moonpool}}{L_{pp} \cdot B} + C_4 \phi_a \frac{\pi}{180} \tag{4}$$

where, $L_{moonpool}$ is the length of the moonpool, $A_{moonpool}$ is the area of the moonpool, $\phi_a\,(\deg)$ is the roll amplitude. Eq. 4 contains four terms, where the first term $C_1 L_{moonpool}/B$ represents that the damping coefficient is related to the length of the moonpool, the second term $C_2 B/\bar{d}$ represents that the damping coefficient is related to the water depth in the moonpool (which is represented by the ship mean draught $\bar{d}$), the third term $C_3 A_{moonpool}/(L_{pp} \cdot B)$ represents that the damping coefficient is related to the opening area of the moonpool, and the fourth term $C_4 \phi_a \cdot \pi/180$ represents that the damping coefficient is related to the roll amplitude.

Table 4: Length of square moonpool

	Full scale (m)	Model scale (m)	$\frac{L_{moompool}}{B}$	$\frac{A_{moonpool}}{L_{pp} \cdot B}$
Case1	5.28	0.126	0.192	0.0080
Case2	7.92	0.188	0.288	0.0181
Case3	10.55	0.251	0.384	0.0322
Case4	13.19	0.314	0.48	0.0503

There are many factors affecting the damping of the moonpool, including the size and shape of the moonpool, whether it features steps, step size, step layout, etc. In this study, a square moonpool without steps is taken as the research model. The length of the square moonpool is shown in Table 4. Based on CFD method, the coefficients of Eq. 4 are obtained through the simulation of roll decay with different moonpool sizes and different rolling amplitudes. Thus, the coefficients in Eq. 4 are solved, which is shown as follows:

$$B_{Pool} = -1.23\frac{L_{moonpool}}{B} + 0.15\frac{B}{\bar{d}} + \\ + 4.126\frac{A_{moonpool}}{L_{pp}\cdot B} - 10\phi_a\frac{\pi}{180} \quad (5)$$

where, $B_{Pool} \le 0$, and B_{Pool} (Nms) is the result of analysis of data at model scale.

The damping coefficients based on simplified Ikeda method are dimensionless results, therefore, the moonpool damping is nondimensionalized as follows:

$$B'_{Pool} = \frac{B_{Pool}}{m\cdot B^2}\sqrt{\frac{B}{2g}} \quad (6)$$

Fig. 9 shows the comparison results of equivalent linear roll damping coefficients obtained by simplified Ikeda supplementary method $B_{\phi NEW}$ and CFD method under different rolling amplitudes and different moonpool sizes. The results show that the equivalent linear roll damping coefficient calculated by the supplementary method in this paper decreases with the increase of moonpool size. Compared with the CFD results, the error is within 5%.

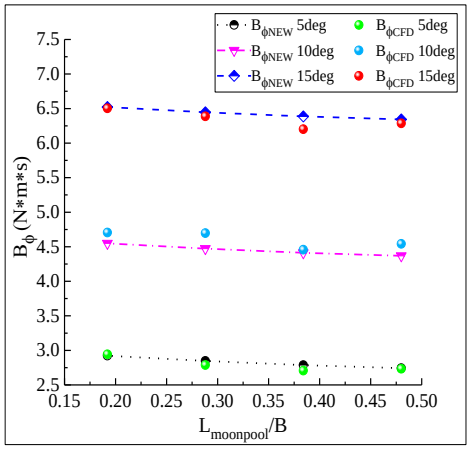

Figure 9 Comparison of equivalent linear roll damping coefficients of OSV under ballast condition

Additional information are now reported changing the loading condition of the OSV from ballast condition to full load condition. The ship's width-to-draft ratio $B/\bar{d}$ decreased from 3.768 to 3.508. Fig. 10 compares ship roll damping coefficients calculated based on supplementary method, simplified Ikeda method and model test for the ballast and the full load conditions. Among them, the roll damping coefficient calculated by model test does not include the influence of steps. According to the results of the influence of the steps in moonpool on roll damping coefficients in Fig. 8, the roll damping coefficients from model tests with steps are reduced by 15% to eliminate the influence of steps on roll damping. The moonpool length is 0.251 m in model scale, which is the same as Case 3 in Table 4. It can be seen that the roll damping coefficients of OSV calculated by the supplementary method are in good agreement with the model test results in both ballast and full load conditions. The results of model test and numerical simulation show that the roll damping coefficients under full load condition are lower than those under ballast condition, and the roll damping coefficient increases nonlinearly with the increase of rolling amplitude. Compared with the model test results, the ship roll damping coefficients calculated by simplified Ikeda method are excessively larger. When the rolling amplitude is 15 deg, the roll damping coefficients calculated by simplified Ikeda method are 29.14% and 33.3% larger than those calculated by the supplementary method in the ballast and full load conditions, respectively. Therefore, the moonpool damping is an important part of ship stability assessment with respect to ship roll damping coefficient.

In the five stability failure modes of the second generation intact stability criteria, the assessment of the excessive acceleration vulnerability criteria is directly related to the equivalent linear roll damping coefficient B_ϕ of the ship.

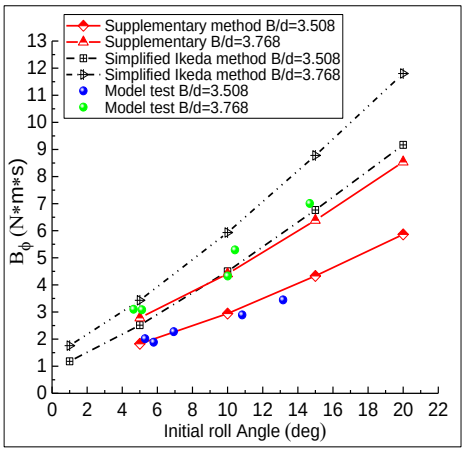

Figure 10 Comparison of equivalent linear roll damping coefficients of OSV under different loading conditions

4. EFFECTS OF MOONPOOL DAMPING ON ASSESSMENT OF VULNERABILITY TO EXCESSIVE ACCELERATION

Taking the failure mode of excessive acceleration as an example, the assessment results of the Level 1 and level 2 vulnerability criteria considering moonpool damping are compared.

The effects of moonpool damping on Level 1 vulnerability criteria assessment

In Level 1 assessment for excessive accelerations, the characteristic roll amplitude corresponds to the roll standard deviation in irregular waves (SDC 3/INF.11, IMO, 2015c), which is shown as follow:

$$\begin{aligned}\sigma_\phi^2 &= \int_0^\infty \int_0^{2\pi} \left|\phi(\omega)\right|^2 D(\beta) S_\zeta(\omega)\, d\omega d\chi \\ &= \int_0^\infty \int_0^{2\pi} \left|\phi(\omega)\right|^2 \frac{2}{\pi}\cos^2\left(\beta - \frac{\pi}{2}\right) S_\zeta(\omega)\, d\omega d\beta \\ &\approx 0.75 \int_0^\infty \left|\phi(\omega)\right|^2 S_\zeta(\omega)\, d\omega\end{aligned} \tag{7}$$

The influence of short-crestedness is considered for using a reduction factor 0.75.

In the simplification process of roll standard deviation calculation, the dominating contribution in the integral comes from the region of frequencies close to the natural roll frequency. Therefore, the natural roll frequency is used. In order to consider the damping of the moonpool, this paper proposes to use the roll amplitude in regular beam waves of unit amplitude ϕ_a, multiplied by the wave elevation standard deviation of the irregular wave σ_z, to represent the ship's characteristic roll amplitude ϕ_{Level1}.

$$\phi_{Level1} = \phi_a \cdot \sqrt{0.75\sigma_z^2} \tag{8}$$

where, the reduction factor of 0.75 is also considered.

According to the 1-DOF motion model, the ship roll amplitude in regular beam waves of unit amplitude ϕ_a can be simplified to obtain the formula related to roll damping coefficient B_ϕ, which is shown as follow:

$$\phi_a = \frac{\mathrm{mg} \cdot GM \cdot r \cdot k}{B_\phi \cdot \omega} = \frac{2\pi \cdot \mathrm{m} \cdot GM \cdot r}{B_\phi \cdot T_{Level1}} \tag{9}$$

where, r is the effective wave slope coefficient, whose calculation method can be found in SDC7/WP.6 (IMO, 2019). For ships with moonpool, B_ϕ can consider the moonpool damping through Eq. 3.

In irregular waves, the standard deviation of wave elevation is calculated as:

$$\sigma_z = \sqrt{m_0} \tag{10}$$

where, $m_0 = \int_0^\infty S_\zeta(\omega) d\omega$.

Since the significant wave height of irregular wave H_s is calculated as:

$$H_s = 4\sqrt{m_0} \tag{11}$$

The standard deviation of the wave elevation σ_z can be calculated by significant wave height and significant steepness, which is shown as follows:

$$\sigma_z = \frac{H_s}{4} = \frac{1}{4} s \cdot \frac{2\pi}{\omega^2 / g} = \frac{s \cdot g \cdot T_{Level1}^2}{8\pi} \tag{12}$$

where, s is the seaway steepness, which is a function of the natural roll period T_{Level1} in Level 1 vulnerability criterion for the excessive acceleration (SDC 7/WP. 6, IMO, 2019).

For the sample ship in this paper, the natural roll period estimated by the vulnerability criteria is 10.70 s, the wave steepness s is 0.0739. The wave elevation standard deviation σ_z is 3.30. Table 5 shows the estimated results of characteristic roll amplitude and lateral acceleration. The roll period estimated by the vulnerability criteria is 12.86% lower than the measured result (the measured natural roll period is 12.28 s). When the measured natural roll period is used, the wave steepness s is reduced to 0.0633. But the wavelength at the roll natural frequency increases, the wave elevation standard deviation σ_z is also increased to 3.73. It can be seen that the lateral acceleration estimated by Level 1 vulnerability criteria is 4.44 m/s^2, which is smaller than the direct measurement result.

Table 5: Comparison of estimated roll amplitude and lateral acceleration (Level 1)

	T_{Level1} (s)	σ_z (m)	ϕ_a (deg/m)	ϕ_{Level1} (deg)	$a_{yLevel1}$ (m/s^2)
Vulnerability criteria	10.70	——	——	13.27	4.44
	12.28	——	——	12.19	3.65
$B_\phi = B_{\phi Ikeda}$	10.70	3.30	11.81	33.80	11.32
	12.28	3.73	10.91	35.22	10.55
$B_\phi = B_{\phi Ikeda} + B_{\phi Pool}$	10.70	3.30	16.23	46.46	15.56
	12.28	3.73	14.99	48.42	14.51
$B_\phi = B_{\phi moedltest}$	10.70	3.30	14.80	42.36	14.19
	12.28	3.73	13.67	44.14	13.23

Model test results	12.28	——	——	18.89	4.45

When Eq. 8 is used to evaluate the Level 1 of excessive acceleration, the lateral acceleration evaluated is much larger than the direct measurement results. This is because the effect of diffraction force is neglected and the calculation of radiant force only takes into account the viscous part in Eq. 9. In the Level 1 vulnerability criteria, the roll damping is simplified. The method proposed in this paper directly adopts more accurate roll damping coefficient to consider the moonpool damping. When the moonpool damping is considered in Eq. 9 ($B_\phi = B_{\phi Ikeda} + B_{Pool}$ and $B_\phi = B_{\phi modeltest}$), the estimated lateral acceleration is larger than the results without considering the moonpool damping ($B_\phi = B_{\phi Ikeda}$). Therefore, the existence of moonpool will increases the occurrence risk of excessive acceleration. It is necessary to consider moonpool damping in Level 1 vulnerability assessment for ships with moonpool.

The effects of moonpool damping on Level 2 vulnerability criteria assessment

In the calculation of the long-term failure probability of excessive acceleration in the Level 2 vulnerability criteria, the calculation equation of lateral acceleration is the same as that of the Level 1 vulnerability criteria. The calculation method of roll amplitude and roll natural period is different from the Level 1. The ship natural roll period in Level 2 is the model test results, and the roll amplitude is calculated by the 1-DOF motion model.

In the 1-DOF motion model, the simplified Ikeda method is recommended in vulnerability criteria to obtain the equivalent linear roll damping coefficient B_ϕ , which does not take moonpool damping into account. For ships with moonpool, the supplementary method proposed in this paper based on simplified Ikeda method can effectively consider moonpool damping.

In SDC 3/WP. 5 (IMO, 2016), an equivalent linear roll damping coefficient for a rolling amplitude of 15 deg is recommended for conventional ships. However, due to the low weather deck of the OSV, the maximum roll angle is 18 deg, which is close to the recommended roll angle. Therefore, Fig. 11 compares the response-amplitude operators of lateral acceleration by using roll damping coefficient at different rolling amplitudes. The black lines in the figure show the results of direct measurements from model tests in regular waves. In the Level 2 vulnerability criteria assessment, the simulation results of 1-DOF motion model are much larger than those of direct measurement. It can be seen that the RAO of lateral acceleration calculated based on the supplementary method is the maximum, while that calculated based on simplified Ikeda method is the minimum. At the peak point of lateral acceleration, when the rolling amplitude for the calculation of equivalent damping is taken as 5 deg, 10 deg and 15 deg, the lateral acceleration calculated based on the supplementary method is 9.57%, 8.32% and 9.30% larger than that calculated using measured damping, respectively. From the perspective of engineering evaluation, the supplementary method can bring more safety margin.

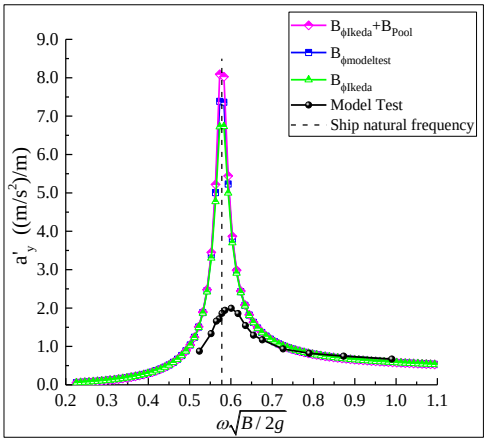

(a) Equivalent roll damping coefficient for 5 degree rolling amplitude

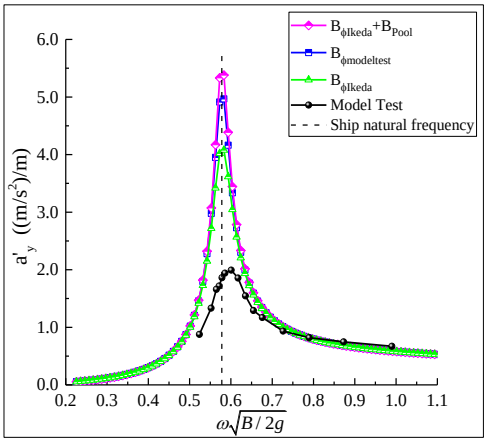

(b) Equivalent roll damping coefficient for 10 degree rolling amplitude

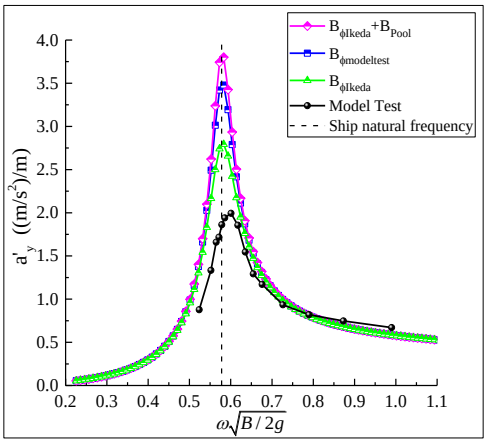

(c) Equivalent roll damping coefficient for 15 degree rolling amplitude

Figure 11 Comparison of lateral acceleration per unit wave amplitude (ballast condition)

Fig. 12 shows the comparison of the long-term failure probability C of the excessive acceleration, where R_{EA2} is the Level 2 threshold value, currently set as 0.00039. It can be seen that the long-term failure probability of ship excessive acceleration based on the supplementary method is the largest, while that based on simplified Ikeda method is the smallest. It is worth noting that the long-term failure probability calculated using simplified Ikeda method to estimate roll damping is smaller than that calculated using roll damping obtained from the model tests. Therefore, when simplified Ikeda method is used to evaluate the stability of ships with moonpool, there may be a risk of insufficient safety margin.

Fig. 12 also shows that when the roll damping coefficient with a rolling amplitude of 15 deg is used to evaluate the Level 2 vulnerability criteria of excessive acceleration, the calculation results based on different roll damping coefficients all show that the ship will not experience excessive acceleration. When the rolling amplitude for damping linearization is taken as 10 deg, the evaluation results based on simplified Ikeda method still show that the ship will not experience excessive acceleration. However, the results based on the supplementary method and the model test method show that excessive acceleration may occur.

As an evaluation of the long-term failure probability of excessive acceleration, the conservative results can decrease the error caused by the 1-DOF motion model and increase the safety margin for ship stability assessment. Therefore, according to the comparison results, the equivalent linear roll damping coefficient for a rolling amplitude of 10 deg is suggested to be used in the Level 2 vulnerability evaluation of the excessive acceleration for the ship with moonpool and lower weather deck.

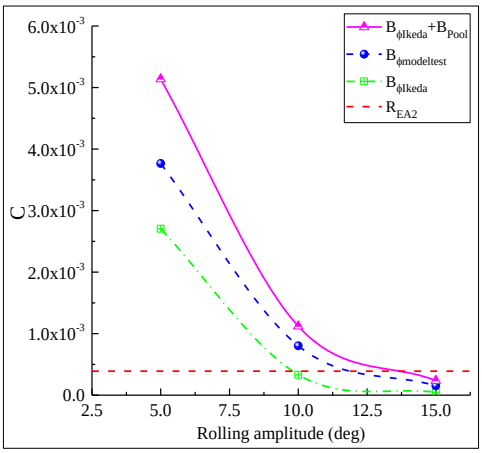

Figure 12 Comparison of the long-term failure probability *C* of excessive acceleration under different method (ballast condition)

5. CONCLUSIONS

As a special type of ship, the examined OSV not only has an extended low weather deck, but also has a moonpool. This study focuses on the Level 1 and Level 2 assessment of vulnerability to excessive acceleration of an OSV. Conclusions are as follows.

Based on simplified Ikeda method, the square moonpool damping is expressed as an independent part. The roll damping coefficients of OSV calculated by the supplementary method are in good agreement with the model test results in both ballast and full load conditions.

In Level 1 vulnerability criteria of excessive acceleration, a supplementary method for estimating ship roll amplitude related to roll damping coefficient is proposed. The results show that it is necessary to consider the moonpool damping in the assessment of Level 1 and level 2 vulnerability criteria of excessive acceleration for ships with moonpool.

In the Level 2 vulnerability evaluation of the excessive acceleration for the ship with moonpool and lower weather deck, the equivalent linear roll damping coefficient for a rolling amplitude of 10 deg is suggested to be used.

The expression of moonpool damping is still needed to be verified, supplemented and perfected by more ships with moonpool.

ACKNOWLEDGEMENTS

This research is financially supported by the Fundamental Research Funds for the Center Universities and the Foundation of National Key Laboratory of Hydrodynamics (JCKY2022201CA02). Authors are grateful to the staff at the Multiple Function Towing Tank of Shanghai Jiao Tong University and students participated in the model test.

REFERENCES

Chen, Z., Cai, S., Ye, J., Lin, X., 2018, "Hydrodynamic performance analysis of drillship with different moonpool openings", *China Water Trans*, 18, 166–168.

Duan, F., Ma, N., Gu, X., Zhou, Y., 2023, "An Improved Method for Predicting Roll Damping and Excessive Acceleration for a Ship With Moonpool Based on Computational Fluid Dynamics Method". *Journal of Offshore Mechanics and Arctic Engineering*, 145(5): 051401.

Guo, X., Lu, H., Yang, J., Peng, T., 2016, "Study on hydrodynamic performances of a deepwater drillship and water motions inside its rectangular moonpool", In: Proceedings of the International Offshore and Polar Engineering Conference, pp. 112–118.

Himeno, Y., 1981, "Prediction of roll damping - State of the art." Report No. 239, Department of Naval Architecture and Marine Engineering, College of Engineering, The University of Michigan, September.

IMO, 2015a, "Comments on pure loss of stability failure mode for a vessel with extended low weather deck", Submitted by Japan, SDC3/6/8, 27 November.

IMO, 2015b, "Comments on the outcome of SDC 2 on the proposed amendments to 2008 IS Code on second-generation intact stability criteria", Submitted by Norway, SDC3/6/4, 12 November.

IMO, 2015c, "Information for criteria and explanatory notes for excessive acceleration stability failure mode", Submitted by Germany, SDC3/INF.11, 13 November.

IMO, 2016, "The vulnerability of ships to the excessive acceleration stability failure mode", Annex 7, SDC3/WP.5, Italy.

IMO, 2019, "Finalization of Second Generation Intact Stability Criteria", Report of the Drafting Group on Intact Stability, International Maritime Organization, SDC7/WP.6, London, UK.

IMO, 2022, "Elements for numerical modelling of roll motion in the vulnerability criteria of the second generation intact stability criteria", Appendix 3, SDC 8/WP. 4/Add. 2, 56.

Kawahara, Y., Maekawa, K., and Ikeda, Y., 2011, "A simple prediction formula of roll damping of conventional cargo ships on the basis of Ikeda's method and its limitation," *Contemporary Ideas on Ship Stability and Capsizing in Waves*. Springer, Dordrecht, 465-486.

Kristiansen, T., Ruth, E., Firoozkoohi, R., Borgen, H., and Berge, B.O., 2014, "Experimental and numerical investigation of ship roll damping with and without bilge keels," Proceedings of the ASME 2014 33rd International Conference on Ocean, Offshore and Arctic Engineering, San Francisco, California, USA, 1-9.

Liu, Z., He, J., Meng, Y., Zhang, H., Zhou, Y., & Tao, L., 2022. "Numerical and experimental study on the influence of a moonpool on motion performance and stability of a drillship", *Ocean Engineering*, 262, 112241.

Liu, Z., He, J., Feng, PY., Zhang, H., Zhou, Y., 2021, "Verification and Analysis of Vulnerability Criteria of Parametric Roll and Excessive Acceleration for Full-Scale Drillship", *SHIP&BOAT*, 32(6): 9-15.

Liu, X., Zhang, H., 2013. "Analysis of motion performance for a deepwater drillship", *SHIP&BOAT*, 24, 12–15.

Song, W., Li, X., Tong, B., 2018., "Influence of moon pool opening on hydrodynamic performance of drillship in wave conditions", *Ship Eng*,40, 15–20.

Sun, C., Yang, J., and Lv, H., 2013, "Numerical investigation on motions of vessel with moonpool in wave conditions", *Ocean Engineering*, 31(4): 21-29.

Wassermann, S., Feder, D.F., and Abdel-Maksoud, M., 2016, "Estimation of ship roll damping – a comparison of the decay and the harmonic excited roll motion technique for a post panama container ship," *Ocean Engineering*, 120: 371-382.

Wei, Y., Yang, J., Chen, G. and Hu, Z., 2011, "The research of moonpool size effect on the hydrodynamic performance of FDPSO", *Proc 30th Int Conf on Offshore, Mech and Artic Eng*, Rotterdam, OMAE, 459–467.

Yao, Z, Guo, Q., Ling, H., Zhou, W. and Zhang, L., 2017, "Hydrodynamic performance of ultra-deep water drilling ship with moonpool", *Ship Engineering*, 39 (12): 22-26.

Zhang, X., Hu, K., Zhou, W., 2016, "Motion Performance of drillship with moonpool", *SHIP&BOAT*, 27, 29–36.

Zhang, L., Yang, Z., Zhao, Z., Cao, K., 2018, "Effect of moon pool resonance on motion performance of ultra-deepwater drillship", *Ship Eng*, 40, 14–18.

Zhang, X, Gu, X., and Ma, N., 2021, "Roll characteristics contributed by a bilge keel using a high-order fractional step finite volume solver," *Ocean Engineering*, 240, 109935.1-109935.15.

Navigating and Manoeuvring of modern Wind powered Ships – Status and Requirements from a legal and practical View

Michael Vahs, Sascha Strasser, Siegfried Wagner, Hochschule Emden/Leer, University of Applied Sciences,
michael.vahs@hs-emden-leer.de

ABSTRACT

Safe and effective navigating and manoeuvring of ships is an essential part of ship operation. The manoeuvrability of ships under sail differs significantly from engine power driven vessels. Ships purely powered by the wind can hardly predict their manoeuvrability as it depends on varying wind conditions and the status or mode of the wind propulsion system, e.g. full sails set or sails reefed. If a sailing vessel and an engine powered ship encounter under risk of collision the international regulations to avoid collision (COLREGs) [IMO, 1972] apply a hierarchical order of ship categories and prescribe manoeuvring action to avoid collision guided by the principle that ships with full manoeuvrability have full responsibility whereas ships restricted in their manoeuvrability are relieved as they cannot contribute effectively to avoid collision. Thus, engine powered vessels have to give way towards sailing vessels. COLREGs take the restricted manoeuvrability of sailing vessels as a fact. Pure sailing vessels have always been part of the shipping fleet and need to be considered for the objective of safe navigation and traffic flow.

Differently, the manoeuvring standards for ships laid down in IMO guideline MSC.137 [IMO, 2002] are addressed to ships of any kind of rudder and propulsion with a length of 100 metres and over, and chemical and gas tankers regardless of the length. It can be assumed that MSC.137 does not consider sailing vessels for their low relevance in commercial shipping. From a regulatory view this could imply that all sailing vessels[1] shall be suited with redundant propulsion to be operated as engine powered vessels. Thus, sailing vessels with engine propulsion can be operated in three different modes: as pure sailing vessels, pure engine powered vessels or as hybrid powered ships. There are no specific regulations and requirements on manoeuvrability of ships operated in these modes nor for the change over from one mode to another. This may turn out to be a "grey zone" for navigators on wind powered vessels of the future.

This paper looks at the manoeuvrability of modern wind powered vessels in regard to regulations and practical requirements for navigation and collision avoidance. The focus is on the applicability of current regulations from the navigator's view based on the operational experience of first modern wind assisted vessels. The legal gaps that are identified and their situational context may lead to insights and approaches for the revision of relevant rules and regulations, examples are given. The paper presents the kick-off phase of the funded "Cargo Sailing Vessel"[2] ship design study performed by Emden/Leer University of Applied Sciences and their partners. An investigation on the manoeuvrability of wind powered ships under operational conditions is in preparation under the project's framework.

Keywords: wind assisted ship propulsion, manoeuvring, sailing vessel, COLREGs.

[1] at least sailing vessels of 100 metres length and over

[2] „Frachtsegler mit alternativen Antrieben"/ "Research for Alternative Propulsion, Sailing Applications and New Technologies" (rasant), funded by the German Federal Ministry of Digital and Transport (BMDV), www.rasant.eu (in prep.)

1. BACKGROUND AND CONTEXT

The upcoming transition of sea transport to climate-neutral operation in the next decades generates an increasing interest in high-performance sail propulsion for commercial shipping, both on freighters and passenger ships. Thus, after a hiatus of about a century, a new generation of commercial sailing ships could be built and launched in the next few years. Existing regulations are partly based on the technical status of the old days of sail. Relevant rules have to be revised and adapted in relation to the new situation. This will only happen gradually and will take time. All parties involved in shipbuilding projects of this kind should contribute to the adaptation process. Technical and operational processes must be carefully analysed, proposals for adaptation developed. Interim solutions based on the recognition of equivalent standards have to be found to accelerate the transition process.

In the following, particularly important issues from the field of maritime rules and regulations in the context of navigation and the required manoeuvrability of ships are identified. It is pointed out that rules of COLREGs and MSC.137 may lead to a different understanding of manoeuvrability requirements in regard to sailing vessels. This could result in in a legal "grey zone" for navigators of wind powered ships. Approaches to possible solutions for the alignment of safety requirements without limiting the use of wind power are discussed. A central question is, if sailing vessels need full manoeuvrability at any time or within an acceptable time frame which is to be defined. The proposals are based on operational experience and experimental data from preceding projects in the design and operation of various wind assisted ships, i.e. BEAUFORT (towing kite), E-SHIP 1 and FEHN POLLUX (both Flettner rotors), presented in [Schlaak et al., 2009], [Schmidt & Vahs, 2013], [Vahs, 2020].

2. MANOEUVRABILITY OF SAILING VESSELS IN GENERAL

Safe and effective navigating and manoeuvring of a ship is an essential part of ship operation. The manoeuvrability of ships under sail differs significantly from engine power driven vessels. Ships purely powered by the wind can hardly predict their manoeuvrability as it depends on varying wind conditions and the status or mode of the wind propulsion system, e.g. full sails set or reefed sails. The manoeuvrability can be roughly estimated by experience from standard manoeuvres under sail such as tacking or jibing. Mathematical prediction models are much more complex than for engine powered ships as introduced in [Eggers & Kisjes, 2023] and [Kontos et al., 2023]. Varying local wind conditions and aerodynamic interaction of all objects and structures in the vicinity still pose problems of predictability at the instance of manoeuvring. However, over centuries sailing vessels had proved their ability to safely perform voyages around the globe including sufficient manoeuvrability for their requirements. Even the principle of tug assistance to enter and manoeuvre in ports was known and applied.

When planning a ship's voyage sufficient manoeuvrability has to be ensured mainly to avoid typical risks of the sea. The voyage plan, a comprehensive scheme of route data and navigation guidance takes risks of navigation into account, e.g. the risk of grounding on the passage of narrow and shallow fairways. This may lead to certain preconditions to be fulfilled before entering the passage or fairway, e.g. wind and sea condition, tides, daylight etc. The voyage plan is a standard instrument for preparing a safe navigation scheme and to handle the risks. It is implemented in the safety management system (SMS) of ships as an important aspect of the International Safety Management (ISM) Code [IMO, 1993]. From this background it can be assumed that sailing vessels pay due regard to their restricted ability in manoeuvring while preparing a voyage plan including all limitations and risks. However, the occurrence of collision risk with another vessel is not explicitly covered by the voyage plan as the event and its boundary conditions are not predictable in advance. A general safeguard is part of the bridge procedures on a ship such as safe passing distances between ships and speed reduction in dense traffic or poor visibility. If a risk of collision occurs the international COLREGs are to be applied.

3. SAILING VESSEL CONCEPT OF COLREGS

If a sailing vessel and an engine powered vessel encounter under risk of collision the COLREGs apply a hierarchical order of ship types resulting in the give way obligation for the engine powered vessel towards the sailing vessel[3]. COLREGs are based on the assumption that pure sailing vessels have been under way for centuries and need to be considered as part of the global fleet mix including sailing pleasure craft. The restricted manoeuvrability of sailing vessels is taken into account by granting them a preferential status in relation to engine power driven vessels with their unrestricted manoeuvrability. There is no obligation for the sailing vessel to start the engine, if available to increase manoeuvrability. Pure sailing is seen as a fixed operational status that may not be changed at all if no engine is available. The COLREGs apply the same concept to other ship categories with restricted manoeuvrability as well, e.g. fishing vessels and vessels with special operational limitations (e.g. buoy tender, dredger, aircraft carrier) or technical failures (rudder, engine)[4].

By definition the COLREGs consider any vessel using its engine additionally to the sails as a power-driven vessel propelled by machinery.[5] Limitations to manoeuvrability caused by sail forces and moments are not legally regarded and have to be managed by the vessel in a safe way. The sailing vessel with engine in operation has to exhibit dedicated lights and shapes to be identified as a power-driven vessel in spite of sails being visible to other ships. Hence, a pure sailing vessel starting its engines instantly changes its legal status which leads to different obligation of action when being under risk of collision to other vessels. Starting engines as a precautionary measure to improve manoeuvrability under sail when approaching other vessels is not incentivised. It yields a more uncomfortable situation requiring full manoeuvrability to give way to other vessels in spite of the adverse impact of sails on manoeuvrability and other operational effects such as unwanted loads on sails and stability. However, there is no precise definition on the technical status of "engines that are in use", e.g. propeller turning or thrust being generated. This may leave some scope of interpretation for precautionary measures as stated above. It yields no systematic approach for the special requirements of modern sail cargo ships with high performance wind power drives. A different definition of the sailing vessel including hybrid propulsion mode could create a clearer picture in regard to manoeuvrability and more safety.

In this context the lack of a clear technical definition of sailing vessels in relation to their sail propulsion system reveals another grey area of COLREGs. From a technical view point any drive creating aerodynamic forces from wind flow could be considered as sails. Some systems require continuous electric power input for operation such as Flettner rotors and suction wings. Though the used power from Diesel generators, fuel cells or batteries has an effect on the energy efficiency balance, it does not change the characteristics of sail drives in regard to the ship's manoeuvrability. However, a modern sail cargo ship may not be identified by the typical visual appearance of traditional sailing vessels. A modern definition of sailing vessels could include all wind powered propulsion systems. This may lead to false interpretations on encountering ships for not identifying modern sail system visually. The automatic identification system (AIS) presents an alternative source of vessel information while transmitting the ship type and operational state according to COLREGs.

4. STANDARDS FOR SHIP MANOEUVRABILITY AND THEIR APPLICATION TO SAILING VESSELS

Traditionally ship designers and builders have relied on navigators' shiphandling abilities to compensate for any deficiencies in inherent manoeuvring qualities of the ship. In 2002 the IMO adopted "STANDARDS FOR SHIP MANOEUVRABILITY"[6] to implement a uniform standard as a reaction to casualties and to increase safety of ships and environmental protection. Thus, an undue burden is not imposed on shiphandlers anymore in trying to compensate for deficiencies in

[3] see COLREGs, rule 18 a)

[4] see COLREGs, rule 3 d), f), g) in context with rule 18 a), b), c)

[5] see COLREGs, rule 3 c)

[6] Resolution MSC.137(76) STANDARDS FOR SHIP MANOEUVRABILITY, adopted on 4 December 2002

ship manoeuvrability. The standards are to be applied to ships of all rudder and propulsion types, of 100 m in length and over, and chemical tankers and gas carriers regardless of the length. This could imply that ships with sail propulsion are included. However, the principles in the annex point out that it should be noted that the Standards were developed for ships with traditional propulsion and steering systems (e.g. shaft driven ships with conventional rudders). Therefore, the Standards and methods for establishing compliance may be periodically reviewed and updated by the Organization, as appropriate, taking into account new technologies, research and development, and the results of experience with the present Standards[7]. From this point it can be concluded that modern sail technology for cargo and passenger ships may require a review of the standards in regard to special characteristics and requirements for ships fitted with wind propulsion.

5. LEGAL INCONSISTENCY AND CONTRADICTIONS FOR MODERN SAILING VESSELS

Currently it seems unrealistic that there will be pure sailing vessels coming up as a new type of "super eco" cargo ship as safety and reliability in operation would be compromised. Modern sail cargo or sail passenger ships are and will be equipped with machinery to be redundantly operated as engine power driven vessels. Hence, there are three different operational modes: as a pure sailing vessel, pure engine powered vessel or as a hybrid ship with both sail and engine power. The change over from one mode to another is not specifically regulated and up to the ship's command. This may be seen as a minor detail not relevant for legal clarification. Perhaps it is a new issue for the operation of modern wind powered ships that has not been considered so far. However, from a legal view it becomes obvious that this issue may lead to contradiction between the application of COLREGs and the Standards for ship manoeuvrability.[8] Whereas COLREGs accept the restricted manoeuvrability of pure sailing vessels as an inherent characteristic the resolution MSC.137 requires a set of manoeuvring characteristics that cannot be fulfilled by pure sailing vessels. A change over to engine power or hybrid operation would be necessary to comply. Further, the question of a limited notice or response time for changing over to full compliance with MSC.137 arises. On the other hand, this change over from sailing to power driven vessel will completely change the application of COLREGs in regard to collision avoidance action. Different rules would have to be applied leading to different obligations and manoeuvring action. All other vessels in the vicinity need to be informed of the changed legal status by navigation lights, shapes and AIS transmission and have to adapt to the new situation. Such change over should be well prepared and not conducted during running action in the course of collision avoidance.

6. APPROACHES FOR IMPROVEMENT

Rules and regulations need to be reviewed for new technologies and developments, here modern sail cargo and passenger ships. In the given example the COLREGs are part of a review. The rules seem not to pay due regard to the technical standards of modern sailing vessels including engines as a redundant power source for the safety of manoeuvring and reliability of operation. For the objective of maximising safety, starting to use the engine should not instantaneously lead to a legal changeover yielding an engine power driven vessel. Starting the engine can be a reasonable measure to increase manoeuvrability of a sailing vessel. Depending on the size and type of sail system its impact on the turning or stopping ability can be significant as long as the system is not furled, retracted or stopped. The changeover of the legal status from sailing to power-driven vessel should rather match the actual manoeuvring characteristics. To overcome the current definition of sailing vessels[9] there could be an adaption to other vessel categories such as "vessel engaged in fishing" or "vessel restricted in her ability to manoeuvre" as per rule 3 d) and g).[10] This would shift the decision from

[7] Annex to Resolution MSC.137(76) STANDARDS FOR SHIP MANOEUVRABILITY, 1.2 Principles

[8] specifically, for sailing vessels of 100 m in length and over, sail chemical tankers and sail gas carriers regardless of the length

[9] see COLREGs, rule 3 c)

[10] Following proposal for reference: The term "sailing vessel" means a vessel which from the nature of her sail propulsion is restricted in her ability to manoeuver as required by these Rules and is therefore unable to keep out of the way of another vessel. The term "sail

the pure criterion "engine used" to a situational decision based on the actual manoeuvrability of a ship using sail propulsion. The approach would follow the general principle of COLREGs to leave the first responsibility for collision avoidance with the superior ship that has unrestricted ability to manoeuvre which is well understood by all navigators.

Resolution MSC.137 leaves similar questions in regard to its practical applicability for modern sail cargo or sail passenger vessels. The general concept of the resolution is to proof specific manoeuvring characteristics in a calm environment. High wind loads and other environmental factors are not addressed. Specific ship types exposed to high wind loads by design, such as pure car carriers or container ships with deck load may not fulfil the manoeuvring criteria at higher wind speeds. The assessment and operational compensation has been left to the navigators so far. However, this principle may change with the requirements of special rules for the classification of wind assisted ships.[11] The requirement to proof manoeuvring criteria under wind load changes the concept and may yield uneven treatment of manoeuvring standards and their application to different ship types. However, for safety aspects it seems to be reasonable to assess the manoeuvrability of ships under higher wind loads. This is a specific issue for ships with sail propulsion as sail forces have a strong impact on the ship's manoeuvrability. Nevertheless, the requirement of full manoeuvrability at any time cannot be fulfilled in a practicable way. The principle of setting a reasonable "notice time period" to prepare the ship for specific manoeuvring requirements is well known on-board ships, e.g. to have engines, thrusters or anchors ready for manoeuvring on demand of the Captain or Pilot. This principle may help to interpret MSC.137 in a practicable way and to increase operational safety of ships with sail propulsion at the same time.

7. MANOEUVRING CONCEPT FOR SHIPS WITH SAIL PROPULSION

A "notice time" in the context of manoeuvring is hereby understood as the time that is needed to arrange for full manoeuvrability required by resolution MSC.137, i.e. keeping the ship within limit values for turning circles and stopping distances. These are so called "emergency manoeuvres" that may need to be initiated primarily for collision avoidance. A ship may not be at any time ready for full manoeuvrability as long as there is sufficient time from "warning" until "full manoeuvrability". Collision warnings are generally generated by plotting functions of the ship's navigation system, i.e. radar and AIS. Typical criteria for danger of collision are the combination of the closest approach (CPA) of two ships passing each other and its countdown time (TCPA). To initiate a safe manoeuvre to avoid collision the manoeuvre should take the own ship's manoeuvrability into account. In the specific case of ships with wind propulsion an adequate "extra" time for achieving full manoeuvrability has to be included into the safety margin of manoeuvre planning. This concept leads to a definition of time or range limits to initiate appropriate action, e.g. start engines, stop wind propulsion system[12], initiate turning circle etc. The manoeuvring concept can be defined for different navigation profiles or modes, such as "open sea", "coastal", "river". The sail systems may be limited to specific performance values within the navigation modes to allow for a shorter or longer notice time period as required by the navigation profile. Looking at average time sequences for collision avoidance in different sea areas the following notice time values could be proposed for discussion and used as an example for the preparation of full manoeuvrability[13]:

- open sea: 12 minutes
- coastal: 6 minutes
- river/port: always full manoeuvrability

The manoeuvring concept implies that for open sea conditions a notice time of 12 minutes is given before reaching a critical approach to other vessels that may require full manoeuvrability. Coastal navigation with a higher density of traffic would require to halve the notice time to 6 minutes. From a technical point the notice time defines the time interval needed to reduce sail power from full (sea mode or costal mode) to a power limit that allows full manoeuvrability in regard to MSC.137. This may include "zero thrust" functions of sail systems. In this context automation technology and

propulsion" includes all technologies that convert atmospheric wind energy directly into thrust.

[11] e.g. DNV DESIGN GUIDELINE: Certification and Classification Procedures associated with installation of a "Flettner" Rotor Unit onboard a classed vessel, Document No.: MCADE452-001 (2016)

[12] e.g. by stopping the rotation of Flettner rotors

[13] time values to be seen as specimen with need of further research work for validation

integration of ship's navigation, manoeuvring and propulsion may play a central role in the system design of modern sail cargo and sail passenger ships.

To go one step further for clear definitions and functional assignments the application of MSC.137 could be clarified and aligned with COLREGs. A vessel using wind propulsion in such way and extent that full manoeuvrability according to the standards of MSC.137 is not given, shall be considered as a "sailing vessel" seen as an operational mode in alignment with COLREGs. A special annex could be added to MSC.137 dealing with ships that are restricted in their manoeuvrability including sailing vessels and, if seen essential, other ship categories as mentioned above. This annex could give guidance for the practice of changing over from one operational mode to another incorporating the principle of an adequate notice time for on-board procedures and safe behaviour in regard to other vessels and the risk of collision.

When reviewing the relevant rules and regulations a change of terms and wordings could be considered as well. To reflect on modern wind propulsion systems and associated changes in technology the term "wind powered vessel" could be used instead of "sailing vessel". A "wind assisted vessel" could be defined more precisely as a vessel with full manoeuvrability as per standards while using a relatively small wind power device to assist the main propulsion.

8. CONCLUSIONS

It has been pointed out that there is no consistent legal concept for wind powered vessels in regard to manoeuvrability and its role in collision avoidance. For navigators the application of COLREGs and MSC.137 seem to bear contradictions. COLREGs do not reward engine assistance for an increase in manoeuvrability resulting in higher safety. MSC.137 does not take sail technologies into consideration and leaves a grey area for sailing vessels. These gaps should be closed for the development of modern sail cargo and sail passenger ships as wind technology bears a significant potential for fuel and emission savings. To ensure operational safety on board wind powered ships technical requirements need to be formulated and met by system developers. However, a review of rules and regulations should be one of the first steps to form a consistent legal base for developers and operators. A view on operational requirements based on safe practice in navigation may lead to approaches for both safety and applicability without much of compromising fuel and emission saving potentials. A risk based approach to manoeuvrability setting notice time intervals to reach a defined state of manoeuvrability is well known in ship operation and could yield a concept for wind powered ships. Minor changes in COLREGs and MSC.137 could lead to clear definitions and operational guidance.

Table 1 summarises proposals for consideration and revision of respective regulations.

Table 1: Proposal for revision

Regulation	Proposals for revision
COLREGs Rule 3 c)	- revise definition of "sailing vessel" based on manoeuvrability and include hybrid propulsion mode whenever manoeuvrability is restricted (see 3 d), 3 g) for reference) - include unconventional wind power propulsion systems such as Flettner rotor, suction wing, kite - change/add method for identification of sailing vessel mode by other ships, e.g. AIS, signal flag - consider to replace the term "sailing vessel" by "wind powered vessel" to reflect on modern technologies
MSC.137 – Standards for Ship Manoeuvrability	- use the manoeuvring standards to define and distinguish "sailing vessel"/ "wind powered vessel" (not complying) from "wind assisted vessel" (complying) - include special requirements and guidance for "sailing vessels"/ "wind powered vessels" (possibly in alignment with other special ship types and/or operational modes) - consider "notice time" as requirement criterion for the change of operational modes, e.g. from sail (restricted manoeuvrability) to engine (full manoeuvrability).

As an outlook, manoeuvring simulation, e.g. with shiphandling simulators could add a scientific tool and methodology for the analysis and prediction of sailing vessels' manoeuvrability under operational conditions. The authors are currently preparing the modelling and simulation of wind

powered vessels for researching the operational requirements in regard to collision avoidance and other safety-critical manoeuvres.

REFERENCES

Eggers, R., Kisjes, A.S., 2023, "WiSP2 Project On Wind Propulsion Performance Prediction Methods And Manoeuvring", Wind Propulsion Conference, Royal Institution of Naval Architects / IWSA, London.

IMO 1972, "Convention on the International Regulations for Preventing Collisions at Sea, 1972 (COLREGs)", 20 Oct.

IMO 1972, "MSC.137(76) – Standards for Ship Manoeuvrability", 04 Dec.

IMO 1993, "Resolution A.741(18) - International Management Code for the Safe Operation of Ships and for Pollution Prevention (INTERNATIONAL SAFETY MANAGEMENT (ISM) CODE)", 04. Nov.

Kontos, S, O Lundbäck, M Kjellberg, E Wilske, and S Werner. 2023. "Manoeuvre Simulations in Design Process of Wind Powered Vessel." Wind Propulsion Conference, Royal Institution of Naval Architects / IWSA, London.

Schlaak, M & Kreutzer, Rudolf & Elsner, R. (2009). Simulating Possible Savings of the Skysails-System on International Merchant Ship Fleets. International Journal of Maritime Engineering - INT J MARIT ENG. 151. 10.3940/rina.ijme.2009.a4.161

Schmidt, A., Vahs, M., „Entwicklung eines innovativen Schiffsantriebes gekennzeichnet durch den Einsatz von Magnus-Rotoren zur Windenergienutzung in Kombination mit einem hierauf abgestimmten Antriebspropeller" (Final Research Evaluation Report on „E-Ship 1"/Enercon, in German Language), Deutsche Bundesstiftung Umwelt, Osnabrück, 2013

Vahs, M., 2020, "Retrofitting of Flettner Rotors – Results from Sea Trials of the General Cargo Ship Fehn Pollux", Transactions of the Royal Institution of Naval Architects Part A: International Journal of Maritime Engineering 162(A4), pp. A-371 - A-379, Oct-Dec 2020

Steering with wind propulsion

Anton Kisjes, *MARIN,* A.S.Kisjes@marin.nl
Rogier Eggers, *MARIN,* R.Eggers@marin.nl
Antoine Bedos, *MARIN,* A.Bedos@marin.nl

ABSTRACT

Although sizeable compared to other energy saving measures, the majority of present installations of wind propulsion now sailing are relatively modest. They are assisting the propulsion of the ship, corresponding to the word *"Assisted"* in the common acronym WASP: "Wind Assisted Ship Propulsion". However, it is seen there is an increase in announcements of projects where the aim is that wind propulsion will on average provide a similar contribution as the propeller, or even the majority. Wind propulsion does not only deliver forward thrust, but also major contributions in side force, heeling and yaw. Theses secondary forces (and moments) influence the performance in straight line sailing, e.g. through lift induced resistance on hull and rudder. This aspect is being covered in literature. However, the impact on (dynamic) course keeping and manoeuvrability does not feature in a lot of publications yet.

Within the WiSP2 Joint Industry Project manoeuvrability and course keeping of wind propelled ships is a subject of research, focusing firstly on modelling methods. The work is also planned to start a discussion on rules and regulations. How do simulated results fare compared to criteria? Making these comparisons already highlighted that rules and regulations, such as manoeuvring standards in IMO Resolution MSC 137(76) are not geared for wind propulsion. Interpretations are required. Eggers & Kisjes, 2023, already provided results for two cases, showing results for different interpretations of the standards. The manoeuvring response showed large variations and heel in a turning circle became particularly significant for certain wind directions.

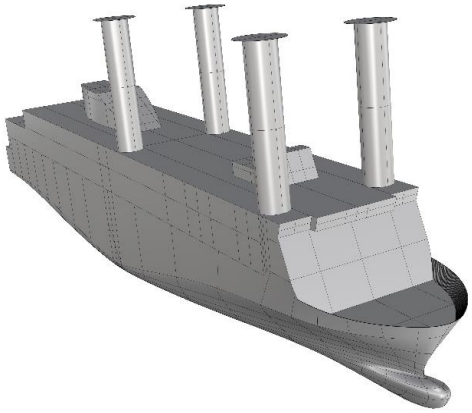

Figure 1: MARIN Ferry case vessel

The published results so far considered Flettner rotors where the controls were fixed: the rotation rate of the rotors was set at the beginning of a manoeuvre, depending on the wind angle and speed in the approach, and was not changed thereafter. This may be a reasonable assumption in some cases. Not all wind propulsion installations have a fast response time; some of them require up to 5 minutes to decelerate. None of the installations known to the authors have an automatic control system developed for manoeuvring. Nevertheless, systems could be adapted and automatic control could be implemented. This paper extends on that previous publication by considering the potential improvement for manoeuvring that can be achieved by fast power reduction or active control.

Keywords: *Wind propulsion, WASP, manoeuvring, MSC 137(76), MARIN Ferry, WiSP*

1. Background

MARIN became active with the resurgence of wind propulsion in commercial shipping in 2013 with background research, involvement in EU projects and organising the BlueWeek (https://blueforum.org). At that time, there were already some (potential) suppliers of wind propulsion systems active and a few design offices and developers were proposing complete ship concepts with wind propulsion. Skysails and E-ship were ahead of their time with products and one ship in operation. What was prevalent at that time is that wind propulsion was hardly acknowledged by the

shipping industry. Whereas there were a lot of reasons for that, a distinct one was that technical information, more specifically promised fuel savings, was often not trusted or understood. Saving predictions were presented at conferences with a wide variety of methods and assumptions, often not documented. This may partially be understandable, because except for the EEDI/EEXIS guidelines (IMO, 2021), there was hardly any guidance. The same was valid for statutory and class regulations. This gap was documented in a report by CE Delft (Nelissen et al, 2017) for the European Commission a few years later. On this premise, the WiSP (phase 1) Joint Industry Project (JIP) started, initiated by MARIN and American Bureau of Shipping (ABS). The project included case studies with performance predictions and gap analyses on rules and regulations. Based on the findings MARIN participated in the update of the EEDI & EEXI guidelines in MEPC.1/Circ896 (IMO, 2021) through delegates Royal Institution of Naval Architects and Comoros.

The momentum on wind propulsion is now rather different. Increased ambition in the industry itself as well as adapted and new regulations have now clearly put shipping on a path towards decarbonisation. Wind propulsion is now often seen as one of the credible solutions. A small selection of trial and monitoring projects (e.g. Hurford, 2019 and Schmidt and Vahs, 2013) have proven the savings. The guidelines for EEDI and EEXI were improved and most class societies came with their own wind propulsion guidelines and rules. So, there is progress. But there is still much to do on topics not yet addressed and improvement of existing standards, rules and regulations to equitably assess (and improve) wind propulsion performance, such as:

- Further improvement of MEPC.1/Cir.896 with guidelines on EEDI / EEXI predictions with wind propulsion.
- Standards for predictions to facilitate investment decisions (higher accuracy) and standards for predictions for larger proportions of wind propulsion.
- Standards for sea trials and monitoring.
- Further adjustment of class rules and statutory regulations suitable for wind propulsion.

Items 1, 2 and 4 have been taken op in the follow-up of WiSP, WiSP2, as described in this paper and other papers.

The WiSP2 Project

WiSP2 (https://www.marin.nl/en/jips/wisp-2) started in 2021 and has since attracted 23 participating organisations. Most organisations are suppliers of wind propulsion systems. WiSP2 also has a design office, technology research centres, consultancies, a flag, and class societies as participants. MARIN and ABS are leading the project. WiSP2 is a Joint Industry Project, which means the funding is primarily brought together by the participants. As it doesn't operate under any specific thematic subsidy program there is the freedom to decide scope with very little bureaucratic overhead. Decisions in the project are confirmed in a democratic manner.

WiSP2 aims to help further decrease barriers for increased uptake of wind propulsion by:

- Improving the knowledge base for performance predictions.
- Improving rules, regulations and standards.
- Showing the potential of wind propulsion.

Improving rules, regulations and standards can of course not be implemented directly inside the project. The focus is rather on doing (case) studies. Recommendations are composed based on results from these case studies. These recommendations are also shared outside the project for possible implementation.

Literature

Not much data is available from literature on manoeuvring of ships with wind propulsion. So the manoeuvring behaviour is, except for a few cases as described below, largely unknown yet.

Eggers and Kisjes, 2023 already published manoeuvring simulations based on work conducted in the WiSP2 project. It demonstrated that simulations could reasonably replicate testing done in the basin with a simplified wind tunnel, using the MARIN Hybrid Transition Coaster (MHTC) case vessel. It also showed a broader exploration of

different wind angles and different ways to interpret the manoeuvring standards in IMO Resolution MSC 137(76), using different interpretations of the initial rudder angles going into zig-zag and turning circle manoeuvres. The results demonstrated an appreciable influence of wind propulsion forces on manoeuvring.

Kontos et al, 2023 also demonstrated good correlation of manoeuvring simulations with model test experiments and showed how simulations, including on a bridge simulator, can be used for design decisions. Focus was on project specific scenarios rather than compliance to the IMO manoeuvring standards.

Vahs, 2019, demonstrated compliance to the IMO manoeuvring standards for a coaster with Flettner rotor on the turning circle and stopping behaviour using a bridge simulator.

The studies referred to above provide valuable information. However, to draw a more broad picture, much more cases should be run in order to determine how the response varies according to ship type, wind propulsion type and relative sizing and different options for control. Moreover, it remains to be argued whether present standards are suitable. The latter is discussed in a dedicated section below.

2. Manoeuvring and Course Keeping Criteria for Ships With Wind Propulsion

With more substantial wind propulsion now entering the market, more and more projects are starting up where the additional aerodynamic forces will influence manoeuvring and course keeping. This leads to the question how the manoeuvring and course keeping performance may be affected and whether there is challenge to comply with existing criteria. A review of existing criteria is given here.

IMO MSC. Resolution 137(76) specifies criteria that are to be verified with zig-zag turning circle and crash stop tests. The interpretation of the criteria is not directly straightforward. Literally, the resolution describes that the criteria should be verified in calm conditions, without wind, which would not present a problem. However, as the intention of the resolution is that ships should be able to make evasive manoeuvres at sea in operational conditions, one may interpret that the criteria should be valid in a relevant wind (and sea) condition too. In fact class societies are now also interpreting it in that way in their guidelines, even if they are mostly not consistent with each other.

Although in the IMO manoeuvring standards, the zig-zag test has some relation to course keeping, a real course keeping scenario is judged to include waves and wind. However, except for military vessels (NATO, 2011), no official criteria exist for this scenario. At best yaw, track and rudder angle variations as observed in simulations, model tests or in operation are judged on an ad hoc basis.

The intact stability code (IMO, 2008) includes a threshold for the maximum heel angle for passenger ships. The code includes an empirical formula from which the resulting (steady) heel angle shall not exceed 10 degrees. It is note that MARIN previously established that the actual (instantaneous) heel in angle in a turning circle may be much higher than the result of the empirical formula (Ferrari et al 2020).

MEPC.1/Circ.896 (IMO, 2021) gives guidance on treatment of innovative energy efficiency technologies, including wind-propulsion, for EEDI & EEXI. Section 2.4.4.4 in that document describes that the verifier may request to demonstrate the vessel's course keeping abilities and rudder response in operational conditions: 'Where the lateral forces and yawing moment are particularly significant, the verifier may request course keeping and rudder angle demonstrations to validate conformity with the operational domain'. This guideline is not yet precise on what exactly these operational conditions should be.

In order to see the effect of wind propulsion, one could argue that the wind speed in which manoeuvring is verified shall not be chosen too small. This can be sailing in demanding conditions such as a rapid change of weather where the vessel experiences high winds, wind gusts or the operator attempts to maximize the use of wind energy in such conditions. In such cases it is important to know what are the operational limits on manoeuvrability and course keeping. For these reasons, moderate to high wind speeds in the range from 6 to 8 Beaufort were selected in two case studies in WiSP2 to evaluate the effect of wind propulsion on the manoeuvring and seakeeping behaviour.

It is noted that the overview of regulations summarised here is focused on the same criteria as used for conventionally propelled ships. It could be considered in the future that ships with wind

propulsion may demonstrate differently that they are operationally safe. However the present paper takes the assumption that the present criteria must be satisfied, possibly with some small changes or interpretations.

One such interpretation is on the "zero rudder angle" used to initiate a manoeuvre. This was researched by Eggers and Kisjes, 2023. It was concluded that a reasonable interpretation is to assume that the zero rudder angle corresponds to the rudder angle required to keep course when initiating a manoeuvre for a specific wind angle and speed at that time.

The present paper specifically focusses on the criteria in IMO Resolution MSC 137(76). While doing that the intact stability code criterion for maximum heel can also verified, though not with the empirical formula.

3. Research Questions

The present paper extends the work as published by Eggers and Kisjes, 2023 for the MARIN Ferry case. Up until now it has been considered that the Flettner rotor wind propulsion system remains operating at the same rotation rate as when initiating the manoeuvre. However, the following questions remained:

1. How is the manoeuvre affected when the rotors are stopped either very quickly or less quickly.
2. What are the options to use the wind propulsion system to aid in steering. What algorithms can be used and what can be the improvement of the manoeuvring response?

4. MARIN FERRY CASE VESSEL

In 2018, MARIN designed the MARIN Ferry, see Figure 1, as a representative modern ferry. The ship features a twin shaft-rudder arrangement. The main particulars of the vessels are indicated in Table 1. See Kisjes et al, 2019 and Ferrari et al, 2022 for more details on the hull form and appendages. Two different skeg variants exist, a short and long skeg. The long skeg is selected for the current application, because a wind-assisted vessel favours the additional side force generation to counter balance the sail forces.

Table 1: Main particulars of the MARIN ferry

Designation	Value	Unit
Length between perpendiculars	190.0	m
Breadth	30.0	
Draught (even keel)	7.0	m
Displacement	25,118.3	t

A 'substantial' sail plan is constructed such that average fuel/emission savings in the order of roughly 20% annually are achievable, depending on the route and the realised winds. As a first indication, steady sailing predictions show that a total of four rotors of each 30.0 m span and 6 m diameter is sufficient to reduce the average net brake power (by also subtracting the Flettner power) by 23% at a chosen design speed of 15 kn for a wind speed of 21 kn from all directions. Two rotors are placed around midship, and two rotors at the deck house, located in longitudinal direction at 98 m and 164 m measured from the aft perpendicular respectively. The Flettner transverse offset from centreline is both 11.5 m to port side and starboard. The frontal and lateral wind area of the superstructure are 428 m^2 and 4848 m^2 respectively.

A transverse stability, GMt, of 3.0 m or more would be more representative for a ferry of this size and without a sail plan. However, when adding four rotors to the upper deck of the vessel, the centre of gravity moves upward. A rough estimation is that the corrected GMt will be in the order of 2.0 m.

5. METHODOLOGY

MARIN's in-house aNySIM time-domain software is used to simulate the vessel in the time domain. Results of captive model tests performed at MARIN were used to derive a complete mathematical model for the hull, propeller and rudder hydrodynamic loads in 4 degrees of freedom. Ferrari et al, 2022 provides further insight on the experiments and the numerical modelling.

The Flettner rotor forces are modelled using lift and drag curve versus spin ratio as shown in Figure 2. The values are averaged for results from literature valid for full scale Reynolds numbers. An optimal Flettner rotation rate is applied, obtained from a very long speed run in which the Flettner rotation rate is varied. The optimal Flettner rotation meets predefined constraints that limit the heel angle at a maximum angle of 5°. For simulations with wind,

the wind loads of the superstructure are modelled as well, based on wind coefficients of a reference ferry.

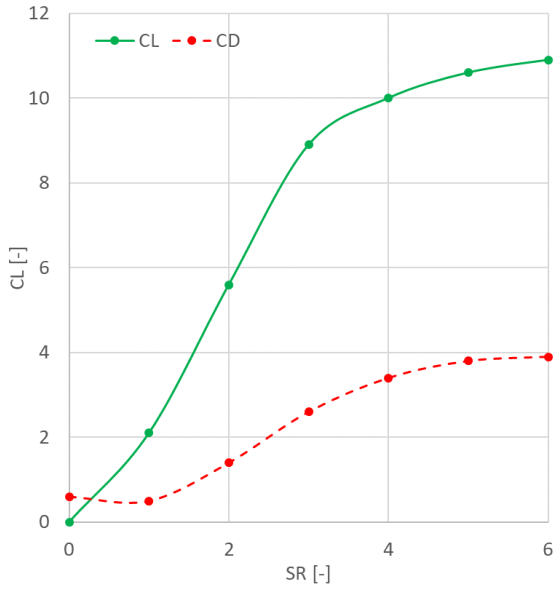

Figure 2: Generic lift and drag curves

6. SIMULATIONS

Simulations were done for the following manoeuvres:

- Zig-zag 10/10 runs where the rudder and yaw checking angle both correspond to 10 degrees.
- Zig-zag 20/20 runs where the rudder and yaw checking angle both correspond to 20 degrees.
- Turning circle runs where the rudder angle is set to 35 degrees.

The definition of these manoeuvres is mandated by the manoeuvring standards as discussed in section 2. The simulations are conducted all in calm water and in three wind speeds: 0 (no wind), 21 kn (top end of Beaufort 5) and 35 kn (start of Beaufort 8) . No wind serves as a reference. 21 kn is judged to be a representative wind speed in operation. It is at the magnitude where class societies appear to expect that the wind propulsion is fully active and should be expected to yield satisfactory manoeuvring performance. 35 kn may be demanding. Depending on the ship type (e.g. stability) some systems may still be fully operational while other systems may be (partially) reefed or powered down.

Finally, the simulations are done for different Flettner rotor configurations and control:

- No wind propulsion and no wind
- Wind propulsion kept fixed at the setting at the approach into the manoeuvre.
- Wind propulsion stopped at the start of the manoeuvre with a relatively slow deceleration of 0.75 RPM/s.
- Wind propulsion stopped at the start of the manoeuvre with fast deceleration of 5.0 RPM/s.
- Active control of the wind propulsion with the target to assist manoeuvring, with fast acceleration or deceleration of 5.0 RPM/s.

Active Flettner control algorithm

With active control the philosophy is that the rotors should assist the steering of the rudder. It is programmed as follows:

- A fixed rotational point, P, is introduced that is a representative value for the pivot point during a manoeuvre. This point is used to compute the yawing moment of the rotors and the rudders, to identify the desired rotation rate rotors. The pivot point is imaginary rotation point, where the ship rotates around under combined drift and rotation. This point, can be determined by:

$$x_{PP} = - v / r$$

  Where, v, is the transverse ship velocity and, r, the rate of turn with respect to the centre of gravity. Here, $x_{PP,}$ is the pivot point forward from the reference point (which is in this case the centre of gravity). Until a fully steady turn is reached, the pivot point changes continuously. Rather than using the instantaneous pivot point, the preference was to keep the rotation point fixed roughly at the bow. This control gave a more favourable manoeuvring behaviour than using the instantaneous pivot point.
- Two predictive Flettner forces are defined that represent the potential forces of all rotors combined for a clockwise and anti-clockwise rotation rate. It is evaluated which one of the these two predictive forces provide the largest yawing moment

around the rotation point P. The sign of the yawing moment must be the same as the yawing moment induced by the steering. Then, the rotor RPM is accelerated or decelerated, depending on the sign. All rotors are controlled by one common Flettner rotation rate variable.

- In case both predictive Flettner forces give an opposite sign of the yawing moment when compared to the yawing moment due to steering, the rotors are decelerated.
- In addition the active control includes a limiter which should throttle down the rotors on large heel angles. This limiter starts to decelerate the rotor when the heel angles exceed 10 deg. However, there can still be an overshoot in heel angle, likely because the deceleration is not fast enough and the dynamic behaviour of the ship in a turn. The maximum rotor RPM that can be set is 150 RPM and the acceleration and deceleration rate equals 5 RPM/s.

The working mechanism of the active control algorithm is further substantiated in Figure 3 to Figure 6. These figures present different time shots for a turning circle to starboard with 35 knots true wind from 315 deg (green arrows). The blue and red arrows indicate the force vector at a spin ratio of 3 for anti-clockwise and clockwise rotation direction respectively.

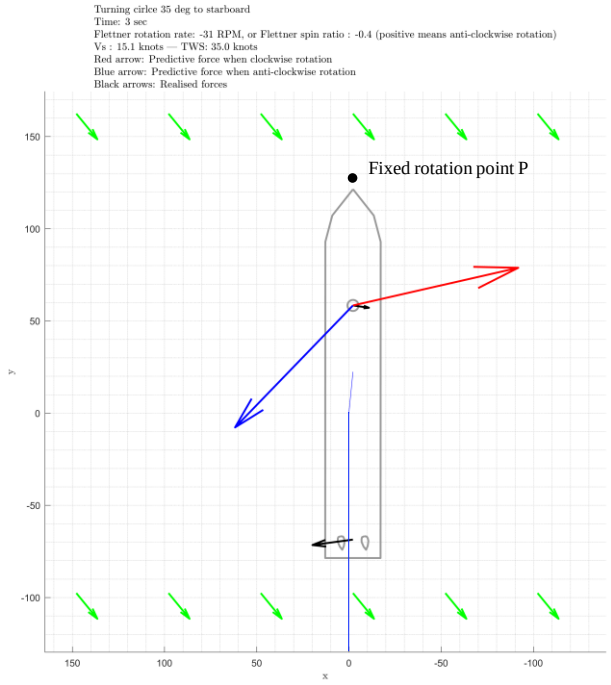

Figure 3: Active Flettner control – initial condition and starting a turning circle 35° to starboard.

The black arrows present the realised total forces of the rudder and rotors.

Figure 3 shows the starting condition of a turning circle to portside. Here, the rotor RPM decelerates until zero. Then, in Figure 4, the rotor accelerates in anti-clockwise direction. This situation remains until the situation in Figure 5. The predictive force cannot provide anti-clockwise yawing moment and consequently, the rotor RPM is decelerated again.

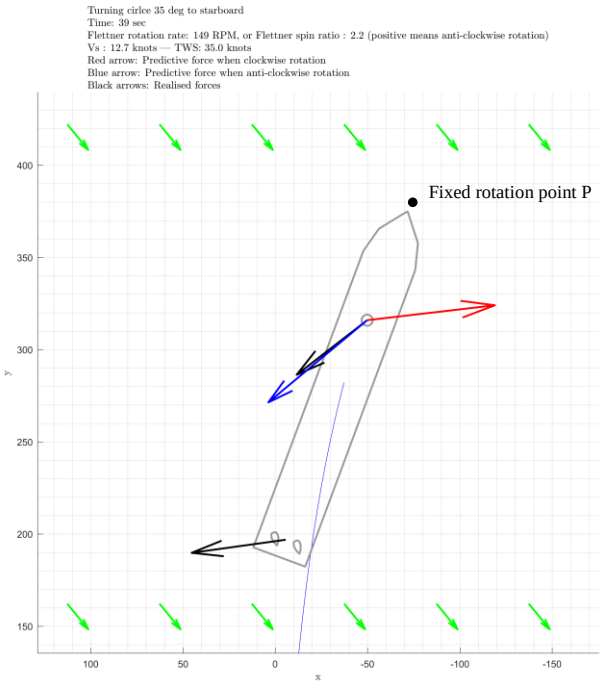

Figure 4: Active Flettner control – accelerating Flettner in anti-clockwise direction.

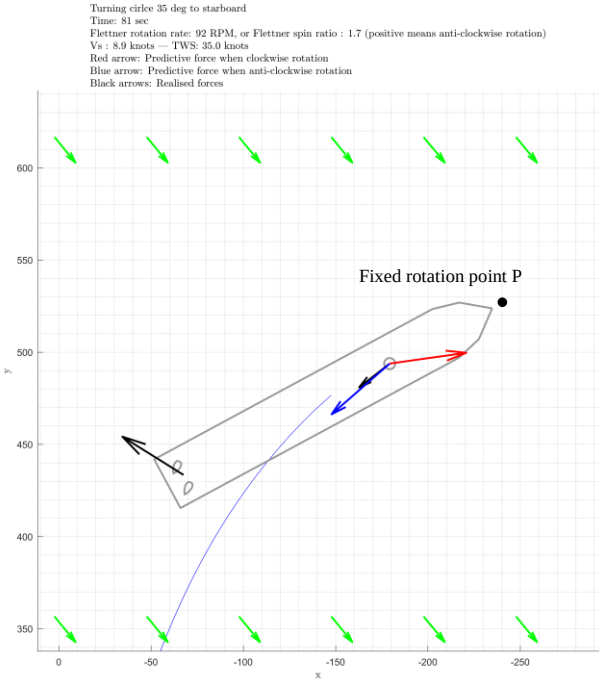

Figure 5: Active Flettner control – decelerating Flettner RPM.

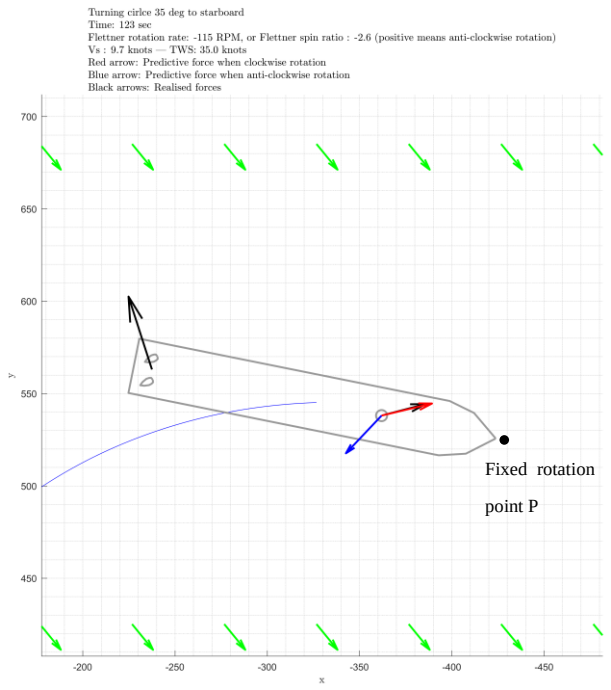

Figure 6: Active Flettner control – accelerating Flettner RPM in clockwise direction.

When the ship rotates further, there comes the moment in Figure 6 that the red arrow can give an anti-clockwise yawing moment. The rotors are accelerated in clockwise direction to realise these forces. This process continues until the ship has completed the entire manoeuvre.

7. RESULTS AND DISCUSSION

The previous work on the MARIN Ferry as reported by Eggers & Kisjes showed that in general the manoeuvring characteristics only worsened, even if the performance was still well within compliance.

Turning circle manoeuvre

The turning circle is a manoeuvre where the required yaw moment to lead the vessel through a turn is consistently, always pointing to the same side. Thus, one would expect that this scenario would be the most straightforward to get better results with Flettner rotors assisting the steering.

Figure 7 shows the tactical diameter in the turning circle. The tactical diameter is the transverse distance that is covered for a 180 degree turn. The results are shown in a polar plot where the radial axis indicates the incoming wind direction. 0 indicates wind from the bow (see schematic representation of a ship in the middle). All turning circles are to starboard. The full lines correspond to identical simulations previously presented by Eggers and Kisjes. The red dashed lines is the maximum allowed tactical diameter by IMO (based on the IMO under limit approach speed of 19.3 kn). The dashed lines indicate new results with different control.

It can be seen that the results with decelerated (stopped) rotors are almost always better than keeping the rotors spinning at constant RPM. Exceptions are for approach wind angles of around 30 and 185 deg. Apparently, in these conditions the rotors are helping to turn the vessel. Otherwise it seems prudent that stopping the rotors is generally better than keeping them spinning. Generally the slower deceleration already manages to get a large part of the benefit that the fast deceleration obtains.

The active control shows that the results generally improve further. Locally, with the initial wind from the starboard quarter, the benefit can be quite large. However, there are also some local spots where the active control shows worse results, such as around 195 and 255 deg, though the exceedance of earlier results is smaller.

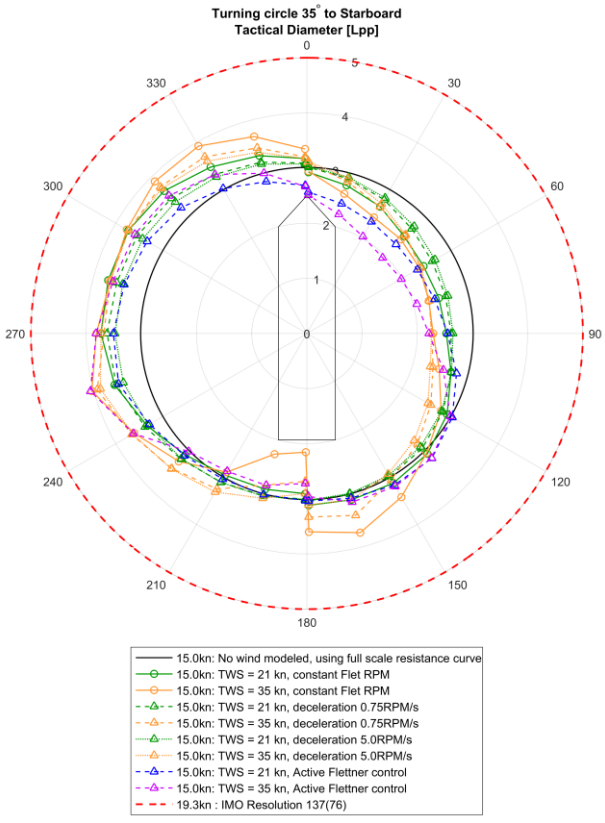

Figure 7: Tactical diameter for turning circle to starboard

Figure 8 shows the Advance, which is the longitudinal distance covered from the start of manoeuvre until reaching a 90 deg heading change.

It can be seen that differences start to become smaller. Still, it helps to stop the rotors. On this fast course change it appears that it is more important to decelerate the rotors fast in order to have a meaningful impact. Finally, active control does generally show a benefit, but the area where it actually performs slightly worse are larger around 30 to 120 deg and 240 deg.

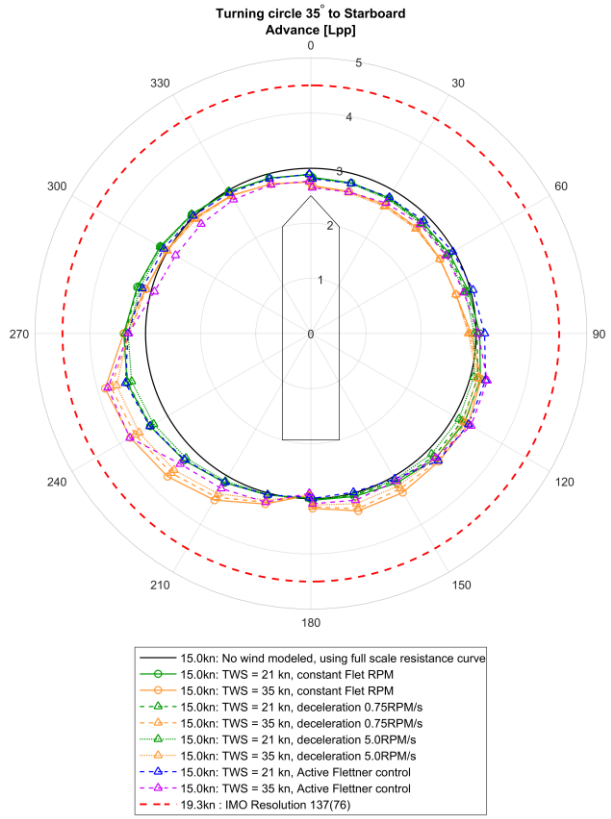

Figure 8: Advance for turning circle to starboard

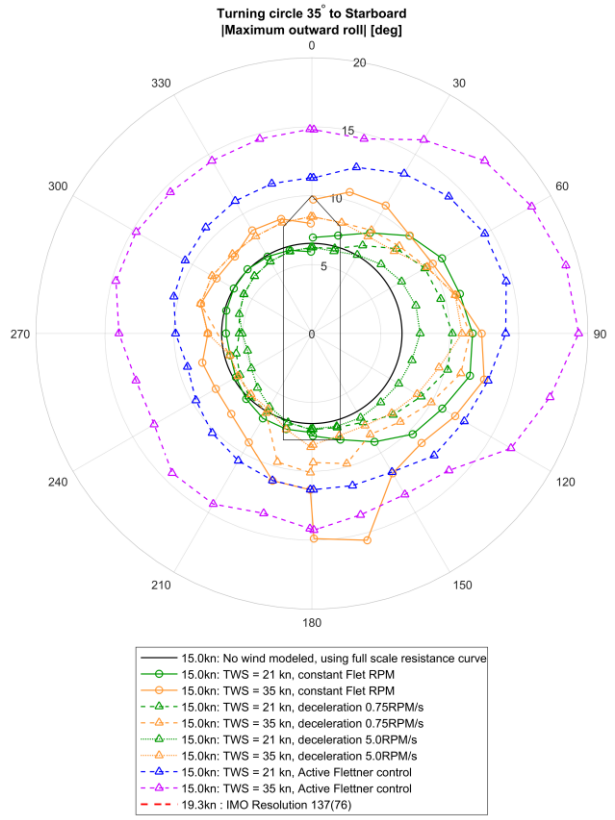

Figure 9: Maximum heel for turning circle to starboard

Figure 9 shows the maximum heel angle in the turning circle. There is a required maximum heel angle on account for turning for passenger vessels in the intact stability code (IMO, 2008). The intact stability code includes an empirical formula from which the resulting (steady) heel angle shall not exceed 10 degrees. Here heel angles of around 15 to 20 degrees are seen. Although strictly speaking the intact stability code does not apply here as it should be calculated with the empirical formula, it is still judged that the resulting heel angle is high. Possibly adjusting the control and/or deceleration speed could lead to a smaller angle. For this vessel, these large heeling angles are judged to limit the applicability of using wind propulsion for steering as a result of the high placement of rotors and the relatively low stability. For other large vessels, such as tankers or bulk carrier such an issue may not exist due to higher stability.

Overall, the position of the Flettner rotors on the MARIN ferry is not optimal for actively aiding the steering. The rotors, being located relatively close to the pivot point of the ship, can only mildly contribute to creating a yawing moment helping the ship to turn. In addition, due to the large superstructure, they

are located high above the waterline, hence contributing to an additional heel angle.

Zig-zag manoeuvre

Figure 10 shows the zig-zag 10/10 first overshoot angle. For many ships this a manoeuvring characteristic for which it is challenging to meet the criterion. However, as can be seen, the MARIN Ferry does not have a problem with this criterion. What can also be seen is that the influence of stopping rotors is hard to see relative to the manoeuvre with keeping rotors running at constant rotation rate. On the other hand, active control shows quite some different behaviour, however not all positive. With wind from the starboard bow, the performance actually worsens quite a lot. This is due to the dynamics at play here.

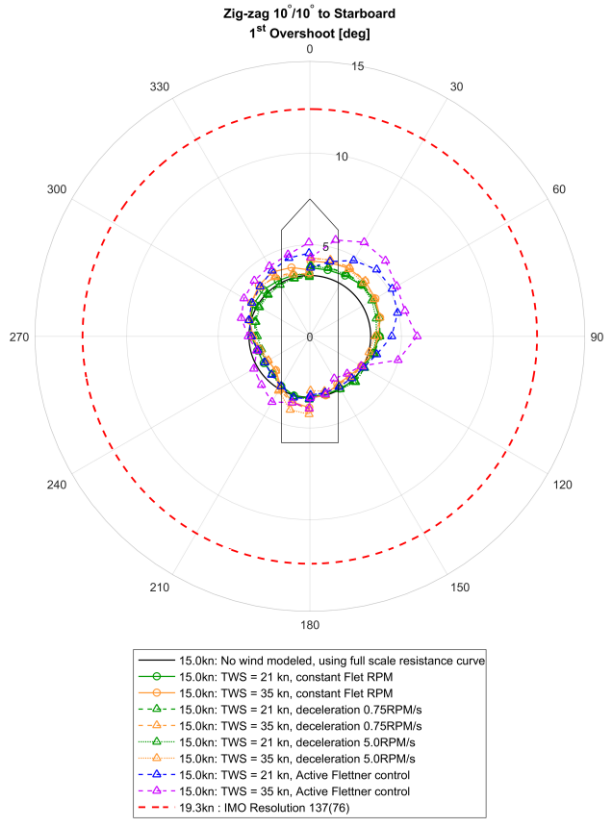

Figure 10: First overshoot angle in zig-zag 10/10 to starboard

Figure 11 shows the initial turning ability, which describes the longitudinal distance travelled until reaching a first heading change of 10 degrees. With the active control, it is observed that all wind angles from port side improve while largely the wind angles from starboard perform slightly worse.

The trends for the zig-zag 10/10 second overshoot and zig-zag 20/20 first overshoot, which are also manoeuvring characteristics to be checked in IMO Resolution MSC 137(76), show very similar trends as the zig-zag 10/10 first overshoot as shown in Figure 10.

A likely reason for seeing less differences in the zig-zag manoeuvres than in the turning circle manoeuvre is that the time period over which the result is determined is much smaller in the zig-zag runs, which gives less time to affect the manoeuvre with control. Moreover, in zig-zag runs, a larger yawing moment generated early in the manoeuvre helps the build-up of yaw rate (leading to a better initial turning ability). However it also increases the yaw rate once the rudder angle (and preferred rotor actuation) is reversed. It then becomes more difficult to stop the yaw moment, leading to a larger overshoot. It is well known that increasing the steering ability (e.g. through larger forces from rudders) can actually lead to worse results on the zig-zag overshoot angles.

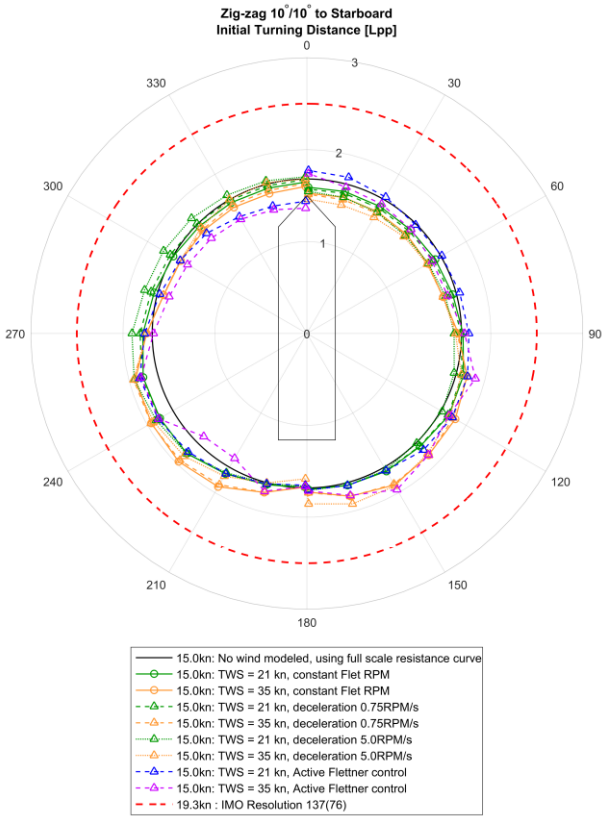

Figure 11: Initial turning ability in zig-zag 10/10 to starboard

Indicative preferred control methods

From this single test case it appears stopping rotors in a manoeuvre is generally a good idea if

sufficient thrust is available from the conventional propulsion. That seems like a prudent thing to do in control systems.

However, the influence from active control is less straightforward. In turning circles, where there is time to set the wind propulsion to a consistent setting that helps the manoeuvre, it seems that active control is beneficial to improve manoeuvring. However, in a scenario like a zig-zag manoeuvre, it appears that wind propulsion may not be suitable for steering based on the present work.

The manoeuvres conducted in the simulations are artificial. Except at a sea trial the same manoeuvres will not be done in actual operation. However, lessons obtained from these artificial simulations can still be applied for actual operation. Based on the results, it appears that when modest steering actions are done in tight areas, it may be smart to power down or stop wind propulsion. In case of larger turns, it may be considered to use the wind propulsion for steering. However the latter should also depend on the roll stability of the vessel and the heeling moment introduced by the wind propulsion.

8. CONCLUSIONS & RECOMMENDATIONS

Related to the studies presented in this paper the following conclusions are drawn.

The results on manoeuvring that were obtained with MARIN Ferry are specific to the case as selected. With its rotor placement relatively far forward, the MARIN Ferry is likely not the best ship to apply active control to improve the manoeuvrability significantly with an influence of wind propulsion. on manoeuvrability.

Nevertheless, the case demonstrated that the impact of wind propulsion on manoeuvring can most easily be mitigated by quickly depowering the wind propulsion system at the time that a manoeuvres starts.

Wind propulsion may be able to improve the manoeuvring capability by using active control. However, the option to do that may be limited by the type of manoeuvre and roll stability of the vessel. In longer manoeuvres where the desired yaw moment is consistently to one side, such as a turning circle, the benefit of using wind propulsion to steer may be more easy to obtain. A more dynamic manoeuvre, such as a zig-zag manoeuvre, may be too quick to be affected by wind propulsion.

To follow up this work, it is firstly recommended to conduct more case studies for manoeuvring with ships including wind propulsion:

- To see how the conclusions from the present work may be valid for other cases as well.
- To see how more aft placement of wind propulsion on board affects the possibilities to steer with the wind propulsion.
- To see how different control methods affect the results.

The work here also gives rise to further scrutiny of the maximum heel angle as specified in the IMO intact stability code. It was known already that the empirical formula generally under predicts the real heel angle in a turn. This may become a more urgent problem with wind propulsion. It is thus recommended to conduct more work for a potentially improved prediction of heel for the purpose of the intact stability code.

In this paper we explored what the influence of control of wind propulsion for better manoeuvring response could be. It seems not problematic to acecpt in regulations that wind propulsion may be depowered when initiating manoeuvres. However, when using wind propulsion to generate forces to assist in steering, a more broad discussion may be required also covering topics such as the requires redundancy in the system that would then be required.

It is reminded that the present study only concerned one case only with very limited variation in control methods. Further case studies need to be done to ascertain the more general validity of the conclusions drawn here.

REFERENCES

Eggers, R., Kisjes, A.S., 2023, “WiSP2 Project On Wind Propulsion Performance Prediction Methods And Manoeuvring”, Wind Propulsion Conference, Royal Institution of Naval Architects / IWSA, London.

Ferrari, V., Tonelli, R., Kisjes, A.S., Hallman, R., 2022, ‘Manoeuvring Experiments, Mathematical Model and Sensitivity Analysis for Test-case Ferry, Trends in Maritime

Technology and Engineering, Guedes Soares, C., Santos, T. A., (Eds.), London, UK: Taylor & Francis Group.

Ferrari, V, H vd Boom, AS Kisjes, and FHHA Quadvlieg, 2020, "Heel Angles in Turn and Passenger Safety." In Sustainable and Safe Passenger Ships. Athens, Greece.

Hurford, A., 2019, 'D2.7 Vessel Performance Final Report (Q1-Q6) for HDV Marine Flettner Vessel Performance Monitoring, Data Analysis and System Modelling Project', Lloyd's Register.

International Maritime Organization (IMO), 2021, MEPC.1/Circ.896, '2021 Guidance on Treatment of Innovative Energy Efficiency Technologies for Calculation and Verification of the Attained EEDI and EEXI'.

International Maritime Organization (IMO), 2008, Intact Stability Code.

International Maritime Organization. (IMO), 2002, Resolution MSC 137(76), "Standards for Ship Manoeuvrability."

Kisjes, A.S., Quadvlieg F., Ferrari, V., 2019, 'Uncertainty Analysis of Free running Manoeuvring Model Tests on a Modern ferry, with the emphasis on heel angles', Proceeding of the 38th International Conference on Ocean, Offshore and Arctic Engineering (OMAE), Glasgow, United Kingdom.

Kontos, S, O Lundbäck, M Kjellberg, E Wilske, and S Werner, 2023, "Manoeuvre Simulations in Design Process of Wind Powered Vessel." Wind Propulsion Conference, Royal Institution of Naval Architects / IWSA, London.

NATO, 2011, STANAG 4721; Common Framework for Naval Surface Ship Manoeuvring Performance and Requirements."

Nelissen, D., Traut, M., Koehler, J., Mao, W., Faber, J, and Ahdour, S., 2017, 'Study on the Analysis of Market Potentials and Market Barriers for Wind Propulsion Technologies for Ships', CE Delft.

Schmidt, Dr.-Ing. A., and Vahs, Prof. M., 2013, 'Entwicklung Eines Innovativen Schiffsantriebes Gekennzeichnet Durch Den Einsatz Von Magnus-Rotoren Zur Windenergienutzung in Kombination Mit Einem Hierauf Abgestimmten Antriebspropeller; Abschlussbericht'.

Vahs, M. 2019. "Retrofitting of Flettner Rotors – Results from Sea Trials of the General Cargo Ship "Fehn Pollux"." Wind Propulsion Conference, Royal Institution of Naval Architects / IWSA, London.

Quantification of modeling uncertainty of a reduced-order model as a validation problem

Vadim Belenky, *David Taylor Model Basin NSWCCD,* vadim.belenky.civ@us.navy.mil
Kenneth Weems, *David Taylor Model Basin NSWCCD,* kenneth.m.weems2.civ@us.navy.mil
Vladas Pipiras, *University of North Carolina, Chapel Hill,* pipiras@email.unc.edu
Themistoklis Sapsis, *Massachusetts Institute of Technology,* sapsis@mit.edu

ABSTRACT

The paper looks into the quantification of modeling uncertainty in the application of Reduced-Order Models (ROM) of ship motion for the characterization of extreme. The focus is on the uncertainty of force models and the propagation of this uncertainty through a dynamical system, with roll damping as an example. The result of this propagation enables a characterization of the response as a random quantity. The modeling uncertainty then can be quantified in statistical sense: as bias and variance.

Keywords: *Reduced –Order Model, Uncertainty Quantification, Uncertainty Propagation, Regression*

1. INTRODUCTION: A LOOK BACK

It is a speculative task to predict the future from the past. Nevertheless, if one engages in a discussion on the future of stability assessment, a certain level of speculation is unavoidable. Furthermore, an interpretation of this past experience may change as time passes.

The last 30 years or research and development in ship stability may be traced to two seeds, both directly related to nonlinearity of ship motions. One is a breakthrough in the theory of oscillators leading to the development of Nonlinear Dynamics (staring from a seminal monograph by Guckenheimer and Holms, 1983). The other is an evolution of numerical ship motion analysis from frequency-domain (e.g. Salvesen et al. 1970) to time-domain (e.g. de Kat and Paulling 1989; Lin and Yu, 1990).

Both of these seeds have led to many significant results, but the format of a workshop paper is not meant for a comprehensive review, so only a few example can be mentioned. Good illustrations of how these "nonlinear dynamics" results have provided an understanding of the very nature of nonlinear ship motion are the transient capsize diagram (e.g. Rainey et al. 1990) and surf-riding and broaching in regular waves (e.g. Spyrou, 1996).

The "numerical" line has largely bifurcated into two approaches: hybrid codes based on potential flow hydrodynamics and full volume viscous flow solvers such as Reynolds-average Navier-Stokes (RANS). Again, this paper does intend to review these numerical methods and tools, a reader is referred to a comprehensive review by Beck and Reed (2001) and its continuation – 15 years later – Reed and Beck (2016).

These two lines do interact, notably when Nonlinear Dynamics is used to interpret the results of numerical simulation. An excellent example is the investigation into the parametric roll accident involving APL China that was described by France et al. (2003). The Mathieu equation was used to show that the observed behavior is caused by parametric resonance. Shin et al. (2003) show motion stability analysis of fold bifurcation, observed in numerical simulation carried out with Large Amplitude Motion Program (LAMP). Spyrou et al. (2009) performed continuation analysis of surf-riding and broaching simulated by LAMP, using a continuation tool originally intended for study of ordinary differential equations. Spyrou and Tigkas (2011) have extended the use of continuation for cases with diffraction and radiation, demonstrating that hydrodynamic memory can be successfully treated by a continuation tool.

This list of "cross-pollination" between dynamical and numerical approaches to nonlinear ship motions and stability in waves is far from being complete and can be further extended. However, even this brief list should be enough to convince a

reader that ordinary differential equations, while being a very simplified models of real physics, has played an indispensable role in the interpretation of the results of numerical simulations of ship motions.

2. A LOOK TOWARDS EXTREMES

The practical application of time-domain simulation tools for the assessment of dynamic stability may incur significant computational costs due to rarity of stability failures in realistic conditions. While computational speed has continued to increase over the last decade, potential flow solvers like LAMP and TEMPEST are still not fast enough to provide the millions of hours needed to collect a sample of sufficient volume for direct counting.

Nevertheless, the ability to evaluate realistic extreme motions (and loads) is of undeniable importance for engineering practice. Time-domain numerical simulation tool can be applied for the assessment of extreme utilizing statistical extrapolation methods (e.g. Themelis and Spyrou 2007). While extrapolation methods are promising, they have not yet completed a transition into everyday practice. Four of these methods were included into a trial use of the Second Generation IMO Intact Stability criteria (Appendix 4 to MSC.1/Circ. 1652).

Another way is obtain extremes is to use a reduced order model (ROM) as a predictor of extreme events (Reed, 2021). The reduced order model used in that study was originally developed for statistical validation of extrapolation methods, so only qualitative validity has been required (Smith, 2019). A recent review of analytical and numerical ROMs was presented by Weems et al. (2022) at the previous Workshop. Further development of a numerical ROM towards quantitative validity is presented at this Workshop by Weems et al. (2023). The simulation tool, described in the cited reference is fast enough get to extremes in very reasonable time.

3. REDUCED-ORDER MODELS (ROM)

If a numerical ROM may become accurate enough to provide the basis for engineering decisions, should a validation and accreditation process, like that described in Reed and Zuzick (2015), be attempted? The short answer is yes, but there are details.

As can be seen from Weems et al. (2022), the core of an effective ROM is a qualitatively-correct model of a force that is believed to be "responsible" for the phenomenon. For example, when considering a capsizing event, the nonlinear hydrostatics are the principle factor. It defines the topology of the phase plane with several equilibria and makes it possible to model the transition between the equilibria. The other forces and effects, including coupling with other degrees of freedom, may be neglected or approximated.

The difference between ROM and an engineering-level simulation tool is somewhat conditional. The latter models more forces, but is limited by a certain physical paradigm. For example, a potential-flow solver assumes inviscid and irrotational flow, a RANS solver assumes continuity of a fluid and operate with Reynolds number averaged over velocity fluctuations. Again, the influence of the not-included forces are approximated with data from experiments or more detailed numerical methods. In that sense, the simulation tool described by Weems et al. (2023) may be seen as a consistent implementation of Froude-Krylov hypothesis, assuming that ship motions do not affect wave.

The increased level of approximation associated with ROMs makes modeling uncertainty a central question of their practical applicability: what level of approximation can be tolerated?

4. ON UNCERTAINTY OF FORCE MODELS

The Merriam-Webster dictionary defines "uncertainty" as a "lack of sureness about someone or something" (https:// www.merriam-webster.com / dictionary/uncertainty). So it can be interpreted as a certain level of lack of knowledge.

4.1 Statistical Uncertainty

The Naval Architecture community is familiar with measurement uncertainty (e.g. ITTC Procedure 7.5-01-03-01), statistical uncertainty (ITTC Procedure 7.5-02-01-08, Pipiras et al. 2018, 2023). The latter reflects an impossibility to obtain an accurate value (i.e. lack of knowledge) of a parameter, characterizing a random quantity from a finite-volume sample.

The statistical uncertainty is unavoidable when dealing with realistic ocean waves, i.e. irregular seas. It has the same influence on high-fidelity models and

ROMs, and is out-of-scope for the present discussion.

4.2 Regression Uncertainty

Regression is traditionally used for the modeling of roll damping in potential-flow simulation tools. The source of data is a roll decay time history, generated with a model test or RANS simulation (e.g. Aram and Park, 2022). Alternatively, a time history of forced roll motion can be used (e.g. Aram et al, 2023). Weems et al. (2023) describe application of regression to model diffraction and radiation forces, based on earlier work of Pipiras et al. (2021, 2022).

While linear equations are used for diffraction and radiation forces in heave and pitch, polynomials (quadratic or quadratic plus cubic) are employed for roll damping. While the later are nonlinear functions, the coefficients are found with a linear regression for all these forces. The squares or cubes of the state valuables are just another predictors that are summed in the force model.

A regression is an approximation, as the polynomial curves do not run exactly through the data points. The deviations of a regression model from the points (the residuals) are assumed to be caused by random reasons and are modeled as independent, normally distributed random variables ε:

$$y = \vec{x} \cdot \vec{c} + \varepsilon \tag{1}$$

where y is an instantaneous value of a force, $\vec{c}$ is a vector of parameter, and $\vec{x}$ is a vector of predictors. For a quadratic plus cubic model of roll damping, it is is expressed as

$$\vec{x} = (1, \varphi_a, \varphi_a^2) \tag{2}$$

where φ_a is the mean roll amplitude in a roll decay test.

Once fitted, the vector $\vec{\hat{c}}$ will contain estimates of linear $(\hat{\delta})$, quaratic $(\hat{\beta})$ and cubic $(\hat{\gamma})$ coefficients for roll damping (symbol "hat" means "an estimate"):

$$\vec{\hat{c}} = \left(\frac{1}{2\omega_0}\hat{\delta}, \frac{4}{3\pi}\hat{\beta}, \frac{3\omega_0}{8}\hat{\gamma}\right) \tag{3}$$

where ω_0 is the natural frequency of roll motion.

When a force is computed with formula (1), the residual ε is not known. As a result, the force become an estimate and is subject for uncertainty. A force modeled with a linear regression is a random quantity, with Student-*t* distribution, and known mean and variance. Details of the regression application procedure and its uncertainty assessment can be found in Aram and Park (2022).

Weems et al. (2022) show an example of application of the Gaussian Process Regression (GPR) to model a roll decay. GPR is a non-parametric regression that models a force as a normally distributed stochastic process with known mean value and covariance functions.

The bottom line is the whenever a force is modeled with regression, the uncertainty originated from the inaccuracy of approximation is treated as a random quantity. The quantification of this uncertainty comes with regression in the form of parameters of a known distribution (usually normal or Student-*t*). The parameters, however, depend on the state variables. For example, the mean value of roll damping, estimated in a "traditional way" from roll decay test, is expressed as (in terms of acceleration and assuming added mass is known):

$$\hat{E}_d(t) = 2\hat{\delta}\dot{\phi} + \hat{\beta}\dot{\phi}|\dot{\phi}| + \hat{\gamma}\dot{\phi}^3 \tag{4}$$

while the estimate of the variance is:

$$\hat{V}_d(t) = \hat{\sigma}^2(1 + \vec{x}^{*T}(t) \cdot \boldsymbol{C} \cdot \vec{x}^*(t)) \tag{5}$$

$\vec{x}^*(t)$ is an affine transformation of the state vector of predictors $\vec{x}$**:**

$$\vec{x}^*(t) = \left(4\omega_0\dot{\phi}, \frac{3\pi}{4}\dot{\phi}|\dot{\phi}|, \frac{8}{3\omega_0}\dot{\phi}^3\right) \tag{6}$$

$\hat{\sigma}$ is an estimate of is the residual standard error

$$\sigma = \sqrt{(\vec{\varepsilon} \cdot \vec{\varepsilon})/(n-p)} \tag{7}$$

where n is a number of points, available from the roll decay test, and p=3 is the number of predictors. $\boldsymbol{C}$ is the unscaled covariance matrix:

$$\boldsymbol{C} = (\boldsymbol{X}^T\boldsymbol{X})^{-1} \tag{8}$$

where $\boldsymbol{X}$ is the matrix of predictors from the roll decay test:

$$\boldsymbol{X} = \begin{pmatrix} 1 & \varphi_{a1} & \varphi_{a1}^2 \\ 1 & \varphi_{a2} & \varphi_{a2}^2 \\ \vdots & \vdots & \vdots \\ 1 & \varphi_{an} & \varphi_{an}^2 \end{pmatrix} \tag{9}$$

and $\varphi_{ai}, i = 1, \ldots, n$ are roll amplitudes from the roll decay test.

In the considered example, a value of the roll damping moment at a particular instant of time t has Student-*t* distribution with n-p degrees of freedom, scaled with $\sqrt{\hat{V}_d(t)}$ and shifted by $\hat{E}_d(t)$. For a

relatively large number of points ($n > 25$ or so), the distribution is practically normal with the mean value $\hat{E}_d(t)$ and the variance $\hat{V}_d(t)$.

For the case considered in Aram et al. (2023), where an entire hydrodynamic roll moment is fitted from forced motion, the number of points is large and the distribution can be assumed to be normal.

4.3 Propagation of Uncertainty: a Linear Example

A dynamical system under deterministic excitation that includes regression-based force model can be considered as a deterministic function of random variables. The simplest example of the propagation of uncertainty can be seen with a linear oscillator under deterministic periodic excitation and estimated linear damping, i.e. an elementary model of ship rolling in regular waves:

$$\ddot{\phi} + 2\hat{\delta}\dot{\phi} + \omega_0^2\phi = \omega_0^2\alpha_e\sin(\omega t) \qquad (10)$$

α_e is an effective angle of wave slope and ω is the wave frequency.

To see the qualitative effect of propagation of uncertainty, another simplification is introduced. The variance of the roll damping moment is assumed constant and some nominal boundaries for damping coefficient (in terms of critical $\hat{\mu} = \hat{\delta}/\omega_0$), are taken; see Figure 1 and Table 1.

Table 1 Parameters of linear oscillator

Parameter	Symbol	Value
Natural frequency, 1/s	ω_0	0.587
Mean value of roll damping coeff. (-)	$\hat{\mu}$	0.092
Lower boundary damping coeff. (-)	$\hat{\mu}_{low}$	0.08
Upper boundary damping coeff. (-)	$\hat{\mu}_{up}$	0.105
Mean value of roll damping coeff. 1/s	$\hat{\delta}$	0.054
Lower boundary damping coeff. 1/s	$\hat{\delta}_{low}$	0.047
Upper boundary damping coeff. 1/s	$\hat{\delta}_{up}$	0.062
Effective angle of wave slope, rad	α_e	0.12
Beg. of wave frequency range 1/s	ω_{beg}	0.2
End of wave frequency range, 1/2	ω_{end}	1.2

A dynamical system (10) is a deterministic function of a random variable. The distribution of this random variable is known, so one can find a distribution of the response. The confidence interval for the response can then be constructed. A simpler way to construct the confidence is a "boundary" method, where all of the calculations are repeated with the input random variable set to the lower and upper boundary of its confidence interval. The results are treated as the upper and lower boundaries of the confidence interval of the response. A justification of this approach can be found in Section 4.4 of Bickel and Doksum (2001).

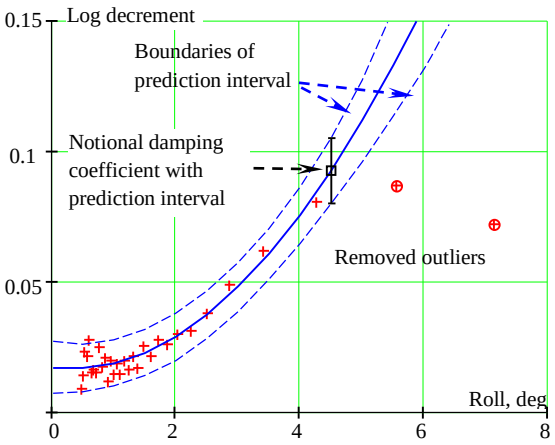

Figure 1. Data source for roll damping: roll decay simulation of ONR tumblehome topside configuration (Aram and Park, 2022).

Figure 2 shows a response curve computed for the upper and lower boundaries of the notional confidence interval for the linear damping coefficient $\hat{\delta}$. As expected, the largest influence of damping uncertainty is around the natural frequency.

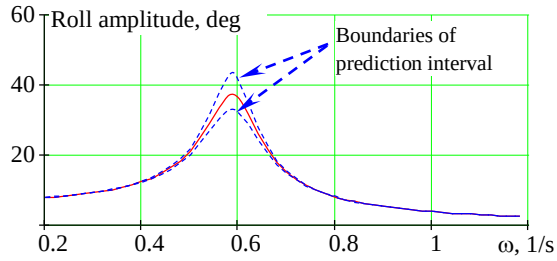

Figure 2. Influence of damping uncertainty on the linear roll response.

4.4 Propagation of Uncertainty: Deterministic Piecewise Linear System

To see the effect of damping uncertainty on the response of a nonlinear system, consider an oscillator with piecewise linear restoring which can be seen as the simplest ROM for capsizing event (Weems et al. 2022):

$$\ddot{\phi} + 2\hat{\delta}\dot{\phi} + \omega_0^2 f^*(\phi) = \omega_0^2\alpha_e\sin(\omega t) \qquad (11)$$

where f^* is piecewise linear restoring shown in Figure 3. Figure 4 shows a response curve computed with the equivalent linearization for a series of sinusoidal excitations with constant amplitude and varying frequencies. For a large enough amplitude of excitation, a fold bifurcation may be expected, where two stable steady-state responses are separated by an unstable solution. As can be seen in Figure 4, the uncertainty in roll damping changes the interval in which the fold bifurcation is observed by a factor of three.

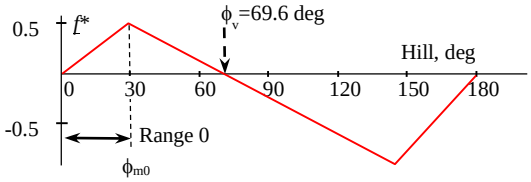

Figure 3 Piecewise linear restoring.

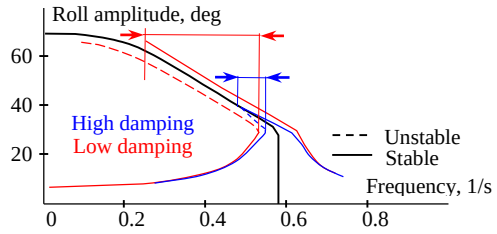

Figure 4. Response curves corresponding to lower and upper boundaries of damping prediction interval

4.5 Propagation of Uncertainty: Piecewise Linear System under Random Excitation

Consider the piecewise dynamical system (11) under stochastic excitation, modeling realistic waves:

$$\ddot{\phi} + 2\hat{\delta}\dot{\phi} + \omega_0^2 f^*(\phi) = \omega_0^2 \alpha_e(t) \qquad (12)$$

where $\alpha_e(t)$ is a stationary Gaussian process.

One of the main advantages of the piecewise linear system (12) is the availability of analytical solutions for the rate of capsizing events and the probability of exceedance of a large roll angle (Belenky et al. 2019). The sample calculations were carried out with the Bretschneider spectrum with a significant wave height of 9 m and modal period of 15 s.

In order to evaluate the strength of the influence of damping uncertainty, the following metric can be used:

$$M = \frac{q_{lw} - q_{up}}{q} \qquad (13)$$

where q is a quantity evaluated with nominal damping (middle of the prediction interval), while q_{lw} and q_{up} correspond to the lower and upper boundaries of the prediction interval, respectively.

Numerical results for the following quantities are in Table 2:

Standard deviation of the linear roll angles and rates (at range 0):

$$\sigma_\phi(\delta) = \sqrt{\int_{\omega_{beg}}^{\omega_{end}} s(\omega) RAO(\omega,\delta)\, d\omega} \qquad (14)$$

$$\sigma_{\dot{\phi}}(\delta) = \sqrt{\int_{\omega_{beg}}^{\omega_{end}} \omega^2 s(\omega) RAO(\omega,\delta)\, d\omega} \qquad (15)$$

where $s(\omega)$ is a spectral density of wave elevations and $RAO(\omega,\delta)$ is a response amplitude operator (RAO) from wave elevation to roll angles.

The rate of upcrossing of the level ϕ_{m0} (see Figure 3) and the probability of capsizing after upcrossing cam be written as:

$$r_{m0}(\delta) = \frac{1}{2\pi}\frac{\sigma_\phi(\delta)}{\sigma_{\dot{\phi}}(\delta)} \exp\left(-\frac{\phi_{m0}^2}{2\sigma_\phi^2(\delta)}\right) \qquad (16)$$

$$P_c(\delta) = \exp\left(-\frac{\dot{\phi}_{cr}^2(\delta)}{2\sigma_\phi^2(\delta)}\right) \qquad (17)$$

where

$$\dot{\phi}_{cr}(\delta) = \lambda_2(\delta)(\phi_{m0} - \phi_v) \qquad (18)$$

$$\lambda_{1,2}(\delta) = -\delta \pm \sqrt{k_1\omega_0^2 + \delta^2} \qquad (19)$$

$k_1 = 0.7$ and $\phi_v = 69.6^0$, see Figure 3.

Rate of capsizing events:

$$r_c(\delta) = r_{m0}(\delta) P_c(\delta) \qquad (20)$$

Probability of exceedance of a large roll angle ($\phi_a > \phi_{m0}$) after upcrossing:

$$P_{\phi_a}(\delta) = \int_{\phi_a}^{\phi_v} PDF_{\phi_a}(\phi,\delta) d\phi \qquad (21)$$

where $PDF_{\phi_a}(\phi,\delta)$ is the probability density of the roll peaks after upcrossing, which can be expressed in the following form for the dynamical system with piecewise linear restoring (Belenky et al. 2019):

$$PDF_{\phi_a}(\phi,\delta) = C_1(\delta)(\phi_v - \phi)^{-\zeta_2(\delta)-1} \qquad (22)$$

$$C_1(\delta) = -\frac{\zeta_2(\delta)}{\lambda_2(\delta)}\left(C_0(\delta)\right)^{-\zeta_2(\delta)} \times PDF_{NC}\left(\dot{\phi}_1,\delta\right) \qquad (23)$$

$PDF_{NC}\left(\dot{\phi}_1,\delta\right)$ is a distribution of the roll rate $\dot{\phi}_1$ at an instant of upcrossing of the level ϕ_{m0} under "no-capsizing" condition:

$$PDF_{NC}\left(\dot{\phi}_1,\delta\right) = PDF\left(\dot{\phi}_1,\delta\right) \times \left(1 - \exp\left(-\frac{\dot{\phi}_{cr}^2(\delta)}{2\sigma_\phi^2(\delta)}\right)\right) \qquad (24)$$

where $PDF\left(\dot{\phi}_1,\delta\right)$ is a distribution of the roll rate $\dot{\phi}_1$ at an instant of upcrossing of the level ϕ_{m0} without "no-capsizing" condition.

$$PDF(\dot{\phi}_1,\delta)=\frac{\dot{\phi}_1}{\sigma^2_{\dot{\phi}}(\delta)}\exp\left(-\frac{\dot{\phi}_1^2}{2\sigma^2_{\dot{\phi}}(\delta)}\right)$$

$$C_0(\delta)=\left(1-\frac{\lambda_1(\delta)}{\lambda_2(\delta)}\right)\left(\frac{\lambda_2(\delta)}{\lambda_1(\delta)}(\phi_{m0}-\phi_v)\right)^{\frac{1}{\zeta_1(\delta)}} \quad (25)$$
$$\times\left(\lambda_1(\delta)-\lambda_2(\delta)\right)^{\frac{1}{\zeta_2(\delta)}}$$

$$\zeta_1(\delta)=\frac{\lambda_1(\delta)-\lambda_2(\delta)}{\lambda_1(\delta)};\ \zeta_2(\delta)=\frac{\lambda_1(\delta)-\lambda_2(\delta)}{\lambda_2(\delta)}$$

The rate of exceedance events is:

$$r_{\phi_a}(\delta)=r_{m0}(\delta)P_{\phi_a}(\delta) \quad (26)$$

As one can see from Table 2, the influence of uncertainty increases with nonlinearity and rarity. While the metric is only about 15-16% for relatively small motions $\phi<\phi_{m0}$, the influence on the rate of upcrossing of the level ϕ_{m0} is about 100%.

Table 2 Influence on uncertainty

Parameter	Symb.	Value
Standard deviation of linear roll, rad	$\sigma_\phi(\delta)$	0.203
Lower boundary for linear roll, rad	$\sigma_\phi(\delta_{up})$	0.188
Upper boundary for linear roll, rad	σ_ϕ	0.221
Metric of influence for linear roll	$M_{\sigma\phi}$	0.162
St. deviation of linear roll rate, rad/s	$\sigma_{\dot{\phi}}(\delta)$	0.122
Lower boundary for linear roll, rad/s	$\sigma_{\dot{\phi}}(\delta_{up})$	0.114
Upper boundary for linear roll, rad/s	$\sigma_{\dot{\phi}}(\delta_{lw})$	0.132
Metric of influence for linear roll	$M_{\sigma\dot{\phi}}$	0.154
Rate of upcrossing of level ϕ_{m0}, s^{-1}	$r_{m0}(\delta)$	4.6 10^{-3}
Lower bound. rate of upcrossing s^{-1}	$r_{m0}(\delta_{up})$	2.8 10^{-3}
Upper bound. rate of upcrossing s^{-1}	$r_{um0}(\delta_{lw})$	7.3 10^{-3}
Metric of influence: upcrossing rate	M_r	0.995
Prob. of capsizing after upcrossing	$P_c(\delta)$	5.9 10^{-3}
Lower boundary for probability	$P_c(\delta_{up})$	2.7 10^{-3}
Upper boundary for probability	$P_c(\delta_{lw})$	0.013
Metric of influence for probability	M_{Pc}	1.711
Rate of capsizings, s^{-1}	$r_c(\delta)$	2.7 10^{-5}
Lower bound. rate of capsizings, s^{-1}	$r_c(\delta_{up})$	7.4 10^{-6}
Upper bound. rate of capsizings, s^{-1}	$r_c(\delta_{lw})$	9.4 10^{-5}
Metric of influence for capsizing rate	M_c	3.198
Prob. of exceedance after upcrossing	$P_{\phi_a}(\delta)$	0.126
Lower boundary for probability	$P_{\phi_a}(\delta_{up})$	0.056
Upper boundary for probability	$P_{\phi_a}(\delta_{lw})$	0.26
Metric of influence for capsizing rate	M_{Pa}	1.624
Rate of exceedance, s^{-1}	$r_{\phi_a}(\delta)$	5.8 10^{-4}
Lower bound. rate of exceedance, s^{-1}	$r_{\phi_a}(\delta_{up})$	1.5 10^{-4}
Upper bound. rate of exceedance, s^{-1}	$r_{\phi_a}(\delta_{lw})$	1.9 10^{-3}
Metric of influence for capsizing rate	M_{ϕ_a}	3.048

The influence on the rare problem (i.e. probability of capsizing or exceedance after the upcrossing) is already 160-170%. The metric of uncertainty influence for the rate of rare events is even larger — about 300%. Notably, the influence of uncertainty is slightly higher for the rate of capsizings than for the rate of exceedances of large roll angle.

4.6 Propagation of Uncertainty with Prediction Interval

The discussion in the previous three subsections used a notional value of a linear damping coefficient with a notional prediction interval computed at the roll amplitude of 4.5 degrees, as shown in Figure 1. If a more formal approach with actual prediction interval is taken, the situation will be more complex. Consider fitting linear damping, using only small roll amplitudes (less than 2 deg.) from Aram and Park (2022). Fitting linear damping limits the regression to an intercept only, which makes it a one-dimensional problem.

The number of predictors is p=1 and there are n=25 data points below 2 deg. available from Aram and Park (2022). The matrix of predictors becomes a vector, consisting of ones:

$$\boldsymbol{X}=\left(\underbrace{1,1,\dots,1}_{n}\right)^T \quad (27)$$

The vector of parameters consists from the single element – the intercept, and is computed as

$$\vec{\hat{c}}=(\boldsymbol{X}^T\boldsymbol{X})^{-1}\boldsymbol{X}\vec{y}=0.019 \quad (28)$$

where $\vec{y}$ is the vector of responses, consisting of logarithmic decrement values corresponding to the mean roll amplitudes below 2 deg.

The standard residual error is:

$$\sigma=\sqrt{(\vec{\varepsilon}\cdot\vec{\varepsilon})/(n-p)}=5.285\cdot10^{-3} \quad (29)$$

The unscaled covariance matrix has only one element:

$$\boldsymbol{C}=(\boldsymbol{X}^T\boldsymbol{X})^{-1}=n^{-1}=0.04 \quad (30)$$

The predicted value is constant, as the model has only intercept, but its variance depends on the mean amplitude:

$$V_d(\varphi_a)=\sigma^2(1+\varphi_a^2\boldsymbol{C}) \quad (31)$$

The boundaries of the prediction interval for the confidence probability $P_\beta=0.95$ are computed with Student-t distribution's 0.975 quantile, corresponding to the $n-p=24$ degrees of freedom: $Q_{St}=Q_{0.975,24}=2.064$, leading to the following prediction interval in terms of the logarithm decrement LD:

$$LD_{lw,up}(\varphi_a)=LD\pm Q_{St}\sqrt{V_d(\varphi_a)} \quad (32)$$

Figure 5 shows the prediction interval plotted for the entire range of mean roll amplitudes available from Aram and Park (2022).

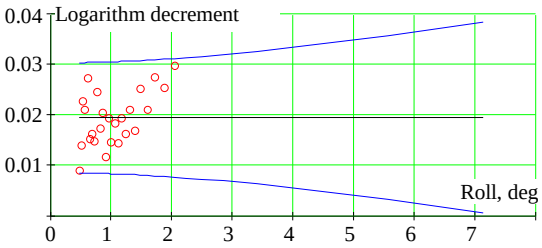

Figure 5. Prediction Interval for Linear Damping

While the damping is linear, the boundaries of its prediction interval are not. To propagate the damping uncertainty, a nonlinear dynamical system needs to be considered. It is a straight-forward task for a deterministic system using numerical integration. However, for the case of stochastic excitation, the uncertainty of the force model needs to be considered together with the statistical uncertainty caused by the finite volume of the sample.

5. MODELING UNCERTAINTY

A complete modeling uncertainty is not limited by the uncertainty of the force models that can be quantified through regression. Even high-fidelity data used for regression may not reflect the complete physical picture, e.g. a rotating arm test characterizes steady flow, while the evolutionary part of a turning maneuver induces an unsteady flow. Another example is that roll decay data do not include information on damping for large roll angles, when a bilge keel comes near or even out of the free surface. Also, not all the forces acting on a ship can be included in the ROM from a practical standpoint. Thus, the propagation the regression-based uncertainty through dynamical system is only part of the answer.

The more general quantification of modeling uncertainty is essentially part of validation, as it reflects how accurate the model describes physical reality, or perhaps, a higher fidelity solution in a multi-fidelity analysis. So, a complete modeling uncertainty requires a validation dataset. The result from the validation dataset is considered to be an ultimate “true value”, while a model is treated as an estimator of the “true value” in a statistical framework. The complete uncertainty of the model is quantified with bias and variance, see Figure 6.

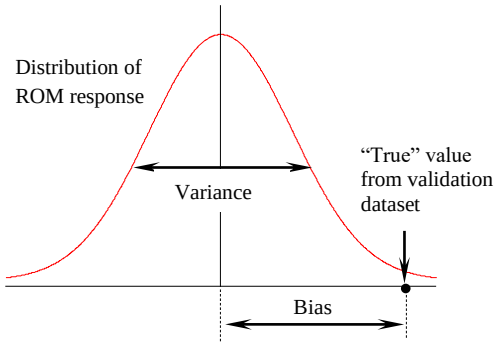

Figure 6. Uncertainty quantification of a model in statistical framework

Zuzick et al. (2014) studied validation in a statistical framework, operating with statistical uncertainty caused by the finite volume of the sample. The idea was to focus on the difference between two population statistics. When the statistical uncertainty of the dynamical system is deterministic and the statistical uncertainty is not present, this difference becomes the bias.

6. SUMMARY AND CONCLUSIONS

The main focus on the paper is on quantification of uncertainty of a Reduced Order Model (ROM) of large-amplitude ship motions. Special attention to quantification of uncertainty is justified by the role ROMs are expected to play of characterization of extreme motions and loads in waves. Quantification of uncertainty of a ROM is a key to its confident application.

The uncertainty of a result obtained with ROM (and any other mathematical model) can be classified in three types:

- Statistical uncertainty, caused by the finite volume of the sample, when the simulation is performed in irregular waves.
- Uncertainty of a force model, resulted from a simplification of physics to represent a force in ROM.
- Modeling uncertainty, caused by not including all the forces into the ROM.

To maintain a focus on the force and modeling uncertainty, regular wave excitation is considered. The force is modeled with a regression, which provides a means for the characterization of uncertainty, whereas prediction interval is the most common form of it.

The uncertainty of a force model is propagated through the considered dynamical system, creating a

prediction interval of a response characteristic. In principle, a distribution for that characteristic may be obtained. The influence of uncertainty may be significantly affected by the nonlinearity of the dynamical system and the rarity of the characterized event.

The characterization of modeling uncertainty requires a knowledge of a "true" value, which can be obtained from high-fidelity numerical model or a model test. The quantification of the complete modeling uncertainty can be done with a bias and a variance, i.e. with statistical framework. The quantification of modeling uncertainty should essentially be considered as a part of the validation process.

The problem of quantification of ROM uncertainty is far from complete. While significant attention has been paid to the propagation of the simplified roll damping uncertainty through the piecewise linear system, the presented consideration is only a first step. The next step is a propagation of actual damping uncertainty, which will require a numerical analysis.

One then needs to study a propagation of uncertainty of a complete set of hydrodynamic forces, of which the roll damping is only a part.

A complete quantification should be attempted, trying to obtain a variance and a bias of the ROM-based estimate. Finally, a problem of adding the statistical uncertainty should be resolved.

7. ACKNOWLEDGEMENTS

The work was supported by the US Office of Naval Research (ONR) under the supervision of Dr. Woei-Min Lin. The participation of Prof. Pipiras and Prof. Sapsis was also facilitated by the NSWCCD Summer Faculty Program, managed by Dr. Jack Price.

REFERENCES

Aram, S. and J. Park, 2022, "On the Uncertainty Quantification of Roll Decay Test," *Proc. 18th Intl. Ship Stability Workshop*, Gdansk, Poland, pp. 21-32.

Aram, S. Weems, K. M. and V. Belenky, 2023, "Towards the Uncertainty Quantification of a Roll Damping Model," *Proc. 19th Intl. Ship Stability Workshop*, Istanbul, Turkey.

Beck, R. F. and A. M. Reed, 2001, "Modern Computational Methods for Ships in Seaway," *Trans. SNAME*, Vol. 109, pp. 1–51.

Belenky, V., Glotzer, D., Pipiras, V. and T. Sapsis, 2019, "Distribution tail structure and extreme value analysis of constrained piecewise linear oscillators," *Probabilistic Engineering Mechanics* Vol. 57, pp 1-13.

Bickel, J. P. and K. A. Doksum, 2001, Mathematical Statistics: Basic Ideas and Selected Topics. Vol. 1, Prentice-Hall, Upper Saddle River, NJ, ISBN 0-13-850363-X.

de Kat, J. O. and J. R. Paulling, 1989, "The Simulation of Ship Motions and Capsizing in Severe Seas," *Trans. SNAME*. Vol. 97. Jersey City, NJ: Society of Naval Architects and Marine Engineers, pp. 139–168.

Glotzer, D., Pipiras, V., Belenky, V., Weems, K and M. Levine, 2023, "Statistical inference for mean and variance of oscillatory processes," *Ocean Engineering, Special Issue on Extreme Stochastic Dynamics of Ships* (submitted).

Guckenheimer J. and P. Holmes, 1983, "Nonlinear Oscillations, Dynamical Systems, and Bifurcations of Vector Fields," Applied Mathematical Sciences, Vol. 42, Springer, N.Y. ISBN 978-0-387-90819-9

France, W. G., Levandou, M. Treakle, T. W., Paulling, J. R., Michel, R. K. and Moore, C. "An investigation of head seas parametric rolling and its influence on Container Lashing Systems," *Marine Technology*, 40(1):1–19, 2003.

IMO MSC.1/Circ.1652. Explanatory Notes to the Interim Guidelines on the Second Generation Intact Stability Criteria, International Maritime Organization, 2023

ITTC Recommended Procedure 7.5-01-03-01 Uncertainty Analysis Instrument Calibration, Rev. 02, 2017

ITTC Recommended Procedure 7.5-02-01-08 Single Significant Amplitude and Confidence Intervals for Stochastic Processes, Rev. 00, 2017

Lin, W.-M., and Yue, D. K. P., 1990, "Numerical Solutions for Large Amplitude Ship Motions in the Time-Domain," Proc. 18th Symp. on Naval Hydrodynamics, Ann Arbor, Michigan, USA, pp. 41–66.

Pipiras, V., Glotzer. D., Belenky, V., Levine, M. and K. Weems, 2018, "On Confidence Intervals of Mean and Variance Estimates of Ship Motions," *Proc. 13th Intl. Conf. on Stability of Ships and Ocean Vehicles STAB 2018*, Kobe, Japan.

Pipiras, V., Belenky, V., Weems, K., Brown, B., Frommer, A. and G. Ouimette, 2021, "Calibrating Multifidelity Ship Motion Codes Through Regression," *Proc. 1st Intl. Conf. on Stability and Safety of Ships and Ocean Vehicles STABS 2021*, Glasgow, Scotland, UK.

Pipiras, V., Howard, D., Belenky, V., Weems, K. and T. Sapsis, 2022, "Multi-Fidelity Uncertainty Quantification and Reduced-Order Modeling for Extreme Ship Motions and Loads," *Proc. 34th Symp. Naval Hydrodynamics,* Washington, D.C., USA.

Rainey, R. C. T, Thompson, J. M. T., Tam, G. W. and P. G. Noble, 1990, "The transient capsize diagram - a route to soundly-based new stability regulations," Proc. of 4th Intl. Conf. on Stability of Ships and Ocean Vehicles STAB 1990, Vol. 2, Naples, Italy, pp. 613-619.

Reed, A.M. (2021) "Predicting Extreme Loads and the Processes for Predicting Them Efficiently," *Proc. 1st Intl. Conf. on Stability and Safety of Ships and Ocean Vehicles STABS*, Glasgow, Scotland, UK.

Reed, A. M and A. V. Zuzick, 2015, "Direct Assessment Will Require Accreditation—What This Means," *Proc. 12th Intl. Conf. on Stability of Ships and Ocean Vehicles STAB 2015*, Glasgow, UK, pp. 51-78.

Reed, A. M and Beck, R. F., 2016, "Advances in the Predictive Capability for Ship Dynamics in Extreme Waves," *SNAME Transactions*, Vol. 124, pp. 2-39.

Salvesen, N., Tuck, E. O. and O. Faltinsen, 1970, "Ship motions and sea loads," *Trans. SNAME*, Vol 78, pp. 250–87.

Shin, Y. S, Belenky, V. L., Lin, W.-M., Weems, K. M., and A. H. Engle, 2003, "Nonlinear Time Domain Simulation Technology for Seakeeping and Wave-Load Analysis for Modern Ship Design," *SNAME Tr.*, Vol. 111, pp. 557-578.

Smith, T. C., 2019, "Validation Approach for Statistical Extrapolation", Chapter 34 of *Contemporary Ideas on Ship Stability. Risk of Capsizing*, Belenky, V., Neves, M., Spyrou, K., Umeda, N., van Walree, F., eds., Springer, 2019 ISBN 978-3-030-00514-6, pp. 573-589.

Spyrou, K., 1996, "Dynamic instability in quartering seas: the behavior of a ship during broaching," *Journal of Ship Research*, Vol. 40, No 1, pp. 46-59

Spyrou, K. J., K. M. Weems & V. Belenky (2009) "Verification of the Patterns of Surf-riding and Broaching by an Advanced Hydrodynamic Code," *Proc. 10th Int'l. Conference on Stability of Ships and Ocean Vehicles STAB 2009*, St. Petersburg, Russia

Spyrou, K. & I. Tigkas (2011) "Nonlinear Surge Dynamics of a Ship in Astern Seas: "Continuation Analysis" of Periodic States with Hydrodynamic Memory," *J. Ship Research*, 55(1):19-28

Themelis, N. and K. J. Spyrou (2007) Probabilistic Assessment of Ship Stability, *Tr. SNAME*, Vol. 115, pp. 181-206

Weems, K. M., Sapsis, T. and Pipiras, V., 2022 "Development of Reduced Order Models for Hydrodynamic Responses", *Proc. 18th Intl. Ship Stability Workshop*, Gdansk, Poland, pp. 285-295.

Weems, K. M., Pipiras, V. and Belenky, V., 2023, "Multifidelity Fast Code for Direct Stability Assessment," Proc. 19th Intl. Ship Stability Workshop, Istanbul, Turkey.

Zuzick, A. V., A. M. Reed, W. F. Belknap & B. L. Campbell, 2014, "Applicability of the Difference Between Population Statistics as an Acceptance Criteria Metric for Seakeeping Validation,". *Proc. 14th Int'l Ship Stability Workshop*, Kuala Lumpur, Malaysia, 9 p.

Damage stability of passenger ships: a multi-modal analysis for time to capsize

Francesco Mauro, *Sharjah Maritime Academy, 180018, Khorfakkan, Sharjah, UAE,* Francesco.Mauro@sma.ac.ae

Dracos Vassalos, *Sharjah Maritime Academy, 180018, Khorfakkan, Sharjah, UAE,* Dvassalos@sma.ac.ae

Donald Paterson, *Sharjah Maritime Academy, 180018, Khorfakkan, Sharjah, UAE,* Donald.Paterson@sma.ac.ae

Hongseok Bae, *Sharjah Maritime Academy, 180018, Khorfakkan, Sharjah, UAE,* Hongseok.Bae@sma.ac.ae

ABSTRACT

After an accident in open seas, the final fate for a damaged ship could be the loss of stability and consequently capsize. The latter may occur even in calm water, but it is more critical and probable in adverse weather conditions, i.e., irregular waves. Identifying a possible capsize event and determining the time that it takes for the ship to capsize is extremely important for safety assessment, meaning whether it would be possible to evacuate the ship for the scenarios considered. In this respect, time domain simulations or model tests should be performed to provide answers to this question. However, in dealing with irregular waves, both approaches are affected by the random nature of the phase spectral components, which leads to a different time to capsize determination at each calculation/run or to the identification of cases where the vessel will not capsize in the analysed time window. Here, a dedicated study is presented to describe the Time to Capsize (TTC) in irregular waves for critical damages. Simulations performed on a real passenger ship, highlight the appearance of more than one capsize mode for the same damage case. A model based on Weibull and Mixed-Weibull distributions has been developed to describe the multi-modal behaviour of the TTC distributions for the analysed damage cases.

Keywords: *Damage stability, Time to capsize, Mixed-Weibull distributions, Extreme value theory, passenger ships.*

1. INTRODUCTION

The damage stability assessment for passenger ships (or ships in general) requires the investigation of the consequences of multiple hazards. Besides standard ship-to-ship collisions, which are included in the SOLAS framework (IMO, 2020), recent enhancements suggest considering also groundings and contacts in the flooding assessment (eSAFE, 2016, Bulian et al., 2020). Such an addition allows for a comprehensive overview of the potential hazards affecting the ship.

However, a thorough damage stability analyses should not be limited to the vulnerability assessment but should include an analysis of risk (Vassalos et al, 2022a, 2023). The damage stability framework developed in the FLARE (2023) project introduces the concept of flooding risk intending to consider first-principles analyses for the risk evaluation through the determination of the Potential loss of lives (PLL). The determination of risk is conceived in a multi-level mode, proposing different levels of approximations for the vulnerability and evacuation analyses (Vassalos et al., 2022b).

To this end, the role of direct flooding simulations is of utmost importance and should not be limited to survivability. A key requirement in the estimation of PLL relates to the evaluation of Time to Capsize (TTC), which could be estimated only through direct flooding simulations.

In the present work, a novel approach is proposed for the estimation of TTC through a detailed analysis of critical damage cases. It is noted that the diverse capsize modes that may occur in irregular waves for the same damage case leads to a multi-modal behaviour in the resulting TTC distribution. Therefore, a model based on Mixed-Weibull distributions is introduced to describe the TTC. This is possible by applying the extreme value

theorem to the capsize problem, considering capsize as a system failure.

The application of Mixed-Weibull distributions to the TTC requires the determination of multiple parameters through a non-linear fitting, performed with a self-developed method based on an evolutionary algorithm (Mauro & Nabergoj, 2017).

Because an accurate description of TTC requires the execution of a large number of repetitions for each damage case, the proposed approach is suggested for the application to critical cases only. Here, an example is provided on a critical damage case for a large cruise ship employed for benchmark analyses in project FLARE (Ruponen et al., 2022b).

2. CAPSIZE OF A DAMAGED SHIP

The most dangerous fate for a ship, in general, and particularly for a passenger ship is a capsize or sinking event as a consequence of stability/buoyancy loss. As the capsize time is short compared to the conventional sinking process, it is extremely important to identify the conditions that may lead to a capsize event and potentially reduce or eliminate their occurrence.

Capsize modes

The identification of a capsize event and the evaluation of the time before this event after a hazard is of the utmost importance for the evacuation analysis of a vessel. In fact, in case damage could potentially lead to the sinking of the vessel, it should be possible to evacuate passengers and crew in less than half an hour. However, capsize may display a different nature depending on the interaction between floodwater and vessel motions and they are usually identified with the flooding state they relate to.

When the flooding process is studied, the following states can be identified after a collision:

- *Transient state*: is the first part of the flooding process. The water rapidly inrushes through the breach, causing a rapid and large heeling into or away from the breach side. The heeling process takes place in a time interval generally shorter than the vessel's natural roll period.
- *Progressive state*: in this stage, the water propagates through unprotected flooding paths within the ship, slowly diminishing stability until the vessel sinks, capsizes or reaches a stationary condition. This phase may take from minutes to hours.
- *Stationary state*: in this phase, there is no more significant water ingress/egress and the average ship motions are almost constant and a function of the external loads only.

An overview of the above-described flooding states is given in Figure 1. In case the capsize occurred during the transient phase, the consequences in terms of loss of lives are extreme, as the phenomenon is too fast to start the evacuation process. When an accident occurred in calm water, then the detection of a capsize is only governed by floodwater progression. In an irregular wave environment, the phenomenon is subject to the randomness of the sea state. In the latter case, it is then not possible to identify a-priori whether the capsize will occur or not in one of the three above-mentioned flooding states.

When a time domain simulation is performed, a capsize event can be easily recognised from the time history of the roll angle. Thus, when the roll signal exceeds a given threshold (generally above 40 degrees) the vessel is considered to have capsized. However, according to different damage stability frameworks, distinct capsize criteria can be found both for calm water and irregular seas:

- *Criterion 1*: SOLAS heeling failure that considers a maximum heeling of 15 degrees.
- *Criterion 2*: ITTC heeling failure that considers a maximum heeling of 30 degrees.
- *Criterion 3*: ITTC criterion on average heeling that considers an average heeling above 20 degrees in an interval of 3 minutes.
- *Criterion 4*: cases where the flooding process is not finished at the end of the simulation.

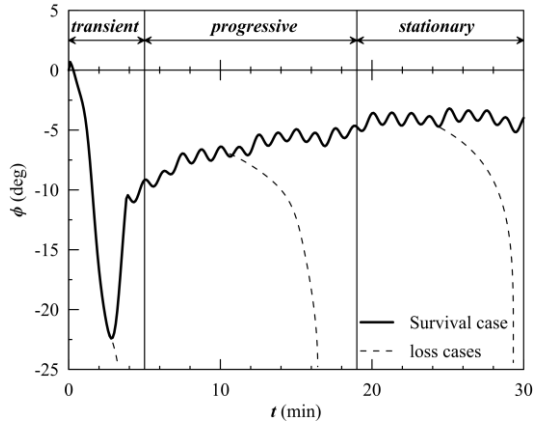

Figure 1: Stages of flooding for a damaged ship.

The first three criteria refer properly to the roll angle time history, whilst criterion 4 infers that the simulation time is not sufficient to cover the whole flooding process of the selected scenario. Thus, this last criterion is not properly a capsize criterion but could indicate a case where the ship loss may occur with a longer simulation time. In any case, all the above-mentioned criteria are not identifying a real capsize. However, they could be handy for the identification of critical cases for ship safety worthy of being analysed in more detail (Mauro et al. 2022a, 2022b).

Time to capsize

When a true capsize is detected, the identification of the TTC is straightforward for the case of calm water, as it is directly extracted from the roll time history of the single simulation:

$$TTC = t_{end} - t_0 \quad (1)$$

where t_{end} is the last time value of the simulation and t_0 is the time corresponding to the beginning of the flooding event. When simulations take place in irregular waves, the TTC is influenced by the randomness of the environment, leading to different TTC results for simulations performed with the same wave parameters. As a result, it is common practice to perform multiple repetitions of the same sea state and use the mean value of the case as a reference for the selected scenario (Cichowicz et al., 2016). In case Monte Carlo simulations are carried out to assess ship survivability, then a cumulative distribution of TTC is found for all the damage cases, considering just a few repetitions per each damage case in waves (Spanos & Papanikolaou, 2014).

However, a reliable evaluation of the possible risk of loss of lives requires the knowledge of TTC for those critical cases that are worthy to be investigated with evacuation analyses (Vassalos, 2022, Vassalos et al., 2023). Therefore, a more accurate and appropriate procedure for TTC determination should be investigated to be applied only to a restricted number of critical cases.

The conventional approaches to TTC do not consider in detail the nature of the capsizes detected during the time-domain simulations. Furthermore, the relatively (or excessively) small simulation time does not allow for recognising properly reliable distributions for the TTC, legitimising the assumption of taking the mean value among the repetitions as significant TTC for further analyses. However, the numerical time-domain simulation codes benchmarking activities within the FLARE project (Ruponen et al. 2022a, 2022b) allow for analysing more in depth single damage case scenarios, comparing 20 repetitions for a single damage scenario. The results obtained with the PROTEUS3 solver for a cruise ship are reported in Figure 2, highlighting the different nature of the capsize within 20 repetitions in irregular waves.

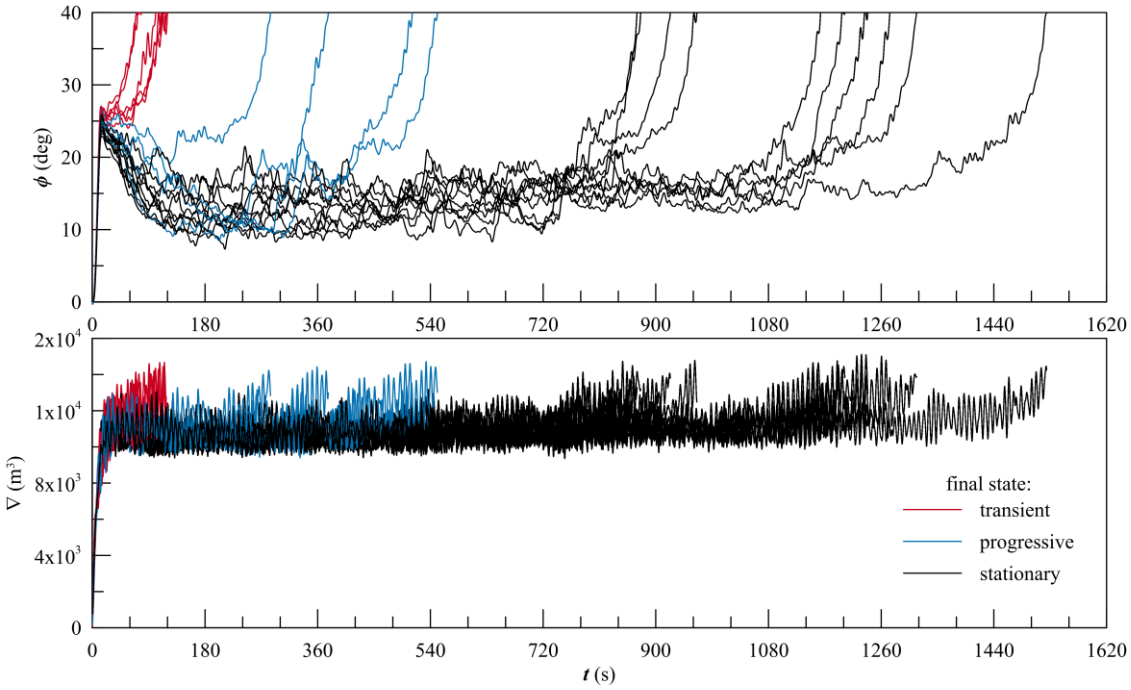

Figure 2: Roll angle (top) and floodwater volume (bottom) time traces for 20 repetitions of the same sea state and damage for the FLARE benchmark cruise ship employing the PROTEUS3 solver.

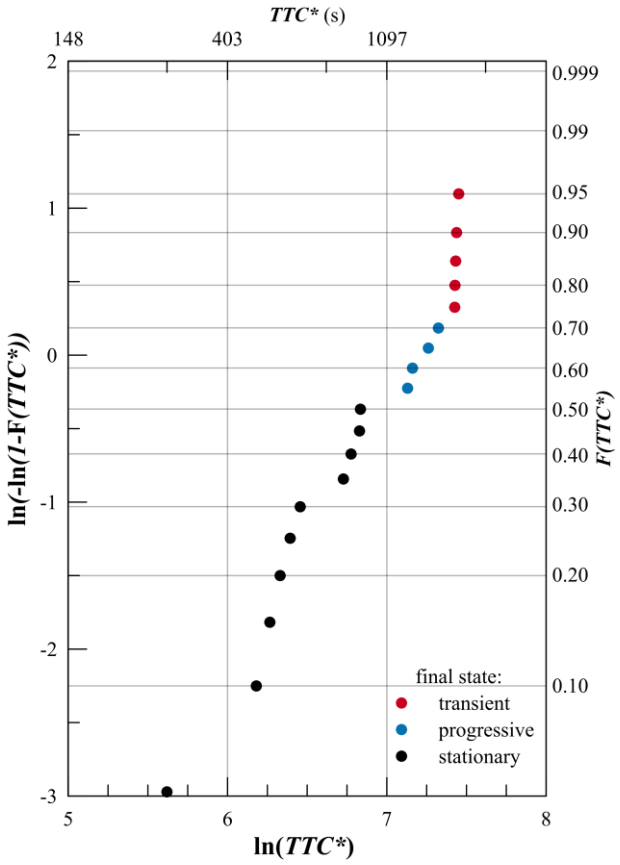

Figure 3: TTC* values representation on the Weibull plot for the FLARE benchmark cruise ship case study.

From Figure 2, it is possible to recognise the three different capsize modes described in the previous section. All 20 repetitions end with a capsize; more precisely, 6 are transient, 4 progressive and the remaining 10 are forced oscillations capsize whilst in what was described earlier as stationary state (stationary state capsize mode). The time trace of the roll angle is not helpful to distinguish between progressive and stationary state capsize modes; however, from a direct time-domain simulation (e.g., performed by PROTEUS 3 software) it is also possible to monitor the amount of floodwater entering/leaving the ship during the flooding process. Therefore, by analysing the water volume (the bottom graph in Figure 2) a distinction can be made between progressive and stationary-state capsize modes.

The simulations show a net distinction between the three different capsize modes, highlighting a grouping of the simulations having similar TTC. Therefore, it is reasonable to assume that the three different capsize modes follow independent distributions instead of a single one. Such an observation requires a more detailed analysis of the TTC estimation, with particular emphasis on finding suitable probabilistic distributions that may be used to describe the various phenomena.

3. MODELLING CAPSIZE AS A SYSTEM FAILURE

Determining suitable distributions to model the TTC is a somewhat new topic in damage stability. It is common practice to assume that TTC is associated with a random Gaussian process and consider the mean of multiple repetitions as a significant value for the analyses.

To enhance the perception of TTC, it could be useful to interpret the capsize as a failure of a system (i.e., the damaged ship). In such a way, it is possible to associate the failure with the commonly used distributions for failure analyses as e.g., Weibull distributions. However, to properly analyse the TTC as a failure it is handy to define an auxiliary time to capsize TTC* defined as follows:

$$TTC^* = t_{\max} - TTC \tag{2}$$

where t_{max} is the maximum allowed simulation time for the damage stability flooding analyses (usually set to 30 minutes). Then, it is possible to adopt for TTC* the common representations for failure cases on the Weibull plot, as shown in Figure 3. On the Weibull plot, a distribution following a 2-parameter Weibull model follows a straight line whilst 3-parameter distributions present only a concavity or convexity. In the given example of Figure 3, it is possible to observe that the different capsize modes are not following a single distribution. Therefore, a more detailed analysis is needed to identify a suitable distribution for the TTC*.

Failure distributions

According to the change of variable identified by equation (2), the minimum values of TTC, corresponding to the transient capsize cases, become the maxima of the TTC*. Therefore, with transient capsize cases being the most critical to assess vessel survivability or PLL, it is extremely important to capture such phenomena, thus reproducing with sufficient accuracy the tale of the TTC* population. To this end, the extreme value theorem could aid in identifying a suitable distribution for the TTC* description.

As for the multiple repetitions of flooding simulations, all capsizes are considered, and the lower limit to define the capsize event is given by the

Fisher-Tippet-Gnedenko theorem (Berliant et al., 1996), stating that the Generalised Extreme Value Distribution (GED) should be used to describe the phenomenon under analysis.

GED can be described by the following cumulative density function:

$$F(x) = e^{-t(x)} \tag{3}$$

where:

$$t(x) = \begin{cases} (1-\beta z)^{-1/\beta} & \text{if } \beta \neq 0 \\ e^{-z} & \text{if } \beta = 0 \end{cases} \tag{4}$$

and:

$$z = \frac{x-\gamma}{\eta} \tag{5}$$

The three real constants in equations (4) and (5) are the shape parameter β, defined in (0,+∞), the scale parameter η, defined in (0,+∞), and the scale parameter γ, defined in (-∞,+∞), The shape parameter value identifies three particular sub-cases of the GPD: the Weibull, the Gumbel and the Frechet distributions, respectively. The Gumbel distribution, obtained for β=0, defines the extremes of populations, which are supposed to follow an exponential distribution. Freshet distribution (β>0) is used for particular populations having a significant amount of data at the tale end (the so-called fat-tale distributions), through a change of sign in the x values. Finally, the Weibull distribution (β>0) represents all the cases not covered by the previous two distributions and is widely used for engineering problems related to defect data analyses.

Here, Weibull distribution is used as the basis for TTC* analyses. Therefore, it is convenient to rewrite equation (5) in the standard form adopted for three-parameters Weibull distribution:

$$F(x) = 1 - e^{-\left(x-\gamma/\eta\right)^{\beta}} \tag{6}$$

Equation (6) is defined for location parameter values such as x> γ. However, for particularly complicated cases subject to high levels of non-linearities (Mauro & Nabergoj, 2016) the use of a simple 3-parameters Weibull distribution is not enough to represent the data. This is the typical case of multi-modal responses, i.e., sample data that could present more than one population. A good representation could be obtained by employing the so-called Mixed-Weibull distribution in such cases. Such distribution is a combination of two or 3-parameters Weibull distributions, resulting in the following cumulative density function:

$$F(x) = 1 - \sum_{i=1}^{N_D} w_i e^{-\left(x-\gamma_i/\eta_i\right)^{\beta_i}} \tag{7}$$

where N_D is the number of subpopulations and w_i are the percentiles of subpopulations in the total population such that $\sum w_i = 1$. The other parameters are the same as for the three parameters Weibull defined in equation (6). There are no limitations on N_D but as N_D increases the number of parameters to estimate increases too. For example, fitting a 2-subpopulation Mixed Weibull distribution requires the estimation of 7 parameters, 3 subpopulations require 12 parameters and so on.

For such a reason, it is necessary to identify a proper method for the estimation of a high number of parameters.

Parameter determination

Different methods can be adopted to estimate the parameters of standard 2-parameter Weibull distribution, like the least-square fitting, the method of moments, the maximum likelihood and so on. All these methods can be extended to the case of a 3-parameter Weibull distribution. Due to the high number of unknowns in the case of a Mixed-Weibull, the aforementioned methods cannot be directly used, and sometimes manual fitting of data is common practice. To set up an automatic process for the parameter estimation, a differential evolution algorithm has been used, which provides an enhanced and extended version of the least square fitting method. The process has been already compared with conventional fitting methods in the case of 2 and 3-parameter Weibull distributions (Mauro & Nabergoj, 2017), highlighting the reliability of the process in case of need for a higher number of unknown parameters. For this reason, the differential evolution approach is here used for the estimation of the unknowns in the fitting of Mixed-Weibull distributions.

4. APPLICATION ON A PASSENGER SHIP

The developed analyses described in the previous sections are applied here on a reference case employed throughout several studies in the FLARE project. The test case refers to a large passenger ship (more precisely a cruise vessel) having the general arrangement shown in Figure 4

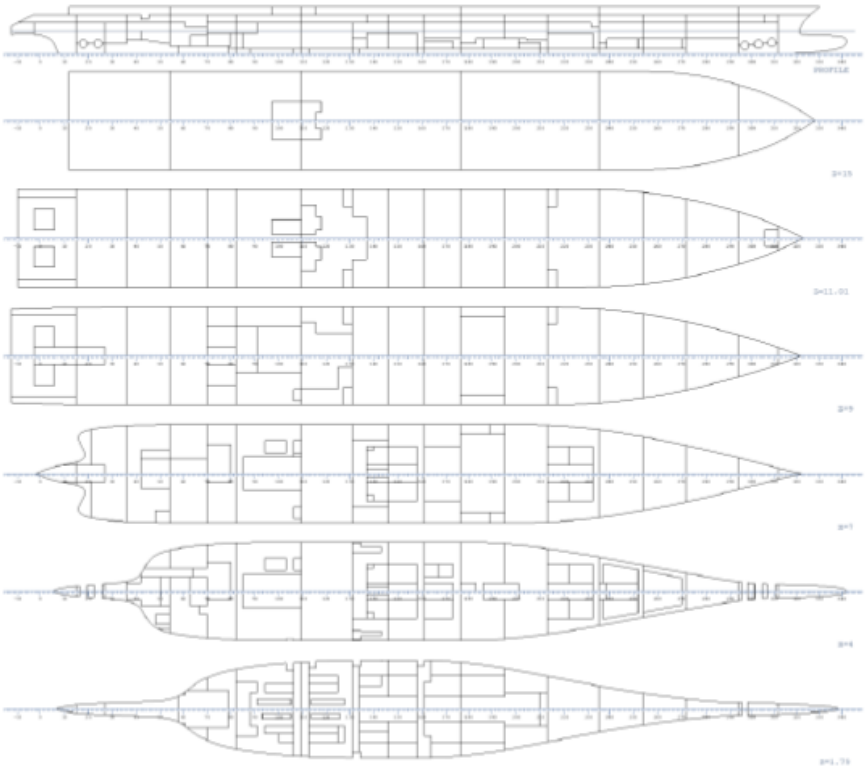

Figure 4: general arrangement of the reference passenger ship.

Figure 5: longitudinal view of the reference damage breach.

Table 1: main characteristics of the reference passenger ship.

Parameter	Value	Unit3
Length overall	300.0	m
Length between perpendiculars	270.0	m
Beam	35.2	m
Subdivision draught	8.2	m
Height at main deck	11.0	m
Metacentric height	3.5	m
Deadweight	8,500	T
Gross tonnage	95,900	T
Number of passengers	2,750	-
Number of crew members	1,000	-

and the main characteristics given in Table 1. The vessel is the same employed for the benchmark studies (Ruponen et al., 2022b) and advanced investigations on first-principles-based damage stability frameworks (Mauro et al., 2022a, 2022b).

Reference damage case

To apply the TTC analyses, a reference damage case has been selected, being the same as the benchmark tests, thus the one shown in Figures 2 and 3 for the time traces and the Weibull plot, respectively. However, the model employed for the benchmark studies refers to a simplified internal layout of the vessel. Here, to address a more realistic case, the full compartmentation of the vessel is used, as it is represented in Figure 4. Such an internal subdivision follows the guidelines for time-domain flooding simulations established and consolidated within the project FLARE (Guarin et al. 2021).

The selected breach damage has a length of 44.2 m, a penetration of 10.0 m a height of 16.0 m starting from a lower vertical limit of 0.0 m.

Figure 5 provides an overview of the breach location and dimension in the longitudinal view of the reference ship. The damage is representative of a significantly large and critical damage for the reference ship, resulting from a preliminary set of calculations. This preliminary set of calculations represents a stress test for the ship, including only damages with the maximum allowable damage length by SOLAS and severe sea states with significant wave height H_S=7.0 metres (Vassalos & Paterson, 2021).

Here, with the 7.0 metres wave height being not realistic as an operational scenario and also outside the reliability bounds of the flooding simulation code, two alternative weather conditions have been considered with H_s=3.75 and H_s=4.25 m.

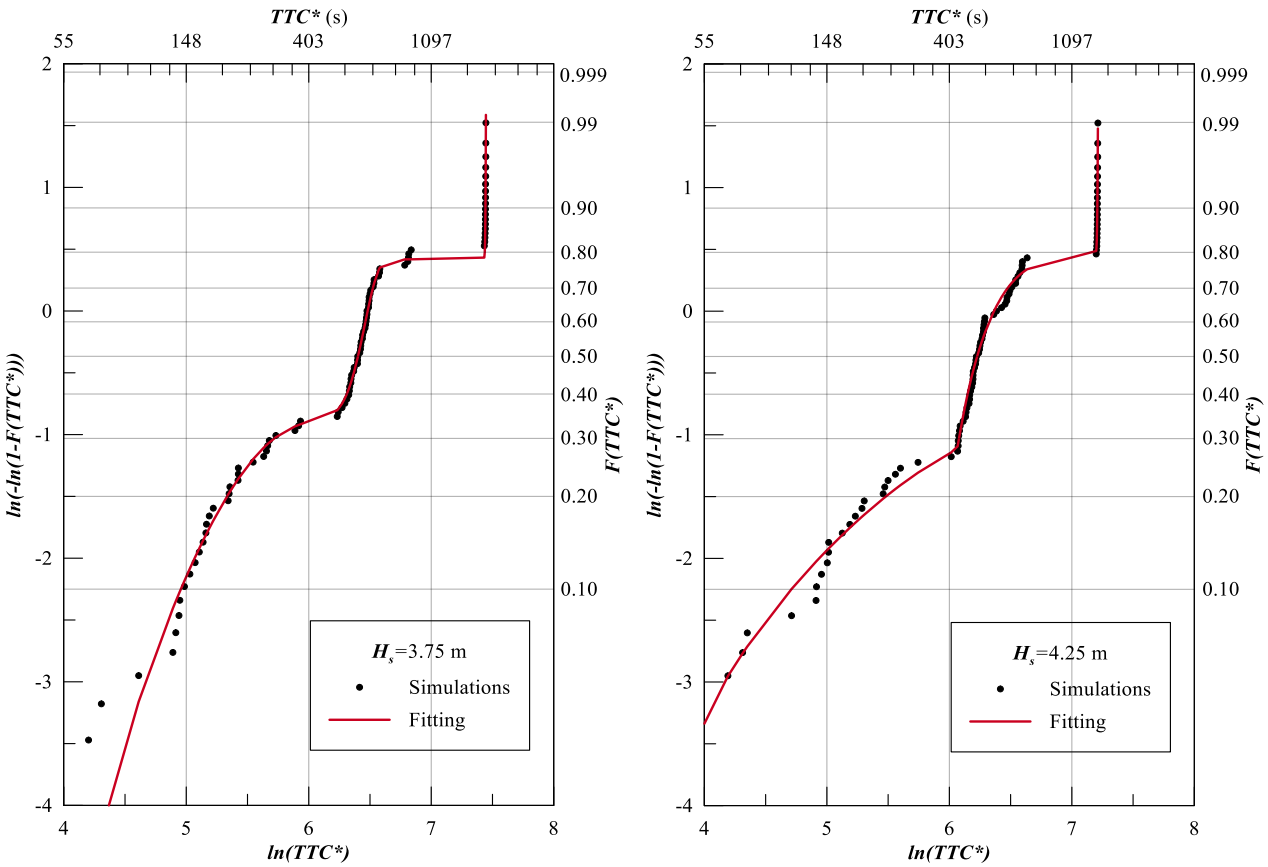

Figure 6: TTC* values and Mixed Weibull fitting on the Weibull plot for the reference damage case with H_s=3.75 m (left) and H_s=4.25 m (right).

Table 2: best-fitting parameters for the Mixed-Weibull distribution on the reference damage case.

	Parameter	Distr. 1	Distr. 2	Distr. 3
H_s=3.75m	η	178.917	310.997	931.324
	β	1.895	5.179	208.190
	γ	39.774	336.768	776.948
	w	0.341	0.273	0.386
	R^2	0.998		
	R^2_{adj}	0.997		
H_s=4.25m	η	253.183	120.584	630.453
	β	0.985	1.099	137.552
	γ	27.707	429.318	721.063
	w	0.346	0.265	0.389
	R^2	0.996		
	R^2_{adj}	0.995		

For both environments, 100 repetitions have been carried out to take into account the random nature of the irregular waves. This number of simulations has been selected in order to perform more than the 20 simulations used for the benchmark analyses so as to have a sufficient number of points necessary to identify the possible distributions describing the different natures of the capsize event

TTC analyses

The reference damage case consists of simulations having a maximum time of 30 minutes, as suggested by past and recent studies on damage stability (Spanos & Papanikolaou, 2014, Guarin et al.,2021, Mauro et al. 2023). All the simulations, both for 3.75 and 4.25 metres of significant wave height, led to the vessel capsizing within 30 minutes. Therefore, the resulting set of 100 capsizes per wave height represents a suitable population for the fitting methodology described in the previous section.

Figure 6 presents the Weibull plane for the distributions of TTC* resulting from simulations together with the fitting curve obtained by the application of the differential evolution algorithm. Even though the fitting seems to capture the population's behaviour well, it was thought appropriate to check the goodness of fit through conventional estimators. In this case, use has been made of the R^2 and R^2_{adj} coefficients, defined as follows:

$$R^2 = 1 - \frac{SS_E}{SS_{tot}} = 1 - \frac{\sum_{i=1}^{n}\left(y_i - y_i^*\right)^2}{\sum_{i=1}^{n}\left(y - \bar{y}\right)^2} \tag{8}$$

$$R^2_{adj} = 1 - \left(1 - R^2\right)\frac{n-1}{n-n_p-1} \tag{9}$$

where y_i are the n observations, y_i^* the predicted values, $\bar{y}$ is the mean value of the observations and

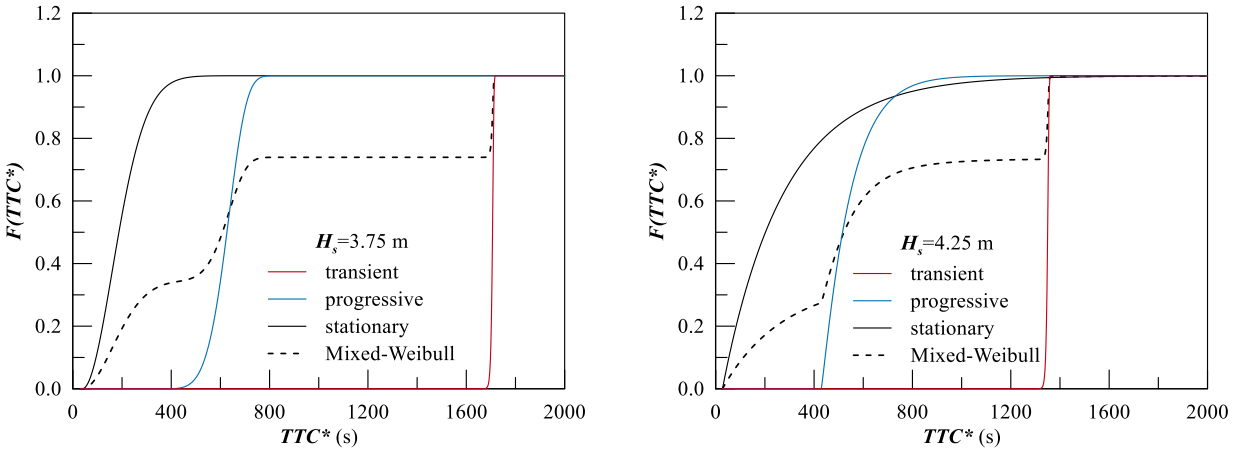

Figure 7: cumulative density functions for the transient, progressive and stationary capsize for the reference damage case considering H_s=3.75 m (left) and H_s=4.25 m (right).

n_p is the number of parameters used in the regression model.

Employing the above indicators makes it possible to evaluate the quality of the proposed regression model. Table 2 gives the obtained regression parameters and the goodness of fit indicators, where it is possible to observe the quality of the regression.

For both analysed cases, the R^2 and R^2_{adj} values are above 0.99, highlighting the good quality of the obtained regression models. The values shown in the table allow for a more accurate description of the distributions that characterise the different capsize modes. The location parameter γ allows for identifying the capsize type. High values of γ refer to the transient capsize as high TTC* corresponds to a low TTC value according to equation (5). Therefore, Distr.3 in Table 2 models the transient case. Adopting the same considerations, Distr.2 is for tor the progressive capsize case and Distr.1 is for the stationary case. The scale parameter η does not add additional considerations for the characterisation of the capsize event. On the other hand, the shape parameter β identifies how the capsizes are distributed along TTC*.

The transient capsizes (Distr.3) present a high β value, which means that they are all distributed along a short TTC* interval. The progressive and stationary capsize present a different shape compared to the transient as they cover a wider interval of TTC*. Considering the case with H_s=3.75 m, the shape parameter for the stationary case (Distr.1) is close to 2, which means it is similar to a Rayleigh distribution. For the same wave height, the progressive case (Distr.2) has a β value close to 5, which means that it follows a general Weibull case. Considering the case with H_s=4.25 m, both progressive and stationary cases have a shape parameter close to 1, which means that the distributions can be approximated by an exponential distribution. Figure 7 shows the cumulative density functions of the individual distributions for transient, progressive, and stationary state capsizes, together with the Mixed-Weibull one. From this picture, all the aforementioned considerations can be easily visualised. The figure highlights the different progressive and stationary capsize behaviour between the two different wave heights tested.

However, by changing the significant wave height, the nature of the distributions for progressive and stationary capsize also vary, suggesting that the general Weibull model is appropriate to cover the possible distributions of the different capsize modes. Adopting simpler distributions commonly used in naval architecture, such as Rayleigh or exponential models, may lead to appropriate fitting only in some particular cases.

As the number of cases analysed in the test is not enough to characterise the parameters of the individual distribution in such a way as to identify simpler formulations for the capsize cases, the Mixed-Weibull model represents a good fitting proposal for all the possible capsize modes.

5. CONSEQUENCES FOR FLOODING RISK ESTIMATION

The characterisation of TTC* (and consequently TTC) through a Mixed-Weibull allows for the opportunity to consider different kinds of significant values for the TTC*. As mentioned, it is common

practice to use the mean among a few repetitions as a significant value for TTC. Here, instead of the mean, different values can be considered, being representative of the analyses of the extreme. From the reported cases, it is evident that a significant part of the capsizes occurs in the transient stage. Thus, this condition is extremely critical for the ship's safety. By considering the mean value of the TTC, leads to a too-optimistic prediction of ship safety.

Such an effect is evident also when the risk of flooding needs to be estimated. In fact, the evaluation of risk through the Potential Loss of Life (PLL) may be strongly influenced by the TTC. By employing a multi-level framework for the evaluation of risk (Vassalos et al. 2023), for the so-called Level-2 prediction, an estimation of the TTC is necessary. In the case of a Level-2.1 prediction, the TTC enters directly into the following empirical formulation for risk:

$$FR = \begin{cases} 0.0 \quad \text{if } TTC > n \\ 0.8\left(1 - \dfrac{TTC - 30}{n - 30}\right) \quad \text{if } 30 \le TTC \le n \\ 1.0 \quad \text{if } TTC < 30 \end{cases} \tag{10}$$

where n is the maximum allowable evacuation time in seconds according to MSC.1/Circ. 1533.

In the case of a Level-2.2 prediction, the TTC needs to be directly compared with the evacuation simulations. In such a case, it is of utmost importance that a reliable value of TTC is used, as the TTC is the time threshold necessary to determine the fatality rate of the analysed evacuation scenario.

Therefore, with a flooding scenario that possibly leads to a transient capsize being much more dangerous than others, the sole adoption of the mean value of multiple repetitions as significant to the risk analysis may lead to an underestimation of the risk itself. As an example, for the case with H_s=3.75 m, the mean value of TTC is 1,160.8 seconds, but considering the extreme events with a percentile of 0.98, the significant TTC drops to 50.5 seconds. With the same assumption, considering H_s=4.25 m, the mean value is 900.0 and the 0.98 percentile is 48.4.

For the cases analysed in this example, a level 2.1 prediction is independent of the TTC, as the TTC is lower than 30 minutes; thus, according to equation (10), the fatality rate *FR* is always equal to 1.0. However, by considering the Level 2.2 prediction, which means a fully direct approach to risk, different TTC led to different fatality rates.

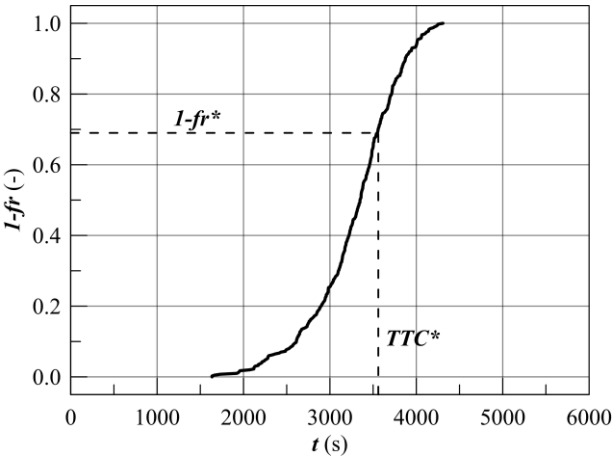

Figure 8: fatality rate estimation from the TTC.

Figure 8 gives an overview of the process necessary to determine the fatality rate from the evacuation analyses curve. Thus, changing TTC induces changes in the *FR* (or 1-*FR* in the graph). This in turn reflects the PLL evaluation, as the risk is given by the following formulation:

$$PLL = p_f \cdot c_f \tag{11}$$

where p_f is the probability of flooding and c_f identifies the consequences of the associated flooding event. The consequences are evaluated from

$$c_f = FR \cdot POB \tag{12}$$

where *FR* is the fatality rate and *POB* is the number of people onboard.

6. CONCLUSIONS

The present paper proposes a novel methodology to determine the Time to Capsize of a damaged ship by applying the extreme value theorem. A Mixed-Weibull model is introduced to capture the three different capsize modes: transient, progressive, and stationary.

Thanks to the application of an evolutionary algorithm, it is possible to automatically fit the 12 parameters needed to characterise the Mixed-Weibull regression model. The provided regressions on two reference cases highlight considerably high goodness of fit, evaluated through both R^2 and R^2_{adj} parameters.

The reference cases have been tested with 100 repetitions per case to capture the random nature of irregular waves. This is a completely different

methodology of estimating TTC, namely, employing the mean of 5 repetitions only. As the number of calculations is significantly high, taking into consideration the amount of time needed to perform a calculation, it is not advisable to perform such a detailed analysis for all the cases being analysed within a damage stability framework, but only on a reduced set of critical cases, in such a way as to inform a forensic analysis of the case itself.

The provided methodology highlights cases that are potentially dangerous for the vessel, as transient capsize may still occur whilst in progressive or stationary stage, something that the conventional methods do not detect as only the mean of five repetitions is considered.

Furthermore, being able to characterise the TTC by means of a mixed distribution may allow for future studies aiming at a fully probabilistic estimation of loss of life after an accident, which means convolute the distribution of the time to capsize with the distribution of the time to evacuate obtained by evacuation analyses.

REFERENCES

Berliant J., Teugels J., Vynkier F., 1996, “Practical Analysis of Extreme Values”, Leuven University Press.

Bulian, G., Cardinale, M., Dafermos, G., Lindroth, D., Ruponen, P., Zaraphonitis, G., 2020, “Probabilistic assessment of damaged survivability of passenger ships in case of grounding or contact”, *Ocean Engineering* 218, 107396.

Cichowicz J., Tsakalakis N., Vassalos D., Jasionowski, A., 2016, “Damage survivability of passenger ships - re-engineering the safety factor”, *Safety* 2(4), pp. 1-18.

Guarin L., Murphy A., Vassalos D., Paterson D., Mauro F., Boulougouris E., 2021, "D5.4 Dynamic vulnerability screening," Project FLARE.

IMO, 2020, “International Convention for the Safety of Life at Sea (SOLAS)”, Consolidated Edition as of 2020.

Mauro F., Nabergoj R., 2016, “Extreme values calculation of multi-modal peak distributions”, Proceedings of the 22nd International Conference Engineering Mechanics 2016, Svratka, Czech Republic, pp. 409-412.

Mauro F., Nabergoj R., 2017, “An enhanced method for extreme loads analysis”, *Brodogradnja* 68(2), pp. 79-92.

Mauro F., Vassalos D., Paterson D., 2022a, “Critical damages identification in a multi-level damage stability assessment framework for passenger ships”, *Reliability Engineering and System Safety* 228, 108802.

Mauro F., Vassalos D., Paterson D., Boulougouris E., 2022b, “Exploring smart methodologies for critical flooding scenarios detection in the damage stability assessment of passenger ships”, *Ocean Engineering* 262, 112289.

Ruponen P., Valanto P., Acanfora M., Dankowski H., Lee G.J., Mauro F., Murphy A., Rosano G., van’t Veer R., 2022a, “Results of an international benchmark study on numerical simulation of flooding and motions of a damaged ropax ship”, *Applied Ocean Research* 123, 103153.

Ruponen P., van Basten-Batemburg R., van’t Veer R., Bu S., Dankowski, H., Lee G.J., Mauro F., Ruth, E., Tompuri M., 2022b, “International benchmark study on numerical simulation of flooding and motions of a damaged cruise ship”, *Applied Ocean Research* 129, 103403.

Spanos D., Papanikolaou, A., 2014, “On the time for abandonment of flooded passenger ships due to collision damages”, *Journal of Marine Science and Technology* 19, pp. 317-327.

Vassalos D., Paterson D., 2021. “Towards unsinkable ships”, *Ocean Engineering* 232, 109096.

Vassalos D., 2022, “The role of damaged ship dynamics in addressing the risk of flooding”, *Ship and Offshore Structures* 17(2), pp. 279-303.

Vassalos D., Paterson D., Mauro F., Mujeeb-Ahmed M.P., Boulougouris E., 2022a, “Process, methods and tools for ship damage stability and flooding risk assessment”, *Ocean Engineering* 266, 113062.

Vassalos D., Paterson D., Mauro F., Murphy A., Mujeeb-Ahmed M.P., Michalec R., Boulougouris E., 2022b, “A multi-level approach to flooding risk estimation of passenger ships”, Proceedings of the SNAME 14th International Marine Design Conference, IMDC 2022, Vancouver, Canada.

Vassalos D., Paterson D., Mauro F., 2023, “Real-time flooding risk evaluation for ship-to-ship collisions based on first principles”, *Ocean Engineering* 281, 114847.

Identification of recurrence in irregular time-series

Dimitris Tsoumpelis, *School of Naval Architecture and Marine Engineering, National Technical University of Athens, Greece,* dimitris_tsoumpelis@mail.ntua.gr

Kostas J. Spyrou, *School of Naval Architecture and Marine Engineering, National Technical University of Athens, Greece*, k.spyrou@central.ntua.gr

ABSTRACT

In the paper is discussed a method developed by the authors for the identification of repetitive patterns within a long time-series. This method is based on the construction of vectors representing short-time portions of the time-series. Similarity (and thus repetition) is determined on the basis of a Euclidian distance metric applied to these vectors. The potential of the method is demonstrated by employing it in the time-series of random wave elevation produced by a power spectrum and also in the corresponding ship roll response, in order to discern repeating patterns in these time-series. Moreover, the method is employed in order to determine wave group patterns in numerical wave elevation records and, in particular, towards assessing their similarity to the predictions of the Quasi-Determinism theory.

Keywords: *Recurrence, time-series, similarity, waves, ship motions.*

1. INTRODUCTION

The task of identification of a pattern (also commonly called "subsequence") in a time-series is a very common one in the area of data-mining. There can be several uses of such an identification scheme. Among these are, in the characterization of outliers or "abnormalities" (Schmidl et al. 2019), in the determination of nonlinear features and non-predictability of a system (Wayland et al. 1994), in motif discovery (Patel et al. 2002), in clustering (He et al. 2003) and, in a recent work of the authors, in the identification of recurrence (Tsoumpelis and Spyrou 2023).

The efficient identification of recurrence in numerical or experimental time-series is a topic that should be of interest to ship and ocean engineering studies. In ship roll simulations, for example, pseudorandom realizations of the excitation are usually created, in order to determine, via direct counting, the statistical characteristics of the responses. To ensure the reliability of the statistical results, spurious repetitions within the long-time realizations must be excluded from the data analysis. In a different direction, it is sometimes desirable to know whether specific patterns are found in some collected time-series. For example, we would like to know whether wave groups appear in wave elevation records and whether their form is close to what the relevant theory would predict.

In the searching process discussed in Tsoumpelis and Spyrou (2023), short subsequences (with duration T_w) were constructed from given time-series with no limitation in their form. These subsequences were represented by sufficiently low-dimensional vectors $\mathbf{X}$. Assume then a certain subsequence, effectively represented by vector $\mathbf{X}_0$, that needs to be checked for the possibility of appearing repeatedly in the time-series. We define a Euclidean distance metric $d(\mathbf{X}, \mathbf{X}_0) = |\mathbf{X} - \mathbf{X}_0|$ of $\mathbf{X}_0$ from any other subsequence $\mathbf{X}$ (of the same duration T_w). Similarity is detected as soon as this distance falls below a predefined small distance threshold (ϵ). Fulfilment of this condition guarantees that the subsequence has reappeared. The scheme provides also the locations in the time-series of all new appearances of the examined subsequence.

Other approaches to recurrence identification have also been discussed in the scientific literature and in relation to a variety of fields. In the Recurrence Quantification Analysis leveraged by Spiegel and Jain (2014), the distances between the pairs of all possible subsequences are computed, resulting in the creation of a *Recurrence Plot*. This plot essentially consists of $N \times N$-points, each of which indicates whether the subsequences i and j ($i, j = 1, \dots, N$) are similar to each other.

Subsequently, various indicators can be computed which quantify the repetitiveness of the analyzed time-series.

Another interesting application is one where similar subsequences are sought in order to minimize the *description length* of a time-series in the context of some data compression scheme. In Rakthanmanon et al. (2011) for example, the authors tried to find non-overlapping subsequences of a time-series, which lead to the optimum bitwise compression of the entire time-series. To this end, reappearing subsequences of various lengths had to be identified in order to be excluded. This would reduce the bit-wise length of the time series, because one would only have to store these shorter parts and the points at which they reappear, in the larger time-series.

In the present work is discussed the application of the recurrence searching scheme of Tsoumelis and Spyrou (2023), in two distinctive directions. In the first, the aim was to quantify the similarity of subsequences belonging to a time-series of a ship's roll motion, given that similarity had been observed in subsequences of the forcing time-series. In the second, the topic of investigation was the form of extreme waves. According to the theory of *Quasi-determinism*, proximal to an extremely high wave, the form of sea elevation in time-space tends to a deterministic profile (Boccotti 1989). Out of the two existing formulations of Quasi-determinism, we chose to adopt the second one and focused on the form of high waves observed in numerical wave realizations. We then compared the randomly generated form of high waves with the corresponding deterministic one supplied by the theory of Quasi-determinism. This comparison was performed by calculating the distance of the original subsequence vector from each candidate subsequence vector.

The paper is organized as follows. In Section 2 we present the simple ship roll model that we employed and in Section 3 we provide a more detailed account of the searching scheme. In Section 4 we discuss about some technical aspects of the method. In Sections 5 and 6 we present the results of the applications and in Section 7 we discuss the results.

2. MATHEMATICAL MODEL

A simple qualitative, rotational oscillator type, ship roll model was adopted, with nonlinear damping and restoring. Below it is written as a two-dimensional system in time normalized by the inertial moment $I + \delta I$:

$$\left\{\begin{array}{c} dx_1 = x_2 \cdot dt \\ dx_2 = \left(-D(x_2) - R(x_1) + m(t)\right) \cdot dt \end{array}\right\} \qquad (1)$$

Where $D(x_2) = b_1 x_2 + b_2 x_2 |x_2|$ is the damping term, $R(x_1) = c_1 x_1 - c_3 x_1^3$ is the restoring term and $m(t)$ is the external forcing from irregular waves. Moreover, x_1 describes the roll angle and x_2 the angle derivative of the ship.

The external moment of the waves acting on the ship consist a Gaussian Process with spectrum $S_{mm}(\omega)$, which is derived by the spectrum of wave elevation $S_{\eta\eta}(\omega)$ with the aid of the response amplitude operator of the ship $RAO(\omega)$. Taking also into account that we have normalized by the inertial moment, the spectrum of forcing moment is:

$$S_{mm}(\omega) = \frac{S_{\eta\eta}(\omega) \cdot |RAO(\omega)|^2}{(I + \delta I)^2} \qquad (2)$$

In our case, the $RAO(\omega)$ -operator has been obtained from Su (2012) who derived it with a strip theory method. In Figure 1 is presented the spectrum of normalized external moment that was employed throughout our studies. The (one-sided) wave elevation spectrum is chosen as a Pierson-Mosckowitz one, calculated as follows:

$$S_{\eta\eta}(\omega) = \frac{5.058 g^2 H_s^2}{T_p^4 \omega^5} \exp\left(-1.25 \frac{\omega_p^4}{\omega^4}\right) \qquad (3)$$

As usual, H_s is the significant wave height and T_p is the modal period. The ship particulars (coefficients of damping and restoring) and the examined sea states are summarized in Table 1. For more information about the ship see also Chai et al. (2015).

For the simulation of a stationary Gaussian process we have adopted the method in Tucker et al. (1984), This method has been reported to reproduce more accurately the statistics of the process and especially those of wave groups. Therefore, we used Eq. (4):

$$\zeta(t) = \sum_{i=1}^{N} Z_i \cdot \sqrt{2S(\omega_i)\delta\omega} \cdot \cos(\omega_i + \varphi_i) \quad (4)$$

In Eq. (4), $S(\omega)$ is the spectrum of the process of interest; $\delta\omega$ is the equidistant step between cyclic frequencies ω_i; φ_i are random phases uniformly and independently distributed in $[0,2\pi)$ and Z_i are Rayleigh independently distributed random variables with parameter $\sigma = \frac{1}{\sqrt{2}}$ so that the mean value $\mathbb{E}[Z_i^2] = \sqrt{2}\sigma = 1$ and thus $\mathbb{E}[\zeta^2(t)] = \sum_{i=1}^{N} S(\omega_i) \cdot \delta\omega$.

Table 1: Ship particulars and sea condition.

Parameter	Value	Unit
c_1	1.153	s^{-2}
c_3	0.915	s^{-2}
b_1	0.095	s^{-1}
b_2	0.0519	$-$
ω_0	1.074	rad/s
H_s	4	m
T_p	11	s

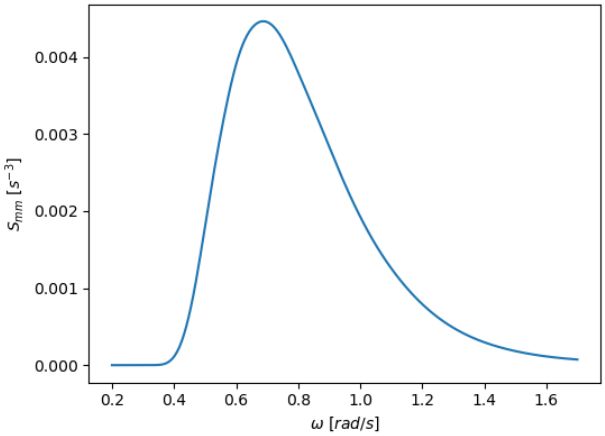

Figure 1: The spectrum of normalized external roll moment which corresponds to a Pierson-Moskowitz spectrum of wave elevation.

3. THE SEARCH METHOD

Let us consider a continuous time-series sampled with a rate which is sufficient for capturing all of the essential information. Then, our time-series is represented via a set of real values $A = \{x(t_i), i = 1, \dots, N\}$. In general, the t_i-values of the sampling are generated by using a step $\tau = t_{i+1} - t_i$. For brevity, we will be writing x_i instead of $x(t_i)$. We define subsequences belonging to the above time-series and having time duration $T_w = k \cdot \tau$ as vectors $\mathbf{X}_i^{T_w} = (x_i, \dots, x_{i+k})$. In order to determine whether two subsequences $\mathbf{X}_i^{T_w}, \mathbf{X}_j^{T_w}$ are similar or not, we compute a slightly modified version of their Euclidean distance:

$$d\left(\mathbf{X}_i^{T_w}, \mathbf{X}_j^{T_w}\right) = \sqrt{\frac{1}{k+1}\sum_{m=0}^{k}\left(x_{i+m} - x_{j+m}\right)^2} \quad (5)$$

We have chosen the Euclidean distance because it is a ubiquitous distance measure in the literature and at the same time its computation can be done very efficiently, as in Yeh et al. (2018). Other popular alternatives of a distance measure are the z-Normalized Euclidean distance and the Dynamic Time Wrapping (DTW) (Xi et al. 2006). The former metric is scale and mean invariant and therefore subsequences of arbitrary amplitude and offset can be identified as similar. The later metric is capable to compare subsequences of different length and allows for parameterization of the subsequences. We have not used such metrics because we wanted the original subsequences to have identical components when the distance between them is zero.

When we want to find subsequences similar to $\mathbf{X}_i^{T_w}$ we first compute the distance with all the subsequences $\mathbf{X}_j^{T_w}, j = 1, \dots, N-k$. We then set a threshold ϵ and define as similar those vectors $(\mathbf{X}_j^{T_w})$ which satisfy:

$$d\left(\mathbf{X}_i^{T_w}, \mathbf{X}_j^{T_w}\right) < \epsilon \quad (6)$$

There are some implications though with this definition, because the j-indexes where Eq. (6) is satisfied appear sequentially, hence corresponding to subsequences which highly overlap and are essentially the same. This problem has been considered from Patel et al. (2002) and we have followed the same practice. That is, whenever there is a sequence of indexes (j) satisfying inequality (6) we choose the one corresponding to the smallest distance.

There are several optimizations that can generally improve the efficiency of the scheme. First of all, for the distance calculation of two subsequences, it is not necessary for all the components of them to be included. Therefore, instead of taking into account components $x_i, x_{i+1}, \dots, x_{i+k}$ with a step τ we can only include $x_i, x_{i+m}, x_{i+2m}, \dots$ with a step $m \cdot \tau$. We have

investigated this topic in our previous work (Tsoumpelis and Spyrou 2023) but we deal with it in more detail in Section 4. Moreover, the searching step with which we increase the value of the j-index is crucial. This is a topic we investigated in Tsoumpelis and Spyrou (2023) in quite a detail and concluded that a step of $\tau = 0.1\ s$ is quite efficient and, at the same time, it does not lead to accidentally overlooking low values of the distance. Regarding the optimization of distance calculation, there are various ways to accelerate its calculation. In the applications we use the algorithm MASS discussed in Yeh et al. (2018), which is a convolutional type of method, and can considerably accelerate the calculations to around 10 times compared to a naive calculation. In Figure 2 we depict on the left two subsequences sampled with high frequency and constant time step; and the subset of components necessary to compute their distance with an accuracy of $\pm 0.01\ [rad]$.

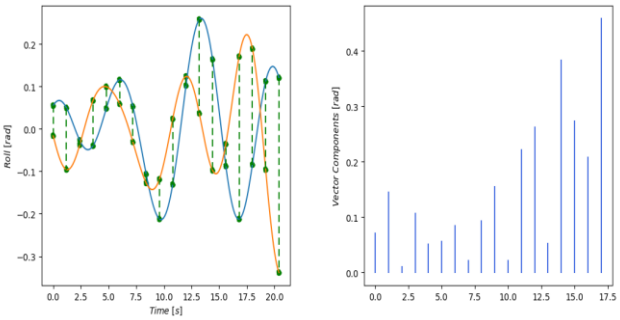

Figure 2:On the left: The continuous subsequences (with blue and orange) and the necessary subset of points to represent them (with green). On the right: the absolute values of the differences of the vector components.

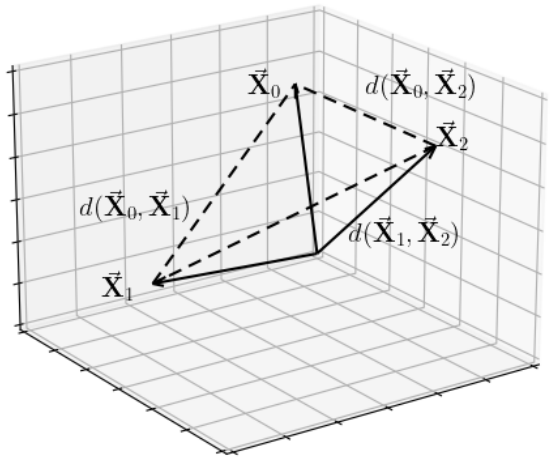

Figure 3: The subsequences represented by three dimensional vectors with solid lines and the distances between them represented by dashed line segments.

Figure 3 offers a basic illustration of the concept. The tested subsequences are depicted as 3-dimensional vectors with solid lines and the distances between those vectors are depicted with dashed line segments.

4. SELECTION OF VECTORS' DIMENSION

In this section we are going to examine in more detail the necessary number of components (n_{nnc}) in order to calculate the distance given by Eq. (5) between two subsequences $\mathbf{X}_i^{T_w}, \mathbf{X}_j^{T_w}$. Eq. (5) is essentially a discrete analog of the integral of the squared difference of the subsequences. Because the subsequences are smooth, since they are derived from either a smooth Gaussian Process or the roll response from it, the error of numerical approximation of the integral tends to zero when the spacing between the components also tends to zero. In practice though, depending on the needed accuracy, there is no reason to increase the components more than a necessary number, because there is no worthwhile improvement in the estimation.

The concept to determine the n_{nnc} is to select two subsequences of a certain length T_w and starting from a very small number of components (say 3), uniformly distribute them within the corresponding time interval and gradually increase their number (up to a number n) untill there is no considerable change in the estimation of the distance. We also define the variability or fluctuation ($fluct()$) of the estimation as:

$$fluct\left(n_0; \mathbf{X}_i^{T_w}, \mathbf{X}_j^{T_w}\right) = \max_{n \geq n_1 \geq n_0} \left\{ \left| d\left(\mathbf{X}_{i,n_1}^{T_w}, \mathbf{X}_{j,n_1}^{T_w}\right) - d\left(\mathbf{X}_{i,n}^{T_w}, \mathbf{X}_{j,n}^{T_w}\right) \right| \right\} \quad (7)$$

In Eq. (7) the extra subscript n_i signifies the number of uniformly spaced components of the corresponding vector [this is a slightly altered definition from the one in our previous work (Tsoumpelis and Spyrou 2023) in order to simplify the formula].

To select the n_{nnc}, we set an accuracy bound ϵ_1 and we define:

$$n_{nnc} = \underset{n \geq n_0 \geq 3}{\operatorname{argmin}} \left\{ fluct\left(n_0; \mathbf{X}_i^{T_w}, \mathbf{X}_j^{T_w}\right) < \epsilon_1 \right\} \quad (8)$$

Since we are dealing with random subsequences, each pair of them is going to yield a different n_{nnc}. Therefore, in order to select a more appropriate n_{nnc}

we randomly choose 10^4 different pairs of subsequences and select the n_{nnc} so that 98% of the pairs satisfies:

$$fluct\left(n_{nnc}; \mathbf{X}_i^{T_w}, \mathbf{X}_j^{T_w}\right) < \epsilon_1 \quad (9)$$

for a given ϵ_1.

In Figures 4 and 5 we depict the percentage of the pairs on the y-axis for which inequality (9) is not satisfied as a function of the number of components used in the x-axis. We have done this procedure for four different T_w and for three different thresholds ϵ_1. With black dashed line we indicate the 2% of remaining pairs which require more components in order to satisfy inequality (9).

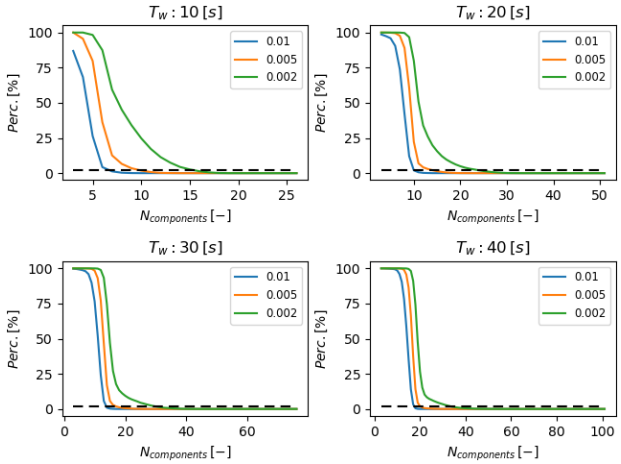

Figure 4: Percentage of subsequences pairs drawn from forcing time-series which do not satisfy inequality (9), as a function of vectors' dimension. With black dashed line is indicated the 2% level.

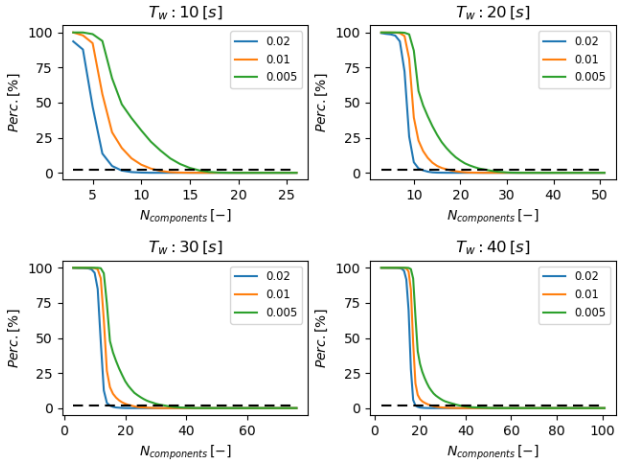

Figure 5: Percentage of subsequences pairs drawn from response time-series which do not satisfy inequality (9), as a function of vectors' dimension. Black dashed line indicates the 2% level.

Figure 4 is for subsequences belonging to time series of forcing and Figure 5 of response. The thresholds we use are different for the two time series because they are adjusted according to their respective standard deviation. The subsequence periods T_w have been determined according to the mean time of one oscillation cycle, so that they correspond to approximately 1 to 4 oscillations respectively.

We notice, as expected, that the smaller threshold ϵ_1 the more components are necessary to reach the same percentage of pairs which satisfy inequality (9). Therefore the three curves of the respective thresholds are quite distinct. We also observe that as T_w increases those three curves are progressively less distinct. In Tables 2 and 3 we include the n_{nnc} for each threshold and T_w for time series of forcing and response respectively.

Table 2: n_{nnc} for the various durations T_w (horizontally) and thresholds ϵ_1 (vertically) for forcing time-series.

$\epsilon_1, T_w[s]$	10	20	30	40
0.01	7	10	14	18
0.005	10	14	17	20
0.002	16	24	29	33

Table 3: n_{nnc} for the various durations T_w (horizontally) and thresholds ϵ_1 (vertically) for response time-series.

$\epsilon_1, T_w[s]$	10	20	30	40
0.02	8	12	15	18
0.01	12	18	22	25
0.005	16	26	32	37

In general, for both time-series we see that in order to transition from the second to the third threshold we need a considerable increase of n_{nnc} and thus we choose the n_{nnc} for the second threshold for each case.

5. CORRELATION OF SIMILARITY BETWEEN FORCING AND RESPONSE

In this application our aim is to investigate the relation of the distance between subsequences belonging to the response time-series when there is a known similarity in the corresponding subsequences belonging to the forcing time-series. More precisely, let's suppose that when steady state has been reached we choose a subsequence $\mathbf{M}_i^{T_w} = (m_i, \dots, m_{i+k})$ of duration T_w from the external moment time-series with corresponding response subsequence $\mathbf{X}_i^{T_w} = (x_i, \dots, x_{i+k})$. If we chose a different $\mathbf{M}_j^{T_w}$ which is completely uncorrelated with $\mathbf{M}_i^{T_w}$ (i.e. sufficient time separates them or they belong to different realizations), but at the same time the following condition holds: $d\left(\mathbf{M}_i^{T_w}, \mathbf{M}_j^{T_w}\right) < \epsilon$,

then how informative is this condition for the value $d\left(\mathbf{X}_i^{T_w}, \mathbf{X}_j^{T_w}\right)$?

We should point out that the duration T_w is a parameter of interest. In case T_w is very small, essentially reducing the subsequences into points, we shouldn't expect significant correlation between them. If, on the other hand, T_w is very large, in case the forcing subsequences are similar, then the corresponding response subsequences would also be similar (except if we were in a regime of chaotic behavior) after a point in time (in the order of the transience decay time) depending on the level of disparity of the initial conditions of the response subsequences. At the same time though, it would also be very improbable to find subsequences that approximately coincide for such a long duration. The interesting part would be to quantify the relation of distances for subsequences of intermediate durations (considerably less than the transient part). Therefore, we search for correlations containing about two oscillation cycles, which corresponds to $T_w = 20s$, whereas the transience period for the oscillator we consider is about $75s$.

We have tried to find out the above relationship between distances for two subsequences which contain extreme response values. In Figure 6 we depict the subsequences of normalized external moment, $m(t)$, with orange; and the corresponding subsequences of response angle, x_1, with blue. We record the distance between subsequences in the forcing time-series when the following condition holds:

$$d\left(\mathbf{M}_0^{T_w}, \mathbf{M}_j^{T_w}\right) < 0.03\ \left[\frac{rad}{s^2}\right] \qquad (10)$$

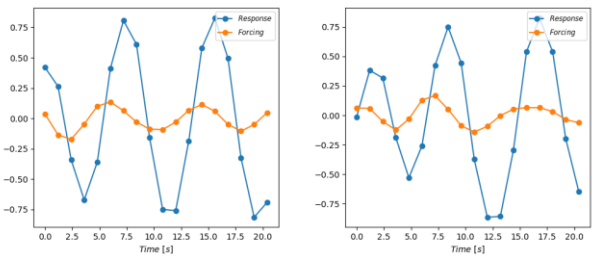

Figure 6: Two pairs of subsequences, where with blue is the response roll-angle and with orange the forcing subsequence.

Then, for the above j-indexes where condition (10) holds we calculate $d\left(\mathbf{X}_0^{T_w}, \mathbf{X}_j^{T_w}\right)$. For comparison we have also calculated $d\left(\mathbf{X}_0^{T_w}, \mathbf{X}_r^{T_w}\right)$, where $\mathbf{X}_r^{T_w}$ is a completely random response subsequence without its corresponding $\mathbf{M}_r^{T_w}$ being subject to any conditon. In Figure 7 we depict the histograms of those distances. With blue is the histogram of distances when the condition (10) occurs and with orange when there is no restriction of this condition.

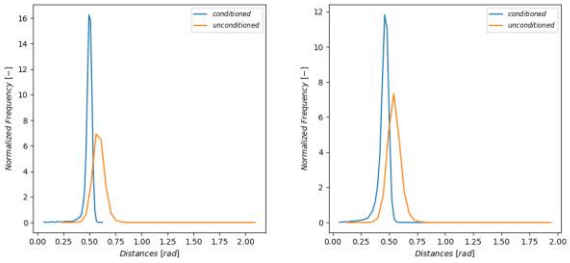

Figure 7: With blue is the histogram of distances between subsequences in the response time-series when the condition (10) holds and with orange is the histogram of distances taken completely at random.

It is obvious that in condition (10) holds then, on average, the distances are considerably smaller than those in case of randomly selected vectors. More precisely, for the left diagram the mean value for the blue and orange histogram is 0.493 and 0.588 respectively and for the right diagram 0.454 and 0.546. For Figure 7 we searched on 20000 time-series of forcing-response each with a duration of about 70 minutes, and we collected about 15000 samples for the blue histogram on the left diagram and 7500 for the one on the left diagram.

6. COMPARISON OF EXTREME WAVES WITH QUASIDETERMINISM

6.1 Overview of the theory

According to the theory of Quasi-determinism the form of the wave elevation both spatially and temporally around a point (X_0, Y_0, T_0) tends to be increasingly deterministic as the height (H) of the incident wave at this point tends to infinity. More precisely, extremely high waves are determined by the ratio $\frac{H}{\sigma} \to \infty$, where σ is the standard deviation of the random process of wave elevation.

There are two formulations of the theory. In the first formulation, also called "New Wave", it is assumed that a very high crest occurs at a given point and the deterministic form is calculated as the most probable form of a Gaussian process subjected to this condition. The initial work about the properties of a Gaussian process in the vicinity of a very high crest was done by Lindgren (1970, 1972). Subsequently, Boccotti (1982) formulated the theory

in a framework of wave environment. This theory is correct up to first order Stokes expansion (i.e. linear waves).

In the second formulation by Boccotti (1989) the condition for the Gaussian process is the occurrence of a very high wave of height H. It was proved that as $\frac{H}{\sigma} \to \infty$ the crest and trough of this high wave tend to obtain heights $\frac{H}{2}$ and $-\frac{H}{2}$ respectively, with the time interval separating them being T^*, which is the abscissa where the autocorrelation of the process obtains its minimum value, i.e. $R(T^*) \leq R(T), \forall\, T \geq 0$. Therefore, for a certain point in space, given the conditions $\eta(0) = \frac{H}{2}, \eta(T^*) = -\frac{H}{2}$, the form of the mean (and most probable) wave elevation is given as:

$$\bar{\eta}(T) = \frac{R(T) - R(T - T^*)}{R(0) - R(T^*)} \frac{H}{2} \tag{11}$$

In Figure 8 has been plotted the mean value of wave elevation at a fixed point in space, normalized by half the wave height.

It is worth mentioning that, according to Boccotti (1989), in a realization of an extreme wave there naturally exists a random portion accompanying the mean (deterministic) wave elevation. It is proved though that this random portion is of the order $O(H^0)$, whereas the mean portion is of the order $O(H^1)$. Therefore, there is going to be some level of randomness in the elevation, but the scale of this randomness is going to vanish compared to the scale of the deterministic portion.

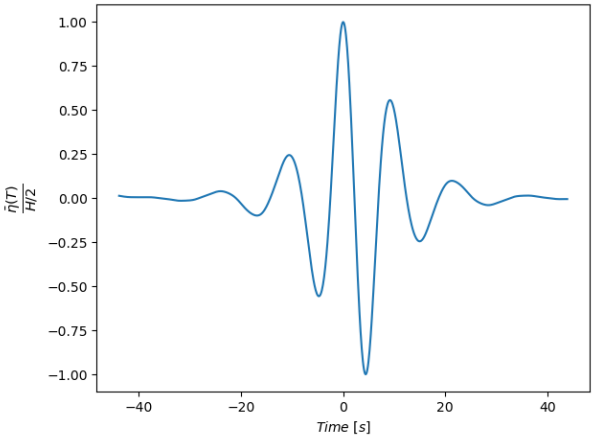

Figure 8: The most probable wave elevation given a wave of extreme height *H* occurs, normalized by half the height of the extreme wave (in the center).

6.2 Comparison with realizations of extreme waves

The theory of Quasi-determinism has been verified both experimentally (see for e.g. Petrova et al. (2011)) and from real wave data from the Baltic sea (Antao 2018). In our work though, we aim to quantify the disparity between the deterministic part that Quasi-determinism dictates and actual realizations of extreme waves. Our aim is to also demonstrate the scale disparity between the deterministic form and the random error.

To this end we follow the subsequent procedure: For a random realization of wave elevation we identify the waves whose height (H) is above a certain threshold. We consider those which are above $H > 5\sigma$. Although extreme waves are considered those with $H > 8\sigma$ we have also included smaller ones to see the applicability extent of the theory. We then compare the random wave we found with the one dictated by the theory using Eq. (11), in which H is the height of the random wave we identified. In order to compare the waves we use the searching algorithm we presented in Section 2.1. More precisely, let's suppose we identify a random wave with $H_r > 5\sigma$. We then initialize a subsequence $\mathbf{X}^{T_{Qd}}$ representing the most probable wave elevation using Eq. (11) with height H_r containing the central wave and some (or none) waves around it having a total duration T_{Qd}. We then compare this subsequence with subsequences of duration T_{Qd} in the vicinity of the random wave we identified (i.e. $\pm\frac{T_{central\_wave}}{2}$ around it). We then choose the subsequence having the smallest distance to the subsequence $\mathbf{X}^{T_{Qd}}$. We then record the height H_r and the minimum distance to analyze their correlation.

We have done this procedure in two variations. In the first variation $\mathbf{X}^{T_{Qd}}$ contains only the central (and highest) wave, whereas in the second one it consists a wave group which includes the wave preceding and succeeding the central one. In Figure 9 we demonstrate a random wave elevation where some 'extreme' waves have been identified and the corresponding most similar wave group is superimposed. The wave group variation is considered in order to investigate the extent of similarity of the theoretical elevation beyond the central wave.

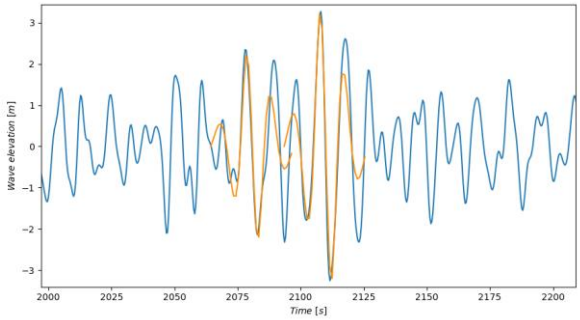

Figure 9: Comparison of two 'extreme' random waves (with blue) and the corresponding wave given from quasideterminism.

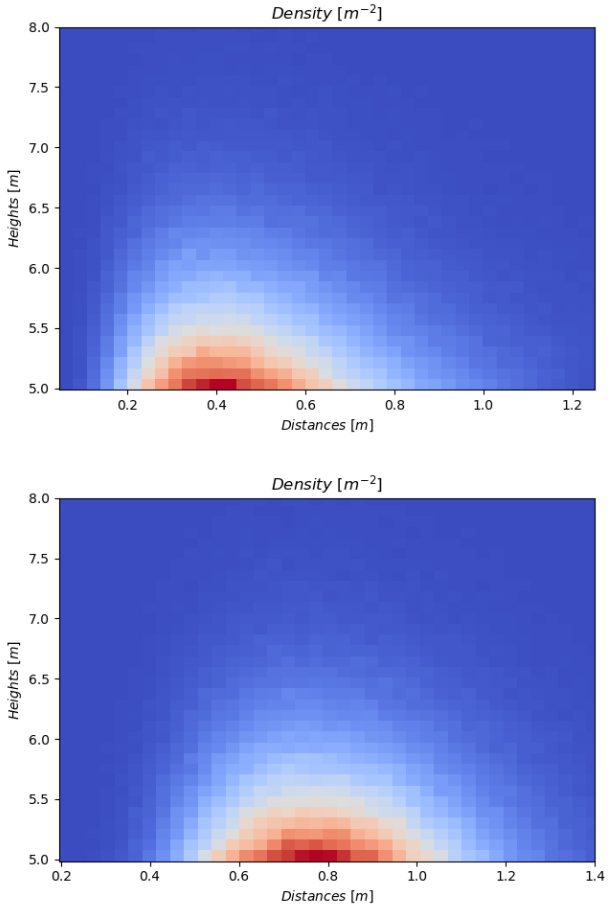

Figure 10: Histogram of wave heights and corresponding distances for the case of one wave (upper) and three waves (lower).

In Figure 10 we have aggregated the pairs of heights and corresponding distances and rearranged them into a histogram for the variation with one and with three waves respectively. In the data we collected, the maximum values of height and distance went up to about $10m$ and $2m$ respectively, but because they are very rare, in Figure 10 we chose to only depict the areas including the main portion of the data. The height of the wave indicates the proximity to the ideal (extreme) scenario. In the sea condition we have considered, it is (cf. Table 1) $\sigma = 1m$. The calculated distance quantifies the disparity between a wave realization of height H and the theoretical form given by Eq. (11).

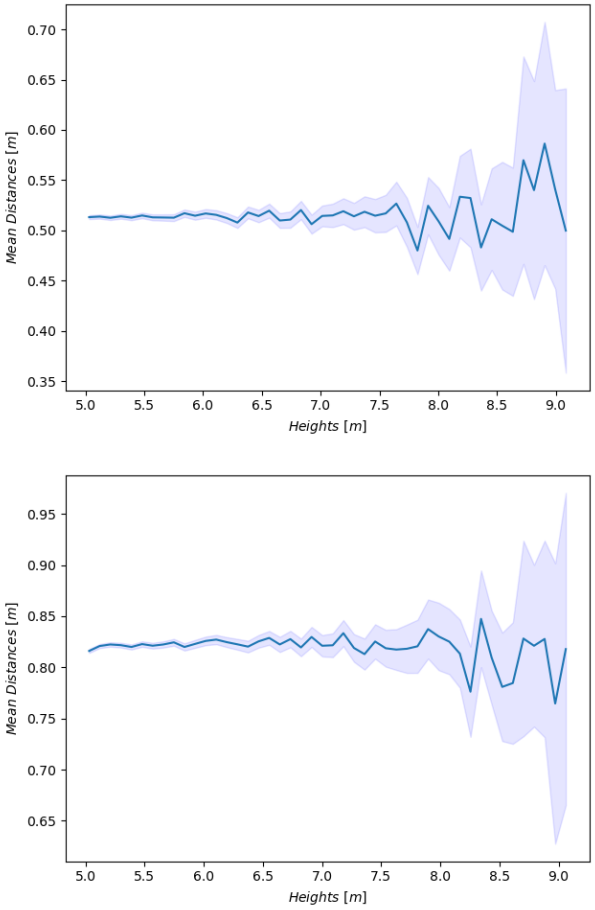

Figure 11: Mean value of distance as a function of the corresponding wave height, along with a 95% confidence interval for the case of one wave (upper) and three waves (lower).

We generally observe that for the case with one wave the mean distance is at around 0.4 meters, whereas for the case of three waves it is around 0.75. It would be more informative though to inspect the mean value of distance with respect to corresponding height. To this end we rearranged the data into bins according to wave height. Then, for each bin, we calculated the mean value of distance for the waves falling into each bin. In Figure 11 we see those mean values and an estimated 95% confidence interval around them. For the derivation of the confidence interval we assumed that the distribution of the mean value follows the student's t-distribution and therefore the limits are given by $\mu \pm t_{a,n-1} \cdot \frac{\sigma_{ML}}{\sqrt{n-1}}$, where μ is the estimated mean value, a the confidence value corresponding to a symmetrical interval, n the number of samples for the

estimations, $t_{a,n-1}$ the value of the inverse c.d.f. of the student's t-distribution with $n-1$ degrees of freedom corresponding to the confidence level a and σ_{ML} the maximum-likelihood estimation of standard deviation of the sample.

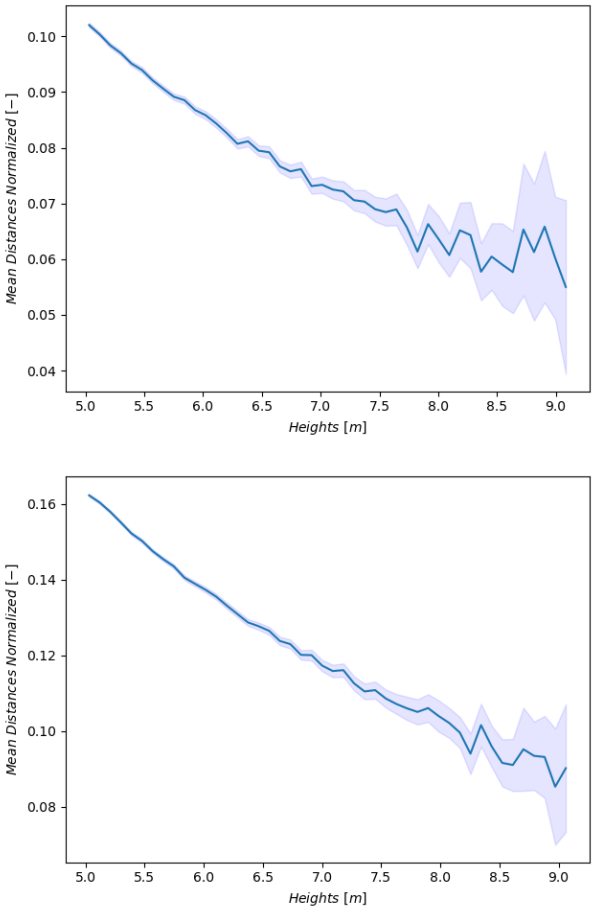

Figure 12: Mean value of distance normalized with wave height as a function of the wave height, along with a 95% confidence interval for the case of one wave (upper) and three waves (lower).

We should point out here that the distance is virtually constant with respect to the wave height as the theory predicts. Therefore, in case we normalize the waves with their corresponding height the disparity between realizations and theory diminishes as the height increases. In Figure 12 we depict the normalized distance with the wave height and see that it indeed decreases.

For the collection of the above data, for each case we calculated 15000 realizations of 70 mins, taking care not to sample from the repeated portion of the realizations. In total, 375000 waves with $H > 5\sigma$ were collected for each of the two cases.

7. CONCLUSIONS

In our work we have introduced the concept of a subsequence, which can be viewed as a generalization of a point value. Moreover, we described an algorithm for identifying similar subsequences to a given one and calibrated its parameters for time series of wave elevation and roll response. Then we made use of the method in two applications.

In the first application we investigated the degree of similarity of subsequences belonging to response time-series when there is a known similarity in their corresponding forcing subsequences. We saw that for two cases of forcing subsequences, if we encounter a forcing subsequence similar to them, then the corresponding response subsequence is going to be noticeably similar to the corresponding response subsequence.

In the second application we compared realizations of extreme waves with the form specified by Quasi-determinism. We found out that the minimum distance is generally smaller when we consider only the central wave compared to when we include adjacent waves. We also verified that the scale disparity between the random portion of the waves and the most probable (deterministic) one is qualitatively in accord with the theory.

REFERENCES

Antão, E. M., 2018, "Verification of Quasi-Determinism theory against Baltic Sea Data", Meteorology Hydrology and Water Management, 6(2), pp.11-20.

Meteorology Hydrology and Water Management, 6(2), pp.11-20

Boccotti, P., 1982, "On ocean waves with high crests", Meccanica, 17, pp. 16-19.

Boccotti, P., 1989, "Quasi-determinism of sea wave groups", Meccanica, 24, pp. 3-14.

Chai ,W., Naess, A., Bernt, J.L., 2015, "Stochastic dynamic analysis and reliability of a vessel rolling in random beam seas", Journal of Ship Research, 59, pp. 113–131.

He, Z., Xu, X., Deng S., 2003, "Discovering cluster-based local outliers", Pattern Recognition Letters, 24(9-10), pp. 1641-1650.

Lindgren, G., 1970, "Some Properties of a Normal Process Near a Local Maximum", The Annals of Mathematical Statistics, 41(6), pp. 1870–1883.

Lindgren, G., 1972, "Local maxima of Gaussian fields", Arkiv for Matematik, 10, pp. 195-218.

Patel, P., Keogh, E., Lin, J., Lonardi, S., 2002, "Mining motifs in massive time series databases", IEEE International Conference on Data Mining 2002.

Petrova, P.G., Arena, F., Guedes Soares, C., 2011, "Space-time evolution of random wave groups with high waves based on the quasi-determinism theory", Ocean Engineering, 38(14-15), pp. 1640-1648.

Rakthanmanon, T., Keogh, E. J. ,Lonardi, S., Evans, S., 2011, "Time Series Epenthesis: Clustering Time Series Streams Requires Ignoring Some Data", IEEE 11th International Conference on Data Mining 2011, pp. 547-556.

Schmidl, S., Wenig, P., Papenbrock, T., 2022, "Anomaly Detection in Time Series: A Comprehensive Evaluation", VLDB Endowment, 15(9), pp.1779-1797.

Spiegel, S., Jain, J. B., Albayrak, S., 2014, "A Recurrence Plot-Based Distance Measure", Translational Recurrences, Springer Proceedings in Mathematics & Statistics, vol 103. Springer, ISBN: 978-3-319-09531-8.

Su, Z., 2012, "Nonlinear response and stability analysis of vessel rolling motion in random waves using stochastic dynamical systems", PhD thesis, Texas A&M University.

Tsoumpelis, D., Spyrou, K. J., 2023, "Identification of recurring patterns and repetitions in time-series, with application to pseudo-stochastic ship rolling", Ocean Engineering, 271, 113717.

Tucker, M.J., Challenor, P.G., Carter, D.J.T., 1984, "Numerical simulation of a random sea: a common error and its effect upon wave group statistics", Applied Ocean Research, 6(8), pp. 118-122.

Wayland R. F., Bromley D., Pickett D., Farrell M. E., Passamante A., 1994, "Dimensionality, prediction, and determinism in the analysis of real broadband data", AIP Conference Proceedings 296, pp. 289-297.

Xi, X., Keogh, E., Shelton, C., Wei, L., and Ratanamahatana, C. A., 2006, "Fast Time Series Classification Using Numerosity Reduction", Association for Computing Machinery, Association for Computing Machinery, ISBN: 1595933832.

Yeh, M. Chin-Chia, Zhu, Y., Ulanova, L., Begum, N., Ding, Y., Anh Dau, H., Zimmerman, Z., Silva, D. F., Mueen, A., Keogh, E., 2018, "Time series joins, motifs, discords and shapelets: a unifying view that exploits the matrix profile", Data Mining and Knowledge Discovery, 32, pp. 83–123.

Real-time onboard flooding risk assessment for passenger ships for ship-to-ship collisions

Dracos Vassalos, *Sharjah Maritime Academy, 180018, Khorfakkan, Sharjah, UAE,* Dvassalos@sma.ac.ae

Donald Paterson, *Sharjah Maritime Academy, 180018, Khorfakkan, Sharjah, UAE,* Donald.Paterson@sma.ac.ae

Francesco Mauro, *Sharjah Maritime Academy, 180018, Khorfakkan, Sharjah, UAE,* Francesco.Mauro@sma.ac.ae

Hongseok Bae, *Sharjah Maritime Academy, 180018, Khorfakkan, Sharjah, UAE,* Hongseok.Bae@sma.ac.ae

ABSTRACT

Software for real-time estimation of flooding risk onboard passenger ships (or ships in general) should be capable of identifying a potential hazard and evaluating a risk level associated with the detected danger. The present work presents a framework for real-time risk assessment in case of potential ship-to-ship collisions. As real-time risk assessment pertains to both phases before and after an accident, the present work focuses on the risk of flooding before an accident occurs. More precisely, the paper describes the step necessary to develop a database-based software for real-time risk assessment during navigation, focusing on the detection and likelihood of possible ship-to-ship collisions potentially dangerous for the ship. As such, the tool should be capable to identify a hazard, evaluating the risk level associated with the hazard and advise the crew of potential risks. The software should work in symbiosis with onboard instrumentation, receiving data from, for example, Radar, GPS and AIS in real-time. Given these inputs, the software should calculate the route of potential striking ships, estimating the possible future collision. Afterwards, in case of possible collisions, the software interrogates a damage surrogate model derived from a database of direct crash simulations, providing in real time a set of potential breaches. Such breaches are then associated with a time to capsize, derived from a survivability surrogate model derived from a set of time-domain flooding simulations. Then it is possible to evaluate risk as the Potential Loss of Life (PLL) in real time. Such an approach is fully based on direct first-principles calculations and compliant with the multi-level framework developed in project FLARE for flooding risk.

Keywords: *Flooding risk, onboard risk evaluation, Passenger ships, damage stability, evacuation*.

1. INTRODUCTION

The survivability assessment of a passenger ship after a flooding event has been always identified with the analysis and judgment of the residual righting lever curve (Rahola, 1939). The approach intrinsically requires the definition of a "sufficient" amount of stability to be compared with the vessels' righting arm for several conditions. However, the meaning of the required "safety" threshold is still not well defined by in-force regulations (IMO, 2009), considering the Required Index R as an acceptance/rejection instrument. The effective meaning of the goal of keeping the vessel upright and afloat has been first discussed in the early 2000s by applying the Risk-Based Design (Papanikolaou, 2009) to the "Design for Safety" of passenger ships. This, in turn, corresponds to ensuring the design of a vessel with a known safety level, which, in case of damage stability, corresponds to a known flooding risk (Vassalos 2009, 2012). The evaluation of such a risk requires the availability of suitable instruments for the understanding of survivability as a function of time (Vassalos et al. 2022a) and advanced analyses to evaluate the evacuation time in case of a flooding casualty (Guarin et al. 2014).

Risk analysis for passenger ships does not cover only the design phase but should also include the operational phase (Du et al. 2020) or the whole life cycle in general (Vassalos et al. 2022b). To this end, risk models for passenger ships should evaluate risk as a combination of susceptibility to an accident and vulnerability to an accident (Goerland and Montewka, 2015). This means estimating accident occurrence and its consequences, as is usual among industries (Aven, 2012). Recent approaches suggest abandoning a rigorous determination of probabilities

in favour of a more in-depth analysis of accident uncertainties (Aven, 2022). Therefore, to reduce uncertainties, the use of first principle-based tools should be pursued for the evaluation of flooding risk.

In this sense, the application of dynamic flooding analysis for the determination of survivability (Mauro et al. 2022) together with the determination of direct crash simulations to determine the breach dimensions (Conti et al. 2022) may tackle the challenge of performing a real-time estimation of risk for onboard applications, employing the Possible Loss of Lives (PLL) as risk metrics (Vassalos et al. 2022c).

The present paper presents a new framework for the real-time risk assessment of passenger ships due to a possible ship-to-ship collision event. The framework employs a multi-level approach to risk allowing for different grades of approximations for the ship's survivability and for the consequences of a possible accident. A notional example highlights the feasibility of the proposed concept for real-time flooding risk assessment onboard passenger ships.

2. MULTI-LEVEL RISK ASSESSMENT

The risk due to flooding can be represented by the Possible Loss of Lives (PLL), which is compliant with the general definition of risk and is defined by the following equation:

$$PLL = p_f \cdot c_f \tag{1}$$

where p_f is the probability of flooding and c_f is the consequence of the flooding event. Both probabilities and consequences can be estimated with different levels of accuracy, extending the findings initially elaborated for damage stability frameworks to risk assessment. This means employing a multi-level approach for the evaluation of *PLL*.

The multi-level approach allows for adopting different levels of confidence for the methods employed to determine the *PLL*. Considering a single possible scenario, equation (1) can be rewritten in the following form:

$$PLL = p \cdot (1 - s) \cdot FR \cdot POB \tag{2}$$

In equation (2) the occurrence is indicated by p and the survivability is expressed by s, commonly used for damage stability analyses, while the consequences are evaluated through the fatalities associated with the event, which means the people on board *POB* times the fatality rate *FR*.

The different values or probabilities related to the occurrence, survivability and fatality are associated with different levels in the risk evaluation process in a multi-level framework, as outlined in Figure 1. More precisely, the occurrence is determined by the preparation of the input and by a Level 1 survivability assessment. Level 1 or Level 2 damage stability calculations define survivability and evacuation handling determines the fatality.

Accordingly, the different levels correspond to different *PLL* levels as it is described in the following sub-sections.

PLL level 1

This approach employs only static damage stability calculations. As such, this method presents a high level of approximation on both survivability and fatalities determination. In fact, the expected number of fatalities depends on the time to capsize of the ship but static analysis does not account for time-dependent phenomena.

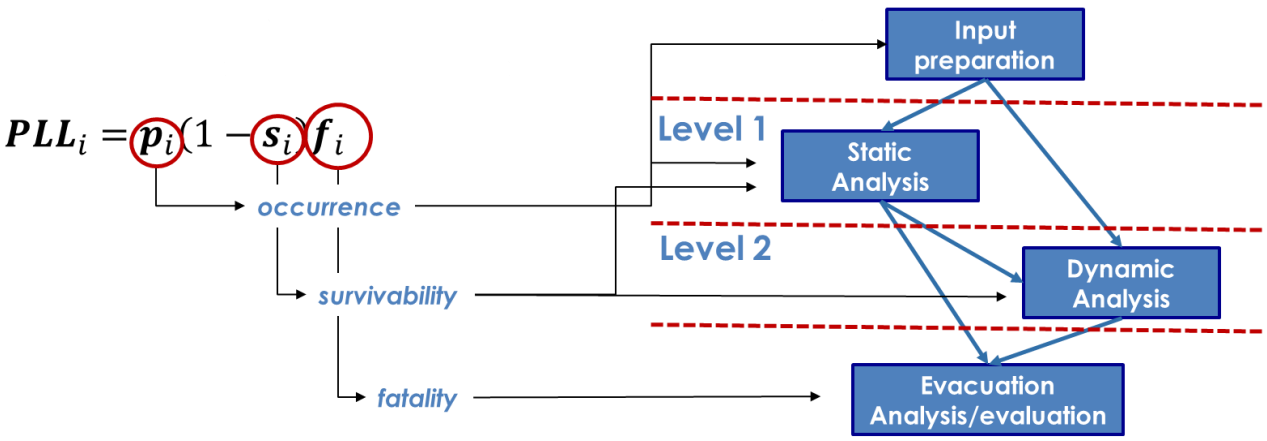

Figure 1: Multi-level framework for flooding risk.

As such, the fatality rate requires an approximated estimation at this stage. To keep the formulation as simple as possible, taking into account the dependencies between survivability and fatality rate, the following simplifying assumptions are made:

$$FR = \begin{cases} 0.8 & \text{if } s < 1 \\ 0.0 & \text{if } s = 0 \end{cases} \quad (3)$$

This simple and conservative approach aligns with the considerations and findings of the EU-founded project EMSA III. This assumption has been further supported by Project FLARE, stating that, considering time-domain flooding simulations, there is evidence that almost 80% of damage scenarios in a survivability assessment are transient capsizes (Paterson et al. 2021), which means conditions where no time for evacuation is available.

PLL level 2

The main parameters for a Level 2 flooding risk estimation are the time to capsize (*TTC*) and the time to evacuate (*TTE*). The *TTC* relates to identifying the time it takes the vessel to capsize/sink after a flooding event. Therefore, an accurate estimate of *TTC* requires the execution of time-domain flooding simulations, abandoning the static approach.

The *TTE* indicates the time needed for an orderly evacuation of passengers and crew onboard a passenger ship after a flooding hazard occurs. Hence, a proper determination of *TTE* requires the execution of advanced evacuation analyses in the time domain. However, the multi-level framework allows for a further simplification of the *FR* determination, allowing for the selection of two sub-levels for a Level 2 analysis.

The first sub-level of approximation, level 2.1, considers time-domain flooding simulations to determine *TTC*. *TTE* does not require evacuation simulations. Therefore, *FR* is determined in an approximate way as a function of TTC according to the following empirical formulations:

$$FR = \begin{cases} 0.0 & \text{if } TTC > n \\ 0.8\left(1 - \dfrac{TTC - n}{30 - n}\right) & \text{if } 30 \le TTC \le n \\ 0.8 & \text{if } TTC > 30 \end{cases} \quad (4)$$

where *n* is the maximum allowable evacuation time in seconds according to MSC.1/Circ. 1533. Therefore, the assumption of equation (4) intrinsically considers the nature of the capsize as a function of *TTC*, considering that is not possible to evacuate the ship in case of a fast transient capsize.

The second sub-level, level 2.2, implies a direct evaluation of the *TTE*. Starting from significant cases where the *TTC* determined through time-domain allows for starting a ship evacuation, motions and floodwater can be imposed to an evacuation software. Such a coupling allows for a direct comparison between the evacuation process and the associated *TTC*. Figure 2 reports the procedure to determine the fatality rate *FR* (*fr* in the picture), which is the result of the intersection between the evacuation curve and the mean time to capsize *TTC** among multiple repetitions of time-domain flooding simulations in irregular waves.

Thanks to this multi-level framework, the single definitions of probabilities and evaluation of survivability and fatalities can be obtained for different phases of the vessel life cycle. Thus, the methodology can be the starting point also for the definition of an application for real-time risk assessment.

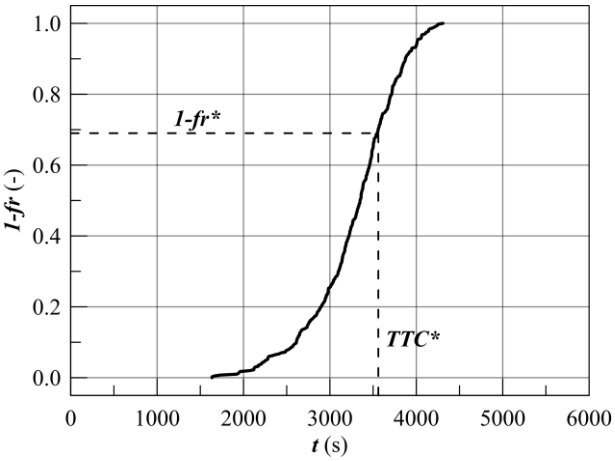

Figure 2: Fatality rate evaluation according to Level 2.2.

3. REAL-TIME RISK ASSESSMENT

The above-described framework for risk assessment is a starting point for the determination of a procedure for real-time risk assessment. Software for real-time risk estimation on-board of passenger ships (or ships in general) should be capable of performing the following tasks:

- Identify potential hazards
- Evaluate risk levels associated with the detected danger.
- (optional) Provide countermeasures to reduce risk.

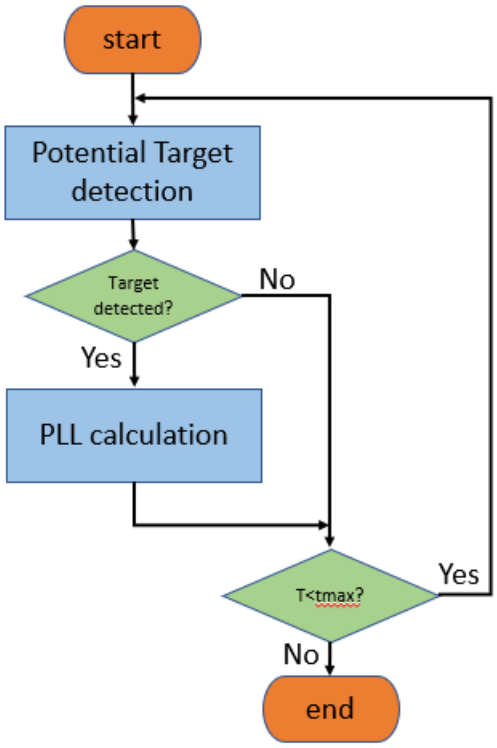

Figure 3: Flowchart of the steps needed for real-time PLL estimation during a voyage.

The last point is set as optional because it pertains to a DSS (Decision Support System), which is outside of the scope of the present work. The proposed approach is oriented to provide a preliminary guideline for the estimation of real-time risk during two phases:

- Before an accident.
- After an accident.

These two aspects require dedicated separate analyses and implementations However, the present work considers only the evaluation of real-time flooding risk before an accident occurs. The evaluation of the risk after an accident requires more insight into the evacuation analysis process.

Going back to the determination of risk assessment in real-time of a potential collision with another ship, the final outcome of the process should be an instantaneous estimation of the *PLL*. Then, the process should follow the steps reported in Figure 3.

As mentioned earlier, the estimation of *PLL* can be performed according to the multi-level framework for risk assessment. The aim is to use first principle-based tools, which means the process should ensure a level 2 estimation of *PLL*. As previous studies within the FLARE project show a minimal difference between level 2.1 and level 2.2 predictions, the real-time risk estimation is here covered up to level 2.1, thus neglecting evacuation analyses.

Figure 4 outlines how a real-time risk estimation tool has to be composed. The first step for an onboard risk assessment tool for ship-to-ship collisions is the detection of a potential hazard, using the data available from the onboard instrumentation (e.g. GPS, AIS, radar, etc...). Such an issue requires estimating the route, speed, and main dimensions of all potential striking ships within a certain distance. Besides, the environmental conditions should be defined from onboard instruments or weather data from local agencies/stations. Subsequently, there is the need to estimate the future path of the target ships, evaluating the most probable collision point, velocity, and encounter angle in case of collision detection. Such actions can be performed by employing different levels of simplifications. Estimation of the route can be performed by consecutive interrogations of GPS, Radar, or AIS data, evaluating the future position of an object based on its actual position, heading, and speed.

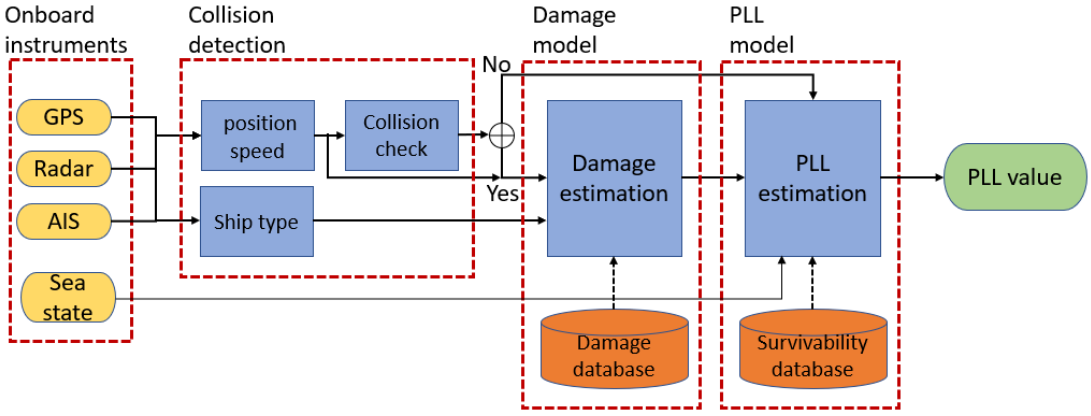

Figure 4: On-board real-time risk estimation outline before accident occurrence.

Table 1: Input needed for an onboard real-time flooding risk assessment.

Input name	unit	Instrumentation
Ship latitude	deg	GPS
Ship longitude	deg	GPS
Ship speed	kn	GPS or Speed mes.
Ship heading	deg	GPS or compass
Target latitude	deg	GPS, AIS, Radar
Target longitude	deg	GPS, AIS, Radar
Target speed	kn	GPS, AIS, onboard PC
Target heading	deg	GPS, AIS, Radar
Target ship type	-	AIS
Target ship length	m	AIS
Target ship breadth	m	AIS
Target ship draught	m	AIS
Significant wave height	m	Wave radar, motions, statistics

The possibility to have multiple sources for the input variables allows for the potential mitigation of loss of data, as, especially for AIS sources, the transmission may not be continuous (Montewka et al., 2021). Table 1 reports the list of inputs needed by the onboard tool together with the associated data source.

The data coming from instrumentation are subject to errors and uncertainties, which, for modelling, requires the knowledge of all the sensors and measuring systems involved in the collision detection tool. However, with this knowledge being unavailable within the FLARE project, a general Gaussian model is considered, sufficiently general to be further extended and modified in subsequent more detailed studies.

According to the adopted assumptions, the uncertainties assume the following form:

$$p(x_i) = \frac{1}{2\pi\sigma_i} e^{-\frac{1}{2}\left(\frac{x_i-\mu_i}{\sigma_i}\right)^2} \quad (5)$$

where μ_i is the signal provided by the instrumentation (interpreted as the mean of the Gaussian process) and σ_i is the standard deviation used to simulate uncertainties.

According to the scheme given in Figure 4, the input data with associated uncertainties enters a damage model, which estimates the dimensions of the breach associated with the collision event. As, due to uncertainties, the input is composed of distributions, the damage model provides output distributions of possible breaches. Subsequently, the breach distribution provides inputs to the survivability model, which evaluates the *PLL* in two steps. First, the *TTC* is evaluated through a surrogate model generated by a database of time-domain simulations referring to critical scenarios for the ship (Mauro et al. 2022). Afterwards, equation (5) is applied to each member of the *TTC* distribution, generating a *PLL* distribution. The real-time *PLL* value is then determined as a Quasi-Monte Carlo integration process on a sample of input values. Such an approach lead to the final calculation of *PLL* with the following formulation:

$$PLL \approx \frac{1}{N_{QMC}} \sum_{i=1}^{N_{QMC}} PLL_i\left(x_{D_i}, V_{T_i}, \beta_{T_i}\right) \quad (6)$$

Where x_D is the longitudinal position of the breach centre, V_T is the target ship speed and β_T is the collision angle. As the core of the process is the determination of the damage model and of the *PLL* model, it is worthy to further describe them in the next sections.

Damage model

The damage model for real-time risk assessment should be based on databases of direct calculations composed of outputs coming from crash analyses. To this end, different software can be employed but a valuable compromise can be given by the super element method, employing SHARP code, which gives results comparable with BEM analyses as tested in dedicated crash analyses benchmark (Kim et al., 2022).

This methodology is capable of providing an estimation of the breach's main dimensions (length L_D, penetration B_D, lower and upper vertical limits z_{LL} and z_{UP}) and the energy absorbed by the impact. The required inputs are the location of the impact x_D, the speed of the target ship V_T, the collision angle β_T and the side of the impact I_{side}. Having as input the outputs of the damage detection module, the SHARP calculation became a suitable method for generating a database of damages. Even though the calculation is quite fast compared to BEM analyses, the required calculation time remains high for a calculation in real-time.

Therefore, an alternative has to be found for the estimation of damage dimensions in real time. SHARP allows for performing a wide set of preliminary calculations that can be used to perform a bulk of initial crash analyses suitable for the generation of an initial database of potential damages. As such, the database gives a sufficiently accurate description of potential damages.

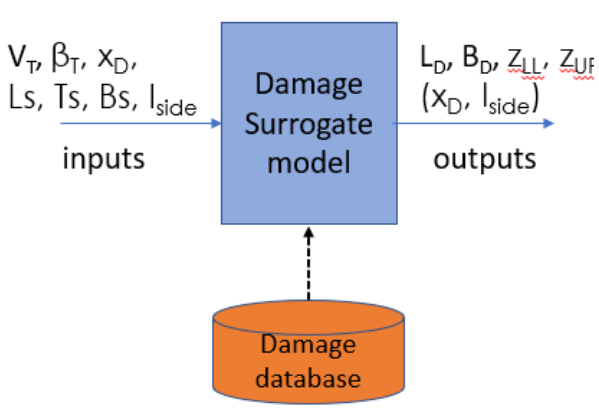

Figure 5: damage model schematisation with inputs and outputs.

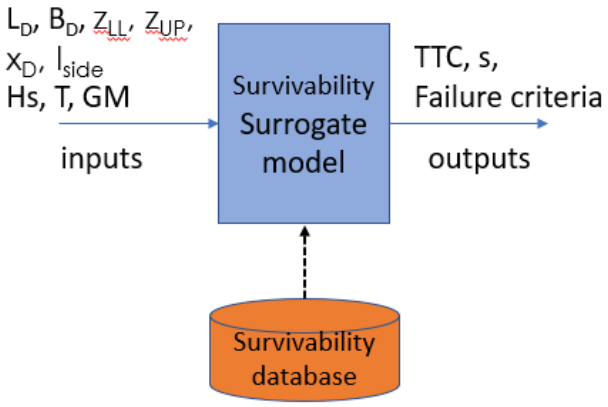

Figure 6: survivability model schematisation with inputs and outputs.

Besides the generation of the database itself, it is necessary to investigate also a method to generate a proper surrogate model from the database, suitable to provide all the relevant information concerning the breach faster than in real-time. Therefore, the general schematisation of the damage model can be the one shown in Figure 5.

From the collision detection model, the values and indicators that are provided to the damage model coincide with the input necessary to identify a SHARP simulation, i.e. the striking ship speed V_T, the relative heading β_T, the collision location x_D, the side identifier Iside and the striking ship main dimensions (*Ls*, *Bs* and *Ts*).

As the provided input to the damage model is subject to uncertainties, it is unlikely to consider such input values are unique and distinct. Therefore, the process considers a distribution of input values, more precisely a normal distribution for each input having the mean as provided by the collision detection model and the standard deviation reflecting the uncertainty of the process (in case it is possible to determine it) or more generally an ignorance factor. A detailed overview of the methodology is given by Mauro et al. (2023).

As a direct consequence, also the provided outputs will be subject to uncertainties and thus provided as distributions instead of single values.

PLL model

After the definition of the real-time damage characteristics through the damage model, the PLL should be evaluated. PLL determination is composed of three steps, as shown in equation (2), necessary to evaluate the case occurrence, the survivability and the fatality rate.

In a real-time risk assessment, the process is not properly the same, as the concept of occurrence is no longer related to the probabilistic distributions of the damages and environmental conditions described for the probabilistic approach to *PLL* calculation. The collision detection model determines the occurrence, which means that once the collision is predicted p is equal to 1, 0 otherwise. More precisely, the effective p is given by the distribution of values given by the collision model, thus it is inherited in the *PLL* model too. The *PLL* model can be then split into two sub-models, one for survivability and one for the fatality rate, to be applied in cascade.

The survivability model is schematised in Figure 6 concerning the surrogate model that should be applied here for the same reasons highlighted for the damage model. A direct method for survivability implies using dynamic simulations that are far away to be directly employed for real-time predictions. Also in this case a database of calculations should be created, taking into consideration the relevant inputs that may affect a dynamic flooding simulation.

A general description of the methods suitable for survivability surrogate model generation is provided in Vassalos et al. (2023).

4. DATABASES CALCULATION EXAMPLE

Hereafter, an example is given of the surrogate models generated from databases of flooding simulations and crash calculations. The test case refers to a cruise ship having the dimensions reported in Table 2. The reference ship is the principal reference hull of the FLARE project, being one of the hull forms used for benchmarking damage stability codes (Ruponen et al. 2022).

Table 2: Reference cruise ship main particulars.

Characteristic	symbol	value	Unit
Length between perpendiculars	L_{PP}	216.8	m
Breadth moulded	B	32.2	m
Depth	D	16.0	m
Design draught	Ts	7.2	m

Furthermore, this ship has been used as a reference for all the developments leading to the establishment of the design phase risk framework. Thus, it gives confidence in the accuracy of results coming out from PROTEUS3 flooding simulations and SHARP crash analyses.

The generation of surrogate models for real-time risk evaluations necessitates the definition of pertinent databases for damage dimensions and survivability. The proper definition of damage and survivability dataset requires the filling of a wide multi-variable space, leading to the execution of a significant number of simulations for either crash or dynamic analyses. The correct minimum number of simulations needed to capture all the possible scenarios has not been yet defined and should be studied in the future. Here, to provide an example of the process an arbitrary number of simulations has been selected, based on the experience with crash analyses and flooding simulations damage screening.

To generate the damage database, a set of scenarios has to be generated from a set of collision simulations between the reference ship and a set of potential striking vessels. Mauro et al. (2023) report the dimensions of the vessels employed as possible striking (target) ships for SHARP collision simulations. Those ships are a representative sample of the worldwide fleet. For this example 11 potential striking ships have been considered, simulating with the super element method 5500 possible scenarios, considering a combination of collision angles (uniformly distributed between 20 and 90 degrees), vessels speed (2,4,6,8,10 m/s), the longitudinal position of impact (uniformly distributed between 0.2 and 0.8 L) and 3 draughts for each vessel.

For the survivability database, it is necessary to evaluate the *TTC* from a set of flooding simulations with PROTEUS3 software. The strategy for creating the database is different from the conventional damage stability assessment according to SOLAS and FLARE design phase framework. Here, instead of performing damage screening on a set of 10,000 damages generated with statutory marginal distributions, a reduced set of 500 breaches is performed employing uniform distribution for the damage characteristics. Such an approach allows for detecting critical cases, giving uniform coverage of all possible breaches that may occur on the reference ship (Mauro et al., 2022).

Thanks to the employment of the QMC sampling method, the coverage of the breach space is in any case more evenly distributed than using conventional MC methods. Therefore, with 500 simulations it is possible to describe with sufficient accuracy the possible breaches that may occur after a collision. As the simulations deals also with irregular waves at the Hs of 1.0, 2.0, 3.0 and 4.0 metres, 10 repetitions per scenario have been carried out to consider the random phases in the wave spectrum. Therefore a total number of 20,500 simulations has been performed on the reference ship, evaluating the *TTC* per each damage case as the mean value among the 10 repetitions. The simulation time has been set to 90 minutes for all the simulated scenarios.

Figure 7 gives an overview of the results obtained from the crash analyses. The figure shows just a part of the data for the sake of brevity, as more detailed analyses require dedicated work and are not in the scope of the present paper and have been provided in Mauro et al. (2023). For damages, the dependency of damage penetration with the position is presented, considering all 11 striking ships (different colours), highlighting the uniformity of results across the length of the vessel.

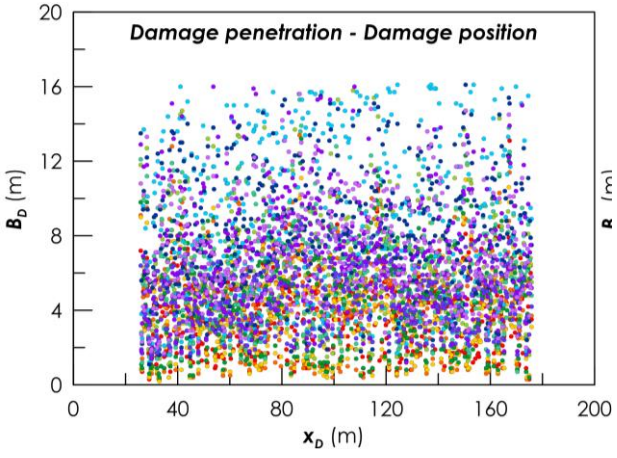

Figure 7: crash simulation results showing the dependence of damage penetration with the damage location.

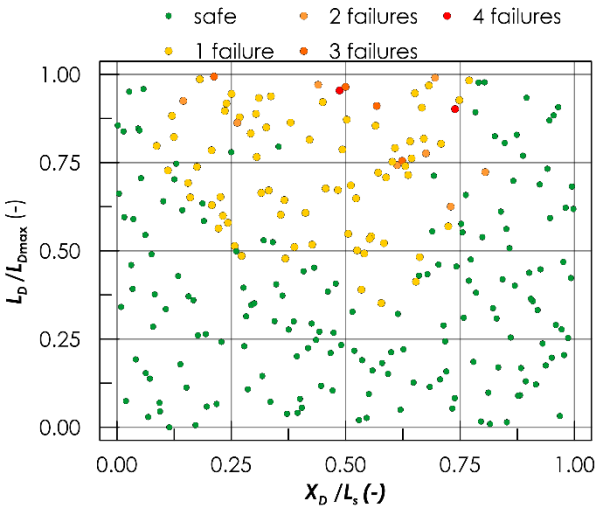

Figure 8: Flooding simulation results with critical damage identification.

Figure 8 shows the results of flooding simulations performed with PROTEUS3, highlighting the damages critical for ship survivability according to the failure criteria defined in Mauro et al. (2022).

The dependency of the damage length with the position is reported for the flooding simulations. For the calm water case, The different colours refer to the number of criteria that failed during the simulations, which means criteria related to the maximum heeling, the average heeling in a given time, and the amount of water entering the ship at the end of the simulations. Such criteria are the standard applied in dynamic flooding analyses. Also in this case it is possible to notice the uniform coverage of the space obtained by applying the QMC sampling. Therefore the two databases cover a possible design space for damages and associated vulnerabilities.

Having two homogeneous databases allows for determining surrogate models to quickly evaluate the damage dimensions and the *TTC*. Here, the models have been derived employing a multiple linear regression technique. For the damage dimensions the variables to be considered are 5, the striking vessel speed, the collision angle, the longitudinal position of damage, the striking vessel draught and the struck vessel draught. Employing a complete 4th-order polynomial regression (except for the two draughts that go up to the 2nd order), the final regression has been obtained removing not significant variables to maximise the goodness of fit of the regression.

Figure 9 shows the predicted/starting values for the damage length, penetration and upper/lower limitations. As reported in the figure, the obtained regressions have a high value for the goodness of fit, thus the model is a good representation of the initial database.

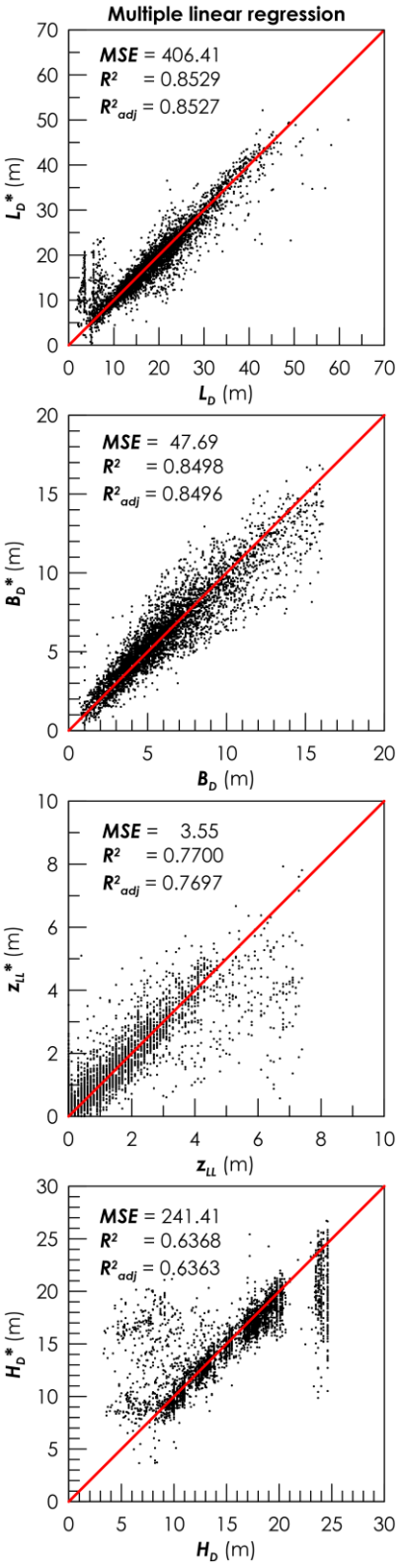

Figure 9: Surrogate models for damage dimensions on the reference ship.

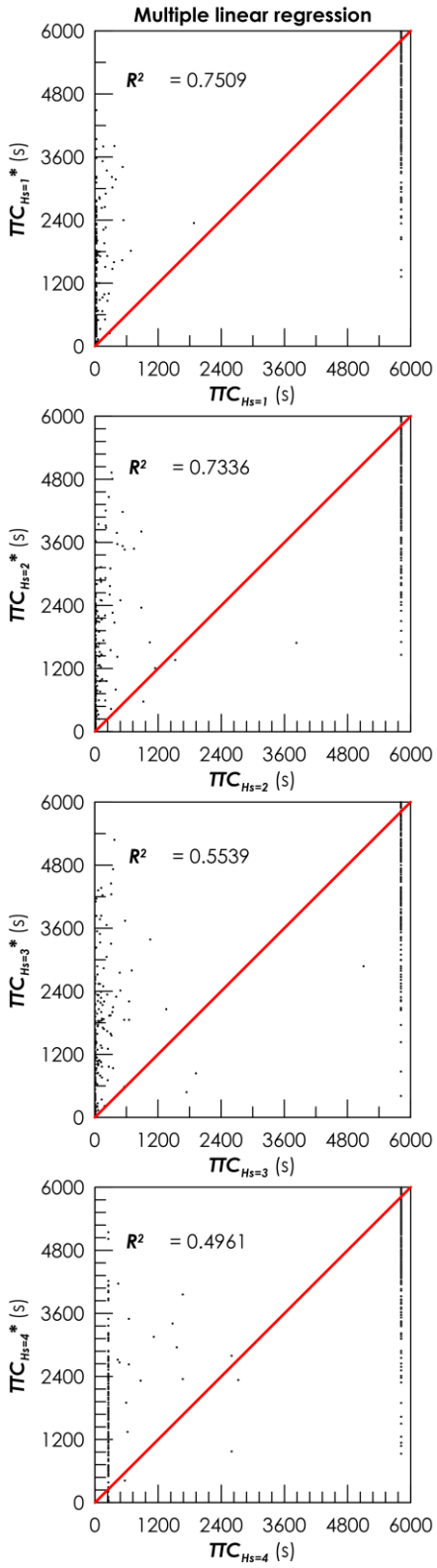

Figure 10: Surrogate models for survivability at *Hs*=1, 2, 3 and 4 metres.

The same has been performed for the TTC. In this case, the initial variables are the damage dimensions and location. However, the goodness of fit is not always giving a real effective matching between predicted and observed data. For this specific TTC case, this is important as a wrong prediction of the variable may lead to a wrong detection between capsize and not capsize of the ship in the same scenario. Figure 10 shows the predicted/starting values for *TTC* in the four irregular wave environments analysed in this example. It can be observed that the predicted and observed values are dense close to the extremities of the *TTC* space, having higher density closer to *TTC*=0 seconds. This happens for all the tested conditions but increasingly the significant wave height strengthens the phenomenon as *TTC* intrinsically reduces. This is a problem for the regression models, as it is hard to reproduce well the behaviour close to the extremities of the domain. Therefore, for *TTC*, the employment of more advanced regression techniques may be suggested.

Notwithstanding the above, the two surrogate models for damage dimension and *TTC* can be used to demonstrate the feasibility of the level 2.1 *PLL* calculation in real time for possible onboard applications.

5. FEASIBILITY FOR ONBOARD APPLICATION

Even though the above-mentioned databases are not yet available for a wide set of passenger ships, it is possible to test with the fictitious models presented afore the capability of the developed approach for the execution of real-time computations. To this end, the process has been implemented with the described surrogate models for breach location and dimensions and the *PLL*. Besides, gaussian errors have been added to the main input to simulate the uncertainties of the sensors producing the inputs to the models. Such a strategy allows for the testing of the calculation procedure and the evaluation of the suitability of a Quasi-Monte Carlo integration to evaluate the real-time *PLL*.

Therefore, the present test follows the subsequent steps for the simulation of a real-time calculation system:

- Generation of arbitrary input data from onboard sensors.
- Addition of Gaussian noise to simulate sensor uncertainties.
- Sample an amount N_{QMC} of breaches from the Gaussian input with a QMC method.
- Evaluate the distribution of the *PLL* at a level 2.1

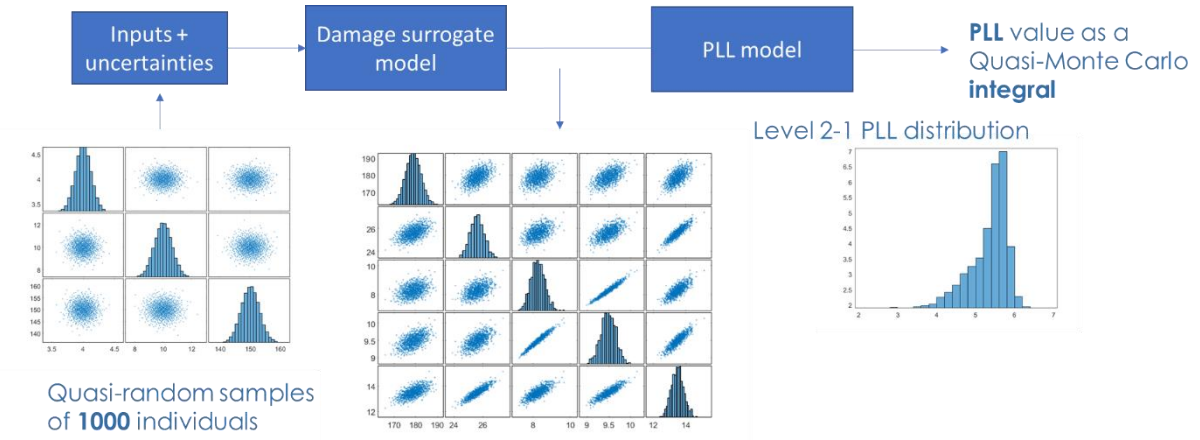

Figure 11: Real-time *PLL* calculation with uncertainties as a QMC process.

Proper modelling of errors and uncertainties requires the knowledge of all the sensors and measuring systems installed onboard and involved in the collision detection tool. Here, the Gaussian model presented in equation (5) is employed because of the lack of specific information on the onboard system's specifications.

In the demonstration, the value modelled with this uncertainty is the target ship speed V_T, the position of the breach centre x_D and the collision angle β_T. The arbitrary standard deviation reference values for the demonstration have been set to 1.5 knots for the speed, 10 metres for the breach position and 5 degrees for the angle. The value is arbitrary and should be not intended to be proposed as the real value to be used on an onboard tool, is just reference input used to test and demonstrate the applicability of the real-time *PLL* calculation.

Figure 11 shows the final process of calculation of real-time *PLL* including the uncertainties in the input values. The total calculation time necessary to estimate the *PLL* is of 0.03 seconds employing a polynomial model for the damages and *TTC*. Thus the process can be applied in real-time computations.

6. CONCLUSIONS

The present paper formalises the concept of real-time risk assessment onboard of passenger ship for the specific case of possible ship-to-ship collisions. The adoption of a multi-level framework established for the risk assessment of passenger ships during the design phase has been modified to accommodate the peculiarities of a real-time prediction. The resulting process allows for the evaluation of real-time risk employing as a metric the *PLL* at a level 2.1.

The work discusses the importance of the strategies and methodologies that should be employed to generate the databases and surrogate models for damage dimensions and survivability by using direct calculations as the primary source.

Finally, The application on a notional example allows for assessing the suitability of the proposed calculation methodology for onboard application in real-time. This conceptual study is the starting point for further investigation on the applicability of better surrogate models and the implementation of realistic errors for onboard instrumentation.

REFERENCES

Aven, T., 2012, "The risk concept -- historical and recent development trends," *Reliability Engineering & System Safety*, 99, p. 33-44.

Aven, T., 2022, "A risk science perspective on the discussion concerning Safety I, Safety II and Safety III", *Reliability Engineering & System Safety*, 217, p. 108077.

Conti, F., Le Sourne, H., Vassalos, D., Kujala, P., Lindroth, D., Kim, S., Hirdaris, S., 2022, "A comparative method for scaling solas collision damage distributions based on a ship crashworthiness application to probabilistic damage analysis of a passenger ship," *Ship and Offshore Structures*, 17(7), pp. 1498-1514.

Du, L., Goerlannd, F., Kujala, P., 2020, "Review and analysis of methods for assessing maritime waterway risk based on non-accident critical events detected from AIS data," *Reliability Engineering & System Safety*, 200, 106933.

Goerland, F., Montewka, J., 2015, "Maritime transportation risk analysis: Review and analysis in light of some foundamental issues," *Reliability Engineering & System Safety*, 138, p. 115-134.

Guarin, L., Hifi, Y., Vassalos, D., 2014, "Passenger Ship

Evacuation – Design and Verification," in 6th International Conference on Virtual, Augmented and Mixed Reality, VAMR 2014 - Held as Part of 16th International Conference on Human-Computer Interaction, HCI International 2014, Heraklion, Crete, Greece.

IMO, 2009, SOLAS-International Convention for the Safety of Life at Sea, London, UK: International Maritime Organisation (IMO).

Kim, S., Taimuri, G., Kujala, P., Conti, F., Le Sourne, H., Pineu, J., Looten, T., Bae, H., Mujeeb-Ahmed M., Vassalos, D., Kaydihan, L., Hirdaris, S., 2022, "Comparison of numerical approaches for structural response analysis of passenger ships in collisions and groundings," *Marine Structures*, 81, 103125.

Mauro, F., Vassalos, D., Paterson, D., Boulougouris, E., "Exploring smart methodologies for critical flooding scenarios detection in the damage stability assessment of passenger ships," *Ocean Engineering*, 262, 112289.

Mauro, F., Vassalos, D., Conti, F., 2023, "Damage surrogate models for real-time flooding risk assessment of passenger ships", *Ocean Engineering*, 285, 115493.

Montewka, J., Manderbacka, T., Ruponen, P., Tompuri, M., Gil, M., Hirdaris, S., 2021, "Accident susceptibility index for a passenger ship-a framework and case study," *Reliability Engineering & System Safety*, 218, p. 1-22.

Papanikolaou, A., 2009, Risk-Based Ship Design, Berlin/Heidelberg, Germany: Springer-Verlag

Paterson, D., Vassalos, D., Boulougouris, E., 2021, "Results of simulation scenarios as input to the flooding risk model," in FLARE, deliverable D4.4.

Rahola, J., 1939, "The Judging of the Stability of Ships and the Determination of the Minimum amount of Stability,".

Ruponen, P., van Basten-Batemburg, R., van't Veer, R., Bu, S., Dankowski, H., Lee, G., Mauro, F., Ruth E., Tompuri, M., 2022, "International benchmark study on numerical simulation of flooding and motions of a damaged cruise ship," *Applied Ocean Research*, 129, 103403.

Vassalos, D., 2009, "Risk-Based Ship Design - Methods, Tools and Applications," in Risk-Based Ship Design, Berlin/Heidelberg, Germany, Springler-Verlaag, pp. 17-98

Vassalos, D., 2012, "Design for Safety, Risk-Based Design, Life-Cycle Risk Management," in 11th International Marine Design Conference (IMDC), Glasgow, Scotland, UK,.

Vassalos, D., Paterson, D., Mauro, F., Mujeeb-Ahmed, M., Boulougouris, E., 2022a, "Process, methods and tools for ship damage stability and flooding risk assessment," *Ocean Engineering*, 266, 113062.

Vassalos, D., Paterson, D., Papanikolaou, A., 2022b, "Impact of life-cycle considerations on internal ship layout for damage stability protection," in SNAME 14th International Marine Design Conference, IMDC 2022, Vancouver, BC, Canada.

Vassalos, D., Paterson, D., Mauro, F., Mujeeb-Ahmed, M., Murphy, A., Michalec, R., Boulougouris, E., 2022c, "A lightning intact and damage stability in a multi-level assessment framework," in 18th International Ship Stability Workshop 2022, Gdansk, Poland.

Vassalos, D., Paterson, D., Mauro, F., 2023, "Real-time flooding risk evaluation for ship-to-ship collisions based on first principles", *Ocean Engineering*, 281, 114847.

Assessment of excessive acceleration of the IMO second generation intact stability criteria for the Offshore Supply Vessel

Erdem Üçer, *Istanbul Technical University,* ucerer@itu.edu.tr

ABSTRACT

The Sub-Committee on Ship Design and Construction (SDC) of IMO (International Maritime Organization) considers the subjects related to ship design and construction including the subdivision and stability. On the meetings of this committee, the guidelines of direct stability assessment procedures for use with the second generation intact stability criteria were discussed. In this study, depending on the procedures of SDC, an evaluation procedure for Lv1 (Level 1) and Lv2 (Level 2) are used to determine the excessive acceleration mode of an offshore supply ship. Firstly, each of these procedures are briefly explained. Then applied to the sample ship which has a length of L_{BP}=41 meters and a displacement of 750 tons. The roll damping coefficients of this vessel are determined by the procedures recommended by ITTC and controlled by the study of Silverman and Pauling on the model studies of an oceanographic ship. For the design draught and the vertical center of gravity value, the sample ship satisfies both the Lv1 criterion considering the simple hydrostatic calculations and Lv2 criterion based on modeling and hydrodynamics. By the increment of h_r value, the height above the estimated roll axis of the location where sailor or passenger are located, the acceleration values of Lv1 increases nearly linear to the threshold value. For the case of Lv2 evaluation of the sample ship, the increment of h_r takes effect after a certain value. After that point the velocity of the increment of the coefficient used in the evaluation of Lv2 rapidly grows. The criterion for Lv2 does not satisfied for smaller values of h_r rather than the criterion for Lv1.

Keywords: *Excessive Acceleration, Intact Stability Criteria, Roll.*

1. INTRODUCTION

The demand in the utilization of marine resources has been rapidly increased after World War II. Therefore, the production and the usage of both offshore platforms and their suppliers, supply vessels have also increased. Examination of the stability of offshore vessels has still an important research topic with the trend of their increasing roles and unpredictable operations that one offshore vessel has throughout its lifespan (Chopra, 2015). Therefore, in this study, the research on the assessment of excessive accelerations of IMO second generation intact stability criteria were conducted for an offshore supply vessel.

There are many researches on developing of second generation intact stability criteria. One of the important research is on that subject is the hydromechanics department report of Naval Surface Warfare Center (Belenky, Bassler and Spyrou, 2011). In that report primarily were addressed on three modes of failure, parametric roll resonance, pure loss of stability and broaching.

The physical background and related mathematical formulations of the pure loss of stability and parametric roll are summarized, the main issues with the new stability criteria are reviewed and benchmark calculation results for 17 different types of ships are discussed by Chung et.al. (2020).

The assessment of excessive acceleration of the IMO second generation intact stability criteria for the tanker (Shin and Moon, 2022) is presented and the evaluation procedure for Lv1 (Level 1) and Lv2 (Level 2) is introduced by focusing on the excessive acceleration mode.

The stability and powering factors in the design of Offshore supply vessels were discussed by the study of Mok and Hill (1970).

A simplified method for the preparation of stability information for offshore supply vessels (Meyer and Feeney, 1981) is presented.

The large amplitude rolling motions of an ocean survey vessel (Falzarano and Mulk, 1994) is examined. Due to their research on the nonlinear and coupled aspects of roll motion, the important parameters that effect roll is obtained.

In the study of Htun et.al (2019), the applicability of the second generation intact stability criteria for preventing pure loss of stability in astern waves to offshore supply vessels (OSV) is investigated by numerical simulations and free-running model experiments of an OSV by changing its length of low weather deck in regular stern quartering waves. It is presented that the effects of water on deck (WOD) on the behavior of the OSV could prevent the occurrence of typical pure loss of stability for the cases of long low weather deck.

In this paper, the characteristics and sections of the sample ship is presented in section 2, the evaluation procedure of the excessive acceleration of IMO second generation intact stability criteria and the sample calculations are presented in section 3 and the conclusion is presented in section 4.

2. SAMPLE SHIP CHARACTERISTIC AND SECTIONS

Offshore supply vessels generally have large beams with respect to their draughts and characteristically their super structures are located at the forward quarter length, leaving about three quarters of deck clear for deck cargo (Mok and Hill, 1970). The transverse sections of sample supply ship used in calculations are shown in the Fig. 1. The sample ship has a length of LBP=41 meters and a displacement of 750 tons. The sections of this vessel is drawn by AutoCAD with the inspiration of the Model 2 in the report of Pauling and Silverman (1966).

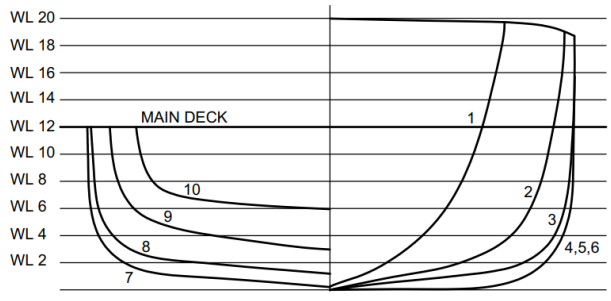

Figure 1: Transverse sections of sample supply ship [9].

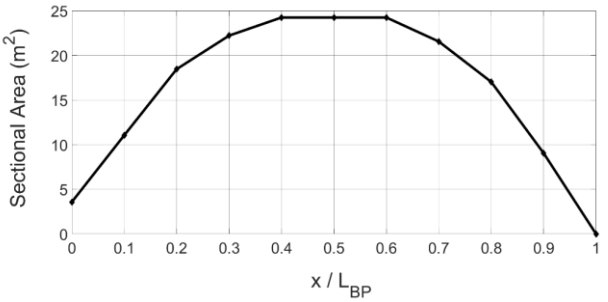

Figure 2: Transverse sections of sample supply ship.

3. EVALUATION PROCEDURE OF THE EXCESSIVE ACCELERATION AND SAMPLE CALCULATIONS

The Lv1 (Level 1) criterion for each loading and position conditions along the longitudinal direction of the ship where passengers or sailor and cargo may be present, is considered to be that the vessel is not vulnerable to excessive acceleration under following conditions given by the expression in Eq .1 (Shin and Moon, 2022).

$$\emptyset_{1/3} \times k_L \times \left(g + \frac{4\ \pi^2 \times h_r}{T_r^2} \right) \leq R_{EA1} \qquad (1)$$

where

$\emptyset_{1/3}$ is the characteristic roll amplitude and determined by Eq. 2, R_{EA1} = 4.64 m/s^2, g is the gravitational acceleration (g=9.81 m/s^2), x is longitudinal distance of the position where sailor or passengers can be located from the aft and of L (ship length) and T_R is the natural roll period (Shin and Moon, 2022).

$$\emptyset_{1/3} = 2\sqrt{m_0} \qquad (2)$$

where m_0 is the area under the curve of the spectral density function of ship response of rolling motion, $S_\emptyset(\omega_e)$ (Bhattacharyya, 1978). The spectral density function of ship response is equal to the product of the spectral density function of the waves, $S_\xi(\omega_e)$ and the response amplitude operator of rolling motion, RAO. ω_e is the encountering frequency of the waves. In this case, the spectrum given in the study of Shin and Moon (2022) is used as the spectral density function of the waves. H_s and T_z are assumed to be 5.5m and 11s respectively. The Response Amplitude Operator is obtained by dividing the ratio of the square of the motion amplitude with the square of wave amplitude. For each wave frequency the roll motion amplitude $\emptyset_a$ is determined by Eq. 3.

$$\emptyset_a = \emptyset_{st} \times \mu_\phi \qquad (3)$$

where $\emptyset_{st}$, the static rolling amplitude is equal to the ratio of the amplitude of exciting moment to restoring constant (Bhattacharyya, 1978). The magnification factor, $\mu_\emptyset$ is determined by the following formula;

$$\mu_\emptyset = \frac{1}{\sqrt{(1-\Lambda^2)^2 + 4\,\kappa^2\Lambda^2}} \quad (4)$$

where Λ is tuning factor, the ratio of frequency of encounter to natural frequency of rolling and κ is the non-dimensional damping factor, the ratio of the roll decaying constant (the ratio of damping moment to double of the total inertia moment of the ship) to the natural frequency of rolling. The damping moment or damping coefficient is determined by applying the procedures recommended by ITTC (2011) and the obtained damping values are controlled by the study of Silverman and Pauling (1966).

k_L is coefficient that reflect the action of roll, yaw, and pitch motions and determined as follows (Shin and Moon, 2022):

$$k_L = \begin{cases} 1.125 - 0.625\ (x/L)\ if\ x < 0.2\ L \\ 1.0\ if\ 0.2\ L \le x\ \le 0.65\ L \\ 0.527 + 0.727\ (x/L)\ if\ x > 0.65\ L \end{cases} \quad (5)$$

h_r is height above the estimated roll axis of the position where sailor or passengers can be located (Shin and Moon, 2022). It is assumed that the roll axis to be located midway between the waterline and the vertical center of gravity and determined by Eq. 6 as shown below.

$$h_r = H - (KG + d)/2 \quad (6)$$

where H is the height of the navigational deck above keel, KG is vertical center of gravity and d is draught.

For Lv2 (Level 2) criterion, the vessel can be judged to be stable from excessive acceleration mode under the following conditions presented in Eq. 7 (Shin and Moon, 2022).

$$C = \sum_{i=1}^{N} W_i \times C_{S,i}\ \le\ R_{EA2} \quad (7)$$

where R_{EA2}=0.00039, $C_{S,i} = e^{-(R_2^2/(2\times\sigma_{LAi}^2))}$, R_2=9.81 m/s^2

The σ_{LAi} is standard deviation of the lateral acceleration at velocity 0 and in a beam seaway determined, shown in Eq. 8 (Shin and Moon, 2022).

$$\sigma_{LAi}^2 = \frac{3}{4}\sum_{j=1}^{N}\left(a_y(\omega_j)\right)^2 S_{zz}(\omega_j)\,\Delta\omega \quad (8)$$

where $\Delta\omega$: Interval of wave frequency=(ω_2-ω_1)/N (rad/s), ω_2: Upper frequency limit of wave spectrum in the evaluation range=min((25/T_r),2.0), ω_1: Lower frequency limit of wave spectrum in the evaluation range=max((0.5/T_r),0.2), N: Number of intervals of wave frequency in the evaluation range, not to be taken less than 100, ω_j: Wave frequency at the mid-point of the considered frequency Interval: ω_1 + ((2j - 1)/2) $\Delta\omega$ (rad/s) (Shin and Moon, 2022).

$S_{zz}(\omega_j)$: Sea wave elevation spectrum is assumed to be composed of the zero-crossing wave period T_z and the significant wave height H_s as shown in Eq. 9 (Shin and Moon, 2022).

$$S_{zz}(\omega) = \frac{H_s^2}{4\pi}\left(\frac{2\pi}{T_z}\right)^2 \omega^{-5} e^{-\left(\frac{1}{\pi}\times\left(\frac{2\pi}{T_z}\right)^4\times\omega^{-4}\right)} \quad (9)$$

$a_y(\omega_j)$: Lateral acceleration is defined as follows:

$$a_y(\omega_j) = k_L \times \left(g + h_r \times \omega_j^2\right) \times \emptyset_a(\omega_j) \quad (10)$$

where, ω_j is the wave frequency and $\emptyset_a$ (ω_j) is the roll amplitude and it is determined by the Eq. 3.

W_i is weighting factor the short-term environmental condition and N is total number of short-term environmental condition (Shin and Moon, 2022).

Fig. 3 shows the Lv1 vulnerability criterion calculation results of excessive acceleration mode. due to h_r. As can be seen from this figure, when h_r is approximately 35m less, the excessive acceleration Lv1 criterion is satisfied.

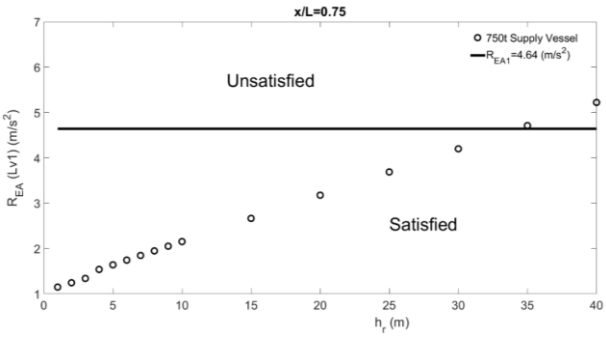

Figure 3: Lv1 vulnerability criterion assessment for excessive acceleration mode of the supply vessel x/L_{BP} = 0.75.

The Figure 4, shows the variation of R_{EA1} due to the location of x. As can be seen from this figure, the highest acceleration occurs the sections near the bow of the ship rather than mid of the vessel.

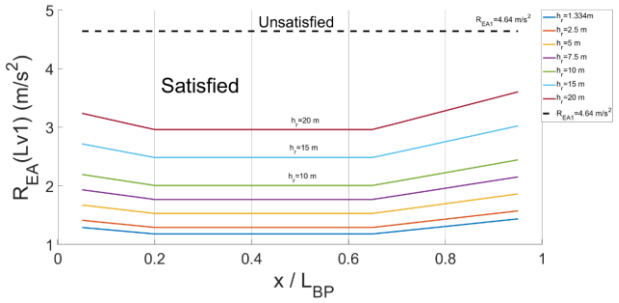

Figure 4: Lv1 vulnerability criterion assessment for excessive acceleration mode of the supply vessel due to x/L_{BP}.

Figure 5 shows the Lv2 vulnerability criterion calculation results of excessive acceleration mode. due to h_r. As can be seen from this figure, when h_r is approximately 21m less, the excessive acceleration Lv2 criterion is satisfied (R_{EA2} = 0.00039).

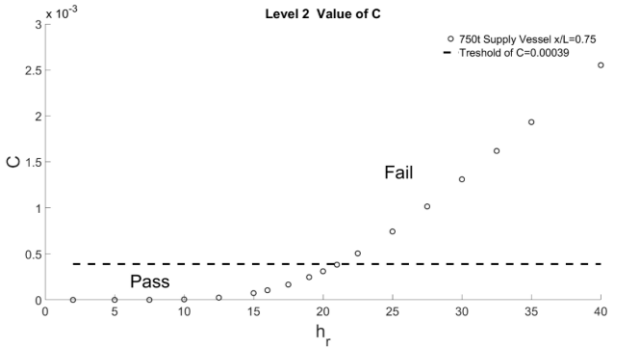

Figure 5: Lv2 vulnerability criterion assessment for excessive acceleration mode of the supply vessel x/L_{BP} = 0.75.

4. CONCLUSION

In this study, depending on the procedures of The Sub-Committee on Ship Design and Construction SDC, an evaluation procedure for Lv1 and Lv2 are briefly explained and then it is used to determine the excessive acceleration mode of an offshore supply ship which has a length of L_{BP}=41 meters and a displacement of 750 tons. The roll damping coefficients of this vessel are determined by the procedures recommended by ITTC (2011) and controlled by the study of Silverman and Pauling (1966).

The sample ship satisfies both the Lv1 criterion considering the simple hydrostatic calculations and Lv2 criterion based on modeling and hydrodynamics for the design draught and the vertical center of gravity value. As can be seen from the figures, when the height above the estimated roll axis of the location where sailor or passenger are located (h_r) increase, the excessive accelerations cause more likely to be unstable of the ship. By the increment of value, (h_r), the acceleration values of Lv1 increases nearly linear to the threshold value. For the case of Lv2 evaluation of the sample ship, the increment of h_r takes effect after a certain value. After that point the velocity of the increment of the coefficient used in the evaluation of Lv2 rapidly grows. The criterion for Lv2 does not satisfied for smaller values of h_r rather than the criterion for Lv1.

This paper is one of the papers that show numerical results in the process of calculating Lv1 and Lv2 for the excessive acceleration. The effect of this regulations are analyzed for the certain type of a ship. As a future study, a more depth analysis can be carried out for different sizes and types of ships.

REFERENCES

Belenky, V., Bassler, C.C., and Spyrou, K.J., 2011, "Development of Second Generation Intact Stability Criteria", Naval Surface Warfare Center Hydromechanics Department Report, West Bethesda, USA.

Bhattacharyya, R. 1978, "Dynamics of Marine Vehicles", Newyork, John Wiley & Sons.

Chopra, G.S., 2015, "Modified Dynamic Stability Criteria for Offshore Vessels", Proceedings of the 12th International Conference on the Stability of Ships and Ocean Vehicles, Glasgow, UK.

Chung, J. et. al, 2020. "Current Status of the 2nd Generation of Intact Stability", *Journal of Ocean Engineering Technology* 34(2), pp. 55-65.

Falzarano, J. and Mulk, M.T.U., 1994, "Large Amplitude Rolling Motion of an Ocean Survey Vessel", Marine Technology 31(4), pp. 278-285.

Htun, S.S. et al. 2019, "Water-on-deck effects on roll motions of an offshore supply vessel in regular stern quartering waves", *Ocean Engineering* 188, pp.1-8.

ITTC, 2011, "Numerical Estimation of Roll Damping", 26th International Towing Tank Conf., Rio De Janerio Brazil.

Meyer, R.B. and Feeney, K.V., 1981, "Simplified Stability Letter for Offshore Supply Vessels", *Marine Tech.* 18(1), pp. 1-9.

Mok, Y. and Hill R.C., 1970, "On the design of offshore supply ships", Offshore Technology Conference, Houston USA.

Pauling, J.R. and Silverman M., 1966, "Model studies for an oceanographic ship derived from an offshore supply vessel". AD0637838.

Shin, D.M. and Moon, B.Y, 2022, "Assessment of Excessive Acceleration of the IMO Second Generation Intact Stability Criteria for the Tanker", *Journal of Marine Science and Engineering 10(2)*, pp.1-13.

Assessment of second-generation intact stability criteria and case study for a Ro-Ro ship

Hasan Islam Copuroglu, *Karadeniz Technical University,* hasancopuroglu@ktu.edu.tr
Emre Pesman, *Karadeniz Technical University,* pesman@ktu.edu.tr
Metin Taylan, *Istanbul Technical University,* taylan@itu.edu.tr

ABSTRACT

In this paper, new intact stability criteria of IMO have been analyzed. The primary goal of the second generation intact stability criterion is to assess a ship's safety level in terms of robust stability measures. However, due to the restricted human resources and facilities required for experimental verification of numerical equipment, such an approach may not be applicable to all new vessels subject to 2008 IS Code. International Maritime Organization (IMO) urges interested parties and Member States to first analyze a ship's risk level using simpler criteria. These are known as vulnerability criteria. In this study, a roro ship has been evaluated according to the 2nd Degree stability criterion and compared with the experimental results.

Keywords: *second generation intact stability criteria, parametric roll, stability of a roro vessel*

1. INTRODUCTION

Since the invention of the first simple boats, ships have been vulnerable to harsh weather. Later, it was understood that ships needed to be more stable in order to prevent capsizing and other stability-related maritime mishaps. The Venetians developed the first recorded written stability criterion in 1255, which calls for driving a nail into a ship's sides to prevent overloading (Nowacki 2003). By passing the Merchant Shipping Act in the late 1800s, the British continued the practice and introduced the draft mark concept. In his doctoral dissertation, Rahola examined ship stability and laid the groundwork for the statistical stability requirements that have been applied up to this point (Rahola 1939). The International Maritime Organization (IMO) takes on all ship-related issues after its establishment, including stability. The "2008 Intact Stability (IS) Code (MSC78/24/1 2003), the most recent and current version of the intact stability requirements, also contains the weather criterion (IS Code 2008).

The IMO SDC7/5 (2020), Umeda (2016), Bassler (2009), and Peters (2011) are only a few of the more than 15 years that the second-generation intact stability criteria have been on the table. The criteria were developed in response to complaints of the limitations of the existing intact stability criteria, which were thought to rely too heavily on a statical background and ignore dynamic environmental impacts (Taylan and Sulus, 2023). The major goal of the second-generation intact stability criteria is to evaluate a ship's level of safety from the perspective of robust stability and to pave the way for the direct application of cutting-edge numerical simulation tools for this evaluation. The main notion is that by using the instruments required to model dynamic ship behavior in random seas, the level of safety of a ship may be determined using a probability measure. This method is known as a direct stability assessment in this context. However, because to the restricted human resources and facilities required for experimental testing of numerical instruments, the installation of such new equipment to all new buildings pursuant to the 2008 IS Code may not be practicable. As a result, IMO urges interested parties and Member States to initially analyze a ship's vulnerability using simpler criteria. These criteria are based on several types of vulnerabilities. If only one ship is vulnerable to a stability failure scenario, a direct stability assessment will be performed on the vessel.

When work on the new criteria began at IMO, the emphasis was on the dynamics of ship motions, which were thought to be the primary cause of the majority of stability-related accidents. The first priority was to include environmental phenomena such as wind and waves. As a result, it was decided that the focus of the criteria should be on ship hydrodynamic properties and related stability

analyses. Following lengthy deliberation, the panel concluded that the new criteria should be based on specific harmful phenomena that would result in a collapse of stability. The incorporation of probabilistic approaches was also on the IMO's agenda. The working group has agreed to look into five forms of motion that ships experience. The structure of the criteria can be seen in Figure 1.

In this paper, new intact stability criteria of IMO have been analyzed. In this study, a roro ship is evaluated according to the 2nd Degree stability criterion and compared with the experimental results. For the wave condition, which is considered the most risky. The ship has no bilge keels to observe the parametric roll motion. Primarily, Level 1 is associated with differences in metacentric heights. The wave crest is inferred depending on the wave trough and the height of the metcentre and is usually sufficient to determine risky ship speeds.

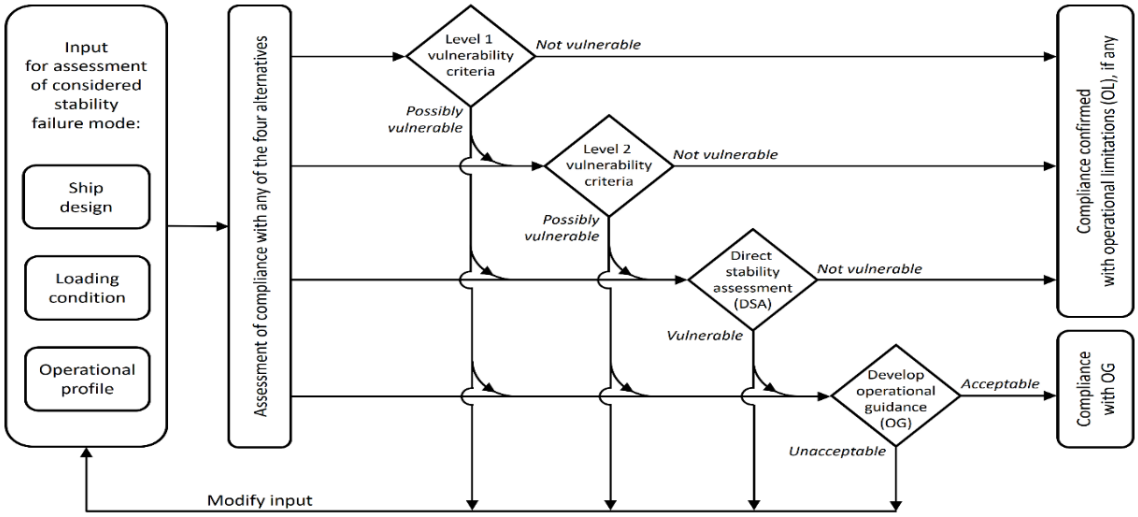

Figure 1. Simplified scheme of the application structure of the second generation intact stability criteria. (IMO, 2020)

$$GM_{min} \geq R_{PLA} \text{ and } \frac{\nabla_D - V}{A_W(D-d)} \geq 1.0 \quad (1)$$

2. CASE STUDY

Sample Ship

The sample ship used throughout the analysis is of a ro-ro form whose experimental tests are carried out at the towing tank of Osaka Metropolitan University-Japan. The experiments are carried out with 6 DOF by a model which has 1/50 scale. The sample ship has no bilge keels and appendages. The main characteristics of the sample ship, named Model 35, is given in Figure 1 and Table 1, respectively.

Table 1: Main characteristics of the sample ship

Type	Δ	LBP	B	d	KG
Ro-Ro	1334.9t	56 m	12.3 m	3.402 m	5.35 m

Level 1 vulnerability criterion for the pure loss of stability failure mode

The sample is considered not to be vulnerable to the pure loss of stability failure mode, if:

and R_{PLA}= *0.05;* GM_{min}=*2.222*

since $GM_{min} \geq R_{PLA}$, this criterion is passed.

Level 1 vulnerability criterion for the parametric rolling failure mode

The sample ship is considered not to be vulnerable to the parametric rolling failure mode if;

$$\frac{\delta GM_1}{GM} \leq R_{PR}\,, \quad \frac{\nabla_D - \nabla}{A_W(D-d)} \geq 1.0 \quad (2)$$

So, $\frac{\nabla_D - \nabla}{A_W(D-d)} = 1.0917$ and this part of the criteria is passed. But since there is no bilge keel on the sample ship $R_{PR} = 0.17$ and $\frac{\delta GM_1}{GM} = 0.2213$ So this part of the criteria is failed.

Level 2 vulnerability criteria for the parametric rolling failure mode

The sample ship is considered not to be vulnerable to the parametric rolling failure mode, if

$$C1 \leq R_{PR1} \text{ or } C2 \leq R_{PR2} \quad (3)$$

Also Level 2 vulnerability criteria for the parametric rolling failure mode wave cases and Ci coefficients for C1 values are given in Table 2 and Table 3.

For each wave specified the requirement for the variation of *GM* in waves is satisfied if:

$$GM(H_i, \lambda_i) > 0 \text{ and } \frac{\delta GM(H_i,\lambda_i)}{GM(H_i,\lambda_i)} < R_{PR} \quad (4)$$

Table 2: Level 2 criteria wave case numbers

Case number	λ_i	H_i	W_i
1	22.574	0.35	0.000013
2	37.316	0.495	0.001654
3	55.743	0.857	0.020912
4	77.857	1.295	0.092799
5	103.655	1.732	0.199218
6	133.139	2.205	0.248788
7	166.309	2.697	0.208699
8	203.164	3.176	0.128984
9	243.705	3.625	0.062446
10	287.931	4.04	0.02479
11	335.843	4.421	0.008367
12	387.44	4.769	0.002473
13	442.723	5.097	0.000658
14	501.691	5.37	0.000158
15	564.245	5.621	0.000034
16	630.684	5.95	0.000007

Table 3: Level 2 criteria Ci coefficients for C1 values

Case number	GM(Hi,λi)	δGM(Hi,λi)	Ci	WiCi
1	2.2155	0.1165	0	0
2	2.2055	0.1505	0	0
3	2.1945	0.3515	0	0
4	2.2005	0.3745	1	0.0927
5	2.2035	0.3345	0	0
6	2.205	0.286	0	0
7	2.209	0.242	0	0
8	2.214	0.204	0	0
9	2.2185	0.1715	0	0
10	2.224	0.145	0	0
11	2.2255	0.1215	0	0
12	2.2245	0.0995	0	0
13	2.2235	0.0815	0	0
14	2.2225	0.0675	0	0
15	2.2225	0.0565	0	0
16	2.222	0.048	0	0

After calculating $C1$, $C1 \leq 0.0928$ and since the R_{PR1}=0.06, the criteria are not corrected the first part of the equation 3 and failed.

In this study, since there are no bilge keels on the sample ship , R_{PR} value is smaller than $\frac{\delta GMi}{GMi}$ while the wavelength is 77.857 m, that is, close to the ship's length, as expected in parametric roll motion, and R_{PR1} in total C1 value is greater than 0.06. This indicates that it does not meet the criteria.

The control of the C2 value is also carried out, despite the fact that the case does not meet the criteria due to the C1 value. In the calculation of the C2 value, 1 degree of freedom numerical time simulation is performed. The following equation is used in the calculation of the roll amplitudes. GZ values are calculated by neglecting viscous effects and ship speed.

$$\ddot{\phi} + 2\mu\dot{\phi} + \beta\dot{\phi}|\dot{\phi}| + \delta\dot{\phi}^3 + \frac{{\omega_0}^2}{GM_0} f(\phi, x) = 0 \quad (5)$$

$$f(\phi, x) = sign(\phi) GZ(|\phi|, x) \quad (6)$$

$$x = Vt - Lfloor\left(\frac{Vt}{L}\right) \quad (7)$$

The value of *C*2 is calculated as an average of values of $C2(Fn_i,\beta_i)$, each of which is a weighted average from the set of waves specified for each set of Froude numbers and wave directions specified.

$$C2 = \left[\sum_{i=1}^{12} C2(Fn_i, \beta_h) + \frac{1}{2}\{C2(0, \beta_h) + C2(0, \beta_f)\} + \sum_{i=1}^{12} C2(Fn_i, \beta_f)\right]/25 \quad (8)$$

The Level 2 criteria Ci coefficients for C2 values in head waves are given in Table 4 and Level 2 criteria Ci coefficients for C2 values in following waves are given in Table 5.

Table 4: Level 2 criteria Ci coefficients for C2 values in head waves

	Speed (m/s)							
Wave Length (m)	…	4.364	3.759	3.086	2.364	1.598	0.808	0
22.574		0	0	0	0	0	0	0
37.316		0	0	0	0	0	0	0
55.743		0	0	0	0	0	0	0
77.857		0	13	23	0	0	0	0
103.655		0	0	0	6	19	0	0
133.139		0	0	0	0	0	0	16
166.309		0	0	0	0	0	0	0
203.164		0	0	0	0	0	0	0
243.705		0	0	0	0	0	0	0
287.931		0	0	0	0	0	0	0
335.843		0	0	0	0	0	0	0
387.44		0	0	0	0	0	0	0
442.723		0	0	0	0	0	0	0
501.691		0	0	0	0	0	0	0
564.245		0	0	0	0	0	0	0
630.684		0	0	0	0	0	0	0

Table x: Level 2 criteria Ci coefficients for C2 values in following waves

	Speed (m/s)							
Wave Length (m)	0	0.808	1.598	2.364	3.086	3.759	4.364	….
22.574	0	0	0	0	0	0	0	
37.316	0	0	0	0	0	0	0	
55.743	0	0	0	0	0	0	0	
77.857	0	0	0	0	0	0	0	
103.655	0	0	0	0	0	0	0	
133.139	16	0	0	0	0	0	0	
166.309	0	0	14	0	0	0	0	
203.164	0	0	0	0	9	0	0	
243.705	0	0	0	0	0	0	0	
287.931	0	0	0	0	0	0	0	
335.843	0	0	0	0	0	0	0	
387.44	0	0	0	0	0	0	0	
442.723	0	0	0	0	0	0	0	
501.691	0	0	0	0	0	0	0	
564.245	0	0	0	0	0	0	0	
630.684	0	0	0	0	0	0	0	

After calculating the C2 values, it can be seen that C2 is 0 and since the R_{PR2} is 0.025 so $R_{PR} \geq C2$ and this part of the criteria is passed.

In the tables above, the equation is solved for each case and the roll amplitudes are obtained with respect to time. Values indicated with 0 in the table indicate cases where the roll motion is damped. Values greater than 0 are the cases where parametric roll motion is seen. It is seen that they meet the stability criterion since the roll amplitudes are not larger than 25 degrees.

Parametric roll motion usually occurs when the wavelength is close to the ship's length. As can be seen from the vulnerability criterion both the C1 table and the C2 table, parametric roll motion can be observed for the case where the wavelength is 77.857 m. In this study, the results obtained from the experiments made for the case where the wavelength is close to the ship's length are also

given and the parametric roll motion phenomenon is examined.

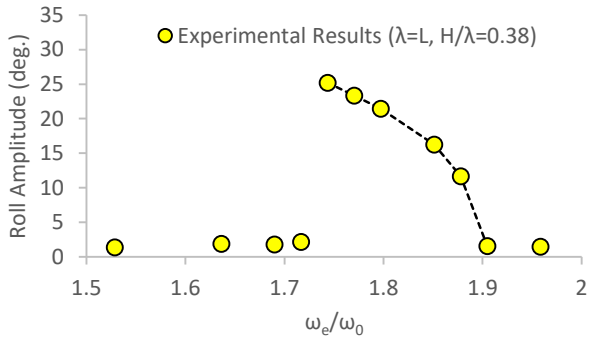

Figure 2. The maximum roll amplitudes obtained from the experiments, depending on the ratio of the encounter frequency to the natural frequency

In Figure 2, the maximum roll amplitudes obtained from the experiments are given, depending on the ratio of the encounter frequency to the natural frequency. As can be seen from the figure, at the ratio of the encounter frequency to the natural frequency of 1.74, the roll amplitudes have exceeded 25 degrees. However, it must be noted that this experimental study is carried out for the case where the ratio of wave height to wavelength was 0.38.

3. CONCLUSION

In this paper, new intact stability criteria of IMO have been analyzed. For the purpose, a case without a roll spine was chosen to observe the parametric roll motion of a ship. Primarily, Level 1 is associated with differences in metacentric heights. The wave crest is inferred depending on the wave trough and the height of the metcentre and is usually sufficient to determine risky ship speeds. In this case study, it is revealed that the case is risky to parametric roll motion for the roll invertebrate condition in the level 1 criterion. Then it was passed to Level 2 criteria. The two conditions that must be met in Level 2 criteria are C1 and C2. For C1 given wave cases, the analysis is done on the basis of metacentric height differences. Accordingly, the ship is again risky in terms of parametric roll, in the case where the wavelength is 77.857 m. C2 criteria, on the other hand, perform the analysis by solving the 1DOF nonlinear equation depending on the GZ moment arm. In this part, there is a limit that the roll amplitudes should not exceed 25 degrees. In this criterion, under no circumstances did the roll amplitudes exceed 25 degrees. The C1 coefficient gives results about risky speeds, while the C2 coefficient directly gives the roll amplitude values. Although it was observed that the roll amplitudes is not exceed 25 degrees in the analysis of the C2 coefficient, it is observed that there is parametric roll motion in the risky condition for the C1 coefficient. This roll amplitude is approximately 23 degrees. According to the Level 2 criteria, even for the case of a roll invertebrate, it is considered risk-free in terms of parametric roll motion compared to the C2 coefficient.

In this study, the experimental results are given for the wave steepness of 0.38 and it is seen that the ship falls into parametric roll motion at large amplitudes (greater than 25 degrees) with an unstable pitchfork bifurcation at low speeds. However, it should be noted that the experiments were performed for the roll invertebrate condition.

Higher stages of the multi-tiered approach involve a more theoretical evaluation of ship motions, even if the initial level is relatively easier and uses traditional and customary ship stability calculations. The ship's ability to operate is limited if any level is failed.

Finally, despite the criteria's promise of a greater safety margin for ships operating in challenging sea conditions, many people are still dubious about it due to its relatively challenging execution procedures.

4. ACKNOWLEDGEMENTS

The experimental study in this paper is carried out at Osaka Metropolitan University, Katayama Laboratory.

The authors sincerely thank the above organization and participants involved.

REFERENCES

Dunwoody A.B., 1989, “Roll of a Ship in Astern Seas – Response to GM Fluctuations”, *Journal of Ship Research* 33(4), pp. 284-290.

IMO 2006, “MSC.1/Circ.1200 - Interim Guidelines for Alternative Assessment of the Weather Criterion”, 24 May.

Kawahara, Y., Maekawa, K., Ikeda, Y., 2009, "A Simple Prediction Formula of Roll Damping of Conventional Cargo Ships on the Basis of Ikeda's Method and Its Limitation", Proceedings of the 10th International Conference on Stability of Ships and Ocean Vehicles, (STAB2009), St. Petersburg, Russia, pp. 387-398.

Bassler, C., Belenky, V., Bulian, G., Francescutto, A., Spyrou, K. and Umeda, N. 2009, "A Review of Available Methods For Application to Second Level Vulnerability Criteria", Proceedings of the 10th International Conference on Stability of Ships and Ocean Vehicles - STAB 2009, Saint Petersburg, pp. 111–128.

Belenky, V.N., Bassler, C.C. and Spyrou, K.J. 2011, "Development of Second Generation Intact Stability Criteria", Naval Surface Warfare Center Carderock Division, Hydromechanics Department Report, pp. 95–107.

Gonzalez, M.M., Casas V.D., Agras D.P. 2013, "Investigation of the Applicability of the IMO Second Generation Intact Stability Criteria to Fishing Vessels" University of A Coruña, Spain.

IMO SDC2/INF.10. 2014, "Second Generation Intact Stability Criteria. Information Collected by Correspondence Group on Intact Stability", Submitted by Japan, London, UK.

IMO SDC7/5. 2020, "Finalization of Second Generation Intact Stability Criteria" Submitted by Japan.

IMO SDC 8/5/Add.2. 2021, "Development of Explanatory Notes to the Interim Guidelines on Second Generation Intact Stability Criteria", submitted by Japan.

IS Code 2008. 2010, "International Code on Intact Stability", IMO, London, UK.

Krüger, S., Hatecke H. 2013, "The Impact of the 2nd Generation of Intact Stability Criteria on Ro-Ro- Ship Design", Proceedings of the PRADS2013, 20-25 October 2013, Changwon City, Korea.

Marlantes, K.E., Kim, S. and Hurt, L.A. 2022, "Implementation of the IMO Second Generation Intact Stability Guidelines", *Journal of Marine Science and Engineering*, 2022, 10, 41.

Nowacki, H. and Ferreiro, L.D. 2003, "Historical Roots of the Theory of Hydrostatic Stability of Ships", Proceedings of the 8th International Conference on Stability of Ships and Ocean Vehicles - STAB 2003, Madrid, Spain.

Peşman, E. and Taylan, M. 2012, "Influence of Varying Restoring Moment Curve on Parametric Roll Motion of Ships in Regular Longitudinal Waves" *Journal of Marine Science and Technology*, Vol.17, No.4, pp.511-522.

Petacco, N., Pitardi, D., Bonvino, C.P., and Gualeni, P. 2021, "Application of the IMO Second Generation Intact Stability Criteria to a Ballast-Free Containership", *Journal of Marine Science and Engineering*, 9, 1416.

Peters, W., Belenky, V., Bassler, C., Spyrou, K., Umeda, N., Bulian, G. and Altmayer, B. 2011, "The second generation intact stability criteria: An overview of development, Transactions" - *Society of Naval Architects and Marine Engineers*, 121, November.

Rahola, J. 1939, "The Judging of the Stability of Ships and the Determination of the Minimum Amount of Stability Especially Considering the Vessels Navigating Finnish Waters", Ph.D. Thesis, Technical University of Finland, Helsinki.

Schrøter, C., Lützen, M., Erichsen, H. 2017, "Sample Applications of the Second Generation Intact Stability Criteria – Robustness and Consistency Analysis", Proceedings of the 16th International Ship Stability Workshop (ISSW2017), 5-7 June 2017, Belgrade, Serbia.

Taylan, M., Sulus, A., 2023, "Assessment of the Second Generation Intact Stability Criteria", 19th International Congress of the International Maritime Association of the Mediterranean (IMAM 2022), pp.133-140, September 26-29, 2022 Istanbul, Turkey.

Umeda, N. and Francescutto, A. 2016, "Current state of the Second Generation Intact Stability Criteria – Achievements and remaining issues", Proceedings of the 15th International Ship Stability Workshop (ISSW2016), 13- 15 June 2016, Stockholm, Sweden.